NASA Technical Memorandum 89810

Reports of Planetary Geology and Geophysics Program—1986

MAY 1987

NASA

NASA Technical Memorandum 89810

Reports of Planetary Geology and Geophysics Program—1986

NASA Office of Space Science and Applications
Washington, D.C.

NASA
National Aeronautics
and Space Administration

**Scientific and Technical
Information Branch**

1987

FOREWORD

This is a compilation of abstracts of reports from Principal Investigators of NASA's Office of Space Science and Applications, Solar System Exploration Division, Planetary Geology and Geophysics Program.

The purpose of this publication is to document in summary form research work conducted in this program over the past year (1986). Each report reflects significant accomplishments within the area of the author's funded grant or contract.

No attempt has been made to introduce editorial or stylistic uniformity; on the contrary, the style of each report is that of the Principal Investigator and may best portray his research.

Joseph Boyce
Discipline Scientist
Planetary Geoscience Program

CONTENTS

CHAPTER 6 - SPECTROSCOPY AND REMOTE SENSING

CHAPTER 1

URANIAN SATELLITES AND RINGS

THE CRATERING RECORD AT URANUS: IMPLICATIONS FOR SATELLITE EVOLUTION AND THE ORIGIN OF IMPACTING OBJECTS.

Robert G. Strom, Department of Planetary Sciences, University of Arizona, Tucson, Arizona 85721

The crater size/frequency distributions on the major Uranian satellites show two distinctly different crater populations of different ages (Smith et al., 1986). Figure 1 is an "R" plot of the size/frequency distributions on Oberon, Titania, Umbriel, Ariel, and the heavily cratered and the resurfaced regions of Miranda. Oberon, Umbriel, and the heavily cratered terrain on Miranda have the same lunar-like size distribution. The crater size/frequency distributions on Titania, Ariel, and the resurfaced areas of Miranda are quite different. They are characterized by an overabundance of small craters and a paucity of large craters relative to Oberon, Umbriel, and the heavily cratered terrain on Miranda. At diameters greater than 30 km, the crater density is significantly less on Titania than Oberon and Umbriel, and progressively decreases from Titania to Ariel to the resurfaced areas of Miranda. Furthermore, the paucity of large craters and a corresponding abundance of small craters becomes more pronounced with decreasing crater density, i.e, with time. This suggests that the objects which caused this younger crater population evolved with time by mutual collision where the collision of large objects produced more and more small ones. If so, they must have been in planetocentric orbits for frequent collisions to have occurred. Since only the young crater population occurs on Titania, the older crater population must have been largely obliterated by a resurfacing event.

Although the young crater population is only recognized on relatively young surfaces, it must also be present on the older heavily cratered surfaces as well. Thus, the old crater population is a mixture of the young population and an original old population that can be recovered by subtracting Titania's young population. This "unmodified" population (curve U1 in Figure 2a) is quite different from other crater populations in the Solar System (see Figure 2a).

Any hypothesis on the origin of the objects responsible for the period of heavy bombardment must account for the occurrence of different crater populations (size/frequency distributions) in different parts of the Solar System. One hypothesis suggests that an early high flux of comets was responsible for the period of heavy bombardment throughout the Solar System (Shoemaker and Wolfe, 1982). To test this hypothesis, a computer simulation using short-period comet impact velocities and a modified Holsapple-Schmidt crater scaling law was used to recover the size distribution of cometary nuclei from the observed cratering record. Figure 2b shows the results of this simulation. It shows that if comets on short-period-like orbits were responsible for the

cratering record, they must have had radically different size distributions in different parts of the Solar System. In fact, their diameters would have to have been on average larger in the inner Solar System where comets rapidly lose mass than at Jupiter where their masses are conserved. This is highly unlikely, and suggests that comets were not responsible for the period of heavy bombardment.

The most likely explanation for the cratering record is that the period of heavy bombardment was caused by different families of accretional remnants indigenous to the system in which the different crater populations occur. Since the same crater population is found on all the terrestrial planets but not Jupiter, this family of accretional remnants was indigenous to the inner Solar System and confined to heliocentric orbits with small semi-major axes (< 3 AU). The satellites of Jupiter, Saturn, and Uranus each have different crater populations suggesting that they were the result of accretional remnants in planetocentric orbits around each of these planets.

Since the young crater population at Uranus shows evidence that it was formed by objects that evolved by mutual collisions in planetocentric orbits, it is quite possible that both crater populations resulted from one family of accretional remnants. The old crater population has a paucity of small craters which is what one would expect from the accretional process where large objects are built from smaller ones. If these objects had their relative velocities increased by close encounters with the satellites, then they could collide, resulting in a progressive depletion of large objects and a corresponding increase in small objects as characterizes the younger crater population. In this case, at least the initial orbits would have low eccentricities and the impact rate would be about the same on all major satellites. Therefore, differences in crater density would represent the relative age of surfaces among the satellites and can be used to date the relative time of resurfacing events. Since the crater density on Oberon and Umbriel is significantly lower than on Miranda, it suggests that both Oberon and Umbriel were resurfaced near the end accretion, and that the sequence of resurfacing events from oldest to youngest was, 1) Oberon and Umbriel, 2) Titania, 3) Ariel, and 4) Miranda.

References:

Smith, et al., Science, 233, p. 43, 1986.
Shoemaker, E.M. and Wolfe, R.F., Satellites of Jupiter, Univ. of Arizona Press, p. 277, 1982.

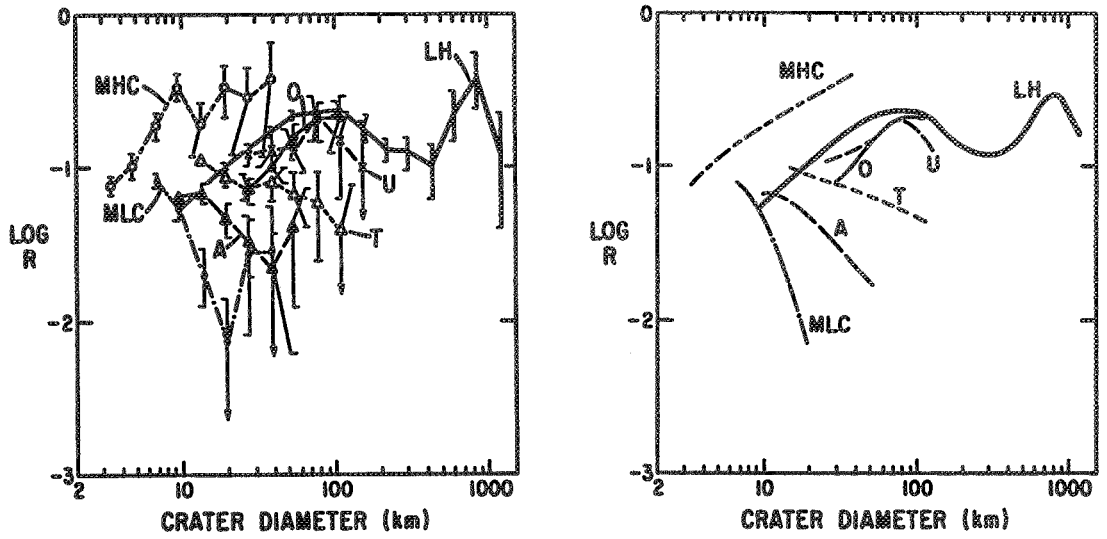

Figure 1. "R" plot of the crater size/frequency distributions on Oberon (O), Umbriel (U), Titania (T), Ariel (A), the heavily cratered terrain (MHC) and resurfaced terrain (MLC) on Miranda, and the lunar highlands (LH).

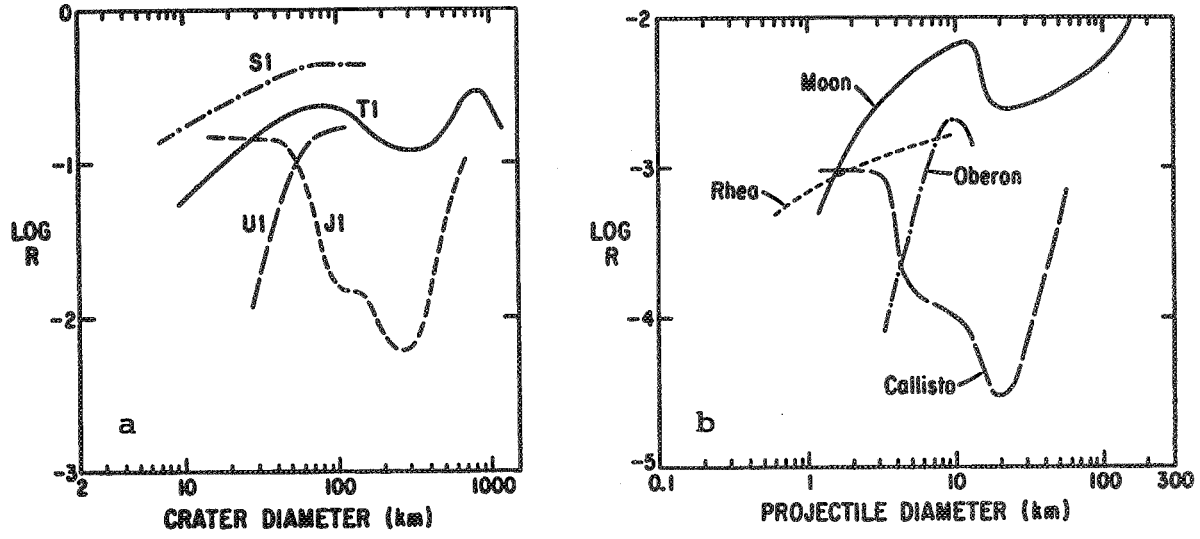

Figure 2. (a) The crater size/frequency distributions representing the period of heavy bombardment on the terrestrial planets (T1), at Jupiter (J1), at Saturn (S1) and at Uranus (U1). (b) The projectile size-frequency distributions for short-period comets recovered from the cratering record.

CRATER MORPHOLOGY AND MORPHOMETRY ON THE URANIAN SATELLITES, Steven K. Croft, Lunar and Planetary Laboratory, University of Arizona, Tucson, Arizona 85721.

Crater Morphology. Fresh craters on the icy Uranian satellites exhibit a range of morphologies similar to craters on the icy satellites of Jupiter and Saturn. Craters on the large satellites Ganymede and Callisto show a progression of crater morphologies with increasing crater diameter: simple craters, complex craters, pit craters, and multiring structures at the largest diameters. Craters on the smaller Saturnian satellites are almost exclusively simple or complex in morphology, pit craters being generally absent. Craters on the Uranian satellites also include simple and complex craters, but no obvious multiring basins occur. However, the two largest craters on Titania, with diameters of about 335 km (about 10°S lat., 280° long.) and 146 km (about -15°, 40°), appear to be pit craters. Complex craters on the Uranian satellites show the same general structural features found in complex craters on the other icy satellites: a) central structures are usually single peaks, circular or linear elongate in planform. A large conical peak approximately 8 km high visible on Oberon's limb is morphologically similar to the distinctive large central peak in Izanagi on Rhea. Albedo patterns and irregularities in Oberon's limb around the peak suggest a crater rim around 300 km in diameter, again comparable to Izanagi. b) Terrace structures are very underdeveloped compared to terraces in complex craters on the terrestrial planets. No true terraces are apparent, and only slump deposits at the bases of rim scarps are found (though this may be a resolution effect). c) The planforms of complex crater rims are frequently polygonal like complex craters on rocky planets.

Simple-Complex Transition Diameters. Estimates of transition diameters from simple to complex crater morphologies are given for the five large Uranian satellites and 1985U1 in Table 1, and plotted with transition diameters on other bodies against surface gravity in figure 1. The transitions on Ariel and Titania are well determined. The other transitions are only bracketed by approximate limits. The lower limit on Miranda is well determined, but the upper limit is set by a single degraded structure that is complex if it is a single crater and not a degraded cluster. The upper limits on Umbriel and Oberon are well defined, but the lower limits are somewhat uncertain due to poor resolution. The lower limit on 1985U1 is based on a single large crater which (again subject to resolution limits) appears to be simple. Two simple theories of crater modification (1,2) suggest an inverse correlation of the transition diameter with surface gravity. The difference in transition diameter between sedimentary (s) and crystalline (c) rocks on the Earth suggest a direct dependence on target strength or

density as well (1,3), a dependence further indicated by the general downward shift of the transition diameters on the icy satellites relative to the rocky terrestrial planets. However, adopting a g^{-1} dependence for the icy satellites seems to indicate two ice sequences: one including Ganymede, Callisto and most of the Uranian satellites, and a second including the Saturnian satellites, Miranda, and Ariel. One might suggest a compositional difference was responsible since the Uranian and Jovian satellites have similar uncompressed bulk-densities while the Saturnian satellites are somewhat less dense, but Titania and Ariel with the best determined transition diameters are on separate "sequences." Apparently other factors affect transition diameters not fully accounted for in current theories.

Possible Large-Scale Impacts. One of the unusual dark structures on Miranda, the "banded ovoid" (1) centered near 15°S lat. and 50° long., occupies a quasi-circular area about 320 km in diameter (figure 1). Crater counts on the dark material and the surrounding light "highlands" demonstrate that the dark terrain is substantially younger than the light terrain. Stereo imagery and limb profiles show that the light terrain slopes down to the contact with the dark terrain, suggesting that the dark terrain fills a previously existing depression. This old depression is inferred to be an impact scar by several observations: 1) strings of overlapping craters morphologically similar to secondary crater chains around large lunar basins extend radially away from the depression center along the terminator. The largest individual craters in the string are 14 to 18 km in diameter, appropriate for a 300 km primary crater (4). 2) Several fractures and two valleys similar to Vallis Bouvard at Orientale Basin on the Moon extend radially from the depression. 3) A tongue of material similar to ejecta deposits around lunar basins obliterates the rim of a 60 km crater ("A") adjacent to the depression and covers most of the floor. 4) Craters on the light terrain fall into two preservation classes: fresh and sharp rimmed, and extremely subdued and degraded with virtually no intermediate states. In addition, a layer of bright material at least 1 km thick appears to cover most of the visible hemisphere (5). Both of these observations may be accounted for if the depression is an impact crater: the light layer representing the thick ejecta blanket that covered and "softened" all pre-existing topography, thus providing a stratigraphic horizon upon which later fresh appearing craters formed.

Another possible modified large-scale impact is located near 10°S lat. and 30° long. on Ariel (figure 2). The structure is a roughly circular depression about 245 km in diameter surrounded by massifs that occur in linear chains that radiate away from the depression center and merge into the surrounding dissected plateau region. An excess of 10-12 km diameter craters that are the right size and radial

distance for a 200-250 km diameter primary crater occur on plateaus surrounding the depression. Several large valleys are also sub-radial to the depression. The floors of the depression and the radial valleys are entirely covered by the smooth material that covers the floors of the large linear valleys to the south and west. The general arrangement is reminiscent of some of the large impact basins on Mars, such as Argyre and Chryse, which act as topographic lows towards which flow has occurred.

References

1. Croft, S.K. (1982) Saturn: Program and Abstracts, p. 77. 2. Melosh, H.J. (1982) J. Geophys. Res. 87, p. 371-380. 3. Pike, R.J. (1980) PLPSC 11th, p. 2159-2189. 4. Croft, S.K. (1986) submitted. 5. Smith, B.A., et al. (1986) Science 233, p. 43-64.

TABLE 1. SIMPLE-COMPLEX CRATER TRANSITIONS ON THE URANIAN SATELLITES

Name	Radius*,km	Density*,g/cm^3	Surface Gravity cm/s^2	Simple-Complex Transition Diam.,km.
1985U1	85 ± 5	(1.4)	(3.3)	>48
Miranda	242 ± 5	1.26 ± 0.39	8.5 ± 2.6	≈ 28 → 41
Ariel	580 ± 5	1.65 ± 0.30	26.7 ± 5.1	13 ± 2
Umbriel	595 ± 10	1.44 ± 0.28	23.9 ± 5.1	≈ 23 → 38
Titania	805 ± 5	1.59 ± 0.09	35.8 ± 2.2	24 ± 2
Oberon	775 ± 10	1.50 ± 0.10	32.5 ± 2.6	≈ 29 → 45

*Radii and densities adapted from Smith et al. (1986) except for density of 1985 U1 which is a nomimal average uncompressed density for other satellites.

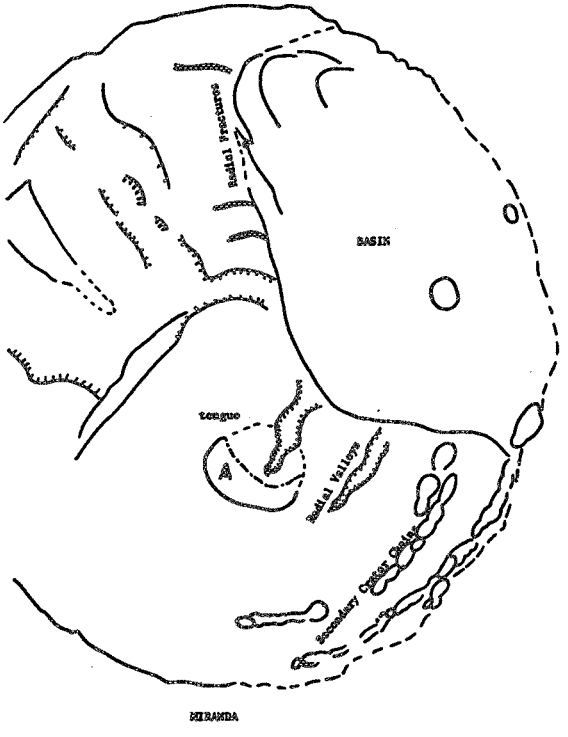

Figure 1.

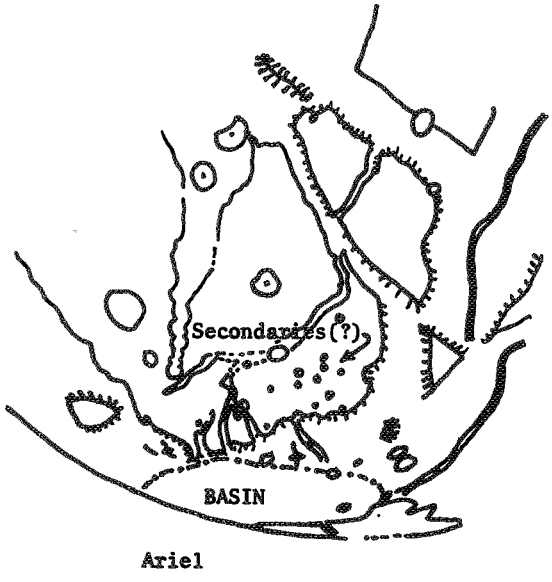

Figure 2.

CRATERING HISTORY OF MIRANDA J.B. Plescia, U.S.G.S., Flagstaff, AZ 86001, and J.M. Boyce, NASA Headquarters, Washington, D.C. 20546

The surface of the southern hemisphere of Miranda imaged by Voyager 2 (Smith et al., 1986) is divisible into two general types of terrain: cratered terrain, characterized by numerous craters and undulating intercrater plains; and basins, circular to rectangular areas of complex morphology having large-scale albedo markings. (The term "basin" is used without a genetic implication.) To determine the relative ages of the terrains and the length of geologic activity, crater-frequency data were compiled for various parts of the cratered terrain and the basins (Table 1).

All of the well-resolved impact craters are either bowl shaped or flat floored; craters having central peaks or rings were not observed. Almost all craters >20 km in diameter are degraded and some are barely detectable. Smaller craters range in appearance from fresh to degraded. Ejecta deposits are generally absent, although two craters are surrounded by low-albedo ejecta material.

The cratered terrain has a varied crater frequency that, in part, is related to position on the satellite. From the anti-Uranian hemisphere (long 180^{o}) to the sub-Uranian hemisphere (long 0^{o}), from areas A to B to C, crater frequencies decrease by an order of magnitude (Table 1). Differences in crater frequencies and the shape of the cumulative size-frequency distributions indicate a resurfacing of the cratered terrain, the sub-Uranian hemisphere having been more affected than the anti-Uranian hemisphere.

Within the cratered terrain in the anti-Uranian hemisphere, near lat -50^{o}, long 180^{o}, the size-frequency distributions correspond to those of steady-state surfaces on the Moon. This correspondence indicates that the cratered terrain is locally saturated with craters <7 km in diameter.

A gradient in the cratering rate from the leading to the trailing hemisphere (Shoemaker and Wolfe, 1982; Horedt and Neukum, 1984) can explain the observed pattern of resurfacing and the correlation of crater frequencies with position within the cratered terrain. The data suggest that Miranda originally was oriented about 90^{o} from its present orientation, such that the most heavily cratered areas that are now near long 180^{o} were originally near the apex of motion (long 90^{o}). Resurfacing within the cratered terrain resulted from the ballistic distribution of ejecta that eroded and buried all craters to some extent but was most effective on the small ones. Apparently, as a result of the formation of the basins, Miranda's moments of inertia were changed, resulting in a reorientation of the satellite.

The banded basin in the leading hemisphere consists of a smooth interior area and a marginal area characterized by albedo banding resulting from concentric, outward-facing scarps. The interior has a higher crater frequency than the margin (Table 1). Although the frequency difference is statistically significant, it may not reflect a real difference in formation ages: the extensive faulting in the margin might have obliterated craters, thereby lowering the observed crater frequency and the apparent age.

The grooved basin in the trailing hemisphere consists of an interior area, characterized by randomly oriented ridges and troughs, and a marginal area, characterized by parallel, closely spaced ridges and grooves. The interior has a significantly higher crater frequency than the margin (Table

1). All of the craters within the margin are superposed; none appear to be affected by the grooving, indicating that the frequency represents a formation age rather than a crater-retention age.

The polar basin was divided into four areas: the bright chevron-shaped feature, grooved area A (near lat -70°, long 300°), grooved area B (near lat -55°, long 340°), and a boundary area that partly surrounds the other areas. Three areas--the chevron, grooved area A, and the boundary area--have similar crater frequencies (Table 1), indicating that they developed contemporaneously. Grooved area B has statistically higher crater frequencies, which may represent a crater-retention rather than a formation age. This area may have formed by the tectonic disruption of adjacent cratered terrain and it may have inherited some preexisting craters. This may explain why the crater frequencies for grooved area B are lower than those characteristic of the cratered terrain but higher than those of a "new" surface of the same age that was originally uncratered.

Crater-frequency data indicate that the cratered terrain is the oldest terrain on Miranda and that it has been locally resurfaced. Ages of the grooved and banded basins are similar but younger than the cratered terrain, and the polar basin is the youngest terrain. Observed crater frequencies on Miranda are, in general, lower than those on any of the other Uranian satellites, indicating that Miranda's surfaces are the youngest in the system. Miranda's relative youth is even more apparent when the increase of the cratering rate inward from Oberon is considered; the cratering rate at Miranda is about 14 times that at Oberon (Smith et al., 1986). Thus, a surface on Miranda dating to the same period as does Oberon's would have about 20,250 craters $\geq$ 10 km in diameter/10^6 km^2. However, the observed crater frequencies on Miranda (Table 1) are several orders of magnitude lower. Apparently, the recorded geologic history of Miranda began after the heavy bombardment had ended and after much of the activity on the other satellites had ceased.

REFERENCES: Horedt, G.P., and Neukum, G., 1984, Icarus, 60, 710-717; Shoemaker, E.M., and Wolfe, R., 1982, Satellites of Jupiter, 277-339; Smith, B. A., et al., 1986, Science, 233, 43-64.

TABLE 1
MIRANDA TERRAIN CRATER FREQUENCIES

REGION	FREQUENCY OF CRATERS ≥ D / 10^6 KM^2 DIAMETER (KM) 1	2	5	10	20
POLAR BASIN					
Grooved A	10763±1345	2523±651	(283±218)	(58± 99)	(12±45)
Grooved B	22038±1805	5916±935	908±366	(227±183)	(60±94)
Chevron	16440±1911	2222±703	(156±186)	(21± 68)	(2±21)
Boundary	8561±1468	1740±662	348±292	(91±151)	(21±73)
Average	15157± 846	3352±398	338±126	(56±51)	(10±22)
GROOVED BASIN					
Margin	(7263±559)	1737±273	355±124	151± 81	(16±26)
Interior	(10325±1042)	3371±596	794±289	206±147	(77±90)
BANDED BASIN					
Margin	(1E5±2206)	(12115± 768)	730±188	115± 75	18±29
Interior	(93886±2057)	(59948±1644)	1307±243	232±102	60±51
CRATERED TERRAIN					
A (-70°/235°)	15599±1789	7800±1265	2175±668	1017±457	(415±292)
B (-40°/270°)	11034±1077	3153±576	736±278	155±126	(44±68)
C (-30°/315°)	7240±800	1126±315	581±123	435±196	177±125
D (-65°/130°)	38312±1880	9045±914	1477±369	233±146	(62±76)
E (-75°/175°)	(30037±3440)	9846±1969	2757±1042	(924±603)	(325±358)
F (-65°/175°)	(32483±1250)	10419±708	2357±337	(667±179)	(235±106)
G (-35°/195°)	(32650±1472)	10325±828	2523±409	598±199	(253±130)
H (-45°/225°)	(25230±1627)	7658±896	2046±463	590±249	(195±143)

Numbers in parentheses are extrapolations of the data to diameters at which craters of a given size were not present (at the large-diameter end) or at which resolution, viewing, or lighting limitations prohibited accurate counting (at the small-diameter end).

The Viscosity of Miranda

P.J. Thomas, R.T. Reynolds, S.W. Squyres and P.M. Cassen

Theoretical Studies Branch, NASA Ames Research Center, Moffett Field, CA 94035.

Voyager 2 images of Miranda reveal a significant history of geological activity. Overlying an apparently ancient, cratered terrain are assemblages of concentric ridges, scarps and dark banded material. Three regions of complex terrain are visible in the Voyager images, which cover virtually an entire hemisphere. These regions are typically $\sim 200km$ in diameter.

Although the concentric ridges have some similarity to the regularity of the grooved terrain on Ganymede, they are also associated with what appear to be extensive flow regions (possibly associated with internal melting) that, in some cases, have modified the geometry of the ridges. Finally, widespread brittle behavior is observed in the form of large faults, scarps and graben up to $15km$ deep.

We examine the problems that evolutionary thermal and structural models of Miranda must face, to provide an convincing explanation for such topographic complexity. The problems center around the requirement that such a small body ($R \sim 242km$) must have a sufficient heat generation mechanism to lower its viscosity substantially. It would generally be expected that a body of such size with such low ambient temperatures ($\sim 50\ K$) would have an extremely rigid surface. While the observed fault regions are consistent with a rigid surface, the high degree of sphericity of Miranda implies a low viscosity material, at least at some time in Miranda's past.

For viscous relaxation on a scale of $L \sim 100km$ to occur over a reasonable timescale ($\tau_r \lesssim 10^9 y$), the dominant viscosity μ determining viscous motion is given by

$$\mu \lesssim \frac{\tau_r L \rho g}{4\pi} \tag{1}$$

where for Miranda $g = 0.09ms^{-2}$ and $\rho = 1200kgm^{-3}$ (Tyler *et al.*, 1986) yielding $\mu \lesssim 10^{22} Pas$. Assuming a Newtonian viscosity law for ice (Weertman, 1970):

$$\mu = \mu_0 \exp\left(A^*\left(\frac{T_m}{T} - 1\right)\right) \tag{2}$$

with parameters appropriate to low-temperature ice $A^* = 25$; $T_m = 273K$; and $\mu_0 = 10^{14} Pas$ (Reynolds and Cassen, 1979), this is appropriate to a temperature T of $157K$, or a temperature $> 100K$ above the ambient temperature.

The two reference models for Miranda that we consider are that (1) the complex terrain was emplaced during a period of reaccretion following a disruptive impact (Smith *et al.*, 1986) in this case the energy required for resurfacing is produced by the release of the potential energy of the reaccreted fragments; or that (2) the complex terrain represents a disturbed region overlying a diapiric instability, similar to a mechanism proposed for the formation of palimpsests on Ganymede (Hale *et al.*, 1980). In the second case the energy required for resurfacing must have an internal origin, such as radiogenic heating or tidal deformation. These two models represent exogenic and endogenic formation models for the complex terrain, respectively. They also permit estimates of dynamic viscosities and associated emergy inputs required by these models.

If population statistics derived for the sizes of comet nuclei are valid for projectiles impacting on Miranda, it is conceivable that Miranda underwent a series of collisions with bodies of sufficient kinetic energy to disrupt it in the first Gy after its initial formation (Shoemaker and Wolfe, 1982; Smith *et al.*, 1986). This model implies that the final stages of reaccretion may have produced the observed terrain patterns by liberation of the gravitational potential energy of the disrupted fragments of the satellite.

While both models must be able to account for Miranda's high degree of sphericity, the reaccretion model faces a more stringent relaxation condition: that relaxation must remove all traces of the impact crater associated with the disruptive impact. Such a crater will have topographic harmonics associated with the rim with wavelengths much smaller than $100km$ and thus much longer relaxation times. For example, to relax crater rims with wavelengths on a scale of $10km$ in $10^9 y$ would require a viscosity of $10^{21} Pas$.

Unfortunately for this model, the energy that can be obtained from reaccretional heating for a body as small as Miranda is limited. The thermal energy retained by Miranda cannot be significantly greater than the binding energy, $\sim 2 \times 10^4 Jkg^{-1}$ which, given a specific heat for ice of $\sim 10^3 Jkg^{-1}K^{-1}$,

predicts a maximum global temperature increase as small as $\sim 20K$. This estimate is in good agreement with more detailed models (Squyres *et al.*, 1986). Of course, local heating arising from point contacts between reaccreted fragments may much greater temperatures in small regions. Furthermore, disruption and reaccretion will dissipate much of this initial energy, tending to produce a more isothermal temperature profile (Ellsworth and Schubert, 1983). One final important problem that this mechanism must face is that, according to various evolutionary models of the icy satellites, radiogenic heating produces a maximum temperature profile for small satellites within the first $\sim 100My$ (Ellsworth and Schubert, 1983; Federico and Lanciano, 1983). This heat will also be dissipated by a cycle of multiple disruption and accretion, if such exists.

We can consider energy constraints on the endogenic model by calculating the ascent time τ_a for a buoyant inviscid sphere (our diapir model) of radius $a = 50km$ at low Reynolds number through a layer of thickness $L = 100km$:

$$\tau_a = \frac{3\mu L}{\Delta\rho g a^2} \tag{3}$$

we assume a density difference $\Delta\rho$ of $300kgm^{-3}$, appropriate to warm pure ice surrounded by material with the mean density of Miranda. Assuming $\tau_a \lesssim 10^9 y$ we obtain $\mu \lesssim 10^{22} Pas$, consistent with the determination above. This value is, however, very much of an upper limit, because Miranda's surface gravitational acceleration was assumed for g. The cooling time for such a diapir is $a^2/\kappa \sim 3 \times 10^8 y$ (where $\kappa \sim 10^{-6} m^2 s^{-1}$). For this ascent time (more reasonable than $10^9 y$ because of the presence of some cratering on the ridged terrain) we have $\mu \lesssim 10^{21} Pas$ which is appropriate, using the viscosity law above, to $T = 166K$, or $\sim 100K$ above Miranda's ambient temperature.

It is possible that extinct radionuclides such as ^{26}Al may have had a significant energy input into Miranda in the past. However, the half life of such elements (typically $\lesssim 10^6 y$) indicates that any resurfacing that occurred as a result would be substantially older than the observed, very lightly cratered terrain on parts of Miranda.

It appears to be clear that some energy source other than accretional heating is required to provide both the spherical shape of Miranda and the evidence of substantial viscous flow activity. The exogenic model requires enhanced temperatures after the last reaccretion, placing serious constaints on short term heating processes. In addition, it has a serious problem in accounting for the absence of small-scale impact features on much of Miranda's surface.

Given the difficulties in finding a suitable energy source capable of raising Miranda's global temperature to a sufficient extent to reduce the viscosity of pure ice adequately, it is possible that mobilization of ice clathrated with CO, N_2 or CH_4 by pressure-solution creep may be an important transport process. Under certain conditions, viscosities many orders of magnitude smaller than those calculated above may be produced by this mechanism (Stevenson and Lunine, 1986).

Since the temperatures determined here lie above the $H_2O.NH_3$ eutectic at $173K$, internal melting may have occurred to some extent. If the flow features were emplaced significantly after the accretional period ($\gtrsim 10^8 y$) then tidal heating alone remains as a plausible energy source. The energy required to produce increases in temperature of the extent calculated for the entire satellite is of the order of $10^{24} J$. If this was expended over the period of $3 \times 10^8 y$ mentioned above, a heating rate of $\sim 10^9 W$, which is $\sim 10^{-4}$ the heating rate associated with Io's tidal flexure. For Miranda no easily indenfiable orbital resonance can account for this enhanced heating (Squyres *et al.*, 1985). However, the effects of mutual satellite pertubations have not yet been considered in full complexity (Dermott and Nicholson, 1986). In conclusion, it should be emphasized that due to the inability of reaccretional heating to provide a important energy input for Miranda, any heating mechanism required by the endogenic model must also be required by the exogenic model.

References

Dermott, S.F. and P.D. Nicholson (1986). *Masses of the satellites of Saturn.* Nature, **319**, 115-120.

Ellsworth, K. and G. Schubert (1983). *Saturn's icy satellites: thermal and structural models.* Icarus, **54**, 490-510.

Federico, C. and P. Lanciano (1983). *Thermal and structural evolution of four satellites of Saturn.* Annales Geophysicae, **1**, 469-476.

Hale, W., J.W. Head and E.M. Parmentier (1980). *Origin of the Valhalla ring structure: alternative models (abstract)*, in *Papers presented to the Conference on Multi-Ring Basins: Formation and Evolution*, pp. 30-32, Lunar and Planetary Institute, Houston.

Reynolds, R.T. and P.M. Cassen (1979). *On the internal structure of the major satellites of the outer planets.* Geophys. Res. Lett., **6**, 121-124.

Shoemaker, E.M. and R.F. Wolfe (1982). *Cratering time scales for the Galilean satellites.* In *Satellites of Jupiter* D. Morrison, ed.), University of Arizona Press, Tucson.

Smith, B.A. and the Voyager Imaging Team (1986). *Voyager 2 in the Uranian System: Imaging Science Results*, Science, **233**, 43-64.

Squyres, S.W., R.T. Reynolds and J.J. Lissauer (1985). *The enigma of the Uranian satellites' orbital eccentricities.* Icarus, **61**, 218-223.

Squyres, S.W., R.T. Reynolds, A.L. Summers and F. Shung (1986). *Accretional Heating of the Satellites of Saturn and Uranus.* This volume.

Stevenson, D.J. and J.I. Lunine (1986). *Mobilization of cryogenic ice in outer Solar System satellites.* Nature, **323**, 46-48.

Tyler, G.L. and the Voyager Radio Science Team (1986). *Voyager 2 radio science observations of the Uranian system: atmosphere, rings and satellites*, Science, **233**, 79-84.

Weertman, J. (1970). *The creep strength of the Earth's mantle*, Rev. Geophys. Space Phys., **8**, 145-168.

MECHANICAL AND THERMAL PROPERTIES OF PLANETOLOGICALLY IMPORTANT ICES Steven K. Croft, Lunar and Planetary Laboratory, University of Arizona, Tucson, Arizona 85721

Two "sequences" of ice composition have been proposed for the icy satellites: 1) a dense nebula model (1) in which C and N are CH_4 and NH_3, yielding, in order of decreasing condensation temperature, hydrated rock, H_2O ice, $NH_3 \cdot H_2O$, CH_4-ice clathrate and finally solid CH_4; and 2) a solar nebula model (2) in which C and N are in CO and N_2 yielding hydrated rock, H_2O ice and finally CO- or N_2-ice clathrate. Careful modeling of the structure, composition, and thermal history of satellites composed of these various ices requires quantitative information on the: 1)density, 2)compressibility, and 3)thermal expansion of the rock and ices (incorporated as an equation of state or EOS), as well as the 4)heat capacity and 5)thermal conductivity. EOS's and thermal data have been given previously for the H_2O ices (3) and CH_4 (4). However, much recent interest in structures of molecular ices by physical chemists has resulted in a large increase in the data available on ices of planetological interest. Thus, data have been gathered from the literature to update equations of material properties for the H_2O and CH_4 ices and to calculate such equations for the first time for NH_3, CO, N_2 and CO_2 ices.

Pure Ice Data. EOS's have been fit to the density data of the molecular ices shown in table 1. The # phases includes the number of solid phases plus one liquid phase (except for $CH_4 \cdot 5.75H_2O$) analyzed for each compound. Compared to silicate minerals, the bulk moduli (K_{oo}) of the ices are one to two orders of magnitude smaller, the K'_p's are about the same, and the K'_T's are about half. The inferred thermal expansions show enormous variability, increasing from rock to H_2O ice to the other molecular ices. The effect is not trivial: increasing the interior temperature of an icy satellite from accretion temperatures near 100°K to around 300°K yields a 0.2% volume increase in the rocks, ≈ 3% increase in the H_2O ices, and > 30% increase in the other molecular ices. The assembled heat capacity data show the same trends, increasing dramatically from rock to H_2O ice to the other ices. Of particular note here is that the heat capacity of rock assumed in previous models was near 1.2 Joules/g°K, appropriate for the high interior temperatures of rocky planets, but far too large for the 100K to 300K temperatures appropriate to the icy satellites. The net affect on icy satellite thermal histories, because of the large mass fraction of the rock, is to shorten the times for internal heating and melting by factors of 2x to 3x. Finally, the assembled thermal conductivity data (figure 1) again show a definite trend: decreasing from rock to H_2O ice to the other molecular ices. Of particular interest is the extremely low thermal conductivity of CH_4-clathrate compared to H_2O ice or rock - a point returned to below.

Binary/Multiple Ice Systems. The simple molecular ices represent end-numbers of more complex ice "minerals" that form when the simple ices are mixed. Ammonia hydrates ($NH_3 \cdot nH_2O$) and ice clathrates (CH_4, N_2, $CO \cdot nH_2O$) are likely forms (5,6). The thermodynamics of ice clathrates have been studied by (7). A preliminary EOS for CH_4- and N_2-clathrates have been constructed here from the meager data available, but much work needs to be done to directly determine thermal expansion and bulk modulus derivatives. Data for the $NH_3 \cdot H_2O$ system are limited: heat capacities and latent heats, liquid densities near room temperature, single density measurements $2NH_3 \cdot H_2O$, $NH_3 \cdot H_2O$ and $NH_3 \cdot 2H_2O$, and some high pressure measurements at

selected compositions (8). Approximate bounds on the thermal and mechanical properties of the ammonia hydrates may be set by looking at the properties of the end-members: NH_3 and H_2O. For example, heat capacity data for the ammonia hydrates are intermediate between ammonia and water. However, actual measurements are preferred and thus analytical, experimental, and theoretical studies of the ammonia hydrates have been initiated. An equation for the density of liquid NH_3-H_2O (at all NH_3 concentrations) has been constructed using previous high temperature data and our own low temperature data. The liquid densities have been combined with thermodynamic and solid density data to determine the low pressure portion of the $NH_3 \cdot 2H_2O$ phase diagram. Combining our results with the high pressure data, we infer at least two solid phases of $NH_3 \cdot 2H_2O$ with the transition near 1kb and with a fairly large density difference. A phase change at such a low pressure is an important one structurally even for fairly small icy satellites.

Applications. Detailed structural and thermal modeling of icy satellites has commenced based on the new data. For example, one of the real surprises of the Voyager Uranus encounter was the presence of endogenic resurfacing and fracturing on tiny Miranda. The implied volume increase of Miranda represented by the fractures is ≈ 6%. How does Miranda become warm enough to exhibit such activity? One possible approach is illustrated by the thermal profiles in figure 2. If Miranda consists of simple ice and rock, the maximum interval temperature rise is ≈ 10°K, perhaps yielding temperatures in the core capable of melting a little CH_4 (if any is present in pure form). Such small amounts would likely freeze en route to the surface. However, if the ice is in the form of CH_4 clathrate, the temperature rise in the core is ≈ 120°K, sufficient to melt CH_4 through much of the interior and probably to drive it through the resulting thin crust to the surface (the dark flows on Miranda may be radiation-darkened CH_4 (9)). Even partial melting of eutectic NH_3-H_2O is possible (depending on boundary conditions). The large internal heating due to clathrate and the presence of molecular ices of high thermal expansivity may also account for the observed fracturing via simple heating and thermal expansion. Thus, the difference between resurfaced Miranda and primitive Mimas may simply be the presence of clathrate. The effects of the clathrate vs. pure ice on larger satellites is not as great (cf. Titania curves in fig. 2) because convection provides a fairly low temperature cutoff (detailed values depend on surface conditions and assumptions concerning viscosity). Thus, the unusual thermal and mechanical properties of the molecular and binary ices suggest a larger range of phenomena than previously anticipated, sufficiently complex perhaps to account for many of the unusual geologic phenomena found on the icy satellites.

References

1. Prinn R.G. and Fegley B. (1981) Ap.J. 249, 308-317. 2. Lewis J.S. and Prinn R.G. (1980) Ap.J. 238, 357-364. 3. Lupo M.J. and Lewis J.S. (1979) Icarus 40, 157-170. 4. Lupo M.J. and Lewis J.S. (1980) Icarus 42, 29-34. 5. Miller S.L. (1985) in Ices in the Solar System, NATO, p. 59-79. 6. Lewis J.S. (1972) Icarus 16, 241-252. 7. Lunine J.I. and Stevenson D.J. (1985) Ap. J. Supp. 58, 493-531. 8. Johnson M.L. et al. (1985) in Ices in the Solar System, NATO, p. 39-47. 9. Smith B.A. et al. (1986) Science 233, 43-64.

TABLE 1. MOLECULAR ICES

Compound	#Phases	K_{oo}	K'_p	K'_T
H_2O	8	114 Kb	5.5	-0.101 Kb/°K
NH_3	4	75	5.5	-0.186
CH_4	4	21	4.9	-0.074
N_2	6	28	3.8	-0.108
CO	5	20	6.6	-0.092
CO_2	3	77	7.0	-0.183
$CH_4 \cdot 5.75H_2O$	1	≈88	(5.5)	(-0.1)

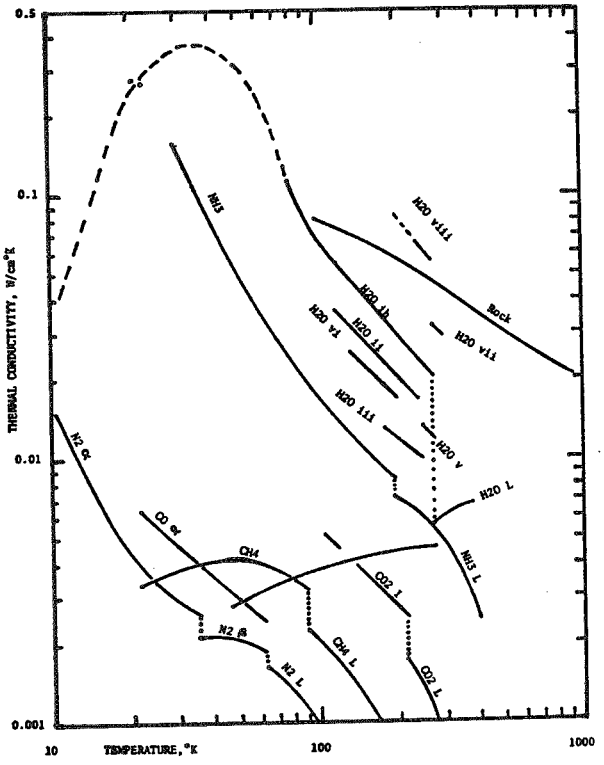

Figure 1.

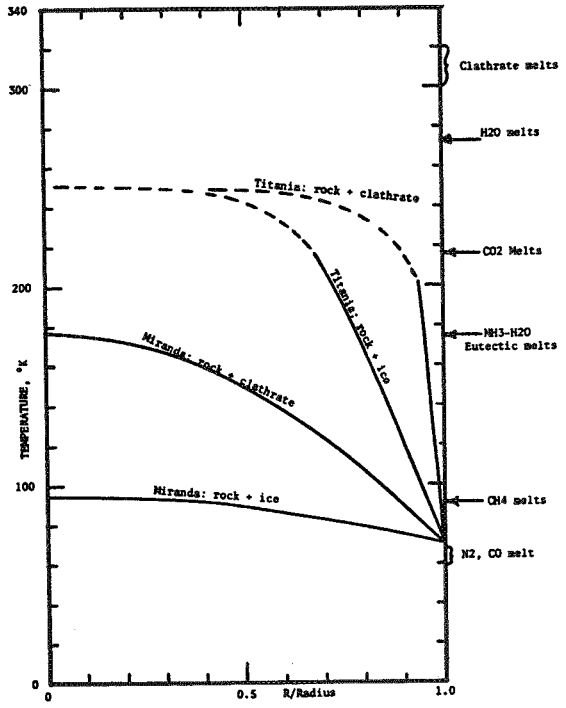

Figure 2.

Could Ariel have been Heated by Tidal Friction?

S. J. Peale (University of California at Santa Barbara)

For significant dissipation in Ariel, one must hypothesize the past existence of an orbital resonance to force and maintain a substantial eccentricity in the orbit. The certain capture of Ariel/Umbriel into a simple eccentricity resonance at the 2/1 commensurability of orbital mean motions had they passed through singles out this strong resonance as the most likely to have had any effect on Ariel's interior. An immediately apparent problem with the occupancy of this resonance is the neccessity for an escape by an unknown mechanism. A lack of resolution of this problem may mean that tidal expansion of the satellite orbits has been insufficient for the 2/1 commensurability to have been encountered, but the striking modifications of Ariel's surface suggests that something much more dramatic has happened. A maximum dissipation occurs when Ariel's eccentricity has been forced to an equilibrium value where the ratio of orbital mean motions of the resonant pair is fixed as the orbits of the satellites continue to expand from tides raised on Uranus. The dissipation is then simply the difference between the rate of work done by the tidal torques from Uranus and the rate of orbital energy increase, where nearly all of the dissipation occurs in Ariel. With dissipation $dE/dt = 0.26nT$ (n = mean motion, T = torque), we can infer a maximum effect on Ariel's thermal history by assuming the longest possible existence of the resonance in equilibrium with the minimum average value of Q for Uranus. $Q_{\min} = 4600$ ($k_2 = .104$) is now determined by Miranda starting at the "standstill" orbit. The maximum dissipation rate in Ariel would have been 7×10^{18} ergs/sec which would drop to 2.3×10^{17} ergs/sec at the last position at which the 2/1 resonance could have existed 2.6×10^9 years later—the resonance being disrupted at least 2×10^9 years ago. The absolute maximum dissipation rate would be reduced both by the time necessary to establish the resonance in the first place and by a consequently larger minimum Q. Subsolidus convection may be able to remove the heat even at the highest rate of deposition without disrupting a rigid lithosphere, but such a conclusion depends on highly uncertain parameters. The actual heating rate has undoubtedly been much less than this maximum, so even the former (unlikely?) existence of a 2/1 resonance may not be sufficient to account for Ariel's smoothed surface. Miranda could never have been trapped in any first order resonance, so its even younger surface is more a mystery.

GEOLOGY AND CRATERING HISTORY OF ARIEL J.B. Plescia, U.S.G.S., 2255 N. Gemini Drive, Flagstaff, AZ 86001, and J.M. Boyce, NASA Heaquarters, Washington, D.C. 20546

The surface of Ariel imaged by Voyager 2 (Smith et al., 1986) can be divided into several types of terrain on the basis of morphology: cratered terrain, subdued terrain, ridged terrain, and plains. Cratered terrain, at lat -20^{o}, long 0^{o} and at lat -30^{o}, long 255^{o}, is characterized by a rolling surface, east- or northeast-trending grabens and scarps, and scattered superposed impact craters. Between the two occurrences of cratered terrain are areas of subdued terrain characterized by highly degraded craters and narrow (<3 km wide) ridges. Ridged terrain bounds the subdued terrain and occurs as narrow bands within it. It is characterized by bands 25 to 70 km wide within which are parallel, east- or northeast-trending ridges and troughs typically about 10 to 35 km apart. Individual ridges and troughs extend 100 to 200 km, but the bands of ridged terrain extend many hundreds of kilometers. At several locations, bands of ridged terrain are continuations of well-defined grabens and follow the same structural trends. Plains fill topographically low areas such as graben floors and irregular depressions. The plains that partly fill the grabens locally exhibit a medial trough from which plains-forming material appears to have flowed out onto the surface.

Crater statistics were compiled for each of the terrain types (Table I). Despite differing morphology, the various terrains on Ariel do not exhibit large variations in crater frequency. The difference in crater frequency between the cratered terrain, the most heavily cratered surface, and the plains, the least cratered surface, is only a factor of 3 to 4, in distinct contrast to the order-of-magnitude differences observed on Miranda (Plescia and Boyce, 1986; Smith et al., 1986).

Crater saturation of the cratered terrain occurs at diameters of about 12 km, whereas that for the subdued and ridged terrains is closer to 7 km, suggesting that the cratered terrain is the oldest of the three. The ridged terrain cuts both the subdued and cratered terrains and is therefore younger than both. The plains, which are not saturated with craters, are the youngest terrain and apparently formed at different periods of time, as indicated by the crater-frequency data.

None of the observed surfaces on Ariel record the period of accretion. If the surface of Ariel were as old as that of Oberon or Umbriel, whose surfaces presumably reflect the period of accretion, it would have a frequency of about 1,800 craters $\geq$ 30 km/10^{6} km^{2}. However, the observed crater frequencies on Ariel are clearly lower (Table 1). The presence of few craters larger than 50 km in diameter also indicates that its observed surface was not formed during accretion. Ariel appears to have been completely resurfaced since it formed.

The extensive network of grabens on Ariel indicates that it has experienced global tensional stresses. Freezing of an initially liquid water interior and the resultant satellite-wide expansion may have produced the necessary global tension. Because the grabens are locally floored by plains, they must have formed, at least in part, during that portion of Ariel's history when new terrains were being formed and when conditions were appropriate for the mobilization of material for resurfacing.

Ariel's geologic history may be better understood by a comparison with that of Dione, which has similar size, density, and surface temperature and for which extensive thermal modeling has been done (Stevenson, 1982; Ellsworth and Schubert, 1983). On the basis of the thermal models for Dione, solid-

state convection within Ariel can be estimated to have lasted for several billion years, a situation conducive to the deformation of the brittle surface layer. Temperatures in excess of the ammonia-water ($NH_3 \cdot H_2O$) eutectic melting point (173 K) might be sustained for the first few hundred million years near the surface and for perhaps 2 billion years at deeper levels. If clathrate dissociation occurred catastrophically (Stevenson, 1982), then resurfacing could have been produced by the explosive eruption of material onto the surface. Because clathrate dissociation at shallow depths (<10 km) can occur at temperatures lower than the melting points of either water ice or ammonia-water ice mixtures, such resurfacing events would have been possible for a longer periods of time than the estimates given above. Thus, it seems that conditions appropriate for resurfacing could have occurred during Ariel's early history.

REFERENCES: Ellsworth, K., and Schubert, G., 1983, Icarus, 54, 490-510; Plescia, J.B, and Boyce, J.M., 1986, this volume; Smith, B.A., et al., 1986, Science, 233, 43-64; Stevenson, D.J., 1982, Nature, 298, 142-144.

TABLE I
ARIEL TERRAIN CRATER FREQUENCIES

REGION	COUNTING AREA KM^2	FREQUENCY OF CRATERS $\geq$ D / 10^6 KM^2 DIAMETER (KM) 2	5	10	20	30	LARGEST CRATER (KM)	DIST. SLOPE
Cratered terrain (lat -20^o, long 0^o)	66962	(22967±586)	2285±185	358±73	75±33	(19±17)	29	2.6
Cratered terrain (lat -30^o, long 255^o)	37684	(63908±1302)	4007±326	849±150	69±43	(34±30)	29	2.7
Subdued terrain (combined areas)	87706	(29663±582)	2497±169	376±66	62±27	33±19	69	2.7
Ridged terrain (combined areas)	46944	(37106±889)	2641±237	547±108	23±22	(18±20)	20	2.7
Plains (lat -45^o, long 320^o)	10740	(24484±1510)	1955±427	162±123	(46±65)	(15±37)	13	2.7
Plains (lat -15^o, long 30^o)	37893	(11365±548)	1311±186	198±72	87±48	34±30	33	2.5
Plains (lat -15^o, long 345^o)	16819	(13769±905)	1873±33	725±208	106±79	(68±64)	24	2.0

Numbers in parentheses indicate extrapolations of the data. At small diameters extrapolations are necessary due to resolution limits, at large diameters because of a lack of craters.

On the Lack of Commensurabilities in the Mean Motions of the Satellites of Uranus and the Resurfacing of Ariel

S. J. Peale (University of Califorina at Santa Barbara)

The lack of commensurabilities among the mean motions of the satellites of Uranus is investigated by determining the probabilities of capture into those orbital resonances which might have been encountered as the satellite orbits expand differentially from tidal torques. For the minimum value of the dissipation function of Uranus $Q_U \approx 6600$, the Miranda/Ariel pair would have passed through the 4/3, 3/2 and 5/3 commensurabilities but with no chance of capture into any of the orbital resonances and consequently no resulting constraints on the orbital evolution. Passage of Miranda through the inclination–type resonances in the wrong direction for capture is unlikely to account for the observed 4° inclination. In contrast the Ariel/Umbriel pair would have encountered the 2/1 commensurability with certain capture into either one or both of two eccentricity–type orbital resonances at 2/1 unless $e_A > 0.027$ and $e_U > 0.023$ as the resonances are approached. It is extremely unlikely that this pair could have avoided being trapped into these resonances if, in fact, they had been encountered. Certain capture of Ariel/Umbriel into eccentricity-type resonances at the 5/3 commensurability would require $e_A < 0.0040$ and $e_U < .0047$, so these resonances could have most likely been traversed. Certain capture of Miranda/Umbriel into the 3/1 eccentricity resonances involving Miranda's parameters would occur if $e_M < 0.0045$ for the simple e–type and $e_M < 0.0084$ for the mixed e–type, which would imply trapping Miranda/Umbriel into this resonance if it were encountered. A possible history for the satellite system would be to avoid traversal of those resonances into which capture was certain. With the potential Love number $k_{2U} = 0.104$ for Uranus, $Q_U \gtrsim 11{,}000$ would mean that Ariel/Umbriel did not encounter the 2/1 commensurability, $Q_U \gtrsim 39{,}000$ avoids the 3/1 Miranda/Umbriel commensurability, and $Q_U \gtrsim 100{,}000$ starts the Ariel/Umbriel outside the 5/3 commensurability leading to virtually no tidal expansion of the orbits at all. An alternative to this uninteresting history is investigated to evaluate the conditions necessary to allow sufficient tidal heating of Ariel for the observed resurfacing. The maximum tidal dissipaton in Ariel (assumed to be locked into the 2/1 eccentricity–type resonance with Umbriel) is determined as a function of Ariel's separation from Uranus. The tidal dissipation for the configuration corresponding to the last possible existence of the resonance is only comparable to a lunar like radiogenic source from the satellite core, but could be about 30 times larger than this value in the earliest past. Countless scenarios can be constructed which could lead to the resurfacing of Ariel in the 2/1 resonance, although the constraints may make them somewhat implausible. In any case, detailed thermal histories of Ariel are not warranted unless and until a supportable means of removing Ariel/Umbriel from the 2/1 resonance is found.

ORBITAL DYNAMICS OF THE URANIAN SATELLITES BASED ON VOYAGER DATA J.B. Plescia, U.S. Geological Survey, 2255 N. Gemini Drive, Flagstaff, AZ 86001

The satellites of Uranus all have significant non-zero eccentricities and in the case of Miranda a significant inclination as well (Table 1). Squyres et al. (1985) studied the time scales and possible energy effects associated with the orbital evolution of these bodies, specifically the eccentricities. However, because of the uncertainty in the sizes and masses (data were based on estimates of Brown et al., 1982 and Brown and Cruikshank, 1983), there was a corresponding uncertainty in the results. The Voyager 2 encounter with Uranus in January 1986 provided more accurate estimates of the masses and sizes of the satellites (Smith et al., 1986). As a result, it seems useful to reexamine the orbital history and possible tidal heating by using the Voyager data. This is particularly relevant because Miranda, which had the largest pre-Voyager size uncertainty, is also the satellite which appears to have undergone the most extensive endogenic evolution.

Miranda and, to a certain extent, Ariel have undergone significant endogenic activity. Crater frequency data for Ariel (Plescia and Boyce, 1986a), in combination with the cratering time scale postulated by Smith et al. (1986), indicate that Ariel's surface is >3.5 Gy old and that no major resurfacing has occurred since. Miranda, on the other hand, has the least cratered surface of any satellite in the Uranian system (Plescia and Boyce, 1986b) and may have surfaces as young as several hundred million years old.

The relevant orbital dynamics equations (Peale, 1977; Peale et al., 1980) follow.

The change in orbital eccentricity (e) with time (t) is

$$de/dt = - (21\ k_2\ n\ M\ r^5\ e)/(2\ m\ a^5\ Q) \qquad (1)$$

where k_2 is the satellite potential Love number, n is the satellite mean motion, m and M are the masses of the satellite and Uranus, r is the satellite radius, a is the satellite semimajor axis and Q is the satellite dissipation function. The equation is an approximation because the term relating to the effect of dissipation within Uranus has not been included. Dissipation within Uranus is negligible and dissipation within the satellite is the dominant term.

The potential Love number (k_2) is

$$k_2 = (1.5)/[1 + (19\ u\ /\ 2\ p\ g\ r)] \qquad (2)$$

where u is the satellite rigidity, p is the satellite density, and g the surface gravity.

Finally, the homogeneous tidal heating rate (E) for a synchronously rotating body is approximated as

$$dE/dt = [(m^2\ n^5\ r)\ /\ (u\ Q)]\ [0.396\ e^2 + 0.0566\ o^2] \qquad (3)$$

where o is the spin obliquity: the angle between the spin vector and the orbit normal. If the satellite is in Cassini spin state 1 (o less than the orbital inclination), there is no obliquity-decay heating. If, however, this is not

the case, the obliquity term can become important.

Assuming u = 4 X 10^{10} dyne cm^{-2}, a value typical for low-temperature ice, and Q = 20, the orbital eccentricity decay times and homogeneous tidal heating rates were calculated (Table 1). These results are similar to those of Squyres et al. (1985) and indicate that the calculated rates are relatively insensitive to the uncertainties in mass and density of the satellites. The calculations indicate that the present eccentricities of Miranda and Ariel should decay on time scales of 10^7 years, whereas those of Umbriel, Titania, and Oberon are stable for 10^8 to 10^9 years. The original eccentricity (e_o) is, however, unknown and could have been quite large.

To make the present orbital eccentricity of Ariel and Miranda long lived, such that a late-stage event to pump up the eccentricity is not neccessary, requires that either u or Q be increased. Neither parameter is well constrained because the interior thermal conditions and compositions of the satellites are uncertain. A Q of >100 would produce an eccentricity decay time of 10^8-10^9 years for Ariel and Miranda. Similarly, increasing u would also lengthen the decay time. Rigidities of 4 X 10^{11} dyne cm^{-2}, similar to rock rather than ice, would increase the decay time to 10^8-10^9 years.

When obliquity heating is not important, the tidal heating rates from eccentricity decay are about one to several orders of magnitude below that of the radioactive heating (Table 1). The low tidal heating and low radioactive heating of Ariel, Umbriel, Titania, and Oberon are consistent with their generally ancient age. Miranda, however, presents a significant problem because of the youthful appearance of its surface.

The inclusion of the obliquity term in equation (3) has important implications for Miranda. If Miranda occupies Cassini state 2 (o greater than the orbital inclination), then the obliquity term in equation (3) becomes important. Assuming that all of the satellites have obliquities equal to their inclinations, the tidal energy produced (II) was calculated (Table 1). For Ariel, Umbriel, Titania, and Oberon, the term remains unimportant because the obliquity is small. However, inclusion of the term for Miranda increases the heating rate by 3 orders of magnitude.

Alternatively, if there is no obliquity heating of Miranda, the eccentricity heating rate can only be raised to approximately that of radioactivity. Enchanced eccentricity heating will result, relative to the model in Table 1, by reducing either Q or u. For Q = 1 and u = 4X10^{10} dyne cm^{-2}, the heating rate is 3.03 X 10^{15} erg sec^{-1}, corresponding to a heat flow of 0.45 ergs cm^{-2} sec^{-1}. For Q = 20 and u = 4 X 10^9 dyne cm^{-2}, the rate is 1.52 X 10^{15} erg sec^{-1}, corresponding to a heat flow of 0.20 erg cm^{-2} sec^{-1}.

REFERENCES: Brown, R.H., and Cruikshank, D.P., 1983, The Uranian satellites: Surface compositions and opposition brightness surges: Icarus, v. 55, p. 83-92; Brown, R.H., Cruikshank, D.P., and Morrison, D., 1982, Diameters and albedos of satellites of Uranus: Nature, v. 300, p. 423-425; Peale, S.J., 1977, Rotation histories of the natural satellites, in (Burns, J.A., ed.) Planetary Satellites, p. 87-112; Peale, S.J., Cassen, P., and Reynolds, R.T., 1980, Tidal dissipation, orbital evolution, and the nature of Saturn's inner satellites: Icarus, v. 43, p. 65-72; Plescia, J.B., and Boyce, J.M., 1986a, Crater frequencies on Ariel, this volume; Plescia, J.B., and Boyce, J.M., 1986b, Miranda cratering history, this volume; Smith, B.A., Soderblom, L.A., et al., 1986, Voyager 2 in the Uranian system: Imaging science results:

Science, v. 233, p. 43-64; Squyres, S.W., Reynolds, R.T., and Lissauer, J.J., 1985, The enigma of the Uranian satellites' orbital eccentricities: Icarus, v. 61, p. 218-223.

Table 1

		Miranda	Ariel	Umbriel	Titania	Oberon
Radius (km)		242±5	580±5	595±10	805±5	775±10
Density (gm cm^{-3})		$1.26^{+0.39}_{-0.39}$	$1.65^{+0.3}_{-0.3}$	$1.44^{+0.28}_{-0.28}$	$1.59^{+0.09}_{-0.09}$	$1.50^{+0.10}_{-0.10}$
Mass (gm)		$7.48^{-}_{-} \times 10^{24}$	$1.35^{-}_{-} \times 10^{24}$	$1.27^{-}_{-} \times 10^{24}$	$3.47^{-}_{-} \times 10^{24}$	$2.92^{-}_{-} \times 10^{24}$
Gravity (cm sec^{-2})		8.52	26.74	23.94	35.76	32.48
Semimajor axis (km)		129783	191239	265969	435844	582596
Eccentricity		0.0027	0.0034	0.0050	0.0022	0.0008
Inclination ^{o}		4.2	0.3	0.4	0.1	0.1
de/dt (Q=20) sec^{-1}		4.79×10^{7}	1.38×10^{7}	1.22×10^{8}	8.16×10^{8}	6.64×10^{9}
tidal heating erg sec^{-1} (Q=20)	*I*	1.52×10^{14}	1.02×10^{16}	1.70×10^{15}	8.18×10^{13}	8.37×10^{11}
	II	1.61×10^{17}	1.36×10^{16}	2.17×10^{15}	8.91×10^{13}	1.41×10^{12}
tidal energy heat flow erg cm^{-2} sec^{-1}	*I*	0.02	0.24	0.04	0.001	0.00001
	II	21.88	0.32	0.05	0.001	0.00002
radioactive heat flow erg cm^{-2} sec^{-1}		0.15	0.93	0.64	1.13	0.91

I does not include the obliquity term in equation (3)
II includes the obliquity term in equation (3).

Why No Orbital Resonances Among the Satellites of Uranus?

S. J. Peale (U. C. Santa Barbara)

Most of the orbital resonances among the satellites of the major planets are thought to have been assembled by differential tidal expansion of their orbits. We can investigate why this has not occurred for the Uranus system by determining the resonances which would have been encountered for various values of Uranus' tidal effective Q. If the minimum Q = 17,000 is assumed for Uranus (from Ariel's proximity to Uranus), Miranda would have passed through the 4:3 and 3:2 orbital resonances with Ariel. As Ariel's orbit expands faster than Miranda's, capture into the Miranda-Ariel resonances is impossible. Althrough the passage of Miranda through the resonances in the wrong direction for possible capture would have increased Miranda's orbital eccentricity and inclination, the latter increase cannot explain the current 4° inclination for Miranda's orbit since the corresponding 6:4 and 8:6 inclination resonance passages would have increased the inclination only a few tenths of a degree. For the same minimum Q, Ariel would have passed through the 2:1 and 5:3 orbital resonances with Umbriel. But Ariel and Umbriel would have been captured into either of the lowest order 2:1 eccentricity resonances with certainty unless $e_A > 0.0224$ and $e_U > 0.0219$ at the time of encounter. As the time constant for damping Ariel's eccentricity from tidal dissipation within the satellite is only about 5×10^7 years (with Q = 100 and rigidity $\mu = 4 \times 10^{10}$ assumed), and Ariel's current eccentricity being only 0.0034, it is very unlikely that Ariel could have avoided capture into the 2:1 libration if the system in fact had passed through this resonance. The Q of Uranus need only be increased to 30,000 to keep Ariel always outside the 2:1 resonance with Umbriel. To avoid certain capture of Ariel–Umbriel in the 5:3 resonance, $e_A > 0.0036$ and $e_U > 0.0059$ at the time of passage. With current eccentricities at 0.0034 and 0.005 respectively, and the fact that eccentricities are *reduced* from initial values upon a probalistic escape from the resonance, it is possible that the system passed through the 5:3 resonance. But if the tidal Q of Uranus is larger than 200,000, Ariel would have started even outside the 5:3 resonance. Since the Q of Jupiter is in the range 6×10^4 to 2×10^6, 200,000 is not an outrageous value of Q for Uranus. This comparison and the possible escape of Ariel-Umbriel from the 5:3 resonance, means that it is not unreasonable that we find no orbital resonances among these satellites.

VOYAGER OBSERVATIONS OF 1985U1. P. Thomas and J. Veverka, Cornell University.

Introduction. Of the 10 small Uranian satellites, 1985U1 is the largest and the only one for which a resolved image was obtained by Voyager 2. In terms of albedo, the other nine satellites seem to be similar to 1985U1 (Smith et al., 1986). Thus the single image of 1985U1 is important in suggesting what these other objects may be like.

Size and Shape. Figure 1 shows the limb and terminator outline of the satellite viewed from 61° latitude, 78° longitude. The limb of the satellite can be measured to subpixel precision by techniques reported by Dermott and Thomas (1986). Scans across the limb can be used to locate the edge of the disk to about 0.3 pixels. The resultant line and sample coordinates are scaled to kilometers using the range and camera focal length (Davies and Katayama, 1981). The center was located approximately from the position of the terminator and from the phase angle. Direct measurement of the long and short dimensions gives 82 km and 77 km, respectively; an ellipse fit to the limb using the same center coordinates gives axes of 78 and 76 km. Thus the satellite's average radius is somewhat less than 77 km, and, at least in the orbital plane, the satellite is not greatly elongated. The dimension perpendicular to the orbital plane is unknown.

Surface Features. One crater, approximately 45 km across, is near the terminator. Two other possible craters are visible, but there is no basis for attempting crater counts, or making any statements concerning crater morphology.

Photometry. We have used a Minnaert function to approximate the photometric behavior of the surface of 1985U1. Such an approximation works well on other Uranian satellites for which extensive data were obtained. Additionally, in the case of 1985U1, the irregular shape of the satellite introduces more serious uncertainties into any photometric analysis than do details of the photometric function employed. We sampled the disk by two methods, one a grid search of every other pixel, the other interactively selected 2×2 pixel boxes. At each point we assumed that

$$I/F = B_0\ (\alpha)\ \mu_0^{\ k}\ \mu^{\ k-1}$$

where $\pi F \cos i$ is incident solar flux, I is scattered intensity, μ_0 is the cosine of the incidence angle (i), μ is cosine of the emission angle (ε), k is the Minnaert limb darkening parameter, and α is the phase angle. Assuming an ellipsoidal shape allows a least squares fit from the Minnaert parameters of B_0 and k. The two sampling methods give nearly identical results:

$$k = 0.65 \pm 0.06 \quad B_0 = 0.043 \pm 0.002$$

These values appear reasonable. For comparison with the Moon at α = 33°, B_0 = 0.058 and k = 0.60 (Helfenstein and Veverka, 1986), while both Titania and Oberon have $k \simeq 0.7$ at this phase angle.

To obtain an estimate of the satellite's geometric albedo and normal reflectance we must extrapolate the B_0 value determined at 33° to $\alpha = 0°$. Considering the overall similarity between the physical properties of 1985U1 and those of Phoebe, a reasonable guess for β_i would be 0.024 mag/deg, the average value found for Phoebe by Thomas et al. (1983). The resulting geometric albedo would be 0.09, with $m_V = 20.5$. Of the five larger satellites of Uranus, Voyager phase data are most complete for Titania. Analysis of disk-resolved photometry shows that for Titania B_0 increases by a factor of 1.63 in going from $\alpha = 33°$ to $\alpha = 0°$, corresponding to an effective value of $\beta_i = 0.016$ mag/deg. Since Titania is considerably brighter than 1985U1, this value is likely to be a lower limit to β_i for 1985U1. Thus, $p > 0.069$ and $m_V < +20.8$, consistent with the estimate made above.

Discussion. In size and shape, as well as in albedo, 1985U1 seems to be generally similar to Saturn's satellite Phoebe. (The average radius of Phoebe is about 110 km.) Although we lack spectral data on 1985U1, if this satellite resembles the other satellites of Uranus for which data are available (Smith et al., 1986), then it has an almost neutral gray color very similar to that of Phoebe. The importance of the 1985U1 image is that it provides the best tie-in of the normal reflectance of any of the newly discovered satellites with that of the five larger ones and with that of the rings. In this respect 1985U1 is considerably darker than the darkest of the larger satellites (Umbriel) and is a little brighter than the currently accepted albedo for the ring particles (about 0.05, according to Smith et al., 1986).

This research was supported by NASA grants NSG 7156 and NAGW-111.

REFERENCES

Davies, M. E., and F. Y. Katayama (1981). Coordinates of features on the Galilean satellites. J. Geophys. Res. 86 (A10), 8635-8657.

Dermott, S. F., and P. C. Thomas (1986). The shape and internal structure of Mimas. For submission to Icarus.

Helfenstein, P., and J. Veverka (1986). Photometric properties of lunar terrains derived from Hapke's equation. For submission to Icarus.

Smith, B. A., L. A. Soderblom, R. Beebe, D. Bliss, J. M. Boyce, A. Brahic, G. A. Briggs, R. H. Brown, S. A. Collins, A. F. Cook II, S. K. Croft, J. N. Cuzzi, G. E. Danielson, M. E. Davies, T. E. Dowling, D. Godfrey, C. J. Hansen, C. Harris, G. E. Hunt, A. P. Ingersoll, T. V. Johnson, R. J. Krauss, H. Masursky, D. Morrison, T. Owen, J. B.Plescia, J. B. Pollack, C. C. Porco, K. Rages, C. Sagan, E. M. Shoemaker, L. A. Sromovsky, C. Stoker, R. G. Strom, V. E. Suomi, S. P.Synnott, R. J. Terrile, P. Thomas, W. R. Thompson, J. Veverka (1986). Voyager 2 in the Uranian system: Imaging science results. Science 233, 43-64.

Thomas, P., J. Veverka, D. Morrison, M. Davies, and T. V. Johnson (1983. Phoebe: Voyager 2 observations. J. Geophys. Res. 88, 8736-8742.

Thomas, P., J. Veverka, and S. Dermott (1986). Small Satellites. In Satellites (J. Burns and M. Matthews, eds.), U. of Arizona Press, Tucson, pp. 802-835.

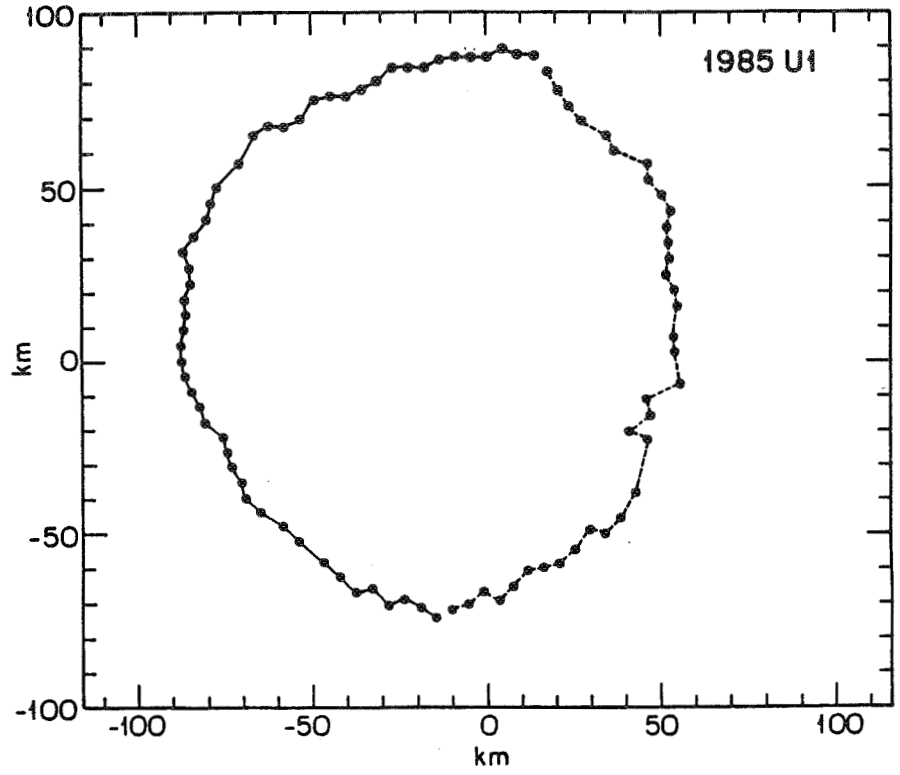

Figure. Outline of limb and terminator of 1985U1. Terminator points connected by dashed lines.

1985U1 Summary

Orbit:	a = 86000 ± 50 km
	P = 18.3 hrs
Spin Period:	Probably synchronous (18.3 hrs)
Size/Shape:	Apparent radii in image: 82 × 77 km
	Ellipse fit: 78 × 76 km
	Average radius: < 77 km
Photometry:	Minnaert parameters at $\alpha = 33°$ $\begin{cases} B_0 = 0.043 \pm 0.002 \\ k = 0.65 \pm 0.06 \end{cases}$
	Estimated geometric albedo 0.07-0.09
	Estimated opposition magnitude m_V ~ +20.5-21

Kinematics and Dynamics of the Uranian Rings

Richard G. French
Dept. of Earth, Atmospheric, and Planetary Sciences
Massachusetts Institute of Technology

A. Test of Self-Gravity Model of Apse Alignment

We have tested the self-gravity model of apse alignment by comparing its predictions about structure within the epsilon ring with an extensive set of observed occultation profiles covering a wide range of ring longitudes. According to the self-gravity model of Goldreich and Tremaine (1979), given a radial mass distribution at one ring longitude, there is a unique distribution of eccentricities across the ring necessary to maintain locked precession. A specific prediction for the epsilon ring is that the radial opacity distribution near periapse and far from periapse would differ significantly, and in particular that the eccentricity gradient across the ring would not be uniform. However, Voyager occultation observations near periapse (Sigma Sgr egress) and near quadrature (radio occultation egress) show very similar shape. The self-gravity model predicts that the near-periapse profile will have its greatest opacity in the inner half of the ring, whereas the observations clearly show that the near-periapse profile has its greatest opacity in the outer half of the ring, just as the near-quadrature profile does.

We conclude that the self-gravity model as presently constructed is inconsistent with the observations. An additional strong test of the model will be possible if the surface mass density of the epsilon ring can be estimated. The model strongly constrains the ring mass by the requirement that the torque on each ring element be just sufficient to maintain the locked precession.

B. Lindblad Resonance Survey

During the past year, we determined that the delta ring has perturbations that are well matched by an m = 2 Lindblad resonant perturbation (French et al., 1986b). Based on the information available at the time, we attributed the perturbation to an unseen small satellite inside the orbit of Miranda. No such satellite was found during the Voyager encounter, but from analysis of the Voyager trajectory the mass of Uranus was determined quite accurately (Tyler et al., 1986). They found a mass ratio of the sun to Uranus of 22905.39 $\pm$ 0.24, whereas we had used Standish and Campbell's (1984) value of 22951 $\pm$ 7, which now appears to be in error by about six times its stated error. The important

consequence is that the mean motion of the m = 2 perturbation pattern corresponds to a resonancce radius lying within a few km of the radius of the delta ring, rather than 41 km away, as we had concluded from the less accurate Uranus mass value. It now seems possible that the delta ring exhibits an internal instability of the sort described by Borderies et al. (1985). Whether or not this is the case can best be settled by determining the ring radii to an accuracy of about one km, to see if the resonance truly does lie within the delta ring. This will be done during the coming year. An addition important test is to see if the Voyager occultation observations match the perturbation pattern found using earlier earth-based observations.

C. Shepherd Satellite Ring Perturbations

We are continuing our investigations of variations of ring width as a function of ring longitude and correlated these results with radial perturbations. In order to do this, we will use occultation observations obtained during May 1985 (French et al., 1985), April 1986, and from Voyager to map the rings in width and radius. This will be the major emphasis of our research in the coming year.

D. Ring Orbit Model Enhancement

We have enhanced our kinematical model of the Uranian ring orbits (French et al., 1986a) to accommodate Voyager observations as well as ground-based occultation observations. Most of the past year has been spent on the development and careful testing of this major extension to our existing computer code. The work is now complete, and we are now able to fit for all ring elements, the direction of the planetary pole, and J2 and J4, using the complete set of earth-based and spacecraft observations. We have tested our results very carefully by writing two sets of independent code, and cross-checking intermediate results with the Voyager Navigation Team, the radio science group at Stanford, and with Philip Nicholson at Cornell. We are in the process of performing a definitive set of orbit fits. Much of our effort will involve sensitivity studies to determine realistic uncertainties for the derived orbital elements.

References

Borderies, N., P. Goldreich, and S. Tremaine (1985). A granular flow model for dense planetary rings. Icarus 63, 406.

French, R. G. et al. (1985). The 4 May and 24 May 1985 occultations by the Uranian rings. Bull. Amer. Astron. Soc., 317, 718.

French, R.G., J.L. Elliot, and S.E. Levine (1986a). Structure of the Uranian rings. II. Ring orbits and widths. Icarus 67, 134.

French, R. G., J.A. Kangas, and J. L. Elliot (1986b). What perturbs the gamma and delta rings of Uranus? Science, 231, 480.

Goldreich, P., and S. Tremaine (1979). Precession of the epsilon ring of Uranus. Astron. J., 84, 1678-1691.

Standish, E. M. and Campbell, J. K. (1984). The masses of the outer planets. Bull. Amer.Astron. Soc.,16,722.

Tyler, G. L. et al. (1986). Voyager 2 radio science observations of the Uranian system: Atmosphere, rings, and satellites. Science, 233,79.

CHAPTER 2

OUTER PLANETS AND SATELLITES

Shapes of Small Satellites. P. Thomas, Cornell University

The accurate measurement of limb coordinates on small satellites is the major technique for evaluating their sizes and shapes in the absence of good stereoscopic image coverage. The shapes of satellites may be clues to their internal structure if they are relaxed into ellipsoids (Dermott and Thomas, 1986). Small satellites appear not to be relaxed and hence their shapes may not help in estimating density or moments of inertia. The distinction between irregular and ellipsoidal satellites can now be made quantitatively with the availability of many accurate limb profiles of satellites. The limb profiles are found to subpixel accuracy (Dermott and Thomas, 1986) and can be fit by ellipses to approximate an average size and shape. The residuals from these fit ellipses provide a convenient and quantitative measure of the topography on the satellites. The standard deviation of the residuals as a fraction of the satellite's radius gives a measure of the departure from a smooth form. Departures from gravitational (and tidal) equipotentials would be greater, but on the average this is a good measure of the relaxed or non-relaxed nature of the shape of the object. Figure 1 plots the standard deviation of residuals of limbs for many small satellites, some of which are averages of several different views; there are many more data to be included for Phobos and Deimos. Mimas, a thoroughly studied equilibrium triaxial ellipsoid, is included, as are preliminary data from the Uranian satellites (Thomas et al., 1986).

The outstanding feature of this plot is the random distribution of shapes for objects smaller than Mimas, and the very smooth forms of larger satellites. The abrupt transition is probably due to a combination of the effects of the ratio of gravitational binding energy (varies as r^5) to the strength binding (varies as r^3) as well as greater relaxation of forms on larger objects due both to higher gravity as well as slight thermal gradients within the objects.

The limb topography is also related to specific forms on the objects, and a systematic survey of these forms on small and larger objects is underway.

This work is supported by NASA Grant NAGW-111.

Reference:

Dermott, S. F., and Thomas, P. (1986). The shape and internal structure of Mimas. For submission to Icarus.

Thomas, P., J. Veverka, T. V. Johnson, and R. Hamilton Brown (1986). Voyager observations of 1985U1. For submission to Icarus.

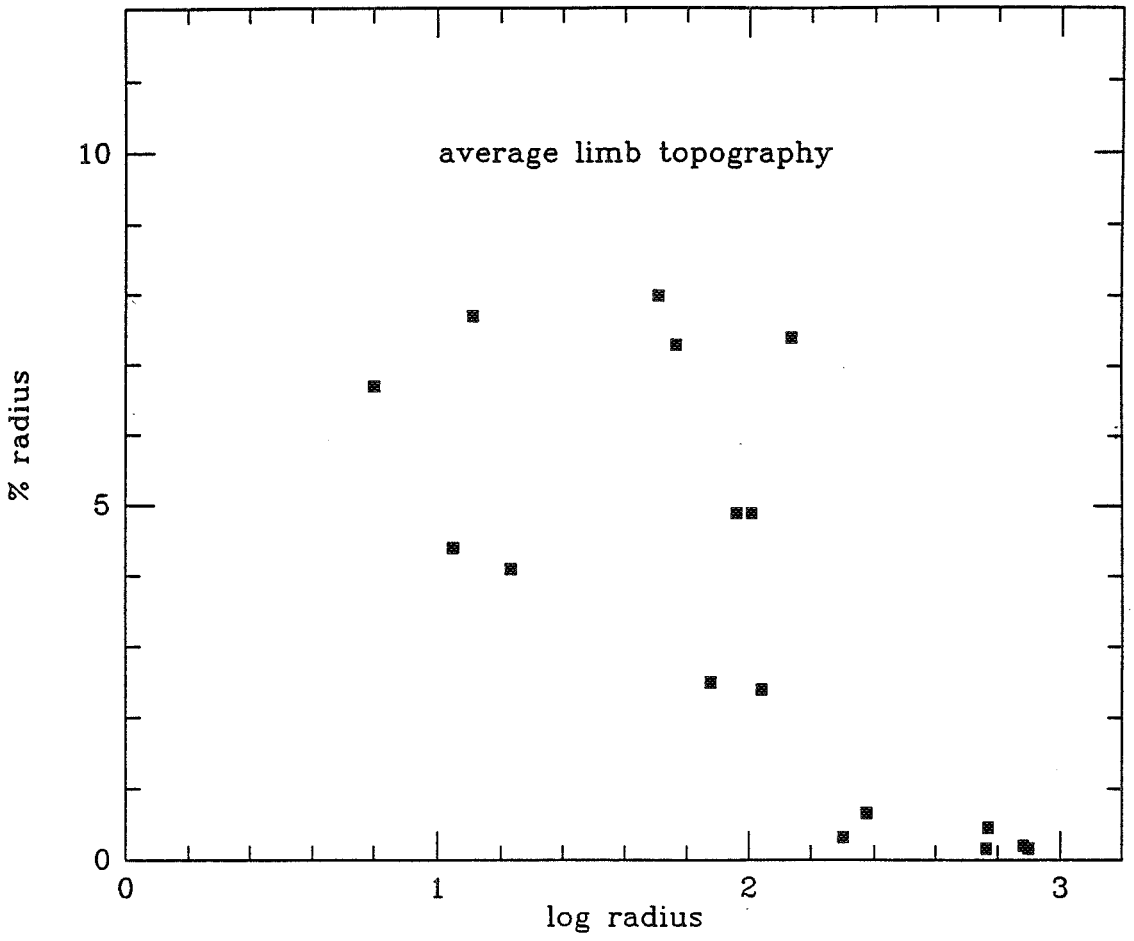

Figure. Standard deviations of limb profiles from fit ellipses. Deviations from equipotential surfaces would be slightly greater. Some data points are averages from several pictures as different perspectives of the same satellite can give very different results. The satellites are Phobos, Deimos, Calypso, 1980S6, Amalthea, Phoebe, Hyperion, Janus, Epimetheus, Mimas, and the major Uranian satellites (Uranian satellite data from Thomas et al., 1986). Other large satellites would plot even closer to the X axis than Mimas and Uranian satellites.

ACCRETIONAL HEATING OF THE SATELLITES OF SATURN AND URANUS

Steven W. Squyres, Cornell University, Ithaca, NY 14853; Ray T. Reynolds and Audrey L. Summers, NASA Ames Research Center; and Felix Shung, Sterling Software, Inc.

Voyager images of the satellites of Saturn and Uranus have shown that these bodies are characterized by remarkable diversity and surprisingly complex geologic histories. Despite their small sizes, a number of the satellites show unambiguous evidence for resurfacing. Satellites that have clearly undergone at least one episode of resurfacing include Enceladus, Dione, Miranda, Ariel, and Titania [1,2]. Less compelling evidence has also been presented for resurfacing on Mimas and Rhea. In the case of Enceladus and perhaps Ariel, tidal dissipation may have been largely responsible for heating the satellites. The energy source that apparently led to melting in the other satellites, however, is less clear. For all the satellites, long-lived radiogenic heating is entirely inadequate to produce melting. We have therefore turned to investigation of accretional heating as a possible energy source. Numerous models of accretional heating of planetary bodies have been developed previously, especially for the terrestrial planets. All such models suffer from a need to select preferred values of critical model parameters in order to obtain meaningful results. Our goal here has been to develop a detailed model for the heating of these small satellites, and then to explore the consequences of variations in the free parameters in the model. Specifically, we attempt to determine for what range of conditions melting will occur in these satellites. Along with varying a number of model parameters, we also consider the important effects of inclusion of small amounts of ammonia and (in the case of the uranian satellites) methane in the system.

We begin with a swarm of bodies from which the satellite will accrete. We allow accretion to take place gravitationally, calculating the amount of heat deposited, the depth over which it is deposited, the subsequent transport of heat within the satellite, the rate of growth of the satellite, and the satellite's evolving internal thermal profile. We consider two reservoirs of particles from which a satellite may accrete: bodies in orbit about the planet (cis-planetary debris) and bodies in orbit about the sun (trans-planetary debris). The initial surface density σ_c of the cis-planetary particle disk is obtained by distributing the present mass of the satellite over an annular region centered on the planet, with inner and outer radii at the distances at which the gravitational attraction of the present satellite is balanced by the attractions of its inner and outer nearest neighbors, respectively. The surface density σ_t of the trans-planetary disk is determined by similarly distributing a small fraction β of the planet's mass over a sun-centered annular region. The impacting particles are assumed to have a density equal to that of the present satellite, and to have a size distribution of the form:

$$\frac{\partial \dot{N}(r_p)}{\partial r_p} \propto {r_p}^{-\alpha} \tag{1}$$

where $\dot{N}(r_p)$ is the number flux of particles of radius r_p, and α is a constant.

In calculating the accretion rate and the impact velocity of the impactors from both particle disks, we follow the formulation of Safronov [3]. We use the Safronov parameter θ_c for the cis-planetary disk, defined by

$$\theta_c = GM_s/R_s{u_c}^2 \tag{2}$$

where G is the gravitational constant, M_s is the mass of the satellite, R_s is the radius of the satellite, and u_c is the velocity of an impactor relative to the circular orbit. The Safronov parameter is related to the eccentricity of the particles in the disk, and is a free parameter in the model. It then follows that the impact velocity v_c is given by

$$v_c = \sqrt{{u_c}^2 + 2GM_s/R_s} \tag{3}$$

and that the mass flux $\dot{M}_c$ is given by

$$\dot{M}_c = \frac{4\pi(1+2\theta_c)}{P_s}\sigma_c {R_s}^2 \tag{4}$$

where P_s is the satellite's orbital period. Following Kaula [4], we also define similar expressions for v_t and $\dot{M}_t$, the impact velocity and mass flux for debris from the trans-planetary disk.

Having developed expressions for the size distribution, impact velocity, and mass flux of particles from both sources, we then calculate deposition of thermal energy by the impact process. We assume that some fraction η of an impactor's kinetic energy is deposited beneath the satellite's surface; η is another free parameter in the model. When an impact takes place, a roughly hemispheric shock wave centered on the impact point is generated. As it passes through the material of the satellite, energy is deposited in that material. The specific energy deposited is largest near the impact, and decreases monotonically with distance from the impact point. We have solved the Rankine-Hugoniot equations for the deposition of specific energy by shock passage, using published experimental data on shock propagation through H_2O ice. The specific energy ϵ deposited as a function of distance r from the impact point is taken to be

$$\epsilon = \epsilon_o (r_i/r)^\gamma \tag{5}$$

where r_i is the impactor radius. Solution of the Rankine-Hugoniot equations for ice show that an expression of this form is appropriate, and give a value of $\gamma = 3.1$. Energy deposition is described by eq. (5) out to the point at which the shock pressure drops below the Hugoniot elastic limit for ice [5], and beyond that point is assumed to be zero. Impacts are assumed to be uniformly distributed over the satellite. Energy deposition is integrated over depth and over the particle size distribution for both impactor sources, so that the total energy deposition as a function of depth is obtained.

The satellite is allowed to grow, increasing in radius as it depletes the particle disks from which it is growing. Simultaneously, we solve the heat conduction equation for the growing satellite, allowing heat to be transported in response to internal thermal gradients. The thermal parameters used are those appropriate for H_2O ice. Near the surface, heat transport will also be significantly influenced by the physical mixing that takes place due to impacts, introducing an additional effective thermal diffusivity. The effective diffusivity due to impact mixing at a depth z is given by

$$K(z) = \frac{1}{2}\dot{n}_z z^2 \tag{6}$$

where $\dot{n}_z$ is the number of times a layer of depth z is turned over by impacts per unit time. We have developed an expression for $K(z)$ based on the regolith mixing model of Gault *et al.* [6]. Growth of the satellite takes place until the source of impactors is exhausted. The free parameters in the model are then β (the fraction of the planet's mass in the trans-planetary disk), θ_c and θ_t (Safronov parameters for impactors in both disks), α (the particle size distribution exponent), and η (the impactor kinetic energy partitioning coefficient).

We have performed two sets of calculations. In the first, we have done a large number of calculations of accretional heating of Saturn's satellite Rhea, allowing for large variations in all the paramters of interest. A sample result is given in Figure 1, for $\beta = 0.001$, $\theta_c = 4$, $\theta_t = 4$, $\alpha = 3.0$, $\eta = 0.2$, and $\gamma = 3.1$. Reasonable variations in β have a negligible effect on the results. Even placing 10% of the mass of Saturn in the trans-planetary nebula has little effect; the reason is that the timescale for accretion from the cis-planetary disk is very short in comparison to that for the trans-planetary disk. Variations in θ_c are important. For large values of θ_c (*i.e.*,

for low impactor eccentricities), accretion times are extremely short; for example, $\sim$ 200 yr for $\theta_c = 50$. Impact velocities are also low, so energy is deposited only very near the surface. In contrast, low values of θ_c lead to longer accretion times ($\sim$ 5000 yr for $\theta_c = 2$), and deeper deposition of energy. Variations in α are also important; smaller values of α mean that more of the mass flux is in large impactors and increases the amount of energy deposited at depth. As one would expect, variations in η have a significant effect on the peak internal temperature achieved.

In the second set of calculations, we have calculated accretional temperature profiles for the inner major satellites of Saturn (Mimas – Rhea) and for all the major satellites of Uranus. The maximum temperatures achieved are: Mimas 83 K, Enceladus 93 K, Tethys 145 K, Dione 158 K, Rhea 195 K, Miranda 82 K, Ariel 164 K, Umbriel 160 K, Titania 214 K, Oberon 199 K. Given the uncertainties in the input parameters, these temperatures may be uncertain by as much as a few tens of degrees. It is clear that temperatures will never exceed 273 K, so melting would not be expected if the satellites were made of pure H_2O ice. However, it is probable that the saturnian satellites contain some NH_3, and it is possible that the uranian satellites also contain some CH_4. A peritectic melt will form in the H_2O – NH_3 system at a temperature of 173 K, and it has been suggested that ice containing CH_4 could be substantially mobilized at temperatures as low as 100 K [7]. Given the uncertainty in the calculations and the likelihood of NH_3 in the saturnian satellites and CH_4 in the uranian satellites, these calculations suggest that, among these satellites, only Mimas and Enceladus cannot have undergone resurfacing as a result of accretional heating.

References: [1] Plescia, J.B., and Boyce, J.M., *Nature* **295**, 285 (1982); [2] Smith, B.A., *et al.*, *Science* **233**, 43 (1986); [3] Safronov, V.S., NASA TT F-677 (1972); [4] Kaula, W.M., *J. Geophys. Res.* **84**, 999 (1979); [5] Gaffney, E.S., in *Ices in the solar system*, Reidel (1985); [6] Gault, D.E., *et al.*, *Proc. Lunar Sci. Conf. 5th*, 2365 (1974); [7] Stevenson, D.J., and Lunine, J.I., *Nature* **323**, 46 (1986).

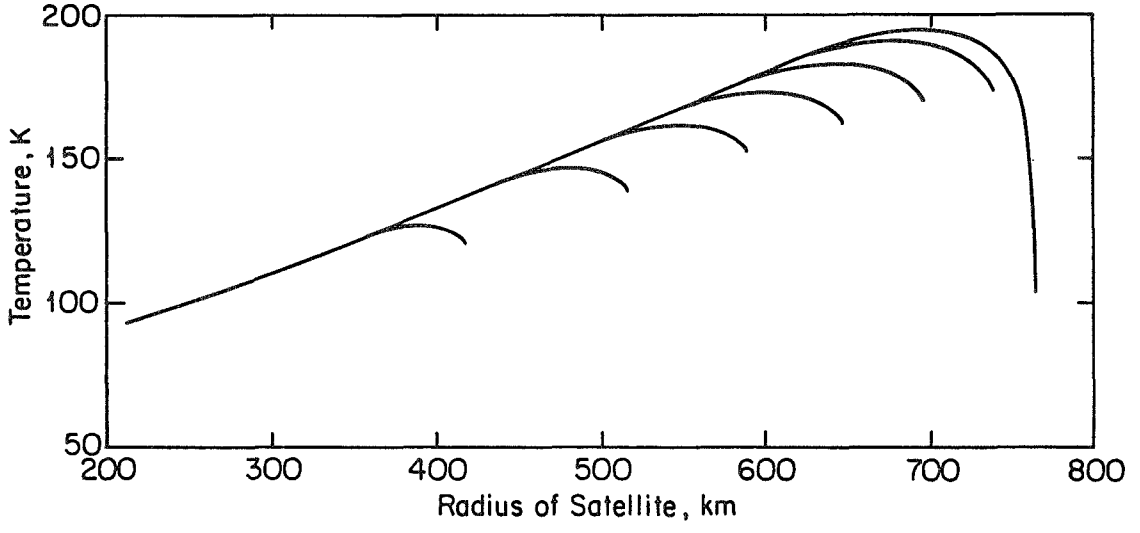

Figure 1 — Calculated thermal profiles within Rhea during accretion. Curves are plotted at equal satellite mass intervals. Total accretion time is $\sim$ 2000 yr.

INVESTIGATIONS OF THE SURFACES AND INTERIORS OF OUTER PLANET SATELLITES

Gerald Schubert
Department of Earth and Space Sciences
University of California, Los Angeles
Los Angeles, CA 90024

Studies under NSG 7315 during 1985/86 include: 1) Tidal heating and the structure and evolution of Io and Europa, 2) Crater relaxation on icy satellites using realistic non-Newtonian ice rheology, 3) Convection through phase transitions in the interiors of icy satellites. The abstracts of published papers on these subjects are reproduced below.

Tidal Heating in an Internal Ocean Model of Europa

M.N. Ross and G. Schubert, ***Nature***, in press, 1986

The tidal response of a three-layer Europa model is calculated. The model consists of an elastic lithosphere (ice shell) above an inviscid water layer (internal ocean) and an elastic core (silicate). The tidal distortion of a decoupled ice lithosphere is a factor of 2 less than previously thought. For a given dissipation factor Q (equal in the ice and silicate) tidal heating in the lithosphere is a factor of 4 less than previous estimates while tidal heating in the core is 30% less. At the current value of orbital eccentricity tidal heating is only marginally able to prevent the internal ocean from freezing; $Q<25$ is required. If Q in the silicate core equals 100 then Q in the ice lithosphere must be less than 17 for an internal ocean to be stable against freezing. If silicate $Q=25$ then lithosphere $Q<37$ is required for internal ocean stability. The persistence of an internal ocean is made somewhat more probable if a low conductivity surface layer insulates the ice lithosphere and raises near surface temperatures above the solar equilibrium value. Cyclical tidal stresses in the lithosphere are currently about 1/10 of the yield strength of ice, making it unlikely that these stresses cause the curvilinear features on Europa.

Finite Element Models of Non-Newtonian Crater Relaxation

P. Thomas and G. Schubert, ***Proc. Lunar Sci. Conf. 17th, J. Geophys. Res.***, in press, 1986.

Models of viscous crater relaxation proposed to date for the icy satellites of the outer solar system assume the behavior of a Newtonian medium, with viscosity η independent of effective stress τ. While this is reasonable if both effective stresses and temperatures are very low, laboratory data on ice indicate that, at effective shear stresses ($\tau \sim$ 0.1 *MPa*) and temperatures (~ 173K) likely to occur in regions underlying craters, non-Newtonian behavior is probable. Such material would have a viscosity-effective stress relation given by $\eta(\tau) \propto \tau^{1-n}$, where $n \approx 4$. It is likely, due to the low activation energy of ice at these temperatures,

that stress differences may affect the profile of relaxing craters to a greater extent than temperature differences. To investigate the effects of a non-Newtonian rheology on the profiles of relaxing craters, two-dimensional finite element simulations have been performed. Initially, effective stresses are highest in the region below the crater center, producing a zone of relatively low viscosity. Relaxation flow forces this region into a convex bulge as the crater relaxes. At later stages, the low viscosity region moves to beneath the crater rim, leading to enhanced relaxation of crater rims, compared to a Newtonian rheology. The reduction of effective stress as the crater relaxes increases viscosity in the region beneath the crater. As a result, relaxation rates are quite rapid compared to those in later stages. This is in marked contrast to the exponential behavior of depth with time associated with Newtonian relaxation. The short relaxation times observed for the craters modelled indicate that a silicate component may be required in the crusts of icy satellites to account for the observed crater populations.

Tidally Forced Viscous Heating in a Partially Molten Io
M.N. Ross and G. Schubert, *Icarus, 64*, 391-400, 1985.

We investigate tidal dissipative heating in two different models of Io. The partially molten asthenosphere model consists of a rigid core and a thin (less than 400km thick) partially molten "decoupling" layer (asthenosphere) surrounded by an elastic lithosphere. In the partially molten interior model the interior beneath the lithosphere is partially molten throughout. The partially molten region in each model is assumed to possess negligible shear strength and to be characterized by a Newtonian viscosity. Tidal deformation and dissipation in the core of the thin asthenosphere model are assumed negligible. Fluid in the viscous layers is forced to circulate by the tidal distortion of the outer shell, modeled here as a sinusoidal variation with time of the distortion amplitude. As a result, heat is generated in the fluid by viscous dissipation. There are two heating mechanisms in our models: "elastic" dissipation in the lithosphere $\propto 1/Q$ and viscous dissipation in the partially molten region. Numerical calculations are carried out for a 90-km-thick lithosphere with Q=100. This thickness maximizes dissipation in a decoupled lithosphere; other reasonable values of lithosphere thickness do not alter our calculations. Under the constraint that total dissipation equals the observed radiated heat loss we derive the viscosity of the partially molten region in each model. We a posteriori evaluate the assumption that the lithosphere is decoupled from the interior by calculating the distortion of an elastic shell due to the viscous stresses on the lower surface of the outer shell. If the interior viscosity is such that the total dissipation is equal to the observed heat flux from Io, viscous stresses produce negligible distortion of a 90-km-thick shell. This validates the assumption of a decoupled shell. The derived viscosity for both models is characteristic of a partially molten rock. In the thin asthenosphere model the derived

viscosity is so low that a very high degree of partial melt is necessary, about 40% crystal fraction in a 400-km-thick asthenosphere and about 0% in a 1-km-thick asthenosphere. In the partially molten interior model the derived viscosity corresponds to a magma with about 60% crystals. Consideration of convective efficiencies demonstrates the plausibility of a stable thermal steady state for both models. A significant portion (75% for Q = 100) of Io's tidal heating can be the result of viscous dissipation in a partially molten region that decouples the outer shell from the interior. The partially molten layer can be considered a "global magma ocean."

Phase Transistions and Convection in Icy Satellites
D. Bercovici, G. Schubert, and R.T. Reynolds,
Geophys. Res. Lett., 13, 448-451, 1986.

The effects of solid-solid phase changes on subsolidus convection in the large icy moons of the outer solar system are considered. Phase transitions affect convection via processes that distort the phase change boundary and/or influence buoyancy through thermal expansion. Linear stability analyses are carried out for ice layers with a phase change at the midplane. Two exothermic phase transitions (ice I - ice II, ice VI - ice VIII) and two endothermic transitions (ice I - ice III, ice II - ice V) are considered. For the exothermic cases, the phase change can either impede or enhance whole-layer convection. For the endothermic cases, the phase change always inhibits whole-layer convection overturn and tends to enforce two-layer convection. These results place some constraints on possible models of icy satellite evolution and substructure.

Crater Relaxation as a Probe of Europa's Interior
P.J. Thomas and G. Schubert, *Proc. Lunar and Planet. Sci. Conf. 16th Planet. Sci. Conf. 16th, J. Geophys. Res., 91*, D453-D459, 1986

Viscous relaxation rates of craters are examined to discriminate among models of Europa's interior. It is shown that the presence of an insulating surface regolith is required for ice lithospheres that do not contain a liquid H_2O layer. Without the presence of such an insulating regolith, relaxation times for craters $\cong$ 100 km in diameter are excessively long (> 1 b.y.) and thus inconsistent with the absence of such features in Voyager images. Finite element calculations indicate that a thick insulating surface frost layer (raising surface temperatures $\gtrsim$ 40 K above the solar radiation ambient temperature of 92 K) allows a 25-km-thick surface viscous layer to relax $\gtrsim$ 100-km-diameter craters on the short timescales ($\cong$ 100 m.y.) required. If the icy lithosphere is 100 km thick (and without a liquid H_2O layer, but containing a subsolidus convecting region), surface temperatures need to be raised 20 K by insulation to allow relaxation of craters in this size range to occur within the required time.

FAILURE STRENGTH OF ICY LITHOSPHERES

M. P. Golombek and W. B. Banerdt (Jet Propulsion Laboratory, Caltech, Pasadena, CA 91109)

It has been widely assumed in the literature that the stresses required for brittle failure of an icy lithosphere under tension are limited by the tensile strength of intact ice. This assumption has led to the widespread use of 2 MPa (20 bars) for the extensional strength of predominantly ice lithospheres (e.g. Ganymede's), based on the unconfined tensile strength of ice near its melting temperature measured by Hawkes and Mellor (1). However, our understanding of the maximum stress levels in the earth's lithosphere are based on the frictional resistance to sliding on pre-existing fractures and not the strength of intact rock in laboratory experiments, which is always greater. Similar friction relations for ice predict maximum stresses that are substantially greater than the apparent tensile strength of intact ice near its melting temperature. At first inspection, then, it appears that ice rich lithospheres would fail under tensional stress by tensile fracture of intact ice rather than sliding on pre-existing fractures. In this abstract we will introduce lithospheric strengths derived from friction on pre-existing fractures and ductile flow laws, derive these relations for icy lithospheres, show that the the tensile strength of intact ice under applicable conditions is actually an order of magnitude stronger than widely assumed, and demonstrate that this strength is everywhere greater than that required to initiate frictional sliding on pre-existing fractures and faults.

The maximum stress levels found in the earth's crust are accurately predicted by Byerlee's law (2,3). This relation is based on laboratory measurements of the frictional resistance to sliding on pre-existing fractures, which occurs at stresses less than those required to break intact rock. Byerlee's law is of the form $t=uS_n+b$, where t is the shear stress, S_n is the effective normal stress (normal stress minus pore pressure), u is the coefficient of friction, and b is a constant. In terms of S_1 and S_3, the maximum and minimum principal effective stresses (stress minus pore pressure), Byerlee's law can be written $S_1=KS_3+B$, where $K=[(u^2+1)^{1/2}+u]^2$, B is a function of b and u, and sliding is assumed to occur on the most advantageous slip plane. Laboratory friction measurements show that u and b are virtually independent of stress (except for a slight change for rocks at 135 MPa), rock type, displacement, surface conditions, and temperature. For this application we will use the friction law for low stress determined by Byerlee (2) $t=0.85S_n$, which has been found to hold for a wide variety of geologic materials, because the appropriate low normal stress friction measurements on ice have not been made. At higher stress we use the friction data measured for ice, u=0.2 and b=10 MPa (4). The higher stress friction data for ice do constrain the applicable low stress friction law to be very close to that for rock, because the lowest normal stress measurements for ice are for S_n=17 MPa (5), which constrains the low stress friction law, that also must pass through the origin, to have a slope only marginally different ($u\geq0.79$) from that determined for rocks (u=0.85). In order for fluid pore pressure to decrease the friction on pre-existing faults and fractures, thereby changing the slope of the brittle yield stress versus depth curve, liquid water must fill the connected pore space. This is not likely to have occurred on the icy satellites given the extremely low surface temperatures (less than 100^{o}K) and reasonable thermal gradients. Because the vertical stress is generally quite close to the lithostatic load (density times gravity times depth) in areas of low relief, this relation

predicts a linear increase in yield stress with depth (Fig. 1).

With increasing temperature, rock and ice deformation occurs by ductile flow. Flow laws for rocks, minerals, and ice have been experimentally determined for stresses up to 1-2 GPa and strain rates down to 10^{-8}/sec. These results can be extrapolated to geologic strain rates via creep equations which generally are of the form $de/dt=A(S_1-S_3)^n exp(-Q/RT)$, where de/dt is the strain rate, R is the gas constant, T is absolute temperature, and A, Q (the activation energy), and n are experimentally determined constants. As a result the ductile strength is negligible at depths where T is high and increases exponentially with decreasing depth. We have used the experimentally determined flow parameters (6,5) for pure ice I_h, $A=1.2x10^{-24}/sec\text{-}Pa^4$, $Q=4.5x10^4$J/mole and n=4.0 extrapolated to geologic strain rates of 10^{-15}/sec (about 3%/m.y.). A surface temperature of 100°K and a thermal gradient of 1.6°/km applicable to the early high temperatures likely in some of the larger icy satellites (e.g. Ganymede, 7) yields the strength envelope illustrated in Fig. 1. It has been shown at high temperatures (i.e. polar conditions on the earth) that the inclusion of a small amount of silicates will greatly increase the creep strength of ice I_h (8). The amount of hardening from the inclusion of small amounts of silicates in the lithospheres of the icy satellites is not known, but for lack of a better constraint we will assume that the hardening resulting from the addition of less than a few percent of silicates in icy satellites lithospheres can be bracketed by an order of magnitude increase in creep strength (e.g. 9).

The failure criterion for a given depth in the lithosphere is determined by the weaker of the frictional or ductile strength at that depth. The yield stress increases with depth according to Byerlee's law until it exceeds that calculated using the appropriate flow law, after which it decreases exponentially with depth. The intersection of the brittle and ductile yield stress curves defines the brittle-ductile transition depth and also the peak stress needed to cause failure of the entire lithosphere. As a result the peak stress needed for lithospheric failure is dependent on the thermal gradient, which causes the ductile flow law to intersect the friction curve at different depths (shallow for high thermal gradients, deep for low thermal gradients). These peak stresses are probably somewhat greater than those actually required to cause failure of the lithosphere because semibrittle and low temperature ductile processes tend to round off the intersection points between the brittle and ductile curves (10).

As can be seen in Fig. 1, the peak stress needed to cause tensile failure of the lithosphere using the above parameters is on the order of 10 MPa (100 bars), although the average stress in the lithosphere is only about half that value. This strength is applicable for large icy satellites (e.g. Ganymede). We have also determined strengths for the smaller icy satellites of Saturn using the appropriate gravities, densities, surface temperatures, and calculated thermal profiles (11) and found all strengths are substantially larger than this value. As a result this value is probably a minimum for the lithospheres of the icy satellites.

Note that this peak stress (10 MPa) is significantly higher than the tensile strength of about 2 MPa used in virtually all previous studies, which is based on the the unconfined tensile fracture strength of ice near its melting temperature. Because failure should occur by the mechanism requiring the lowest stress, it would appear on first inspection that tensile fracture of intact ice is the relevant mode of fracture for icy satellites. However it can be shown using a Griffith failure criterion and taking the vertical lithostatic load into account that the stress difference for failure due to the tensile fracture of intact material at depth z is given

by $S_1-S_3=S_o+pgz$ for $S_1-S_3<4S_o$ and by $S_1-S_3=4[(S_opgz+S_o^2)^{1/2}-S_o]$ for $S_1-S_3>4S_o$, where p is density, g is gravitational acceleration, and S_o is the unconfined tensile strength (e.g. 12). The first of these relations describes the opening of tension cracks, which occurs when the confining pressure is relatively low. The second relation describes shear failure in tension (or compression), which is the mode of failure when the confining pressure is too great for open tension cracks to form. The depth of transition between the two modes of tensile failure is given by $z=3S_o/pg$ (about 5 km for S_o=2.5 MPa on a satellite with a gravitational acceleration similar to that of Ganymede). The curve for failure due to fracture of intact ice is plotted in Fig. 1, where it can be seen that frictional failure is preferred at all depths for the assumed material parameters of ice. This conclusion is borne out by the experimental results, in which ice samples failed due to frictional sliding along pre-existing saw cuts rather than initiating new fractures (4). Note also that if the tensile fracture strength of intact ice increases with decreasing temperature, as is the case for the compressional fracture strength (13), the curve for fracture of intact ice under tension will move to the left and frictional failure will be even more favorable. Similar results are also obtained for other choices of failure criteria. Thus the failure strength of an icy lithosphere is significantly greater than has been previously assumed.

In conclusion, because the tensile strength of intact ice increases markedly with confining pressure, it actually exceeds the frictional strength at all depths. Thus, icy lithospheres will fail by frictional slip along pre-existing fractures at yield stresses greater than previously assumed rather than opening tensile cracks in intact ice.

References (1) Hawkes & Mellor (1972) J Glaciol 11, 103. (2) Byerlee (1978) Pageoph 116, 615. (3) Brace & Kohlstedt (1980) JGR 85, 6248. (4) Beeman et al. (1984) EOS 65, 1077. (5) W. Durham, written com. (6) Durham et al. (1983) P14LPSC JGR 88, B377. (7) Golombek & Banerdt (1986) Icarus Nov. 86. (8) Baker & Gerberich (1979) J Glaciol 24, 179. (9) Friedson & Stevenson (1983) Icarus 56, 1. (10) Kirby (1980) JGR 85, 6353. (11) Ellsworth & Schubert (1983) Icarus 54, 490. (12) Jaeger & Cook (1976) Fund. Rock Mech. (13) Parameswaran & Jones (1975) J Glaciol 14, 305.

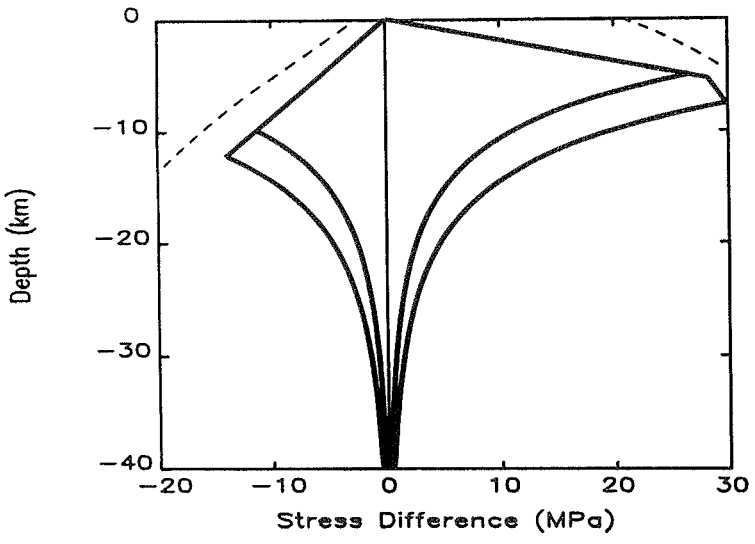

Fig. 1. Brittle and ductile yield stress versus depth curve for compression (to the right) and extension (to the left), with a peak stress of 10 MPa (see text for discussion). The dashed lines show the failure strength of intact ice as a function of depth assuming a Griffith failure criterion. Because stresses required to break intact rock are greater than those required to initiate sliding on pre-existing fractures, lithospheric failure occurs by frictional sliding on pre-existing fractures.

STUDIES OF OUTER PLANET SATELLITES, MERCURY, AND URANUS

William B. McKinnon and Paul M. Schenk, Department of Earth and Planetary Sciences and McDonnell Center for the Space Sciences Washington University, Saint Louis, MO 63130.

Ring Geometry on Ganymede and Callisto

Arguments have been made, based on geometry, for both an impact and an internal origin for the ancient, partially preserved furrow system of Ganymede. Zuber and Parmentier (1984) concluded that furrows were not concentric, but could be impact related if multiringed structures on icy satellites are initially noncircular. We examine the geometry of the Valhalla ring structure on Callisto in order to assess the circularity of an unmodified ring system. Despite prominent local meandering, the only gross deviations from concentricity in the Valhalla system are found in the outer north-east quadrant of the system. Here, a number of ring segments intersect small circles about the center at angles up to 30°. The Ganymede furrow system was remapped to make use of improvements in coordinate control. The least-squares center of curvature (determined using natural weighting) for all furrows in Marius and Galileo Regio is -20.7°, 179.2°. Furrows in Marius and Galileo Regio are reasonably concentric, and are much more circular than previously estimated and probably once covered at least an entire hemisphere of Ganymede. Thus we find furrow geometry is consistent with an impact origin (Schenk and McKinnon, 1986, 1987). Deviations of some furrows from concentricity about the center of curvature, on the scale of those found at Valhalla, do exist. As in the case of Valhalla these variations are principally confined to outer regions of the structure, and are interpreted as inherent properties of multiringed structures on icy satellites. The cause(s) of this may be in the ring formation mechanism itself, but are more likely due to variations in preexisting lithospheric mechanical properties. The perceived present nonalignment of the assumed originally concentric furrows has been used to argue for large-scale lateral motion of dark terrain blocks in Ganymede's crust, presumably in association with bright terrain formation. The overall alignment of furrows as well as the inherent scatter in centers of curvature for subregions of Galileo and Marius Regio do not support this hypothesis.

Primitive Material on Ganymede and Callisto

The surfaces of the two outermost Galilean satellites may record the influx of carbonaceous and "ultracarbonaceous" material in the Jupiter region (McKinnon and Schenk, 1986). Major albedo units on both satellites are spectrally red as determined by Voyager (excepting the brightest craters on Ganymede), and increasing redness is correlated with decreasing albedo and increasing crater density (age). Present optical, infrared, and microwave data indicate very ice-rich optical surfaces and regoliths, globally averaged, for both bodies. Together, these argue for the presence of an exogenic, dark, reddish, contaminant. Regionally, the darkest and reddest units on Ganymede are dark-ray craters, although they are not as dark as Iapetus dark material or even as dark as Callisto dark terrain. In some cases they are no more red than nearby dark terrain, and one large dark-ray crater, Kittu, is actually spectrally neutral (in the visible). If the rays are areal mixtures of ice-free and ice-rich materials, then the non-ice portion may in most cases be analogous to D-type "ultracarbonaceous" material, and in the case of Kittu, "ordinary" C-type material. The best model for formation of dark rays involves the creation of a lag deposit in the ejecta of projectiles of rare low velocity or composition or both (Conca, 1981). We infer the compositional class to be (mostly) either D-class asteroids or comets (possibly silicate-enriched). We cannot rule out the impact of C asteroids coupled with spectral modification by the Jovian magnetosphere, but Kittu makes this hypothesis less likely. Terrain contamination by the integrated effects of dispersed D asteroid ejecta and infalling D-type meteoritic dust is also plausible, if accumulation preceded crater retention in the heavily cratered terrains. D-type objects are also the most likely ones available in the Jovian region; C types may have only dominated Jupiter-crossing objects during dispersal of the main asteroid belt by Jupiter,

apparently near the time the protojovian nebula itself dispersed if the flat spectra of the "captured" outer Jovian satellites are to be explained. "Himalia-dust" alone cannot account for the contamination of the surfaces of Ganymede and Callisto without spectral alteration. Work on this topic is continuing.

Tectonics of Caloris Basin, Mercury

Caloris is in many ways a unique basin compared with its lunar counterparts (McKinnon, 1986a). As a multiringed basin. Although youthful and vast, most of its multiringed elements are obscured. Ring segments immediately outside the Caloris Montes lie at diameter ratios smaller than 1.4. If the ridge systems and concentric arches of the basin floor indicate buried rings, their spacings are consistent with the inter-ring distances outside the basin rim and indicate an upper limit to the thickness of the impact-defined lithosphere of ~120 km. As a volcanic center. The smooth plains fill, presumably volcanic, is extraordinarily deep if it is required to completely bury ring topography; alternatively, the mercurian lithosphere may not be as buoyant as that of the moon. Later lunar basin volcanism usually occurs near the basin periphery; at Caloris this apparently corresponds to the emplacement of the smooth plains in an annulus surrounding the basin. That this annulus may be nearly complete is supported by radar and earth-based visual observations. All these volcanic manifestations provide a model for intercrater plains formation. The only lunar analogue to this volcanic style might be the Oceanus Procellarum basalts, if they are viewed as a partial annulus surrounding the Imbrium basin. As a mascon. Topographic depression and ridge formation imply that the basin floor subsided under a load, but the predominantly concentric orientation of the ridges is not consistent with a central mascon (radial ridges are predicted) unless basement ring structure controls tectonic orientation or the scale of the load is larger than Caloris itself. The latter may be consistent with a broad withdrawl of magma to form the smooth plains, as advocated by Dzurisin (1978). The final tectonic episode appears to be uplift and extension of the basin floor, and thus any present mascon is likely to be associated with the exterior smooth plains. The effects of such a ring load were investigated (McKinnon, 1979) using the thick-plate theory of Melosh, in which shell curvature is parameterized. The main characteristics of the predicted tectonic pattern are normal faulting within the basin and thrust faulting beneath the ring load, both in agreement with observation. The dominant concentric trend of the basin normal faults is consistent with the ring load hypothesis provided the elastic lithosphere of Mercury was $\lesssim$125 km thick at the time of faulting. Although this solution is approximate due to the great scale of the structure compared to Mercury's radius, it suggests that central concentric normal faults are characteristic of annular loading in the long-wavelength limit. (The dominant long-wavelength component of the annular load is second order, and thus equivalent to the tidal despinning problem. Concentric normal faults within the basin are predicted in this case.) Simple updoming within the basin would produce normal faults of predominantly radial orientation. A lower limit to the elastic lithosphere thickness (~75 km) is set by requiring sufficient deviatoric stress to initiate faulting for reasonable load magnitudes (consistent with photogeological observation, radar subsidence profiles, and limits to the contribution to J_2).

Microwave Interferometry of the Deep Atmosphere of Uranus

A less-appreciated feature of the Uranian microwave spectrum is its apparent flatness at wavelengths longward of ~6 cm. From the suite of measurements made by various workers during 1978-1979 (the Uranus spectrum can be time-variable), averaged brightness temperatures at 6, 13, and ~20 cm can be estimated as 251±5, 255±18, and 265±45 K. The last figure includes a strenuous attempt to measure the 21-cm brightness temperature with the Owens Valley three-element interferometer. Eighty hours of integration over five days yielded a value of 240±63 K (McKinnon et al., 1981). More recent higher-precision VLA measurements by Jaffe et al. (1984) and de Pater (Gulkis and de Pater, 1984) give brightness temperatures ranging between ~225-235 K at 6 cm and ~240 at 21 cm, suggesting that the averages above were biased upward or that the decimeter flux has fallen in recent years. In either case there is no evidence that the spectrum is steeply rising with

wavelength, and it may well be flat. We originally considered three explanations: a subadiabatic region, a high surface, and a rapid increase in microwave absorption below some level. The first two were rejected on physical grounds. I examine the last by calculating theoretical brightness temperatures by standard methods, incorporating the Voyager 2 radio occultation profile as the upper boundary condition (McKinnon, 1986b). One class of model atmosphere has only molecular hydrogen and water vapor as opacity sources. (This may actually occur if a super-massive water cloud [>several 100 x solar adundance] traps essentially all the available ammonia deep in the cloud.) As long as the water abundance is greater than a few times solar, then the calculated spectrum is rather flat, ranging between ~270 and ~290 K as the wavelength varies from 6 to 21 cm. Although this spectrum is two warm to fit the decimeter data, emission from a water-cloud deck may account for the 270 K warm regions seen in 6-cm VLA maps. The decimeter brightness spectrum requires that the water abundance of the deep atmosphere not be so great that a sensible amount of ammonia vapor is not distributed between the base of the water-ice cloud and the top of the probable NH_4SH cloud. Including ammonia in the brightness temperature modeling, using abundance profiles calculated by S.K. Atreya (in the manner of Atreya and Romani [1985]) and Fegley and Prinn (1985), shows that disk-averaged brightness temperatures in the 6-21 cm range are well fit by a deep atmosphere with abundances of water and ammonia of ~20 x solar. In this sense, ammonia has been detected on Uranus. Any global abundance determination is suspect, however, because the disk-resolved VLA maps show strong latitudinal variation in ammonia abundance. Perhaps the polar regions, which are ammonia-free at the wavelengths discussed here, are more representative of the deep atmosphere, thus implying a much greater enhancement in water and ammonia (>several 100 x solar) at deep levels. The detectable ammonia in the Uranian atmosphere at equatorial and mid-latitudes may be due to convective lofting.

Ackowledgement. Research on outer planet satellites is supported by NASA grant NAGW-432. Research on Mercury and Uranus is a continuation of long-standing work, and is independently supported.

References

Atreya S.K. and P.N. Romani (1985) In Recent Advances in Planetary Meteorology, 17-68; Conca J. (1981) Proc. Lunar Planet. Sci. Conf. 12B, 1599-1073; Dzurisin D. (1978) J. Geophys. Res. 83, 4883-4906; Fegley B. and R.G. Prinn (1985) Nature 318, 48-50; Gulkis S. and I. de Pater (1984) In Uranus and Neptune, NASA Conf. Pub. 2330, 225-262; Jaffe W.J., G.L. Berge, T. Owen and J. Caldwell (1984) Science 225, 619-621; McKinnon W.B. (1979) Eos Trans. AGU 60, 871; McKinnon W.B. (1986a) Mercury Conference Abstracts, 18; McKinnon W.B. (1986b) Bull. Am. Astron. Soc. 18, 765; McKinnon W.B. and P.M. Schenk (1986) Eos Trans. AGU 67, 1073; McKinnon W.B., G.L. Berge and D.O. Muhleman (1981) Eos Trans. AGU 62, 941; Schenk P.M. and W.B. McKinnon (1986) Bull. Am. Astron. Soc. 18, 759-760; Schenk P.M. and W.B. McKinnon (1987) Icarus, submitted; Zuber M.T. and E.M. Parmentier (1984) Icarus 60, 200-210.

SO_2 ON IO: A THERMODYNAMIC PERSPECTIVE

Aaron P. Zent and Fraser P. Fanale, Planetary Geosciences Division, Hawaii Institute of Geophysics University of Hawaii, Honolulu, Hawaii

The presence of condensed SO_2 on Io mandates a finite abundance of SO_2 vapor which must be present, regardless of plume activity. Currently, even the order of magnitude of the ambient SO_2 pressure is unknown. However, a number of models indicate that the pressure may be near saturation much of the time. Among the models that suggest atmospheric pressure does not approach saturation is that of Matson and Nash, [1983], who base their model in part on the argument that Io's surface must have a very high porosity, and in part on the argument that the particulate material in Io's volcanic plumes has a very fine grain size. This implies that a significant amount of cold, particulate, surface area is likely to be in diffusive contact with an SO_2 atmosphere that probably at least approaches saturation locally.

These conditions indicate that adsorption of SO_2 may be important SO_2 adsorbate. We have measured the adsorption of SO_2 on particulate sulphur, and examined the equilibrium between adsorbed SO_2, SO_2 vapor, and SO_2 ice based upon our measurements and simple thermodynamic considerations.

Measurements of SO_2 adsorption on particulate sulphur at conditions near those of Io were made on a Numinco Model MIC 103 00R Surface-Area Pore-Volume Analyzer. Adsorption data were gathered at 178K, 193K and 225K. These are higher than surface temperatures on Io, which peak around 130K. The SO_2 vapor pressure (1 to 10^3Pa) also exceeds Io surface pressures. The adsorptive behavior of the system must be extrapolated to Io conditions.

The most rigorous extrapolation method of which we are aware is one presented by Anderson et al. [1967]. They showed that it is possible to compute adsorption isotherms for temperatures below those covered in adsorption measurements via the equation

$$\ln\left[\frac{(P^a/P^i)_2}{(P^a/P^i)_1}\right] = \frac{(\Delta H_{va} - \Delta H_{vi})\,(T_2 - T_1)}{RT_1T_2} \qquad (1)$$

Where P^a and P^i are the vapor pressures over the adsorbed phase and the solid phase, respectively. The subscript 1 refers to state variables at condition 1, where data are available, and 2 refers to state variables at condition 2 for which we would like to calculate the relative vapor pressure. ΔH_{va} is the change in partial molar enthalpy in going from the vapor to the adsorbed phase, and ΔH_{vi} is the same quantity for the vapor to ice phase change.

In order to use Eq.(1), we must know $\Delta H_{vi}(T)$ and, from the data, we must find $\Delta H_{va}(T)$. ΔH_{va} is found by solving the Clausius-Clapeyron equation at points of constant adsorptive coverage. Since the data are not at constant adsorptive coverage we must fit a curve to the data and read equilibrium pressures at constant adsorptive coverage from that.

We are then able to extrapolate our adsorption isotherms to lower temperatures via Eq.(1). In all cases, our isotherms agree with the data to better than a factor of 2.5; the average precision of the data is ±50%.

At a fixed temperature, the equilibrium vapor pressure over adsorbed SO_2 may be thought of as an extensive property of the system; it increases as the mass of SO_2 in the system increases. The equilibrium vapor pressure over ice however is intensive; it does not matter how much SO_2 is in the solid phase, the vapor pressure depends only on temperature. That means that at a fixed temperature, there is a maximum adsorptive coverage, which occurs at the point at which the equilibrium

vapor pressure over the adsorbed phase is equal to the vapor pressure over ice. Thereafter, any additional SO_2 present in the system must exist as ice.

We should now be able to calculate the maximum adsorptive coverage in terms of volume of SO_2 per unit mass of sulphur, although we consider this an intermediate data product. We would really like to know the maximum coverage of SO_2 in terms of number density *per unit surface area* of sulphur (i.e. the monolayer coverage). We need to represent our results in this way because the specific surface area of S on Io is unconstrained, but the upper limit on the number density of the coverage, which is more closely related to the chemical potential, must be the same in the laboratory as on Io.

Fortunately, adsorption measurements provide concurrent measurements of specific surface area through application of BET theory [Brunauer et al., 1938]. We calculate BET surface areas, assuming the size of the adsorbed SO_2 molecule is ~ $30A^2$. We use the mean specific surface area of ~ 5×10^{-3} m^2 g^{-1} indicated in our analysis to calculate maximum coverage for sulphur at Io conditions.

This relationship is shown in Figure 1, along with the data. Each of the isotherms is truncated against the vapor pressure curve for SO_2 ice (solid line). A very simple expression can be written to describe the maximum amount of adsorbed SO_2 per square meter of sulphur, at any temperature.

$$\text{Max } \rho_a = \exp(aT-b) \qquad (2)$$

where a = 0.1673 K^{-1}, and b = 33.89, and ρ_a is the density of adsorbed SO_2 in terms of g SO_2 m^{-2}S. If the maximum surface temperature on Io is around 130 K, the maximum abundance of adsorbed SO_2 on Io is around 5×10^{-6} g SO_2 m^{-2} S. At disk average temperatures of 90 K, the maximum adsorbed SO_2 capacity cannot be more than 6.6×10^{-9} g SO_2 m^{-2} S. If more SO_2 is present in the system at these temperatures, it will exist as ice.

To understand why our results constitute a new perspective, we must examine the previous estimates of SO_2 adsorption on Io.

Unpublished adsorption measurements of SO_2 on S obtained by Fanale and Laue, at warmer, higher pressure, conditions suggested that up to a monolayer of SO_2 could be adsorbed onto S at low relative pressures. It was more or less accepted that at lower pressures and temperatures characteristic of Io, the adsorptive coverage should be about the same, around a monolayer [e.g. Fanale et al., 1982]. Let us examine how many monolayers our current analysis indicates. The upper limit of adsorptive coverage is around 5×10^{-6} g SO_2 m^{-2}sulphur at 130K (Fig. 1). This mass represents around 4.7×10^{16} molecules per square meter. If we assume that each adsorbed molecule occupies $30A^2$, the maximum number of adsorbed SO_2 molecules occupies no more than 1.4×10^{-2} m^2. Thus ~ 1.4×10^{-2} is the maximum number of adsorbed monolayers, well over an order of magnitude less than previously believed. Nash [1983] calculated that 0.5 monolayers of adsorbed SO_2 would be required to create the 30% 4–μm absorption. We argue that the maximum adsorbed SO_2 coverage must be significantly less than 0.5 monolayers, making spectroscopic detection of adsorbed SO_2 highly problematic.

The question of how important the adsorbed phase on Io is, now becomes largely a question of what the adsorbent is.

We selected sulphur as our adsorbent because it is clear that sulphur allotropes constitute a significant fraction of Io's surface. To the extent that elemental sulphur dominates the Ionian surface, we have excellent confidence in our results. However, the Na and K in the magnetosphere require the presence of other phases on the surface.

The importance of the adsorbed phase in suppling the magnetosphere, and in diurnal exchange of SO_2 with the atmosphere, depends on the abundance and adsorptive capacity of other surface materials, as well as on the specific surface area of the sulphur on the Io surface. Nash [1986], in experiments on vacuum sublimation of solid sulphur, identified a very fluffy form which results from preferential sublimation of ring sulphur (S_8) over polymeric sulphur. Such a filamentary residue might be expected to have a very high surface area, and hence render the surface adsorbed phase a significant sink by mass, although monolayer coverage would remain very small.

REFERENCES

1. Anderson, et al., *Science, 155*, 319-322, 1967.
2. Brunauer, S., et al., *J. Am. Chem. Soc., 60*, 309-319, 1938.
3. Fanale, F. P., et al., In: *Satellites of Jupiter* (Morrison, D., ed.), 756 - 781. 1982.
4. Matson, D. L., and Nash, D. B.,. *J. Geophys. Res., 88*, 4771-4783, 1983.
5. Nash, D. B., *Icarus, 54*, 511-523, 1983.
6. Nash, D. B., In: *Lunar and Planetary Science. XVII*, pp. 603-604, 1986.

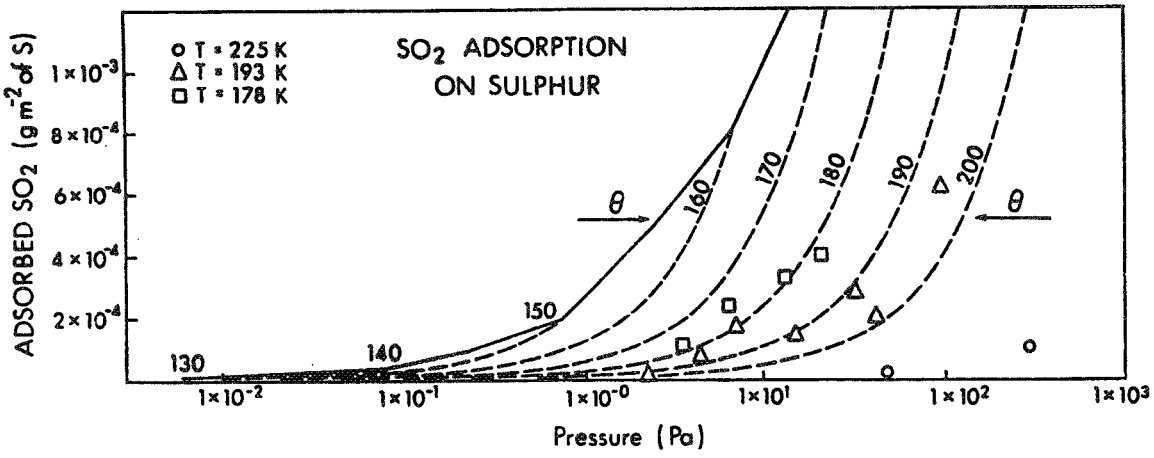

Fig. 1 - The pressure temperature field tangential to that of Io. The isotherms are found from Eq. (1) (dashed lines) and each is truncated at the vapor pressure over SO_2 ice (solid line). Coverage corresponding to one monolayer is indicated by the arrows (θ). On Io, (T< 130K), adsorption is limited to a fraction of a monolayer by equilibration with ice.

INVESTIGATIONS OF PLANETARY RING PHENOMENA

Joseph A. Burns, Cornell Universitlly

Faint planetary rings--their dynamical behavior and physical properties--have been the main focus of research efforts during the past year. A reanalysis of the structure and physical properties of the Jovian ring system was completed and will be published shortly (2). Jupiter's ring is composed of i) a flattened main ring ($t \lesssim 300$ km) that terminates abruptly at its outer edge, and that has features associated with the two known embedded moonlets, ii) a toroidal halo that rises quickly at the main ring's inner edge to a half thickness of $\sim 10^4$ km and fades into the background at $\sim 1.4\ R_J$, and iii) the exterior "gossamer" ring (see last year's progress report) that is only 1/20 as bright as the main ring and that is enhanced at synchronous orbit. The ring is reddish like nearby Amalthea and its particles have a power law size distribution of slope $-2.5(\pm 0.5)$ in the range $\sim 0.1\text{-}100\ \mu$m.

We have examined the motion of weakly-charged dust through Jupiter's gravitational and magnetic fields (1). Resonances occur where the frequency of the perturbing Lorentz force matches a grain's natural orbital frequency; near such resonances, large radial and out of plane motions appear. Ongoing research shows that during passage through such resonances large vertical amplitudes develop and persist; the boundaries of the jovian halo are near such locations. Current studies include the character of stochastic variations in a particle's electric charge and the orbital consequences of this, an analytical investigation of resonance passage, the details of the dust-plasma interaction, and application to other ring systems.

Several topics concerning features of Saturn's rings have been addressed. Cuzzi and Burns (4) have shown that depletions in MeV charged particles measured by Pioneer 11 near the F ring are only partly caused by the ring and thus that unobserved localized clouds of debris must be present. We hypothesize that these faint clouds are ejecta thrown off during collisions amongst moonlets (radius 0.1-10 km) which populate the entire annulus between the orbits of the shepherds. We have developed a self-consistent scenario in which mutual collisions of unseen parents generate debris clouds, which then shear out and become part of an overall patchy background of faint material; the particles comprising the background are continually re-accreting onto the parents, only to be thrown off in some later collision. According to this model, about 10^2 clouds (with $\tau \sim 10^{-3}\text{-}10^{-4}$ and $\sim 10^2$ km x 10^4 km size) should be present at any typical time. With a steep size distribution of parents, even the F ring itself could be the outcome of a collision between two of the largest moonlets, in which case the F ring is a temporary feature of the ring system. We suggest that arcs like those in

Neptune's retinue may be produced by this scheme. Kolvoord (7) has developed a perturbation routine to study the orbital consequences of an embedded moonlet on a narrow ring and is presently incorporating an exterior satellite perturber into his program as well as considering the consequences of particle collisions within the narrow rings.

Showalter and co-workers (3) have interpreted quasi-periodic optical depth variations that were found on either side of the Encke gap as the gravitational "wakes" of a moonlet orbiting near the gap's center and at a longitude of 32°. A single moonlet of ~10 km radius is able to produce the observed features. Studies of the signal scatter of the PPS occultation data by Showalter and Nicholson (8), initiated under this grant, give promise of providing an independent measure of the size distribution of ring particles.

The origin and fate of Uranian ring dust is presently being studied (6). Such ring particles have brief lifetimes primarily due to sputtering and orbital collapse under atmospheric drag. An unresolved quandary is that abrupt transitions in ring brightness observed at interior ringlet edges seem to imply that the expected orbital evolution does not proceed. The dust discovered on ring plane crossing at 4.57 R_U must have nearby sources; its broad and asymmetric distribution about the planet's equatorial plane suggests that resonant electromagnetic forces are at work (5).

Our studies of faint rings are pertinent to the possible presence of fine material near Neptune; such grains could prove hazardous to Voyager 2 as it swings through the ring plane on its way toward a flyby of Triton; we have been helping to advise the Voyager project office on the potential danger to this precious spacecraft.

Several review articles were also prepared during the funding period. They concerned dust motion (9), planetary rings (10), satellites (11), and satellite orbital evolution (12).

1. L. Schaffer and J.A. Burns (1986). The dynamics of weakly-charged dust: Motion through Jupiter's gravitational and magnetic fields. Jnl.Geophys.Res. 92, in press. Abstracts in BAAS 17, 921; BAAS 18, 777-778 and 838, Nat'l Congress Applied Mech. Paper F3a (Austin, June 1986).

2. M.R. Showalter, J.A. Burns, J.N. Cuzzi and J.B. Pollack (1986). Jupiter's ring system: New results on structure and particle properties. Icarus 69, in press.

3. M.R. Showalter, J.N. Cuzzi, E.A. Marouf and L.W. Esposito (1986). Satellite "wakes" and the orbit of the Encke gap moonlet. Icarus 66, 297-323.

4. J.N. Cuzzi and J.A. Burns (1986). Charged particle depletion surrounding Saturn's F Ring: Evidence for a moonlet belt. Icarus, submitted; Abstracts in BAAS 17, 922; 18, 768; EOS 67, 1077.

5. D.A. Gurnett, W.S. Kurth, F.L. Scarf, J.A. Burns, J.N. Cuzzi and E. Grun (1986). An analysis of micron-sized particle impacts detected near Uranus by Voyager 2. Jnl.Geophys.Res., in preparation; Abstract in EOS 67, 340.

6. J.A. Burns, L.E. Schaffer, J.N. Cuzzi, and D.A. Gurnett (1986). Dust in the Uranian system: Its origin and fate. BAAS 18, 770-771.

7. R.A. Kolvoord (1986). The effect of an embedded satellite on narrow rings using a perturbation approach. BAAS 18, 771.

8. M.R. Showalter and P.D. Nicholson (1986). Saturn's rings through a microscope: Constraints on particle size from the Voyager PPS scan. BAAS 18, 767.

9. J.A. Burns (1986). The motion of interplanetary dust. In Evolution of the Small Bodies in the Solar System (M. Fulchignoni and L. Kresak, Eds.), in press.

10. J.A. Burns (1986). Rings around planets. In Evolution of the Small Bodies in the Solar System (M. Fulchignoni and L. Kresak, Eds.), in press.

11. J.A. Burns (1986). Some background about satellites. In Satellites (J.A. Burns and M.S. Matthews, Eds.), University of Arizona Press, 1-38.

SUBCENTIMETER-SIZE PARTICLE DISTRIBUTION FUNCTIONS IN PLANETARY RINGS FROM VOYAGER RADIO AND PHOTOPOLARIMETER OCCULTATION DATA

Howard A. Zebker, Jet Propulsion Laboratory, G. Leonard Tyler and Essam A. Marouf, Stanford University.

Analysis of measurements of the scattered and direct components of Voyager 1 radio occultation signals at 3.6- and 13-cm wavelengths yields estimates of the distribution functions of supracentimeter-size particles and thickness of relatively broad (>1000 km wide) regions in Saturn's rings (Tyler at al.,1983; Zebker et al., 1985; Zebker and Tyler, 1984). The amplitude of these signals is mostly unaffected by particles smaller than a wavelength in size, thus the distribution of these particles in the rings cannot be determined by analysis of the amplitude data alone. If, however, measurements of signal amplitude at a shorter wavelength are combined with the previously analyzed data, we can constrain the shape of the distribution functions characterizing the smaller particles. In particular, the additional measurement of amplitude at 0.26 μm wavelength from Voyager photopolarimeter occultation observations (Esposito et al., 1983) allows inference of subcentimeter-size distribution functions for a number of relatively narrow (30-100 km wide) embedded ringlets in Saturn's ring C and the Cassini division. These data are available from the January, 1986 Uranian ring occultation also, and this same technique can be used to estimate corresponding distributions for the Uranian ringlets.

If we consider size distributions of arbitrary form, many solutions are found that are consistent with the three available observations of signal amplitude. In order to limit the formal solution set to functions that are likely on a geophysical basis, we constrain the solutions to be of the power-law form with sharp lower- and upper-size cutoffs. We calculate the best-fit power law (in the least-square-error sense) to the three observations at three wavelengths for several of the embedded Saturn ringlets-- the results are tabulated in Table 1. We note that in each case but two the inferred power law index is approximately 3, which is similar to the power law that describes the distribution of supracentimeter particles in the broad ring features. Thus, it is likely that accumulations of particles in the embedded features are distributed similary to the particles in the rings as a whole, and that the forces responsible for the creation and maintenance of of the embedded features are not highly size-selective in nature.

Mie scattering theory predicts that the measured phase of the radio occultation signal is highly sensitive to particles ranging from 0.1 to 1.0 wavelengths in size, thus additional constraints on the subcentimeter-size distribution functions for both the Saturn and Uranus rings can in principle be derived from radio phase measurements. However, the observed phase and amplitude data from both sets of occultations cannot be reconciled with classical Mie theory. Discrepancies of up to a factor of three are found between predicted and measured values for nearly all physically-likely distribution functions. We have attempted to account for these differences by introducing terms in the Mie equations representing proximity effects of particles (see Zebker et al., 1985) and also for non-sphericity of the particles, however a reasonable match between theory and observation has not been found. We are beginning to investigate new models of scattering by dense particulate media in order to understand the limitations of the Mie approach, and this area of investigation remains as future work.

References:

Tyler, G.L., E.A. Marouf, R.A. Simpson, H.A. Zebker, and V.R. Eshleman, The microwave opacity of Saturn's rings at wavelengths of 3.6 and 13 cm from Voyager 1 radio occultation, ICARUS 54, 160-188, 1983.

Esposito, L.W., D.L. Coffeen, C.W. Hord, A.L. Lane, M. O'Callaghan, R.B. Pomphrey, M. Sato, K.E. Simmons, and R.A. West, Voyager photopolarimeter stellar occultation of Saturn's rings, J. GEOPHYS. RES. 88, 8643-49, 1983.

Zebker, H.A., and G.L.Tyler, Thickness of Saturn's rings inferred from Voyager 1 observation of microwave scatter, SCIENCE 223, 396-98, 1984.

Zebker, H.A., E.A. Marouf, and G.L. Tyler, Saturn's rings: particle size distributions for thin-layer models, ICARUS 64, 531-548,1985.

Table 1. Saturn Ringlet Distribution Functions

Ringlet location km from Saturn center		Power law index	Lower size cutoff, m	Upper size cutoff, m
Start	Stop			
79230	79260	3.7	0.00316	0.316
84780	84930	2.7	0.00005	0.100
85670	85695	3.6	0.00316	0.178
85930	85970	2.8	0.00032	0.100
86400	86580	2.8	0.00018	0.100
87185	87210	3.0	0.00003	0.178
87300	87325	3.2	0.00178	0.178
87500	87580	3.2	0.00002	3.162
88380	88723	3.1	0.00003	10.00
89800	89930	3.3	0.00178	0.316
90420	90600	2.9	0.00006	10.00

Observational Studies of Saturn's Rings

Carolyn C. Porco, Lunar and Planetary Lab/Department of Planetary Science, University of Arizona, Tucson, Az. 85721.

The objective of this work is to investigate several noteworthy pheonomena in Saturn's rings which have until now received an inadequate amount of attention. Among these are the periodic variation of the 'spokes' in the B ring and eccentric features throughout the rings.

One of the major discoveries by Voyager has been the existence of eccentric features within the predominantly circular rings of Saturn (Smith *et al.* 1981,1982). Several of these nonaxisymmetric features are narrow elliptical rings which share many characteristics with the rings of Uranus (Porco 1983; Porco *et al.* 1984a). In recent work, two new narrow ringlets have been added to the list of eccentric features in the rings of Saturn (Porco and Nicholson 1986). The ringlet at $1.95R_s$ sits in the Huygens gap outside the outer B ring edge and together they comprise an interesting dynamical system. The B ring edge, also a major eccentric feature which clearly owes part of its shape and kinematics to the nearby 2:1 inner Lindblad resonance with the satellite Mimas (Porco *et al.* 1984b), is not completely described by a simple $m = 2$ radial distortion expected from this resonance. The 'Huygens' ringlet behaves, to first order but not entirely, as do the majority of $m = 1$ narrow ringlets in the solar system precessing around an oblate planet (Fig. 1a). In addition, it does not exhibit the positive linear width-radius relation found for many narrow ringlets like the ϵ, α, and β rings of Uranus (Fig. 1b). Voyager Imaging and occulation (RSS, PPS, UVS) data are now in hand, as well as image-processing software which allows accurate absolute positional measurements to be made in Voyager imaging data. Work is in progress to re-examine this region of Saturn's rings and to study the possibility of a dynamical interaction between the outer B ring edge, the Huygens ringlet, and the nearby Mimas 2:1 resonance. An understanding of the kinematics and dynamics of this region promises to yield important clues to a matter of great interest in both theoretical and observational ring studies: the behavior of ring particles in regions of high optical depth like the outer B ring.

Ever since the Voyager discovery of the broad-band, impulsive Saturn Electrostatic Discharges (SED) whose spectrum is akin to that of lightning, it was speculated that the spokes observed in Saturn's B ring might be the visible manifestation of the SED. It has been known for some time that the variation of spoke activity in Saturn's B ring is modulated at a period equal to 641 ± 5 minutes, within observational uncertainty equal to that of Saturn's magnetic field, $639.4 \pm .05$ minutes (Porco and Danielson 1984). However, the SED's have modulation period of 610 ± 5 minutes (Evans *et al.* 1981), significantly different that the magnetic field period. There is a strong suggestion of a peak at a period of 610 minutes in the spectrum of spoke activity (Fig. 2) and current work is focussed on the investigation of this feature (Porco and Haemmerle 1987) and the problem of the physical connection, if any, between spokes and the SED.

Evans, D. R., et al. (1981). *Nature* **292**, 716-718.

Porco, C. C. (1983). Ph. D. dissertation, California Institute of Technology

Porco, C. C. and Danielson, G. E. (1984). The kinematics of spokes. Proceedings of the IAU Colloquium # 75, *Planetary Rings*, A. Brahic, Ed., CNES, Toulouse, France.

Porco, C., et al. (1984a). *Icarus* **60**, 1-16.

Porco, C., et al. (1984b). *Icarus* **60**, 17-28.

Porco, C. C. & Nicholson, P. D. (1986). *Icarus* , Submitted.

Porco, C. C. & Haemmerle, V. R. (1987). In preparation.

Smith, B. A., et al. (1981). *Science* **212**, 163-191.

Smith, B. A., et al. (1982). *Science* **215**, 504-537.

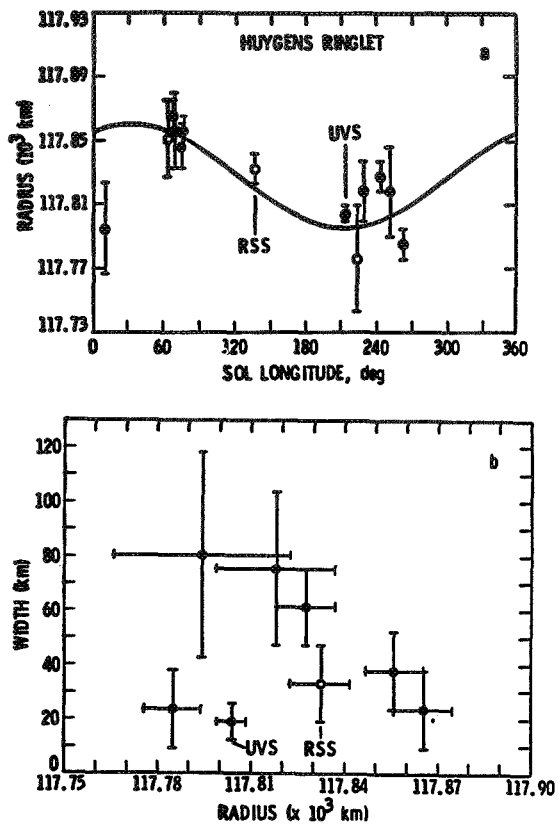

Fig 1. a. The radius-longitude data obtained from Voyager imaging and occultation experiments and the best fitting co-planar elliptical model for the Huygens ringlet at 1.95 Rs. The data points (open circles - Voyager 1; filled circles - Voyager 2) have been precessed to a common epoch. b. The radius-width data for the Huygens ringlet. Both figures from Porco (1983).

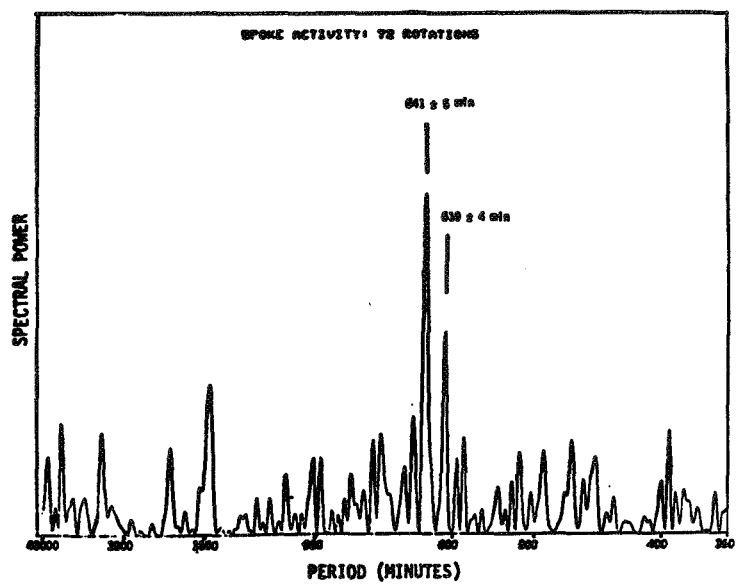

Figure 2. Fourier power spectrum of spoke activity observed on the morning ansa in Voyager 2 Imaging data spanning 72 Saturn rotations. The highest peak at 641 ± 5 min occurs very close to the magnetic field period (639.4 min). The next highest peak at 610 ± 4 min may indicate a relationship between spokes and SED's which have a period of 610 min. Figure from Porco and Danielson (1984).

The Production of "Braids" in Saturn's F Ring

Jack J. Lissauer and Stanton J. Peale (UCSB).

Two models are presented to explain the "braided" structure observed in some Voyager images of Saturn's F ring. A braided pattern can be produced from an initially uniform, circular, narrow ring, which orbits past a nearby satellite (resulting in a wavy pattern) and then is doubled back upon itself due to gravitational accelerations from an embedded moonlet (Figure 1). Viewed from the frame which rotates with the moonlet's orbital angular velocity, the trajectories of the ring particles traverse one end of the now classic horseshoe orbit. At least one (and probably both) of the F ring shepherding satellites is massive enough to produce the required wavy pattern; an icy moonlet 5-10 km in radius would be massive enough to subsequently cause the ring particles to horseshoe into irregular, short braided strands. Alternatively, if the F ring is composed of two well-separated strands prior to the passage of the shepherding moon, then the differing wavelengths of the wavy patterns induced in the two strands and the subsequent drift in relative phase can lead to a regular, lengthy braided pattern, without the need for an embedded moonlet. (Figure 2).

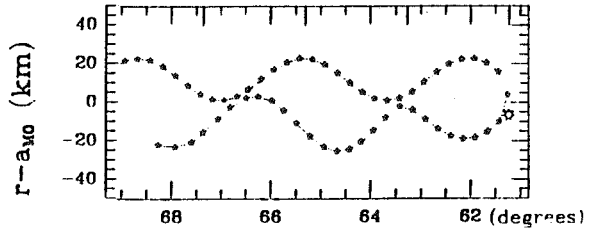

Fig. 1: Single strand Shepherd plus moonlet perturbations.

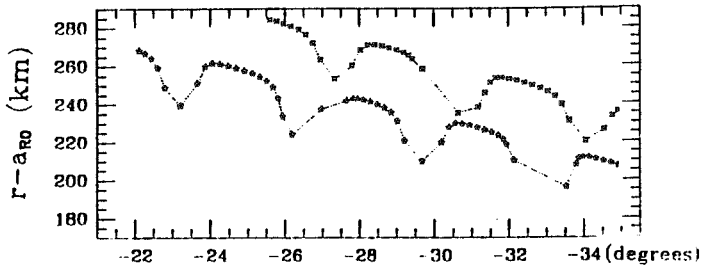

Fig. 2: Two strands, shepherding perturbations only.

Experimental Studies On the Impact Properties of Water Ice

F.G. Bridges, D.N.C. Lin, and A.P. Hatzes
Physics Dept. and Board of Studies in Astronomy and Astrophysics,UCSC

We have continued our experimental studies on the impact of ice particles at very low velocities. These measurements have applications in the dynamics of Saturn's rings. Initially data was obtained on the coefficient of restitution for ice spheres of one radius of curvature. The type of measurements have now been expanded to include restitution data for balls with a variety of surfaces as well as sticking forces between ice particles. We have made significant improvements to this experiment, the most important being the construction of a new apparatus. Previous measurements were made using iceballs mounted on a disk pendulum which could be made to oscillate for very long periods (40-60 secs). This pendulum was placed in a styrofoam cryostat and cooled using liquid nitrogen. Although this setup was adequate for performing the first measurements, it suffered from several drawbacks. First of all the the cryostat used was not completely air-tight. Not only did this preclude the taking of measurements under vacuum conditions, but atmospheric water vapor was able to leak into the apparatus, thus making it very difficult to make measurements with iceballs that were completely free from any frost on the impact surface. Secondly, this cryostat was only able to reach temperatures of around 170°K and only for short periods of time. Measurements of the velocity were made by bouncing a laser beam off a mirror mounted on the axis of the pendulum. This reflected beam would sweep past a photocell device prior to and after each collision. The time required for the beam to sweep past the cell was a measure of the velocity of the iceball. This detector enabled us to measure the coefficient of restitution accurately down to a velocity of 0.02 - 0.05 cm/sec. Reliable data on the coefficient of restitution is needed for velocities below this.

The new apparatus consists of a smaller version of the disk pendulum and a stainless steel, double-walled cryostat. The new apparatus has proved to be a significant improvement over the old one. Measurements can now be made at temperatures near 90°K, comparable to the temperature of the environment of Saturn's rings, and with much greater temperature stability. With the recent acquisition of a diffusion pump, the iceball chamber can now be evacuated to a pressure of 10^{-5} torr. For the actual measurement of the velocity a capacitive displacement device (CDD) is now used. This device consists of a set of parallel plates mounted near the top of the disk pendulum. These plates rest between a similar set mounted on the cryostat. As the pendulum oscillates the plates on the pendulum swing between those on the cryostat. This device then measures the varying capacitance of the plate system and converts this to a voltage as a function of time which is directly related to the displacement of the pendulum. The sensitivity of the CDD enables us to obtain accurate measurements of the coefficient of restititution for velocities near 0.005 cm/sec, even for moderately short periods of oscillation of the pendulum (10-15 secs). The CDD also has an advantage over the photocell detector in its ability to measure the displacement of the pendulum as a function of time during the entire collision. This device not only improves the accuracy of our measurements but makes it possible to obtain data on the contact time of the collision.

With the old apparatus ice spheres were made by freezing water in tennis ball molds. This had the disadvantage that variations in the shape of the contact surface could not be controlled. We now use a precision aluminum mold for producing ice spheres with a radius of curvature of 2.5 cm. We also have additional molds for freezing different radii of curvature on the ice spheres. Figure 1 shows typical data on the coefficient of restitution for smooth, frost-free ice spheres with different radii of curvature (2.5, 5, 10, and 20 cm) and taken at the same temperature ($123K°$). The most obvious feature of these figures is that the dependence of the coefficient of restitution on the radius of curvature in the range of .05-1.0 cm/sec is quite weak. As one goes to higher velocities ($> 1cm/sec$) the differences in the coefficient of restitution between the various ice spheres becomes more noticeable, with spheres with the larger radius of curvature being more elastic. In the range of 0.1-1.0 cm/sec the data for all four ice

spheres can be fit by either a linear or an exponential function with the exponential form providing the slightly better fit. Data taken at velocities greater than 2 cm/sec should better distinguish between the two laws, and these measurements are currently in progress. Using a function of the form $\epsilon(v) = Ce^{-\gamma v}$ to fit the data in figure 1, one finds that there is very little variation in C among the different iceballs (C$\sim$ 0.9); however there is a noticeable trend of decreasing γ with larger radius of curvature. The behavior of γ versus R, the radius of curvature is shown as an insert in figure 1. It is a linear relation of the form $\gamma(R) = 0.41 - 0.1R$. For the 5, 10, and 20 cm radii iceballs only the exponential fits to the data are shown.

A large effect on the coefficient of restitution can be caused by the condition of the contact surface before the collision. We find that a roughened contact surface or the presence of frost can cause a much larger change in the restitution measure than the geometrical effect of the radius of curvature. Figure 2 shows data taken during one run using an ice sphere that had a radius of curvature of 20 cm. Circles represent data taken while the iceball had a relatively smooth surface. Triangles represent data taken using the same ball after the cryostat had been evacuated for several minutes at a relatively high temperature (T=210°K). This allowed the ball to sublimate and thus created a roughened surface on the ball. Crosses represent data taken after water vapor was blown across the surface of the same iceball thus allowing frost to form. An even further reduction in the coefficient of restitution is evident. At a velocity of 0.5 cm/sec the sublimated iceball was 20% more inelastic than the smooth ball at the same velocity while the frosted ball was 30% more inelastic. This is much larger than the variation in the coefficient of restitution at a given velocity between different iceballs with the same radius of curvature, which can be as large as 10%.

Work is now in progress to further quantify the effects of sublimation and frosting. We have recently completed a gas handling system that enables us to deposit carbon dioxide, methane, or ammonia on the surface of the iceball. Effects on the restitution measure with these substances present will also be examined.

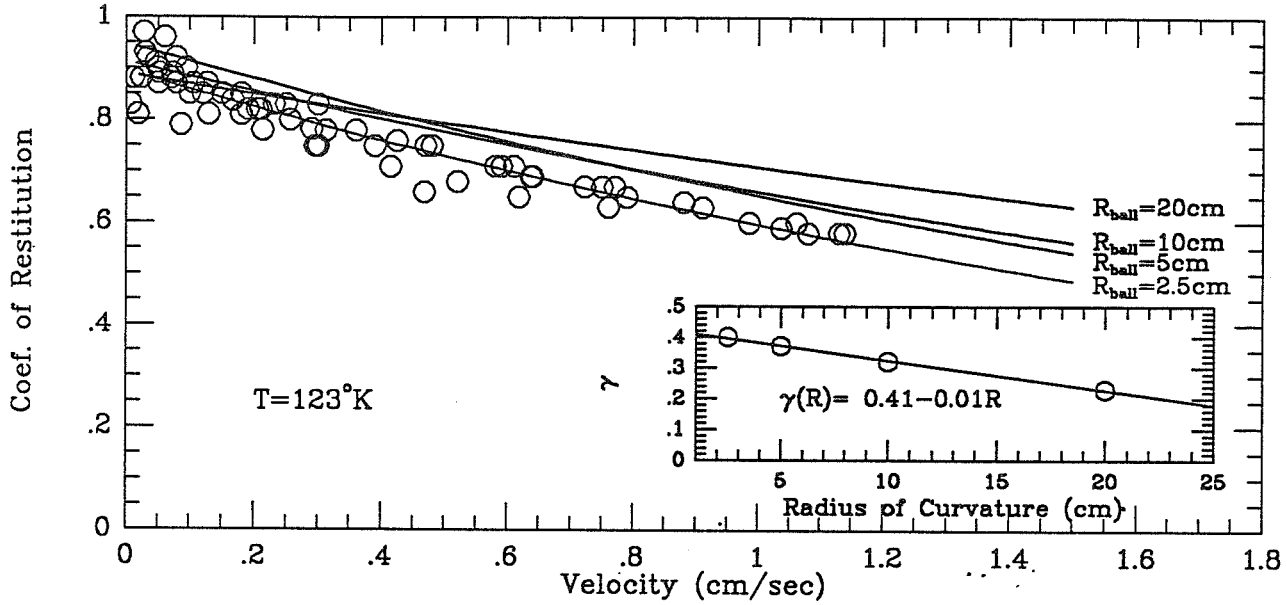

Fig. 1: Typical data taken with a smooth iceball of radius 2.5cm (circles). Lines represent exponential fits to the data of the form $\epsilon(v) = Ce^{-\gamma v}$. Fits to the data for balls with larger radii of curvature are also shown. Insert shows behavior of γ with radius of iceball.

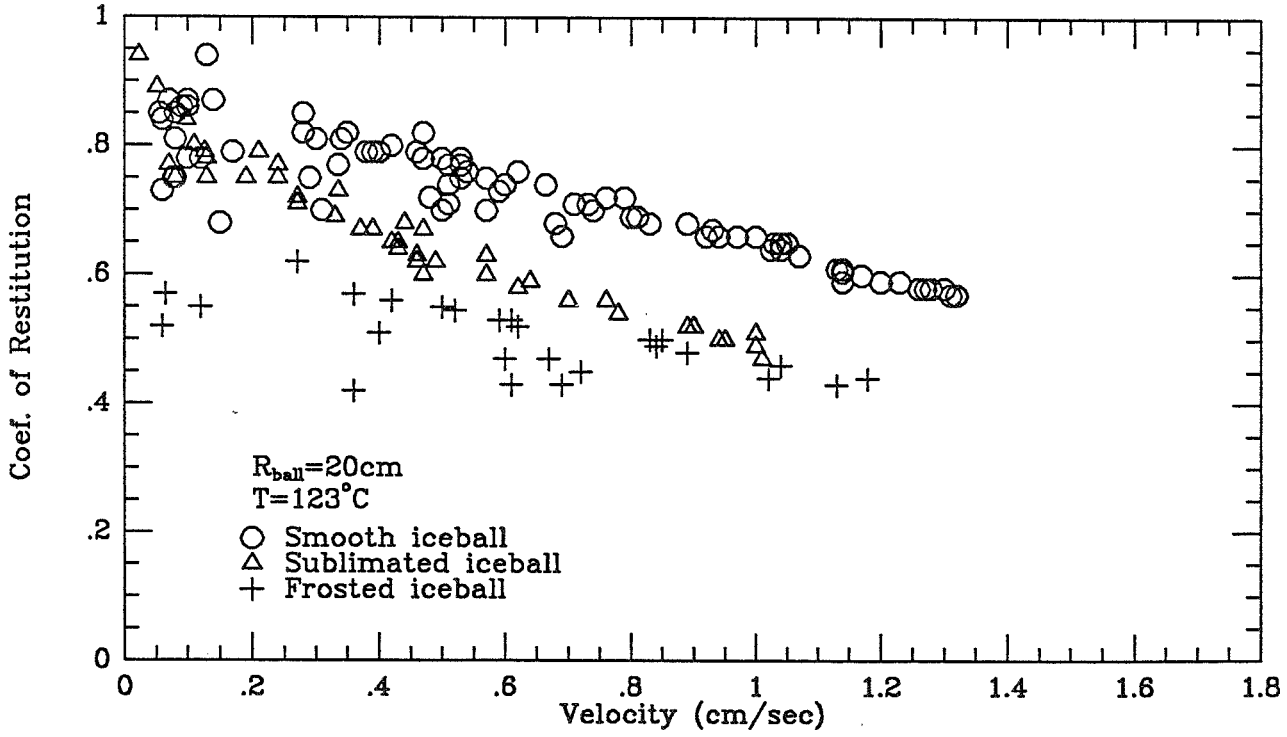

Fig. 2: Restitution data for an iceball with 20cm radius of curvature. This shows the changes in the coefficient of restitution after the ball is sublimated (triangles) and then frosted (circles).

CHAPTER 3

COMETS AND ASTEROIDS

TEMPERATURES AND MINIMUM THICKNESS OF THE INACTIVE SURFACE LAYER OF COMET HALLEY

F. P. Fanale and J. R. Salvail, Planetary Geosciences Div., Hawaii Inst. of Geophysics, Univ. of Hawaii, Honolulu, HI.

The effects of a nonvolatile mantle on the thermal state of a comet nucleus are investigated. Our original computer model (Fanale and Salvail, 1984) was modified so that temperatures can be computed through a thin dust mantle to the center of a 5 km spherical nucleus in the orbit of P/Halley. No attempt is made to simulate the formation of a mantle. Results are obtained for various specified values of initial mantle thickness and thermal conductivity to determine their effects on temperature profiles through the mantle. The minimum thickness of mantle that can withstand ejection by sublimating gasses is also calculated as a function of mantle thermal conductivity. This is assumed to occur when the vapor pressure at the ice interface exceeds the lithostatic pressure of the mantle. Calculations were performed for ten or more orbits until temperatures in the mantle reached a near steady state. Results indicate that mantles as thin as 4 cm and 14 cm, for thermal conductivities of 600 and 6000 ergs/cm-s-K, respectively, will remain intact. Surface temperatures as high as 511K at perihelion and 400K at the position of spacecraft encounter were computed at 0° latitude for an upright, rotating nucleus. Ice interface temperatures were raised by different amounts during each orbit, depending on mantle thickness and thermal conductivity, until steady state was reached. After temperatures in the mantle reached a steady state, ice surface temperatures were constant throughout the orbit due to the large difference in the thermal conductivities of the mantle and the more compact icy nucleus. These results imply that relatively small nonvolatile masses emplaced randomly in comet nuclei could produce an irregular, permanently mantled surface and could also account for the apparently random location of active areas.

Reference

Fanale, F.P. and J.R. Salvail (1984). An idealized short period comet model: Surface insolation, H_2O flux, dust flux and mantle evolution. Icarus 60, 476-511.

COMET THERMAL MODELING

Paul R. Weissman, Jet Propulsion Laboratory, Pasadena, CA 91109, and Hugh H. Kieffer, U. S. Geological Survey, Flagstaff, AZ 86001

The past year has been one of tremendous activity because of the appearance of Halley's Comet. Observations of the comet have been collected from a number of sources and compared with the detailed predictions of the comet thermal modeling program. Spacecraft observations of key physical parameters for the cometary nucleus (size, albedo, dust-to-gas ratio, etc.) have been incorporated into the thermal model and new cases run. These results have led to a much better understanding of physical processes on the nucleus and have pointed the way for further improvements to the modeling program.

A new model for the large-scale structure of cometary nuclei was proposed in which comets were envisioned as loosely bound agglomerations of smaller icy planetesimals, essentially a rubble pile of primordial dirty snowballs. In addition, a study of the physical history of comets was begun, concentrating on processes during formation and in the Oort cloud which would alter the volatile and non-volatile materials in cometary nuclei from their pristine state before formation. Dr. Gary Herman of Tel Aviv University spent one year at JPL as a NRC post-doc working on two interesting research tasks: internal temperatures in icy nuclei, and radiative transfer in dusty cometary comae.

The thermal modeling of Halley's Comet has shown that the asymmetric behavior of Halley's light curve pre- and post-perihelion cannot be explained by heat flow into sub-surface layers on the inbound leg of the orbit, providing an additional energy source as the comet moves away from perihelion. Within 2 AU of the sun, high values of surface thermal conductivity can yield post-perihelion brightenings of only about 10 or 20%, as compared to the 100 to 200% brightenings that are actually observed. Previous models which suggested this behavior did not allow for radiative cooling of the cometary nucleus at night.

The correct explanation for post-perihelion brightening appears to be seasonal changes on the inclined, rotating nucleus. As a result of the comet's highly eccentric orbit, as it rounds perihelion there is a very abrupt change in the declination of the sub-solar point from the southern to northern hemispheres of the nucleus. On the way towards perihelion the northern hemisphere receives only modest heating, in fact, none around the circumpolar region. The sudden change post-perihelion, at a time when the comet is very close to the sun, causes rapid temperature increases and resulting thermal stresses. The compressional hoop stresses on the non-volatile cometary crust material causes cracking and strike-slip fractures. Plates of crustal material are broken loose from the nucleus and substantial new areas of fresh ice are exposed beneath the crust. The activity continues to build as the sun moves northward in declination following perihelion. Eventually, the decreasing solar insolation as the comet moves away from the sun causes the activity to subside.

Activity is less on the inbound leg because of two factors. First of all, the heating is more gradual and the thermal stresses can be accomodated more readily without catastrophic failure of the non-volatile crustal material. Second, the gradual heating likely depletes near surface layers of volatiles while building a thicker non-volatile crust layer over the ice.

Detailed solutions for the seasonal behavior of the Halley nucleus are sensitive to rotation pole orientation. However, all the suggested pole orientations for Halley are within about 40 degrees of each other, with suggested obliquities of 20 to 30 degrees. Other factors such as the nucleus rotation period, a still poorly determined parameter, and the triaxial spheroid shape of the nucleus also will affect the detailed gas production rates that are derived from the comet model as a function of orbital position.

Comparison of the comet thermal model results with the observed behavior of the Halley nucleus versus heliocentric distance showed that the fraction of active sublimating area on the nucleus surface was not constant throughout the orbit but changed in unpredictable ways (though consistent with the seasonal dependence explanation above). This is further proof of the heterogeneous nature of the nucleus and of cometary phenomena in general.

The surface heat flow becomes important with regard to the behavior of the nucleus at large heliocentric distances where the energy going into heat flow is comparable to that going into sublimation. For high heat flows the comet does not "turn on" until relatively close to the sun, while for low heat flow the coma can become visible at over 6 AU from the sun. Given the observed turn on of the Halley coma at 5.8 AU inbound in early 1985, one can set an approximate value for the thermal conductivity of about one-tenth that of solid crystalline water ice. This is a relatively low conductivity, though not as low as observed for some dusty satellite regoliths in the solar system.

The proposed new model for cometary nuclei, known as the "primordial rubble pile," considered what a cometary nucleus should look like based on present scenarios for planetesimal formation in the outer solar system, and attempted to explain a variety of observed cometary phenomena. The lack of major energy sources means that cometary material will likely not be brought together into a single, well consolidated body, but will retain the composite structure of an agglomeration of smaller dirty ice snowballs. Phenomena such as cometary outbursts and splitting might be explained by such a structure, as smaller pieces break off to become secondary nuclei, and freshly exposed faces result in sudden brightening and activity from the main nucleus. Evidence from radar studies of large debris clouds around nuclei tends to support this suggestion of a possible "rubble pile" structure, with small debris being briefly elevated off the nucleus surface and then falling back very slowly in the weak cometary gravity field.

Imaging of the Halley nucleus did not have sufficient resolution to determine if the primordial rubble pile model is correct. Giotto images did show a highly irregular nucleus with surface roughness on the order of 10% the mean radius, or more. But better images, presumably from the CRAF mission, will

be needed to resolve this question. In addition, it is possible that after long years of physical evolution, the original rubble pile structure of the nucleus is hidden by external modification and mass movement.

Dr. Herman developed a detailed analytical solution to the nucleus heating problem and a one-dimensional numerical model of the means by which cold nuclei from the Oort cloud warm as both their perihelia and orbital semimajor axes decrease. He showed that previous models were inaccurate because they ignored surface heat flow. The internal temperature is a complex function of both the comet's semimajor axis and eccentricity, as well as the nature of the ice making up the nucleus, i.e., amorphous versus crystalline. The time required for the nucleus to reach equilibrium temperature is often quite long, exceeding the dynamic time scale for substantial changes in the comet's orbit due to close planetary encounters.

Another research effort was concerned with radiative transfer in dusty cometary atmospheres. It had been shown that a dusty coma can increase the total energy reaching the cometary nucleus as a result of multiple scattering and thermal emission by the dust. Dr. Herman showed that most past estimates of this phenomena tended to over-estimate the effect, and that it was difficult to get a large energy increase. However, the coma does serve to redistribute energy around the cometary nucleus, illuminating the night hemisphere while cutting down the total radiation reaching the dayside. This would lead to a more isothermal nucleus when the coma opacity was high. A Monte Carlo simulation of the radiative transfer by Dr. Herman and Dr. H. Salo showed that a modest, on the order of 10%, increase in total flux reaching the nucleus was possible, if one assumed forward scattering particles ($g = 0.7$), and an accelerating dust velocity due to entrainment in the evolving gas.

Finally, an analysis of possible mechanisms for modifying cometary nuclei during their formation stages, and/or during their long residence time in the Oort cloud was begun. Because of the small size of the nuclei and their formation in zones far from the sun where orbital velocities are small, their total gravitational potential energy and degree of compaction is probably quite small. The radii of the cometary nuclei are sufficiently small that they were likely not substantially heated by long-lived radio-isotopes. Short-lived isotopes like aluminum 26 may have melted the interiors of comets, but only if comets formed over a time span short as compared to the lifetime of that radionuclide. That appears to be unlikely. Sputtering of nucleus surfaces by galactic cosmic rays is an important process, removing much of the volatiles and polymerizing all the carbon compounds down to a depth of a meter or more. This leads to the interesting possibility that comets may have already developed non-volatile crustal layers before they entered the planetary system. Although comets might accrete a thin veneer of interstellar dust and gas while resident in the Oort cloud, it appears more likely that hypervelocity impacts by interstellar dust grains result in a net erosion of the cometary surfaces, though the effect here is only on the order of centimeters, as compared with modification to a depth of a meter or more by cosmic rays. Thus, comets may not be as entirely pristine as originally thought, and it will be important to consider these various modification processes in interpreting the results form the Halley's Comet missions, and from future missions such as CRAF and CNSR.

THE LOSS AND DEPTH OF CO_2 ICE IN COMET NUCLEI

F. P. Fanale and J. R. Salvail, Planetary Geosciences Div., Hawaii Inst. of Geophysics, Univ. of Hawaii, Honolulu, HI.

An analytical model has been developed to simulate the material differentiation of a cometary nucleus composed of water ice, putative unclathrated CO_2 ice and silicate dust in specified proportions. Selective sublimation of any free CO_2 ice present in a new comet would produce a surface layer of water ice and dust overlying the original CO_2 rich material. This surface layer reduces the temperature of buried CO_2 ice and restricts the outflow of gaseous CO_2. On each orbit, water sublimation at smaller heliocentric distances temporarily reduces the thickness of the water ice and dust layer and liberates dust. Most of the dust is blown off the nucleus, but a small amount of residual dust remains on the surface. (cf. Houpis et al., 1985) Our model includes the effects of nucleus rotation, arbitrary orientation of the rotation axis, latitude, heat conduction into the deep interior of the nucleus and restriction of CO_2 gas outflow by the water ice and dust layer, features that were not included in the Houpis et al. model. Specifically, we investigate the effects of the permeability of the surface water ice layer, the nucleus rotation rate and the latitude. The loss rate of CO_2 and the resultant depth of CO_2 ice are shown to be most sensitive to the permeability of the water ice and dust layer. For a homogeneous, initially unmantled comet placed in the orbit of comet Halley, it is shown that the CO_2 ice attains a steady state or cyclic relationship between CO_2 depth and orbital position within several revolutions. If the nucleus contains 25% by mass of CO_2, our results indicate that CO_2 ice is always within several meters from the surface at any location for a nucleus of low obliquity and that CO_2 ice is nearest to the surface at the equator shortly after perihelion. Under these conditions the sublimation of CO_2 ice is always significant and becomes the dominant gaseous species beyond 4AU. This result is probably generally valid for unmantled portions of most comets and qualitatively simulates the behavior of an abundant, highly volatile component in an H_2O/silicate matrix. Comparison of these and similar results with observations could yield information regarding the permeability and chemical composition of cometary material and suggest sampling strategies to minimize fractionation effects.

Reference

Houpis, H.L.F., W.H. Ip and D.A. Mendis (1986). The chemical differentiation of the cometary nucleus: The process and its consequences. Astrophysical J., in press.

DYNAMICS OF LONG PERIOD COMETS

Paul R. Weissman, Earth and Space Sciences Division, Jet Propulsion Laboratory, Pasadena, CA 91109 USA

The appearance of Halley's Comet in 1985-86 and the related emphasis on research on physical models of cometary nuclei, led to a more moderate pace for the dynamical studies of the Oort cloud and the motion of long-period comets this year. Specific areas studied included the dynamical evolution of cometary showers as a result of stars passages through the inner Oort cloud and the possible relationship to observed stepwise mass extinctions at geological boundaries, revised estimates for the total mass of comets in the Oort cloud as a result of lessons learned from the spacecraft encounters with Halley's Comet, and study of the possible dynamical sources for the short-period comets in the solar system as part of a wider study of physical processing of cometary nuclei prior to their becoming visible comets.

The work on cometary showers used a Monte Carlo simulation of the evolution of cometary orbits under a combination of planetary, nongravitational, and stellar perturbations, and with physical removal by disruption, sublimation of all volatiles, and collision. A major cometary shower lasts about 2 to 3 Myr after the initial perturbation, with peak flux rates of about 9,000 comets crossing the Earth's orbit per year (600 times the usual flux). The average comet makes 8.5 returns with an average lifetime of about 0.8 Myr. Such an intense random shower would be caused by a one solar mass star passing 3,000 AU from the sun, would be expected perhaps once every 500 Myr, and might produce on the order of 20 significant impacts on the Earth.

The actual mechanism for initiating showers was found to be quite interesting. As compared with Hill's (1981) simple loss cone analysis, it was found that the total number of comets entering the planetary region was somewhat less, and the fraction perturbed to small perihelia (Earth-crossing orbits) was lower still. In addition, the intensity of showers dropped off sharply with more distant stellar passages, roughly as the inverse square of the encounter distance. The number of comets peturbed into the inner solar system is very much a function of the distribution of orbital semimajor axes in the inner Oort cloud; the figures above reflect an inner cloud that is only modestly centrally condensed. If the distribution of orbits in the cloud is steeper then distant encounters would be less effective at inducing large numbers of comets into cometary showers.

The timescales for cometary showers and that for disruption of terrestrial environments as revealed in the fossil record at extinction boundaries, are comparable. This does not prove a causal relationship and may be entirely coincidental, but it does demonstrate that comet showers may provide a plausible explanation for some biological extinction events. The main problem with this hypothesis is that extinctions are roughly 10 times more frequent than the expected rate of major cometary showers.

The estimated mass of comets in the Oort cloud has increased dramatically as a result of the revised estimate for typical cometary albedos based on the Halley spacecraft encounters. The term "dirty snowball" has tended to mislead people into thinking that comets were relatively bright objects, perhaps gray in color. In fact, comets are really "frozen mudballs" with the low albedo of their non-volatile constituents. While lowering the albedo causes an increase in the mass estimate, other factors such as shape, improved population estimates based on new dynamical modeling, and the fraction of active area on the nucleus, serve to reduce the total mass estiamte. Using a revised albedo of 0.05 based on the Halley encounters, it was found that the mass of comets in the outer, classical Oort cloud was 25 Earth masses, and the mass of the inner Oort cloud which serves as a reservoir to replenish the outer cloud is perhaps 250 Earth masses. The latter estimate is highly uncertain because of the lack of detailed dynamical modeling of the inner Oort cloud to date. Also, present attempts to estimate the density of cometary nuclei based on modeling of nongravitational forces on Halley are still highly uncertain.

The question of the source of the short-period comets is one that has taken on new meaning becaue of the proposed spacecraft missions to comets. To interpret the cosmochemical record found in comets it is necessary to know where they formed, and where they have been since their formation. Halley results have already shown that the comet appears to have formed from the same material as the rest of the planetary system. But the dynamical history of Halley prior to its being peturbed into its present orbit remains a mystery. The classical view is that short-period comets are long-period comets from the Oort cloud, captured by Jupiter perturbations. Recently, it has been shown that the inner Oort cloud should provide a dynamically more efficient source as comets trickle across Neptune's orbit and are passed down by planetary perturbations into the inner solar system. However, Halley's retrograde orbit argues against this (for Halley only) because the comets derived from the inner Oort cloud should be in direct orbits. Because of the chaotic nature of cometary orbit evolution, and the large number of comets we have to deal with, it is difficult to rule out any dynamical path for the origin of Halley or any other short-period comet. Work on this problem will continue.

OBSERVATIONS ON THE MAGNITUDE-FREQUENCY DISTRIBUTION OF EARTH-CROSSING ASTEROIDS

Eugene M. Shoemaker, U.S. Geological Survey, Flagstaff, AZ 86001
Carolyn S. Shoemaker, Arizona Research and Technology, Flagstaff, AZ 86002

During the past decade, discovery of Earth-crossing asteroids has continued at the pace of several per year; the total number of known Earth crossers reached 70 as of September, 1986. These objects comprise 36 numbered and 34 unnumbered asteroids, 11 of which are lost; 6 are Atens, 41 are Apollos, 22 are Earth-crossing Amors, and one of the Earth crossers has a present perihelion distance of greater than 1.3 AU. The sample of discovered Earth crossers has become large enough to provide a fairly strong statistical basis for calculation of mean probabilities of asteroid collision with the Earth, the Moon, and Venus. It is also now large enough to begin to address the more difficult question of the magnitude-frequency distribution and size distribution of the Earth-crossing asteroids.

Absolute V magnitude, H, has been derived from reported magnitudes for each Earth crosser on the basis of a standard algorithm that utilizes a physically realistic phase function (Minor Planet Circular 10193). On average, $H = V(1,0) - 0.3$, where $V(1,0)$ is the absolute magnitude based on a linear phase function. Fairly reliable observations of magnitude are available for most numbered Earth crossers, but observations are sparse for unnumbered objects and commonly consist only of visual estimates of B made from photographic plates. In the latter case, the derived value of H is calculated only to the nearest half magnitude.

The derived values of H range from 12.88 for (1627) Ivar to 21.6 for the Palomar-Leiden object 6344, which is the faintest and smallest asteroid discovered. The absolute magnitude of Ivar is close to the magnitude threshold for completeness of discovery of asteroids in the inner part of the main asteroid belt. It is possible that one or two more Earth crossers as bright or brighter than Ivar remain to be discovered, but it is unlikely that there are as many as ten. Completeness of discovery drops with increasing magnitude. Shoemaker et al. (1979) estimated the population of Earth crossers to $V(1,0) = 18$ (equivalent to $H = 17.7$) at ~1300; the observed number at $H = 17.7$ is 50, which corresponds to an estimated completeness of discovery of about 4%.

If we adopt the estimate of 1300 for the total number of Earth crossers brighter than $H = 17.7$ and assume that the number brighter than $H = 12.88$ does not exceed 3 Earth crossers, a plausible magnitude-frequency distribution for the population to $H = 17.7$ can be represented approximately by

$$N = 3.17\ e^{-1.28\ (13-H)}, \qquad (1)$$

where N is the cumulative frequency (fig. 1). This distribution corresponds to a monotonically decreasing completeness of discovery with increasing magnitude above 13.2, which is expected from circumstances of asteroid discovery. The distribution represented by eq. (1) is much steeper than the estimated average magnitude-frequency distribution of main belt asteroids,

which can be represented approximately by

$$N \propto e^{-0.9(-H)}, \qquad (2)$$

To the extent that Earth-crossing asteroids are derived as collision fragments from main belt asteroids, the size and magnitude distribution of Earth crossers can be expected to be steeper than those of main belt asteroids. Most collision fragments that become Earth-crossing objects probably are displaced in orbital element phase space into secular resonances by impulses of the order of hundreds of meters per second. Small collision fragments tend to receive larger impulses than large fragments, and small fragments probably are delivered preferentially to secular resonances and ultimately to Earth-crossing orbits.

The exponent (size index) of the cumulative size-frequency distribution of the impactors that produced the post-mare lunar craters ≥10 km diameter has been estimated at -1.62 (Shoemaker, 1983). A power function of the diameter with this exponent corresponds to an exponential magnitude-frequency distribution for the impacting objects of the form

$$N \propto e^{\frac{-1.62}{5 \log e}(-H)} = e^{-0.75(-H)}, \qquad (3)$$

under the condition that the range of albedo is similar for objects of different sizes. This derived magnitude distribution for post-mare impactors is much flatter than eq. (1) and also is flatter than the magnitude distribution of discovered Earth-crossing asteroids in the range $13 \leq H \leq 16$ (fig. 1). If 1300 is adopted as the cumulative number to H = 17.7, then the number of objects predicted by (3) at H = 13 is 30 times higher than the number observed. Conversely, if discovery of Earth crossers were considered complete at H = 13, then fewer objects than have already been discovered to H = 17.7 would be predicted by (3). From the ratio of the frequency of discovery of new Earth-crossing asteroids to the frequency of accidental recovery of those already known, it is certain that the number remaining to be found to H = 17.7 is many times greater than the number now known. If it is assumed that most 20-km-diameter, post-mare impact craters have been produced by asteroid impact, then the difference in exponent between (1) and (3) suggests that no more than 1/3 of the craters with diameters ≥50 km were formed by Earth-crossing asteroids. The large lunar craters probably have been formed chiefly by impact of comets.

References

Shoemaker, E.M., Williams, J.G., Helin, E.F.,and Wolfe, R.F., 1979, in Asteroids, ed. T. Gehrels: Tucson, University of Arizona Press, p. 253-282.

Shoemaker, E.M., 1983, Ann. Rev. Earth Planet. Sci. 11, p. 461-494.

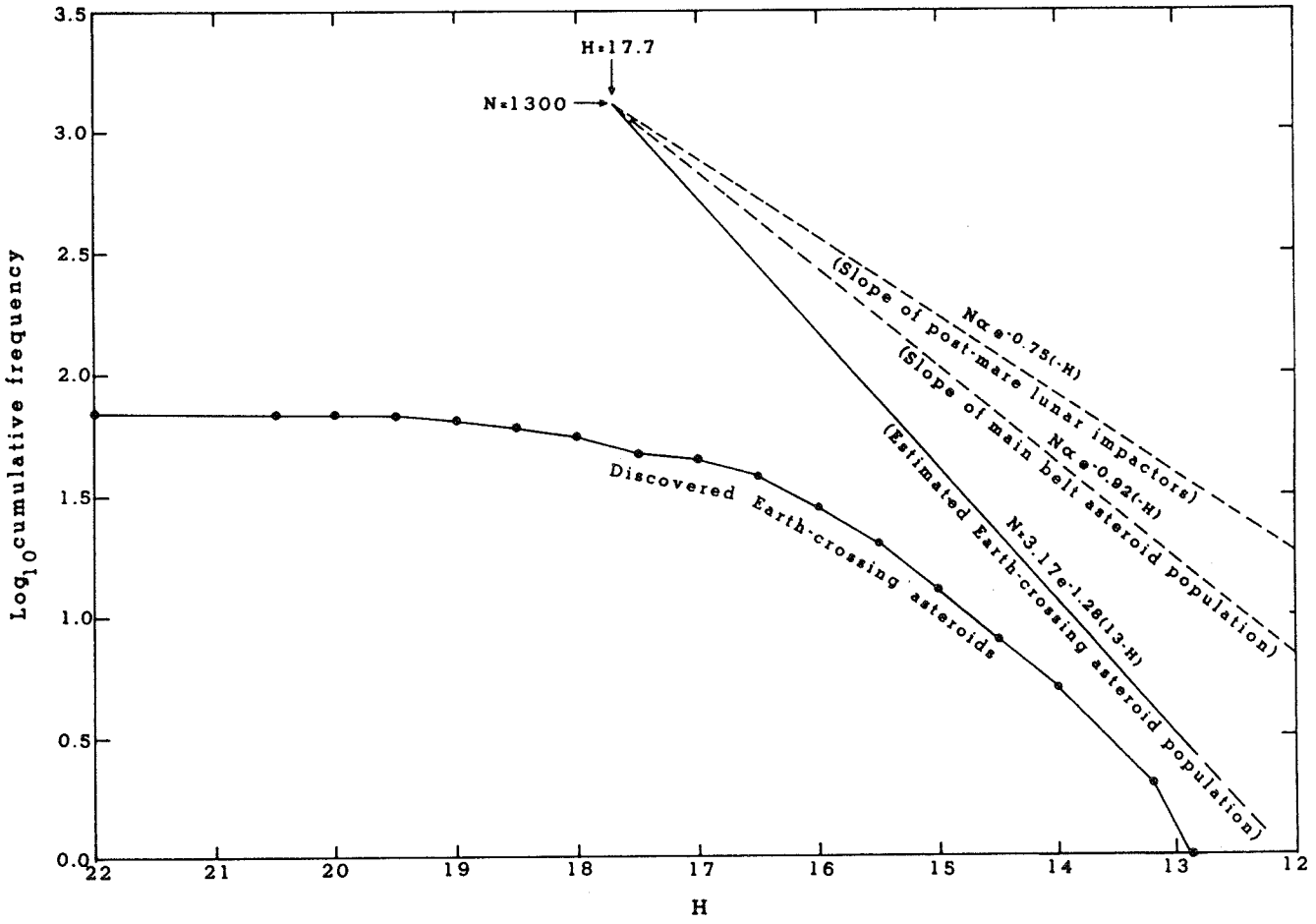

Figure 1. Magnitude-frequency distribution of Earth-crossing asteroids.

ASTEROID FAMILIES, DYNAMICS, AND ASTROMETRY

J. G. Williams and J. Gibson
Jet Propulsion Laboratory, Pasadena, CA, 91109

The proper elements and family assignments for the 1227 Palomar-Leiden Survey asteroids of high quality have been tabulated and included in a paper which is in press in Icarus. In addition to the large table, there are also auxiliary tables of Mars crossers and commensurate objects, histograms of the proper element distributions, and a discussion. Probably the most important part of the discussion describes the Mars crossing boundary, how the closest distances of approach to Mars and Jupiter are calculated, and why the observed population of Mars crossers should bombard that planet episodically rather than uniformly.

A start has been made on classifying families, the debris left over from collisions between asteroids, based on the relative sizes of the members, particulary with respect to the largest object, and where the largest object(s) lies in the family. The taxonomic classes of the members are also being compared. This undertaking is about 30% complete. Very few families appear to have resulted from total disruption and dispersal of the parent body.

Analytical work has been done to derive velocity distributions of family forming events from proper element distributions subject to assumptions which may be appropriate for cratering events. The more conventional approach uses an "average" value for the two orbital angles (true anomaly and argument of latitude); the family distributions can also be combined assuming a uniform distribution of the angles to get an overall velocity distribution. All researchers who have tried to get velocity distributions have found that the results from the different proper elements differ radically, with the semimajor axis giving the least and the inclination giving the largest velocities (by a factor of two or three). It is usual to dismiss this discrepancy by attributing it to the accuracy of the proper elements. While this was a plausible explanation 20 years ago, improvements in the calculation of proper elements and the presence of small structure in some families (there is a very tight core in family 38 and the inclination spread of family 128 is quite narrow) argue otherwise. Selection effects may be present in the less well populated families, but the strong asymmetry is also present in the more populous families. On the assumption that the effect is real, several possible causes have been considered, but all seem to be flawed. For example, the passage of weak secular resonances after family formation would scatter e and sin i without scattering a, but it would also leave a boxy morphology which is not seen. It has to be said that this asymmetry is not understood, but it could be an important problem.

During the past year software has been developed for a microcomputer to permit plotting the proper elements. Three orthogonal views are generated and stereo pairs can be printed when desired. This program was created for the study of asteroid families (a similar capability of long standing on a mainframe computer was lost when the high resolution graphics capability

was removed). In a cooperative effort with E. Tedesco and G. Veeder this software has been used to examine a sample of the best physical properties data that they have amassed. This work is presently ongoing, but so far Pv and two colors permit ten plausible taxonomic classes to be recognized.

The astrometry task is directed toward measuring and reducing positions on faint comets and the minor planets with less common orbits. The obsevational material is CCD frames taken with the Palomar 1.5m telescope. There is a need to measure Schmidt plates because the CCD is too small to capture an array of reference stars with known positions. It is necessary to use an existing plate to measure the fainter stars on the CCD frame with respect to the less common catalogue stars. During the past year positions of 10 comets and 16 different asteroids have been published on the Minor Planet Circulars. Many of these were early or late observations which particularly strengthen the orbit determination. In summary, asteroid positions were given on 10 planet crossers (1981 PB, 1981 VA, 1982 HR, 1982 TA, 1985 JA, 1985 PA, 1985 TB, 1985 WA, 1985 XB, and 1986 EB), 1 Pallas-type object (1986 AE), and 5 more ordinary minor planets. The comets were 1980 XI (Encke), 1982 i (Halley), 1985 f, h, j, k, and p and 1986 a, b, and c. These comet and asteroid positions were published on Minor Planet Circulars 9844, 9845, 9849, 9984, 9993, 9994, 10006, 10092, 10200, 10204, 10224, 10226, 10272, 10369, 10370, 10469, 10477, 10478, 10487, 10488, 10591, 10592, 10595, 10596, and 10690.

1986 DA AND 1986 EB: M-CLASS ASTEROIDS IN NEAR-EARTH ORBITS

Jonathan Gradie, Planetary Geosciences Division, HIG, 2525 Correa Road, Honolulu, HI 96822 and Edward Tedesco, Jet Propulsion Laboratory, Pasadena, CA 91109.

The earth-approaching asteroid population is composed of asteroids in orbits with lifetimes short compared with the age of the solar system. These objects which are comprised of Aten, Apollo, and Amor asteroids must be replenished from either cometary or mainbelt asteroid sources since lifetimes against collision with or ejection by a planet are on the order of 10 to 100 million years. Without a source, the number of such objects, postulated to be as large as 1,500 (Shoemaker, 1979), would be quickly depleted. Suggestions for sources has ranged from cometary (Opik, 1951) to a combination of asteroidal and cometary (c.f. Shoemaker, 1979; Wetherill, 1986). A cometary source implies that the compositions consistent with the non-volatile remnants of a comet (Hartmann, et al., 1986) where as an asteroidal source would imply that the compositions consistent with the asteroidal source region.

The physical study of Earth-approaching asteroids is constrained by the generally long period between favorable apparitions and poorly known orbits. For example, although 88 such asteroids have been discovered through 1985 only 47 had orbital elements sufficiently reliable to receive permanent numbers (Hahn, 1986). For this reason, these objects must be studied as "targets of opportunity" as soon as they are discovered and before orbital elements are firmly established and a permanent number is assigned. Such is the case for objects 1986 DA and 1986 EB.

1986 DA and 1986 EB were discovered on 16 February 1986 by M. Kizawa, Shozouka, Japan and on 4 March 1986 by E. Shoemaker and C. Shoemaker, Palomar Observatory, respectively (IAU Circ. 4181 and 4191). 1986 DA is a member of the Amor group since its orbital elements cause it to cross the orbit of Mars but not the Earth whereas 1986 EB is a member of the Aten group since its orbital elements cause it to cross the orbit of the Earth even though its semimajor axis is less than 1 AU.

Broadband spectrophotometry on the Johnson UBVR system and the Eight-Color Asteroid Survey system (Tedesco, et al., 1982) were obtained at Kitt Peak National Observatory and on the Johnson JHK system and at 10 and 20 microns at the NASA Infrared Telescopy Facility at Mauna Kea Observatory (Tedesco and Gradie, 1987). These observations were used to determine the absolute visual magnitudes and to derive the visual geometric albedos and diameters on the IRAS system (Lebofsky, et al., 1987) given in Table I.

Table I. UBV colors and mean albedos and diameters.

Object	H	G	U-B	B-V	pv	Diameter (km)
1986 DA	15.94	0.25	0.21	0.70	0.14	2.3
1986 EB	15.94	0.25	0.24	0.71	0.19	2.0

The UBV colors and the albedos are enough to uniquely classify these two objects on the taxonomic system of Gradie and Tedesco (1982) as class M, the first of these objects to be found in the planet crossing population.

The spectral reflectance properties and geometeric albedos of the M-class asteroids are consistent with compositions analogous to the iron-nickel meteorites or the enstatite-metal assemblages of the enstatite chondrites (Zellner, 1979). Radar observations by Ostro, et al. (1985) of the M-class asteroid 16 Psyche indicate a body nearly entirely of metal. These results imply that both 1986 DA and 1986 EB are probably nearly entirely metallic in composition, perhaps similar in gross composition to the iron meteorites.

The identification of two objects probably of entirely metallic composition has important implications for 1) the origin of the objects currently found in near-earth orbit, 2) the timescales for the delivery of iron meteorites to the earth and 3) the sources of raw materials for space industrialization.

Tedesco and Gradie (1987) examine the issue of the source(s) of the near-Earth asteroids population by comparing the classifications on the scheme employed by Gradie and Tedesco (1982) of 38 such asteroids. Those asteroids for which an unambiguous C, S, or M classification could not be assigned were called "Others" (e.g. D, E, F, P, R or unclassifiable). Five objects were classified as C, twenty-four as S, two as M (1986 DA and 1986 EB), and seven as "Other". The predominance of the well-known C, S, and M classes of asteroids (>80%) in this population strongly suggests that the source region is the asteroid belt unless cometary nuclei are compositionally indistinguishable from the C, S, and M class of asteroids. Furthermore, the presence of M-class asteroids in the near-Earth population argues that the source in the asteroid belt must be close to the 3:1 and 5:2 Kirkwood gaps since these are the only regions in the belt where M-class asteroids are found.

If the source of most of the near-Earth objects is indeed the asteroid belt as our observations suggest, then a method for removing extinct nuclei of short period comets must be found since the rate of production of short period comets from the long period comets is relatively large. We suggest that the lack of a large number of objects with compositions consistent with that expected for short period comets, i.e., dark and spectrally reddened (Hartmann, et al., 1986), argues that either the majority of comets lack cohesive, volatile-free cores and end up as meteor streams or the core of a comet may be so friable that it cannot survive intact as long as asteroidal material.

The two metallic objects , 1986 DA and 1986 EB, provide examples of near-Earth, intermediate parent bodies of some iron meteorites. Using the meteorite production model of Greenberg and Chapman (1983) we calculate that half of the iron meteorites should come from these two objects. These irons should have cosmic-ray exposure ages of < 100 million years, the mean lifetime of most objects in planet-crossing orbits. However, the cosmic-ray

exposure ages of nearly all iron meteorites measure to date are 4 to 20 times older which implies that these irons came directly from the asteroid belt as meter-sized objects without the need for an intermediate parent body. This discrepancy suggests that either that meteorite production from near-Earth iron objects is extremely inefficient or, as Wasson (1985) points out, the small number of irons with cosmic-ray exposure ages less than 200 million years my be the result of experimental bias.

Finally, we note that 1986 DA and 1986 EB, if indeed similar in gross composition to the iron-nickel meteorites, could prove to be valuable sources of raw materials for space industrialization since relative transportation costs to and from these objects could be greatly reduced. Such objects would contain not only iron (90-95 wt%) and nickel (5-10 wt%) but also cobalt (0.6 wt%) and sizeable trace amounts of other elements including gold, platinum group metals.

REFERENCES

Gradie, J. and Tedesco, E.F. (1982). Science 216, 1405.

Greenberg, R. and Chapman, C. R. (1983). Icarus 55, 455.

Hartmann, W.K., Tholen, D.J. and Cruikshank, D.P. (1986). Bull. Amer. Astron. Soc. 18, 800-801.

Lebofsky, L.A., Sykes, M. V., Tedesco, E.F., Veeder, G.J. Matson, D.L., Brown, R.H., Gradie, J., Feierberg, M.A., and Rudy, R.J. (1987). Icarus, in press.

Opik, E.J. (1951). Proc. Ropy. Irish Acad. 54A, 165.

Ostro, S.J., Campbell, D.B. and Shapiro, I.I. (1985). Science 229, 442.

Shoemaker, E.M., Williams, J.G., Helin, E.F., and Wolfe, R.F. (1979). In Asteroids edited by T. Gehrels (Univer. Arizona Press, Tucson), p.253.

Tedesco, E.F. and Gradie, J. (1987). Astron. J., submitted.

Tedesco, E.F., Tholen, D.J. and Zellner, B. H. (1982). Astron. J. 87, 1585.

Wasson, J. (1985). Meteorites. (W. H. Freeman and Company, New York).

Zellner, B. H. (1979). In Asteroids, edited by T. Gehrels (Univ. Arizona Press, Tucson), p. 783.

EVOLUTION OF THE INNER ASTEROID BELT: PARADIGMS AND PARADOXES FROM SPECTRAL STUDIES. Michael J. Gaffey, Department of Geology, West Hall, Rensselaer Polytechnic Institute, Troy, New York 12180-3590.

Recent years have witnessed a significant increase in the sophistication of asteroidal surface material characterizations derived from spectral data. An extensive data base of moderate to high spectral resolution, visible and near-infrared (~0.35-2.5μm) asteroid spectra is now available (1-4). Interpretive methodologies and calibrations have been developed to determine phase abundance and composition in olivine-pyroxene assemblages and to estimate NiFe metal abundance from such spectra (5-7). A modified version of the asteroid classification system more closely parallels the mineralogic variations of the major inner belt asteroid types (8). These improvements permit several general conclusions to be drawn concerning the nature of inner belt objects; their history, and that of the inner solar system; and the relationship between the asteroids and meteorites.

Essentially all large inner belt asteroids have - or are fragments of parent bodies which have - undergone strong post-accretionary heating, varying degrees of melting and magmatic differentiation, and subsequent collisional disruption. The surfaces of the dominant S-type asteroids appear mostly to be the exposed metal-rich internal layers of differentiated or partially differentiated parent planetesimals (7,9). The shift from an S-type dominated inner belt population to a C-type dominated outer belt population (10) appears to be primarily the result of post-accretionary heating of the inner belt and not the signature of a radial compositional gradient in the original solar nebula. The S-type asteroids are predominantly olivine-metal assemblages with a relatively minor pyroxene component [ol/px$\gtrsim$2.5] (3,9), but exhibit a significant range of variation. These asteroids show a systematic, but not yet well characterized, mineralogic variation with semi-major axis. Large S-type family asteroids exhibit greater lightcurve amplitudes in general than large non-family S-objects, and the mineralogic range among members of the S-families is much smaller than the range in the background S-type population. This suggests that the S-type asteroid families represent relatively recent ($\lesssim$4byr) collisions onto the cores of previously disrupted parent bodies. A variety of additional constraints (heating requirements for small bodies, rarity of pure olivine mantle fragments, meteorite heating ages) suggest that the thermal evolution of the inner belt occurred very early, followed quickly by disruption during single collision events with an intruding flux of large planetesimals, similar to those invoked to abort the growth of Mars (11).

REFERENCES: (1) Chapman, C.R. and Gaffey, M.J. (1979) in Asteroids (T. Gehrels and M.S. Matthews, Eds.), U. Arizona Press, pp. 655-687. (2) Zellner, B., Tholen, D.J., and Tedesco, E.F. (1985) Icarus 61, 355-416. (3) Feierberg, M.A., Larson, H.P., and Chapman, C.R. (1982) Astrophys. J. 257, 361-372. (4) Bell, J.F., Hawke, B.R., Owensby, P.D., and Gaffey, M.J. (1985) Bull. Am. Astron. Soc. 17, 729. (5) Adams, J.B. (1974) J. Geophys. Res. 79, 4829-4836. (6) Cloutis, E.A., Gaffey, M.J., Jackowski, T.L., and Reed, K.L. (1986) J. Geophys. Res., submitted. (7) Gaffey, M.J. (1986) Icarus, in press. (8) Tholen, D.J. (1984) Ph.D. Diss., U. Arizona, Tucson. (9) Gaffey, M.J. (1984) Icarus 60, 83-114. (10) Gradie, J., and Tedesco, E. (1982) Science 216, 1405-1407. (11) Weidenschilling, S.J. (1975) Icarus 26, 361-366.

This research has been supported under NASA Grant NAGW-642.

Meteorite Spectroscopy and Characterization of Asteroid Surface Materials

Michael J. Gaffey, Geology Department, Rensselaer Polytechnic Institute, Troy, New York 12180-3590.

The purpose of this research effort is to improve our understanding of the origin, evolution, and inter-relationships of the asteroids; of their relationships to the meteorites; and of the conditions and processes in the early inner solar system. The surface mineral assemblage and the surface heterogeneity of selected minor planets is determined from analysis of telescopic spectra to provide the data base to accomplish these goals.

The asteroids represent the sole surviving, in situ remnants of the population of planetesimals which accreted to form the Earth and other terrestrial planets. The meteorites are samples of some of these asteroidal bodies, but the specific source bodies of the individual meteorites or meteorite groups have not been established. Thus the detailed meteoritic evidence cannot be directly placed into a spatial context in the early solar system. The meteorites provide a good "clock" for events and conditions in the late nebular and early accretionary period of solar system history, but they provide a poor "map".

The analysis of asteroidal visible and near-infrared (VNIR) reflectance spectra compliments meteorite studies as a means of probing the late nebular through early post-accretionary period of solar system history. Although surface material characterizations from VNIR reflectance spectrophotometry cannot achieve the detail or the level of sophistication attainable in the laboratory analysis of meteoritic specimens, such remote sensing studies do provide valuable and unique information on material whose location in the early solar system can be established with some certainty. Asteroid spectral studies also provide insight into the incompleteness in the meteorite sample and into the types of additional assemblages which are present on asteroids.

The particular type of material present on a specific asteroid provides direct insight into the nebular or post-accretionary processes in the early solar system at that particular semi-major axis. As the number of characterized asteroids increases, so does the completeness of this "map" of early processes and conditions. The combination of temporal constraints from meteoritic studies and spatial constraints from asteroid spectral characterizations provides the most powerful available means of investigating the formation epoch.

This research program involves five complimentary efforts, including:

1) the development of quantitative interpretive calibrations and procedures for the analysis of VNIR spectral data from laboratory spectral studies of the meteoritic and meteorite-like assemblages which are appropriate analogues to asteroidal materials [e.g. Gaffey, 1986a; Cloutis et al., 1986],

2) the reduction and calibration of high precision VNIR telescopic data of asteroids selected as particularly relevant to major issues in asteroid or meteorite science,

3) the analysis of that asteroid VNIR spectral data using the most sophisticated available interpretive calibrations and methodologies to derive quantitative or semi-quantitative determinations of surface mineralogy, phase abundance, and the mineralogic nature and lateral extent of large scale lithologic units on the surface [e.g. Gaffey, 1983, 1984],

4) the utilization of these surface material characterizations to constrain the evolution of individual asteroids, such as the presence and intensity of any post-accretionary thermal events, the degree of metamorphism or magmatic differentiation, and the nature and extent of

the subsequent collisional processes [e.g. Gaffey, 1984], and 5) the synthesis of this information on individual asteroids into models of the inter-relationships between the various asteroid groups, the post-accretionary collisional and thermal history of regions and populations in the asteroid belt, and the implications for the accretion and early evolution of the terrestrial planets [e.g. Gaffey, 1986b].

This multidiscipline approach, combining in a single program all the major aspects of the work, has proven particularly efficient. It allows each aspect to be better focused on the central issues. For example, calibration work can be better directed toward satisfying the most pressing needs in the interpretive area; the observations can be specific to the questions being addressed rather than simply part an uncoordinated general survey; and the analysis can effectively communicate its most urgent needs for specific calibrations or for observations of a particular type.

However, in any asteroidal research beyond the most general type of survey observations (i.e. in the first pass, one observes whatever happens to be available), the quality of the scientific contribution which is produced depends significantly on the appropriateness and sophistication of the formulation of the original question. A major focus of this research program is the issue of asteroidal thermal and collisional evolution.

The relative proportion of S-type asteroids decreases rapidly with increasing semi-major axis across the asteroid belt. This has been interpreted to indicate that either: a) the belt represents a transition region between the zones of formation of ordinary chondrite-type and the carbonaceous chondrite-type assemblages by nebular processes, or b) the inner portion of the belt has undergone a strong post-accretionary heating event which altered the original material in that region.

In the first alternative, the general population pattern in the belt is the fossil signature of the radial compositional variation of the accreting solar nebula. In principle, once that pattern is understood, the temperature and pressure of the nebula could be strongly constrained at that particular distance from the proto-sun. In the second case, the radial variation in the asteroid population is the signature of a radially dependent heating event in the early post-accretionary period which was superimposed upon the previous nebular material. It is plausible or probable that such a heating event would have also affected the planetesimals in the zones of the terrestrial planets. In that case, the early thermal structure and processes (core formation, atmospheric outgassing rates, etc.) of the terrestrial planets, which accreted from such a population of planetesimals, would be a strong function of the thermal state these planetesimals. An Earth accreted from warm, magmatically differentiated planetesimals would have a profoundly different early history than one accreted from cold, undifferentiated planetesimals, even though both would have chondritic bulk compositions.

To date, essentially all available spectral evidence has strongly indicated that the large S-type asteroids are predominantly thermally evolved, magmatically differentiated bodies [see, Gaffey, 1984; Gaffey, 1986a,b). It is also now evident that the variation in UBV colors of the S-type asteroids with semi-major axis (Dermott et al., 1985) is a manifestation of a systematic mineralogic variation within the S-type population, these objects becoming more metal- and pyroxene-rich and more olivine-poor with increasing orbital distance (Gaffey, 1986b). This pattern is the reverse of that expected from an undifferentiated, chondritic planetesimal population. The relationships indicate that indeed the S-type are primarily thermally-evolved bodies, and that the innermost S-type objects underwent the most intense heating and differentiation while the outer S-types underwent substantial reduction of oxidized iron with either

strong metamorphism or partial melting. Work is underway using 52-color survey spectra (Bell et al., 1985) to refine this picture.

Analysis of rotationally resolved reflectance spectra has been used to derive a litholoic unit map for 4 Vesta (Gaffey, 1983; and in preparation), to investigate asteroid surface heterogeneity (Gaffey, et al., 1982), and to test the chondritic affinities of 8 Flora (Gaffey, 1984).

Present work is concentrated on 15 Eunomia, the largest S-type asteroid. Observations in December, 1981 produced 101 24-filter spectra (0.35-1.00um) and 66 120-channel VNIR CVF spectra (0.65-2.55um). These exhibit rotational variations which are being analyzed to determine the nature of the hemispheric mineralogic variations which produce the variations.

In addition, the flux variations in each filter or channel provides a lightcurve for Eunomia at that bandpass. In a cooperative program with S.J. Ostro (JPL), these monochromatic lightcurves are being inverted by his technique (Ostro and Connelly, 1984) to derive an equivalent equatorial profile of the body. Since the physical shape of the body is invariant, differences between the profiles at different wavelengths must arise from surface reflectance variations. Combined with the subhemispheric mineralogic variations determined from the analysis of the spectra at different rotational aspects, the variations of the complex profile within and outside mineralogically diagnostic spectral intervals will permit determination of lithlogic boundaries and, if Eunomia is an intact core fragment, constrain the litho-stratigraphic structure within the parent planetesimal. This should significantly increase our understanding of the nature of the magmatic differentiation processes in asteroid sized bodies.

References

Bell, J.F, B.R. Hawke, P.D. Owensby, and M.J. Gaffey (1985) The 52-color asteroid survey: Results and interpretation. Bull. A.A.S. 17, 729.

Cloutis, E.A., M.J. Gaffey, T.L. Jackowski, K.L. Reed (1986) Calibrations of phase abundance, composition, and particle size distribution for olivine-orthopyroxene mixtures from reflectance spectra. J. Geophys. Res. 91, 11,641-11,653.

Dermott, S.F., J. Gradie, and C.D. Murray (1985) Variation of the UBV colors of S-class asteroids with semimajor axis and diameter. Icarus 62, 289-297.

Gaffey, M.J. (1983) The asteroid (4) Vesta: Rotational spectral variations, surface material heterogeneity, and implications for the origin of the basaltic achondrites. Lunar Planet. Sci. XVI, 231-232.

Gaffey, M.J. (1984) Rotational spectral variations of Asteroid (8) Flora: Implications for the nature of the S-type asteroids and for the parent bodies of the ordinary chondrites. Icarus 60 83-114.

Gaffey, M.J. (1986a) The spectral and physical properties of metal in meteorite assemblages: Implications for asteroid surface materials. Icarus 66, 468-486.

Gaffey, M.J. (1986b) Evolution of the inner asteroid belt: Paradigms and paradoxes from spectral studies. Meteoritics 21.

Gaffey, M.J., T. King, B.R. Hawke, and M.J. Cintala (1982) Spectral variations on asteroidal surfaces: Implications for composition and surface processes. in Workshop on Lunar Breccias and Soils and Their Meteoritic Analogs (G.J. Taylor and L.L. Wilkening, Eds.), LPI TR 82-02, Lunar and Planetary Institute, Houston, pp. 40-43.

Ostro, S.J. and R. Connelly (1984) Complex profiles from asteroid lightcurves. Icarus 57, 443-463.

SOURCE OF THE OPTICAL RED-SLOPE IN IRON-RICH METEORITES. Daniel T. Britt, Carle M. Pieters, and Peter H. Schultz, Department of Geological Sciences, Brown University, Box 1846, Providence, RI 02912.

The relationship between ordinary chondrites and the S-type asteroids is an unresolved issue in meteorite science. S-type asteroids exhibit a positively red-sloped spectrum that has been interpreted to indicate the presence of elemental iron on their surfaces. Some workers [1] suggest that S-type asteroids represent undifferentiated parent bodies of ordinary chondrites on which regolith processes have enhanced the spectral signature of metallic iron relative to laboratory samples. Other workers [2] interpret the red-slope spectra in S-types to indicate the presence of relatively large amounts of elemental iron and suggest that the differentiated meteorites are better analogs. The issue hinges on the amount and form of iron required to produce a spectral red-slope.

Investigators using integrating-sphere spectrometers [3] note that iron-rich meteorites exhibit a strong and characteristic red-slope in the visible and near-infrared wavelengths. Optical constants measured at normal incidence for iron [4] and for iron-nickel alloys [5] also predict a red-sloped spectrum. The effect of viewing geometry on the reflectance of iron meteorites has been investigated using NASA's RELAB facility located at Brown University [6]. Figure 1 shows the spectra of a clean, smooth portion of a nickel-iron meteorite taken from several viewing geometries (these data are relative to the reflectance of halon and are displayed on a logarithmic scale). A striking feature of these results is that iron's characteristic red-slope appears only in the specular portion of the reflectance. All the non-specular geometries exhibit flat, featureless spectra with the relative brightness being a function of the angular distance from the specular reflection. These results suggest that the diffuse reflectance spectrum of iron and any iron-rich complex surface is a weighted average of specular and non-specular components; the degree of "redness" is a function of the amount of the specular component included in the measurement. As a test of this hypothesis, bi-directional spectra were obtained of a complex iron surface (an 8 mm crater produced in an experimental hypervelocity, metal on metal, impact on the same iron meteorite [7]). The spectrum of the crater on the meteorite exhibit a red-slope of 30%. The proportions of shadow and specular, near-specular, and non-specular reflectance were estimated for the meteorite crater, and a linear mixing model was applied using the spectra of figure 1. Less than 0.2% of the specular component was required to accurately model the red-slope of the meteorite crater.

CONCLUSIONS: The characteristic red-sloped spectrum of iron-rich meteorites is produced by only the specular component of the reflectance. Complex metallic surfaces can be modeled as linear mixtures of specular and non-specular components. It is the geometry of the metal on a surface and its interaction with surrounding material, rather than the absolute amount of metal, that determine the redness of resulting spectra. In order to distinguish between ordinary chondrite and differentiated parent bodies it is important to understand how regolith processes affect the nature and form of metal on asteroid surfaces.

REFERENCES: [1] Feierberg, M.A., et al. (1982) *Astrophys. J. 257*, p 361-372. [2] Gaffey, M.J. and McCord, T.B. (1978) *Space Sci. Rev. 21*, p 555-628. [3] Gaffey, M.J. (1976) *J. Geophys. Res. 81*, p 905-920. [4] Bolotin, G.A., et al. (1969) *Phys. Metal. Metallography 27*, p 31-41. [5] Sasovskaya, I.I. and Noskov, M.M. (1974) *Phys. Metal. Metallography 37*, p 45-52. [6] Pieters, C.M. (1983) *J. Geophys. Res. 88*, p 9534-9544. [7] Matsui, T. and Schultz, P.H. (1984) *Proc. Lunar Planet. Sci. Conf. 15th*, in *J. Geophys. Res. 89*, p C323-C328

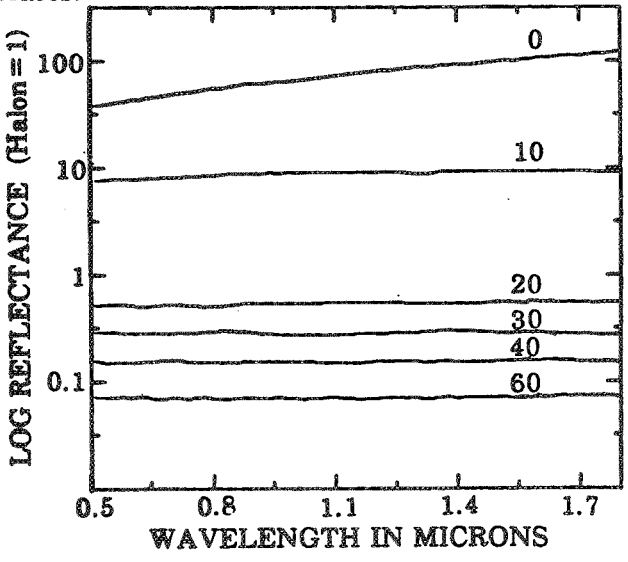

FIGURE 1: Bi-directional reflectance of iron meteorite sample. Labels are in degrees from specular reflection.

A SEARCH FOR SPECTRAL ALTERATION EFFECTS IN CHONDRITIC GAS-RICH BRECCIAS.

J. F. Bell (Hawaii Institute of Geophysics, Honolulu HI 96822) and Klaus Keil (Institute of Meteoritics, Univ. of New Mexico, Albequerque NM 87131)

INTRODUCTION: The photons reflected by planetary surfaces do not penetrate the surface by more than a few millimeters, even in the most transparent minerals. Thus the large number of visual and IR reflection spectra of asteroids obtained with telescopes (and in the future by spacecraft) sample only the very uppermost regolith. However these spectra are usually compared with lab spectra of solid meteorites derived from the asteroidal bedrock. Solid meteorite fragments are pulverized to simulate the scattering conditions in the upper regolith. This methodology implicitly assumes that the regolith-forming process on asteroids changes only the particle size and does not introduce spectral effects due to glass formation, solar wind implantation, etc. On the Moon, very strong weathering effects (mostly related to the formation of glassy agglutinates) exist in the uppermost regolith which largely conceal the absorption features of minerals, except in very fresh craters. While it is generally agreed that lunar-style glass formation is a very minor process in asteroidal regoliths due to the lower impact velocities, several workers have proposed alternate weathering effects to account for various mysteries connected with asteroid spectral interpretation (e.g. Pieters 1984; T.V.V. King et al. 1984; McFadden and A'Hearn 1986; Weatherill, personal communication, 1984). A small subset of meteorites, the solar-gas-rich breccias, apparently preserve portions of the uppermost regolith complete with alteration effects characteristic of long exposure to the space environment. Typically, areas of fine-grained matrix in these meteorites are rich in implanted solar wind gases, particle tracks left by galactic cosmic rays and solar flares, and small fragments of exotic meteorites classes, apparently projectile material which has survived low-velocity impacts. These effects indicate that this matrix material once resided on the optical surface of an asteroid, was turned over by regolith gardening, lithified by an impact, ejected, and transported to Earth. (A similar history is inferred for many lunar samples, including lunar meteorites). Large clasts in the same breccias usually are devoid of these effects in their interiors, which were protected from direct exposure to space. If any unknown weathering effect exists in the uppermost regolith of asteroids which significantly affects current interpretations of their composition, it should be evident in a spectral difference between gas-rich matrix and gas-poor clast interiors. We have carried out a systematic search for such effects to test the hypothesis that they could make ordinary-chondrite material resemble the common Class S asteroids.

MEASUREMENTS: Several samples of gas-rich breccias were selected, including slabs of the Kapoeta howardite, the ordinary chondrites Dubrovnik, Cangas de Onis, and Dimmit. Numerous 0.8-2.5 micron reflection spectra of selected areas on sawed or broken surfaces were measured with the Planetary Geosciences Division spectrogoniometer. While these spectra are not directly comparable to those of powdered samples (the continnua are systematically bluer), comparisons within the data set should reveal any spectral differences due to space weathering.

RESULTS: Kapoeta: Spectra of eucritic clasts resemble those of powdered eucrites. Spectra of dark gas-rich matrix are very similar except

for slight reduction in band depths. Both lower albedo and reduced band depths are probably due to mild shock effects. Dubrovnik: All spectra very similar and resemble powdered ordinary chondrites, with pyroxene band depths reduced relative to eucrites due to presence of dispersed iron particles. Cangas de Onis: Spectra similar to Dubrovnik. A few highly shocked dark veins have anomalously shallow bands, but gas-rich and gas-poor regions are very similar. Dimmit: This meteorite contains a clast of impact melt rock in a chondritic matrix, representing the most extreme form of altered regolith. Spectra of this clast have very deep pyroxene bands. They closely resemble those of the eucritic clasts in Kapoeta, and earlier published eucrite spectra. This may be due to the lack of metal in the Dimmit clast; it appears to be a fragment of a large melt pool in which the metal component settled out.

IMPLICATIONS FOR ASTEROIDS: These results indicate that unknown regolith processes do not conver the ordinary-chondrite parent bodies with an altered layer exhibiting S-class spectral properties. This is consistent with recent interpretations of the new Q-class of asteroids as the ordinary-chondrite parent bodies. However, significant spectral effects do occur in asteroid regoliths: A) Darkening and suppression of absorption bands in highly shocked material, as seen previously in the so-called "black chondrites"; B) Segregation of metal in large impact melt pools on chondritic asteroids, which may have achondritic spectra. Neither of these effects is likely to be significant in interpreting current integral-disk spectra, but should be searched for in spectral maps returned by future spacecraft.

REFERENCES:

King, T. V. V. (1984). Spectroscopic evidence of regolith maturation. Meteoritics, 19, 251-252.

McFadden, L. A., and M. F. A'Hearn (1986). Asteroid composition and meteorite origins. In NASA TM-88383, p. 14.

Pieters, C. (1984). Asteroid-meteorite connection: Regolith effects implied by lunar reflectance spectra. Meteoritics, 19, 290-291.

ANALYTICAL ELECTRON MICROSCOPY OF FINE-GRAINED PHASES IN PRIMITIVE INTERPLANETARY DUST PARTICLES AND CARBONACEOUS CHONDRITES.

Ian D. R. Mackinnon, Frans J. M. Rietmeijer, Department of Geology, University of New Mexico, Albuquerque NM 87131 and David S. McKay, Mail Code SN4, NASA Johnson Space Center, Houston TX 77058.

Exploration of the Solar System by spacecraft over the past few decades has not only provided an enhanced appreciation of the geological diversity within planetary bodies, but also a greater understanding of the origin and evolution of our Solar System and perhaps others within the galaxy. A fundamental component of this understanding involves the compilation and analysis of chemical, physical and mineralogical data on the smaller bodies within the Solar System. These bodies (or their fragments) probably contain a record of processes occurring early in the evolution of the Solar System. In general, the fine-grained fractions (i.e. <1 μm) of solid materials in primitive meteorites and micrometeorites are the most likely hosts for this record of early Solar System processes [1]. Any study of early Solar System processes should involve (a) characterization of known extraterrestrial materials intersecting Earth orbit [2,3], (b) an understanding of possible contaminants both in low Earth orbit and the upper atmosphere [4,5], (c) experimental verification of basic phenomena occurring in a stellar environment [6] and (d) the production of realistic models on aspects of Solar System evolution [1,7]. In the current phase of this research program, all approaches have been utilized and highlights of this work are given below.

In order to describe the total mineralogical diversity within primitive extraterrestrial materials, individual interplanetary dust particles (IDP's) collected from the stratosphere as part of the JSC Cosmic Dust Curatorial Program [8] have been analysed using a variety of AEM techniques. Identification of over 250 individual grains within one chondritic porous (CP) IDP shows that most phases could be formed by low temperature processes [2] and that heating of the IDP during atmospheric entry is minimal and less than 600°C [2, 9]. This observation agrees with more recent entry temperature estimates based upon solar flare track data. We have suggested that layer silicates observed in these IDP's could have formed by low temperature (cryogenic) alteration of precursor silicates [2]. In a review of the mineralogy of IDP's [1], we also suggest that the occurrence of other silicates such as enstatite whiskers is consistent with formation in an early turbulent period of the solar nebula during which C/O and Mg/Si ratios enhance condensation at temperatures <1000°C.

Considerable attention has been paid to carbon-rich phases in IDP's and at least three different forms have been identified [1]. Earlier work on poorly-graphitised carbons (PGC's) has shown that the basal spacing of synthetically-formed PGC varies with formation temperature [10]. This structure-temperature relationship has been proposed as a new type of cosmothermometer for primitive extraterrestrial materials [11]. This temperature dependence has been confirmed for naturally occurring PGC's in terrestrial environments [11,12]. The lower graphitisation temperatures predicted for carbonaceous chondrite and IDP PGC's also reflects the presence of catalysts during the graphitisation process [11]. Use of this cosmothermometer on observations of PGC's in carbonaceous chondrites or IDP's [11,12] provides a record of the last temperature event experienced by the

host body. Other types of carbon observed in IDP's include the polymorph carbon-2H, and we propose that this type of carbon formed by hydrous pyrolysis of precursor hydrocarbons [14]. A collaborative laser microprobe study on carbon-rich IDP's, previously characterized by AEM, provides inconclusive results on the presence of interstellar carbon [15] though they are consistent with previous ion microprobe studies.

Micrometeorites captured in low Earth orbit have also allowed a fortuitous calibration of orbital capture techniques for future dedicated Shuttle or Space Station missions [16]. Components returned from the Solar Maximum satellite have been exposed to space for about four years and thus, contain a continuous record of the local micrometeorite and debris environment by way of impact features (i.e. craters and penetration holes) with associated projectile residues and adhered solids [3]. Electron optical analyses of the returned Solar Max surfaces show that solid residue from the projectiles survived impact due, in part to the multi-layer design of thermal blankets and the variable approach velocities of impacting bodies [17]. Analysis of solid particles associated with impact features readily allows the identification of orbital debris, such as paint particles [16], as well as at least two types of micrometeorites: Mg-Fe silicates and Fe-Ni sulphides [3,16]. Detailed AEM observations on Mg-Fe silicate particles show that (a) they are Mg-rich olivines with a chemical signature similar to olivine in CM chondrites and (b) these olivines did not melt upon impact and survived impact without appreciable shock metamorphic effects, such as lattice distortion [18]. These observations provide an important database for the capture of pristine micrometeorites by Earth-orbiting capture cells or comet coma dust sampling devices [16,17].

Experimental confirmation of fundamental chemical and physical processes in a stellar environment, such as vapor phase condensation, nucleation, and growth by annealing, is an important aspect of astrophysical models for the evolution of the Solar System. For example, the microstructural development of refractory smokes can provide significant constraints on the kinetics of particle growth and accumulation in a stellar environment. Characterization of laboratory-produced smokes has shown that both infra-red spectroscopy and X-ray diffraction fail to detect the very initial stages of crystallite development during high temperature annealing of "amorphous" smokes [6]. Detailed AEM study indicates that microcrystallites of forsterite may directly condense from an MgO-SiO vapor phase system or form metastably shortly after condensation [6]. With annealing, both compositional and structural transformations of the MgO-SiO smokes occur and have been documented using the AEM [6]. Similar textural and structural observations have been presented for the ultra fine-grained minerals in four anhydrous chondritic IDP's, and are interpreted as evidence for annealing in the early history of the Solar System [15,19,20,25].

An inherent limitation of terrestrial-based laboratory experiments on particle condensation, nucleation and growth from a vapor phase is the influence of the Earth's gravity during smoke production. To overcome this experimental limitation, suggestions on the development of a particle (or "dust") facility on board the Shuttle, and ultimately, upon the Space Station have been proposed [21,22]. This potentially rich area for experimental confirmation of fundamental astrophysical concepts has also received attention with respect to understanding solar nebula physico-chemical processes such as turbulence and particle aggregation [23,24].

On a larger scale, the possible relationships between chondritic IDP's and chondrite meteorite components have also been investigated [1,25]. In one case, there may be mineralogical similarities between an IDP and the matrices of CO/CV chondrites or unmetamorphosed unequilibrated ordinary chondrites [25]. However, in general, a detailed comparison of chondritic IDP and carbonaceous chondrite mineralogies shows significant differences between the types of silicate minerals as well as the predominant oxides [1]. In a continuing effort to characterize the fine-grained matrix of carbonaceous chondrites, detailed structural and morphological studies of the mineral tochilinite have been presented [26]. This work arises from the suggestion that the commonly-known "poorly-characterized-phases" (PCP's) can in fact be identified as members of the mixed-layer tochilinite mineral group or as coherent intergrowths of tochilinite and serpentine [27]. This is a critical observation for models of CM matrix formation as tochilinite paragenesis, though incompletely studied, appears restricted to very specific environments on Earth [28].

References:

1. Mackinnon IDR and Rietmeijer FJM (1986) Rev. of Geophysics, in press.
2. Rietmeijer FJM and Mackinnon IDR (1985) J. Geophys. Res., 90, D149-D155.
3. Rietmeijer FJM et al., (1986) Adv. Space Res., in press.
4. Mackinnon IDR (1986) LPI Tech Rpt. 86-05, 68-72.
5. Rietmeijer FJM (1986) LPI Tech. Rpt. 86-05, 80-82.
6. Rietmeijer FJM et al., (1986) Icarus, 65, 211-222.
7. Rietmeijer FJM (1986) Nature, 313, 293-249.
8. Mackinnon IDR et al., (1982) J. Geophys. Res., 87, A413-A421.
9. Mackinnon IDR and Rietmeijer FJM (1984) Nature, 311, 135-138.
10. Rietmeijer FJM and Mackinnon IDR (1985) Lunar & Planet. Sci. XVI, 700-701.
11. Rietmeijer FJM and Mackinnon IDR (1985) Nature, 315, 733-736.
12. Lumpkin GR (1986) Lunar & Planet. Sci. XVII, 504-505.
13. Lumpkin GR (1986) Lunar & Planet. Sci. XVII, 502-503.
14. Rietmeijer FJM and Mackinnon IDR (1986) Nature, in press.
15. Carr, RH et al., (1986) Meteoritics, 21, in press.
16. McKay, DS et al., (1986) LPI Tech Rpt. 86-05, 72-75.
17. Rietmeijer FJM (1986) Rpt on Multi-Comet Mission, in press.
18. Blandford GE et al., (1986) Lunar & Planet. Sci. XVII, 56-57.
19. Rietmeijer FJM and McKay DS (1986) Lunar & Planet. Sci. XVII, 710-711.
20. Rietmeijer FJM (1986) Meteoritics, 21, in press.
21. Nuth JA et al., (1985) SSPEX Workshop, 62-63.
22. Nuth JA et al., (1985) In: Micro-gravity Particle Research on the Space Station, 2-8.
23. Mackinnon IDR and Rietmeijer FJM (1985) In: Rpt. on a Workshop on Experimental Cosmo-chemistry in the Space Station, 15-16.
24. Iversen J et al., (1985) SSPEX Workshop, 7-12.
25. Rietmeijer FJM and McKay DS (1985) Meteoritics, 20, 743-744.
26. Zolensky ME and Mackinnon IDR (1986) Am. Mineral., 71, 1201-1209.
27. Mackinnon IDR and Zolensky ME (1984) Nature, 309, 240-242.
28. Zolensky ME (1984) Meteoritics, 19, 346-347.

ASTEROID LIGHTCURVE INVERSION

Steven J. Ostro, Jet Propulsion Laboratory, Pasadena, CA 91109
Robert Connelly, Cornell University, Ithaca, NY 14853

One of the most fundamental physical properties of any asteroid is its shape, i.e., its dimensions. Lightcurves provide the only source of shape information for most asteroids. Unfortunately, the functional form of a lightcurve is determined by the viewing/illumination geometry ("VIG") and the asteroid's light-scattering characteristics as well as its shape, and in general it is impossible to determine an asteroid's shape from lightcurves (1). The best one can do is to derive a shape constraint that is useful and takes advantage of all the information in the lightcurve.

We have introduced a technique called convex-profile inversion (CPI) that obtains a convex profile, $\underline{P}$, from any lightcurve (2). If certain ideal conditions are satisfied, then $\underline{P}$ is an estimator for the asteroid's "mean cross section", $\underline{C}$, a convex set defined as the average of all cross sections C(z) cut by planes a distance z above the asteroid's equatorial plane. $\underline{C}$ is therefore a 2-D average of the asteroid's 3-D shape. The ideal conditions are that (A) all C(z) are convex; (b) the asteroid's scattering law is geometric, so brightness is proportional to the projected visible, illuminated area; (C) the VIG is equatorial, i.e., the asteroid-centered declinations δ_E and δ_S of the Earth and Sun are zero; (D) the solar phase angle $\phi \neq 0$.

The first three conditions are unlikely to ever be satisfied exactly, but the issue here is the extent to which their violation degrades the validity of $\underline{P}$ as an estimator for $\underline{C}$. Laboratory simulations suggest that modest, "topographic" concavities play a relatively minor role in determining the form of a lightcurve (3). Similarly, numerical experiments indicate that systematic errors introduced by small (several-degree) violation of Condition C are not severe (4). The bulk of available polarimetric and spectrophotometric data show that whereas "hemispheric" albedo variations can be detected at about the several percent level for several asteroids [e.g., (5)], the forms of most broadband optical lightcurves seem less sensitive to surface heterogeneity than to gross asteroidal shape.

Geometric scattering is expected to be an excellent approximation close to opposition (6), but a poor approximation far from opposition (7). This is an unfortunate circumstance, because CPI's ability to reveal odd harmonics in $\underline{C}$ improves as ϕ increases. The systematic error introduced by non-geometric scattering will depend on the 3-dimensional shape as well as on the VIG. Hence, the nature and magnitude of this error will be to invert several lightcurves obtained under nearly ideal VIG but at a variety of solar phase angles, use the weighted mean profile as an estimate of $\underline{C}$, and use the variance in the profiles to gauge hte severity of systematic error.

What can an opposition lightcurve tell us about an asteroid's shape? At $\phi = 0$, CPI yields a profile $\underline{P}_S$ as an estimator for $\underline{C}_S$, the "symmetrization" and the ratio β, of the profile's maximum breadth to its minimum breadth, remain intact.) Moreover, Condition A need not hold at opposition, and if it does not, then $\underline{C}_S$ is the symmetrization of the asteroid's mean convex envelope, or "hull".

Opportunities for reliable estimation of $\underline{C}_S$ should be much more abundant than those for estimation for $\underline{C}$ for several reasons. First, the VIG required for reliable estimation of $\underline{C}_S$ occurs much more frequently than that for estimation of $\underline{C}$. Second, to assess how close the VIG is to ideal, we want to know the direction of the asteroid's spin vector when estimating $\underline{C}$, but we just need to know the direction of the asteroid's line of equinoxes when estimating $\underline{C}_S$. Third, as noted above, geometric scattering is most valid close to opposition. Finally, as shown by Russell (1), it is easy to test the hypothesis that the ideal conditions required for reliable estimation of $\underline{C}_S$ ($\delta_E = \delta_S = \phi = 0$ and geometric scattering) actually hold; if the lightcurve has any odd harmonics, the conditions are violated.

$\underline{C}_S$ is the symmetrized average of all C(z) and constitutes the optical extraction of shape information from an opposition lightcurve, just as $\underline{C}$ constitutes the optimal extraction of shape information from a non-opposition lightcurve. If an estimate of $\underline{C}$ were free of systematic errors, its symmetrization would look the same as an estimate of $\underline{C}_S$, so we can use opposition lightcurves to qualify the interpretation of non-opposition lightcurves.

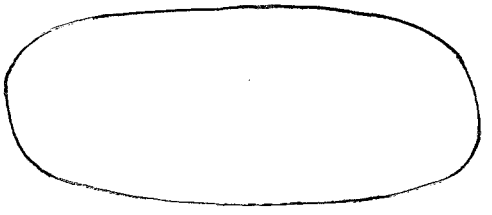

This profile is our estimate of $\underline{C}_S$ for asteroid 624 Hektor from CPI of a lightcurve obtained by Dunlap and Gehrels (8) at ϕ - 4^o. The pole directions estimated by those authors and by Magnusson (9) indicate that $|\delta_E|$, $|\delta_S| < 10^o$. The constancy of Hektor's color indices with rotational phase (8) results of Russell's Fourier test, and the goodness of fit of CPI's model lightcurve to the data concur in supporting the expected high reliability of this estimate.

The profile has $\beta = 2.5$ and is distinctly non-elliptical. Since the mean cross section of an ellipsoid rotating about a principal axis is an ellipse, our results suggest that neither the asteroid nor its convex hull are ellipsoids. On the other hand, our results are quite consistent with many other models for Hektor's 3-D shape, including a cylinder with rounded ends (8), a dumbbell (10), and various binary configurations.

REFERENCES: 1) Russell H.N. (1906), Astrop. J. 24, 1-18. 2) Ostro S. J. and Connelly R. (1984), Icarus 57, 443-463. 3) Barucci M.A. and Fulchignoni M. (1981), in Asteroids, Comets, Meteors (C.-I. Lagerkcist and H. Rickman, Eds.), pp. 101-105. 4) Ostro S. J., Dorogi M.D., and Connelly R. (1985), Lunar Plan. Sci. 16 Abstracts, 637-638. 5) Gaffey M. J. (1984), Icarus 60, 83-114. 6) French L. M. and Veverka, J. (1983), Icarus 54, 38-47. 7) Lumme K. and Bowell E. (1981), Astron. J. 86, 1694-1704. 8) Dunlap J. L. and Gehrels T. (1969), Astron. J. 74, 796-803, Fig. 8. 9) Magnusson P. (1986), Icarus, in press. 10) Hartmann W. K. and Cruikshank D. (1978), Icarus 36, 353-366. 11) Weidenschilling S. L. (1980), Icarus 44, 807-809.

Accumulation of the Planets

G. W. Wetherill, DTM, Carnegie Institution of Washington

A. Early Stages of Planetary Growth.

In modelling the accumulation of planetesimals into planets, it is appropriate to distinguish between two stages:

(A) An early stage, during which $\sim$ 10 km diameter planetesimals accumulate locally to form bodies $\sim 10^{25}$ g in mass. During this stage, it is useful to treat the bodies as particles, analogous to gas molecules in the kinetic theory of gases.

(B) A later stage in which the $\sim 10^{25}$ g planetesimals accumulate into the final planets. During this stage it is likely that bodies will become well-mixed as a consequence of radial excursions and the "giant" impacts will occur. During this stage it is better to trace the orbital evolution of the larger individual bodies.

Previous work on the early stage has been extended by use of new expressions developed by G. R. Stewart of the University of Virginia to describe the changes in velocity of the bodies as a consequence of mutual gravitational perturbations, collisions, and gas drag. The contribution of one of these terms, "dynamical friction", has not been included in any earlier calculations, and all previous workers have neglected at least one of the other terms as well.

In the terrestrial planet region, an initial planetesimal swarm corresponding to the critical mass of dust layer gravitational instabilities is considered. It is assumed these bodies have an initial exponential mass distribution $dN \alpha e^{-m/m_o} dm$ where $m_o = 3 \times 10^{18}$ (11.5 km diameter) and an initial relative velocity of 11 m/sec, and the gas density to be 1.18×10^{-9} g/cm^3. The continuous distribution is modelled as an assemblage of 10^8 bodies divided into 22 "batches", each batch containing bodies of equal mass distributed over a zone of width $\Delta a = 0.02$ A.U. The size and velocity evolution of each batch is followed through successive time steps by calculating the effects of gravitational perturbations, collisions, gas drag, merger, and fragmentation. When appropriate, the effect of low velocities on the gravitational cross-section was included.

For a continuous initial size distribution, as assumed by previous workers, an orderly growth is found, the early stage of accumulation ending when most of the mass of the terrestrial planet region is concentrated in $\sim$3000 bodies ranging from $\sim 10^{24}$ g to $\sim 10^{25}$ grams in mass at the time ($\sim 10^6$ years) that eccentricities rose to $\sim$.01.

"Runaway accretion", in which most of the mass of the zone becomes concentrated in a single low eccentricity $\geq 10^{26}$ g body in $< 10^5$ years, was found to require a discontinuous initial mass distribution, i.e. a "seed" at the upper end of the distribution. The size of the seed required is somewhat dependent on the parameters assumed for gas drag and fragmentation. For the more plausible values, a "seed" 2 to 3 times the mass of the 2nd largest body is required. The presence or absence of such seeds is not at present predictable. For this reason, it is permissible to speculatively entertain models in which volatile-rich seeds are formed beyond the "snow line" of the solar nebula at $\sim$5 A.U., but not in the asteroid belt and the terrestrial planet region. This could be a factor in facilitating the rapid growth of planetesimals of Jupiter and Saturn, despite the relatively long accumulation times conventionally associated with these large heliocentric distances.

B. Late Stages of Planetary Growth.

Our previous work on this problem has concentrated on the larger terrestrial planets, Earth and Venus. Because of their smaller size and less "averaging", the

present state and chemical composition of Mercury and Mars may be expected to be more diagnostic of events during planet formation.

In order to understand better the accumulation history of Mercury-size bodies, 19 new Monte-Carlo simulations of terrestrial planet growth have been calculated. Three cases are presented, involving different assumptions regarding the initial state of the final stage of planetary accumulation and the degree and ease with which planets can be collisionally disrupted. It is found that the same conditions that lead to Mars-size giant impacts on Earth and Venus imply a more catastrophic fragmentation history for Mercury-size bodies and the fragments from which they accumulated. In accordance with these results, it may be speculated that the large iron core of Mercury may be a consequence of a giant impact that removed the silicate mantle from a previously differentiated body. Less extreme fragmentation events may also contribute to chemical fractionation processes for which bodies in this mass range may be especially susceptible. It is also found that planets of the size and position of Mercury will accumulate material originating over the entire terrestrial planet range of heliocentric distances. This tends to reduce the relative importance of more primordial chemical fractionation processes.

C. Primitive Earth-approaching Bodies (Meteorites, Apollo-Amors, Meteors).

A Monte Carlo technique has been used to investigate the orbital evolution of asteroidal collision debris produced interior to 2.6 A.U. It is found that there are two regions primarily responsible for production of Earth-crossing meteoritic material and Apollo objects. The region adjacent to the 3:1 Jovian commensurability resonance (2.5 A.U.) is unique in providing material in the required quantity and orbital distribution of the ordinary chondrites. This region should also supply a comparable preatmospheric flux of carbonaceous meteorites. This work has been extended to include the innermost asteroid belt. The innermost asteroid belt (2.17 to 2.25 A.U.), via the υ_6 secular resonance, provides a flux $\sim$9% that of the ordinary chondrites, and appears to be the strongest candidate for the basaltic achondrite source region. It is unlikely that a significant number of meteorites originate beyond 2.6 A.U. It is speculated that enstatite achondrites are derived from the Hungaria region, interior to the main belt, and that iron and stony-iron meteorites originate from many main belt sources interior to 2.6 A.U.

The same techniques have been extended to include the origin of Earth-approaching asteroidal bodies. It is found that these same two resonant mechanisms predict a steady-state number of Apollo-Amor about 1/2 that estimated based on astronomical observations. There are some types of observed Apollo-Amor orbits that are observationally overpopulated by a factor of 10 - 30 when compared with predictions of the asteroidal source model. These deficiencies are remedied by postulation of additional production of Apollo-Amor objects as outgassed comets at a rate of $\sim 10^{-5}$ yr^{-1}.

Particularly puzzling questions are raised by sun-approaching bodies, and attention is being given to these. Two Apollo objects have perihelia <0.2 A.U. and aphelia <2.5 A.U. (1566 Icarus and 1983TB). The latter is associated with the Geminids, the second most prolific of the annual meteor showers. At least 1% of the Prairie Network fireballs are in similarly small orbits; because of selective effects the fraction must be higher (e.g. Geminids were excluded in reducing the data). These orbits are unstable on a time scale of $\sim 10^7$ years and a fairly productive source is required. None of the known mechanisms (either cometary or asteroidal) for supplying Earth-crossing material can accomplish this.

This lack of correspondence with known cometary and asteroidal material has been extended by examination of the atmospheric trajectories of six -5 to -8 magnitude meteors: three bright Geminids reported by Jacchia and three non-Geminid Prairie Network fireballs in similar Sun-approaching orbits. These objects, both Geminid and non-Geminid, also show physical similarities to one another. All of them are Ceplecha and McCrosky type I fireballs, in this way we have identified as ordinary chondrites. Their ratio of photometric/dynamic mass is at least as small, and often smaller than ordinary chondritic fireballs, a further indication of strong, dense bodies. They are clearly unlike typical Taurids (Comet Encke) and other cometary fireballs which fragment more easily and are probably of lower density.

These bodies, however, have much lower ablation coefficients ($\sigma \sim 5 \times 10^{-13}$ sec^2/cm^2) than ordinary chondritic asteroidal fireballs ($\sigma \sim 2 \times 10^{-12}$ sec^2/cm^2). If loss by ablation were all that mattered, a Geminid would retain 4% of its initial mass while penetrating the atmosphere, despite its entry velocity of 36 km/sec. Nevertheless, they fail to fully decelerate in the atmosphere, instead they disappear at velocities of 17-32 km/sec at dynamic pressures of $\sim 10^7$ $dynes/cm^2$. For this reason, their breaking strength appears to be no greater than ordinary chondrites, despite all this other quantitative evidence for "toughness". The relatively small mass ($\sim 1 - 100g$) of these bodies makes it difficult to know whether or not any possibly collectible material survives their apparent disappearance. Measurement and reduction of larger Geminids on fireball network photographs could permit addressing this question.

CHAPTER 4

COSMOGONY AND DYNAMICS

Protostellar disks and the Primitive Solar Nebula

P. M. Cassen, J. B. Pollack, T. Bunch
O. Hubickyj, P. Moins
NASA Ames Research Center
Moffett Field, CA 94035
C. Yuan
City College of New York
New York, NY 10031

(1) Turbulence in the solar nebula. This is a new project that we expect to figure prominently in our future work. The objective is to obtain quantitave information on the turbulent transport of mass, angular momentum and energy under the conditions that characterized the solar nebula, by direct numerical calculations. These calculations have been made possible by research conducted on new supercomputers (Cray XMP and Cray 2) by the Ames Computational Fluid Dynamics Branch, with whom we have established a strong collaboration. Techniques have been developed that permit the accurate representation of turbulent flows over the full range of important eddy sizes -- from the largest scales at which energy is deposited in turbulent motions, down through the inertial sub-range, to the small scales at which viscous dissiptaion becomes important. So far, these techniques have been applied (and verified) primarily in mundane laboratory situations, but they have a strong potential for astrophysical applications.

Most current models of the solar nebula are based on the hypothesis that turbulent stresses drive its evolution. But disagreement exists on the effectiveness, or intensity, of the turbulence. All models are burdened by untested assumptions regarding the details of the driving mechanisms, the vertical distribution of dissipated energy, and the all-important effects of rotation. Our approach is to conduct a sequence of numerical experiments to evaluate the Reynold's stress tensor, turbulent heat transfer rate, turbulent dissipation rate, and turbulent kinetic energy spectrum, as functions of position, for conditions relevant to the solar nebula. Emphasis is placed on the variation of these properties with appropriate nondimensional quantities (such as the Rayleigh, Taylor, and Prandtl numbers), so that relations can be derived that will be useful for disk modeling under a variety of hypotheses and initial conditions. In these experiments, we intend to examine separately the characteristics of three potential sources of turbulence in the nebula: thermal convection, mass infall from outside the nebula, and shear in the angular velocity.

The codes that were developed for engineering purposes require modification and generalization in a number of areas to realize their full potential for nebula studies, and this is where our efforts have been devoted so far. Calculations of Benard convection and convection driven by internal heat sources have been performed. Diagnostics have been devloped that permit easy examination of turbulent correlation coefficients, energy spectra, mean variable profiles, all evaluated at selected locations in the computational grid. The convection results

have been compared with detailed experimental results and those of other numerical computations to the point where we are confident that our resolutions, computational grid size, integration time, etc. are adequated. We are now embarking on a series of experiments that will become progressively more general and complex, as we (1) obtain results for parameter ranges more relevant to nebula studies (e.g. low Prandtl numbers) that have not been previously examined, and (2) include more physical effects that will be necessary for our goal of understanding nebula turbulence.

(2) Self-gravitating Disk Models. Most models of the solar nebula ignore the self-gravity of the disk compared to that of the protosun. In many circumstances this is a good approximation, but it is clearly inadequate for gravitational instability of the disk, to form spiral density waves, planets or multiple star systems, say, should treat the gravitational field of the disk self-consistently. So far, this has only been attempted in studies that use hydrodynamical codes to calculate the collapse of protostellar clouds. However, the results of theses calculations are usually not the formation of a solar nebula-like disk, but rings or ring fragments (see review by Bodenheimer and Black, in Protostars and Planets, U. of Arizona Press, 1978), or in some cases, thick disks that are subject to non-axisymmetric instabilities (Boss, Icarus, 61, 3, 1985). In some cases, an ad hoc turbulence is added to transport angular momentum outward, allowing a disk to form (Morfill et al., in Protostars and Planets II, U. of Arizona Press, 1985). These results contrast with semi-analytic calculations of cloud collapse by Terebey et al. (Ap. J., 286,529,1984), which suggest that a slowly rotating cloud can collapse directly to a disk.

In order to examine the ring/disk formation question, as well as to provide a convenient method for studying self-gravitating disk models for other purposes, we have devised a method whereby (nearly) arbitrary distributions of mass and angular momentum in spherically symmetric protostellar clouds can be mapped into corresponding distributions in infinitely thin self-gravitating disks, under the assumption of strict angular momentum conservation. The method is based on Toomre's (Ap. J., 138, 385, 1963) Bessel integral formulation for the mass distribution in flattened galaxies. Solution of an integral equation, by an iterative method, is required; but what appears to be an excellent first approximation for the mass distribution in the disk can be found analytically for many cases. These preliminary results agree very closely with the corresponding results of Cassen and Moosman (Icarus, 48, 353, 1981) for inviscid disks. Furthermore, they suggest that disks (rather than rings) can form a wide range of initial cloud conditions, even at high rotation rates, as long as enough accretional energy can be radiated away so that the thin disk approximation is valid. Calculations of the cooling of the post-accretion shock gas indicate that this is the case. The implication is that numerical collapse calculations must resolve the accretion shock cooling region very well in order to get accurate results, even on the basic question of ring- vs. disk formation.

(3) Analysis and interpretation of meteoritic inclusions. Examination of the components of the Allende meteorite has continued, along with the development of a model postulated to explain the observed thermal processing of CAIs (see Bunch et al., Lunar Planet. Sci. XVI, 97, 1985; Cassen et al. ibid. 117, 1985; Bunch et al., Lunar Planet. Sci. XVII, 87, 1986). The essence of the hypothesis is that the secondary processing exhibited by these objects resulted from an episode of aerodynamic heating most plausibly attributed to entry into the atmosphere of a large planetisimal. Microprobe and SEM analyses performed this year indicate that "classic" chondrules and ferro-magnesium aggragataes in Allende may also have experienced thermal processing related to the growth processes of a parent body. Details are provided in the attached Appendix. Synthesis of this data, along with an evaluation of other heating mechanisms, are currently in progress. The implications of our conclusions with regard to the Allende parent body are that it was a large (~1,000 km radius) body possessing a substantial (but perhaps transient), dusty atmosphere.

Timescales for Planetary Accretion and the Structure of the Protoplanetary Disk

Jack J. Lissauer (U. California, Santa Barbara)

Models of planetary accretion which assume the mass of condensable matter in the protoplanetary disk was equal to that present in the planets today predict accretion timescales for the outer planets $\gtrsim 10^8$ years. Such timescales are inconsistant with observations of star forming regions, which suggest that most of the gas in disks around one solar mass stars is removed in a few x 10^6 years. This paper outlines a unified scenario for solar system formation consistent with astrophysical constraints. Jupiter's core could have grown by runaway accretion of planetesimals to a mass sufficient to initiate rapid accretion of gas in times of order of $5 \times 10^5 - 10^6$ years, provided the surface density of solids in its accretion zone was at least 5-10 times greater than that required by minimum mass models of the protoplanetary disk. The inner planets and the asteroids can be accounted for in this picture if the surface density of the solar nebula was relatively uniform (decreasing no more rapidly than $r^{-\frac{1}{2}}$) out to Jupiter's orbit. The total mass of the protoplanetary disk could have been less than one tenth of a solar mass provided the surface density dropped off more steeply than r^{-1} beyond the orbit of Saturn. The outer regions of the nebula would still have contained enough solid matter to explain the growth of Uranus and Neptune in $5 \times 10^6 - 10^8$ years, together with the coincident ejection of comets to the Oort cloud. The formation of such a protoplanetary disk requires significant transport of mass and angular momentum, and is consistent with viscous accretion disk models of the solar nebula.

Formation of Giant Molecular Clouds in Global Spiral Structures: The Role of Orbital Dynamics and Cloud-Cloud Collisions.*

W. W. Roberts, Jr., G. R. Stewart (U. Virginia)

We investigate the different roles played by orbital dynamics and dissipative cloud-cloud collisions in the formation of giant molecular clouds (GMCs) in global spiral structures. The interstellar medium (ISM) is simulated by a system of particles, representing clouds, which orbit in a spiral-perturbed, galactic gravitational field. Detailed comparisons are made between the results of cloud-particle simulations in which the cloud-particles collide inelastically with one another and give birth to and subsequently interact with young star associations and the results of stripped-down simulations in which cloud-cloud collisions and star formation processes are omitted. Large "GMC-like" associations of smaller clouds are efficiently assembled in spiral arms and subsequently dispersed in interarm regions largely by the orbital dynamics alone. The overall magnitude and width of the global cloud density distribution in spiral arms is very similar in the collisional and collisionless simulations. The results suggest that the assumed number density and size distributions of clouds and the details of individual cloud-cloud collisions have relatively little effect on these features. In the simulations with shorter mean free paths, pronounced shock-like density and velocity profiles occur. In the simulations with longer mean free paths and in the collisionless simulations, we find more symmetric, less shock-like density and velocity profiles. The natural tendency of orbits to crowd together in spiral arms is enhanced by the temporary trapping of clouds in spiral arm potential minima for periods up to 50 Myr. Dissipative cloud-cloud collisions play an important steadying role for the cloud system's global spiral structure. Dissipative cloud-cloud collisions also damp the relative velocity dispersion of clouds in massive associations and thereby aid in the effective assembling of GMC-like complexes. The assembly of these GMC complexes from smaller clouds is remarkably efficient even if collisional coalescence of individual clouds is inefficient.

*Work supported in part under NSF grant AST-82-04256 and NASA grant NAGW-929.

ANALYSIS OF PLANETARY EVOLUTION WITH EMPHASIS ON DIFFERENTIATION AND DYNAMICS

William M. Kaula and William I. Newman
University of California, Los Angeles

Task #1: Collapse of the Proto Solar System Cloud

In order to address the early stages of nebula evolution, we are developing a three-dimensional collapse code which includes not only hydrodynamics and radiative transfer, but also the effects of ionization and, possibly, magnetic fields. We intend to focus on understanding the properties of a protostellar cloud which lead to the formation of a Jupiter-like second largest body, since such a body would have had a significant influence on the subsequent dynamics of the circumsolar material from which the planets formed. Ultimately, we intend to couple this collapse code with the accretionary N-body being developed in task #2 which addresses the problem of planet formation.

Over the past few months, we have developed a numerical model for protostellar collapse similar to one developed by Boss in 1979. We are developing a hydrodynamic scheme that minimizes the effect of numerically-induced artificial diffusion and expect to improve upon the overall accuracy by replacing the first order finite difference scheme with a higher order difference scheme or, preferably, a spectral or Galerkin technique.

In order to define the specific numerical technique that we intend to use, we have surveyed the current literature for a method which minimizes boundary errors while remaining computationally efficient. Glatzmaier (1984) developed spectral and Galerkin techniques to model magnetohydrodynamic problem in solar physics, methods that are well-suited to the protostellar collapse problem. However his model accommodates only the shell of a sphere. Currently, we are adapting this technique to full spherical geometry by reducing the lower boundary to the sphere's center. Thus we hope to minimize the problem of artificial diffusion and develop an accurate means for dealing with the inner region of the nebular cloud where the important physical changes take place.

Task #2: Formation of the Post-Jovian Planets

As part of our examination of solar system evolution, we have developed an N-body code describing the latter stages of planet formation from the accretion of planetesimals. It is based on Aarseth's (1972) scheme and is a sixth order, three dimensional code which solves the equations of motion precisely for N mutually attracting bodies. In practice, the run-time for such a code varies as N^3. It is our goal to reduce this cubic exponent through efficient vectorization.

To test our code for accuracy and run-time efficiency, and to develop a stronger theoretical foundation for our study, we have used it to study problems in orbital dynamics. This summer, we examined resonant interactions between Neptune and Pluto, with Jupiter as the single other perturbing body. We observed significant exchange of angular momentum over the equivalent of 1.9 million years. Our results support conclusions made by others (Nacozy and Diehl; 1978, Williams and Benson, 1971), who found that resonance improved the stability of the Neptune-Pluto system. We have reproduced periodicities they found in eccentricity and inclination. Understanding such resonant effects is basic to understanding mechanisms which may be important to solar system formation. Other planetary problems we shall examine are the stability of orbits between Jupiter and Saturn, possible rounding of Neptune's orbit by smaller bodies, and the effect due to the 2:1 resonance with Jupiter on diffusion of planetesimal sized bodies at that orbit. The last problem is essential to a theory of planet formation.

In the beginning of this year, we converted our code to run on the CRAY computers at Los Alamos National Laboratory, and later at the San Diego Supercomputer Center. The Neptune-Pluto problem took nearly two hours of computer time. In anticipation of problems with many more bodies, we have updated the subroutines which perform the force calculations to enhance vectorization. These routines occupy approximately 90% of the CPU time used by our program. Test runs show that the combined effect of moving the code onto the CRAY and vectorizing the force routines has been a twelvefold increase in speed over that of scalar machines.

The next step in suiting our code for planetesimal accretion is to invoke the ability to handle collisions. We have now written the routines to identify and service two-body interactions. With this capability, we intend next to compare our results to those of other investigators, such as Wetherill (1985). Wetherill simulated the accumulation of 500 moon-sized bodies in a gas free environment. His Monte Carlo simulations typically produced four roughly earth sized planets in the order according to mass like that of our own solar system. We shall examine the sensitivity of the outcome (i.e. number and location of planets) to initial conditions. We also intend to develop more precise values for certain parameters, such as gravitational cross section, collision frequency and impact energies, which are essential to analytical treatment of the problem.

Task #3: Regional Tectonics of Venus

We are performing a regional analysis of the correlation between the gravity and topography fields of Venus, in an effort to determine the small and intermediate scale subsurface structure. This subsurface structure will provide us with valuable information concerning the depth of compensation, flexural rigidity of the lithosphere, thermal profile, and ultimately, the tectonic regimes characterizing Venus. Knowledge of Venus tectonics will then allow us to make inferences concerning reasons for the apparent differences between the earth and Venus in terms of global tectonics.

The analysis of the gravity and topography of Venus is done using a two-dimensional Fourier admittance function technique, developed by Dorman and Lewis (1970) and McNutt (1979). This technique allows us to analyze the correlation between gravity and topography at different wavelengths, and to compare these correlations with model admittances. The main complication involved with this technique is the nature of the Venus gravity measurements. While a vertical gravity field is required for this admittance analysis, the Pioneer Venus Orbiter data consists of accelerations measured in the line-of-sight (LOS) direction - that is, accelerations along a line between the Venus surface, the spacecraft, and earth.

We have written the computer programs necessary to convert this LOS gravity field to vertical gravity using quadratic sum minimization, an inverse method described by Kaula (1966), Jackson (1979), and Jackson and Matsu'ura (1985). This method combines the measured data, using a matrix representing the complete LOS observation geometry, the LOS data, and a covariance matrix of the measurement errors, with a priori information, in the form of a covariance matrix of resolving errors. This method involves two major parts. The first is representation of the LOS observation geometry in a 2^{o} by 2^{o} matrix form, involving averaging of the spacecraft altitudes, LOS azimuths and declinations, and the LOS gravity measurements. The solution of this problem is nearly complete. The other part involves the quantification of the a priori assumptions on the form of a covariance matrix. The assumption being made is that the topography and compensation are linearly related, but we don not know the amplitude (i.e. the depth of compensation) of this relationship. It now appears the best way to deal with this problem is to use a range of

depths of compensation for our covariance matrices, and find the one which minimizes the chi-squared residuals. The programming for this method is also nearly completed.

Choosing regions of study based on evidence of consistent tectonics has also been a problem. Division of the surface into radar units based on reflectivity and rms slope (Davis et al., 1986, Head et al., 1985) shows very complex relationships. Since the LOS gravity and topography show good correlation on a long-wavelength, regional scale, we have decided to delineate regions based on topography, and will use the residuals of the admittances to help decide if this delineation is justified. The programs to invert the data and solve for the equivalent surface mass distribution, and hence the vertical gravity field, have been completed, as have the programs to determine the admittance functions for the regions. Theoretical models have been derived for various compensation mechanisms for comparison with these results. All these programs have been tested with synthetic data and actual data is now being compiled. Preliminary results are expected shortly, to be followed by appraisal and interpretation.

Task #4: Contrasts in the Evolutions of Venus and Earth

The analyses related to the Earth's archean are being pursued.

REFERENCES

Aarseth, S.J., 1972. "Direct Integration of the N-Body Problem," in M. Lecar (ed.), *Gravitational N-Body Problem* (Dordrecht, Holland: D. Reidel), 373.

Ahmad, A., and Cohen, L. 1973. "A Numerical Integration Scheme for the N-Body Gravitational Problem," *J. Comp. Phys.*, *12*, 389.

Boss, A.P. 1979. *Theoretical Models of Stellar Formation*, Ph.D. Thesis, University of California, Santa Barbara.

Davis, P.A., Kozak,, R.C., and Schaber, G.C. 1986. "Global radar units on Venus derived from statistical analysis of Pioneer Venus orbiter radar data," *J. Geophys. Res.*, *91*, 4979.

Dorman, L.M., and Lewis, B.T.R. 1970. "Experimental isostasy - 1. Theory of the determination of the Earth's isostatic response to a concentrated load," *J. Geophys. Res.*, *75*, 3357.

Glatzmaier, G.A. 1984. "Numerical Simulations of Stellar Convective Dynamos. I. The Model and Method," *J. Comp. Phys.*, *55*, 461.

Head, J.W., Peterfreund, A.R., Garvin, J.B., and Zisk, S.H. 1985. "Surface characteristics of Venus derived from Pioneer Venus altimetry, roughness, and reflectivity measurements," *J. Geophys. Res.*, *90*, 6873.

Jackson, D.D. 1979. "The use of a priori data to resolve non-uniqueness in linear inversion," *Geophys. J. Roy. Astr. Soc.*, *57*, 137.

Jackson, D.D., and Matsu'ura, M. 1985. "A Bayesian approach to nonlinear inversion," *J. Geophys. Res.*, *90*, 581.

Kaula, W.M. 1966. *Theory of Satellite Geodesy* (Waltham, Mass.: Blaisdell).

McNutt, M. 1979. "Compensation of oceanic topography: An application of the response function technique to the Surveyor area," *J. Geophys. Res.*, *84*, 7589.

Nacozy, P.E. and Diehl, R.E. 1978. "A Discussion of the Solution for the Motion of Pluto," *Celestial Mechanics*, *17*, 405.

Wetherill, G.W. 1985. "Occurrence of Giant Impacts During the Growth of the Terrestrial Planets," *Science*, *228*, 877.

Williams, J.G. and Benson, G.S. 1971. "Resonances in the Neptune-Pluto System," *Astron. J.*, *76*, 167.

Evolution of Planetesimal Velocities[1]

Glen R. Stewart
University of Virginia

George W. Wetherill
Department of Terrestrial Magnetism
Carnegie Institution of Washington

Abstract

A self-consistent set of equations for the velocity evolution of a general planetesimal population is presented. The equations are given in a form convenient for calculations of the early stages of planetary accumulation, when it is necessary to model the planetesimal swarm by the methods of gas dynamics, rather than follow the orbital evolution of individual bodies. To illustrate the relative importance of the various terms of these equations, steady state velocities of a simple planetesimal population, consisting of two different sizes of bodies, are calculated. Dynamical friction is found to be an important mechanism for transferring kinetic energy from the larger planetesimals to the smaller ones, providing an energy source for the small planetesimals that is comparable to that provided by the viscous stirring process. When small planetesimals are relatively abundant, gas drag and inelastic collisions among the smaller bodies are of comparable importance for dissipating energy from the population.

---

[1]This research was sponsored by the National Science Foundation under grants AST-82-04256 and MCS-83-04459 and by NASA under grants NSG-7437, NAGW-398, and NAGW-929.

ACCUMULATION OF SOLID BODIES IN THE SOLAR NEBULA

S.J. Weidenschilling and D.R. Davis
Planetary Science Institute, Tucson, AZ 85719

The earliest stage of accumulation of solid bodies in the solar system, i.e., the formation of planetesimals from dust, occurred in the presence of the gaseous component of the solar nebula. The effects of the gas on these particles via aerodynamic drag must be understood in order to produce physically plausible models of this process. There are major uncertainties in nebular properties, e.g., its mass (or the gas density), lifetime, and degree of turbulence. The enigmatic textural and mineralogical properties of primitive meteorites suggest that we still do not understand the formation of their parent bodies. Weidenschilling (1980) modeled the settling of dust to the central plane of the nebula. He argued that coagulation of grains during settling could be expected due to van der Waals surface forces, and was probably necessary for the formation of planetesimals. Coagulation causes settling to be non-homologous; i.e., a small fraction of the total dust content arrives at the central plane as large aggregates, while most of the mass remains suspended. Recently Nakagawa et al. (Icarus 67, 375, 1986) criticized this work because it assumed the dust motions were always controlled by the gas, whereas the reverse would be true (dust controlling gas) at sufficiently high dust density. However, their conclusion was based on an analytic homologous settling model. Weidenschilling has re-examined this problem numerically, using a higher spatial resolution near the central plane than previously employed. He found that the first-formed aggregate layer is thinner than found earlier (~10 km thick at 1 AU for a low-mass nebula), and containing $\leq 10^{-3}$ of the total surface density solids. The ~meter-sized aggregates are so widely separated that they behave independently; i.e., there is no stage at which the dust dominates the motion of the gas. Earlier, Weidenschilling (1980) had suggested that planetesimal formation would involve gravitational instability in a layer of >m-sized aggregate bodies. These new results imply that gravitational instability might be avoided entirely, due to the extremely low surface density of the initial layer, with planetesimals forming entirely by collisional coagulation.

An important property of the solar nebula is the non-Keplerian rotation of the gas due to a radial pressure gradient (Weidenschilling, MNRAS 180, 57, 1977). The resulting headwind" on the planetesimals causes their orbits to decay. Weidenschilling and Davis (Icarus 62, 16, 1985) examined the combined effects of gas drag and gravitational perturbations of a planetary embryo on the orbital evolution of planetesimals. They showed that planetesimals could be trapped in stable orbits at commensurability resonances (ratio of periods (j+1)/j, where j is an integer). The resonant perturbations pump up eccentricities to an equilibrium value e(eq) that is independent of planetesimal size. The eccentric orbits cause collisional comminution of the planetesimals. Weidenschilling and Davis suggested a scenario in which this phenomenon allows an early-formed embryo to prevent the growth of rivals, while it grows rapidly by capture of small fragments that are brought through the resonances by drag.

Weidenschilling and Davis have continued their investigation of resonant planetesimal orbits, using analytic and numerical methods. Three dimensional orbit integrations have shown that there is no significant pumping of inclinations; the planetesimal swarm remains highly flattened, with a high collision rate. The rate of eccentricity pumping at a resonance can be expressed as $de/dt \simeq (e(eq)-e)/\tau$, where the time constant τ is independent of the embryo mass or the resonance order, j. τ does depend on the damping coefficient, i.e., τ is proportional to the planetesimal size and inversely proportional to the gas density. A typical value for a low-mass nebula is $\tau \sim 10^3$ yr for a km-sized body at 1 AU. In the outer nebula, with much lower gas density, $\tau \sim 10^7$ yr for a similar body. Thus, large planetesimals at Neptune's distance may not reach e(eq) before the nebular gas is dissipated. The presence of fine dust that is coupled to the gas increases the effective density, and can shorten τ. Collisions with other large planetesimals on Keplerian orbits have no effect on τ, but can decrease the value of e(eq).

Another important consideration for evaluating the effects of resonant trapping is the width of a resonance, i.e., the range of semimajor axis (or mean motion) over which a planetesimal responds to the resonant perturbations. As with any simple damped oscillator, lower damping (a larger planetesimal or lower gas density) produces a narrower resonance peak near exact commensurability; higher damping yields a broader range of response with a lower peak. Using analytic resonance theory (cf. Greenberg, Icarus 33, 62, 1978), it can be shown that the width of a resonance varies slowly with order j, and is proportional to the square root of the product of the gas density, the perturbing embryo's mass, and the planetesimal's size. In a lower-mass nebula containing an Earth-mass embryo, the effective resonance width for a km-sized planetesimal is typically $\sim 10^{-4}$-10^{-3} AU. If a planetesimal has a close encounter or collision with another body, so that its semimajor axis is changed by more than the resonance width, it may pass through the resonance without being trapped. Larger bodies have narrower resonances (less damping), and so require smaller perturbations; also, their larger τ values make it more likely that they will experience a collision or encounter before their eccentricities can be pumped up. Thus, resonances are "transparent" to large bodies. This effect alters the accretion scenario that was proposed by Weidenschilling and Davis. There is a minimum planetesimal size that allows trapping; below that size drag dominates and forces bodies through any resonances. The matter accreted by a planetary embryo is probably bimodal. Much of the mass, especially in the early stage of accretion, will consist of small ($<<$1 km) fragments. The late-accreted mass will include bodies that have grown large enough ($>>$1 km) to be unaffected by resonances. This scenario can yield rapid growth of the cores of the giant planets while providing a population of large impactors that produce their obliquities.

A more detailed description of this work was presented at the symposium "Origin and Evolution of Planetary and Satellite Systems," Potsdam, GDR, October 1986, and has been submitted to Gerlands Beiträge zur Geophysik. This work was supported by NASA Planetary Geophysics/Geochemistry Program, Contract NASW-3214.

A Scaling Law for Accretion Zone Sizes

Yuval Greenzweig and Jack J. Lissauer (University of California at Santa Barbara)

Current theories of runaway planetary accretion require small random velocities of the accreted particles. Two body gravitational accretion cross sections, which ignore the tidal perturbations of the Sun, are not valid for the slow encounters which occur at low relative velocities. Wetherill and Cox (*Icarus* **63**, 290, 1985) have studied accretion cross sections for rocky protoplanets orbiting at 1 AU. Using analytic methods based on Hill's lunar theory (Petit and Henon, *Icarus* **66**, 536, 1986) one can scale these results for protoplanets that occupy the same fraction of their Hill sphere as does a rocky body at 1AU. Generalization to bodies of different sizes is achieved here by numerical integrations of the three body problem. Starting from initial positions far from the accreting body, test particles are allowed to encounter the body once and the cross section is computed. A power law is found relating the cross section to the radius of the accreting body (of fixed mass). The value of the exponent varies with the initial distribution of inclinations of the test particles. It is found that for an initial distribution of planar circular orbits, with uniform semi-major axes spacing, the cross section obeys an $r^{\frac{1}{2}}$ power law. For nonplanar circular-orbit distributions, and fixed small inclination, the cross sections behave approximately as r. Variable non-zero inclination distributions result in intermediate power law dependences. These power laws are valid for the range of parameters of interest to runaway accretion theories of the planets, but different results apply in satellite systems near Roche's limit.

URANUS AND NEPTUNE: QUESTIONS AND POSSIBLE ANSWERES

Reynolds, R. T. and M. Podolak*, NASA Ames Research Center,
Moffett Field, CA 94035

Uranus and Neptune are of special interest for theories of the origin of the solar system, because they represent a special class of objects intermediate in composition between the giant hydrogen-rich planets Jupiter and Saturn, and the small, rocky, terrestrial planets. Their structure and composition should provide important clues to the origin of the solar system (1,2). In order to compute models of the internal structure, using high pressure equations of state for the materials believed to constitute those planets, it is necessary to measure several parameters characterizing these palnets. Their masses and radii have been known to sufficient accuracy for many years, and recently J_2 and J_4 (respectively the quadrupole and 16-pole moments of the gravitational field) have been determined for Uranus (3) and moments J_2 for Neptune (4). Until the Voyager flyby, however, the rotation period for Uranus was not well constrained and various observations placed it in the neighborhood of 16 hrs. (5). It is interesting that, although this is a shorter period than the 18 hrs determined photometrically for Neptune (5), Neptune has the larger J_2.

We have constructed a detailed set of theoretical models which consist of a core of "rock" (MgO, SiO, Fe, and Ni in solar proportions), surrounded by an envelope of "ices" (H_2), CH_4 and NH_3 in solar proportions), surrounded, in turn, by an envelope of these same "ices" mixed with H_2 and He (6). We found although the ratio of "ices" to "rock" was nearly the same for the two planets, the internal arrangement was very different in the two cases, a situation very difficult to explain in terms of current pictures of planet formation. We suggested (7) that the period measured photometrically for Neptune is influenced by surface features caused by the motion of Rossby waves in the upper atmosphere, and , in fact, the body of the planet rotates more quickly. Such a shorter period is, indeed, indicated by new measurements of the oblateness (8). The recent Voyager flyby of Uranus has fixed its rotation period at just over 17 hours, narrowing the difference between the two models, but by no means eliminating it. Hopefully, the Voyager encounter with Neptune will help resolve the issue.

The new improved rotation period, combined with the latest values for J_2 and J_4 have raised problems in the understanding of Uranus' structure independently of a comparison with Neptune. We have found that none of the models computed previously (fig.1) could be made to fit with this new set of observational data. Instead it was necessary to assume that Uranus has an anomalously high ratio of "ices" to "rock",

some five times the solar value (9)! Such a high value (fig. 2) may be a natural outcome of an accretion mechanism we have begun to investigate. As a planetesimal approaches a protoplanetary atmosphere with some impact parameter, it may (depending on its composition) lose a significant amount of mass and be captured by the protoplanet, or lose very little, and escape to space. Since ice is more volatile, an icy planetesimal will lose mass at larger impact parameters, and hence the cross section for capture will be larger for icy planetesimals than for rocky ones. This provides a possible mechanism for greatly enhancing the ice to rock ratio over the solar value. This mechanism is currently being explored.

REFERENCES

1. Podolak, M. and R. T. Reynolds (1984). Consistency tests of theories from models of Uranus and Neptune. Icarus **54**, 102-111.
2. Podolak, M. and R. T. Reynolds (1985). What have we learned from modeling giant planet interiors? In Protostars and Planets II (D. Black and M. S. Matthews, eds.) Univ. Arizona Press pp. 847-872.
3. French, R. G., J. L. Elliot, and S. E. Levine (1985). Structure of the Uranian rings II. Perturbations of the ring orbits and widths. Icarus **76**, 134-163.
4. Harris, A. W. (1984). Physical properties of Neptune and Triton inferred from properties of Triton. In Uranus and Neptune (J. T. Bergstralh, ed.) pp. 357-373 NASA CP-2330.
5. Belton, M. J. S. and R. Terrile (1984). Rotational properties of Uranus and Neptune. In Uranus and Neptune (J. T. Bergstralh, ed.) pp. 327-347 NASA CP-2330.
6. Podolak, M. and R. T. Reynolds (1981). On the structure and composition of Uranus and Neptune. Icarus **46** 40-50.
7. Podolak, M., R. Young, R. T. Reynolds (1985). The internal structures and relative rotation rates of Uranus and Neptune Icarus **63**, 266-271.
8. Lellouch, E., W. B. Hubbard, S. Sicardy, F. Vilas, and P. Bouchet (1986). The 1985 August 20 occulation by Neptune: The central flash determination of Neptune's oblateness and methane atmospheric mixing ratio. Preprint
9. Podolak, M. and R. T. Reynolds (1986). The rotation rate of Uranus, its internal structure, and the process of planetary accretion. Submitted Icarus.

*Permanent address: Dept. of Geophysics and Planetary Sciences, Tel Aviv University, Israel.

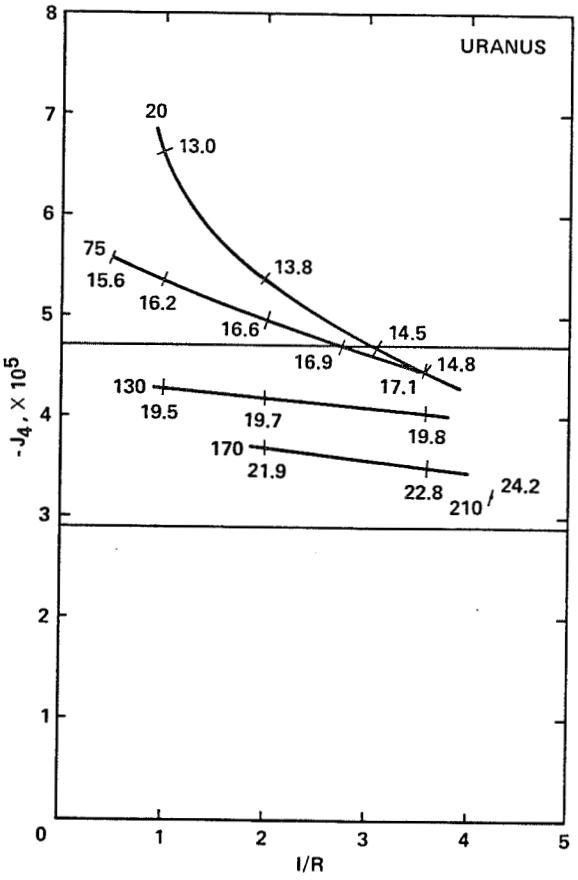

Fig. 1 J4 as a function of the ice/rock ratio for former Uranus models. Parameter on right gives enhancement of volatiles in envelope over solar composition. Tick marks along curve give rotation period required for fit to J2. Horizontal lines show former limits on observed value of J4.

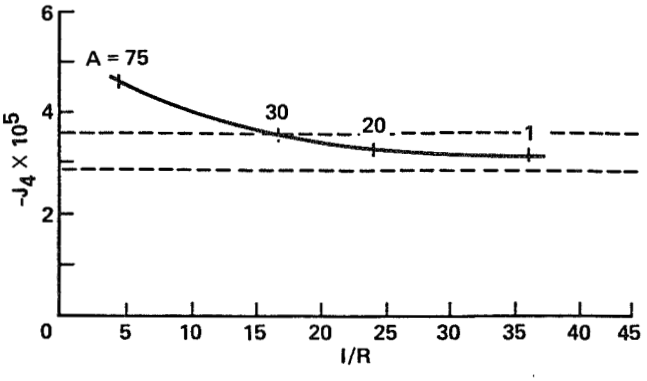

Fig. 2 J4 as a function of the ice/rock ratio for current Uranus models with 17.24 hr period. Tick marks show enhancement of volatiles in envelope. Horizontal dashed lines show current limits on J4.

COLLISIONAL AND DYNAMICAL PROCESSES IN MOON AND PLANET FORMATION

C.R. Chapman, D.R. Davis, S.J. Weidenschilling, W.K. Hartmann and D. Spaute
Planetary Science Institute

We report research on a variety of dynamical processes relevant to the formation of planets, satellites and ring systems. Our main focus has been on studies of accretionary formation of early protoplanets using a numerical model, structures and evolution of ring systems and individual bodies within planetary rings (Davis et al., Science 224, 1984; Weidenschilling et al., in Planetary Rings, p. 67, 1984) and theories of lunar origin (Weidenschilling et al., in Origin of the Moon, p. 731, 1986; Hartmann, in Origin of the Moon, p. 579, 1986).

Our earlier work on planetary accretion has been in the context of gas free accretion. However, a significant area of recent Planetary Science Institute research concerns the effects of gas drag and resonances on the accretion of planets. While at present there does not appear to be a strong requirement for the presence of gas during formation of the terrestrial planets, there is increasing support for the idea that the giant planets formed by accumulation of massive solid cores that eventually captured gas from the solar nebula (Bodenheimer and Pollack, Icarus 67, 391, 1986). Models for accretion that do not consider affects of gas drag on planetesimal dynamics are unable to produce such cores on reasonable timescales.

Weidenschilling and Davis (Icarus 62, 16,1985) under a separately funded program showed that orbital decay due to gas drag and resonant gravitational perturbations lead to stable trapping of planetesimals at commensurability resonances with a planetary embryo. The synergistic effect of drag and resonances allows a planetary embryo to pump up eccentricities of smaller planetesimals to values much larger than those due to random encounters. Eccentricities of a few x 10^{-2} are induced for plausible nebular models, independent of the sizes of planetesimals. The close spacing of resonances ensures that different resonant orbits overlap, and cross the non-resonant orbits between them. The high relative velocities, ~1 km/sec, cause comminution of the planetesimals. This process could allow an early-formed planetary embryo to inhibit the growth of potential rivals, and to dominate the zone covered by overlapping resonances (up to the 2/3 exterior resonances). That scenario alleviates the tendency of numerical accretion models to produce too many, closely-spaced small planets. Weidenschilling and Davis noted that if resonances were completely effective for inhibiting accretion, the spacing of planetary orbits would approximate their actual values. However, whether this process would yield a single embryo or several in a given zone depends on details of the size distribution and its rate of change, impact strengths of planetesimals, nebular structure, etc. Detailed numerical simulations are needed to determine the likely range of outcomes.

We are examining in this program the range of outcomes by numerical simulations of accretion with resonance effects due to an early-formed planetary embryo. Our approach uses a varient of the method of Spaute et al., (Icarus 64, 139, 1985). We have been aided in this effort by collaboration with Dr. Spaute, who has been in residence at PSI during 1985-86. The simulation computes the outcome of collisions among

planetesimals in as many as 50 narrow radial zones spanning a range of semimajor axis; bodies in different zones interact when their eccentricities allow their orbits to cross. This spatial resolution allows explicit inclusion of e-pumping at discrete resonances in specific zones, and the transfer of mass between zones by collisions and drag. Resonance effects -- de/dt, size limits for trapping, resonance widths, etc. -- are parameterized from results of Weidenschilling and Davis (1985) and Weidenschilling (1986, submitted to Gerland-Beiträge zur Geophysik).

These simulations involve a determination of the probability density for collisions between bodies in overlapping orbits, with a Monte Carlo determination of the specific interactions. Collisional outcomes, ranging from accretion to complete disruption, depend on impact speeds and the assumed mechanical properties of the planetesimals. In addition, the radial movement of matter between zones due to secular decay of planetesimal orbits is accounted for. A major limitation at present is the lack of detailed information on the distributions of sizes and orbital elements of the planetesimals. Due to the complexity of the program, only mean values for the size, eccentricity, and inclination are computed in each radial zone. However, these quantities can be weighted (e.g., acording to mass or cross-sectional area, as appropriate) for assumed power-law size distributions.

Fig 1 shows the results for one such simulation. An embryo of mass $3 \times 10^{-7} M_{\odot}$ (one Mars mass) is assumed present at 1 AU, and the effects of its perturbations on a swarm of planetesimals with initial mean radius 1 km is computed. After a model time of 550 yr, ecentricities have increased signficantly at resonances. The mean size has decreased sharply at those locations due to collisional comminution, while accretion occurs in the relatively quiescent zones between the non-overlapping low-order resonances. The evolution of eccentricities is dominated by resonant perturbations, so any uncertainties in the effects of mutual gravitational stirring of planetesimals are unimportant to the outcome. Some low-order information on the size distribution can be obtained from the number of shatttering events that yield power-law fragment distribution; several tens of percent of the total swarm has been processed through such events and can be brought to the embryo for accretion. Future efforts will be directed toward computing more detailed size distributions.

Hartmann, also working with our visiting scientist, D. Spaute, has undertaken an investigation of the accretional evolution in a circumterrestrial (or generally, circumplanetary) cloud of debris. Hartmann and Spaute visualize the creation of a chaotic, spheroidal or flattened cloud by an unspecified process (such as giant impact?) in a "stage 1." They then investigate "stage 2," the collisional evolution that follows from specified parameters of mean e, i, material properties, etc. in the cloud. This study used a variant of the accretion numerical model by Spaute et al. (1985) which models growth at different distances from a primary. For this work, Hartmann has updated and modified the treatment of some of the material parameters based on our experimental results. Preliminary results

suggest the very rapid collapse of a chaotic cloud into a flattened ring, faster growth on the inner edges of the cloud, and a transition from fragmentation to accretion as energy dissipation reduces collision velocities. Thus, if a giant impact threw out a cloud of debris, accretion might occur first in the inner part of the cloud. A sufficiently large satellite accreted inside the synchronous point would spiral inward, but such a satellite accreted just beyond the synchronous point would spiral outward, sweeping up the rest of the debris. This could account for lunar formation.

We are currently reviewing our numerical models for calculating collisional outcomes and orbital stirring due to gravitational encounters. These algorithms were developed about ten years ago and while they have been updated occasionally, there has never been a comprehensive review of them in light of new experimental and theoretical results. We have undertaken a complete review and updating of these models. In particular we will use the much more extensive collisional database that now exists (e.g. review by Fujiwara, Mem. Soc. Astron. Ital. 57, No. 1, 47, 1986) and new scaling relationships (Holsapple and Housen Mem. Soc. Astron. Ital. 57, No. 1, 65, 1986; Housen et al., JGR 88, 2485, 1983) to revise as needed the predictions of our collisional outcome model. Recent work on gravitational stirring by Stewart and Wetherill (LPSC XVII Abstracts, 827) 1986, Carusi et al. (BAAS 18, No. 3, 776, 1986) and Wetherill and Cox (Icarus 63, 290, 1985) will be used to test and improve as needed our present algorithm for modeling this very important effect for planetary accretion.

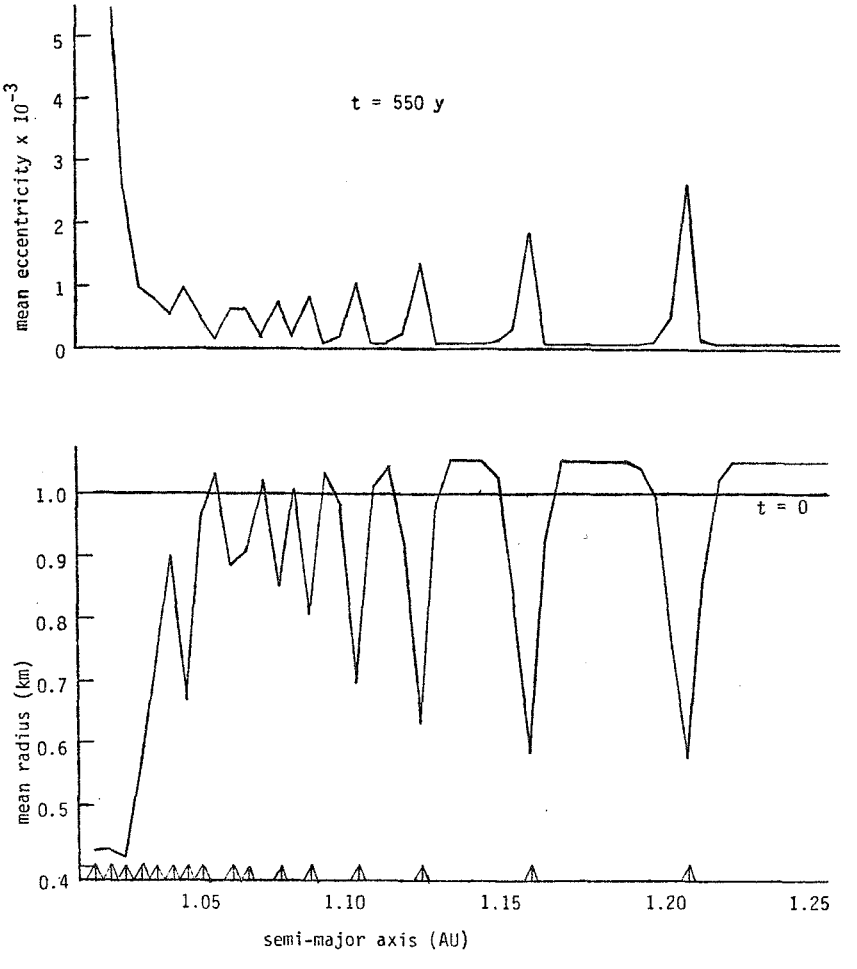

Dynamical Constraints on the Orgin of the Moon

A. P. Boss (DTM Carnegie Institution of Washington) and S. J. Peale (University of California at Santa Barbara)

Dynamical studies dealing with the orgin of the Moon are described and are used to try to eliminate dynamically impossible or implausible theories of lunar orgin. The orgin of the Moon is discussed within the context of the general theory of terrestrial planet formation by accumulation of planestesimals. The past evolution of the lunar orbit is of little use in differentiating between the theories, primarily because of the inherent uncertainty in a number of model parameters and assumptions. The various theories that have been proposed are divided into six catagories. Rotational fission and disintegrative capture appear to be dynamically impossible for viscous protoplanets, while precipitation fission (precipitation of Moon–forming material from a hot, extended primordial atmosphere of volatilized silicates), intact capture, and binary accretion appear to be dynamically implausible. Precipitation fission and binary accretion suffer chiefly from having insufficient angular momentum to form the Moon, while intact capture requires forming the Moon very close to the Earth without encountering any perturbations prior to capture. The only mechanism proposed so far that is apparently not ruled out by dynamical constraints and that also seems the most plausible involves formation of the Moon following a giant impact that ejects portions of the differentiated Earth's mantle and parts of the impacting body into circumterrestrial orbit. The Moon must have accreted subsequently from this circumterrestrial disk. The giant impact model contains elements of several of the other models and appears to be dynamically consistent with the absence of major satellites for the other terrestrial planets. While the giant impact mechanism for forming the Moon thus emerges as the theory with the least number of obvious flaws, it should be emphasized that the model is relatively new and has not been extensively developed nor thoroughly criticized. Much further work must be done to learn whether the giant impact mechanism for lunar formation can be made into a rigorous theory.

LUNAR SCIENCE FROM LUNAR LASER RANGING

J. G. Williams, X X Newhall, and J. O. Dickey
Jet Propulsion Laboratory, Pasadena, CA 91109

Seventeen years of lunar laser ranging data have been analyzed to determine lunar second-degree moment differences, third-degree gravitational harmonics, Love number, rotational dissipation, and retroreflector coordinates. The range accuracy improves through the time span until 3-5 cm accuracies have been achieved since 1985. The retroreflectors were located at the Apollo 11, 14, and 15 sites and the Lunakhod 2 site. The results from the solution are:

	Value Units	Error 10^{-6}
(C-A)/B	631.93	0.76
(B-A)/C	227.95	0.06
C30	-8.3	0.7
C31	35.2	12.
S31	2.9	3.4
C32	4.812	0.035
S32	1.682	0.019
C33	1.66	0.22
S33	-0.30	0.07

A more accurate value of C31 is available from previous analyses of lunar orbiting satellite Doppler tracking data. Two additional lunar solution parameters are the potential Love number, $k = 0.027 \pm 0.006$, and the rotational dissipation, $kT = 0.0048 \pm 0.0002$ days. The coordinates of the retroreflectors were determined with accuracies of a few meters. These results are to be published in the proceedings of the international symposium titled Figure and Dynamics of the Earth, Moon, and Planets.

SOLAR SYSTEM DYNAMICS

Jack Wisdom, Department of Earth, Atmospheric and Planetary Sciences, Massachusetts Institute of Technology, Cambridge, Massachusetts 02139

I. Rotational Dynamics of Irregularly Shaped Satellites

All irregularly shaped natural satellites tumbled chaotically at the point of capture into synchronous rotation.

The basic mechanism governing the tidal evolution of the spins and obliquities has been well understood since the work of George Darwin (1879). If the spin angular velocity is large the obliquity is driven to a equilibrium value between 0 and 90°. As the spin is slowed by tidal friction the equilibrium obliquity decreases. If the orbit is fixed, the equilibrium obliquity goes to zero as the spin angular velocity approaches twice the mean orbital motion. For smaller angular velocities the obliquity is zero. Spin-orbit resonances are encountered as the spin rate is reduced and the rotation may or may not be captured in a spin-orbit resonance with calculable probability (Goldreich and Peale, 1966). If the non-synchronous spin-orbit resonances are avoided, the spin continues to decrease until synchronous rotation is established.

A dramatic exception to the regular tidal evolution envisioned in the standard scenario is provided by the chaotic tumbling of Saturn's satellite Hyperion (Wisdom, Peale, and Mignard, 1984). The chaotic tumbling of Hyperion is a consequence of its highly aspherical shape, to some extent the large orbital eccentricity ($e \approx 0.1$), and the fact that the spin rate of Hyperion has been brought by tidal friction to be nearly synchronous with the orbital mean motion.

For other irregularly shaped satellites this picture of steady evolution to synchronous rotation must also be revised. All resonances are surrounded by a chaotic zone (see Chirikov, 1979). The width of the chaotic zone surrounding the synchronous spin-orbit state may be estimated. It turns out to be linearly proportional to the orbital eccentricity, but exponentially dependent on the parameter which measures the out of roundness of the satellite. Thus the chaotic zone surrounding the synchronous state may be significant for an irregularly shaped satellite even if the eccentricity is not as large as that of Hyperion. This prediction has been verified numerically. A remarkable fact is that this chaotic zone seems to always be attitude unstable just as it is for Hyperion. Even Deimos which has an anomalously low eccentricity of 0.0005 has a non-negligible chaotic zone which is attitude unstable. In all cases the timescale for the spin axis to fall away from the orbit normal is only a few orbit periods; the attitude instability is very strong. Thus all the irregularly shaped satellites in the solar system, regardless of their orbital eccentricity, tumbled chaotically at the point of capture into synchronous rotation.

Dissipation within a chaotically tumbling satellite is significantly greater than in a synchronously rotating satellite. If a secular change in the angular momentum of the satellite can be ruled out, then the dissipation within the satellite leads to a decrease in the orbital eccentricity. It is plausible, but not yet proven, that tidal friction will not give a secular change in the angular momentum of a chaotically tumbling satellite because, speaking qualitatively, the motion is so irregular the tides do not know which way to push. Once this is rigorously justified then the anomalously low eccentricity of Deimos can be explained as resulting from the dissipation in Deimos during the chaotic tumbling phase. In any case, the chaotic tumbling phase must be taken into account in the orbital histories of the natural satellites.

This work has been submitted to Icarus.

II. Origin of the Kirkwood Gaps

We have used the Digital Orrery (Applegate, et al. 1985) to systematically explore the phase space of the elliptic restricted three body problem near the principal commensurabilities (2/1, 5/2, 3/1, and 3/2). The results for the 3/1 commensurability are in close agreement with those found earlier with the algebraic mapping method (Wisdom 1981, 1983). Large chaotic zones are associated with the 3/1, 2/1 and 5/2 resonances, where there are gaps in the distribution of asteroids. The region near the 3/2 resonance, where the Hilda group of asteroids is located, is largely devoid of chaotic behavior. Thus there is a qualitative agreement between the character of the motion and the distribution of asteroids.

The detailed comparisons (using the representative plane method of Wisdom, 1983) between the distribution of asteroids and the chaotic zones do not show perfect agreement. While the boundaries on the large semimajor axis side are in good agreement, there is in each case a small region at fairly low eccentricity on the small semimajor axis side of the gaps where there are no asteroids and also no chaotic behavior. Unfortunately, the interpretation of this result is not straightforward. There are three possibilities: (1) The planar elliptic approximation is not a sufficiently accurate representation of the motion near the principal commensurabilities. (2) The void on the representative plane represents a sufficiently small phase space volume that asteroids were simply unlikely to be found there. (3) Cosmogonic mechanisms such as resonance sweeping (Henrard and Lemaitre, 1983, and Torbett and Smoluchovski, 1980) have been operative. The first possibility has been examined by integrating several test particles in the field of the major planets with the Digital Orrery. Five test particles were started in the region in question and integrated for five million years each. Of the five test particles three turned out to be chaotic. This gives strong support to the conclusion that the discrepancy is primarily due to the use of the elliptic restricted approximation in the systematic exploration. Most likely a combination of the first two possibilities can fully account for the differences between the systematic exploration and the observed distribution, but resonance sweeping can not yet be ruled out. We intend to resolve this question soon.

The existence of chaotic zones at the principal commensurabilities does not by itself explain the existence of the Kirkwood gaps. We must also understand the mechanism whereby asteroids on chaotic orbits are removed. We have used the Digital Orrery to approach this problem as well. Again, five test particles were integrated in the field of the major planets for five million years each. Each one was started in the 2/1 chaotic zone. Of these five, two reached eccentricities above 0.6, which makes them Mars crossing. In both cases they went to large eccentricity by a path that temporarily took them to high inclination ($i > 20°$). (Recall that the integrations by Froeschlé and Scholl (1981) of Giffen's (1973) 2/1 chaotic orbit seemed to show that there was a maximum eccentricity. Their integrations were performed in the planar approximation.) This is quite an interesting result. This is the first example in the solar system where a phenomenon seems to depend on the interconnectedness of the chaotic zone in many dimensions (the so-called "Arnold web", see Chirikov, 1979). Sweeping by Mars thus appears to be a plausible removal mechanism, though it seems likely that longer integrations will reveal Jupiter itself to be the culprit.

References

Applegate, J.F., Douglas, M.R., Gürsel, Y., Hunter, P. Seitz, C. and Sussman, G.J. 1985. *IEEE Trans. Comput.* **C34**, 822.

Chirikov, B.V. 1979. *Phys. Rep.* **52**, 263-379.

Darwin, G. 1879. *Phil. Trans.*, Part I.

Froeschlé, C., and Scholl, H. 1981. *Astron. Astrophys.* **93**, 62.
Giffen, R. 1973. *Astron. Astrophys.* **23**, 387.
Goldreich, P. and S.J. Peale 1966. *Astron. J.* **71**, 425.
Henrard, J., and Lemaitre A. 1983. *Icarus* **55**, 482.
Torbett, M. and Smoluchowski, R. 1980. *Icarus* **44**, 722.
Wisdom, J. 1983. *Icarus* **56**, 51.
Wisdom, J., S.J. Peale and F. Mignard 1984. *Icarus* **58**, 137-152.

Orbital Resonances, Unusual Configurations and Exotic Rotation States among Planetary Satellites

S. J. Peale (University of California at Santa Barbara)

Several examples of satellite dynamics are presented where significant progress has been made in understanding a complex problem, where a long–standing problem has finally been solved, where newly discovered configurations have motivated novel descriptions or where an entirely new phenomenon has been revealed. The origin of orbital resonances is shown in the demonstration of the evolutiona of a pair oa planetary satellites through a commensurability of the mean motions by a sequence of diagrams of constant energy curves in a two–dimensional phase space, where the closed curve corresponding to the motion in each successive diagram is identified by its adiabatically conserved area. All of the major features of orbital resonance capture and evolution can be thus understood with a few simple ideas. Qualifications on the application of the theory to real resonances in the solar system are presented. The two–body resonances form a basis for the solution of the problem of origin and evolution of the three body Laplace resonance among the Galilean satellites of Jupiter. Dissipation in Io is crucial to the damping of the amplitude of the Laplace libration to its observed small value. The balance of the effects of tidal dissipation in Io to that in Jupiter leads to rather tight bounds on the rate of dissipation of tidal energy in Jupiter. Motion in the relative horseshoe orbits of Saturn's coorbital satellites is described very well by a simple expansion about circular reference orbits. The coorbitals are currently very stable, and their relative motions can be used for the determination of the masses of both satellites. Pluto and its relatively large satellite Charon form an unusual system where the relative size and proximity of Charon lead to a most probable state where both Pluto and Charon are rotating synchronously with their orbital motion. The normal tidal evolution of a satellite spin toward shychronous rotation is frustrated in the case of Saturn's satellite Hyperion where gravitational torques on the large permanent asymmetry cause it to tumble chaotically. Observations of Hyperion's lightcurve are consistent with the chaotic rotation but do not verify it with certainty.

Dynamics of Satellites, Asteroids, and Rings

Stanley F. Dermott, CRSR, Cornell University

Work is in progress on: (a) determining the shapes and the internal structures of satellites (with Peter Thomas of Cornell University); (b) investigating the tidal heating of Miranda (with Renu Malhotra of Cornell University and Carl Murray of Queen Mary College, London); (c) investigating the dynamics of arc-like rings (with Carl Murray); and (d) determining the structure of the zodiacal cloud as revealed by IRAS (with Philip Nicholson of Cornell University). Significant progress has been made in (a) the determination of the shape and the internal structure of Mimas and (b) understanding the dynamical evolution of Miranda's orbit.

(a) The Shape and Internal Structure of Mimas

Limb profiles from the six best Voyager images have been used to determine the shape of the satellite. Correction of image distortions allows coordinates on the limbs to be located with an accuracy of approximately one-half picture element: about 0.5 km for the two best images and between 1 and 2 km for the other images. Ellipses fit to the limbs show that the shape of Mimas is well-represented by a triaxial ellipsoid: it is the smallest satellite observed for which this is possible. The ratio of the differences of the axes , $(b - c)/(a - c)$, is 0.27 ± 0.04, indicating that the satellite is close to hydrostatic equilibrium. This is the first observation of a satellite in the solar system with a triaxial equilibrium figure. Using the satellite mass determined by Kozai (1957) from observations of the libration period and the libration amplitude of the Mimas-Tethys resonance, and a second-order theory for the ellipsoidal figure of equilibrium, we deduce that the satellite has a mean radius $\langle R \rangle$ of 198.9 ± 0.6 km, a mean density of 1.137 ± 0.018 g/cm^3 and that the difference between the long and short axes, $a - c$, is 17.0 ± 0.7 km. The expected value of $a - c$ for a comparable, but homogeneous satellite in hydrostatic equilibrium is 20.3 ± 0.3 km. We conclude that Mimas is probably differentiated and may have a rocky core of radius $(0.43 \pm 0.10) \langle R \rangle$. The material outside the core probably has a mean density of 0.98 ± 0.08 g/cm^3, consistent with that of uncompressed water-ice. The rock/ice ratio (by weight) of Mimas is probably a factor of 2 lower than the cosmic ratio: Mimas is markedly deficient in rock. This work represents the first determination of the internal structure of a satellite in the solar system, other than the Moon, and is likely to shed light on the accretion of satellites. Preliminary considerations favor the idea of heterogeneous accretion (Dermott and Thomas, 1986).

(b) Tidal Heating of Miranda

This work is part of a continuing effort to understand the dynamics of the Uranian satellite system. We showed that the theory previously used to find the masses of the Uranian satellites from their orbital precession rates contained a fundamental error (Dermott and Nicholson,

1986). Thus, we were able to predict that the pre-Voyager masses of the satellites would prove to be incorrect. This prediction has now been proved to be right.

We have now analyzed the evolution of the Uranian satellite orbits due to tidal dissipation in the planet and have calculated the change in the orbital elements due to passage through low-order orbit-orbit resonances. We have succeeded in showing that the orbital eccentricity of Miranda would have been dramatically increased by these passages and that the subsequent tidal damping of this eccentricity would have heated the satellite. We have also calculated the change in the orbital inclination of Miranda on passage through the same set of resonances. The calculated change is large enough to account for the present very high orbital inclination of Miranda. Thus, we consider that we have found a dynamical solution for both the bizarre appearance of Miranda observed by Voyager and the anomalous orbital inclination (Malhotra, Dermott and Murray, 1986).

(c) Dynamics of Arc-Like Rings

The location and the stability of the Lagrangian equilibrium points in the restricted circular three-body problem have been examined under a variety of drag forces. Linear stability analysis and numerical integration confirm that, contrary to what might be expected from simple energy arguments, the L_4 and L_5 points can be asymptotically stable under the action of certain drag forces, despite being points of potential maxima. The results have been extended to the horseshoe regime where the radial oscillations of the particle are small compared with the width of the horseshoe path in the rotating reference frame. In this case, the behavior of the Jacobi constant averaged over the horseshoe path determines the stability and the sense of evolution of the particle. If the drag force varies as v^p, where v is the velocity of the particle in the inertial frame, then the value p = 2 is critical for both the tadpole and the horseshoe regimes. Stability is ensured if sign($\dot{a}$) x sign (2 - p) is negative.

A similar analysis can be applied to any particle in a co-rotating arc. These results may have important implications for the stability of arcs of ring material where the dynamical effects of drag can counteract the spreading due to particle collisions (Murray and Dermott, 1986).

(d) Structure of the Zodiacal Cloud as Revealed by IRAS

The IRAS Zodiacal History File, which contains the all-sky survey data, is now to hand at Cornell. Software has been written to Fourier analyse the data and thereby separate the smooth large-scale zodiacal background from the narrower dust bands. Our preliminary results were described in a paper read at the Uppsala Asteroid, Comets and Meteors meeting (Dermott, Nicholson, and Wolven, 1986).

We have previously shown that the dust bands may be debris associated with the Hirayama asteroid families, in particular, the Eos and Themis families, and we have predicted (a) that the ecliptic latitudes of the dust bands should vary with ecliptic longitude and (b) that the central dust band should be split (Dermott et al., 1984, and Dermott et al., 1985). We now have evidence supporting both of these predictions. In particular, we have evidence showing that the central dust band is indeed split and that the separation in latitude of the two components is consistent with that expected for debris derived from the Themis family. This has important implications for the origin of the particles in the zodiacal cloud.

References

1. Dermott, S. F., Nicholson, P. D., and Wolven, B. (1986). Preliminary Analysis of the IRAS Dust Data. In "Asteroids, Comets and Meteors II" (eds. C-I. Lagerkvist and H. Rickman) Uppsala, 583-594.

2. Dermott, S. F., Nicholson, P. D., Burns, J. A., and Houck, J. R. (1985). An Analysis of IRAS' Solar System Dust Bands. IAU Colloquium No. 85, "Properties and Interaction of Interplanetary Dust" (ed. Giese, R.H. and P. Lamy), D. Reidel Pub. Co., 395-409.

3. Dermott, S. F., Nicholson, P. D., Burns, J. A., and Houck, J. R. (1984). Origin of the Solar System Dust Bands discovered by IRAS, Nature, 312, 505-509.

4. Dermott, S. F. and Nicholson, P. D. (1985). Masses of the Satellite of Uranus. Nature 319, 115-120.

5. Dermott, S. F, and Thomas, P. C. (1986). The Shape and Internal Structure of Mimas. B.A.A.S. 18, 761.

6. Malhotra, R., Dermott, S. F., and Murray, C. D. (1986). Tidal Heating of the Uranian Satellites. B.A.A.S. 18, 785.

7. Murray, C. D., and Dermott, S. F. (1986). Dynamical Effects of Drag on Particles in Corotational Resonances. B.A.A.S. 18, 778.

Hamiltonian Theory of Nonlinear Waves in Planetary Rings*

G. R. Stewart (U. Virginia)

Nonlinear spiral density waves have been observed at several locations in Saturn's rings. Our theoretical understanding of these waves was substantially advanced by the recent derivation by Shu et al. (1985) and Borderies et al. (1985) of a nonlinear dispersion relation which generalizes the linear relation found earlier by Lin and Shu.[1,2] The purpose of this abstract is to report the derivation of a Hamiltonian field theory for nonlinear density waves. Starting from the Hamiltonian for a discrete system of gravitating streamlines, an averaged Hamiltonian is obtained by successive application of Lie transforms. The transformation may be carried out to any desired order in q, where q is the nonlinearity parameter defined in the above references. Subsequent application of the WKB approximation yields an asymptotic field Hamiltonian. Both the nonlinear dispersion relation and the wave action transport equation are easily derived from the corresponding Lagrangian by the standard variational principle.

*Work supported in part under NSF grant AST-82-004256 and NASA grant NAGW-929.

---

[1]Shu et al., *Ap. J.* 291 (1985) 356
[2]Borderies et al., *Icarus* 63 (1985) 406

Planetary Ring Dynamics and Morphology

Jeffrey N. Cuzzi, Ames Research Center, principal investigator
Richard H. Durisen, Indiana University, coinvestigator
Frank H. Shu, U. C. Berkeley, coinvestigator

F ring moonlet belt paper: We are happy to have finished our long-overdue paper on the moonlet belt for which we find evidence in the region between Saturn's close-in ringmoons Pandora and Prometheus, the so-called F ring shepherds. In this paper, Cuzzi and J. Burns show how the little-noticed observations of magnetospheric electron density by Pioneer 11 imply substantial, ongoing injections of mass into the 2000 km region noted above which surrounds the F ring. We present a hypothesis that these events (which require the appearance of the mass equivalent of a 100 m radius ice particle every few hours) result naturally from interparticle collisions between the **smaller** members of an optically thin belt of moonlets. The moonlets in the belt may have radii ranging from about 100 meters to somewhat less than 10 km, and continually sweep up the ejecta produced by these collisions, keeping the F region relatively, but not completely, clear in steady state. We show that the **larger** members of this same population, numbering perhaps less than a dozen, produce much more massive clumps of particles when they collide, but that their collisions are far less common. In fact, it is possible to choose a reasonable parent size distribution that produces simultaneously the many small events responsible for the Pioneer electron density observations and rare large events that would lead to rings much like the F ring in mass and structure. These large clumps become strands when differential motion spreads the material longitudinally, and may exist for years before succumbing to the perpetual sweeping action of surrounding moonlets.

We thus raise the possibility that the F ring is not necessarily a primordial structure relying on "shepherding" by Pandora and Prometheus to keep it from spreading, but merely one of a series of transient features which come and go in response to occasional creation and continuing removal. The mysterious kinks in the F ring would be easily explained by occasional close passages by moonlets with sizes too small in general to be visible to the Voyager cameras, and its unusually small particle sizes by the fact that the F ring particles are really only a recently lost regolith produced initially by meteoroid bombardment. Even the multistranded nature of the F ring may be explained by this hypothesis, if the regoliths of two colliding bodies retain some memory of their pre-collision orbits.

We suspect that new insight into similar dynamical puzzles, such as incomplete ring arcs known to exist in Saturn's Encke gap and in the ring systems of Uranus and Neptune, will be gained from use of this theoretical framework. It may even help us understand the existence of the eight inner rings of Uranus, which seem to have no major shepherds to maintain them from spreading over the age of the solar system. These and the diffuse dust bands discovered by Voyager in the inter-Uranian-ring regions may indicate a situation similar to that which we describe for the F ring.

The concept of an intimate mix of rings and ringmoons in a highly interactive situation just outside Saturn's Roche limit, and the increasing evidence for moonlets embedded within Saturn's main rings (Showalter et al. 1986), provide us with new constraints on the properties of planetary ring systems. These new results seem to increasingly support some variation of the concept first presented by Shoemaker that sizeable moons precede or accompany ring formation, and that meteoroid bombardment of such moons, which is increasingly focussed and intense in regions closer to a planet, results in smaller and more numerous moon fragments closer to the planet. In addition, we suspect that more detailed future studies of the dynamical behavior of the F-region moonlet belt, which seems to lie outside Saturn's Roche limit, may have much to teach

us about planetary accretion.

First erosion manuscript about half done: We are about halfway through with the first of an anticipated series of papers on transport of mass and momentum by meteoroid ejection in planetary rings. The first paper (somewhat too rough to be distributed as yet) provides the theoretical framework of the numerical solution and some illustrative examples for certain simple ejecta distributions. It will describe how transport of mass and angular momentum by both ejecta and viscosity has been included in the formulation, and what typical results demonstrate. A companion manuscript will describe our development of the ejecta distribution in a realistic case including all known cratering ejecta distributions and accurate distributions of incident meteoroid flux which reflect aberrations due to the orbital motion of both Saturn and the ring particles, as well as the impact probability which depends on incident direction and velocity as well as on the optical depth of the local ring material. Extension of certain of these dynamical concepts has been made to demonstrate the inability of "late heavy bombardment" impacts to desynchronize satellite spins (Lissauer 1985).

Uranus Ring ring structure and photometry: We are conducting photometric analysis of the Uranian rings , working with others of the Voyager imaging team. The color of the rings has been carefully constrained using our image analysis system to average hundreds of pixels along the only barely visible rings. The improvement in SNR allows ring spectral contrast to be measured to the 15% level or so; the rings seem to have the same relatively colorless spectrum between 0.41 and 0.56 microns as the Uranian satellites and carbonaceous chondrites. In a complementary effort, we are analysing the Voyager images over the entire range of illumination and viewing geometry, using radiative transfer modeling to determine the dust content of the rings and the reflectance of the ring material. The dust content is extremely low in all nine main rings. The ring material is about as dark as the darkest primitive carbonaceous chondrites, and perhaps as dark as Halley. These new results are in agreement with pre-Voyager estimates reported last year(Cuzzi 1985). A paper on the ring color has been submitted to Icarus. One will shortly be written on the dust content and reflectance properties.

Jupiter ring paper finished: We have completed a paper describing our image processing and analysis of the Jovian ring system (enclosed), and the paper has been accepted for publication in **Icarus**. This work was primarily the thesis research of Mark Showalter, although general theoretical collaboration, radiative transfer modeling, and about half of the image processing were supported or materially aided under this RTOP. This task resulted in a significantly different view of the structure of the Jovian ring and the discovery of a new exterior "gossamer" ring, as reported last year.

A ring photometry and structure: Progress continues in photometric and structural studies of the A ring of Saturn. This work, primarily the thesis research of Luke Dones, is aimed at determining the distribution of "dust" as a dynamics tracer in and out of spiral density wavetrains in different regions of the A ring. Our ultimate goal here is to better understand the complex process of wave damping, which is less effective in higher optical depth regions due, according to a theory we developed under this grant, to the lower random velocities therein (Shu et al. 1985). We expect that these differences will manifest themselves in the fractional dust abundance. We have obtained improved constraints on the phase function and albedo of the macroscopic particles in the rings, and soon hope to solve for the dust fraction and its variation between unperturbed and perturbed regions.

Solution of this problem has been complicated by the poorly constrained azimuthally

variable brightness shown by the A ring; that is, in order to determine a phase curve that can constrain the fractional abundance of dust, we need first to determine how certain of the brightness observations may be corrupted by the azimuthal variation, which seems to have an amplitude of as much as 40% in certain cases and is poorly constrained as to how the phase of the effect changes with viewing geometry. We continue to spend a reasonable amount of effort trying to understand the systematics of this effect, at least to the extent possible to avoid having it bias our primary results.

Improvements to image processing system: The powerful and flexible image processing system which we developed, support, and continually upgrade under this RTOP provides a major facility for about ten researchers. We hope to maintain the ability to support both resident and visiting scientists interested in ring studies, and to be able to provide analysis in support of research tasks initiated by others than imaging team members. For instance, we recently were able to rapidly address questions posed by members of the PPS team on some apparent anomalies in the Uranian ring structure, and by a member of the Electric Field Analyser team on the possibility of detecting extended regions of dust at the location of Voyager ring plane crossing. Most recently, we have implemented on-line inspection and display programs for accessing the full stellar and radio occultation data sets. We actively pursue the use of computer telecommunications and data transfer between interested ring scientists. The programmer/analyst time required to maintain this system and support occasional users, as well as to actually perform much of the basic data analysis, is funded partially under this RTOP and is our fundamental limitation. For the sake of economy, we will continue to run interactively on the Ames Space Science Division VAX'es (11/785 and 8600) for the near future.

Bibliography:

Cuzzi, J. N. (1985) Rings of Uranus: not so thick, not so black, Icarus, 63, 312-316

Cuzzi, J. N. and J. A. Burns (1986) Charged Particle depletions surrounding Saturn's F ring - evidence for a moonlet belt; Icarus, submitted

Lissauer, J. J. (1985) Can cometary bombardment disrupt synchronous rotation of planetary satellites? J. Geophys. Res., 90, 11289-11293

Ockert, M. E., J. N. Cuzzi, and C. C. Porco (1986) Uranian rings: photometry from Voyager; paper presented at Paris DPS meeting, October 1986

Porco, C. C., J. N. Cuzzi, M. E. Ockert, and R. J. Terrile (1986) The color of the Uranian rings; Icarus (submitted)

Showalter, M., J. N. Cuzzi, E. A. Marouf, and L. W. Esposito (1986), Satellite wakes and the orbit of the Encke gap moonlet; Icarus, 66, 297-323

Showalter, M. , J. A. Burns, J. N. Cuzzi, and J. B. Pollack (1986), Jupiter's ring: new results on structure and particle properties, Icarus, in press

Shu, F. H., L. Dones, J. J. Lissauer, C. Yuan, and J. N. Cuzzi (1985), Nonlinear spiral density waves: viscous damping, Astrophys. J., 299, 542-573

Dynamical Studies of Saturn's Rings

Philip D. Nicholson, Astronomy Department, Cornell University, and Carolyn C. Porco, Lunar and Planetary Laboratory, University of Arizona.

We are currently pursuing several investigations of Saturn's rings, employing data from three Voyager experiments: radio science (RSS), stellar occultation (PPS), and imaging. These investigations, which are concentrated on the poorly-understood but regularly-organized C ring, include a search for eccentric or inclined features; a photometric study of regions of different optical depth; an analysis of wavelike structures at three locations; and a study of the size-distribution of meter-sized particles (with M. Showalter of NASA-Ames Research Center). Recent results from these investigations are summarized here.

a) Eccentric features in the C ring.

Of 35 well-defined features examined in the outer C ring, only 4 show rms deviations from circularity in excess of 2.0 km. These features form the inner and outer edges of two relatively opaque ringlets which lie in, or adjacent to, two narrow gaps at radii of 1.470 R_S and 1.495 R_S (1 R_S = 60,330 km). The 16 km wide 1.470 R_S ringlet, with a radial amplitude of $\pm$2.2 km, appears to owe its eccentricity to perturbations by the 2:1 inner Lindblad resonance with the satellite Prometheus, although it is possible that the ringlet is freely precessing instead (Porco and Nicholson, 1985).

The 64 km wide ringlet at 1.495 R_S, on the other hand, is almost certainly a freely precessing ellipse, similar to the previously studied Maxwell ringlet (Porco et al., 1984). Its radial amplitude is $\pm$ 3.9 km. These results contradict the expectation that the edges of these two ringlets would be perturbed by two nearby Mimas 3:1 resonances, and call into question the role played by these resonances in forming the surrounding gaps.

(b) Wavelike structures in the C ring.

Much of the fine scale structure in the A ring, and a smaller portion of that in the B ring, has been shown to be due to density waves and bending waves driven at resonances with external satellites (e.g., Holberg 1982; Esposito et al., 1983). Perhaps because of the weaker resonances in this region, no such waves have yet been identified in the C ring. There are, however, three wavelike features associated with narrow gaps at 1.28 R_S, 1.470 R_S, and 1.495 R_S. We have

examined these waves in both the RSS and PPS data, and attempted to fit both density wave models and models describing perturbations by moonlets orbiting within the gaps to the observations.

Rather surprisingly, no model has been found which satisfactorily accounts for either the 1.470 or 1.495 R_s waves, although 14-20 complete oscillations are observed. The wave at 1.28 R_s, with ~15 oscillations, has the characteristics of a density wave, but the associated resonance appears to be far too weak to account for the wave's observed amplitude, Furthermore, the gap associated with the wave, with a width of 15 km, appears only in the RSS occultation data, suggesting either temporal or longitudinal variability, or extreme particle size segregation.

(c) Particle size distributions

We have shown (Showalter and Nicholson, 1986) that the statistical properties of the Voyager PPS stellar occultation data are incompatible with simple photon (i.e., Poisson) statistics. An improved statistical model has been developed, which takes into account the random distribution of finite-sized particles within the rings. When applied to the PPS data, this model yields different, but internally consistent, results for the 4 principal ring regions. For power law size distributions of plausible slopes ($d(\log n)/d(\log r) > -5$), the maximum particle size is found to be $r(max) \leq 3$m in the C ring, $\leq$ 5m in the Cassini Division, and ~10m throughout the A ring. The B ring shows a gradient in r(max), from ~5m in the inner region to 10-15m in the outermost region. Our results are consistent with average size distributions obtained for the C and A rings by Zebker et al. (1985), based on scattering cross sections at radio wavelengths, but offer the first detailed insight into variations in the size distribution.

References:

Elliot, J.L. and Nicholson. P.D. (1984). In Planetary Rings, R. Greenberg and A. Brahic, Eds., Univ. of Arizona Press.

Esposito, L.W., O'Callaghan, M., and West, R.A. (1983). Icarus 56, 439.

Holberg, J.B. (1982). Astron. J. 87, 1416.

Porco, C.C., and Nicholson, P.D. (1985). BAAS 17, 716.

Porco, C.C., Nicholson, P.D., Borderies, N., Danielson, G.E., Goldreich, P., Holberg, J.B., and Lane, A.L. (1984). Icarus 60, 1.

CHAPTER 5

PLANETARY INTERIORS, PETROLOGY, AND GEOCHEMISTRY

HIGH PRESSURE COSMOCHEMISTRY OF MAJOR PLANETARY INTERIORS: LABORATORY STUDIES OF THE WATER-RICH REGION OF THE SYSTEM AMMONIA-WATER

Malcolm Nicol, Mary Johnson, Steven Boone, and Hyunchee Cynn
Department of Chemistry and Biochemistry
University of California, Los Angeles, CA 90024

Models of the major planets and their satellites make simple, rather arbitrary assumptions concerning deep interiors. "Rock" cores or "ice" (water-ammonia-methane) layers are often invoked without considering thermodynamic consistency. The behavior of "gas-ice" mixtures at very high pressures, however, is poorly understood. When this project began, few measurements existed on binary or multicomponent gas-ice systems at pressures of the order of 1 GPa. We set out, therefore, to determine some relevant pressure-temperature-composition (P-T-X) regions of the hydrogen (H_2) - helium (He) - water (H_2O) - ammonia (NH_3) - methane (CH_4) phase diagram. These experiments, and theoretical modeling of the relevant phases, are needed to interpret ice-gas systems of planetary interest.

Our first goal was to show that the data needed to characterize compositions and structures of a multi-phase, multi-component system at very high pressures can be obtained with reasonable precision. We began with water-rich solutions of ammonia for several reasons. These mixtures are relevant to planetary interiors and are relatively easy to prepare. A few parts of the relevant P-T-X space had been determined. These include: the P-T surfaces of pure water [see, for example, Mishima and Endo ,1980] and pure ammonia [Mills et al., 1982] and the T-X surface of ammonia-water at atmospheric pressure [Rollet and Vuillard, 1956] which includes two water-rich compounds ammonia dihydrate ($NH_3 \cdot 2H_2O$) and ammonia hydrate ($NH_3 \cdot H_2O$). The dihydrate is the ammonia-bearing phase most likely to occur near the surfaces of icy planets. Recent models [Lunine and Stevenson, personal communication] suggest that both dihydrate and hydrate are important in the evolution of the interior and surfaces of the icy satellites. The work was begun by Ms. Andrea Koumvakalis and Dr. Mary Johnson [Johnson et al., 1985] and is being continued by Mr. Steven Boone and Mr. Hyunchee Cynn.

Even for this relatively simple system, many experimental problems had to be overcome. The structures of some of the solids are very different from the structure of the liquid. These solids are difficult to grow, and liquid or a glassy solid often persists metastably at conditions where crystals should form. Ice VI and ammonia dihydrate are very troublesome. Despite many attempts to overcome this metastability, it is not clear that equilibrium boundaries have been established among these phases and the liquid. All of the phases also are colorless; and the structures and vibrational spectra of many of the phases are not known. Thus, we learned to identify phases by shapes and birefringence. These observations do not identify phases unambiguously; however, they help us us to determine how to grow authentic samples of pure phases.

A manuscript submitted to the **Journal of Geophysical Research** during August 1986 describes Dr. Johnson's studies of the phase diagram of

$(NH_3)_x(H_2O)_{1-x}$ at pressures to 5 GPa, temperatures from 240 to 370 K, and ammonia compositions to 50%. Particularly careful studies were made near 5, 10, 15, 20, 25, 30, and 34% in an effort to resolve questions about metastability of the liquid and possible differences between visual work in the diamond-cell and thermophysical measurements in a large piston-cylinder apparatus. Dr. Johnson showed that melting at 20% NH_3 and higher compositions is complex; the composition of the high-temperature solid phase varies with both temperature and time; and the phase diagram can be reasonably well constrained by these data. Other results obtained from Dr. Johnson's work are:

1. At 25° C and lower temperatures, five well characterized and well behaved phases were observed, including: liquid; ice VI; ice VII; an ammonia hydrate; and an ammonia dihydrate.

2. At 3.45 GPa, dihydrate reconstitutes into myrmekitic intergrowths of Ice VII with a higher-relief phase which seems to be isotropic. The high-pressure phase was shown to have a composition near $NH_3 \cdot H_2O$. The transition is either independent of temperature or has a negative P-T slope. Hydrate plus Ice VII remains stable at room temperature to 14.7 GPa. Whether the low-temperature and high-pressure hydrates are equivalent must still be examined.

3. To the limits of precision of this study, none of the boundaries between solid phases of water ice are shifted by the presence of ammonia, although melting is suppressed in the expected manner.

4. At room temperature, the Ice VI-dihydrate-liquid eutectic is at 17 atom percent ammonia and 1.58 GPa. The eutectic curve as a whole may be fit by the equations: $T = 174 + 1.125\ P - 0.0229\ P^2$ ($r = 0.83$) and $X = 13.35 + 0.0252\ P$ ($r = 0.96$). 5. The dihydrate-liquid field has an unusually-shaped region of stability. Dihydrate becomes very prominent in the high pressure regieme. At room temperature, dihydrate melts at 0.88 GPa.

Mr. Steven Boone is extending the visual studies system in the diamond-anvil high pressure cells, especially near 33% NH_3.

Mr. Hyunchee Cynn used the data obtained by Dr. Johnson to grow single crystals of ammonia dihydrate at room temperature and has begun to determine their structures by x-ray diffraction. Preliminary data suggest that dihydrate has a monoclinic-B structure. The lattice constants were: $a = 709.80$ pm, $b = 568.86$ pm, $c = 886.64$ pm, $\alpha = 90.008°$, $\beta = 109.545°$, and $\gamma = 90.401°$. While the diffraction work continues, Mr. Cynn also has grown single crystals of dihydrate for Raman and infrared spectroscopy.

Drs. Johnson and Nicol are involved in two other projects of planetary interest. (1) Chemical reactions during shock compression of simple molecules are being followed by spectroscopy in order to evaluate how the reactions affect the interpretation of equation of state data obtained by shock methods. (2) Temperature and x-ray diffraction measurements are being

made on resistively heating wires in diamond-anvil cells in order to obtain phase and structural data relevant to interiors of terrestrial planets.

Shock compression data are the other major source of equations of state for H-C-N-O compounds at pressures and temperatures inside planets. However, many compounds undergo chemical reactions during shock compression. The products and kinetics of these reactions are not understood, and the effects of the reactions have not been fully considered in reducing shock wave data to equations of state. With benzene as a prototype, we use molecular emission spectra to detect products of these shock reactions at pressures between 20 and 65 GPa and temperatures between 2000 and 5000 K.[Johnson et al., 1986] The spectra show many bands of C_2 and other small molecules. Recent experiments with doubly-shocked material suggest that kinetics of the post-shock reactions can be followed.

Another shock wave project involves a "synthetic Uranus", a solution of iso-propanol, ammonia, and water with C:N:O compositions of cosmic abundance. In addition to the spectroscopy, shock equations of state and electrical conductivities of this "planet" are being measured. Other starting mixtures also will be studied in order to determine whether the results depend strongly upon the initial chemical species.

Drs. Boehler, Johnson, and Nicol also developed techniques for measuring the temperatuers of resistively-heated iron and other metals in gasketed diamond-anvil cells.[Boehler et al., 1986] Dr. Boehler has applied these techniques to determination of the phase diagram of iron and, with collaborators from Paris VI, Paris-Nord, Riso, and HASYLAB, they are obtaining high-pressure, high-temperature x-ray diffraction data for alpha, gamma, and epsilon iron that are needed to understand the nature of the Earth's core.

REFERENCES

Boehler, R., M. Nicol, C.-S. Zha, and M.L. Johnson, 1986, Physica B **139/140**, 916-918.

Johnson, M.L., M. Nicol, and N.C. Holmes, 1986, in Y.M. Gupta, ed., **Shock Waves in Condensed Matter** (Plenum, New York) 201-206.

Johnson, M. L., A. Schwake, and M. Nicol, 1985, in Klinger J. et al., eds., **Ices in the Solar System** (D. Reidel, Doerdrecht) 39-47.

Mills, R.L., D.H. Liebenberg, and Ph. Pruzan, Ph. (1982), **J. Phys. Chem. 86**, 5219.

Mishima, O., and S.J. Endo, 1980, **J. Chem. Phys. 73**, 2454.

Rollet, A.-P., and G. Vuillard, 1956, **Comptes. rendus Acad. Sci. Paris 243**, 383.

EXPERIMENTS PERTAINING TO THE FORMATION AND EQUILIBRATION OF PLANETARY CORES

Principal Investigator: Raymond Jeanloz
Dept. Geology and Geophysics
University of California
Berkeley, CA 94720

I

High-Pressure Metallization of FeO and Implications for the Earth's Core

Elise Knittle and Raymond Jeanloz

The phase diagram of FeO has been experimentally determined to pressures of 155 GPa and temperatures of 4000 K using shock-wave and diamond-cell techniques. We have discovered a metallic phase of FeO at pressures greater than 70 GPa and temperatures exceeding 1000 K. The metallization of FeO at high pressures implies that oxygen can be present as the light alloying element of the Earth's outer core, in accord with the geochemical predictions of Ringwood. The high pressures necessary for this metallization suggest that the core has acquired its composition well after the initial stages of the Earth's accretion. Direct experimental observations at elevated pressures and temperatures indicate that core-forming alloy can react chemically with oxides such as those forming the mantle. The core and mantle may never have reached complete chemical equilibrium, however. If this is the case, the core-mantle boundary is likely to be a zone of active chemical reactions.

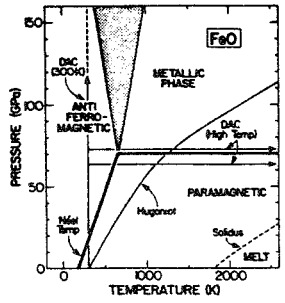

Figure 1. Phase diagram of FeO based on high-pressure experiments with the diamond cell (DAC) and by shock-wave techniques (Hugoniot). Diamond-cell experiments have been carried out both at room temperature (300 K) and at combined high temperatures and pressures, as indicated on the figure. The phase boundaries between antiferromagnetic (nonmetallic), paramagnetic (nonmetallic), and metallic phases are shown by heavy lines and a shaded region; the latter reflects the uncertainty in the slope of the boundary. The solidus is given by a dashed line.

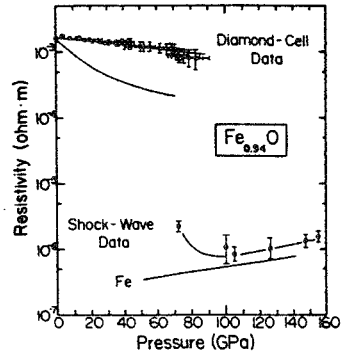

Figure 2. Room-temperature diamond-cell (0 to 83 GPa) and high-temperature shock-wave (72 to 155 GPa) electrical resistivity data for FeO. Shock-wave resistivity measurements for iron [Keeler and Mitchell, 1969] are summarized (solid line) to illustrate that the resistivity of FeO is metallic at elevated pressures and temperatures. The three order of magnitude difference in resistivity between the diamond-cell and shock-wave measurements at 80 GPa cannot be explained as a temperature effect on semiconducting FeO. The dashed line is the calculated resistivity for semiconducting FeO at high temperature. At 72 GPa and 1200 K (the calculated Hugoniot temperature) the predicted resistivity is still two orders of magnitude higher than that observed in the shock-wave experiments.

II

The Melting Curve of Iron to Over 100 GPa and of Iron Sulfide to Over 60 GPa

Quentin Williams and Raymond Jeanloz

We have measured the melting curve of Fe and FeS to pressures exceeding 100 GPa and 60 GPa, respectively, using a laser-heated diamond cell. Temperatures of the samples were determined spectroradiometrically, and melting was determined based upon a combination of visual observation during heating and of textural observations on the quenched samples. To avoid chemical reaction with the diamond anvils, all samples were suspended in an Al_2O_3 (ruby) matrix. Our results for iron agree with previous measurements below 7 GPa, and indicate a melting temperature of 4100 (±200) K at 100 GPa. By extrapolation, we find that the melting temperature of iron at the pressure of the core-mantle boundary (136 GPa) is 4500 (±300) K. Our data for FeS suggest an initially steeply rising melting curve (temperature of 3000 K at 50 GPa), with greater curvature at high pressure than that observed for iron. We find no evidence for the hot iron samples reacting with the ruby when they are solid, but both molten Fe and molten FeS appear to react significantly with the oxide at elevated pressures.

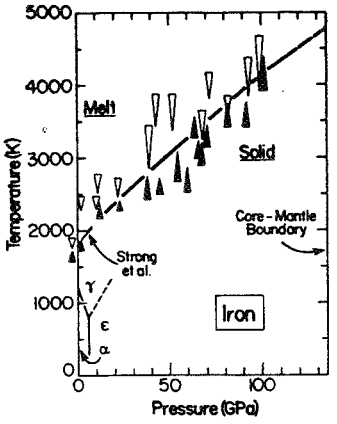

Figure 3. Bounds on the melting curve of iron from static experiments as a function of pressure. Solid triangles represent the highest temperature measured on solid iron samples at a given pressure, while open triangles indicate the lowest temperature of liquid samples. Lengths of symbols reflect the statistical uncertainty in temperature from the relevant spectral fit. The low-pressure melting curve of Strong et al. (2) is also shown, along with the phase equilibria of the known iron crystalline phases: α represents the body-centered-cubic structure, ε the hexagonal close-packed structure, and γ the face-centered cubic structure.

Melting of Troilite at High Pressure in a Diamond Cell by Laser Heating

William A. Bassett and Maura S. Weathers
Dept. Geological Sci., Cornell U., Ithaca, N.Y. 14853

We have assembled a system which allows us to measure melting temperatures at high pressures. Figure 1 is a schematic diagram of our apparatus. The sample is heated with radiation from a YAG laser (λ = 1.06 um), either continuously or in a Q-switched mode. The Q-switch can be used to produce individual pulses of 100-200 nsec duration. The power of each pulse is of the order of 1,000 watts. The laser can be triggered by the computer (Fig. 1) at the same time that the photodiode array starts to collect a series of spectra. The beam is reflected downward through a microscope objective, through the upper diamond anvil, and focused onto the sample. The laser light is thereby strongly converging onto the sample, producing intense heating only at the sample and not within the diamond anvils. The heated area is ~10 um in diameter. A vidicon system is used to observe the sample during heating.

Incandescent light from the heated sample passes back through the objective lens into a grating spectrometer. The spectrum of the incandescent light is received by the photodiode array and stored in the multichannel analyzer. These data can then be transferred to floppy disk for analysis. A curve-fitting program is used to compare the spectra with standard blackbody curves and to determine the temperature.

Pressure is measured by the ruby fluorescence method. A frequency-doubling crystal is placed in the laser beam to produce green light having a wavelength of 530 nm. This light, when focused onto particles of ruby inside the diamond cell, excite fluorescence. The wavelength of the emitted red light can then be used to measure the pressure. The pressure is measured at room temperature by this method.

We have tested our apparatus by melting several different materials. These materials provide various criteria for determining whether or not melting has occurred. Our technique in these experiments is to bracket the melting temperatures of the materials. During each laser pulse a spectrum of the emitted incandescent light is collected and stored. It is necessary to remove the sample and look for evidence of melting using optical and electron microscopy. We have used various criteria in different samples to establish whether or not melting has occurred, including the formation

of droplets from elongate fibers of platinum, formation of droplets from angular particles of silicon and diamond, formation of a groove with ridges on a diamond face, encapsulation of droplets of the pressure medium within diamond (Gold et al, 1984), and holes melted through tungsten foil. We have also inferred melting from electron diffraction patterns of samples (Weathers and Bassett, 1986).

The samples which are loaded into the diamond anvil cells consist of a mixture of small grains (<10 microns) of the actual sample (e.g., graphite, troilite, diamond, iron, etc.) and a pressure medium (e.g., LiF, NaCl, or KBr). Usually between 20 and 50 grains in each sample are heated using the laser radiation. The position of each heated grain is recorded on a photograph. When the sample is removed from the diamond cell, the pressure medium is slowly dissolved in alcohol so that the grains maintain their relative positions and can be identified from the earlier photographs. The dissolution of the pressure medium is done so that the sample is deposited on a grid which can be put directly into the electron microscope.

We are studying the melting behavior of natural troilite (FeS). Powdered troilite mixed with NaCl at ~200 kbar was laser-heated. Our initial transmission electron microscopy study showed that we successfully melted grains of the troilite, converting angular particles into spherical grains (Fig. 2). An example of a preliminary temperature determination is shown in Figure 3. A blackbody curve for 2800 K was fitted to the processed spectrum which represents a grain of troilite that melted at 5 kbar. Further analyses of temperatures obtained at various pressures, combined with determinations of whether or not the heated grains melted will allow us to bracket the melt curve for troilite.

Gold, J.S., Bassett, W.A., Weathers, M.S., and Bird, J.M. (1984) Melting of diamond, Science 225, 921-922.

Weathers, M.S., and Bassett, W.A., Melting of carbon at 300 kbar, submitted, Phys. Chem. Min.

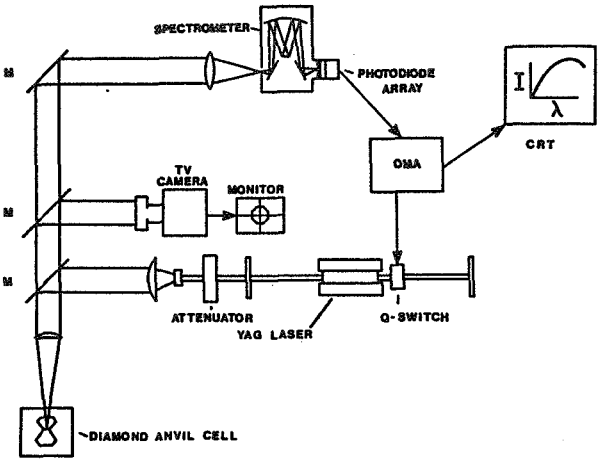

Figure 1. Diagram showing our experimental apparatus for melting materials at high pressures and determining temperatures. The YAG laser can be rapidly pulsed using the Q-switch. The intensity of the laser light is controlled by means of an attenuator. The laser beam is focused onto the sample in the diamond cell. A beam-splitter mirror allows a portion of the light to be used to monitor the sample during the experiment. The incandescent light given off by a heated sample is directed to the grating spectrometer and photodiode array. Spectra collected by the photodiode array are stored in the computer controlled optical multichannel anlyzer and are later processed to determine temperature.

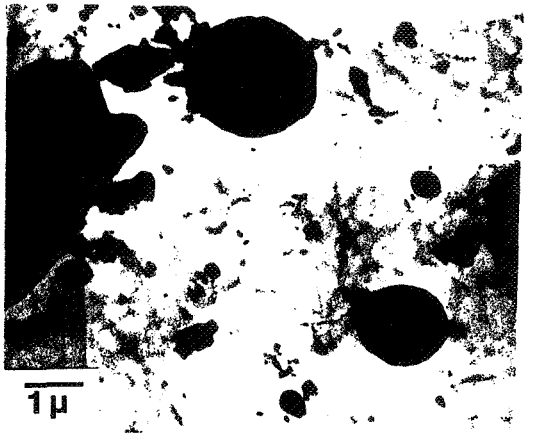

Figure 2. Transmission electron image of spherical grains of troilite (FeS). These grains, which were originally angular, were melted by laser-heating.

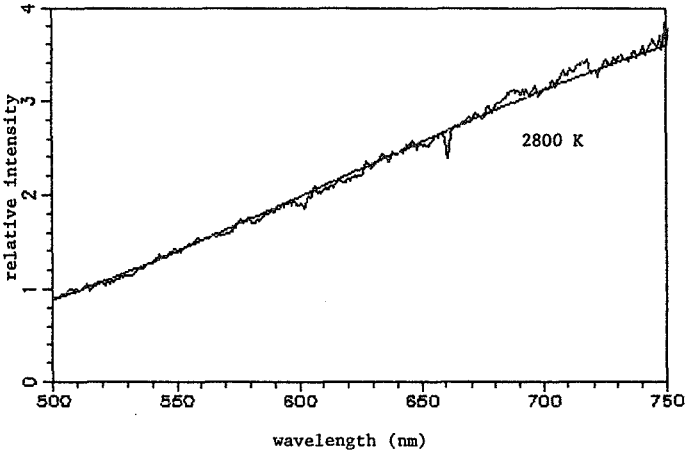

Figure 3. Processed spectrum from a heated grain of troilite fit to a blackbody curve of 2800 K. The pressure at the time of heating was 5 kbar. This spectrum is from a grain that showed evidence of melting.

PROPERTIES OF PLANETARY FLUIDS AT HIGH PRESSURE AND TEMPERATURE

W. J. Nellis, D. C. Hamilton, N. C. Holmes, H. B. Radousky, F. H. Ree, M. Ross, D. A. Young, and M. Nicol*
Lawrence Livermore National Laboratory, University of California
Livermore, CA 94550

*University of California, Los Angeles, CA 90024

The outer planets Uranus and Neptune are thought to consist of the "ices" H_2O, CH_4, NH_3, and possibly CO, CO_2 and N_2.[1] The envelopes of these planets, as well as those of Jupiter and Saturn, are composed of H_2 and He.[1] In order to derive models of the interiors of these planets we have been studying the equations of state and electrical conductivities of these molecules at high dynamic pressures and temperatures. This study is timely because of the recent Voyager II flyby of Uranus, which measured the magnetic field distribution and the rotation rate of the magnetic field, which gives the rate of rotation of the interior of the planet.[2] The gravitational moments derived from the rotation rate put constraints on the mass distribution. Thus, equations of state of representative materials are needed to model the chemical composition. The magnetic field requires information on the electrical conductivities of representative materials to develop dynamo models. The condensed gases in these planets were compressed isentropically starting from very low density and temperature. By virtue of their large masses, however, interior temperatures and pressures are quite large. For Uranus the conditions in the "ice" layer range between 0.2-6 Mbar and 2000-7000 K.[3] Shock compression of liquids achieves virtually the same states in the laboratory.

Interest has been generated in the interior of Uranus because of its unusual magnetic field with an offset tilted dipole moment of 0.23 gauss R_U^3, whose dipole axis is tilted about 60° from the axis of rotation and centered at about 0.3 R_U, where R_U is the radius of Uranus.[2] Thus, material at substantially larger radii than 0.3 R_U must be contributing to the dynamo. This means that data we obtain using our two-stage light-gas gun at pressures up to ~ 2 Mbar and temperatures up to 5000 K are especially relevant for constructing models of the interior.

During the past year we used the fast optical pyrometer developed the previous year to complete shock temperature measurements for N_2 and CH_4. Nitrogen can exist inside Uranus by virtue of the decomposition of NH_3, whose shock temperature we measured previously.[4] The nitrogen temperature data showed that it undergoes a continuous phase transition to a dense, stiff, monatomic, diamond-like phase above 0.3 Mbar and 6000 K. The temperature data allowed us to demonstrate <u>shock-induced cooling</u> (a first), that $(\partial T/\partial P)_V < 0$ in the transition region (as predicted), and the existence of crossing isotherms in P-V space.[5] The shock-induced cooling is caused by absorption of internal energy by dissociation. Since N_2 at room temperature does not dissociate at static pressures up to 1.3 Mbar,[6] the transition in the shock-wave

experiments must be temperature-driven. Because of the high temperatures inside Uranus, the same phenomena would be expected there also. Thus, it is quite likely that the lower ice region is composed of stiff, diamond-like H, C, N, O phases. In contrast, our two shock temperature points near 0.4 Mbar and 4000 K for liquid CH_4 are in good agreement with the published prediction, which assumes shocked methane is in the molecular phase.[7]

Electrical conductivities measured for shocked liquid CH_4 show that its conductivity is substantially lower than that of H_2O. Our results for N_2 show that our maximum observed value at 0.6 Mbar is comparable to the maximum conductivity we measured for H_2O, but the conductivity of H_2O is much higher than for N_2 below 0.6 Mbar.

In order to find materials with higher electrical conductivities than observed so far for individual fluids and which may be necessary to derive a Uranian dynamo theory, we have started to investigate fluid mixtures. We have devised a mixture we call "synthetic Uranus," which is based on estimates of the composition of Uranus, proposed to be mostly H_2O and H_2. We have made a liquid with a 4:1 ratio of H to O, corresponding to an equimolar mixture of H_2O and H_2, and also with concentrations of C and N such that the ratios of the concentrations of O to C and O to N correspond to the ratio of their cosmic abundances (7:4 for O to C and 7:1 for O to N).[8] Three shock-wave equation-of-state points were measured between 0.15 and 0.78 Mbar. This mixture has the same shock P-V curve as H_2O when scaled to the appropriate initial molar volume. This fluid has a relatively high conductivity at ambient. Our preliminary data does not allow us to say that its conductivity is larger than that of water at higher pressures and temperatures. Work is continuing on this point.

Our research plans are to complete our measurements of shock temperatures, emission spectroscopy, and electrical conductivities of the "ices," H_2, and "synthetic Uranus" and to develop techniques to measure the same properties in quasi-isentropically compressed fluids. This technique would cause the specimens to track states closer to the planetary isentropes; that is, at relatively higher densities and lower temperatures than the shock data.

Work performed under the auspices of the U.S. Department of Energy by the Lawrence Livermore National Laboratory under contract number W-7405-ENG-48.

REFERENCES

1. D. J. Stevenson, "Interiors of the Giant Planets," Annu. Rev. Earth Planet. Sci. 10, 257 (1982).

2. N. F. Ness, M. H. Acuna, K. W. Behannon, L. F. Burlaga, J. E. P. Connerney, R. P. Lepping, and F. M. Neubauer, "Magnetic Fields at Uranus," Science 233, 85 (1986).

3. W. B. Hubbard and J. M. MacFarlane, "Structure and Evolution of Uranus and Neptune," J. Geophys. Res. 85, 225 (1980).

4. H. B. Radousky, A. C. Mitchell, W. J. Nellis, and M. Ross, "Shock Temperature Measurements in Ammonia," in Shock Waves in Condensed Matter, edited by Y. M. Gupta (Plenum, New York, 1986), pp. 467-472.

5. H. B. Radousky, W. J. Nellis, M. Ross, D. C. Hamilton, and A. C. Mitchell, "Molecular Dissociation and Shock-Induced Cooling in Fluid Nitrogen at High Densities and Temperatures," Phys. Rev. Lett. (in press - November 10, 1986 issue).

6. R. Reichlin, D. Schiferl, S. Martin, C. Vanderborgh, and R. L. Mills, "Optical Studies of Nitrogen to 130 GPa," Phys. Rev. Lett. 55, 1464 (1985).

7. M. Ross and F. H. Ree, "Repulsive Forces of Simple Molecules and Mixtures at High Density and Temperature," J. Chem. Phys. 73, 6146 (1986).

8. D. J. Stevenson, "Condensed Matter Physics of Planets: Puzzles, Progress and Predictions," in High Pressure in Science and Technology, Vol. III, edited by C. Homan, R. K. MacCrone, and E. Whalley (North-Holland, New York, 1984), pp. 357-368.

GRAVITY DATA ANALYISIS

William L. Sjogren
Jet Propulsion Laboratory, Pasadena, CA 91109

Three different efforts have been worked. The first is the reduction of raw Doppler data from the Apollo 15 subsatallite to produce acceleration profiles as a function of latitude, longitude and altitude (~15,000 new observations). The second is an investigation related to fitting long arcs of Pioneer Venus Orbiter tracking data. The third effort was the study of gravity/topography ratios which were found to have a linear trend with longitude.

Raw Doppler data from the Apollo 15 subsatellite have been archived for the past 15 years. These data have now been reduced and put in a form compactible with user-friendly software (Geophysical Data Facility (GDF) which is being sponsored by the Lunar and Planetary Institute). Approximately 150 orbits (~15,000 acceleration observations) covering a $\pm 30^{\circ}$ band of latitude with varing space altitude are plotted and described in a report entitled "User's Guide to the JPL Doppler Gravity Data Base" JPL publication 86-16. These data have been distributed to NSSDC and LPI.

Fitting long arcs of Pioneer Venus Orbiter data (>3 orbits) became a problem a few years ago when a global 10th degree and order gravity field (Mottinger et al, 1985) was being estimated. Only realistic results for the field could be obtained when short arcs of data were used (~1 to 2 orbits). Since then many tests and empirical models have been evaluated to explain the poor fits to the observations. Presently we are obtaining some encouraging results where excellent data fits have been obtained over eight orbits. It is somewhat premature to state that the previous problem is understood. It appears that significant perturbations are being produced by the high frequency (local) gravity anomalies. The introduction of many near surface mass disks in a global sense is very effective. This work will continue.

The ratios of observed gravity to theoretical gravity based on topography (ρ = 2.7 gm/cc) were calculated for 35 well defined Venusian gravity anomalies as displayed by Sjogren, et al. 1980. The anomalies were significantly greater than 5 milligals and were located between -15° latitude and 42.5° latitude. Theoretical gravity profiles were generated using USGS topography (Pettengill, et al., 1980) gridded on $2^{\circ} \times 2^{\circ}$ spacing. The extent of the topography was 60° east and 60° west of the feature being evaluated. It also extended from 60°N to 30°S and was isostatically compensated uniformly at 100 km. Some typical profiles for four features are shown in figure 1. The dotted line is gravity while the solid line is theoretical gravity based on topography having a density of 2.7 gm/cc and being compensated at 100 km. Figure 2 shows the plot of the ratios of gravity to topography. There appears to be an increasing trend in the ratios from 60°E longitude. At least two of these ratios had previously been confirmed by other investigations (Bills, Esposito, Reasenberg) for Aphrodite Terra and Beta Regio. Shallower compensation for Aphrodite Terra and deeper compensation for Beta Regio are the generally accepted statements in the literature. These new results seem to indicate that there is a definite trend eastward and possibly some internal dynamic process may be the cause of it. Certainly the 300 km isostatic depth of compensation for Beta Regio (Esposito, et al.) seems unrealistic and therefore dynamic forces sup-

porting it would be a more acceptable model. If this is so, this result may indicate a time sequence in the age of topography. This report is presently in peer review at Icarus where Sjogren, Trager and Saunders are authors.

REFERENCES

1. Bills, B.G. (1983), Gravity, topography and crustal evolution of Venus, Icarus, 56, 345-371.
2. Esposito, P.B., W.L. Sjogren, N.A. Mottinger, B.G. Bills, and E. Abbott (1982), Venus gravity: Analysis of Beta Retio, Icarus, 51 448-459.
3. Mottinger, N.A., W.L. Sjogren and B.G. Bills (1985), Venus Gravity: A Harmonic Analysis and Geopysical Implications, J. Geophys. Res., 90, C739-C756.
4. Pettengill, G.G., E. Eliason, P.G. Ford, G.B. Loriot, H. Masursky, and G.E. McGill (1980), Pioneer Venus radar results: Altimetry and surface properties, J. Geophys. Res., 85, 8261-8270.
5. Sjogren W.L. R.J. Phillips, P.W. Birkeland, and R.N. Wimberly (1980), Gravity anomalies on Venus, J. Geophys. Res., 85, 8295-8302.
6. Reasenberg, R.D., A.M. Goldberg, and I.I. Shapiro (1982), Venus: Comparison of gravity and topography in the vicinity of Beta Regio, Geophys. Res. Lett., 9, 637-640.

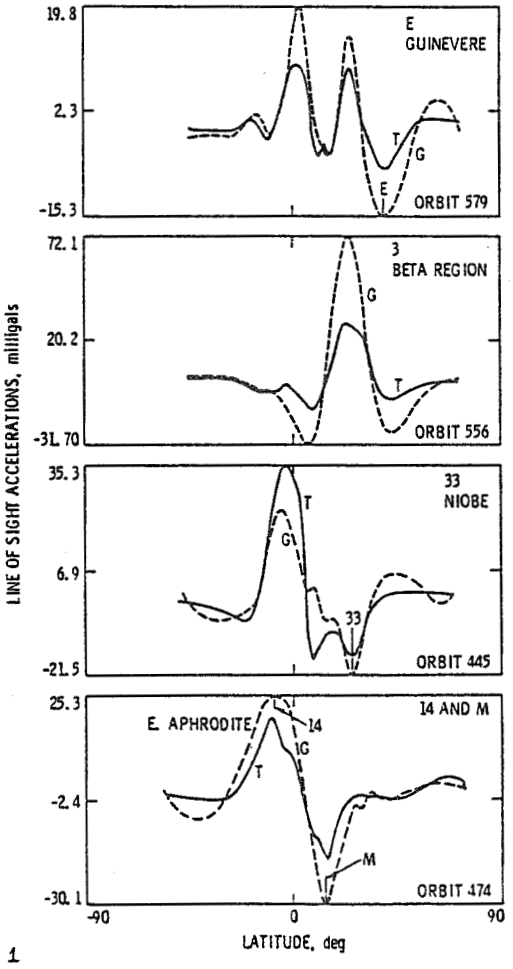

Figure 1

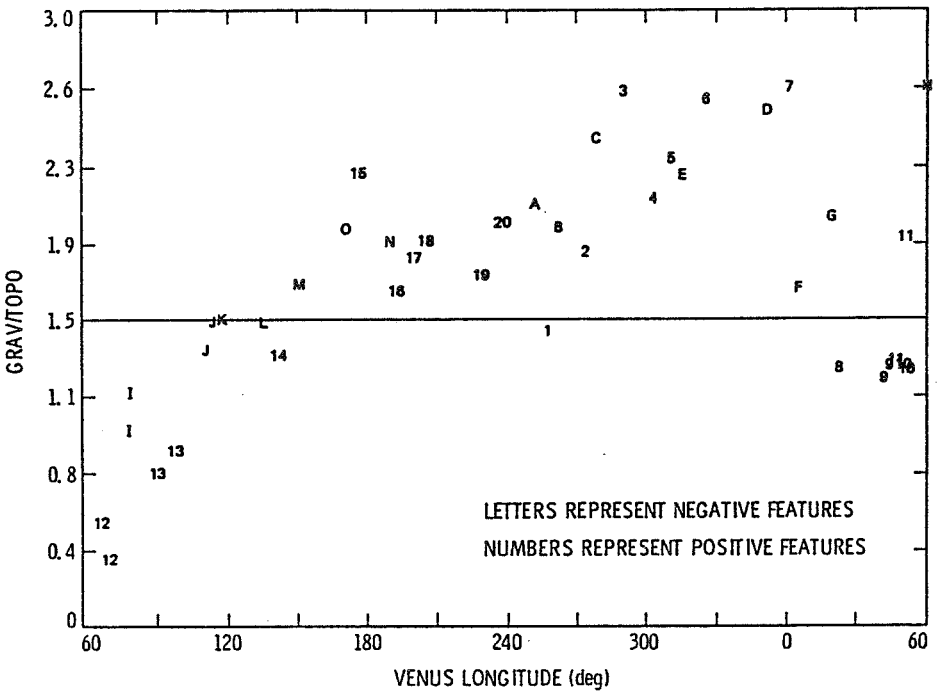
3.0
2.6
2.3
1.9
1.5
1.1
0.8
0.4
0
GRAV/TOPO
60
120
180
240
300
0
60
VENUS LONGITUDE (deg)
LETTERS REPRESENT NEGATIVE FEATURES
NUMBERS REPRESENT POSITIVE FEATURES

2

Figure 2

The Origin of Polarity Asymmetries in the History of the Geomagnetic Field

E. H. Levy, Lunar and Planetary Laboratory and Department of Planetary Sciences, University of Arizona, Tucson, Arizona 85721.

Paleomagnetic studies of the behavior of Earth's magnetic field suggest that the field has exhibited persistent polarity asymmetries throughout recent geologic time, with relative amplitudes of the lowest several multipole moments differing between the "normal" polarity state and the "reversed" polarity state. This paper examines the behavior of magnetohydrodynamic stationary modes in the presence of an imposed weak magnetic field originating separately from the dynamo. A rare class of stationary states is found that exhibit high sensitivity to the presence of weak imposed fields. The amplitude of the difference between the total fields of opposite polarity is much larger than the amplitude of the imposed nondynamo fields. It is proposed that Earth's magnetic field operates in such a mode, highly sensitive to the presence of an ambient field. An argument, based on the possible mechanisms of dyanamical equilibration of dynamo magnetic fields, is given to explain why the terrestrial dynamo should choose to operate in one of these rare states. Implications are discussed for the general mechanism of dynamo magnetic field equilibration in planets.

Magnetic Flares in the Protoplanetary Nebula and the Origin of Meteorite Chondrules

E. H. Levy and S. Araki, Lunar and Planetary Laboratory and Department of Planetary Sciences, University of Arizona, Tucson, Arizona 85721.

Meteoritic chondrules apparently resulted from very rapid, transient, and short-lived heating events in the otherwise much cooler protoplanetary nebula where the meteorites formed. This paper proposes and analyzes a model for the chondrule forming heating events based on magnetohydrodynamic flares in the corona of the protoplanetary nebula which precipitate energy in the form of energetic plasma along magnetic field lines down toward the face of the nebula. It is found that flare energy release rates sufficient to melt prechondrular matter, leading to the formation of chondrules, can occur in the tenuous corona of a protostellar disk. Energy release rates sufficient to achieve melting require that the ambient magnetic field strength be in the range that has been inferred separately from independent meteorite remanent magnetization studies.

Generation of a Dynamo Magnetic Field in a Protoplanetary Accretion Disk T. Stepinski and E. H. Levy, Lunar and Planetary Laboratory and Department of Planetary Sciences, University of Arizona, Tucson, Arizona 85721.

A new computational technique is developed that allows realistic calculations of dynamo magnetic field generation in disk geometries corresponding to protoplanetary and protostellar accretion disks. The approach is of sufficient generality to allow, in the future, a wide class of accretion disk problems to solved.

In this initial study, the basic modes of a disk dynamo are calculated. Spatially localized oscillatory states are found to occur in Keplerian disks. A physical interpetation is given that argues that spatially localized fields of the type found in these calculations constitute the basic modes of a Keplerian disk dynamo.

These results and the computational technique have general applicability to a variety of other cosmical disk systems including disk galaxies and high energy accretion disks around black holes and compact stars.

The Steady State Toroidal Magnetic Field at the Core-Mantle Boundary S. J. Pearce and E. H. Levy, Lunar and Planetary Laboratory and Department of Planetary Sciences, University of Arizona, Tucson, Arizona 85721.

Recent measurements (Lanzerotti, et al., 1985) indicate that the strength of the toroidal magnetic field at Earth's core-mantle boundary is comparable to the strength of the poloidal field--5 to 10 gauss. Illustrative calculations are given to show that this result is an inevitable result of the external boundary condition on the core, in which the mantle electrical conductivity is several orders of magnitude lower than that of the core. The measurements are shown to imply that the internal core toroidal magnetic field is in the range of several hundred gauss. Thus the measurements imply that Earth's core contains a strong toroidal magnetic field and support the idea that Earth's dynamo--and, by implication, other planetary magnetic fields--involves efficient toroidal magnetic field generation through strong differential rotation.

LUNAR MAGNETIZATION CONCENTRATIONS (MAGCONS) ANTIPODAL TO YOUNG LARGE IMPACT BASINS, R. P. Lin, and K. A. Anderson,* Space Sciences Laboratory, University of California, Berkeley, CA 94720, L. L. Hood, Lunar and Planetary Laboratory, University of Arizona, Tucson, AZ 85711

Electron reflection measurements from the Apollo 15 and 16 subsatellites show that patches of strong surface magnetic fields ranging in size from less than ~7 km, the resolution limit of the observations, to greater than 500 km, are distributed over the surface of the Moon (1, 2). With the exception of a few regions — Rima Sirsalis (3) and Reiner Gamma (4) — no obvious association to surface geology has been found. In the ±35° latitude band covered by the electron reflection measurements, the largest concentration of surface magnetic fields extend in a chain from ~E160 S30 east and south to ~W115 S20 (Figure 1). In the north a large magcon is located at ~N10-25 E85-110. The southern chain includes the intense magnetic region near Van de Graaff initially found from Apollo subsatellite magnetometer measurements (5). The orbiting magnetometer also observed the anomaly centered at ~W125 S23, at the northeastern end of the southern chain (6). We have previously noted that these large regions are approximately antipodal, i.e. located diametrically opposite, to large circular impact basins (7). The southern chain appears to be composed of three regions corresponding to the antipodes of the Imbrium, Serenitatis and Crisium basins. The large northern magnetized region is antipodal to Orientale.

We have examined the antipodes of the 23 ringed impact basins identified by Wilhelms (8) for which electron reflection measurements are available. Measurements (in 1¼° × 1¼° pixels) located within an antipodal region equal in diameter to the basin itself were used to form distributions of the surface magnetic fields for each basin (Figure 2). The median surface magnetic field for each basin antipode is plotted in Figure 3, where the basins are arranged in order of increasing age. Strong magnetic fields are obtained for antipodes of the young ringed impact basins, but significantly weaker fields are found for older basins. Strong median magnetic fields are obtained at the antipodes of three young ringed impact basins, Orientale, Imbrium and Serenitatis. The median magnetic field at the antipodes of 20 other ringed basins are significantly weaker. With one possible exception, all these basins are older than the three young basins just referred to.

Large impacts could produce significant modification of the antipodal region either by focusing of impact generated seismic waves (9) or by clustering of secondary ejecta. Seismic waves may produce and enhance deep fractures in the antipode region. If an underlying layer of the lunar crust was uniformly magnetized over a very large region, possibly over the entire Moon, then the surface field from such a layer will be small except at the edges of the region. Deep fractures produced at the antipodes of impact basins will result in discontinuities in the magnetized layer, which would result in strong surface magnetic fields.

Alternatively, antipodal magnetic anomalies could mean that the basin-related secondary ejecta may have become highly magnetized, possibly in a strong ambient or impact generated magnetic field.

The apparent temporal variation of the magnetic fields for the basin antipodes may reflect real variations in the lunar magnetic field. Paleomagnetic data (10) suggest that a lunar "magnetic epoch" of strong fields occurred approximately at the time of formation of the youngest impact basins. However, the lack of strong antipodal fields for older basins may also be the result of more extensive gardening which has removed any strong magnetization signature.

REFERENCES

(1) Lin R. P., Anderson K. A., Bush R., McGuire R. E., and McCoy J. E. (1976) *Proc. Lunar Sci. Conf. 7th*, pp. 2691-2704.

(2) Lin R. P. (1979) *Proc. Lunar Sci. Conf. 10th*, pp 2259-2264.

(3) Anderson K. A., Lin R. P., McGuire R. E., McCoy J. E., Russell C. T., and Coleman P. J. Jr. (1977) *Earth Planet. Sci. Lett. 34*, pp. 141-151.

(4) Hood L. L., Coleman P. J. Jr., and Wilhelms D. E. (1979) *Proc. Lunar Sci. Conf. 10th*, pp. 2235-2257.

(5) Russell C. T., Coleman P. J. Jr., Fleming B. K., Hilburn L., Ioannides G., Lichtenstein B. R., and Schubert, G. (1975) *Proc. Lunar Sci. Conf. 6th*, pp. 2955-2979.

(6) Hood L. L. (1979) *Papers presented to the Conference on Origins of Planetary Magnetism*, 8-11 November 1978, Lunar and Planetary Institute, Houston, Texas.

(7) Lin R. P., El-Baz F., Hood L. L., Runcorn S. K., Schultz P. H. (1980) (abstract) *Lunar Planet. Sci. XI*, p. 626.

(8) Wilhelms, D. E. (1979) *NASA Rep. Planetary Geology Program 1978-1979* Washington, D.C., Tech. Mem. 80339.

(9) Schultz P. H., and Gault D. E. (1975) *The Moon 12*, pp. 159-177.

(10) Cisowski S. M., Collinson D. W., Runcorn S. K., Stephenson A., and Fuller M. (1983) *J. Geophys. Res. 88, Suppl.*, pp. A691-A704.

* Also Physics Department.

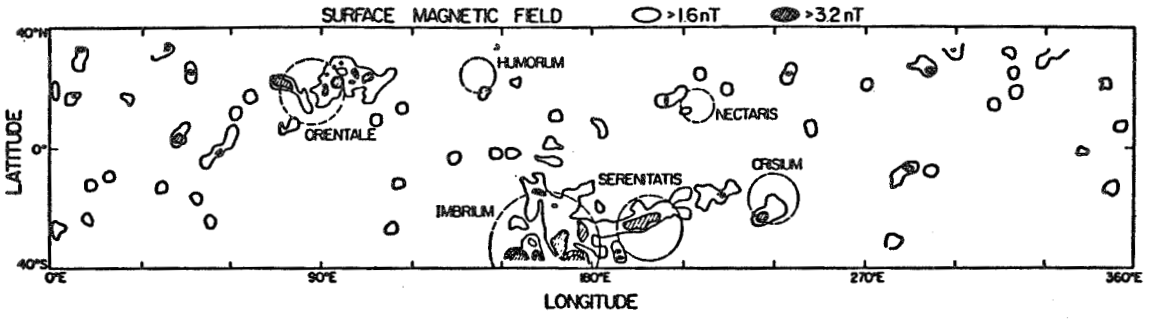

Figure 1 (above). A contour map of the strongest surface magnetic fields measured by the electron reflection method. The circles indicate the antipodes of large impact basins.

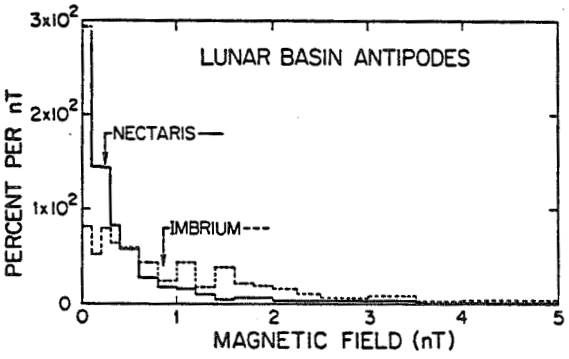

Figure 2 (left). The distribution of 1¼° × 1¼° magnetic field samples in the antipodal region for the Nectaris and Imbrium basins. The arrows indicate the median field value.

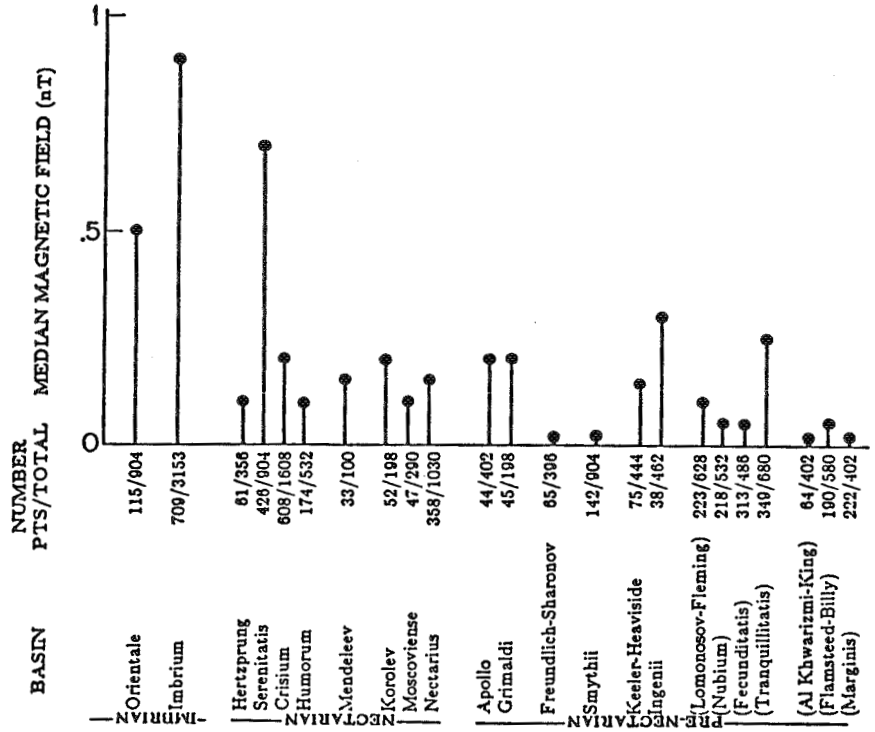

Figure 3. The median magnetic field for the antipodal regions of 23 impact basins. The number of samples and the total number possible for the antipodal region are given to provide an indication of the coverage.

Implications of Convection in the Moon and the Terrestrial Planets

Donald L. Turcotte, Department of Geological Sciences, Cornell University, Ithaca, NY 14853-1504

During the past year we have worked on two principle lines of research:

1) The early thermal and chemical evolution of the moon. The work on the evolution of isotopic systems on the moon has now been published (1). The rubidium-strontium, neodymium-samarium, and uranium-thorium-lead systems were studied. The relation of source region heterogeneity to the mixing associated with mantle convection was considered. We are continuing this line of research by studying the chemical evolution of the moon and terrestrial planets by means of parameterized convection. One aspect of our studies is the concentration of trace elements including the heat producing elements into the crust thus influencing the rate of mantle convection. A second aspect of our studies is the delamination of planetary lithospheres as a cooling mechanism and as a means of returning trace elements to the planetary interior.

2) Fractals. Our group is the only group working on the application of fractal concepts to planetary geology and geophysics. With the current explosion of interest in and research on fractals this promises to be a most rewarding line of research. Our initial results have been quite exciting. Our first application of the fractal concept was to fragmentation including the frequency-size distribution of meteorites, asteroids, and particulate matter produced by impacts. This work has now been published (2). We have continued our fractal research on geophysical spectra. Global spectra are available for topography and geoid on the Earth, Venus, Mars, and the moon. If the spectral energy density has a power law dependence on wave number a fractal is defined. The topography spectra for the earth is a well-defined fractal with $D = 1.5$; this corresponds to Brown noise with the amplitude proportional to the wave length. Although there is more scatter for the other planetary bodies, the data for Mars and the moon correlate well with the data for the earth. Venus also exhibits a Brown noise behavior but with a smaller amplitude. The power law dependence of the Earth's geoid is known as Kaula's law. We show that uncompensated Brownian topography gives a power law dependence that is in good agreement with Kaula's law. However, the required amplitude is only 8% of the observed topography. This ratio increases to 72% for the moon. This work was presented at the 17th Lunar and Planetary Science Conference, Houston, Texas, March 17-21, 1986 (3) and has been written up and accepted for publication in the Proceedings (4).

(1) D.L. Turcotte and L.H. Kellogg, Implications of isotope data for the origin of the Moon, in Origin of the Moon, W.K. Hartmann, R.J. Phillips and G.L. Taylor, eds., Lunar and Planetary Institute, 311-330 (1986).

(2) D.L. Turcotte, Fractals and fragmentation, J. Geophys. Res., 91, 1921-1926 (1986).

(3) D.L. Turcotte, A fractal approach to planetary spectra, Lunar Planet. Sci. XVII, 905-906 (1986).

(4) D.L. Turcotte, A fractal interpretation of topography and geoid spectra on the earth, moon, Venus, and Mars, J. Geophys. Res., in press (1986).

Global Petrologic Variations on the Moon: A Ternary-Diagram Approach

Philip A. Davis and Paul D. Spudis, Branch of Astrogeology, U.S. Geological Survey, Flagstaff, Arizona 86001

Approach. We have used the ternary-diagram approach outlined herein in an attempt to show on a single map as much detailed geochemical information indicating petrologic variations within the lunar crust as possible. We confine the presentation of our ternary-diagram analysis and subsequent discussion of the results to use of the Fe (wt%) versus $(Th/Ti)_c$ variation diagram, because these data include only the Apollo gamma-ray orbital data, which have more global coverage (about 19%) than that of the X-ray orbital data (about 9%). The $(Th/Ti)_c$ ratio represents the observed Th/Ti ratio normalized to C1 chondrite values. We produced an error database for Fe and $(Th/Ti)_c$ by the standard method of determining error from counting statistics to take into account the analytical errors associated with the Fe and $(Th/Ti)_c$ data in the present analysis.

The method starts by establishing a ternary reference diagram whose three sides are each divided into eight segments. Each ternary subdivision is assigned a distinct color; the colors represent a spectral continuum from red to green to blue to red. The center of the diagram is a trianglar area representing approximately equal proportions of each apex, and it is thus assigned a gray color. Assignment of rock end-member compositions to the three apexes allows rock or soil compositions that are binary or ternary mixtures of these three end members to be represented as continuous colors in the visible spectrum.

Each of the end-member Fe and $(Th/Ti)_c$ compositions is an average calculated from values reported in the literature. The Mg-suite (troctolite and norite) and KREEP rocks are represented by the red apex, the mare basalt by green, and the ferroan anorthosite by blue. Thus, we can now assign a color from the ternary reference diagram to each pixel in the orbital geochemical databases, using the Fe-concentration and $(Th/Ti)_c$-ratio values of the pixel and the ternary apexes. The relative proportion of each of the three compositional end members (apexes) needed to produce the observed composition of a particular pixel is determined trigonometrically. Once the pixel's location within the diagram has been determined, the color at that location is assigned to that pixel's position in a new image or map file. This process is then repeated for every pixel within the orbital databases. Also, the frequencies of occurrence of pixels at a particular ternary composition are accumulated within a ternary scattergram.

Certain pixels within the Fe and $(Th/Ti)_c$ databases have high uncertainties, mostly because of their low orbital accumulation times. To determine the effects of these errors on the areal abundance of units within the classification map, we decreased by increments the amount of error that pixels could have in terms of Fe and $(Th/Ti)_c$ before being excluded from the classification map. The following discussion pertains to the classification map (not shown) in which pixels that have errors greater than 75% are excluded. This level of error exclusion provides a reasonable amount of certainty for the remaining unit pixels and their areal abundances.

Discussion. Examination of the classification map allows easy determination of (1) the global spatial distribution of end-member compositions, (2) the transitional spatial relations between end-member compositions, and (3) quantitative estimates of the relative proportions of each end member at each pixel location within the orbital groundtracks. The use of elemental ratios in our analyses, instead of the commonly used elemental bivariate diagrams

[1,2], shows geologic information that is otherwise hidden in individual elemental databases.

The Apennine Bench region is shown to have a composition corresponding to a mixture of KREEP and mare basalt, which is consistent with the results of previous studies [3,4]. Other areas of Mg-suite/KREEP material are in the farside highlands near Van de Graaff (18°-29°S, 175°-171°W), within the Hertzsprung basin (3°-5°S, 125°-130°W), and south of Mare Smythii and west of Pasteur Crater (7°-15°S, 76°-98°E). The first two of these KREEP-rich highland areas coincide with areas of highland crustal thinning [5,6] that are covered by the orbital gamma-ray data. An inverse relation between Th concentration and highland crustal thickness has been reported by [7]. The preliminary elemental concentrations obtained by [8] suggest that the Van de Graaff region may have a "granitic" rock composition, similar to that of sample 12013. Generally, the average composition of lunar granites is lower in Fe, Ti, and Mg and significantly higher in K and Th than that of KREEP basalts. The Fe and Ti concentrations of these three highland areas are indeed lower than that at any of the three nearside high-KREEP areas, possibly because of the proximity of maria to the KREEP-rich areas; however, the three highland KREEPy areas do not appear to be associated with extensive mare deposits. For K, [9] have presented preliminary gamma-ray data showing the Van de Graaff region to have only 880 ppm K, whereas they report the Fra Mauro region as having 2680 ppm K. This significantly lower K value for Van de Graaff strongly suggests that these KREEP/Mg-suite highland areas (at least those near Van de Graaff) are not composed of "granitic" rock. They are most likely either "KREEPy basalts" [10] resulting from volcanism propagated by crustal thinning in these areas, or the remnants of an Mg-suite pluton exposed by an early impact event (such as the South Pole-Aitken basin; [11]).

Our classification map also shows that, at the spatial resolution (about 100 km) of the gamma-ray instrument, the central regions of most major maria have relatively pure mare-basalt compositions. Only Mare Tranquillitatis appears to have compositions transitional between mare basalt and ferroan anorthosite, which is probably the result of the addition of underlying anorthositic highlands debris to mare-basalt regoliths by vertical mixing through relatively thin, young, blue mare-basalt flows [12,13]. At Aristarchus, the unit map indicates a mixture of KREEP, mare basalt, and ferroan anorthosite, which grades into a more KREEP- and mare-basalt-rich unit at the north border of the groundtrack. The presence of these two units can be attributed to the relatively thin, young, blue mare-basalt flows in these two areas [14] that mixed with underlying KREEP- or Mg-suite-rich highland terrain. This underlying material is present at relatively shallow depth, as indicated by its exposure within Aristarchus Crater [15,16].

A series of relatively young lava flows with well-developed flow fronts occur in southwestern Mare Imbrium [17]. In addition to their striking morphological development, remote-sensing data indicate that these lava flows are rich in Ti [14], relatively rich in Th (8.0 ppm; [18]), and young (less than 2.0 b.y. old; [19]). These high-Ti, KREEP-rich lavas are represented on our petrologic map by two units of mostly mare basalt with some KREEP component.

Another interesting area is within and near the Balmer basin on the lunar eastern limb (10°-15°S, 75°E). The position of this zone correlates with the light plains fill of the Balmer basin, which has been described previously as KREEP-rich, mare-like deposits [10,20]. Our classification map shows these plains to represent roughly an equal mixture of anorthosite, mare basalt, and KREEP/Mg-suite material. The identification of dark-halo craters in this

region [20,21] supports the suggestion that light plains in the region thinly mantle buried, KREEP-rich mare-basalt flows. These basalt flows are probably older than 3.9 b.y. because they are buried by highland plains of Imbrian to Nectarian age [22]. It thus appears that the ancient lunar maria (older than 3.9 b.y.) had a diversity of chemical compositions, ranging from "normal" chondritic Th/Ti values to more KREEP-rich varieties.

The lunar surface represented by the Apollo orbital groundtracks is shown to consist of 8.4% relatively pure (85%) ferroan anorthosite, even though pixels that have high compositional uncertainties were excluded. Deleting the maria from these data raises this value to 12.9%. Most of the lunar highlands is composed of four units. Considering the areal percentages of the groundtracks and the modal amounts of the end-member components for these four units results in an average highland composition of 68% ferroan anorthosite, 29% mare basalt, and 3% KREEP/Mg-suite rocks. This resultant rock composition approximates that of "anorthositic gabbro" and is consistent with our previous analyses [23]. This composition may represent the average composition of the upper half of the highlands crust [24].

Significant amounts of mare basalt (21.1% of the Apollo groundtrack) occur within the highlands (mostly on the eastern limb and farside highlands), as indicated by the areal distribution of a unit composed of 65% ferroan anorthosite, 3% KREEP/Mg-suite, and 32% mare basalt. Its areal distribution coincides with mapped occurrences of highland plains that display dark-halo craters [19,21], for which spectral data indicate the presence of excavated mare basalt [25]. This coincidence suggests that mare volcanism occurred within these highland areas before the end of the final heavy bombardment. We do not, however, dismiss the possibility that this unit may represent some type of highland gabbro or a mixture of Mg-suite rocks with an as-yet-unsampled mafic rock type that has a subchondritic Th/Ti ratio.

References. [1] Clark, P. E. et al. (1978) PLPSC 9, 3015; [2] Clark, P. E., and B. R. Hawke (1981) PLPS 12B, 727; [3] Hawke, B. R., and J. W. Head (1978) PLPSC 9, 3285; [4] Spudis, P. D. (1978) PLPSC 9, 3379; [5] Frontispiece (1976) PLSC 7; [6] Bills, B. G., and A. J. Ferrari (1977) JGR 82, 1306; [7] Metzger, A. E. et al. (1977) PLSC 8, 949; [8] Metzger, A. E. et al. (1974) PLSC 5, 1067; [9] Parker, R. E. et al. (1981) LPS XII, 811; [10] Hawke, B. R., and P. D. Spudis (1980) Proc. Conference on the Lunar Highlands Crust, 467; [11] Wilhelms, D. E. (1984) Moon, in The Geology of the Terrestrial Planets, NASA SP-469, 106; [12] Horz, F. (1978) PLPSC 9, 3311; [13] Whitford-Stark, J. F., and J. W. Head (1980) JGR 85, 6579; [14] Pieters, C. (1978) PLPSC 9, 2825; [15] McCord, T. B. et al. (1972) JGR 77, 1349; [16] Guest, J. E., and P. D. Spudis (1985) Geol. Mag. 122, 317; [17] Schaber, G. G. (1973) PLSC 4, 72; [18] Etchegaray-Ramirez, M. I. et al. (1983) PLPSC 13, JGR 88, A529; [19] Schultz, P. H. and P. D. Spudis (1983) Nature 302, 233; [20] Hawke, B. R. et al. (1985) Earth Moon Planets 32, 257; [21] Schultz, P. H., and P. D. Spudis (1979) PLPSC 10, 2899; [22] Wilhelms, D. E., and F. El-Baz (1977) USGS Map I-948; [23] Davis, P. A. and P. D. Spudis (1985) PLPSC 16, JGR 90, D61; [24] Spudis, P. D., and P. A. Davis, in press, PLPSC 17, JGR; [25] Hawke, B. R., and J. F. Bell (1981) PLPS 12B, 665.

A CHEMICAL AND PETROLOGICAL MODEL OF THE LUNAR CRUST.
Paul D. Spudis and Philip A. Davis, U.S. Geological Survey, Flagstaff, AZ 86001

It has long been recognized that the lunar crust is chemically and petrologically heterogeneous, although the exact details of its structure remain contentious. Various models of lunar crustal structure have been proposed that invoke lateral heterogeneity [e.g., 1], vertical variations [2,3], or both [4]. Recently, we presented the results of our attempts to make petrologic maps of the lunar highlands from orbital geochemical data [5]. These maps provide data on petrologic variations in the uppermost lunar crust. Moreover, recent studies have clarified the process involved in multi-ring basin formation [e.g., 6, 7], resulting in models that permit us to use basin as probes to understand the composition of the lower crust. Thus, it is now appropriate to reevaluate a variety of remote-sensing and lunar sample data to determine the probable chemical and petrologic structure of the lunar crust.

Composition and structure of the upper crust. The average composition of the highland crust under the Apollo 15 and 16 orbital groundtracks is that of "anorthositic gabbro" (Al_2O_3 26-28%) [5]. Within this area of coverage is considerable petrologic variation, ranging from deposits of "pure" anorthosite to KREEP basalt [5]. Our efforts to map highland rock types used the Fe - Th/Ti chemical plot; such a variation diagram readily separates the ferroan anorthosites (believed to be original crustal products of lunar primordial differentiation [8]) from the Mg-suite rocks and KREEP. Of the eleven petrologic units mapped in [5], five have "chondritic" Th/Ti ratios, indicating affinity with the ferroan anorthosite suite rather than with the Mg-suite or KREEP. These units make up over 80% of the toal highland region covered by the Apollo orbital data. Assuming that the Apollo groundtracks are representative of the whole Moon, we conclude that rocks of the Mg-suite represent a minor fraction of the upper lunar crust. The dominance of Mg-suite rocks in the sample collection is probably more apparent than real and may be mostly due to the emphasis placed on study of pristine clasts from highland breccias.

A consequence of the heavy bombardment of the lunar crust was the development of a thick, brecciated debris layer, the "megaregolith" [9]. The thickness of this layer has been estimated as 1-2 km [10-11] to as much as 40 km [12]. Because of the general paucity of pristine plutonic rocks and the lunar cratering history implied by the apparent 3.92 b.y. age of the Nectaris Basin [13,14], we favor values of tens of kilometers for megaregolith thickness. Mixing in such a debris layer would be dominantly vertical, analogous to mixing in the thinner regoliths developed on mare basalt flows. Such mixing would preserve "outcrops" of pure rock types such as those on the petrologic maps [5].

Composition of the lower lunar crust. Evidence for lower crustal composition comes from the composition of multi-ring basin ejecta. Of the eleven basins covered by Apollo orbital chemical data, nine display enrichments of norite in their continuous near-rim deposits, in contrast

to the more anorthositic compositions of the interbasin terrain. Moreover, the relative fraction of norite in basin ejecta determined by mixing models increases with increasing basin diameter [4,5]. Assuming these relations to be non-coincidental, we suggest that the lower crust is composed dominantly of noritic rocks ($Al_2O_3 \sim 20\%$). Additional evidence for this noritic composition comes from the (probably) polymict "Very High Aluminum "(VHA) and "low-K Fra Mauro" (LKFM) basalt rocks, which appear to be basin impact melts [14]; these rocks are noritic in bulk chemistry. Given estimated formation energies of impact-basins [15,16] and projectile penetration depths [6], we consider most basin impact melts to have been generated at depths of about 30 to 60 km in the lunar crust. If VHA and LKFM basalt does represent basin impact melt, these rocks provide direct evidence for a noritic lower crust. To explain the lack of lunar mantle material in impact melts, Ryder and Wood [2] suggested that a noritic LKFM layer exists midway in the crust. Analysis of both the geologic settings of the Apollo landing sites [17,18] and particle movements during cratering flow [6,19] suggest such a crustal structure is not a requirement, as the basin impact melt sampled during Apollo missions should be contaminated with only shallow-level clasts. We believe that the available data are consistent with the hypothesis that the lower lunar crust is composed dominantly of norite.

A lunar crustal model. Our lunar crustal model is shown in Figure 1. It has essentially two-layers: anorthositic mixed rocks overlie a generally noritic crystalline basement. The contact between these layers is probably gradational on a scale of kilometers. The Mg-suite comprises a series of plutons, some of them layered, that are a subordinate fraction of the crustal volume. In this model, the crust is laterally and vertically heterogeneous on a scale of tens of kilometers.

Our model has several implications for lunar crustal origin and evolution. Concurring with previous suggestions (see review in [8]), we believe that a global magma system produced an original ferroan anorthosite crust by plagioclase flotation and olivine/pyroxene sinking. As the crust grew downward and the mantle upward, the residual liquid had a noritic composition [2,20]; this layer formed the noritic lower crust and eventually, a layer of material (KREEP substratum; Fig. 1) greatly enriched in incompatible trace elements [20,21]. Partitioning of incompatible elements into this KREEP layer was not totally efficient, resulting in the production of KREEP-rich norites in the lower crust [2]. Concurrent with this episode was intrusion of Mg-suite rocks to form plutons within the original anorthositic crust. This activity was virtually complete by 4.36 b.y. ago [22]. Massive extrusions of mare basalts [5] and continued heavy bombardment of the crust followed until about 3.85 b.y. ago. During this interval, the hot, low-density KREEP material migrated upward [23] and was disseminated through most of the lower crust. Thus, basins forming around 3.9 b.y. ago incorporated a KREEP trace-element pattern into their noritic impact melts ("Melt rocks"; Fig. 1). In the Imbrium region, KREEP basalts were erupted on the surface both before [24] and after [25] the Imbrium impact. After the heavy bombardment ended, mare basalts continued to be extruded, forming the visible maria. Continued study of lunar samples and new remote-sensing

data from the proposed Lunar Geoscience Observer Mission will be required to assess the validity of this lunar crustal model.

References: [1] James, O.B. (1980) PLPSC 11, 365. [2] Ryder, G. and Wood, J.A. (1977) PLSC 8, 655. [3] Charette, M.P. et al. (1977) PLSC 8, 1049. [4] Spudis, P.D. et al. (1984), LPS XV, 812. [5] Davis, P.A. and Spudis, P.D. (1985) PLPSC 16, JGR 90, D61. [6] Croft, S.K. (1981) PLPSC 12A, 207. [7] Spudis, P.D. et al. (1984) PLPSC 15, JGR 89, C197. [8] Warren, P.H. (1985) Ann. Rev. Earth Planet. Sci. 13, 201. [9] Hartmann, W.K. (1973) Icarus 18, 634. [10] Short N. and Forman, M. (1972) Mod. Geol. 3, 69. [11] Horz, F. et al. (1976) PLSC 7, 2931. [12] Cashore, J. and Woronow, A. (1985) PLPSC 15, JGR 90, C811. [13] James, O.B. (1981) PLPSC 12B, 209. [14] Spudis, P.D. (1984) PLPSC 15, JGR 89, C95. [15] Baldwin, R. (1963) Measure of the Moon, U. Chicago, 488 p. [16] Grieve, R.A.F. and Dence, M.R. (1979) Icarus 38, 230. [17] Head, J.W. and Settle, M. (1976) Imb. Consort. 1, 5. [18] Spudis, P.D. (1982) Ph.D. Thesis, ASU, 291 p. [19] Grieve, R.A.F. et al. (1977) Imp. Explos. Crater, 791. [20] Wood, J.A. (1972) Icarus 16, 462. [21] Warren, P.H. and Wasson, J.T. (1979) RGSP 17, 73. [22] Lugmair, G.W. and Carlson, R.W. (1978) PLPSC 9, 689. [23] Shirley, D.N. and Wasson, J.T. (1981) PLPSC 12B, 965. [24] Hawke, B.R. and Head, J.W. (1978) PLPSC 9, 3285. [25] Spudis, P.D. (1978) PLPSC 9, 3379.

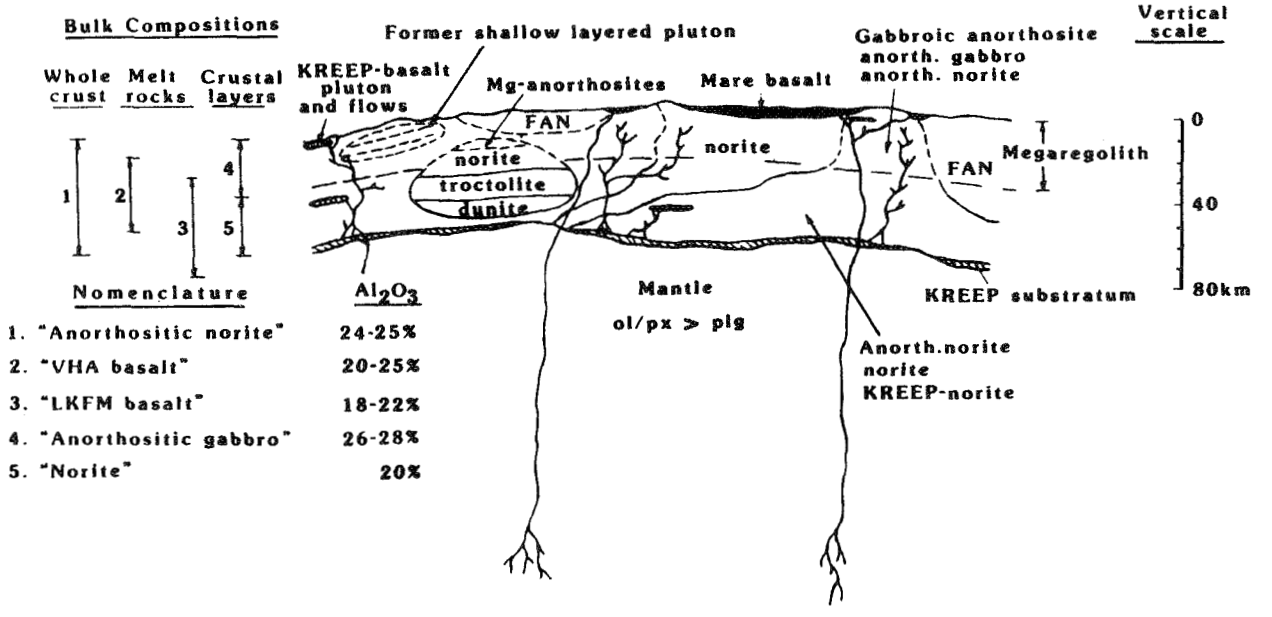

Figure 1. Proposed model of the lunar crust. FAN refers to ferroan anorthosite. Provenance of bulk compositions indicated at left by arrows. See text for discussion.

CALCIUM CARBONATE AND CALCIUM SULFATE IN MARTIAN METEORITE EETA79001.

J. L. Gooding (a) and S. J. Wentworth (b). (a) SN2/Planetary Materials Branch, NASA/Johnson Space Center, Houston, TX 77058. (b) Lockheed/EMSCO, Mail Code C23, NASA/JSC, Houston, TX.

Introduction. If shergottite meteorites are rocks ejected from Mars by impact cratering, then they might be expected to contain samples of Martian weathering products. Indeed, sulfur- and chlorine-rich minerals of apparently pre-terrestrial, low-temperature origin were previously found in samples of the shergottite, Elephant Moraine, Antarctica A79001 (EETA79001) [1,2]. Further work on additional samples has revealed the occurrence of calcium carbonate [3] and calcium sulfate in the same meteorite.

Occurrence of Carbonate and Sulfate. Chips of glassy Lithology C of EETA79001 were studied by scanning electron microscopy (SEM) and energy-dispersive x-ray spectrometry (EDS) to determine the mineralogy and petrogenesis of the glass that was shown by others [4,5] to contain trapped Mars-like gases. Calcium carbonate was identified as massive to acicular crystals for which Ca, C, and O were the major elements. Calcium sulfate was identified as prismatic-acicular crystals with Ca and S as the major elements. Additional SEM/EDS work is in progress to better more identify the minerals and their parageneses.

Ca-carbonate occurs in at least three locations in EETA79001, all of which are closely associated with glassy Lithology C. The largest deposit occurs as a drusy halo around a large glassy vug at the center of the meteorite. A second, more modest deposit occurs near the large deposit but in association with a separate, smaller glass pocket. The third deposit was recognized only after SEM/EDS reconnaissance of a chip from its glass-pocket host. The two macroscopically visible central deposits are not connected to the surface of the meteorite by any obvious system of fractures. In addition, parallel studies of demonstrably Antarctic (surface-located) weathering products in EETA79001 and other meteorites from the same field locality [6] failed to find Ca-carbonate as a terrestrially formed phase. Therefore, present physical evidence supports pre-terrestrial origin of the carbonate. Stable-isotopic analyses of C and O in the carbonate are in progress by our collaborators and should help to positively establish whether the carbonate formed in Antarctica. If an Antarctic origin can be excluded, then origin of the carbonate on Mars would become the favored interpretation.

Pre-terrestrial origin of Ca-sulfate in EETA79001 is less clear. Gypsum is a known Antarctic weathering product in the exterior of EETA79001 and in other Antarctic meteorites [6]. However, the sole occurrence of Ca-sulfate documented to date in interior samples of EETA79001 is in the intensively studied sample 27 glass pocket which has yielded the highest concentrations of trapped Mars-like gases [4,5]. Furthermore, the possibly pre-terrestrial Ca-sulfate occurs as euhedral crystals, some of which are crystallographically oriented inclusions in quench-textured pyroxenes. Other Ca-sulfate crystals in the same sample are intimately associated with Ca-carbonate and also appear to be unmelted relics. The Ca-sulfate is volumetrically less abundant than the Ca-carbonate and probably will not be separable in sufficient quantities for conventional isotopic analyses.

Implications for Martian Geology. Gooding and Muenow [2] previously hypothesized that origin of the unusual glass pockets in EETA79001, and concomitant trapping of Martian atmospheric gases, was related to shock-induced melting of pre-existing weathered (or deuterically altered) areas in the target rock. New evidence for relict grains of carbonate and

sulfate minerals in the gas-rich glass supports the Gooding-Muenow hypothesis, reiterating the unique nature of EETA79001 and the nearly inescapable conclusion that it is a Martian rock. Accordingly, the case for using EETA79001 and other shergottites for deriving geochemical properties of Mars seems to be strengthened.

Various workers have speculated about possible storage of major amounts of carbon dioxide as carbonates in the Martian regolith [7-9] although attempts to find direct evidence for carbonates in remotely-sensed data for Mars have produced negative results [10,11]. Therefore, if further work demonstrates that Ca-carbonate in EETA79001 is pre-terrestrial in origin, then we will have probably achieved the first confirmation of carbonates on Mars. In that case, geological and paleoclimatological studies of Mars need not dwell on whether carbonates exist but can concentrate on determining locations, ages, and abundances of carbonate deposits.

References:

[1] Gooding J. L. and D. W. Muenow (1985) Repts. Planet. Geol. Geophys. Program - 1985, NASA Tech. Memo. 88383, 161-163.
[2] Gooding J. L. and D. W. Muenow (1986) Geochim. Cosmochim. Acta, 50, 1049-1059.
[3] Wentworth S. J. and J. L. Gooding (1986) Meteoritics, 21, in press.
[4] Bogard D. D. and P. Johnson (1983) Science, 221, 651-654.
[5] Becker R. H. and R. O. Pepin (1984) Earth Planet. Sci. Lett., 69, 225-242.
[6] Gooding J. L. (1986) Geochim. Cosmochim. Acta, 50, 2215-2223.
[7] Fanale F. P. (1976) Icarus, 28, 179-202.
[8] Kahn R. (1985) Icarus, 62, 175-190.
[9] Haberle R. M. (1985) Nature, 318, 599-600.
[10] Singer R., T. B. McCord, R. N. Clark, J. B. Adams, and R. L. Huguenin (1979) J. Geophys. Res., 84, 8415-8426.
[11] Roush T. L., D. Blaney, T. B. McCord, and R. B. Singer (1986) Lunar Planet. Sci. XVII, Lunar and Planetary Institute, Houston, 732-733.

The Case for A Wet, Warm Climate on Early Mars

J.B. Pollack, J.F. Kasting
NASA Ames Research Center, Moffett Field, CA 94035
S.M. Richardson
Iowa State University, Ames, Iowa 50011
K. Poliakoff
I.M.I. Inc., San Jose, CA

The theoretical arguments are presented in support of the idea that Mars possessed a dense CO_2 atmosphere and a wet, warm climate early in its history. Calculations with a 1-D radiative-convective climate model indicate that CO_2 pressures between 1 and 5 bars would have been required to keep the surface temperature above the freezing point of water early in the planet's history. The higher value corresponds to globally and orbitally-averaged conditions and a 30% reduction in solar luminosity; the lower value corresponds to conditions at the equator during perihelion at times of high orbital eccentricity and the same reduced solar luminosity.

The plausibility of such a CO_2 greenhouse is tested by formulating a simple model of the CO_2 geochemical cycle on early Mars. By appropriately scaling the rate of silicate weathering on present Earth, we estimate a weathering time constant of the order of several times 10^7 years for early Mars. Thus, a dense atmosphere could have persisted for a geologically significant time period ($\sim 10^9$ years) only if atmospheric CO_2 was being continuously resupplied. The most likely mechanism by which this might have been accomplished is the thermal decomposition of carbonate rocks induced directly and indirectly (through burial) by intense, global scale volcanism. For plausible values of the early heat flux, the recycling time constant is also of the order of several times 10^7 years. The amount of CO_2 dissolved in standing bodies of water was probably small; thus, the total surficial CO_2 inventory required to maintain these conditions was approximately 2 to 10 bars. The amount of CO_2 in Mars' atmosphere would eventually have dwindled, and the climate cooled, as the planet's internal heat engine ran down. A test for this theory will be provided by spectroscopic searches for carbonates in Mars' crust.

THE ROLE OF REGOLITH ADSORPTION IN THE TRANSITION FROM EARLY TO LATE MARS CLIMATE

F.P. Fanale, S.E. Postawko, A.P. Zent, and J.R. Salvail, Planetary Geosciences Div., Hawaii Instit. of Geophysics, Univ. of Hawaii, Honolulu, HI 96822

The total degassed CO_2 inventory on Mars is currently thought to be the equivalent of about 3.0 bars or less (1). Using a surface pressure of ~1 bar, several radiative transfer models for early Mars have been advanced (2) proporting to show that a significant greenhouse effect could have characterized the early Mars environment, possibly explaining the intense channeling of the most ancient Mars terrain.

We have reexamined those models with regard to the effect that regolith adsorption may have had. In our model, we take into account: 1) the atmospheric greenhouse effect, 2) the existence, mass, and temperature of any cap, 3) the partition of CO_2 between the atmosphere-cap system and the regolith as required by the latitudinal temperature distribution, and 4) atmospheric heat transport.

We solve simultaneously for all these interdependent variables for cases involving realistic total CO_2 inventories, a variety of published greenhouse models, and both current and lower solar constants.

To describe regolith adsorption properties we use the mineralogically insensitive adsorption relationship developed by Zent et al. (3), which is normalized to be consistent with observed surface properties of Viking-sampled soil (4). We should point out that adsorption is relatively more effective under current Martian conditions than at the higher temperature and pressure conditions that may have characterized the early Martian environment. However, the regolith currently has adsorbed 10 - 100 times the atmospheric CO_2 inventory, whereas in most models the removal of only half the original atmospheric CO_2 inventory would be sufficient to destroy the strong greenhouse effect.

Resulting scenarios fall into several classes. Either: 1) The greenhouse effect is so weak that a cap exists throughout the period of growth of several hundred meters of regolith. In this case the surface environment is essentially unaffected by the development of any reasonably postulated regolith; or 2) A cap exists initially, but is sufficiently small that the growth of >100m or so of regolith causes a significant repartitioning of CO_2 molecules among the three parts of the system and the equilibrium solution finally involves no cap. In this case the regolith has no effect on the atmospheric pressure and resulting temperatures until the cap disappears. However, once the cap disappears, the effect of further regolith growth is to dramatically lower atmospheric pressure and hence surface temperatures; or 3) A substantial greenhouse effect exists initially, and there is no cap initially. In this case, also, regolith growth to a depth of several hundred meters dramatically lowers atmospheric pressures and surface temperatures, and the effect of the regolith is important from the outset.

In all scenarios which start out with surface pressures on the order of 1 bar, high pressures and temperature conditions are truncated by the growth of only a few hundred meters of regolith, ultimately leading to present Mars conditions. It might be argued that while the development of a regolith a few hundred meters thick in early Mars history is likely in view of the existence of the ancient cratered terrain, it is unreasonable to postulate a much lower regolith thickness at the very outset. We point out, however, that it is not literally the thickness of the regolith that is the critical parameter, but rather its total surfac area. Weathering products such as palagonites and nontronites typically exhibit specific surface areas for CO_2 adsorption of tens to

hundreds of square meters per gram, whereas basalts typically exhibit specific surface areas ofa fraction of a square meter per gram to several square meters per gram. Thus, although we represent the "regolith growth" as a physical thickening (keeping the specifc surface area equal to the Viking derived value), the acutal case involves the product of both actual thickening and a great increase due to an increased abundance of weathering products. While the precipitation of carbonates has probably been an important process during Mars history (5), the rates at which this process could have taken place under early Mars conditionswould have dropped sharply once liquid water was fairly scarce. Furthermore, conditions under which liquid water was available may have involved efficient recycling of carbonate so that steady state conditions rather than irreversible CO_2 removal prevailed. In contrast, the growth of regolith surface area demands corresponding and predictable CO_2 removal from the atmosphere-cap system and is, as shown here, fully capable of terminating any enhanced temperature regime on early Mars in the absence of any other effects. To put it another way, total degassed CO_2 inventories of <2 bars and the existence of substantially higher temperatures than present are compatible; total degassed CO_2 inventories of <2 bars, substantially higher temperatures than present, and a regolith qualitatively comparable to the present one are not compatible.

More recent calculations (6) have shown that when reduced solar radiation is taken into account ~5 bars of CO_2 is necessary to raise average surface temperatures on Mars above freezing. Calculations are presently under way to determine the effect of regolith adsorption in the evolution of this large amount of atmospheric CO_2.

REFERENCES

(1) J.B. Pollack and D.C. Black (1982), *Icarus*, **51**, 169-198. (2) M.I. Hoffert, et al. (1980), *Icarus*, **47**, 112-129. (3) A.P. Zent, et al. (1986), *MECA Symposium on Mars: Evolution of its Climate and Atmosphere*, 109-111. (4) E.V. Ballou, et al. (1978), *Nature*, **271**, 644-645. (5) R. Kahn (1985), *Icarus*, **62**, 175-190. (6) J. Kasting (1986), *MECA Symposium on Mars: Evolution of its Climate and Atmosphere*, 50-52.

CHAPTER 6

SPECTROSCOPY AND REMOTE SENSING

OXIDIZED BASALTS ON THE SURFACE OF VENUS: COMPOSITIONAL IMPLICATIONS OF MEASURED SPECTRAL PROPERTIES - C. M. Pieters, W. Patterson, S. Pratt, J. W. Head, (Dept. of Geol. Sci., Brown Univ., Providence, RI 02912) and J. Garvin (NASA, Goddard)

Introduction: Both the reflectance properties and the geochemistry of a few areas on the Venusian surface have been measured by the series of Venera landers. These data, coupled with laboratory reflectance measurements of rocks and minerals at the high temperatures characteristic of the Venusian surface, are used to infer the oxidation state of iron in surface minerals based on observed spectral characteristics.

Reflectance properties of the surface of Venus were measured by the Venera 9 and 10 landing crafts which contained two wide angle photometers, one oriented away from the surface and the other oriented toward it, each with five spectral channels covering the spectral range from about 0.5 to 1.0 μm (1) . The Venera 13 and 14 landers contained multispectral scanners that obtained color panorama images of the surface at three wavelengths in the visible (2). Other experiments on Venera 13 and 14 measured the geochemistry of surface material demonstrating that the surface is basaltic in general character with a FeO content of approximately 9% (3). The mineralogy of the surface is unknown. The oxidation state of surface material is also not certain, although a reducing environment has been suggested from indirect evidence (4). A better description of the current surface environment and mineralogy will set limits to the possible geochemical interactions between surface and atmosphere, essential information for understanding the recent evolution of the planet.

Spectral Reflectance Properties of the Surface of Venus: Five band spectra of the surface obtained by Veneras 9 and 10 are shown in Figure 1 (from 1). The surface at these locations is dark and without significant color in the visible, but exhibits a substantial increase in reflectance beyond 0.7 μm. Possible sources of error in the near-infrared have been seriously considered, and are not expected to alter these measurements substantially. Information from the Venera 13 and 14 panoramas indicate the surface is similarly very dark in the visible (2). Further processing of the panoramas for spectral information (6) has shown both the rocks and soil to be essentially grey (to ± 10%) in these visible channels (wavelengths shown on Figures 1 and 4). Although examination of the spectral character of unknown phases expected for this CO2 environment have not been completed (e.g. 6), ferric oxides in oxidized basalt would be distinguished by a characteristic ferric absorption edge (7) normally observed near 0.55 μm, as in Figure 2. The combined data for the surface of Venus, however, are not consistent with the typical room-temperature spectra shown in Figure 2 of either unoxidized basalts [which exhibit dark, relatively *flat* continua beyond 0.7 μm, commonly with superimposed ferrous absorption bands] or oxidized basalts [which derive their characteristic 'red' coloration from the ferric absorption edge *near 0.55 μm*].

Laboratory Reflectance Measurements at High Temperatures: The strength, and often energy, of absorption features is known to be affected by temperature. Many measurements have examined low temperatures (7,8) with application to Mars and asteroids. Significant variations also noted at elevated temperatures (e.g. 9) indicate that only high-temperature spectra should be used for interpretation of the Venera data. Recent laboratory (RELAB) measurements have shown this to be critically true for the ferric oxides: the characteristic absorption edge moves more than 100nm to longer wavelengths from 25 to 500°C (Figure 3). This is most likely due to broadening of intense charge transfer absorptions at shorter wavelengths.

Discussion and Conclusions: Venera reflectance data are compared in Figure 4 with high temperature spectra of the same basaltic materials in Figure 2. The dark, flat unoxidized basalts are still inconsistent with the Venera data in the near-infrared. Basaltic material with a ferric component, however, would satisfy both the increase in reflectance beyond 0.7μm as well as the dark, relatively colorless character in the visible. We therefore conclude that basaltic surfaces of Venus represented by these measurements either contain minerals with uncommon characteristics, or, more likely, are relatively oxidized.

Acknowledgments: Use of the RELAB facility at Brown University (supported by NAGW-748) is gratefully acknowledged. Discussions with Soviet colleagues from the Vernadsky Institute, IKI, and GOSNIZIPR as part of a more detailed joint analysis of Venera lander color images were most helpful during this study.

References. 1) Economov et al, 1980, *Icarus, 41*, p65; 2) Selivanov et al, 1983, *KOSM. ISSLED 21*, no.2, p 176, p183; 3) Surkov et al., 1984, PLPSC 14, *JGR,89*, B343; 4) Florensky et al. 1983, LPS XIV p203; 1983 *KOSM, ISSLED, 21*, no.3, p351; 5) Pieters et al., 1985, Bull. Am Astr. Assoc.17, no 3,p722; 6) J. Gooding, Planetary Geology reports (unpublished); 7) Morris et al, 1985, *JGR,90*, no. B4, p3126; 8) Singer and Roush, 1985, *JGR*, in press; 9) Osborne et al., 1978, PLPSC 9th, p2949; Shankland et al., 1979, *JGR, 84*, no. B4, p1603; Parkin et al., 1980, LPS XI, p854.

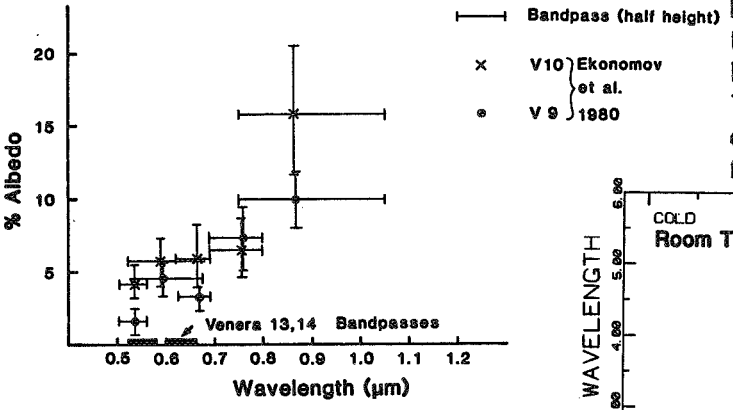

Figure 1. [left] Reflectance properties of the Venusian surface at the Venera 9 and 10 landing sites (from Economov et al., 1980). The bandpasses for the Venera 13 and 14 cameras are shown at the bottom of the figure.

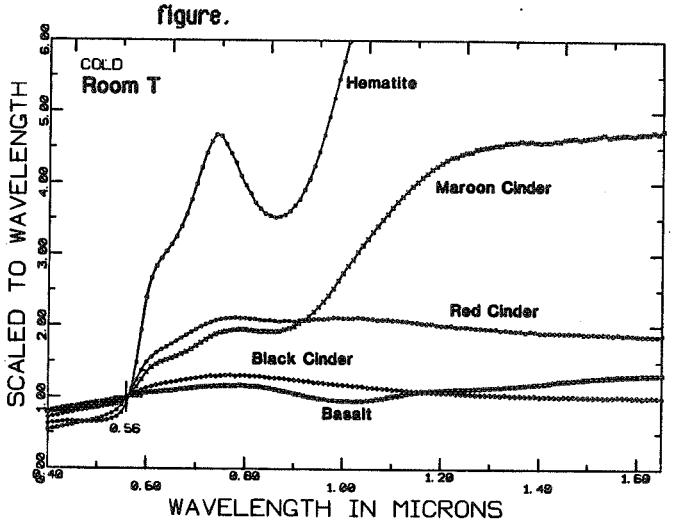

Figure 2 [right]. Reflectance spectra (0.4 to 1.6 μm) of typical basaltic materials at 25°C. The 'Basalt' is a tholeiite from Taos, NM; the three cinders are from Mauna Kea, HI. The 'Red Cinder', 'Maroon Cinder', and Hematite exhibit the characteristic absorption edge near 0.55 μm due to ferric iron.

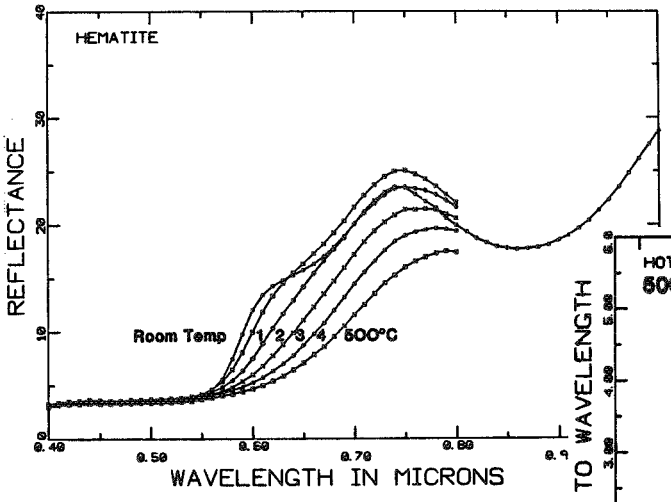

Figure 3 [left]. Reflectance spectra (0.4 to 0.8 μm) of the ferric oxide hematite at temperatures ranging from room temperature (25°C) to 500°C. The trends observed are reversible. [Note wavelength scale is expanded compared to Figs 1,2,4.]

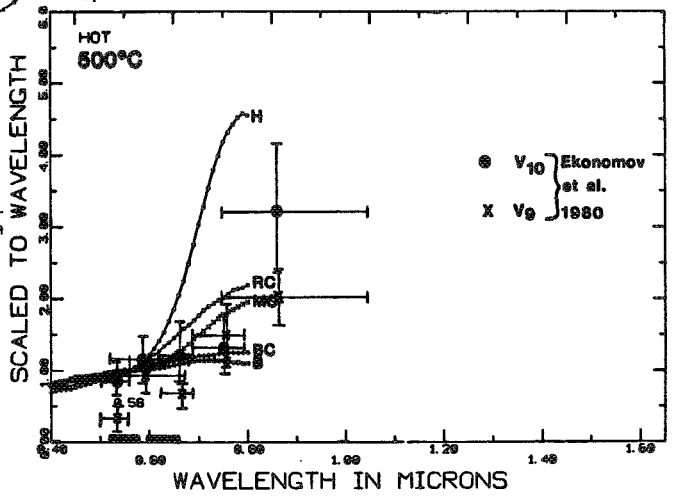

Figure 4 [right]. Reflectance spectra (0.4 to 0.8 μm) of the same basaltic materials at 500°C. Due to the high reflectance in the near-infrared, only ferric containing basaltic material is consistent with the Venera spectra.

VARIATIONS OF MARTIAN SURFACE ALBEDO: EVIDENCE FOR YEARLY DUST DEPOSITION AND REMOVAL

Philip R. Christensen, Dept. of Geology, Arizona State University, Tempe, AZ, 85287

Dust deposition and removal is an important process in the evolution of the martian surface. Mars has been observed to have variable surface markings from the earliest telescopic views of the planet. These changes have since been seen to be related to aeolian activity, primarily through the reworking of bright dust deposited following major global dust storms (1,2). Viking Infrared Thermal Mapper (IRTM) observations of albedo have also revealed significant changes in surface brightness through time, again primarily associated with major global dust storms (3,4). All of these observations indicate that there is a significant amount of dust that is deposited during the decay of global storms which is subsequently reworked and redistributed. The purpose of this study is to determine the degree, spatial distribution, and timing of the deposition and removal of dust-storm fallout, and to relate the current patterns of dust deposition and removal to the long-term evolution of the martian surface.

A model has been proposed (5) for the development of regional dust deposits that form through the preferential accumulation of dust-storm fallout into specific northern hemisphere regions. In this model, dust is deposited uniformly during the decay phase of each major storm, but is subsequently removed only from regions that are seen today as classic dark areas. Thus, dark regions remain unmantled by dust, whereas bright regions have developed a 1-2 m thick mantle of fine, bright dust (5). This model can account for the high thermal inertia (coarse) material observed in dark regions, together with their relatively high rock abundance (6), and low albedo. Conversely, bright regions have fine particles (5-40 μm) and fewer exposed rocks, presumably due to mantling of the coarse material by dust.

In order to directly observe the seasonal changes in surface brightness associated with dust deposition and removal, the albedo of specific regions in both hemispheres has been determined through time. The IRTM data were collected into 1° latitude by 4° longitude bins, at 3 hour intervals for each 10° of L_s. Using these data, the albedo changes for a given area have been investigated from the beginning of the Viking mission (L_s 84°), through the first (L_s 190-240°) and second (L_s 270-340°) global dust storms that occurred in 1977. Global data are available through L_s 120° of the second year, allowing a year to year comparison of surface albedo.

The albedo variations as a function of season are shown in Figure 1 for representative bright and dark regions. All of the areas studied show a marked increase in brightness associated with the two global storms, due primarily to the presence of dust in the atmosphere. The increase in brightness, even for bright regions, indicates that the albedo and scattering phase function of suspended dust varies from dust on the surface. The maximum brightness at the peak of the second storm was nearly equal for most bright and dark regions, indicating that the atmospheric dust was optically thick. For some dark regions, however, such as Solis Planum, the albedo remained relatively low even at the height of the storm activity, suggesting that the atmospheric dust was not globally uniform nor well mixed. Many areas show a non-uniform decrease in brightness during the decay phase, again suggesting spatial variations in dust load and non-uniform mixing, possibly due to episodic injection of dust into the atmosphere locally (7).

The albedo of most regions had returned to the pre-storm value by L_s 355°, indicating that the atmosphere had cleared to pre-storm levels by that time. This conclusion is supported by Viking lander observations, which show that the opacity over the two lander sites had decreased to

pre-storm levels by L_S 360° (7). Therefore, surfaces that remained brighter after L_s 360° than they were prior to the two storms are thought to be covered by a thin layer of bright dust fallout.

The distribution of surfaces that remained bright following the storms, and those where the surface quickly returned to its pre-storm albedo follow a consistent pattern. The albedo of bright regions, such as Arabia and Tharsis, rapidly returned to pre-storm values, and was close to the albedo of the previous year (Fig. 1a). Many dark regions also darkened to nearly their pre-storm levels by L_s 360° (Fig. 1b). This pattern holds particularly well for southern hemisphere dark regions. This behavior is consistent with the model of deposition described above; in dark regions the dust is rapidly removed with little net accumulation, whereas in bright regions a dust mantle already exists so that the deposition of additional bright dust does not affect the surface albedo.

There are several dark regions that differ from the general trends described above and provide insight into the level of dust activity that occurs throughout the year. Syrtis Major and Acidalia Planitia are among the few regions that remained significantly brighter at L_s 360° than they were before the global storms began. These areas did, however, continue to darken with time, returning to nearly their pre-storm albedo by L_s 120° (Fig. 1c). It is interesting to note that the albedo of these and some other regions was still slightly higher at this time than it was the previous year, suggesting that some dust still remained on the surface. This finding is consistent with observations at the Viking lander 1 site where dust was deposited following the global storms and was not removed until over a year later (8). These observations support the hypothesis that Syrtis Major and Acidalia Planitia act as local dust sources during inter-storm periods, producing enhanced dust loading in the northern hemisphere (9).

In summary, observations of seasonal changes in surface albedo reveal regional differences in the deposition and subsequent erosion of dust-storm fallout. Southern hemisphere dark areas quickly return to close to their pre-storm albedos, suggesting rapid removal of any dust that was deposited. Northern hemisphere dark regions are brighter post-storm, but gradually darken to pre-storm levels over a Mars year. In doing so they act as local sources of dust during otherwise clear periods. Dust does not appear to be removed from bright regions, resulting in the 1-2 m thick deposits observed today.

References

1) Thomas, P. and J. Veverka, 1979, *J. Geophys. Res., 84*, 8131-8146.
2) Veverka, J., P. Thomas, and R. Greeley, 1977, *J. Geophys. Res., 82*, 4167-4187.
3) Pleskot, L.K. and E.D. Miner, 1981, *Icarus, 45*, 179-201.
4) Lee, S.W., 1986, submitted to Icarus.
5) Christensen, P.R., 1986, *J. Geophys. Res*, in press.
6) Christensen, P.R., 1986, submitted to Icarus.
7) Pollack, J.B., D.S. Colburn, R. Kahn, J. Hunter, W. Van Camp, C.E. Carlston, and M.R. Wolfe, 1977, *J. Geophys. Res., 82*, 4479.
8) Arvidson, R.E., E. Guinness, H.J. Moore, J. Tillman, and S.D. Wall, 1983, *Science, 222*, 463-468.
9) Christensen, P.R., 1982, J. *Geophys. Res., 87*, 9985-9998.

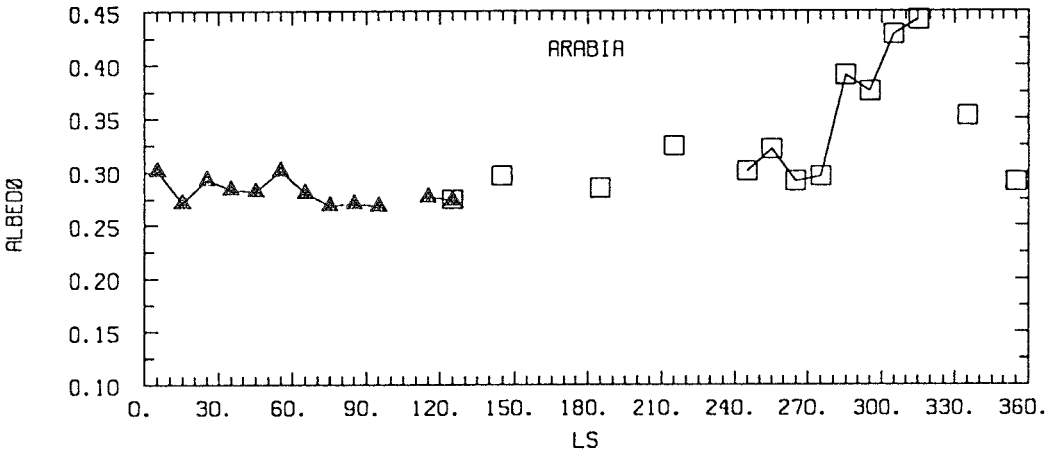

Figure 1. Variation of albedo with season. Open squares represent data from the first year following the arrival of Viking at Mars. a) Arabia, typical of bright region behaviour.

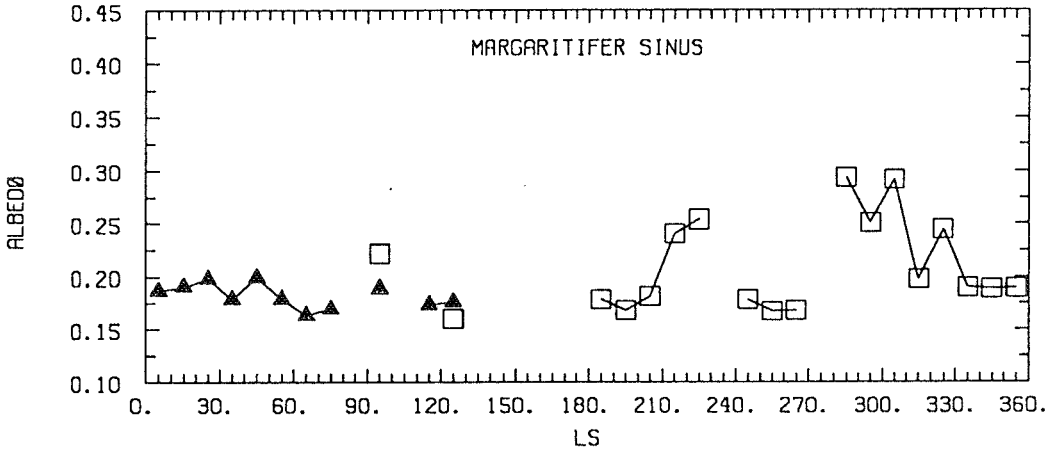

Fig. 1b). Margaritifer Sinus, representative of southern hemisphere dark regions.

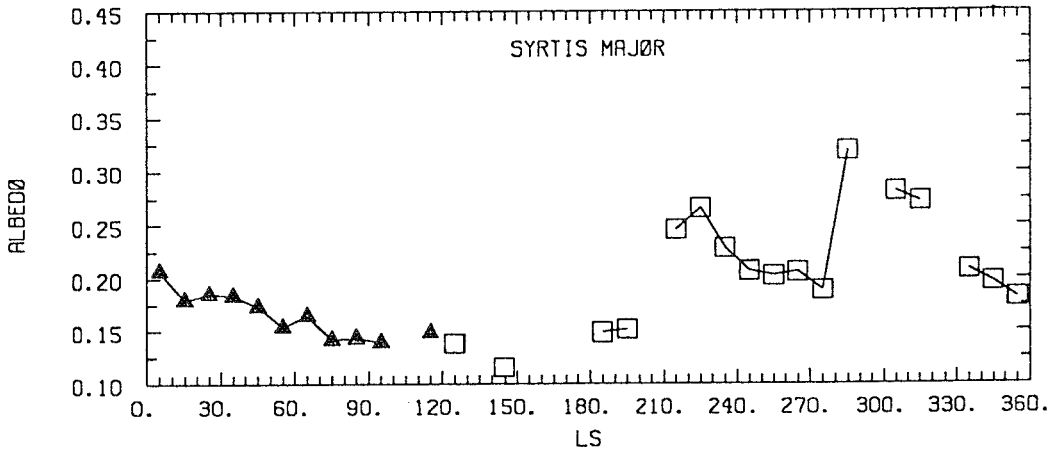

Fig.1c). Syrtis Major, showing the long residence time of dust on the surface in northern hemisphere dark regions following the global dust storms.

ON THE SPECTRAL REFLECTANCE PROPERTIES OF MATERIALS EXPOSED AT THE VIKING LANDING SITES

E. Guinness, R. Arvidson, M. Dale-Bannister, McDonnell Center for the Space Sciences, Department of Earth and Planetary Sciences, Washington University, St. Louis, MO 63130, R. Singer, E. Bruckenthal, Planetary Geosciences Division, Hawaii Institute of Geophysics, University of Hawaii, Honolulu, HI 96822.

Reflectance data derived from Viking Lander multispectral data were used to characterize the types of soils and blocks exposed at the landing sites and to search for evidence of relatively unaltered igneous rocks. Despite past research efforts [1-5], there has yet to be a comprehensive examination of the multispectral data that combines testing of the Camera radiometric calibrations, explicitly removing the effects of atmospheric attenuation and skylight, and quantitatively comparing the corrected data to reflectance data from laboratory materials. This abstract summarizes our work Guinness et al. [6] which reports such comprehensive efforts. Bi-directional reflectances for blue (0.40-0.52 μm), green (0.50-0.59 μm), and red (0.60-0.74 μm) channels were determined for 31 block and soil exposures at the Viking Landing sites. In order to interpret the mineralogy of the landing site materials, the Lander data were compared to laboratory spectra of selected materials and Earth-based telescopic spectra of Mars after the laboratory and telescopic data were resampled to the Lander bandpasses.

The uncertainty in the Lander reflectance estimates must be well-known in order to compare Lander data acquired by the four different Cameras and to compare Lander reflectance estimates to laboratory reflectance data. Preflight calibrations were tested by analyses of the brightness values obtained from sunlit and shadowed gray patches mounted on the Landers, which have well-defined Lambertian scattering characteristics. Except for Camera 2 on Lander 1, the results were consistent with the combined 8% uncertainty in the radiometric calibrations measured in the preflight tests [7], 3% uncertainty in the analog-to-digital conversion [8], and the uncertainty in the optical depth value. We concluded that the preflight calibrations for the color channels are still valid (with the possible exception of Camera 2 on Lander 1) and that reflectances can be computed with an uncertainty of about ±10% due to radiometric calibration and analog-to-digital conversion uncertainties. Partially shadowed RTC images acquired with the three infrared channels suggested that there have been changes in the calibration constants of the infrared channels or wavelength dependent changes in the spectral responsivity functions. Both types of changes were predicted from modeling of neutron induced degradation of the infrared channels [7]. As a result, the infrared channels are poor prospects for extraction of absolute reflectance. More importantly, it is difficult to make comparisons with laboratory samples since we cannot determine the nature of the wavelength dependent changes to the responsivity functions. Thus, we limited our analysis of absolute reflectances to data from the blue, green, and red channels from the 3 Cameras where the preflight calibration data are still valid. However, it was clear from the RTC data that voltage versus RTC gray patch reflectance was still linear for the infrared channels. This suggested that the IR channel detector sensitivities were still linear, although absolute values and IR spectral properties were questionable. Thus, the infrared channels were used to explore relative brightness variations with wavelength, albeit in more qualitative ways than with the blue, green, and red channels.

Laboratory analogs used for this analysis were chosen primarily for their compositional and spectral relevance to Mars, based on the interpretation of, for example, Viking Lander chemical measurements and Earth-based telescopic reflectance spectra [9-11]. Samples included the ferric oxides hematite, goethite, and limonite, two Hawaiian palagonitic soils, hematitically altered

volcanic cinders, and seven mafic igneous rocks (fresh and weathered surfaces of each). Four telescopic spectra were chosen as representative data in the spectral region of interest, including a bright region and a dark region observation from both the 1969 [12] and 1973 [13] oppositions. The comparisons of the Lander reflectance data to laboratory spectral data was primarily based on spectral shape. The blue, green, and red reflectances can be used to characterize spectral shape in terms of spectral curvature and slope. The red/green reflectance ratio divided by the green/blue reflectance ratio was used to measure spectral curvature. We found that this curvature parameter was related to ferric oxide mineral type as well as degree of crystallinity in laboratory samples. Larger values of curvature would, for example, be consistent with greater degrees of ferric iron crystallinity because the green channel is sensitive to the depth of the ferric iron absorption near 0.45-0.54 μm. This measure was also very sensitive to the spectral difference between mineral phases such as hematite and goethite. In addition, we used the ratio of the red and blue reflectances to measure the slope of the spectra. The red/blue ratio will generally increase as the degree of oxidation of iron bearing materials increases [14-15].

The variations in bi-directional reflectance in the visible and relative brightness in the infrared for Lander soils and blocks can best be explained by varying composition (i.e., degree of oxidation, mineralogy, and crystallinity) among the different samples. The darkest, grayest block surfaces are consistent with laboratory reflectance spectra of mafic rocks, thinly coated with ferric iron-rich palagonite. Such a result is consistent with the low relative reflectance for the dark facets determined from images acquired with the infrared channels. More rigorous determination of substrate rock composition (e.g., ultramafic, basalt, or basaltic andesite) requires complete spectral data in the near-infrared region. Most other block surfaces are consistent with thin to optically thick covers of palagonitic material [10]. Limited exposures of soil have blue, green, and red reflectances that are similar to palagonitic material. One soil exposure has a spectral shape that is similar to a sample of hematitically altered volcanic cinder. The bulk of the soils sampled and a few block surfaces have spectra with steeper slopes and larger curvatures than the palagonite analog. In particular, one reasonable interpretation is that the most commonly sampled soil exposed at the landing sites may have a greater degree of ferric iron crystallinity than the palagonite analog. These soils could also be an intimate mixture of palagonitic material and other materials not seen in end-member form. But, if intimate mixing occurs, these other materials would need an even greater slope and curvature than the observed soils, and be presumably even more different from material seen on block surfaces in terms of the degree of ferric iron crystallinity.

The distinctly different spectral shape of most observed soils as opposed to blocks imply that soils at the landing sites have not been produced by local weathering of blocks. Even if mixing occurs between material weathered from blocks and a soil end-member not exposed at the landing site, it implies that soils at the landing sites are not predominantly derived from local weathering of blocks. A more plausible scenario is one where soils are created globally by a number of processes that operated at higher rates earlier in geologic time. For example, Baird and Clark [16] make compelling arguments that soils are derived from mafic to ultramafic source blocks in some isochemical process. Palagonitization of basaltic magmas and basaltic glass have also been proposed as an important mechanism [17-18]. The materials would then be transported and would accumulate at a variety of locations. Once deposited, further erosion would sort the material, and evaporation of fluids would lead to generation of duricrust. At least at the

landing sites, blocks would have been steadily added to the site by impact events and exposed to slow, perhaps steady state weathering generating only a small amount of soil. This scenario implies that the bulk of the soil at the sites carries little information about the local geology.

REFERENCES CITED

[1] Huck, F., and others (1977), *J. Geophys. Res., 82,* 1977.
[2] 2) Strickland, E., (1979), *Proc. Lunar Planet. Sci. Conf. 10th,* 1979.
[3] Evans, D., and J. Adams, (1979), *Proc. Lunar Planet. Sci. Conf. 10th,* 1829-1834.
[4] Guinness, E., (1981), *J. Geophys. Res., 86,* 7983-7992.
[5] Adams, J., and others, (1986), *J. Geophys. Res., 91,* 8098-8112.
[6] Guinness, E., and others, (1986), *Proc. Lunar Planet. Sci. Conf. 17th,* in press.
[7] Patterson, W., and others, (1977), *J. Geophys. Res., 82,* 4391-4400.
[8] Huck, F., and others, (1975), *NASA Tech. Memo. X-72692.*
[9] Singer, R., (1980), *Lunar and Planet. Sci. XI,* 1045-1047.
[10] Singer, R., (1982), *J. Geophys. Res., 87,* 10,159-10,168.
[11] Singer, R., and E. Strickland, (1981), *Lunar and Planet. Sci. XII,* 999-1001.
[12] McCord, T., and J. Westphal, (1971), *Astrophysical Journal, 168,* 141-153.
[13] McCord, T., and others, (1977), *Icarus, 31,* 293-314.
[14] Evans, D., and others, (1981), *Proc. Lunar Planet. Sci. Conf. 12th,* 1473-1479.
[15] McCord, T., and others, (1982), *J. Geophys. Res., 87,* 10,129-10,148.
[16] Baird, A., and B. Clark, (1981), *Icarus, 45,* 113-123.
[17] Soderblom, L., and D. Wenner, (1978), *Icarus, 34,* 622-637.
[18] 18) Allen, C., and others, (1981), *Icarus, 45,* 347-369.

SPECTRAL MIXTURE MODELING: FURTHER ANALYSIS OF ROCK AND SOIL TYPES AT THE VIKING LANDER SITES

John B. Adams and Milton O. Smith
Department of Geological Sciences
University of Washington, Seattle, WA 98195

We have applied a new image-processing technique to Viking Lander multispectral images (Adams et al., 1986). Spectral endmembers were defined that included soil, rock and shade. Mixtures of these endmembers were found to account for nearly all of the spectral variance in a Viking Lander 1 image, thus one spectral type of soil and one type of rock mixed in various proportions accounted for the observed "color" differences.

Further work on the Viking Lander 1 image has solved the problem of the nature of a minor spectral endmember that we originally identified as being due to secondary illumination effects. That endmember can now be shown to be the result of lighting effects (especially near-far/field spectral phase changes) and the effects of a foreground misregistration of the three IR bandpass images with the three visible bandpass images in the original Viking data. The misregistration of the data is not apparent when viewing individual bandpass images or color composites; however it is distinct in the RMS (root mean squared) error image which displays the accumulated error between the model image and the real image. The pixels with high RMS error do not correspond spectrally or spatially to reasonable soil or rock types, however they force the introduction of another spectral endmember.

The misregistration was corrected by Dr. E. Guinness at Washington University (St. Louis). When the spectral mixing model was calculated for the rectified images using rock, soil and shade as endmembers the RMS error image showed only a weak spectral phase shift from near to far-field, and no additional endmember was required. These results further emphasize the usefulness of the mixing model for isolating geologically meaningful spectral variance from that introduced by the imaging system or by lighting effects.

Analysis of other Viking Lander 1 and 2 images shows that the spectral phase effect is strong at certain lighting geometries. In all cases the effect is expressed as a gradual shift in the reflectance spectra of all objects from near field to far field. The spatial patterns of these shifts are unrelated to geological features. However, the phase effect must be isolated and removed in order to compare soil or rock spectra in different parts of an image.

We have applied the mixing model to other Lander 1 and 2 images using the same spectral endmembers for soil and rock that fit the data in the Viking Lander 1 image. The objective has been to test for the presence of other soil and rock types by analysing the RMS error images. Materials that appear spectrally different from the endmembers (and their mixtures) used in the model appear bright in the RMS error image. Preliminary results show that the same soil and rock types carry through all images studied at both Viking sites, however there are important local exceptions where areas of spectrally different rocks also occur. As discussed above we can establish that these spectral differences are not produced by lighting effects or by system defects. An evaluation of the nature and extent of these new spectral rock types is underway.

REFERENCE

Adams, J.B., Smith, M.O., and Johnson, P.E., Spectral mixture modeling: A new analysis of rock and soil types at the Viking Lander 1 site, J. Geophys. Res., 91, 8098-8112, 1986.

HISINGERITE AND IDDINGSITE ON MARS: Degradation of Iron-Rich Basalts.
Burns, Roger G., Department of Earth, Atmospheric and Planetary Sciences, Massachusetts Institute of Technology, Cambridge, MA 02139.

Iron-rich basalts, which erupted onto the surface of Mars from massive shield volcanoes such as Olympus Mons, have undergone extensive alteration to produce regolith dominated by Si, Fe, Al, Mg, Ca, S, and perhaps Na and H_2O or OH^-. The modal mineralogy of martian regolith is believed to be dominated by clay silicates, such as the smectites iron-rich montmorillonite or nontronite, coexisting with poorly crystalline and magnetic iron oxides, and Ca-Mg sulphates or hydroxo ferric sulfate minerals (e.g. jarosite) [1]. The phyllosilicate and ferric oxide phases were deduced to be poorly crystalline [2] in order to account for reflectance spectral profiles of Mars' surface in the visible-near infrared region [3]. Such phases also constitute iddingsite, a deuteric alteration product of olivine in basalts, which has been identified in meteorites believed to have originated from Mars. Paragenetic evidence summarized here indicates that hisingerite, too, may have formed during the evolution of martian regolith.

Numerous terrestrial occurrences of hisingerite, possessing vitreous luster, conchoidal fracture and pulverizing to orange-brown powder which resembles the color of martian regolith, have been documented [4]. Hisingerite is formed by deuteric and late-stage alteration of pyroxenes and olivine in mafic igneous rocks, particularly those associated with sulfide ore deposits [5,6]. Apparently, acidic solutions formed during the dissolution of sulfide mineralization has led to the formation of hisingerite in crusts, fracture fillings and cooling joints of iron-rich basaltic host-rocks. Similar environments of chemical weathering may also exist on Mars [1,7]. Hisingerite was once regarded as poorly crystalline iron-rich smectite or nontronite [4]. However, recent electron microscopy and X-ray studies [5,6] have revealed hisingerite to have an amorphous or gel structure containing a disordered array of $[FeO_6]$ octahedra and $[SiO_4]$ tetrahedra. It is just this coordination environment and degree of crystallinity that matches materials simulating the spectral properties of bright regions of Mars [5]. Therefore, hisingerite and basic ferric sulfate minerals (e.g. jarosite) appear to be major contributors to remote-sensed reflectance spectral profiles of Mars [8].

[1] Burns, *Nature*, **320**, 55 (1986); [2] Sherman *et al.*, *JGR*, **87**, 10169 (1982); [3] Singer, *Adv. Space Sci.*, **5**, 59 (1985); [4] Brigatti, *Proc. Int. Clay Conf., Bologna 1981*, 97-110 (1982); [5] Eggleton, *Clays & Clay Minerals*, **32**, 1 (1984); [6] Shayan, *Clays & Clay Minerals*, **32**, 272 (1984); [7] Burns, *JGR*, in press; [8] Research supported by NASA grant number NGR 7604.

GOSSANS ON MARS: SPECTRAL FEATURES ATTRIBUTED TO JAROSITE.
Burns, Roger G. (Department of Earth, Atmospheric and Planetary Sciences. Massachusetts Institute of Technology, Cambridge, MA 02139.

Summary. Jarosites, $(K^+,Na^+,H_3O^+)(Fe^{3+},Al^{3+})_3(SO_4)_2(OH)_6$, which are present in terrestrial gossans capping oxidized sulfides associated with mafic igneous rocks, may also be present in martian regolith. Spectral characteristics of jarosites, attributed to Fe^{3+} in the visible region and to water or hydroxyl groups in the infrared region, are also displayed in remote-sensed reflectance spectra of bright regions of Mars' surface. The occurrence of jarosite in the regolith would imply that acidic permafrost and sulfide ores exist beneath the surface of Mars.

Introduction. The Viking XRF experiment detected high sulfur and iron contents in the martian fines [1]. These elements are believed to exist as oxidized SO_4^{2-} and Fe^{3+} species, respectively [2]. Although the majority of ferric iron on Mars is probably derived from chemical weathering of ferromagnesian silicates, some Fe^{3+} may have originated from oxidation of iron sulfides present as accessory minerals in iron-rich basalts or as massive pyrrhotite ores associated with ultramafic igneous rocks. Several hydroxo ferric sulfate minerals could be stabilized at low temperature and pH conditions in martian permafrost [3]. However, as a constituent of martian regolith, jarosite is the prime candidate because in arid regions on Earth it is associated with mixtures of poorly crystalline ferric oxides ("limonite") and silica (jasper) found in gossans. Spectral features summarized here of assemblages containing jarosites and poorly crystalline FeOOH plus silica or clay silicates match closely profiles measured in remote-sensed reflectance spectra of Mars.

Spectra. Reflectance spectra of ubiquitous bright dust and soil on Mars in the near UV-visible region are highly diagnostic of ferric iron [4]. Distinguishing features include a slope change at 0.5-0.6 μm and a broad band centered at 0.8-0.9 μm. A variety of candidate ferric-bearing phases have been suggested [4,5], and it is generally agreed that Fe^{3+} occurs in amorphous or poorly crystalline hydrated ferric oxide-silica gel and clay silicate phases. However, jarosite has similar spectral features in the UV-visible region [6]. In the near infrared, spectral features between 1.4-1.7 μm, around 2.3-2.4 μm, and at 2.9 μm have been assigned to H_2O and OH^- in phyllosilicates. Again, jarosite spectra possess similar features [7]. In addition, the mid-infrared feature near 9 μm observed in suspended martian dust [2] also occurs in spectra of jarosites.

Formation of Jarosite. Near-surface oxidation of sulfides on Earth proceeds by electrochemical processes involving oxygenated groundwater and dissolved Fe^{3+} ions [8,9]. Primary pyrrhotite in mafic igneous rocks is oxidized by Fe^{3+} to secondary pyrite well below the water table ($Fe_7S_8 + 6Fe^{3+} = 4FeS_2 + 9Fe^{2+}$). Nearer the water table, oxidation of pyrite occurs ($4FeS_2 + 2H_2O + 15O_2 = 4Fe^{3+} + 8SO_4^{2-} + 4H^+$), leading to dissolved Fe^{2+}, Fe^{3+}, and SO_4^{2-} in acidic groundwater, in which complex ferric ions predominate (e.g. $FeSO_4^+$, $FeOH^{2+}$, etc.). Monodispersed sols of hydronium jarosite (carphosiderite) may form by reactions involving these complex ions ($2FeSO_4^+ + FeOH^{2+} + 6H_2O = (H_3O^+)Fe_3(SO_4)_2(OH)_6 + 4H^+$), or by direct oxidation of dissolved Fe^{2+} ($6Fe^{2+} + 4SO_4^{2-} + 11H_2O + 3/2\ O_2 = 2(H_3O^+)Fe_3(SO_4)_2(OH)_6 + 4H^+$). In the presence of alkali metal cations and Al derived from chemically weathered feldspars in basalt, extremely insoluble jarosites are precipitated. Stability relationships [10] indicate that jarosite compositions as sodic and aluminous as $(K_{0.5}Na_{0.5})(Fe_{0.5}Al_{0.5})_3(SO_4)_2(OH)_6$ are stable at pH 5 and 298°K. Below the freezing point of water, they might be stable to pH 6 and form near permafrost on Mars.

Applications to Mars. Independent evidence for the occurrence of jarosite on Mars stems from its suggested presence in shergottite and nakhlite meteorites [11,12]. The existence of jarosites on Mars provides important clues about the inventory of volatiles, degassing of the mantle, evolution of the atmosphere, and acidity of groundwater and permafrost there [2,3,9]. The presence of jarosite in the highly colored gossan-like regolith might also indicate that massive sulphide ore deposits occur beneath the permafrost of Mars [13].

References.

[1] Clark *et al.*, *JGR*, **87**, 10059 (1982); [2] Clark & Baird, *JGR*, **84**, 8395 (1979); Clark & van Hart, *Icarus*, **45**, 370 (1981); [3] Burns, *Nature*, **320**, 55 (1986); [4] Singer, *Adv. Space Sci.*, **5**, 59 (1985); [5] Sherman *et al.*, *JGR*, **87**, 10169 (1982); [6] Hunt & Ashley, *Econ. Geol.*, **74**, 1613 (1979); [7] Hunt, *Geophysics*, **44**, 1974 (1979); [8] Blain & Andrew, *Minerals Sci. Engng*, **9**, 119 (1977); [9] Burns, *JGR*, in press; [10] Hladky & Slansky, *Bull. Mineral.*, **104**, 468 (1981);[11] Smith & Steele, *Meteoritics*, **19**, 121 (1984); [12] Gooding, *Geochim. Cosmochim. Acta*, **50**, 2215 (1986); [13] Research supported by NASA grant number NSG 7604.

CHARACTERIZATION OF SURFICIAL UNITS ON MARS USING VIKING ORBITER MULTISPECTRAL IMAGE AND THERMAL DATA

M.A. Presley and R.E. Arvidson, McDonnell Center for the Space Sciences, Dept. of Earth and Planetary Sci., Washington University, St. Louis, MO 63130; and P.R. Christensen, Dept. of Geology, Arizona State University, Tempe, AZ 85287

The topography of the northern hemisphere of Mars is dominated by three areas of high elevation (up to 5 km above the datum for Elysium and Arabia, and up to 27 km for Tharsis) separated by areas of low elevation (about 1 to 2 km below the datum). Albedo and thermal properties correlate fairly well with this regional topography [1]. The high elevation areas have relatively high albedos (0.32 - 0.33) and low thermal inertias ($< 2.5 \times 10^{-3}$ cal·cm^{-2}s$^{-1/2}$K^{-1}), while the lower elevation areas generally have lower albedos (< 0.15) and higher thermal inertias (5 - 14). In order to examine these correlations on a more local scale, a detailed study was conducted [2] of the types and origins of materials exposed in the central equatorial region (335°W - 15°W, 10°S - 30°N). The region is part of the heavily cratered terrain, located on the western edge of Arabia where the topography is changing from the high elevations of Arabia in the east to lower elevation in the west. This area was selected because it displays a wide variation in color, albedo and thermal properties over a small area of the planet and has good data coverage, relatively free from dust and haze.

Three surficial units can be distinguished in this region on the basis of spectral reflectance properties determined from radiometrically calibrated Viking Orbiter color images and thermal properties determined from the Viking Infrared Thermal Mapper. These units are: (1) a bright red unit that has a relatively high reflectance in both red (average reflectance of type area = 0.17) and violet wavelengths (0.06) and a low fine component thermal inertia (modal value of the unit = 2.4); (2) a dark violet unit that has a relatively low reflectance in both red (0.10) and violet wavelengths (0.05) and a relatively high thermal inertia (6.4); and (3) a brown unit that has a reflectance that is relatively low in the violet wavelengths (0.04), but intermediate in value relative to the other units in the red wavelengths (0.13), and a thermal inertia that is also intermediate in value (4.6). Reflectance values for the region produce two trends. These trends suggest that a bright red end-member material is mixing with each of the darker end-members. The darker units, however, do not mix with each other.

These units can be mapped to contiguous, well defined locations by use of simple parallelepiped techniques. Material that produces the brighter reddish trend, at the apex of the two mixing trends, is located in the east where it corresponds to Arabia and in the very south where it corresponds to Deucalionus Regio. Dark violet material is located in the south and southwest where it corresponds to Sinus Meridiani and Sinus Sabaeus. The dark violet material also exists as dark splotches in large craters within the Oxia Palus quadrangle, as well as dark streaks associated with the splotches. Brown material is located in the north to northwest where it is the dominant unit in the western half of the Oxia Palus quadrangle. In addition to the contiguous units, bright red material can be found as bright crescents within the large craters in Oxia, opposite to the dark splotches, and as bright margins surrounding the dark streaks.

Color/albedo boundaries are relatively sharp and distinct in all places, yet they are not correlated with abrupt changes in regional morphology, as determined from medium and high resolution Viking Orbiter images, nor do they exhibit any systematic correlation with topographic boundaries. Crater statistics, derived from high resolution Viking Orbiter images and Mariner 9 A-frames, indicate that the units are indistinguishable in terms of age, and that only a relatively minor amount of crater obliteration (< 0.008 μm/year depositional rate) could have occurred over the past several billion years.

A major objective of the Mars Observer Mission is to map the physical, elemental and mineralogical characteristics of the surface, for the purpose of characterizing both the surficial materials and bedrock geology. The results of this study [2] suggest that the dark violet unit is probably composed of sand-sized deposits [3]. The bright red unit is composed of dust, probably a globally homogenized deposit emplaced during dust storms [4 and 1]. The thermal inertia of the brown unit, and the lack of mixing between the brown and the dark violet units, are consistent with significant duricrust formation in the brown unit, as suggested by Kieffer et al. [5]. This possibility is supported by Viking Lander color data. Duricrust exposed at the Viking 1 Lander site occupies the same relative position on a two-dimensional histogram of the number of pixels as a function of their red and blue albedos for Frame A168 (VL1, Sol 28), as the brown unit does on a red-violet histogram from Viking Orbiter Apoapsis color. These data support the possibility of extensive duricrust formation and exposure in the brown unit.

If there are significant amounts of duricrust within the brown unit, then the thermal inertia of the unit suggests that the matrix must be composed of very fine-grained sand or dust. Thus the brown unit may be composed of fine-grained bright red material that has been cemented to produce a duricrusted surface. Although the resultant spectra of matrix and cement would not be a simple linear addition of end-member spectra, since the cement would probably form an intimate mixture [6] with its matrix, the spectra would nonetheless be intermediate between those of the cement and the matrix. A salt that is transparent in the visible, such as Kieserite, $MgSO_4 \cdot H_2O$, which has been suggested as a likely candidate at the Viking Lander sites by Toulmin et al. [7], could not produce a composite spectra for the brown unit that is lower in albedo than the red unit. Trans-opaque minerals, such as iron sulfates (Quenstedtite, $Fe_2(SO_4)_3 \cdot 10H_2O$, for example [8]), however, may present some interesting possibilities, and spectral properties of such compounds should be investigated.

Another possibility is that the brown unit is simply a lag deposit composed of a mixture of particles with an effective grain size in the range of fine sand. This is also consistent with Viking Lander observations. Viking Lander high resolution color images synthesized by Dale-Bannister [9] show exposures of brown and bright red materials, with the brown materials underlying the brighter, redder deposits. Only the redder deposits form tails or drifts, suggestive of eolian deposition. The absence of dark violet materials in these images is consistent with Viking Orbiter Apoapsis color data, which show only brown and bright red materials in the region of the Chryse Landing site.

A global view shows that both the bright red material and the brown material occupy large regions of the planet, regardless of morphology or

inferred geology. Together with the results summarized here, this observation implies that these two units are thin eolian deposits completely decoupled from the underlying bedrock. The higher elevations of the bright red unit imply that deposition and/or erosion are being controlled by topography. Data utilized in this study are insufficient to determine whether the dark violet unit is locally derived from bedrock, or whether it is also a thin eolian deposit. Earth-based spectra of the dark regions, however, indicate that Fe^{2+} absorptions around 1 μm vary with location on the planet. These are believed to reflect differences in the mafic mineralogy, primarily pyroxenes and olivines [10]. These variations suggest that the dark material is derived from local sources. Since the material of the dark violet unit is the most likely to be derived from bedrock, data collection by the Mars Observer Mission should concentrate on these areas, and other dark regions like them. At any rate, a major problem in analyzing Mars Observer data will be in determining to what extent a surficial material may be related to underlying crustal geology or to laterally homogenized eolian deposits.

REFERENCES:

[1] Christensen, P.R. (1986), Regional dust deposits on Mars: Physical properties, age, and history, *J. Geophys. Res.*, **91**, 3533-3545.

[2] Presley, M.A. (1986), The origin and history of surficial deposits in the central equatorial region of Mars, MA Thesis, Washington University

[3] Christensen, P.R. (1983), Eolian intracrater deposits on Mars: Physical properties and global distribution, *Icarus*, **56**, 496-518.

[4] Christensen, P.R. (1982), Martian dust mantling and surface composition: Interpretation of thermophysical properties, *J. Geophys. Res.*, **87**, 9985-9998.

[5] Kieffer, H.H., Davis, P.A. and Soderblom, L.A. (1981), Mars' global properties: Maps and applications, *Proc. Lunar Planet. Sci. Conf.*, **12B**, 1395-1417.

[6] Singer, R.B. (1981), Near-infrared spectral reflectance of mineral mixtures: Systematic combinations of pyroxenes, olivine, and iron oxides, *J. Geophys. Res.*, **86**, 7967-7982.

[7] Toulmin, P.T., III, Baird, A.K., Clark, B.C., Keil, K., Rose, H.J., Jr., Christian, R.P., Evans, P.H. and Kelliher, W.C. (1977), Geochemical and mineralogical interpretation of the Viking inorganic chemical results, *J. Geophys. Res.*, **82**, 4625-4634.

[8] Clark, B.C. (1978), Implications of abundant hygroscopic minerals in the Martian Regolith, *Icarus*, **34**, 645-665.

[9] Dale-Bannister, M.A. (1986), Synthetic high resolution color slides from Viking Lander imaging data, Washington University.

[10] McCord, T.B., Huguenin, R.L., and Johnson, G.L. (1977) Photometric imaging of Mars during the 1973 opposition, *Icarus*, **31**, 293-314.

CO_2: ADSORPTION ON PALAGONITE AND THE MARTIAN REGOLITH

Aaron P. Zent, Fraser P. Fanale and Susan E. Postawko, Planetary Geosciences Division, Hawaii Institute of Geophysics, University of Hawaii, Honolulu, Hi.

If there was ever sufficient CO_2 in the martian atmosphere to engender a greenhouse effect sufficient to raise the surface temperature above 273 K, most of that CO_2 is missing today.

Pollack et al., (1986) calculated that, even if reduced solar luminosity is accounted for, 0.75 bars of CO_2 could have provided surface temperatures greater than 273K at restricted times and places. We consider 0.75 bars to be the lower limit on the early atmospheric CO_2 abundance necessary for a greenhouse effect.

Known reservoirs of CO_2 do not hold anywhere near 0.75 bars. Only 8 mbar is currently in the atmosphere, less than 10 mb has escaped to space (Pollack and Yung, 1980), and no more than a few mbar are in the permanent south polar cap reservoir (Fanale et al., 1982). In the absence of a deep subsuction mechanism, the remainder must have been lost to space, or be stored in the regolith, either as carbonate rock or in the adsorbed state.

Based on laboratory measurements of CO_2 adsorption on basalt and nontronite, (Fanale et al., 1982), suggested that it is unlikely that the regolith could have adsorbed more than about 0.28 bars of CO_2.

The possible scenarios for the evolution of the martian climate are likely to lie along a continuum whose end members may be defined as follows:

1) The abundant erosional features indeed indicate the presence of fresh liquid water (eutectic = 273K) on the martian surface. That water was stablized by the presence of a massive CO_2 atmosphere, at least 0.4 bars of which cannot be accounted for in known reservoirs, and which presumably exists as carbonate in the regolith.

2) The erosional activity was accomplished mainly by Martian brines (Brass, 1980) with depressed eutectics. In this case, sapping, and not rainfall is involved, and the difficulties associated with fresh water erosion are mitigated, but not removed. A greenhouse may still be required, but less than 0.75 bars would be necessary, and it may be that the entire CO_2 inventory necessary for a greenhouse effect of the required magnitude could be accommodated today in the adsorbed state without recourse to carbonates.

In the interest of determining an upper limit on the adsorptive capacity of the martian regolith, we recently examined the results of Fanale and Cannon, (1971,1974) for CO_2 adsorption on nontronite and basalt. There appeared to be a strong proportionality between the capacity of the adsorbent and its specific surface area. In order to investigate the hypothesis that the specific surface area of the adsorbent could be used to constrain its adsorptive capacity, even in the absence of mineralogical information, we performed additional adsorption measurements of CO_2 on palagonites from Mauna Kea, Hawaii. We chose palagonites because they are a weathering product of basaltic glass and form a good spectral and chemical analog to the Viking soils (Evans and Adams, 1980, Singer, 1982). Weathering products generally dominate adsorption behavior, and nontronite is now in disfavor as a Mars analog material because of features in its spectrum which are undetectable or absent in Mars' spectrum.

Determining the relative importance of surface area and mineralogy is important becasue *in situ* measurements of specific surface area for Martian materials

exist, whereas no determination of mineralogy has ever been made.

Adsorption measurements were made on a Micrometrics AccuSorb 2100E Physical Adsorption Analyzer. We found that our data were reproducible to approximately 40% at low adsorptive coverage, but that precision increased to better than 20% at higher coverage. The desorption branches of the isotherms were reproducible, provided the preceding adsorption branches were carried up to near saturation. Unfortunately, the high saturation pressure of CO_2 complicated this in higher temperature data runs. However, the BET surface area, which we calculated for each isotherm, provides another check on internal consistency. Performing a least-squares fit on the data, we find that the data can be fitted to a curve of the form

$$\rho_a = \delta\, P^{\gamma}\, T^{\beta} \qquad (1)$$

where δ = 27.93, γ = 0.171045, and β = -1.44675. Here P is in mm Hg, and T is degrees Kelvin. The associated error in this equation is ±20%, based on the spread in the data.

Normalizing for the surface area of all three minerals, decreases the uncertainty associated with not knowing the composition of the adsorbent to less than a factor of three from approximately a factor of 13. We believe that accounting for specific surface area provides a significant improvement in our estimate of the capacity of a mafic particulate adsorbent at Mars-like conditions. More importantly, it provides a description of the response to temperature variation which is less mineralogy-dependent and more useful in predicting climate change than those used in the past.

For the purposes of this study, we therefore assume that an equation can be written which describes CO_2 adsorption on any basalt or basaltic weathering product in terms of temperature, P_{CO_2} and the specific surface area of the material, without regard to mineralogy. We do not apply this equation to temperature and pressure conditions which differ from the conditions at which the data were gathered. The complete data set for all minerals was used to fit that equation. The equation which best describes the general CO_2 adsorptive behavior of particulate mafic rocks and their weathering products is

$$\rho_a = A_s \delta\, P^{\gamma} T^{\beta} \qquad (2)$$

Where A_s is the specific surface area of the material in ($m^2\, g^{-1}$), and P and T are as above. In this case $\delta = 5.9629 \times 10^4$, γ = 0.364391, and β = -3.83415. A check of this equation indicates that it predicts adsorptive capacity to within a factor of three for those mafic rocks and weathering products for which CO_2 adsorption data are available, regardless of precise mineralogy.

If we are granted the indulgence of scooping up a few cubic centimeters of soil and extrapolating to the entire unconsolidated regolith, we can use Eq.(2) to draw some constraints on the partitioning of CO_2 in the martian regolith.

Fanale et al. (1982) presented a model of the martian climate in which they considered regolith adsorption to be the primary reservoir of exchangeable CO_2. They presented results based on basalt and nontronite, and described cap formation and atmospheric pressure as a function of obliquity. We have reconfigured that model, eliminating explicit assumptions of mineralogy, and substituting Eq.(2) with $A_s = 17\ m^2\, g^{-1}$.

There are two independent variables in the current configuration of this model. One is the amount of *exchangeable* CO_2, (i.e. adsorbed, atmospheric, or cap CO_2). The other variable is the depth of the regolith, which essentially determines the total surface area available for adsorption. This model is useful because if we specify the depth of the regolith that is in diffusive contact with the atmosphere, then there is a unique amount of exchangeable CO_2 that is compatible with, 1) the current atmospheric pressure, and 2) the absence of a significant current polar CO_2 reservoir. Our model allows us to find that amount of exchangeable CO_2.

The depth of the regolith in our model is not the depth of crustal fracturing, but a conceptual construct. It is the equivalent depth of a model regolith, with specific surface area 17 $m^2 g^{-1}$, in diffusive contact with the atmosphere. A relatively small thickness of this idealized regolith would be the equivalent, in terms of total surface area, of a rather extensive real regolith, with sills, blocks, adsorbed H_2O and probably extensive permafrost. Our model indicates that even 500m of this ideal, highly adsorptive regolith could hold no more than 0.19 bars.

There are reasons to place a lower limit on regolith thickness as well. If we fix the total amount of outgassed CO_2, and make the regolith progressively shallower, the concentration of carbonate in the regolith must increase, assuming that CO_2 displaced from adsorbate would remain in the regolith. Eventually, a finite amount of carbonate should be present at the surface. Nonetheless, there is no spectral evidence for the existence of carbonates on Mars. That argues against a massive carbonate deposit of unconstrained mass as a panacea for models involving massive greenhouse effects early in martian history. Nonetheless, it is clear that some reservoir over and above adsorbate is almost certainly necessary.

This model allows us to make some estimates of exchangeable CO_2 abundances without knowing much more than we do now about martian volatile history. All atmospheric pressure vs. obliquity curves cross at obliquity 25° and pressure 7.5 mbar, as would be expected since the pairs of independent variables were chosen to be consistent with current conditions. However as long as the exchangeable CO_2 abundance and regolith depth are chosen with those constraints in mind, atmospheric pressure and cap formation as a function of obliquity is only weakly dependent on the specific parameters we chose. The actual mass of the polar cap at low obliquity of course does depend strongly on total exchangeable CO_2, but the atmospheric pressure does not at any obliquity.

REFERENCES

1. Brass, G. W., *Icarus*, **42**, 20-28, 1980.
2. Evans, D. L., and Adams, J. B. *Proc. Lunar and Planet. Sci. Conf. 11th.* 757 - 763, 1980.
3. Fanale, F. P., and Cannon, W. A., *Nature*, **230**, 502-504, 1971.
4. Fanale, F. P., and Cannon, W. A. *J. Geophys. Res.* **79**, 3397-3402, 1974.
5. Fanale, F. P., et al., *Icarus*, **50**, 381-407, 1982.
6. Pollack, J. B., and Y. L. Yung, *Ann. Rev. Earth Planet. Sci.*, **8**, 425-487, 1980.
7. Pollack, J. B., et al., Submitted to: *Icarus*, 1986.
8. Singer, R. B., *J. Geophys. Res.*, **87**, 10,159-10,169, 1982.

INVESTIGATION OF MARTIAN H_2O AND CO_2 VIA GAMMA-RAY SPECTROSCOPY

Steven W. Squyres, Cornell University, Ithaca, NY 14853, and Larry G. Evans, Computer Sciences Corporation, Beltsville, MD 20705.

Earth-based and spacecraft investigations of Mars have shown that H_2O and CO_2 are the two most important volatile species on the planet. While major advances have been made concerning the evolution and present state of H_2O and CO_2 on Mars, many unanswered questions remain. The upcoming Mars Observer mission will include in its payload a gamma-ray spectrometer. This instrument will measure the spectrum of gamma radiation emitted by the planet. From the measured gamma-ray spectrum, it is possible to infer a considerable amount of compositional information. Particularly, the experiment will enable study of the spatial and temporal distribution of H_2O and CO_2 in the near-surface martian regolith.

The presence of H_2O can be investigated directly by measurement of the 2.223 MeV gamma-ray line of H. Because H is the most important element for moderating the neutrons produced by cosmic-ray interactions with the surface, it can also be investigated by the direct or indirect determination of the fast to thermal ratio of the neutron albedo flux. In general, for materials with high H concentrations, the total neutron flux consists of proportionally more thermal neutrons and the flux peaks at shallower depths than for materials with low H concentrations. The neutron fast/thermal ratio may be determined indirectly from the gamma-ray spectrum. Prompt capture lines result primarily from interactions of nuclei with thermal neutrons, while inelastic scattering lines result primarily from interactions with fast neutrons. Some elements, such as Si and Fe, emit strong lines of both types. One may therefore examine ratios of inelastic scatter to prompt capture line strengths for these elements, and acquire information regarding the H distribution that is similar to what one would acquire directly from fast/thermal neutron ratios. The 2.223 MeV gamma-ray flux is an indicator of the amount of H in the upper few tens of g cm^{-2}, while the inelastic/capture ratio for Si or Fe is related to the amount of H in the upper $\sim$ 100 g cm^{-2} or more. It is therefore possible to obtain information about the vertical distribution of H. CO_2 is more difficult to detect, but it may be possible to determine the thickness of a layer of CO_2 frost by direct detection of C or by inference from attenuation of gamma rays from underlying material.

We wish to determine how effectively questions regarding the distribution of H_2O and CO_2 on Mars may be addressed with orbital gamma-ray data. Our approach is straightforward. We have identified several unanswered questions regarding martian H_2O and CO_2. These include: *(1)* What is the ice/dust ratio of the polar layered deposits? *(2)* What is the thickness of the polar perennial ice? *(3)* What is the thickness of the CO_2 that covers the southern perennial ice? *(4)* What is the thickness of the seasonal CO_2 frost caps? *(5)* How much H_2O is there in the seasonal frost cap? *(6)* How does the distribution of subsurface ice vary with latitude and geologic material? *(7)* What is the degree of hydration of minerals making up the martian surface? *(8)* Are there near-surface liquid water "oases" in Solis Lacus or elsewhere? For each question, we have formulated a simple multi-layer model of the martian surface. In each model, the martian surface is composed of one or two horizontal layers. If one surface layer is present, it is taken to be semi-infinite; if two surface layers are present, the upper one has some variable thickness and the lower one is semi-infinite. A layer may be composed of H_2O, CO_2, or soil with a composition like that at the Viking landing sites, or some homogeneous mixture of two of these materials. In two-layer models in which one layer is a mixture of two materials, the other layer is always composed of a single material. Each model therefore can be completely described by no more than two parameters. As an example, the problem of detection of subsurface ground ice is modeled with a variable-thickness upper layer of pure soil,

and a semi-infinite lower layer of intermixed soil and H_2O. In this case, the two parameters are the thickness of the upper layer and the soil/H_2O mass ratio of the lower layer. For each model, we calculate the gamma-ray spectrum that will be observed by a spacecraft in orbit. All of the calculations include atmospheric attenuation and emission. We then examine ways in which the observed spectrum can be interpreted to yield unique determinations of values for the parameters of interest.

In order to predict the expected gamma-ray fluxes from the surface of Mars and the sensitivity of the Mars Observer gamma-ray spectrometer experiment, the neutron spatial and energy distributions in the near-surface materials must be modeled. We use a primary cosmic-ray spectrum and resulting secondary neutron source distribution like that for the Moon. We then calculate the resulting neutron spectrum and distribution for the surface and atmosphere under consideration using the ANISN code. This is a discrete ordinate code that solves the neutron transport equation by evaluating the flux for discrete directions, positions, and energies. The code is one-dimensional, and uses 100 neutron energy groups and 100 spatial intervals with a spacing of 5 g cm^{-1}.

Once the neutron spatial and energy distributions have been determined, we calculate the discrete line gamma-ray fluxes produced by neutron interactions. For capture lines, the calculated thermal flux is used with the appropriate thermal neutron capture cross-sections and gamma-ray yields to calculate the gamma-ray line flux. Inelastic scatter gamma-ray fluxes are calculated in a similar manner with the inelastic scatter cross-sections integrated over energy at each depth. Production of gamma rays by natural radionuclides is also calculated. All gamma-ray line strengths are corrected for attenuation in the martian surface and atmosphere. The gamma-ray background is calculated from the observed lunar background, scaled to Mars from gamma-ray transport results.

Combining line strengths, background strength, detector characteristics, and counting time, we may estimate the quantitative uncertainty of the measurements to be made. For our calculations, we used the area, energy resolution, and efficiency of a laboratory 120-cm^{-3} HPGe detector, and a counting time of 38 hr. This period corresponds to the total integration time for a single gamma-ray spectrometer resolution element (about 300 km diam.) near the poles over one martian year.

We have considered a total of five models:

Model 1: Intermixed Soil and H_2O: This model can be used to address problems such as the ice/dust ratio of the layered deposits, the dust content of the north polar perennial ice, and the degree of hydration of hydrated silicates. Sample results are given in Figure 1, where we plot two observed line strength ratios as a function of the mass fraction of H_2O present. For small amounts of H_2O, optimum results are given by the ratio of Si inelastic capture to prompt capture line strengths, while for larger amounts of H_2O, optimum results are obtained by using the ratio of H (2.223 MeV) to Fe (capture). For a simple model such as this, it should be possible to determine the H_2O content to a high degree of accuracy.

Model 2: Soil over Soil + H_2O: This model consists of two layers: a pure soil layer of variable thickness over a semi-infinite layer of soil + H_2O with a variable H_2O mass fraction. This model can be used to address the distribution, depth, and concentration of ground ice (or liquid). Figure 2 plots Si(inelastic/capture) *vs.* H/Fe(capture). Solid curves are contours of constant H_2O mass fraction in the lower layer, and dashed curves are contours of constant thickness of the upper layer. For data falling in the region where the curves are separated, it will be possible to determine both the thickness of the upper layer and the ice mass fraction of the lower layer.

Model 3: H_2O over Soil + H_2O: This model can be used to address the thickness of the north polar perennial ice, which lies atop the layered deposits. Calculations like those in Figure 2 show that unique solutions are possible, but the uncertainties are large. However, if we assume that we know the ice fraction of the lower layer *a priori*, (as might be possible from an independent measurement of the ice content of exposed layered deposits) determination of the ice layer thickness can be improved very substantially.

Model 4: CO_2 over Soil + H_2O: This model can be used to address two problems. In the extreme of very high H_2O mixing ratio in the lower layer, it can be used to investigate the thickness of the CO_2 layer atop the south polar perennial ice. In the extreme of a very low or zero H_2O mixing ratio in the lower layer, it can be used to address the problem of the thickness of the seasonal CO_2 frost cap. Again, unique solutions are possible, but the uncertainties are large in some cases. However, if we know the H_2O content of the lower layer *a priori* (as would be the case if it were determined when the CO_2 layer was absent), uncertainties again can be very substantially reduced.

Model 5: CO_2 + H_2O over Soil: This model can be used to address the H_2O content of the seasonal frost cap. Unique solutions are found for both adjustable parameters, with small uncertainties.

These results indicate that the Mars Observer gamma-ray spectrometer will be a very powerful tool for investigating the distribution and stratigraphy of volatiles on Mars. It is important to note that the results here do not include the substantial additional information about the neutron energy spectrum that will result from the GRS's neutron mode. With this mode, it should be possible to determine fast/thermal ratios directly, providing an independent check on the gamma-ray results, and increasing the overall certainty in the results.

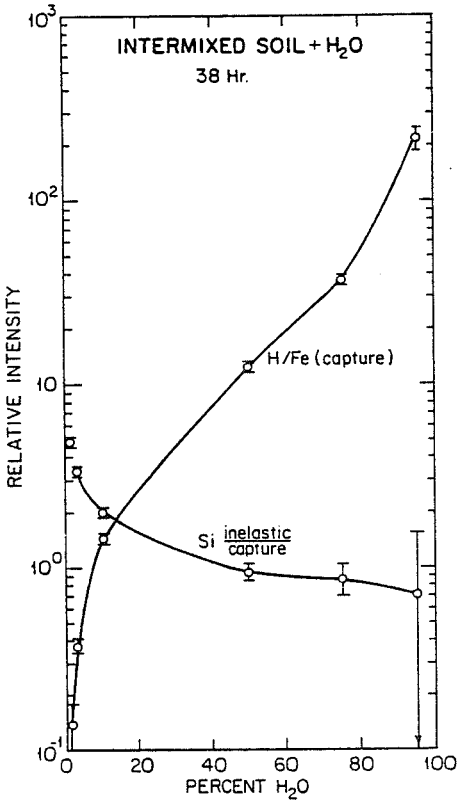

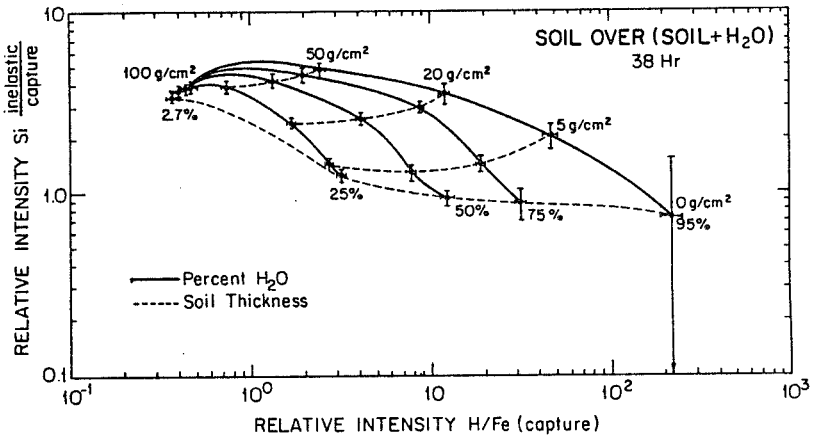

Figure 1 (left)
Figure 2 (above)

REFLECTANCE SPECTRA OF MAFIC SILICATES AND PHYLLOSILICATES FROM .6 TO 4.6μm;
Ted L. Roush, Robert B. Singer, and Thomas B. McCord, Univ. Hawaii, Planetary Geosciences Div., Hawaii Inst. Geophysics, 2525 Correa Rd., Honolulu, HI 96822

INTRODUCTION Spectral reflectance, obtained by spacecraft and earth-based telescopic observations, is the dominant method of collecting mineralogical information concerning the surface properties of solar system objects. Our ability to interpret this data, in terms of the identity and abundance of minerals present on a surface, is important for addressing more general questions concerning the origin and evolution of that body as well as the solar system as a whole. The reflectance of geologically important materials in the 0.3 to 2.5μm wavelength region has been the subject of intense laboratory research for many years(1,2,3,4,5). However, there has been a paucity of research concerning the reflectance behavior of geologic materials in the 2.5 to 4.6μm wavelength region.

The mapping spectrometers on future spacecraft missions, such as Galileo and the Mars Orbiter, are designed to return spectral reflectance data from 0.7 to 5.2μm. Thus, it is important for interpretation of such data to expand laboratory reflectance measurements to include the longer wavelength region. The study presented here provides empirical laboratory data concerning the reflectance behavior of geologically important materials in the 2.5 to 4.6μm wavelength region.

EXPERIMENTAL METHOD For this study two infrared, cooled, circular variable filter (CVF) spectrometers with InSb detectors were used and the combined wavelength coverage spanned the .65 to 4.5μm wavelength region. In both instruments the detector, filter, and other internal components are operated at liquid nitrogen temperature (77 K). The spectral resolution ($\Delta\lambda/\lambda$) of both CVF's is about 1.5%.

The mafic samples were chosen to represent minerals which result in mafic to ultramafic assemblages. All the mafic samples were dry sieved to the <38μm grain size. The phyllosilicates were chosen to represent a variety of structural types and amounts of natural hydration states. All phyllosilicate samples were dry sieved to the 38-45μm grain size. Additionally, a palagonite was included in the sample suite since this material has been suggested as a Mars soil analog material(6,7). The 2-3μm grain size of the palagonite was separated by liquid suspension in methanol.

All samples were placed in a furnace prior to being situated in an environment chamber. The environment chamber was flushed with inert nitrogen gas during the entire data collection and heating sequence. The samples were allowed to equilibrate in the nitrogen environment for thirty minutes before room temperature spectral data were collected. The samples were then heated at 200°C for thirty minutes and subsequently allowed to cool to room temperature before additional data were collected.

BACKGROUND Electronic transitions of the first transition element series, especially the petrologically significant cations Fe^{2+} and Ti^{3+}, result in absorptions in the visible and near-infrared (0.3 to 2.5μm) region of the electromagnetic spectrum(8), and are due to ions located within specific crystallographic sites. Hence, from the spectra direct information is obtained concerning the chemistry and crystal structure of the material.

For the silicates and of this study, the most important species which have vibrationally induced absorptions are the H_2O molecule and the OH^- ion. The H_2O molecule has strong absorption features located near 2.9μm (O-H asymmetric stretch), 3.0μm (H-O-H bend overtone), and 3.1μm (O-H symmetric stretch)(9). Overtones and/or combinations of these bands can occur near 0.94, 1.135, 1.38, 1.45, and 1.88μm(9). There is a fundamental of the OH^- group located near 2.75μm and the first overtone is located near 1.4μm(9). Additionally, bands in the 2.2 to 2.4μm region involve a combination of the OH^- fundamental with a X-OH bending mode (where X is usually Al or Mg)(9).

DISCUSSION The results of the spectral measurements for the mafic silicates are presented in Figures 1 to 3. All spectra, except the plagioclase, exhibit electronic absorptions located near 1 and/or 2μm which are due to Fe^{2+} located in octahedral crystallographic sites. These absorptions remain unchanged after heating. Additionally, all spectra have an absorption centered near 3μm which is due to H_2O. This absorption changes in intensity, and in some cases shape, after heating. We believe these changes represent the removal of physically adsorbed H_2O from the sample. The continued presence of the 3μm band band in the spectra of all samples after heating implies that H_2O bearing contaminants are present, or alternatively, the samples

contain fluid inclusions.

The results of the spectral measurements for the phyllosilicates are presented in Figures 4 and 5. Kaolinite and pyrophyllite have types of structures which typically accommodate little cationic substitution and hence do not incorporate interlayer H_2O(10). Before and after heating, the spectra of both samples exhibit strong absorption bands located near 2.75μm, due to OH^-, and the spectra after heating show minor changes due to the removal of physically adsorbed H_2O. This spectral behavior is illustrated in Figure 4 for kaolinite.

The Na-Montmorillonite (Fig. 5) has a structure which has abundant cationic substitution and its open nature results in the presence of interlayer H_2O(10). The spectrum of the sample before heating exhibits a broad 3μm band and narrower but pronounced 1.9μm band both due to H_2O and bands located near 1.4 and 2.8μm both due to OH^-. After heating, the spectrum exhibits the effects of removing the physically adsorbed, and possibly some of the interlayer, H_2O. The 1.9 and 3.0μm bands have decreased in intensity, while the band near 2.8μm has become more pronounced.

The palagonite spectrum (Fig. 6) before heating shows a strong, broad 3μm absorption and a weak absorption near 1.9μm, both indicate the presence of H_2O. After heating, the spectrum shows virtually no 1.9μm band and the 3μm band although slightly reduced in intensity still remains very prominent. We believe the physically adsorbed H_2O has been removed, so the continued presence of the 3μm band indicates abundant H_2O. The spectral behavior of the 3μm band is reminiscent of the plagioclase.

CONCLUSIONS This study has provided valuable spectral reflectance information about mafic silicates and phyllosilicates in the 2.5 to 4.6μm wavelength region. In this wavelength region we have shown that the reflectance of these materials is strongly affected by the presence of H_2O and OH^-. Therefore, the identification of these absorbing species is greatly enhanced.

The reflectance behavior of mafic silicates beyond 2.5μm can provide additional information about the chemical composition of the pyroxenes by revealing the long wavelength edge of the clinopyroxene absorption band located near 2μm. For Mercury, the Moon, Earth, Mars, and the asteroids this provides additional information which enhances our ability to map changes in the mineral composition and abundance across the surface of a planetary body.

The reflectance of phyllosilicates beyond 2.5μm provides additional information concerning the potential for identifying compositional and water content variations of these minerals. Since OH^- is structurally bound to octahedrally coordinated cations in phyllosilicates, the substitution of various cations should result in the shifting of absorptions due to the OH^--metal vibrations. Additionally, absorptions due to interlayer H_2O can be expected to vary as a function of amount of water available on the surface. In the case of Mars, a map of water content variation could identify possible sources and/or sinks of weathering products on a global scale and allow the study of water transport on the surface.

The spectral reflectance behavior of the palagonite beyond 2.5μm implies that the water contained within the sample is not composed solely of physically adsorbed water. Thus, the palagonite, if located in the desiccated Martian environment, could provide an exchange mechanism for atmospheric water vapor by trapping and releasing physically adsorbed water. The palagonite, during its initial formation, also provides a more permanent mechanism for removal of atmospheric water from the Martian environment.

ACKNOWLEDGEMENTS This research was supported by NASA grants NSG 7590 and NSG 7312.

REFERENCES 1)Hunt, G.R. and J.W. Salisbury, *Mod. Geol.*, *1*, 283-300, 1970. 2)Hunt G.R. and J.W. Salisbury, *Mod. Geol.*, *2*, 23-30, 1971. 3)Adams, J.B., *J. Geophys. Res.*, *79*, 4829-4836, 1974. 4)Singer, R.B., *J. Geophys. Res.*, *86*, 7967-7982, 1981. 5)Clark, R.N., *J. Geophys. Res.*, *86*, 3074-3086, 1981. 6)Evans, D.L. and J.B. Adams, *Proc. Lunar Planet. Sci. Conf. 11th*, 757-763, 1980. 7)Singer, R.B. *J. Geophys. Res.*, *87*, 10159-10168, 1982. 8)Burns, R.G., *Mineralogical Applications of Crystal Field Theory*, 1970. 9)Hunt, G.R., *Geophysics*, *42*, 501-513, 1977. 10)Deer, W.A., R.A. Howie, and J. Zussman, *An Introduction to the Rock Forming Minerals*, 1966.

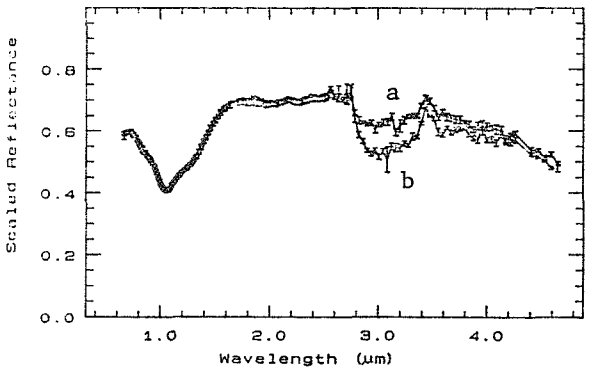

Figure 1. Reflectance spectra of olivine (Fo_{89}) before (b) and after (a) heating. The absorption centered near of 1μm is due to the presence of Fe^{2+} and is unaffected by heating. The decrease of the absorption located near 3μm upon heating is due to the loss of physically adsorbed H_2O.

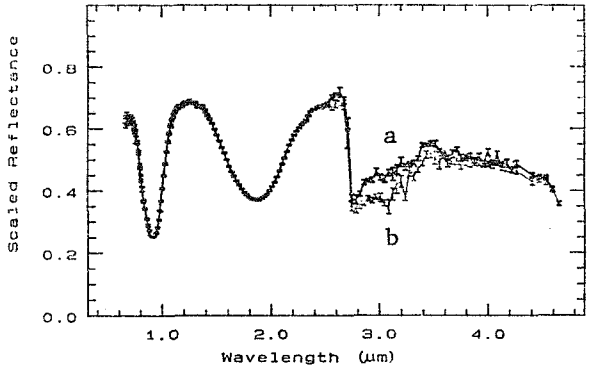

Figure 2. Reflectance spectra of orthopyroxene (En_{86}) before (b) and after (a) heating. The absorptions located near 1 and 2μm are due to the presence of Fe^{2+} and are not affected by heating. Because this sample contains tremolite as a contaminant, after heating the 3μm band depth decreases, due to the loss of physically adsorbed H_2O, and the relatively narrow absorption located near 2.75μm, due to OH^-, is more pronounced.

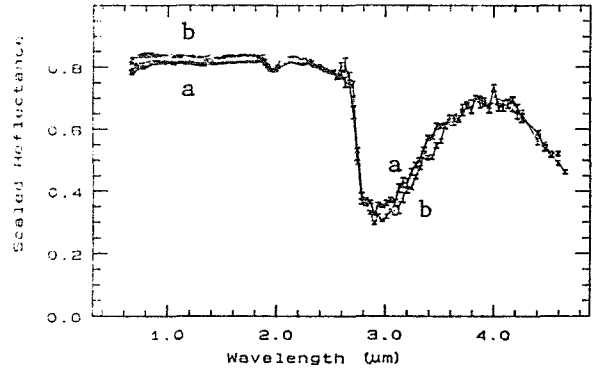

Figure 3. Reflectance spectra of plagioclase (An_{55}) before (b) and after (a) heating. The spectra of this mineral exhibit the strongest 3μm of all the mafic silicates due to the presence of fluid inclusions in the sample. Since the H_2O in the fluid inclusions is not easily lost upon heating, the minor spectral changes indicate solely the loss of physically adsorbed H_2O.

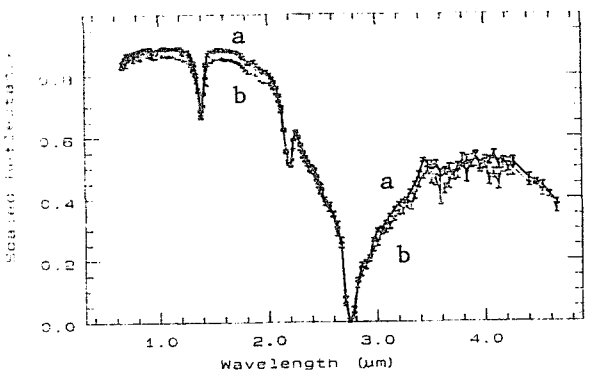

Figure 4. Reflectance spectra of kaolinite ($Al_2Si_2O_5(OH)_4$) before (b) and after (a) heating. The spectra exhibit OH^- vibrational absorptions near 1.4, 2.2, and 2.75μm. The spectral changes due to heating indicate the loss of physically adsorbed H_2O.

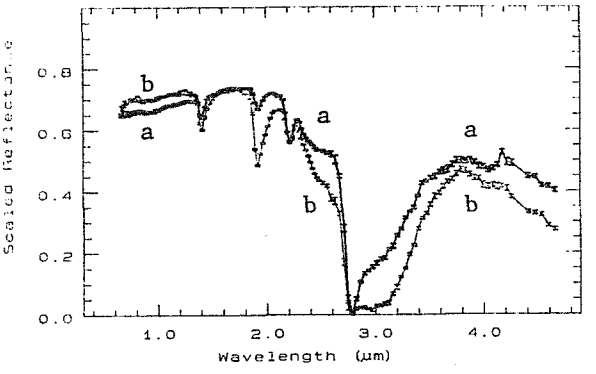

Figure 5. Reflectance spectrum of Na-Montmorillonite (nominally, $(½\ Ca,Na)_{0.7}(Al,Mg,Fe)_4[(Si,Al)_8O_{20}](OH)_4\ nH_2O$) before (b) and after (a) heating. Before heating the spectrum of this sample exhibits absorptions due to H_2O near 1.9 and 3.0μm and OH^- near 1.4 and 2.2μm. After heating the spectrum exhibits the effects of removing physically adsorbed, and potentially interlayer H_2O, by the reduced intensity of the 1.9 and 3.0μm bands and the OH^- band near 2.8μm is more pronounced.

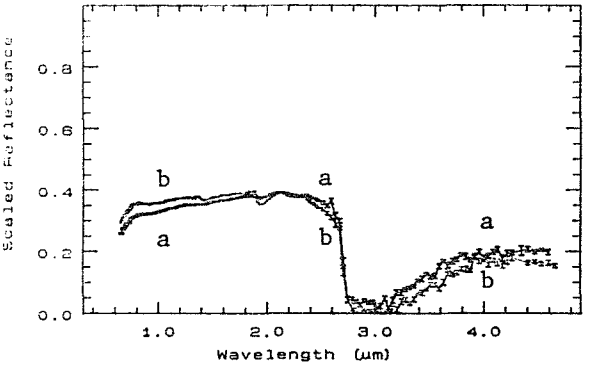

Figure 6. Reflectance spectrum of palagonite before (b) and after (a) heating. Before heating the spectrum of this sample exhibits a weak 1.9μm band and a strong 3μm band both indicative of H_2O. After heating the spectrum exhibits a very weak 1.9μm band implying removal of H_2O, yet the 3μm band remains prominent. This spectral behavior is very reminiscent of the plagioclase.

SPECTRAL EFFECTS OF DEHYDRATION ON PHYLLOSILICATES; E.A. Bruckenthal and R.B. Singer, Planetary Geosciences Division, Hawaii Institute of Geophysics, 2525 Correa Road, Honolulu, HI 96822

INTROUCTION Six phyllosilicates have been progressively dehydrated under controlled conditions in an effort to study the spectral effects of their dehydration. Justification for the study may be found in both terrestrial and planetary soil science applications. For example, we know through spectroscopic observations of Mars and several asteroids[1,2] that their surfaces contain ubiquitous hydrated silicates. However, due to the anhydrous nature of the extraterrestrial environment, one would not expect these soils to exist in the same hydration states as they do on Earth. Furthermore, spectroscopy provides a tool which probes the internal structures of these clays as they undergo changes. Thus, the spectra obtained at each level of hydration provide information which may be used in future spectroscopic observations of other planets, as well as a data set which complements the existing body of terrestrial soil knowledge.

SAMPLES AND EXPERIMENTAL METHODS Samples were chosen to represent a range of both crystalline and X-ray amorphous soil components. The four crystalline clays include dioctahedral and trioctahedral endmembers of t-o and t-o-t type clays, as well as species characterized by extensive substitutions in their tetrahedral and octahedral layers. Serpentine, $Mg_3Si_2O_5(OH)_4$, represents an endmember (negligible cationic substitution) tricotahedtal t-o clay, while talc, $Mg_3Si_4O_{10}(OH)_2$, is an endmember trioctahedral t-o-t clay. Ca-montmorillonite was chosen as a dioctahedral smectite, while saponite represents the trioctahedral smectite group. Both smectites have the general formula, $(½\ Ca,Na)_{0.7}(Al,Mg,Fe)_4(Si,Al)_8O_{20}(OH)_4\ nH_2O$.

The final two clays studied are Big Island palagonites -- X-ray amorphous, low temperature alteration products of basaltic volcanic glass. The two differ in that the Pahala Ash is more completely weathered, more incipiently crystalline, and significantly more hygroscopic than the Mauna Kea palagonite.

Each clay was ground and dry-sieved to <38 μm, and then equilibrated in a high humidity (>95%) environment. An environment chamber which allows spectrophotometric observations at non-ambient conditions was used in conjunction with a custom-built furnace. Each sample was heated to eight elevated temperatures (120, 160, 200, 250, 300, 400, 600, and 750° C.) in an inert, dry nitrogen atmosphere. Spectra were obtained at room temperature and after heating to each of the aforementioned target temperatures.

BACKGROUND In order to understand the nature of clay dehydration, a brief introduction to the different species of hydration is helpful. The four species of hydration which exist include three forms of adsorbed water and one form of hydroxyl ions.

The first of three types of adsorbed water is found in pores, on surfaces, and around the edges of particulate samples of all clay minerals, regardless of type. It consists of loosely bound H_2O molecules held only by Van der Waals' forces and is called *physically adsorbed water*.

The second and third forms of adsorbed water, found almost exclusively in t-o-t layer clays, refer to those H_2O molecules which are bound more tightly to a clay mineral than physically adsorbed water. Although capable of being removed at low temperatures, these molecules are bound to the basal surfaces of a clay by forces of a more electrostatic nature. This species will be referred to here as *surface-bound water*. Often surface-bound water grades into physically adsorbed water at some distance from the basal surface.

Very similar and difficult to distinguish from surface-bound water are those H_2O molecules bound to cations which have been adsorbed between layers in smectite clays. A distinction must be made between this *cation-bound water* and surface-bound water because researchers have shown that cation-bound water is held much more tightly, and driven off at much higher temperatures, than surface-bound water[3,4].

The final form of hydration consists of those OH molecules which comprise portions of the clay structure through their presence in an octahedral layer. This species of hydration will be referred as *structural hydroxl ions*, and its loss from a clay as dehydroxlation.

INTERPRETATION The plots which follow illustrate spectral changes observed with increasing temperature for three of the six samples investigated. Only those temperatures at which significant changes occurred are shown. Numbers in bold type represent the temperatures associated with each sample.

Talc

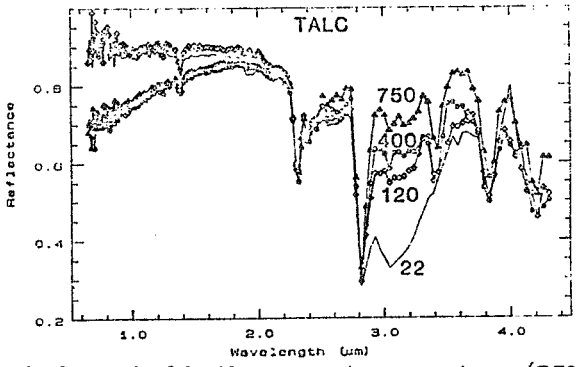

Spectral features to be noted in the room temperature (22° C.) spectrum above include the following: 1) a sharp, 1.4 μm band due to both OH and H_2O 2) a broader 1.9 μm H_2O band 3) a broad, shallow 2.2 μm cation-OH feature 4) very sharp, well-defined 2.3 and 2.4 μm Mg-OH bands 5) a strong OH fundamental near 1.8 μm, and 6) a broad, deep 3.1 μm H_2O absorption. Upon heating to 120°C., physically adsorbed water contributing to the 1.9 and 3.1 μm bands is driven off, dramatically lessening the strength of both features. By 400°, more tightly held water molecules have begun to leave the structure, reducing 1.4 μm band depth, completely eliminating the 1.9 μm band, and further reducing the 3.1 μm band. Limited cationic substitution has attracted surface and/or cation bound water molecules to a few interlayer sights, and sufficient kinetic energy is now available to begin removing them. Most likely some of this water is reincorporated back into the structure to cause the oxidation which is apparent as a slope change between 0.65 and 1.8 μm. Upon heating through 750° C., talc continues losing its most tightly bound H_2O, as shown by the continued decrease in 3.1 μm band strength.

Montmorillonite

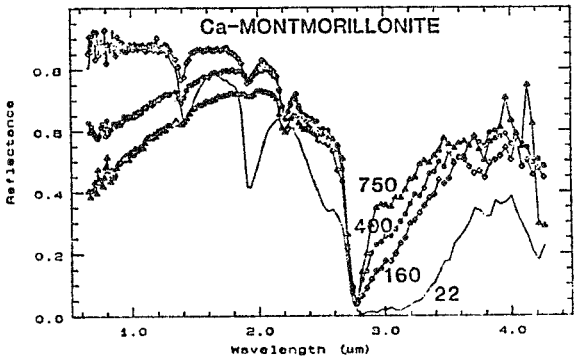

Salient spectral features in the room temperature smectite spectrum include the following: 1) a deep, asymmetric 1.4 μm OH + H_2O band, 2) a deep asymmetric 1.9 μm absorption, 3) a 2.2 μm Al-OH band, and 4) complete saturation in the region between ~2.75 and 3.2 μm, which includes both OH and H_2O fundamentals. As physically adsorbed water is lost through 160°, both the 1.4 μm and 1.9 μm bands decrease in strength, narrow and become more symmetric. This occurs because the molecules which contribute to their absorptions are in more well-defined crystalline sites. When

the water bands decrease in strength, they are less able to mask other absorptions, and the apparent 2.2 μm band increase is due to this effect. At longer wavelengths, both the 2.9 and 3.1 μm H_2O fundamental bands lessen dramatically, eliminating saturation in the 3 μm region. Loss of tightly held, surface-bound water by 400° contributes to a decrease in band strength at 1.4, 1.9, 2.9, and 3.1 μm. Very likely the increased slope between 0.6-1.8 μm is due to cation oxidation by some of this released water. By 750° structural reorganization begins to occur. The 1.4 μm band is now both broad and very weak, suggesting a disruption of sites in which OH is commonly located as well as its loss from the clay. The miniscule 1.9 μm feature indicates that little H_2O remains, a conclusion substantiated by the weak 2.9 and 3.1 μm bands. Incipient structural reorganization is also indicated by a broadening of the 2.2 μm Al-OH absorption.

Palagonite

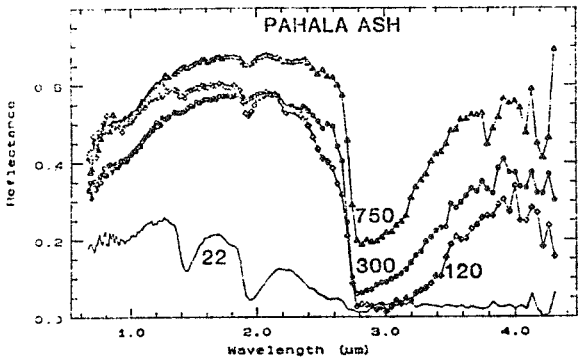

At room temperature the hygroscopic palagonite displays the following four features: 1) a broad Fe^{+2} electronic transition band centered near 1 μm, suggesting the presence of some short range crystalline order, 2) a deep, asymmetric 1.4 μm H_2O + OH band, 3) a deep, asymmetric 1.9 μm H_2O band on which the resolution of a 1.7 μm shoulder feature is evidence for *extreme* hydration, and 4) complete saturation of the 2.7-4.3 μm region. Heating to 120° drives off the most loosely bound water molecules, decreasing the strength of the 1.4 and 1.9 μm features and easing saturation between 3.1-4.3 μm. Lessening these H_2O features enables a previously masked 2.2 μm Al-OH band to be seen. More water, and loosely held OH molecules are driven off by 300°. The lack of a well defined crystalline network eliminates the distinction of *structural* OH ions; hydroxyls are held much less tightly and may be driven off at lower temperatures than in crystalline clays. Removal of some hydroxyls eliminates the 1.4 μm band and lessens the 2.75 μm band. However, the distinct 2.2 μm Al-OH feature indicates that tightly bound hydroxyl ions are still held. By 400° loss of these tightly held hydroxyls begins, indicated by reduction and broadening of the 2.2 μm band and continued reduction of the 2.75 μm band. More H_2O is also lost by this temperature, and lessening 1.9, 2.9, and 3.1 μm bands reflect this change. The trends noted above continue through 750°.

REFERENCES: 1) Feierberg, M.A., Lebofsky, L.A., and H.P. Larson (1981) Spectroscopic evidence for aqueous alteration products on the surfaces of low-albedo asteroids, Geoch. Cosmoch. Acta 45, 971-981. 2) Pimentel, G.C., Forney, P.B., and K.C. Herr (1974) Evidence about hydrate and solid water in the Martian surface from the 1969 Mariner infrared spectrometer, JGR 79, No. 11, 1623-1634. 3) Mackenzie, R.C., *The Differential Thermal Investigation of Clays*, Mineralogical Society, London, 1957, p. 144-145. 4) Grim, R.E., *Clay Mineralogy*, 1st ed., McGraw-Hill, New York, 1953, p. 176-177.

ACKNOWLEDGEMENTS: This research was funded by NASA Planetary Geology and MDAP grant NSG-7590.

Studies of the scattering/absorption properties of minerals

Roger N. Clark

U.S. Geological Survey, Mail Stop 964, Box 25046, Federal Center
Denver, CO 80225

An understanding of the scattering and absorption properties of a planetary regolith is important for understanding remote sensing data from spacecraft and earth-based telescopes. One way to study these properties is to measure the reflectance of powdered minerals and mineral mixtures in the laboratory. This has been and continues to be a major task of many laboratories. However, the possible combinations of mineral mixtures, grain sizes, and viewing geometries are virtually infinite. Another approach to this study is by radiative transfer models. The Hapke reflectance theory (Hapke, 1981) is one such theory that has been verified by several investigators (e.g. Clark et al., 1986 and references therein). Using the Hapke theory, the scattering and absorption properties can be quickly computed as a function of wavelength, grain size, and viewing geometry for pure minerals as well as mineral mixtures.

Reflectance spectra were computed for water ice and ammonia ice mixtures as functions of weight fraction, grain size, and viewing geometry to simulate possible outer-solar-system satellite surfaces. This exercise has shown several interesting aspects of scattering and absorption from a particulate surface that have not been previously realized. As might be expected, as the grain size of a pure water ice or pure ammonia ice is increased from very small ($< 1\mu m$), the absorptions increase in depth. However, at some grain size, depending on the fundamental band strength, the bands become saturated and their apparent depth decreases. This band saturation is described in Clark (1981) for water ice.

In a mineral mixture, if the grain sizes are held constant and the weight fractions are varied, the observed absorption bands change along with the weight fraction. As the weight fraction increases, the apparent absorption bands for that species tend to become more apparent (Figure 1). However, if the grain sizes are varied and the weight fraction is held constant, the apparent absorption bands still vary (Figure 2)! This is because the photons are encountering grains according to the projected surface area (of the grain), so either weight-fraction or grain-size changes will affect the relative surface area encountered. The implications of this fact are profound for laboratory studies of mineral mixtures. A simple weight-fraction series is not adequate for deriving a calibration curve of abundance. The calibration curve depends strongly on the grain sizes. Because of band saturation, the relative band depths are not the same at different grain sizes when the grain-size ratios (of minerals in a mixture) are held constant. The only solutions are either to measure all possible grain sizes and weight fractions to derive calibration curves, or to use a radiative transfer model like the Hapke reflectance theory.

As a next step in the understanding of scattering in a particulate surface, viewing geometry was added to the model calculations. It was found that viewing geometry had only a small effect on the reflectance

levels and observed band depths. Generally, it was found that extreme viewing geometry ranges (incidence and emission angles near 80°) were similar to changes in grain size of only factors of two or three.

Everyday experience gives a qualitative understanding of viewing geometry effects on a multitude of objects; a colored object or a typical powdered mineral can be held at different orientations and the colors do not change significantly. However, if two powders are mixed or ground to smaller grain sizes, the colors can change dramatically, even if the viewing geometry is not changed.

In conclusion, reflectance spectra of planetary surfaces are most affected by the weight fraction and grain sizes of the minerals in the surface. The reflectance can range from 1.0 to about 0.01 by changing the grain size or weight fraction, a factor of 100. Viewing geometry changes the reflectance by about 25% or less.

References

Clark, R.N., Water Frost and Ice: The Near-Infrared Spectral Reflectance 0.65-2.5 μm, *J. Geophys. Res.*, **86**, 3087-3096, 1981.

Clark, R.N., K.S. Kierein, and G.A. Swayze, Experimental Verification of the Hapke Reflectance Theory 1: Computation of Reflectance as a Function of Grain Size and Wavelength Based on Optical Constants: *J. Geophys. Res.* submitted, 1986.

Hapke, B., Bidirectional reflectance spectroscopy 1. Theory. *J. Geophys. Res.* **86**, 3039-3054, 1981.

Figure Captions

Figure 1. The reflectance spectra for mixtures of water and ammonia ice are shown for a constant grain size. As the weight percent of ammonia is increased, the ammonia bands (e.g. the 2.2-μm bands) become more prominent.

Figure 2. The reflectance spectra are shown for 70-weight-percent water ice and 30-weight-percent ammonia ice mixtures with varying grain sizes. As the grain size of the ammonia ice increases, the ammonia bands become smaller and the spectrum appears more like that of water ice.

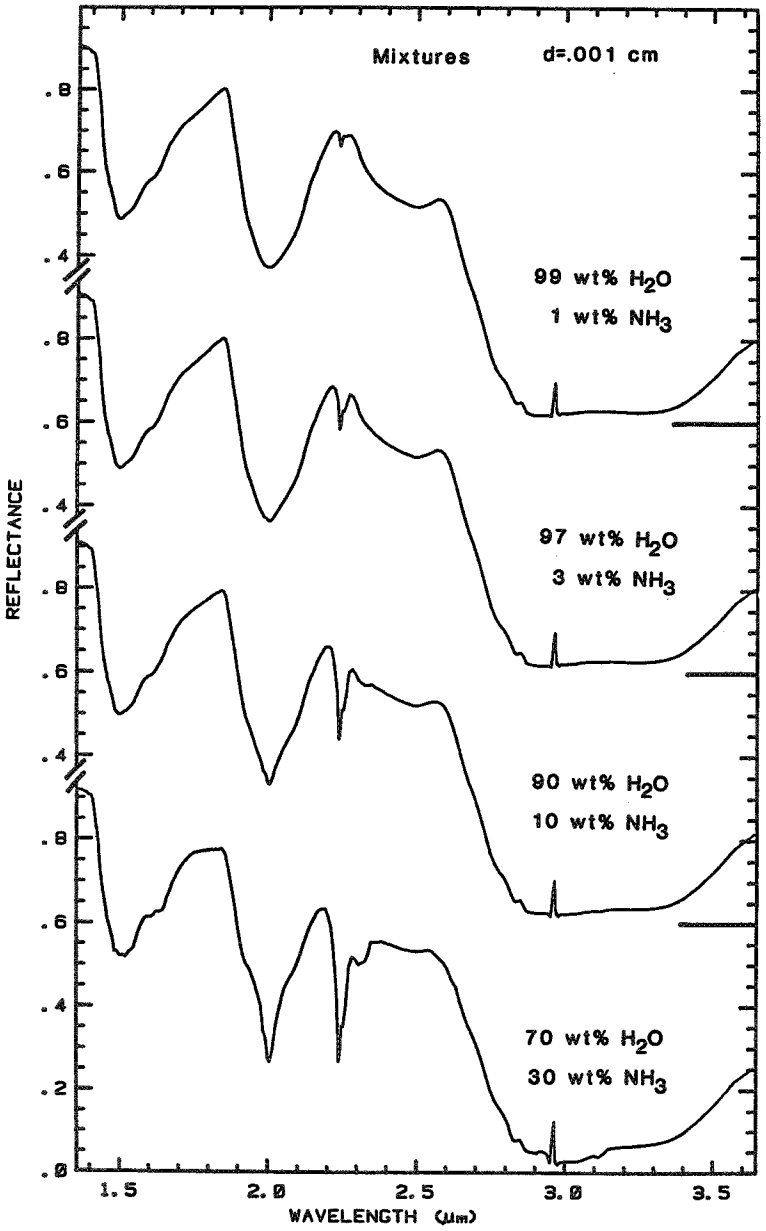

Figure 1

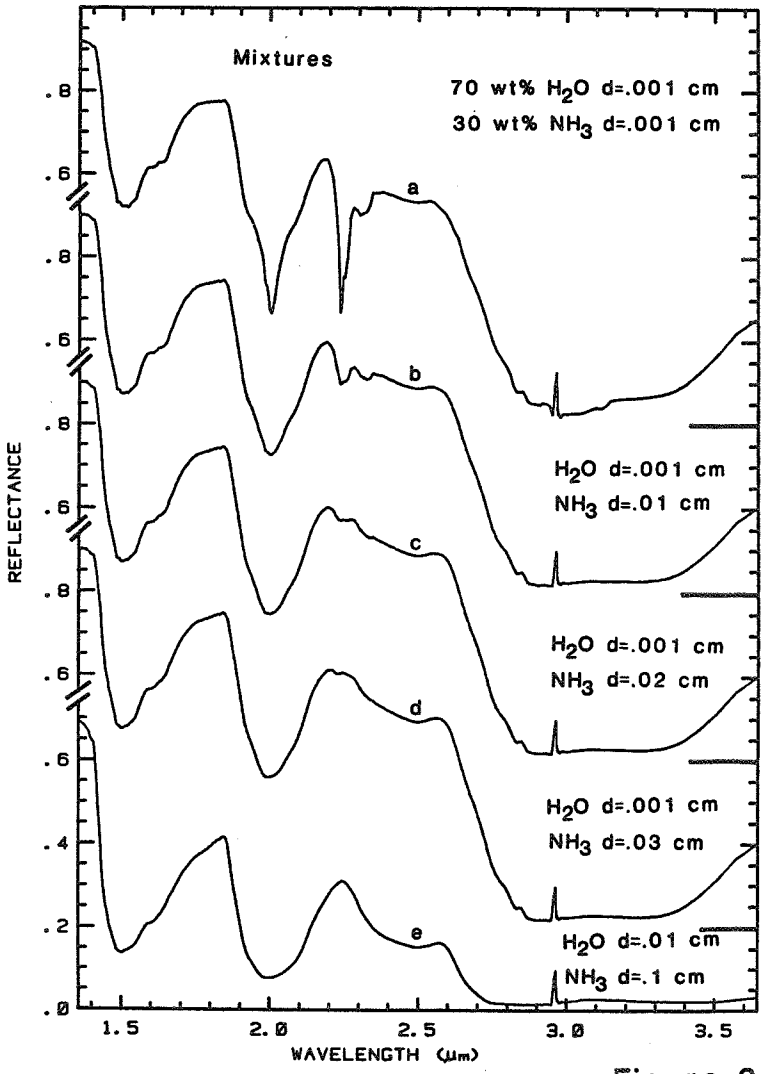

Figure 2

MID-INFRARED SPECTROSCOPIC INVESTIGATION W-16, 305 10-37915

John W. Salisbury, U.S. Geological Survey; Louis Walter, Goddard Space Flight Center, and Norma Vergo, U.S. Geological Survey

This research effort includes: 1) the development of new instrumentation to permit advanced measurements in the mid-infrared (2.5-25.0 μm) region of the spectrum; 2) the development of a spectral library of well-characterized mineral and rock specimens for interpretation of remote sensing data; and 3) cooperative measurements of the spectral signatures of analogues of materials that may be present on the surfaces of asteroids, planets or their moons.

New Instrumentation: Although bidirectional reflectance data in the 3-5 μm region of the spectrum can be used directly to predict the spectral behavior of a low temperature (less than 5C°) remotely sensed surface, emittance begins to dominate over reflectance at higher temperatures or longer wavelengths. Then, directional spectral emittance (i.e. in the direction of the observer) dominates. In order to predict the spectral behavior of remotely sensed surfaces under these conditions, it is necessary to measure directional hemispherical reflectance (Nicodemus, 1965).

A close approximation of directional hemispherical reflectance can be determined with an integrating sphere. The inside of the sphere must, however, be coated with a diffusely reflecting gold surface in order to function properly in the mid-infrared. We have contracted for the construction of such a sphere, which is to be delivered in November and will undergo its first tests in December, 1986. This sphere will provide the first spectral reflectance data of minerals and rocks from which directional spectral emittance can be confidently predicted.

More detailed, though much more time-consuming, measurements of directional reflectance can be made with a bidirectional reflectance device with adjustable angles of incidence and reflectance. Such a device is currently being designed at Goddard Space Flight Center and is due for completion in April, 1987. This device should make possible confirmation that the spectral contrast of a reflectance measurement at zero phase angle will be unaffected by particle size, as predicted by Salisbury and Eastes (1985). If so, reflectance measurements using lasers from orbiting spacecraft will avoid the ambiguities inherent in measurements of the spectral emittance of materials of different particle sizes.

Spectral Library: A library of mineral spectra has been started using a fixed angle bidirectional reflectance attachment. Relatively pure minerals, generally obtained from the Smithsonian collection, were crushed and further purified by hand picking. They were then checked for purity and further characterized by petrographic microscope (L. Walter), X-ray diffraction (N. Vergo), and electron microprobe (L. Walter) techniques. Thus, all samples studied have high purity so as to avoid spectral anomalies, and have been well characterized both mineralogically and chemically.

So far, more than 100 mineral samples have been processed and approximately 87 selected for spectral signature measurements (J. Salisbury). For each sample, the reflectance spectrum of the solid material is recorded, preferably in different crystallographic orientations, and then reflectance spectra are obtained of 74-250 μm and 0-74 μm size ranges. Finally, a small portion of the 0-74 μm size range is ground to less than 2 μm and incorporated into a KBr pellet for a transmittance measurement.

The procedure described above yields a variety of spectral data appropriate for different observational conditions or for surfaces of different particle size ranges. One important result of these early measurements is to show that quite different spectral features must be measured in remote sensing of coarse and fine particulate surfaces. This is illustrated in Figures 1 and 2, which show reflectance spectra of olivine (11% forsterite) from 4600 cm^{-1} (2.17 μm) to 400 cm^{-1} (25.0 μm). In both spectra a less than 30 μm particle size range was used, but firmly packed in Figure 1 and sifted in Figure 2. Packing increases the effective particle size (Salisbury & Eastes, 1985), resulting in prominent reflectance peaks (reststrahlen bands) associated with the molecular vibration bands. Of special interest is the double peak due to the Si-O stretching vibration between 1000 cm^{-1} (10 μm) and 800 cm^{-1} (12.5 μm), because it is in the region of terrestrial atmospheric transparency. A reflectance spectrum of the same olivine sample sifted into the sample holder (Fig. 2) shows that this reststrahlen band has greatly decreased in spectral contrast due to the increased porosity (Salisbury & Eastes, 1985). It also shows a completely new spectral feature in the form of the broad peak centered about 700 cm^{-1} (14 μm). This peak is not directly related to the molecular vibration bands, but is instead associated with transparent behavior due to the low absorption coefficient between the stretching and bending vibrations at longer wavelength (Salisbury et al, 1986). We have been able to show, however, that the wavelength of this transparency peak is just as diagnostic of composition as are those of the reststrahlen bands. Thus, compositional remote sensing of a fine particulate surface using the transparency peak can be accomplished despite the loss of spectral contrast of the reststrahlen bands that make them difficult to detect (Salisbury and King, in preparation).

Cooperative Efforts: Several colleasuges have an interest in the mid-infrared spectral signatures of meteorites, proton bombarded frost residues and even more exotic materials that may be analogues of materials present on the surfaces of asteroids, planets or their moons. We encourage the use of our facility to obtain spectra of these analogues for comparison with telescopic spectral data. To date, we have had such cooperative efforts with Dale Cruikshank of the Un. of Hawaii; Tom Jones, a graduate student of John Lewis' at the Lunar and Planetary Laboratory of the Un. of Arizona, Tucson; and Trude King of the University of Hawaii and the USGS, Denver.

References

Nicodemus, F.E., 1965, Directional reflectance and emissivity of an opaque surface: Applied Optics, v 4, p. 767-773.

Salisbury, J.W. and Eastes, J.W., 1985, The effect of particle size and porosity on spectral contrast in the mid-infrared: Icarus, v 64, p. 586-588.

Salisbury, J.W., Hapke, Bruce, and Eastes, J.W., 1986, Usefulness of weak bands in mid-infrared remote sensing of particulate planetary surfaces: Journal of Geophysical Research (in press).

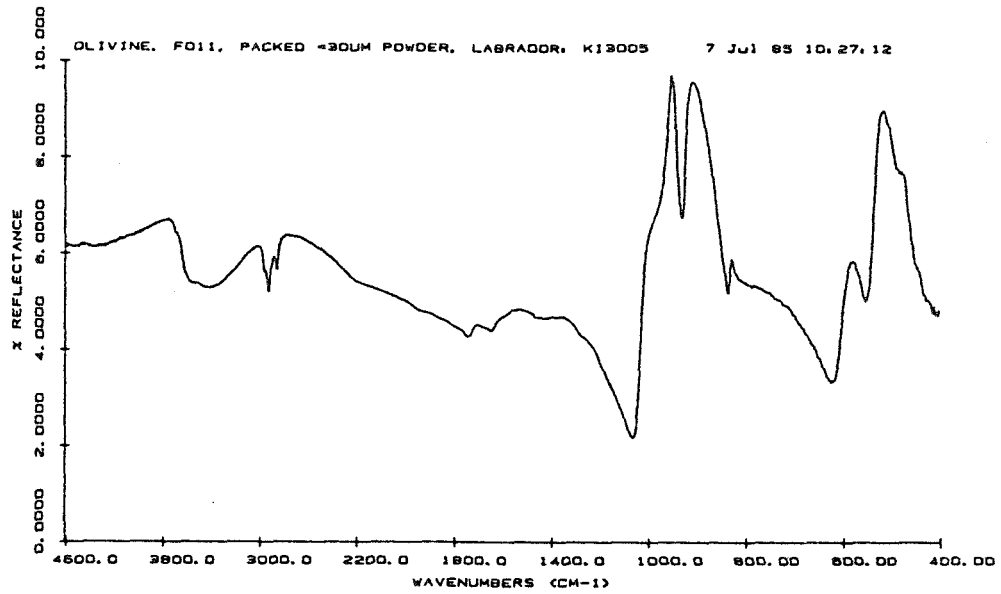

Figure 1. Bidirectional reflectance spectrum of packed olivine powder (less than 30 um).

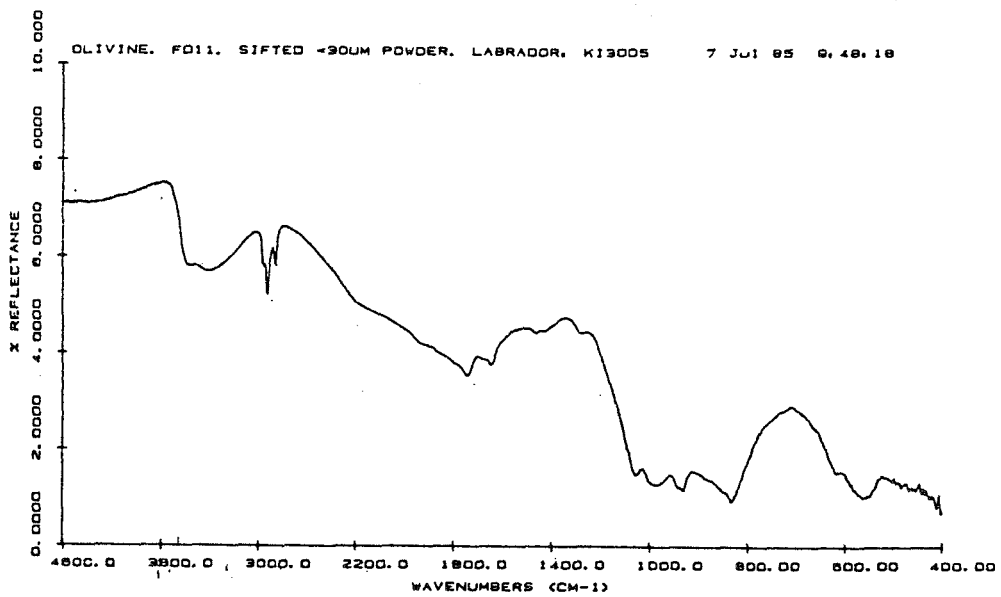

Figure 2. Bidirectional reflectance spectrum of sifted olivine powder (less than 30 um).

THERMAL-INFRARED SPECTRAL OBSERVATIONS OF GEOLOGIC MATERIALS IN EMISSION

Philip R. Christensen and Sharon J. Luth, Department of Geology, Arizona State University, Tempe, AZ 85287.

Thermal-infrared spectroscopy provides a powerful tool for determining the composition of planetary surface materials. Virtually all silicates, carbonates, sulfates, phosphates, oxides, and hydroxides have thermal-infrared spectral features associated with the fundamental vibrational motions of the major ionic groups in the crystal structure. The vibrational frequency of these motions, and therefore the wavelength of energy absorbed, varies with both the ionic composition and crystal lattice structure. This variability provides a direct means of identifying the composition of many geologic materials, and for interpreting the crystal structure, and therefore the mineralogy of these materials. Because rocks are composed of mixtures of mineral phases, this technique also permits the petrology of the rocks and soils exposed at the surface to be determined.

The Thermal Emission Spectrometer (TES) instrument is a thermal-infrared spectrometer that is currently being developed for use on the Mars Observer mission. To support this investigation, a series of laboratory measurements of candidate martian materials has been initiated. These observations are intended to characterize the spectral properties of geologic materials in emission, and to study a variety of processes and surface modifications that may influence or alter the spectra of primary rock materials.

Pioneering studies of the thermal-infrared absorption characteristics of minerals were have been performed (Lyon, 1962, 1964; Farmer, 1974; Hunt and Salisbury, 1974, 1975, 1976). The vast majority of these studies have measured the spectral properties of materials in either transmission or reflection, whereas remote sensing observations of planetary surfaces measure the amount of energy emitted. In theory, reflectance measurements can be related to emission measurement assuming Kirchoff's law, where the fraction of emitted (ε) and reflected (R) energy are related by:

$$\varepsilon = 1 - R$$

However, this relationship is only strictly valid for measurements of the total hemispherical reflection and emission from a mat surface, rather that the reflection from a polished surface as is often measured (Hunt and Vincent, 1968).

In the studies reported here, we have acquired thermal-infrared spectra of materials in emission. These observations were acquired using the prototype TES brassboard spectrometer. This instrument is a Fourier transform interferometer, which covers the spectral range from 7 to 18 μm at a spectral resolution of 5.5 cm^{-1} (0.055 μm at 10 μm wavelength). This resolution is approximately a factor of two better than will be achieved with the Mars Observer instrument, allowing the detailed spectral properties to be investigated and interpreted. The instrument is controlled, the spectra are acquired, and the data are processed and analyzed using an IBM PC-XT microcomputer.

To acquire a spectra the sample is heated in a temperature-controlled oven for 4-6 hours to achieve a uniform temperature throughout the sample. At present, only solid rock samples have been investigated, in order to minimize the effects of temperature gradients within the samples, which are known to cause uncertainties in the observed spectral

properties (Logan and Hunt, 1970; Logan et al., 1975). The samples are removed from the oven and their spectra acquired within 20 sec to again minimize the effects of temperature gradients. Spectra are also acquired of a very accurately controlled blackbody reference surface, and of liquid nitrogen to determine the instrument response and background emission respectively. This suite of observations permits absolute determination of the emissivity of the sample, provided that the kinetic temperature of the sample is known. Because of the difficulty in measuring and interpreting the surface temperature of the sample, the temperature is determined by fitting a blackbody curve to the observed spectra. This technique is illustrated in Figure 1. The Michelson mirror position is accurately determined using a visible light interferometer to count the fringe patterns of a neon light source. This standard technique permits an absolute wavelength determination to be made that is accurate and repeatable to approximately 0.01 μm at 10 μm. Double-side interferograms are acquired to permit phase offsets and non-linearities in the beamsplitter and interferometer to be removed.

Figure 1a shows the initial spectrum acquired for a quartz crystal, together with the best-fit blackbody curve used to estimate the sample temperature. Figure 1b show the same data after the observed spectrum has been divided by the blackbody to determine the emissivity of the crystal. Figure 2 shows a similar set of spectra taken of a basalt sample returned from the Cima volcanic field in the Mojave desert, California. This sample was acquired from a flow surface contained within a region imaged by the Thermal Infrared Mapping Spectrometer (TIMS) airborne instrument (see Kahle and Goetz, 1983). Figure 3 gives the emissivity of a carbonate sample acquired from within the same TIMS scene.

These spectra confirm that thermal emission spectra contain the same absorption features as have been previously observed in transmission and reflection spectra, and demonstrate the successful utilization of the TES prototype instrument to obtain relevant spectra for analysis of rock and mineral composition.

References

Farmer, V.C. (edt.), 1974, The Infrared Spectra of Minerals, Mineralogical Society, London, 539 pp.

Hunt, G.R., and R.K. Vincent, 1968, The behavior of spectral features in the infrared emission from particulate surfaces of various grain sizes, J. Geophys. Res., 73, 6039-6046.

Hunt, G.R., and J.W. Salisbury, 1974, Mid-infrared spectral behavior of igneous rocks, Environ. Res. Paper 496-AFCRL-TR-74-0625, 142 pp.

Hunt, G.R., and J.W. Salisbury, 1975, Mid-infrared spectral behavior of sedimentary rocks, Environ. Res. Paper 510-AFCRL-TR-75-0256, 49 pp.

Hunt, G.R., and J.W. Salisbury, 1976, Mid-infrared spectral behavior of metamorphic rocks, Environ. Res. Paper 543-AFCRL-TR-76-0003, 67 pp.

Kahle, A.B., and A.F.H. Goetz, 1983, Mineralogic information from a new airborne thermal infrared multispectral scanner, Science, 222, 24-27.

Logan, L.M. and G.R. Hunt, 1970, Emission spectra of particulate silicates under simulated lunar conditions, J. Geophys. Res., 75, 4983-5005.

Logan, L.M., G.R. Hunt, and J.W. Salisbury, 1975, The use of mid-infrared spectroscopy in remote sensing of space targets, in Infrared and Raman Spectroscopy of Lunar and Terrestrial Minerals, C. Karr, (ed.), Academic Press.

Lyon, R.J.P., 1962, Evaluation of infrared spectroscopy for compositional analysis of lunar and planetary soils, Stanford Research Inst. Final Report Contract NASA 49(04).

Lyon, R.J.P., 1964, Evaluation of infrared spectrophotometry for compositional analysis of lunar and planetary soils: Part II: Rough and powdered surfaces, NASA Contractor Report CR-100, 172 pp.

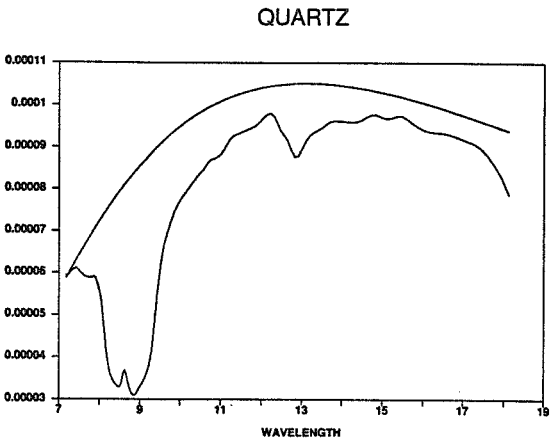

Fig. 1a

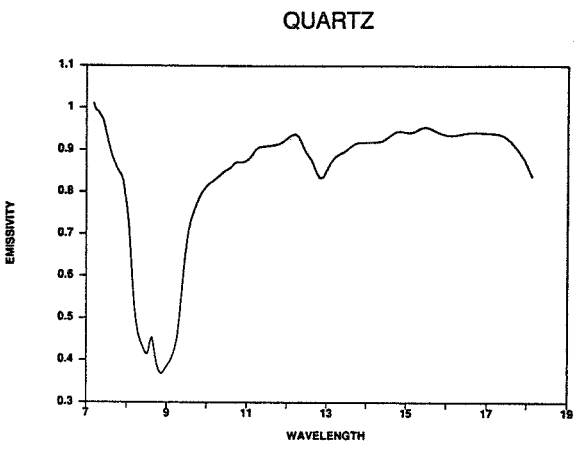

Fig. 1b

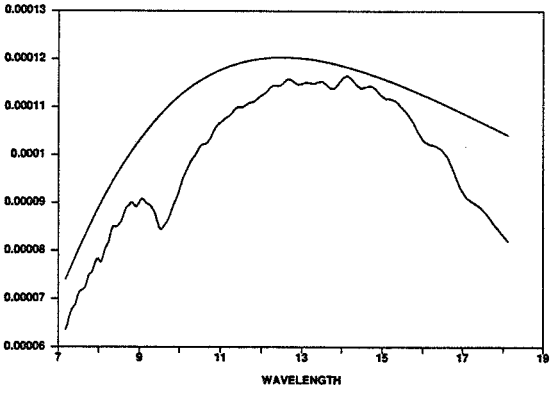

Fig. 2a

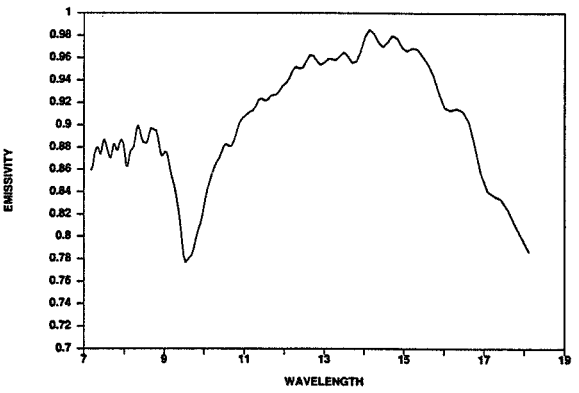

Fig.2b

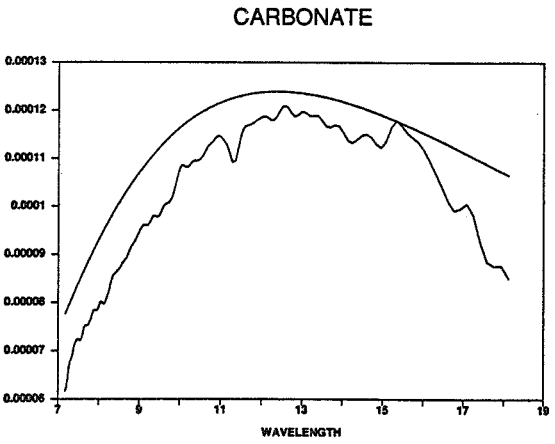

Fig. 3a

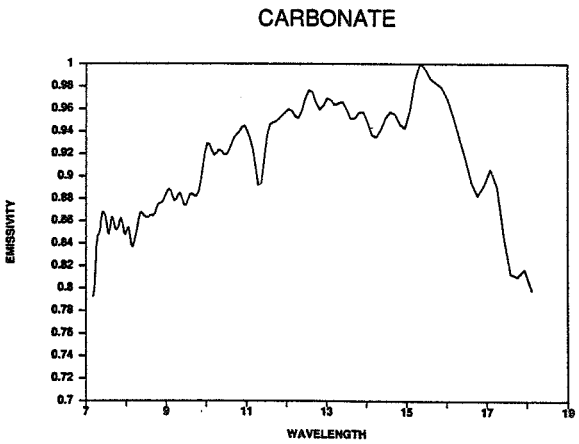

Fig. 3b

Bidirectional Reflectance Properties of Planetary Surface Materials

B. Buratti, W. Smythe, R. Nelson, V. Gharakhani (JPL/Caltech), B. Hapke (U. of Pittsburgh)

The JPL spectrogoniometer is capable of measuring the bidirectional reflectance properties of planetary surface materials for arbitrary viewing geometries including small phase angles (Smythe et al., 1986a,b). These measurements depend on the textural characteristics of the regolith, particularly its packing state, and the albedo of the surface, which dictates the degree of multiple scattering. In general, porous, dark surfaces should exhibit the largest opposition surges. Our laboratory measurements on the JPL spectrogoniometer over the past year have concentrated on separating the effects of surficial texture and albedo. Figure 1 (Smythe et al.) for example, which represents a comparison of compacted and fluffy basalt, demonstrates that if all other factors such as normal reflectance and composition are equal, less densely packed surfaces exhibit more sharply peaked phase curves near opposition.

However, dark, porous surfaces are not the only ones with large opposition effects. Although very dark materials (e.g., carbon black) exhibit large surges, our measurements of compact barium sulfate show significantly non-linear increases in intensity, similar to, though somewhat smaller than the large surges exhibited by very dark materials (e.g. carbon black).

The range of materials measured over the past year include charcoal, several types of basalt, barium sulfate, sulfur, sugar, magnesium oxide, several clays, and halon.

Understanding the opposition effect requires a threefold attack: laboratory measurements, the comparison of these measurements with remote sensing observations, and the development of a theoretical model to describe both sets of data. We have extended our comparisons of laboratory measurements to remote sensing data. Figure 2 shows a comparison of IUE observations of Io with our measurements of fluffy basalt (~90% void space) and a theoretical model. The UV geometric albedo of Io is comparable to the normal reflectance of our sample. Our results suggest a fluffy regolith for Io, similar to that expected from the deposition of material falling from volcanic plumes. This result contrasts with our finding last year that Europa most likely has a compact surface with about 25% void space.

A number of technical improvements have been made to the goniometer during the past year. First, the quartz beam splitter we utilized to achieve normal incidence and emergence angles introduced unacceptable secondary reflections into our apparatus. A pellicle beam splitter manufactured by Oriel Corporation was substituted with success -- the secondary reflections disappeared entirely. Secondly, we found that mechanical stability is a major controlling factor in achieving small phase angles. We found that sufficiently accurate alignment of the laser, beam splitter, sample holder, and detector could be attained only by completely substituting optical XYZ mounts for optical rails and jacks.

We incorporated a Mie scattering program into our theoretical model (Buratti, 1985). The purpose of this approach was to explain the opposition surges we observed in samples that are not dark and porous. As yet we have not been able to explain these surges as Mie scattering phenomena.

REFERENCES

Buratti, B., 1985. "Application of a Radiative Transfer Model to Bright Icy Satellites." ICARUS, 61, 208-217.

Smythe, W., Buratti, B., Nelson, R., Hapke, B., Gharakhani, V., 1986a. "Reflectance Measurements of Planetary Surface Materials at Small Phase Angles." B.A.A.S., 19, p. 761.

Smythe, W., Buratti, B., Nelson, R., Hapke, B. Gharakhani, V., 1986b. "A Spectrogoniometer for Measuring Planetary Surface Materials at Small Phase Angles." Applied Optics, submitted.

This work was supported by Grant # NAS 7-918.

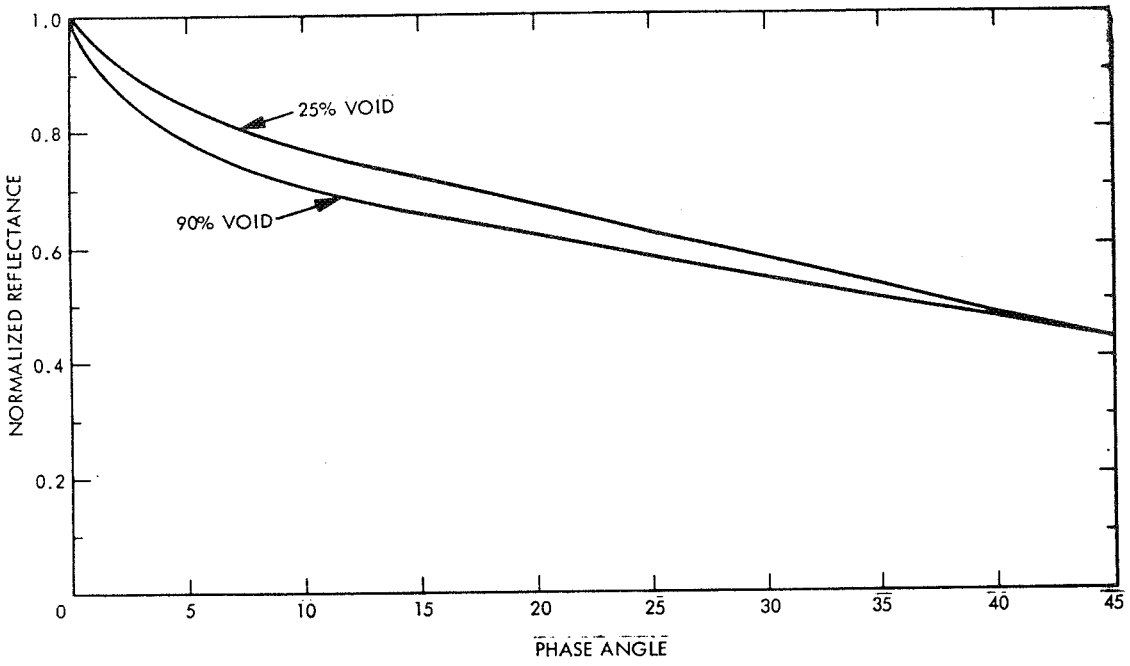

Figure 1. A comparison of fluffy (~90% void) basalt and dense (~25% void) basalt showing that fluffy regoliths exhibit larger opposition surges than dense ones.

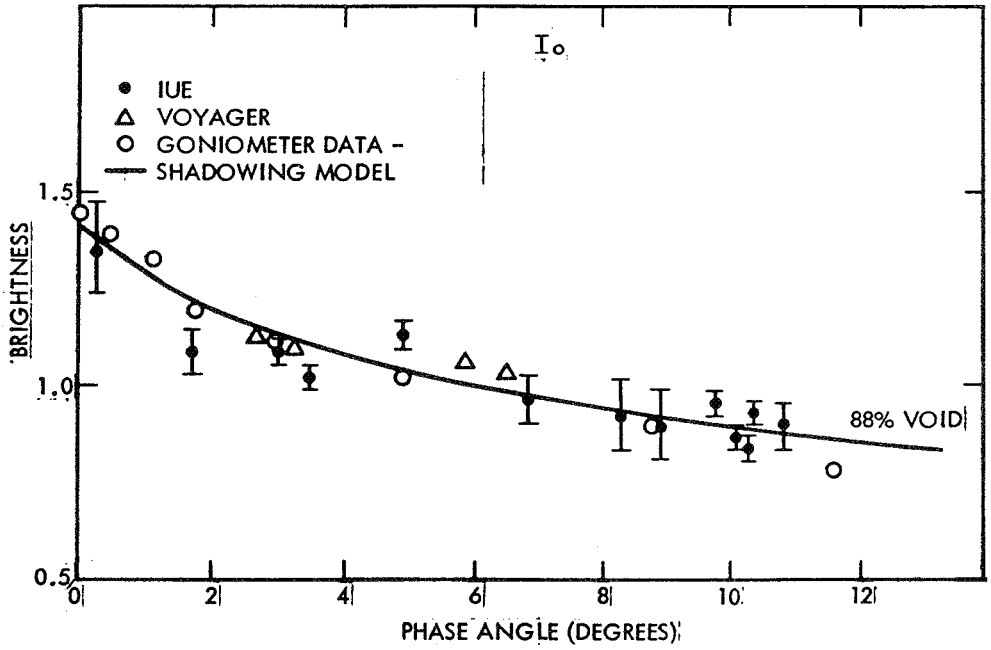

Figure 2. A comparison of fluffy basalt of about 90% void space with remote sensing observation of Io and our theoretical model. Data are normalized to unity at 6 degrees.

Atlas of Reflectance Spectra of Terrestrial, Lunar and Meteoritic Powders and Frosts from 92 to 1800 nm

Jeffrey Wagner, Bruce Hapke and Eddie Wells
Dept. of Geology & Planetary Science, Univ. of Pittsburgh

The reflectance spectra of powdered samples of selected minerals, meteorites, lunar materials and frosts are presented as an aid in the interpretation of present and future remote sensing data of solar system objects. Spectra obtained in separate wavelength regions have been combined and normalized, yielding coverage from 92 to 1800 nm. Spectral features include relfectance maxima in the far UV region produced by valence-conduction interband transitions, and reflectance minima in the near UV, visible and near IR regions, produced by charge transfer and crystal field transitions. Specific maxima and minima are diagnostic of mineral type and compostion; additionally, the minerals present in mixtures such as meteorites and lunar samples can be determined.

DECONVOLUTION OF SPECTRA FOR INTIMATE MIXTURES John F. Mustard, Carle M. Pieters and Stephen F. Pratt, Brown University, Providence, RI 02912.

Visible to near-infrared reflectance spectra of macroscopic mixtures have been shown to be linear combinations of the reflectances of the pure mineral components in the mixture (1). However, for microscopic or intimate mixtures the mixing systematics are in general non-linear (2,3). The systematics may be linearized by conversion of reflectance to single-scattering albedo (w), where the equations which relate reflectance to w depend on the method of data collection (bihemisphericial, directional hemisphericial, or bi-directional reflectance) (4). Several recently proposed mixing models may be used to estimate mineral abundances from the reflectance spectra of intimate mixtures. These models are summarized below and a revised model is presented.

Johnson *et al* (5) present a semi-empirical mixing model based on the work of Hapke (4). They used directional-hemisphericial reflectance data measured in the laboratory and combined pure mineral spectra to fit the spectrum of a mixture using an iterative least squares approach. Although the fits of endmember spectra to mixture spectra were within experimental error, the predictions of mineral abundances were 2% to 30% from the actual values. A more recent approach has been to apply principal components analysis (PCA) to collections of laboratory and lunar spectral data measured as or, converted to directional-hemisphericial reflectance (6,7). This technique may be used to determine the type of mixing (macroscopic *vs.* intimate), identify the potential endmembers from a suite of spectra and estimate the relative proportions of endmembers in a sample. The advantages of PCA are the identification of endmembers with limited *a priori* knowledge and approximate mixing relations between endmembers. The disadvantages are that it requires careful interpretation of the principal axis of variation and the quantitative determination of endmember abundances becomes complex for mixtures containing more than two components.

We have used a similiar curve fitting approach as Johnson *et al* (5) with the following exceptions. We use a non-iterative (*i.e.* linear) least squares approach and the data, measured as bi-directional reflectance with incidence and emergence angles of 30° and 0° were converted to w by the following simplified version of Hapke's (4) equation for bi-directional reflectance

$$r(i,e) = \frac{w}{4(\mu + \mu_0)}(2.2 + H(\mu)H(\mu_0)) \qquad H(\mu) = \frac{1+2\mu}{1+2\mu\gamma} \qquad (1)$$

where r is the measured reflectance, i is the incidence angle, e is the emergence angle $\mu = \cos(e)$, $\mu_0 = \cos(i)$ and $\gamma = (1-w)^{1/2}$. Hapke (4) predicts that for intimate mixtures, the mean single-scattering albedo is related to the single-scattering albedo of each of the components by

$$w(\lambda) = (\sum_i w_i(\lambda) M_i p_i d_i)/(\sum_i M_i p_i d_i) \qquad (2)$$

where M_i, p_i, and d_i are the mass fraction, density and mean particle diameter of each of the i-components in the mixture. The endmember mineral spectra were combined to fit the measured mixture spectra by a single least squares inversion of equation (2). The fractional contribution of each endmember is given by the relative geometrical cross section (f) where $f_j = (M_j/p_j d_j)/(\sum_n M_n/p_n d_n)$ for the jth component of an n-component mixture.

This model was tested with two mixture series composed of 45-75 um particles: an anorthite-enstatite series (two minerals of similiar overall albedo) and an olivine-magnetite series (two minerals with strongly different overall albedos). The quality of the least squares fits as determined by the standard deviation are not greater than 5×10^{-3} in all cases. The standard deviation is determined by curve shape only and is not sensitive to the effects of sample preparation which may result in up to a 2% offset in the measured reflectance curves (5). Shown in Fig. 1 are the observed and least squares fit spectra for the anorthite-enstatite mixture series.

The computed and actual values for f are shown in Figs. 2 and 3. It is evident from Fig. 2 that, for mixtures of comparable albedo, equations (1) and (2) can be used to predict the known fractional abundances to within the experimental error. This degree of accuracy is more than sufficient for the purposes of estimating surface mineral abundances from known or assumed endmembers. The simplified version of Hapke's (4) equation is less satisfactory for mixtures containing low albedo materials as shown in Fig. 3. The model consistently overpredicts the olivine content and underpredicts the magnetite abundance. The systematic deviation of computed from actual values of f for the mixtures containing low albedo minerals suggests that either a more rigorous treatment of Hapke's (4) equations is needed or an empiricial adjustment to equation (1) will allow a more accurate solution to be developed.

These data indicate that the simplified version of Hapke's equation for bi-directional reflectance (equation (1)) may be used to deconvolve reflectance spectra into mineral abundances if appropriate endmembers are known or derived from other techniques. For surfaces that contain a significant component of very low albedo material, a somewhat modified version of this technique will need to be developed. Due to the nature of equation (2) above, this model can also be easily expanded for use with multicomponent mixtures. Since the abundances are calculated using a non-iterative approach, the application of this method is especially efficient for large spectral data sets, such as those produced by mapping spectrometers (NIMS,AVIRIS, *etc.*)

References: (1) Singer, R.B., and McCord, T.B. (1979) *Proc. Lunar Planet. Sci. Conf. 10th.* 1835-1848. (2) Nash, D.B., and Conel, J.E. (1974) *J. Geophys. Res.* **79**, 1615-1621. (3) Singer, R.B. (1981) *J. Geophys. Res.* **86**, 7967-7982. (4) Hapke, B. (1981) *J. Geophys. Res.* **86**, 3039-3054. (5) Johnson, P.E., Smith, M.O., Taylor-George, S., and Adams, J.B. (1983) *J. Geophys. Res.* **88**, 3557-3561. (6) Smith, M.O., Johnson, P.E., and Adams, J.B. (1985) *J. Geophys. Res.* **90**, C797-C804. (7) Johnson, P.E., Smith, M.O., and Adams, J.B. (1985) *J. Geophys. Res.* **90**, ,C805-C810.

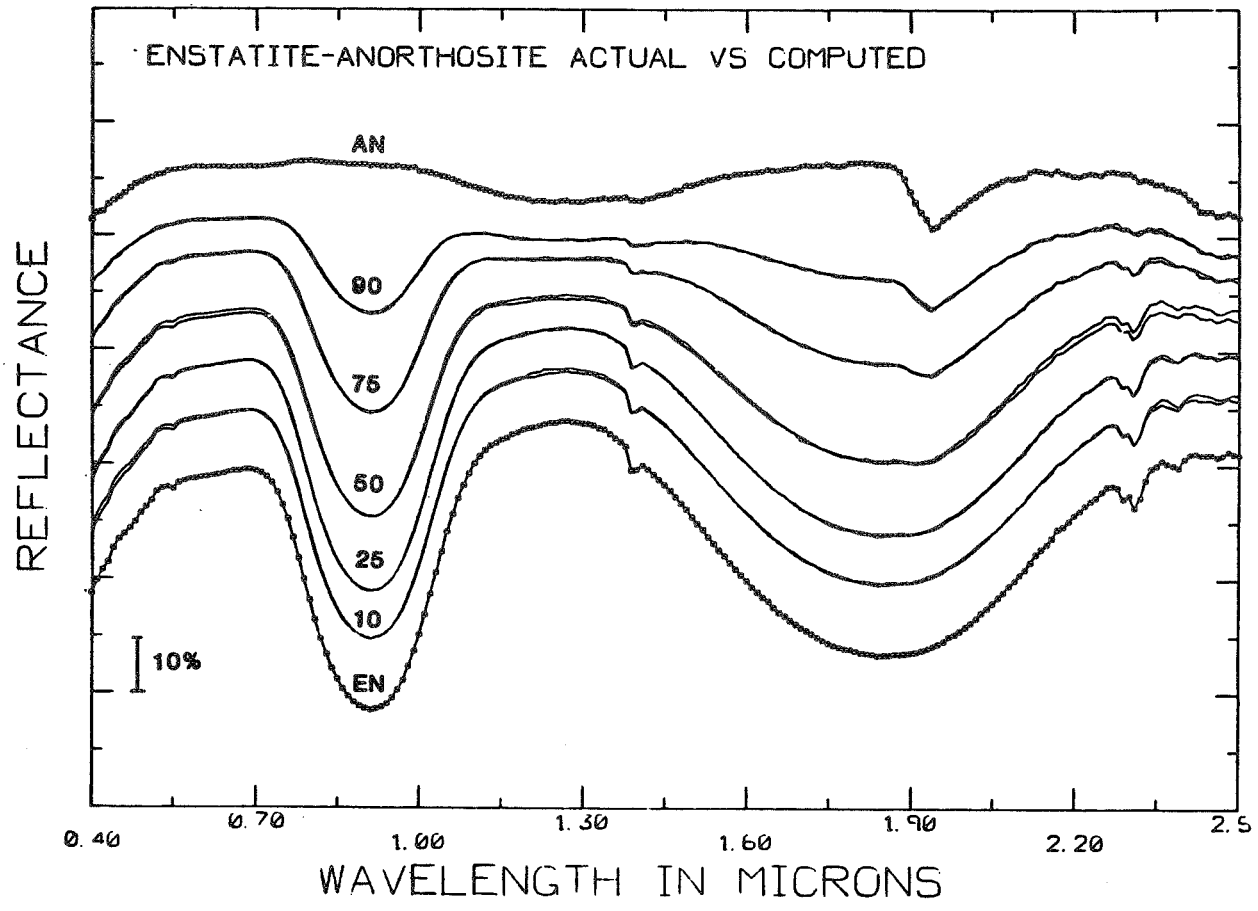

Figure 1. Actual and calculated bi-directional reflectance spectra for the anorthite-enstatite mixture series. The dotted curves, labelled AN for anorthite and EN for enstatite, are the endmember spectra used to model the mixture spectra. The smooth curves are the actual and calculated spectra plotted together. The number located in the 0.9 um. absorption band corresponds to the % mass of anorthite in the mixture. Each pair of calculated and actual spectra are offset for clarity and to emphasize the quality of the curve fits. At this scale there is almost no difference between the claculated and actual spectra.

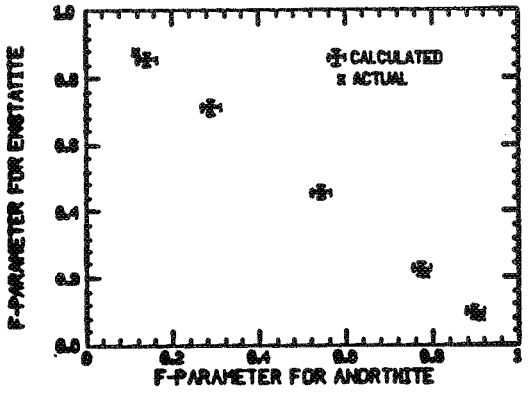

Figure 2. Actual and calculated relative geometricial cross sections (f-parameters) of anorthite and enstatite plotted against one another for the mixture series shown in Fig. 1. The calculated values are obtained from the curve fitting technique described in the abstract. The calculated values are generally within 1.5% of the actual values which is adequate for estimating mineral abundances in the mixtures.

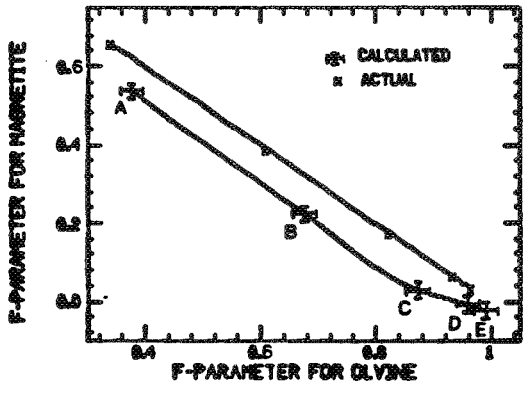

Figure 3. This is the same type of plot as in Fig 2 for the olivine-magnetite mixture series. The letters correspond to the mass fraction ratios where A=25/75, B=50/50, C=75/25, D=90/10, E=95/5, and the first number is the % mass of olivine in the mixtures. The lines between data points were added to emphasize the systematic overprediction of olivine content and underprediction of magnetite content.

COMPOSITIONAL INFORMATION FOR THE MOON: SOME CHARACTERISTICS OF CURRENT NEAR-IR SPECTRA (TELESCOPIC AND LABORATORY)

- Carle M. Pieters, Dept. Geological Sciences, Brown University, Providence, RI 02912

Introduction. During the Apollo program the spectral reflectance characteristics of a variety of lunar samples were measured in the laboratory by John B. Adams. Results of these measurements were reported in a series of papers by Adams and McCord (e.g. PLSC of 1970, 71, 72, 73). Most of these studies were directed toward understanding the nature and composition of lunar soils, since the vast majority of remote measurements are derived from the uppermost surface soils. These laboratory measurements were essentially discontinued with the close of the Apollo program. Later, in the late 1970's, telescopic instruments were developed that allowed high precision near-infrared spectra, comparable in spectral resolution to the laboratory data, to be obtained for individual lunar areas 3-20 km in diameter using telescopes at the high-altitude Mauna Kea Observatory (1). For the last decade near-infrared spectra for small lunar areas have been painstakingly obtained by researchers from the Univ. of Hawaii and from Brown University. Such telescopic spectra, with the 'ground truth' foundation from lunar samples, have been used extensively by these lunar scientists to address a multitude of problems in lunar science. Summaries of the compositional information inherent in the telescopic spectra can be found in (1,2,3). Much of the near-infrared spectral reflectance data from both laboratory and telescopic measurements have recently been compiled in comparable formats and an initial comparative assessment of the available data using selected measured spectral parameters has been made. The objective is to develop a framework for the systematics of lunar near-IR spectra in order to better interprete spectra of unknown materials in terms of useful compositional information.

Spectral Parameters. Each spectrum was first classified according to its general character. Major categories indicated in the key accompaning Figures a-d account for about 2/3 of the data. A variety of parameters sensitive to mineralogy and alteration products were measured for each spectrum: center of an absorption band near 1 μm, strength of the band, band width, band symmetry, continuum slope (near the 1 μm band), etc. These particular properties were chosen because important lunar minerals (high- and low-Ca pyroxenes, olivine, glass, plagioclase) have characteristic absorptions that affect the strength and nature of these parameters in diagnostic ways (1,2,3). Examples of the relation between some of these spectral parameters for the two collections are shown in figures a-d. Each spectrum was also assigned a relative quality factor from 1 to 5; only quality 1 and 2 have been used in these figures.

Telescopic Data. The current data base includes almost 350 individual spectra for about 210 areas 3 to 15 km in diameter (independent measurements are required for most areas). If data scattered among researchers is included, the lunar collection could be about 1/3 larger. Although some attempt has been made in recent years to assure most important geologic units are included in the collection, the survival of data acquisition programs depends on productive science, and the data collection is necessarily biased toward areas studied for specific topics (mare soils, Copernicus and its rays, highland craters, etc.).

Laboratory Data. The Adams' spectra include almost 420 spectra of ~150 lunar samples. About 70% are lunar soils representing all Apollo sites, as well as Luna 20 and 24. Although the scale of a laboratory sample is about 10^6 times smaller than the area of telescopic measurements, the two types of data are directly comparable for the relatively well-mixed lunar soils. However, for lunar rocks and minerals, and especially for breccias, the collection of sample spectra is incomplete due to the difficulty of obtaining or identifying materials from limited samples that are representative of a rock, a site, or even the moon as a whole. Not all lunar rock types identified are represented by sample spectra.

Comparisons. The two collections are not expected to be entirely similar for the reasons mentioned above concerning completeness. A few well-known lunar spectral properties are evident in both, such as the systematic variation in pyroxene composition (detected by band position and strength) between the highlands (Lo-Ca) and mare (Hi-Ca). Note, however, that an additional gabbroic (Hi-Ca px) component can be detected (longer band center) in many highland craters of Fig. d(3). As an example of

compositional inferences, consider the glassy samples (such as 74220, 15401 and a synthetic Apollo 12 glass) which systematically exhibit wider bands than the main trends of rocks and soils in Fig. a. The pyroclastic mantling material at Aristarchus, Sulpicius Gallus, and Sinus Aestuum exhibit similiarly broad bands, implying Fe-bearing glass deposits (4). Olivine, such as that at Copernicus' central peak (CP) has similar properties, but can often be distinguished from glass by other characteristics such as albedo. The region marked 'OP' on Fig b and d include soils from the young Hi-Ti basalts of the western maria. These represent soils for which no samples exist (dotted areas on Figs. a and c) but which clearly contains substantial olivine or glass(5).

Acknowledgments: This research is supported by NASA grant NAGW-28. **References.** 1) McCord et al., 1981, *JGR, 86*, no. B11, p10883; 2) Pieters 1978, LPSC9th, p2825; 3) Pieters,1985, *Revs. Geophys.*, in press; 4) Gaddis et al., 1985, *Icarus,61*, p461; 5) Pieters et al, 1978, *JGR, 85*, no. B7, p3913.

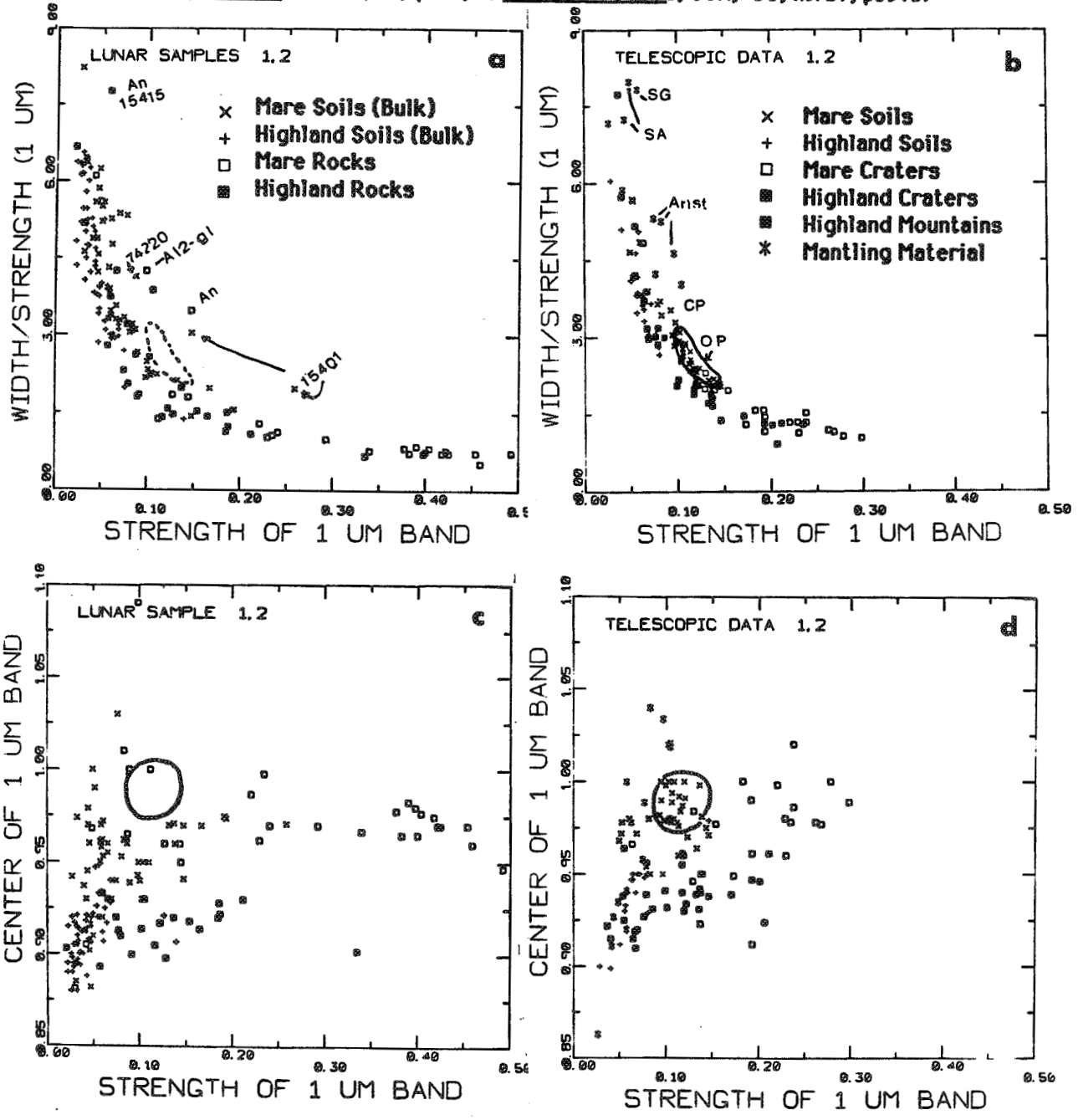

Compositional Stratigraphy of Crustal Material from Near-Infrared Spectra

C. M. Pieters (Brown University)

The walls and ejecta surrounding large impact craters 40-100 km in diameter expose the first few kilometers of crustal material at the target site just below the surface. Central peaks of such craters expose material derived from greater depths (~4 - 10 km) [eg. Grieve and Head, LPSC 14]. High spatial resolution measurements of the composition of material associated with such craters can be used to probe the subsurface crust. An earth-based telescopic program to acquire near-infrared spectra of freshly exposed lunar material now contains data for 17 large impact craters with central peaks. Noritic, gabbroic, anorthositic and troctolitic rock types can be distinguished for areas within these large craters from characteristic absorptions in individual spectra of their walls and central peaks. Norites dominate the upper lunar crust while the deeper crustal zones also contain significant amounts of gabbros and anorthosites. Examples of the compositional stratigraphy of the lunar highland crust observed at specific craters include (subsurface crust - deeper crust):

Aristarchus: gabbro + troctolitic gabbro - gabbro [Lucey et al LPSC 16]
Bullialdus: gabbro - norite
Copernicus: norite - troctolite [Pieters et al, *JGR 90*, 12,393]
Eratosthenes: norite - gabbro
Langrenus: norite throughout
Lansberg: norite - norite (with clinopyroxene)
Theophilus: norite - anorthosite
Tycho: gabbro throughout

When the complexity of planetary crusts are compared, the Moon is often considered a relatively simple and homogeneous end-member in terms of crustal formation processes as well as the mixing that must have occurred during the extensive early bombardment history. These data for material associated with large craters, however, indicate that not only is the lunar crust highly heterogeneous across the nearside, but that the compositional stratigraphy of the lunar crust is also nonuniform. If such diversity occurs for even this small planet, crustal complexity should be expected for other planetary bodies to be studied. For maximum compositional information using advanced sensors on future missions (Galileo, MO, LGO) measurement strategy should include high spatial and spectral resolution data in and around large impact craters.

PRELIMINARY RESULTS OF SPECTRAL REFELECTANCE STUDIES OF TYCHO CRATER

B.R. HAWKE, C.R. COOMBS, P.G. LUCEY, and J.F. BELL, Planetary Geosciences Division, Hawaii Institute for Geophysics, University of Hawaii, 2525 Correa Road, Honolulu, HI 96822; R. JAUMANN and G. NEUKUM, DFVLR, 8031 Wessling, W. Germany; C.M. PIETERS, Department of Geological Sciences, Brown University, Providence, RI, 02912.

INTRODUCTION

Spectral studies of lunar craters and their ejecta deposits provide valuable information about the composition of the lunar crust as well as insights into the impact cratering process. Materials from a variety of depths have been excavated by these impacts and deposited in a systematic manner around the craters. Hence, information concerning vertical and lateral changes in the composition of the lunar crust can often be obtained by careful analysis of spectral data of these ejecta deposits. Results of multispectral imaging studies of Tycho, Aristilus, Lalande, and Kepler were published by Hawke *et al.* (1979).[1] Lucey *et al.* (1986)[2] more recently have published the results of a spectral reflectance study of Aristarchus crater and its deposits. This paper presents the preliminary analysis and interpretation of near-infrared spectra obtained for both the interior and exterior deposits associated with Tycho crater. Specifically, our objectives were: 1) to determine the composition and stratigraphy of the highland crust in the Tycho target site, 2) to determine the likely composition of the Tycho primary ejecta which may be present in ray deposits, 3) to investigate the nature of spectral units defined in previous studies, 4) to further investigate the nature and origin of both the bright and dark haloes around the rim crest, and 5) to compare the compositions determined for the various Tycho units with those of Aristarchus crater as well as "typical" highlands deposits.

METHOD

Near infra-red spectra (0.6 - 2.5 μm)for small (~2 km) areas in and around Tycho were obtained at the Mauna Kea 2.24-m telescope using the Planetary Geosciences Division indium antimonide spectrometer. Extinction corrections were made using the techniques described by McCord and Clark (1979).[3] Analyses of absorption bands and continuum slopes were made using the

methods presented by McCord *et al.* (1981).[4] Spectra were collected for the following areas: 1) the southwest crater wall, 2) the northern rim, 3) the southwest floor, 4) the eastern floor, 5) the central peak, 6) the northeast ejecta blanket, and 7) the dark halo north of the crater. The residual absorption spectra (after continuum removal) are shown in Figure 1.

RESULTS AND DISCUSSION

The spectra obtained for areas on the interior of Tycho exhibit similar spectral features. These include relatively strong 1μm absorption bands whose minima are centered between 0.97 and 0.99 μm and shallow to intermediate continuum slopes. The spectra generally exhibit indications of a 1.3 μm feature consistent with the presence of Fe^{2+}-bearing plagioclase feldspar. The strong 1 μm absorption features indicate a dominant high-Ca clinopyroxene component. These spectra are all Type G as defined by Pieters (1986).[5] The material exposed on the interior of Tycho is a gabbroic assemblage with compositions ranging between gabbro and anorthositic gabbro.

The spectrum that we obtained for the Tycho central peak is slightly different from that presented by Smrekar and Pieters (1986).[6] Their spectrum exhibits a shallower continuum slope, a deeper 1 μm band centered at a slightly longer wavelength (0.99 μm vs. 0.98 μm), and a well-defined 1.3 μm absorption feature. Their spectrum was collected for a larger area of the Tycho central peak and may better represent the character of peak as a whole than does the one we present in Figure 1.

Spectra were also obtained for Tycho ejecta deposits. Hawke *et al.* (1979)[1], noted that the Tycho rim crest is surrounded by two spectrally distinct haloes. The inner, bright halo is narrow, discontinuous, and poorly developed south of the crater. The outer, dark halo is more extensive and continuous and extends in places to almost one crater diameter from the rim crest. One spectrum was collected for an area just north of the Tycho rim crest. This area appears to be typical of the inner, bright halo. The spectrum is almost identical to those obtained for interior units and a similar composition is implied.

The spectrum obtained for a portion of the dark halo north of Tycho is very different from those of the interior units. This spectrum exhibits a wide, relatively shallow absorption feature centered at 1.01 μm, a 1.3 μm absorption, and a relatively steep continuum slope. This spectrum is very similar to that

presented by Smrekar and Pieters (1986)[6] for a portion of the dark halo southwest of Tycho. They interpreted their spectrum as indicating the presence of pyroxene, Fe-bearing feldspar, and a significant component of Fe-bearing impact melt glass. We agree with this interpretation and suggest that the dark halo north of the crater is composed of a similar assemblage.

The spectra of spots inside of Tycho show, in the context of the highlands thus far investigated, the greatest similarity to certain spectra obtained for features in the Aristarchus region (i.e., Class 1) of Lucey *et al.* (1986).[2] However, the suite of spectra obtained for Tycho exhibits a different trend than that of the Aristarchus spectra in terms of band center versus width. Aristarchus spectra show a strong correlation between band center and width which Lucey *et al.* (1986)[2] attributed to a variation in olivine content in the highland units in the region. This is not the case at Tycho. Apparently, olivine is absent or present in only minor amounts in the Tycho region.

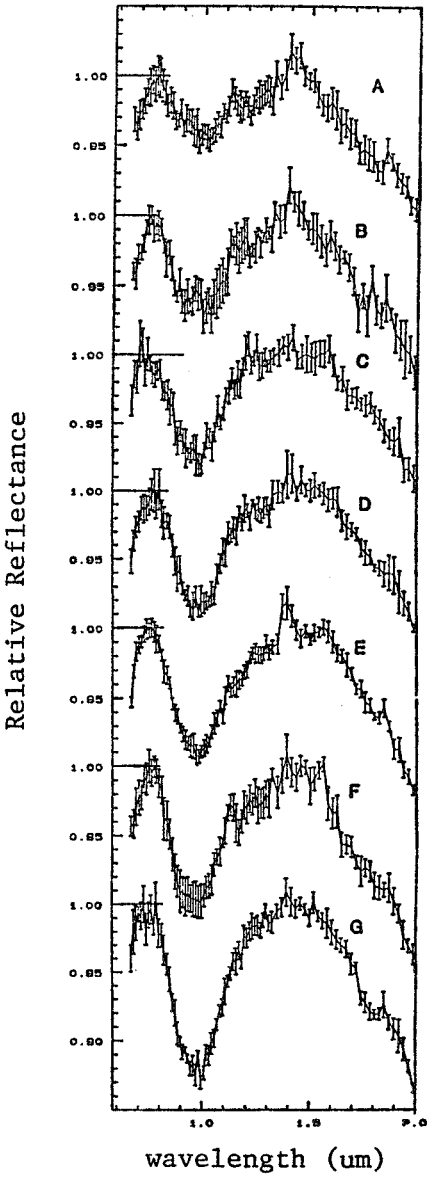

FIGURE 1:
Spectra of locations of Tycho crater interior and exterior deposits, with straight line continua removed. (A) Dark halo, north (B) Northeast ejecta (C) Southwest wall (D) Southwest floor (E) East floor (F) North rim (G) Tycho central peak.

REFERENCES:

1) B.R. Hawke *et al.* (1979), Conf. on the Lunar Highlands Crust. 50; 2) P. Lucey, *et al.*, (1986), PLPSC 16, in press; 3) T. McCord and R. Clark (1979), Pub. Astron. Soc. Pac., 91, 571; 4) T. McCord, *et al.*, (1981) JGR, 86, 10883; 5) C. Pieters (1986), Rev. Geophysics, in press; 6) S. Smrekar and C. Pieters (1986), Icarus, in press.

Preliminary Results of Geologic and Remote Sensing Studies of Rima Mozart

C.R. COOMBS and B.R. HAWKE, Planetary Geosciences Division, Hawaii Institute of Geophysics, University of Hawaii, 2525 Correa Rd., Honolulu, HI 96822.

The nature and origin of lunar sinuous rilles have long been the subject of major controversy. Lunar sinuous rilles typically occur on mare surfaces, though a few cross highland terrains. Suggested origins for sinuous rilles vary widely: 1) erosion by nuees ardentes (Cameron, 1964), 2) fluvial erosion (Urey, 1967; Gilvarry, 1968; Lingenfelter *et al.*, 1968; Schubert *et al.*, 1970), 3) tectonic features of tensional origin (Quaide, 1965) 4) formation as lava tubes and channels during lava emplacement (Kuiper *et al.*, 1966, Greeley, 1971, Oberbeck *et al.*, 1969) or, during the draining of a lava lake (Howard *et al.*, 1972), 5) incision of channels by thermal erosion and/or turbulent flow through the channels (Carr, 1974; Hulme, 1973).

It is very unlikely that nuees ardentes would form the smooth sinuous channels on the lunar surface. On the Earth they form hummocky channels and dunes, not smooth curvy channels. Though a morphologic similarity to terrestrial fluvial features has been noted (Urey, 1967; Gilvarry, 1968, Lingenfelter *et al.*, 1968), a fluvial origin for lunar rilles has long been discounted due to the anhydrous nature of the returned lunar samples (e.g. Taylor, 1975). The similarity of certain lunar rilles to terrestrial channels of fluvial origin merely suggests an origin by fluid flow, though water is not necessarily the erosive agent (Oberbeck *et al.*, 1971). Terrestrial lava tubes and channels often originate at vent craters or depressions associated with regional tectonic features such as faults, fissures, or fracture systems that often form concentric to calderas (Greeley, 1971). Similarly, many lunar sinuous rilles are located in areas of structural weakness and often tend to follow pre-existing structural trends. However, the presence of elongate "head" craters, levees, and the fact that lunar sinuous rilles may extend for large distances without offset or mirror images on either side helps negate an origin soley by extensional tectonics.

Lunar sinuous rilles are also similar to terrestrial lava channels and collapsed lava tubes in that they commonly originate at irregular shaped "head" craters, trend down-slope, are discontinuous in areas (tube formation and/or collapse?), taper out at distal ends, and may form distributaries. Thermal erosion and turbulent flow may help explain the extent of lunar sinuous rilles, but it can not explain the formation of meanders that are commonly associated with lunar rilles.

In order to better understand the processes responsible for the formation of lunar sinuous rilles, we have conducted a study of Rima Mozart using a variety of geologic, photographic, and remote sensing data. The apparent source of this rille is located in a highlands unit of known composition (i.e., KREEP basalt; Hawke and Head, 1978; Spudis, 1978; Spudis and Hawke, 1986) and it was hypothesized that thermal and mechanical erosion played an important role in the formation of Rima Mozart. Excellent photographic, topographic, multispectral, and radar data exist for this rille. The purpose of this paper is to present the preliminary results of an analysis of this data.

Rima Mozart is a 40 km-long lunar sinuous rille located near the SE rim of Imbrium basin (25°21''N, 359°03''W). It is situated about 100 km southwest of the Apollo 15 landing site. It is 250 - 500 m deep and is incised into the volcanically derived KREEP basalts of the Apennine Bench Formation and dark mare basalts surrounding the rille (Figure 1).

Photographic data indicates the presence of two volcanic source vents for Rima Mozart. Now girdled by dark mare-type material, these vents appear to have formed in the underlying Apennine Bench Formation (Figure 1). The primary source vent, Kathleen, is an elongate crater (5 x 3 km) in the Apennine Bench Formation. From Kathleen, Rima Mozart follows a dominant NW/SE structural trend (Swann, 1986) until terminating 30 km to the east. About 10 km from the termination of Rima Mozart the second elongate (2 x 1 km) source vent, Ann, is joined to the main channel by a secondary rille. Evidence of spatter surrounding Ann strongly supports the volcanic origin of this feature. At the distal end of Rima Mozart, the rille terminates at Michael, a possible "sink" crater. The crater Michael may be connected to the NE-trending Rima Bradley, to the southeast, through a conduit and/or underground plumbing system marked by a collapse feature , Patricia. This possible extension of Rima Mozart joins Rima Bradley at a NW/SE angle, reflecting the dominant structural trend of the region.

We suggest that Rima Mozart, like many other lunar sinuous rilles, is most likely formed by a combination of events. Rima Mozart does follow a pre-existing, dominant, NW/SE structural trend suggesting the influence of structural features on the rille, however, the tectonic influence is not the sole source for the formation of the rille, as suggested by the presence of two volcanic source vents and spatter present around Ann. We suggest that the rille formation began with an explosive eruption at Kathleen which later calmed down to a pulsating, high volume, low-viscosity lava flow. The rapid effusion rate of the magma as well as its high temperature and turbid nature helped carve the

sinuous rille into the fractured and structurally weak Apennine Bench Formation underneath. Similar eruptions and subsequent flows were also created at Ann and joined to the main channel by a NE-trending secondary rille. Rapid and turbulent lava flows continued to form Rima Mozart through a distributary system of channels and/or tubes that paralleled the underlying, pre-existing structure of the Apennine Bench Formation until reaching the terminus at Michael.

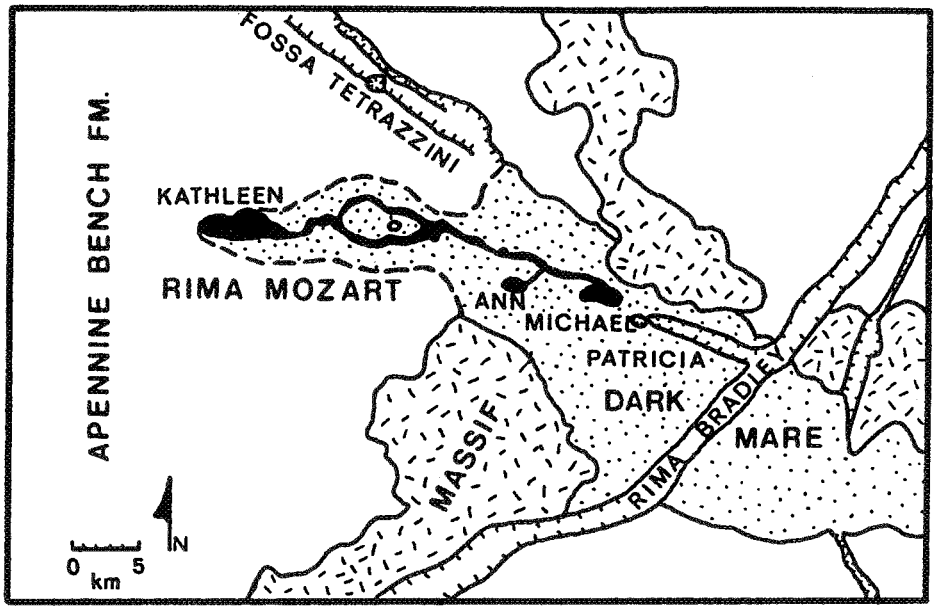

FIGURE 1: A sketch map of the Rima Mozart region showing the locations of the two surce vents, Kathleen and Ann, and the "sink" crater, Michael.

REFERENCES: (1) Cameron, W.L. (1964), IGR, 69, 2423; (2) Urey, H.C. (1967), Nature, 216, 1094; (3) Gilvarry, J.J. (1968), Nature, 218, 336; (4) Lingenfelter, R.E., Peale, S.J. and Schubert, G. (1968), Science 161, 266; (5) Schubert, G., Lingenfelter, R.E. and Peale, S.J. (1970), Rev. of Geophys. and Space Phys., 8, 199; (6) Quaide, W. (1965), Icarus, 4, 374; (7) Kuiper, G.P, Strom, R.G., LePoole, R.S. (1966), JPL Lab. Tech. Rept., 32-800; (8) Greeley, R. (1971), Science, 172, 722; (9) Oberbeck, V.R., Quaide, W.L. and Greeley, R. (1969), Modern Geology, 1, 75; (10) Howard, K.A., Head, J.W. and Swann, G.A. (1972), Proc. 3rd Lunar Science Conf., Vol.2, 1; (11) Carr, M.H. (1974), Icarus, 22, 1; (12) Hulme, G. (1973), Modern Geology, 4, 107; (13) Taylor, S.R. (1975), Lunar Science- A Post Apollo View, 1; (14) Swann, G.A. (1986), LPSC XVII, 855; (15) Hawke and Head (1978), Proc. 9th Lunar Planet. Sci. Conf., 3285; (16) Spudis (1978), Proc. 9th Lunar Planet. Sci. Conf., 3379 ; (17) Spudis and Hawke (1986), Proc. Apollo 15 Conf., 105.

PHOTOMETRIC PROPERTIES OF LUNAR TERRAINS DERIVED FROM HAPKE'S EQUATION.
Paul Helfenstein and Joseph Veverka, Center for Radiophysics and Space Research, Cornell University, Ithaca, NY 14853-6801.

Hapke's bidirectional reflectance equations [1,2,3] provide the most rigorous available description of photometric behavior in terms of physically meaningful parameters. In the newest version [3], six model parameters characterize photometric properties: The efficiency with which average particles scatter and absorb light is described by single scattering albedo, w. The opposition effect, a surge in brightness observed in particulate surfaces near zero phase [4,5,6,7, 8,9,10] is characterized by two parameters; h, which relates its angular width to the combined effects of regolith compaction and particle size distribution, and S(0), the contribution of singly scattered light primarily by first-surface reflection at zero phase. The particle phase function is a Legendre polynomial with first and second order coefficients b and c, respectively. Finally, $\bar{\theta}$, is an average topographic slope angle providing a measure of sub-resolution scale macroscopic roughness.

The complexity of Hapke's equation and comparatively large number of model parameters makes the unique solution of meaningful parameter values difficult. Reliable methods for simultaneously solving all six parameters from remotely-sensed data needs development and testing. The primary objective of this study is to derive Hapke parameters for the lunar surface from both disk-integrated and disk-resolved photometric data. The Moon is the only extraterrestrial body for which samples have been returned to Earth for laboratory analysis, for which extensive manned and unmanned geological field observations have been conducted, and for which corresponding regional photometric measurements have been obtained over adequate ranges of illumination and viewing geometry. The derivation of physically and geologically meaningful parameters from the existing lunar photometric data set is an important test of the usefulness of Hapke's equation in remote sensing applications where surface-based ground truth measurements are unavailable. Hapke's parameters for the Moon also provide a foundation for the comparison of parameters derived from other planetary surfaces.

Visual disk-integrated phase curve data were obtained by renormalizing and combining the measurements of Russell [11,12], Rougier [13], and Shorthill *et al*. [14] to the precise photoelectric measurements of Lane and Irvine [15], which covered a slightly smaller range of phase angles. The combined data were subdivided and averaged in phase angle bins having the following intervals: data in the range of 0°- 10°were divided into 2.5° bins, data in the range of 10° - 30° were divided into 5° bins, and data in the range of 30° to 150° were divided in 10°bins. Lunar disk-resolved reflectance data were a subset of the extensive measurements tabulated by Shorthill *et al*. [14] who divided terrains into three groups on the basis of their normal albedoes, A_n. We have preserved their classification system and used data for thirty-two dark lunar terrains ($0.06< A_n <0.09$), twenty-five average terrains ($0.10< A_n <0.12$), and thirty bright terrains ($0.13< A_n <0.16$) in their catalogue. We combined all similar terrain classes into three groups and renormalized all brightness measurements to group-mean albedoes. Average brightnesses, incidence angles (i), and emission angles (e) were determined at each phase angle (α) in each group.

Hapke's equation was fit to the disk-integrated phase curves and disk-resolved data for dark, average, and bright terrain classes using an iterative, non-linear least-squares algorithm described by Helfenstein [16]. Parameters were initially determined from the disk-integrated data, and the result was applied as a first-guess to the iterative solution of parameters for individual terrain classes. Table 1 lists our numerical results. The visual phase curve computed from the best-fit is presented with the averaged disk-integrated data in Figure 1. Figure 2 shows plots of the disk-resolved data normalized to corresponding brightnesses predicted from the disk-integrated solution under the same illumination and viewing geometries. The curves in Figure 2 represent the similarly normalized brightnesses predicted from disk-resolved solutions for all points such that $i=e=\alpha/2$.

Disk-integral photometric properties of the Moon and Mercury at visual wavelengths are known to be remarkably similar [17]. Our value of w, S(0), b, and $\bar{\theta}$ are nearly identical to those found by Veverka *et al*. [18] for Mercury. Our value of h (0.07) falls in between Veverka *et al*.'s Mercurian value (0.08) and the 0.05 value derived from lunar farside data [19] by Hapke [3]. Disk-integrated and disk-resolved solutions are mutually consistent. The value of each disk-integrated parameter lies between end-member dark and bright terrain values, and does not differ strongly from the average albedo terrain value.

Systematic trends in disk-resolved parameters can be identified in Table 2. Not surprisingly, values for single scattering albedo (w) of the dominantly anorthositic average and bright terrains are significantly larger than the value for the basaltic dark terrains (mare). Decreasing values of b for dark through

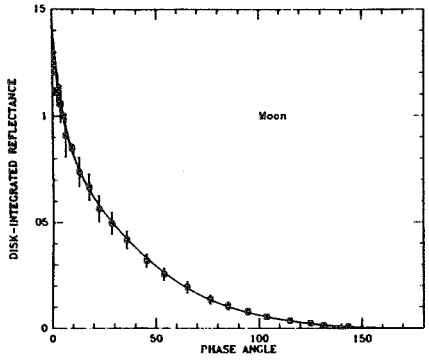

Table 1: Hapke Parameters for Lunar Terrains

	w	h	S(0)	b	c	$\bar{\theta}$
Disk-Integrated	0.21	0.07	0.71	0.29	0.39	20.0°
Disk-Resolved Dark	0.12	0.12	0.51	0.41	0.10	8.1°
Disk-Resolved Average	0.25	0.06	0.78	0.33	0.37	20.6°
Disk-Resolved Bright	0.33	0.05	1.03	0.26	0.45	24.0°

Figure 1 (left): Predicted lightcurve and averaged disk-integrated data (one sigma error bars), normalized to geometric albedo at zero phase.

Figure 2 (bottom): Averaged disk-resolved data normalized to predicted brightness from disk-integrated solution. a) dark terrains, b) average terrains, c) bright terrains. Curves represent predicted normalized brightnesses for hypothetical points on the surface such that $i=e=\alpha/2$.

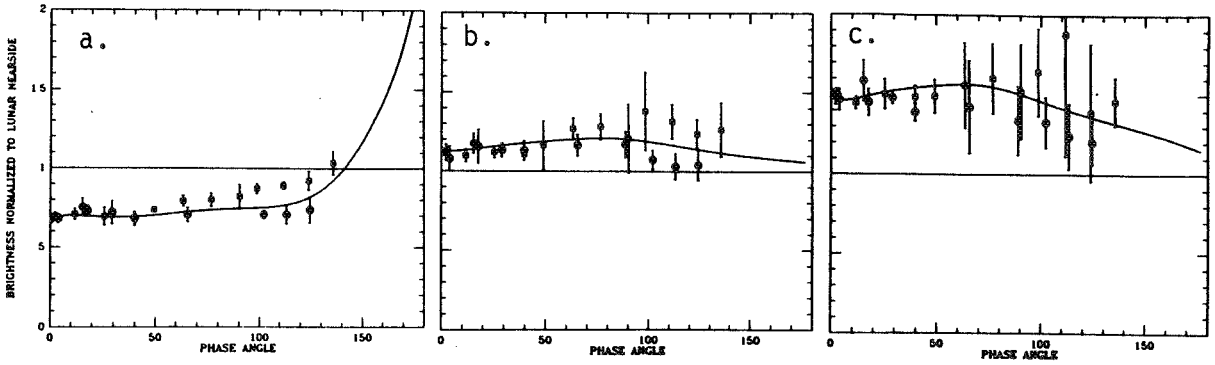

bright terrains indicate that dark regoliths are, as expected, more backscattering than those in average and bright lunar terrains. Values of h likewise decrease from dark through bright terrains indicating that the angular width of the opposition effect is greatest for mare. This would suggest either that mare soils have lower surface porosities, or that they have a slightly different characteristic regolith particle-size distribution. Since porosities over most of the lunar surface are known to be remarkably similar (~45%) [20,21,22], the difference is most likely due to a greater abundance of fine grains (<20 μm) in lunar highlands regoliths [23]. The total amplitude of the opposition surge, $B_0 = S(0)/w\{1+b+c\}$, for dark terrains is larger than for average and bright terrains. This appears to be a consequence of the fact that in opaque particles a larger fraction of singly scattered light at zero phase comes from first surface reflection, S(0). The average macroscopic roughness ($\bar{\theta}$) of dark terrain is significantly lower than that of average and bright terrains. The ratio of of $\bar{\theta}$ for bright terrain to $\bar{\theta}$ for dark terrain is 2.5. This value corresponds to subcentimeter scales and compares well to the ratio of 2.0 derived from radar RMS slopes of highland (β=8°) and mare (β=4°) at 13 cm wavelengths [24].

Acknowledgement: This research was supported by NASA grant NSG-7606.

REFERENCES: [1] Hapke, B. (1981) JGR 86, 3039-3054. [2] Hapke, B.(1984) Icarus 59, 41-59. [3] Hapke, B. (1986) Icarus 67, 264-280. [4] Seeliger, H.(1887) Abhandl. Bayer. Akad. Wiss. Math.-Natur. 16, 405-516. [5] Seeliger, H. (1895) Abhandl. Bayer. Akad. Wiss. Math. Natur. 18, 1-72. [6] Hapke, B. (1963) JGR 68, 4571-4576. [7] Hapke, B. (1966) Astrophys. J. 71., 333-339. [8] Bobrov, M. (1970) In Surfaces and Interiors of Planets and Satellites, Acad. Press, NY. [9] Gehrels, T., et al., (1964) Astron. J. 69, 826-852. [10] Irvine, JGR 71, 2931-2937. [11,12] Russell, H. (1916) Astrophys. J. 43, 103 & 173. [13] Rougier, M. (1933) Ann. Obs. Strasbourg 2, 205-339. [14] Shorthill, R., et al., (1969) NASA Contr. Rep. CR-1429, 405 pp. [15] Lane, A. and W. Irvine (1973) Astrophys. J. 78, 267-277. [16] Helfenstein, P.(1986) Ph.D. Thesis, Brown Univ.,Providence, RI, 414 pp. [17] Hapke, B. (1977) Physics of Earth and Planet. Interiors 15, 264-274. [18] Whitaker, E. (1979) Icarus 40, 406-417. [19] Veverka, J. et al., (1986) in preparation. [20] Houston, W., et al.(1972) Proc. LPSC III, 3255-3263. [21] Carrier, W., et al.(1972) Proc. LPSC III, 3223-3234. [22] Carrier, W., et al.(1974) Proc. LPSC V, 2361-2364. [23] McKay, D., et al.(1974) Proc. LPSC V, 887-906. [24] Tyler, G. (1979) Icarus 37, 29-45.

Bidirectional Reflectance Spectroscopy
4. The Extinction Coefficient and the Oppostion Effect

Bruce Hapke
Dept. of Geology & Planetary Science, Univ. of Pittsburgh

Icarus 67, 264-280 (1986)

The extinction coefficient and the opposition effect in a particulate medium are discussed. Simple analytic expressions that describe these quantities are rigorously derived using a few physically realistic mathematical approximations. The particles of the medium may have a distribution of sizes and the particle density is allowed to vary with depth. The xpression for the extinction coefficient is valid for both large and small porosities and is more accurate than the one commonly used. The opposition effect arises from the hiding of extinction shadows and occurs even if the particles are transparent. The angular half-width of the opposition peak is shown to be equal to the ratio of the average particle radius to extinction length at unit slant path optical depth in the medium, and depends on both the filling factor (ratio of bulk to solid density) F and the particle size distribution.

To illustrate the theory it is fitted to observations of the moon, an asteroid and a satellite of Uranus; Europa is also discussed. For the moon a value of F=0.41 is derived, in good aggrement with data on Apollo soils. For Oberon, the width of the oppositon effect peak gives F=0.10, which is similar to values for terrestrial frosts and snow. Thus, the narrow opposition effects of the Uranian satellites do not require any unusual particles or microstructures on their surfaces. More photometric observations of Europa are needed.

On the Sputter Alteration of Regoliths of Outer Solar System Bodies

Bruce Hapke

Icarus **66**, 270-279 (1986)

This paper discusses several processes that are expected to occur when the porous regoliths on bodies without atmospheres in the outer solar system are subjected to energetic ion bombardment. The conclusions reached in many of the papers involving sputtering published in the planetary literature are qualitatively or quantitatively incorrect because effects of soil porosity have been neglected. It is shown theoretically and experimentally that porosity reduces the effecitve sputtering yield of a soil by more than an order of magnitude. Between 90 and 97% of the sputtered atoms are trapped withn the regolith, where they are factionated by differential desorption. Experiments indicate that more volatile species have higher desorption probabilities. This process is the most importanbt way in which alteration of chemical and optical properties occurs when a regolith is sputtered. When a basic silicate soil is irradiated these effects lead to sputter-deposited films enriched in metallic iron, while O, Na and K are preferentially lost. The Na and K are present in the atmosphere above the sputtered silicate in quantities much greater than their abundances in the regolith. Icy regoliths of SO_2 should be enriched in elemental S and/or S_2O. This prediction is supported by the probable identification of S_2O and polysulfur oxide bands in the IR spectra of H-sputtered SO_2 reported by Moore (1984, Icarus **59**, 114). When porous mixtures of water, ammonia and methane frosts are sputtered, the loss of H and surface reactions of C, N and O in the deposits should produce complex hydrocarbons and carbohydrates, some of which may be quite dark. Such reactions may have played a role in the formation of the matrix material of carbonaceous chondrites prior to agglomeration.

Charged Particle Modification of Surfaces in The Outer Solar System

R.E. Johnson, Univ. of Virginia

Voyager reflectance spectra data have indicated clear leading/trailing differences in the albedo of the icy Galilean and Saturian satellites. For the Galilean satellites, these have been analyzed by Nelson, et al. and, more recently, by McEwen. They have described the longitudinal dependence of this data and attempted to interpret this in terms of plasma and meteorite modification of the surface. Primary attention has been paid to Europa at which the leading/trailing differences are the largest.

Recently we have reanalyzed this data extracting the single grain (particle) albedo, w, and constructing the Espat-function, $W=(1-w)/w$ from this. Because w is near unity, $W \sim 2\alpha D$ where α is the absorption coefficient and D the grain size. In doing so we find a direct comparison to the longitudinal plasma bombardment flux for the first time (see figure). This occurs primarily in the UV and is probably due to an asorption associated with implanted S, as the UV band of Voyager overlaps the IUE data of Lane et al. We also can now unravel the relative importance of grain size effects and implant impurity effects.

Work supported by NASA grant NAGW-186

Clarke, R.N., et al. Icarus 56 (1983) 233
Lowe A.L. et al. Nature 292 (1981) 38.
McEwen, A.S. Icarus (in press) (1986).
Nelson, M. et al. Icarus 65 (1986) 129

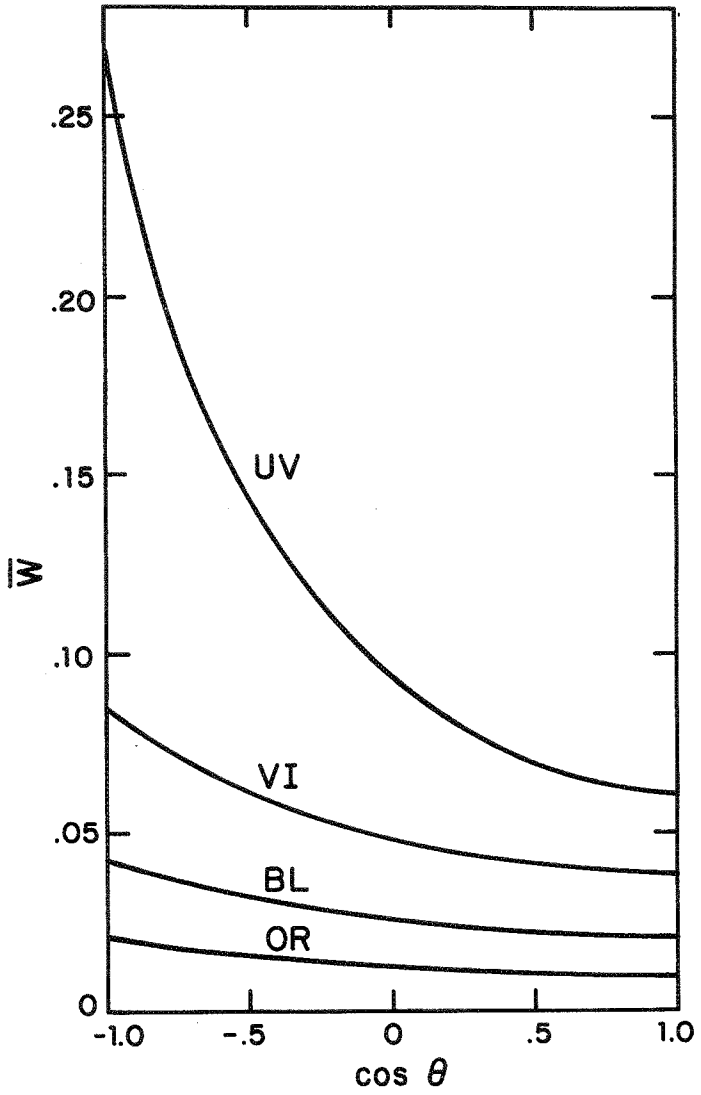

Smoothed values of Espat Function vs. cosine of logitude from apex of motion

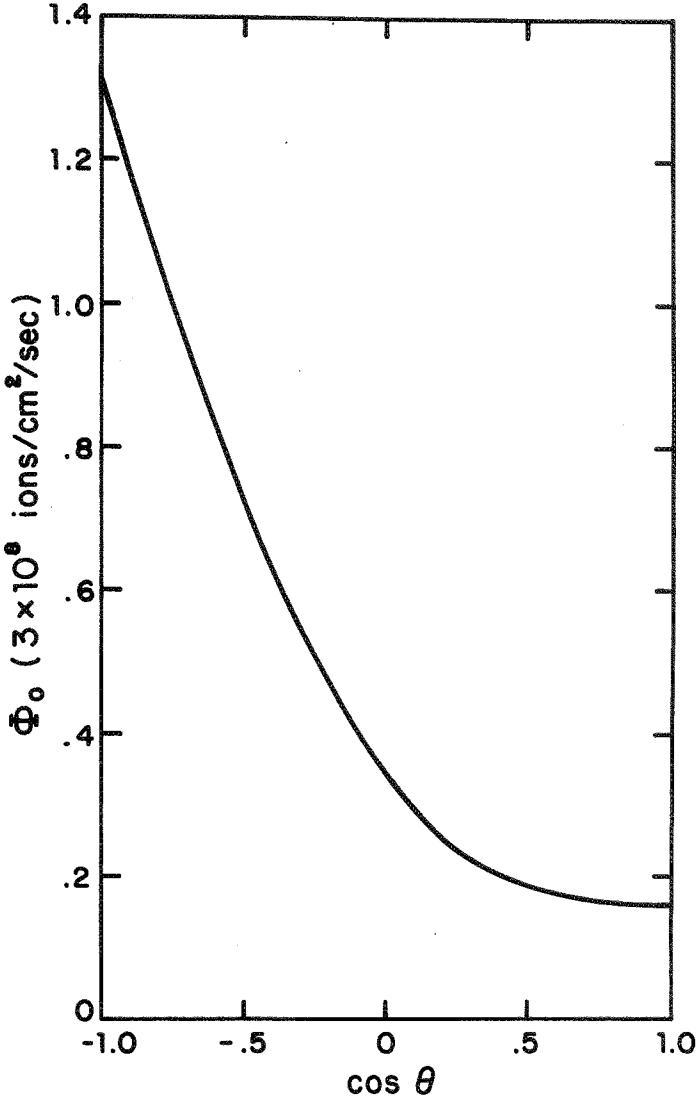

Equitorial Flux of sulfur ions bombarding Europa vs. longitude

IO: COMPARISON OF PHOTOMETRIC SCANS PRODUCED BY THE MINNAERT AND HAPKE FUNCTIONS. Damon P. Simonelli and Joseph Veverka, Cornell University.

Experience has shown that the empirical Minnaert function is a very useful approximation to real photometric behavior near opposition (phase angle $\alpha = 0°$), but that in general it cannot accurately model photometric scans across the face of even a homogeneous planet at higher phase angles (see for example Goguen, 1981). Given recent work on fitting the rigorous Hapke photometric function to Voyager data for Io (Simonelli and Veverka, 1986), we can test to what degree the Minnaert function breaks down in the case of Ionian materials by comparing photometric scans produced by the two approaches.

At phase angles $\alpha = 2$, 10, 30, 60, and 90°, we have computed scans of the reflectance along the photometric equator (photometric latitude $\Psi = 0°$) and mirror meridian (photometric longitude $\omega = \alpha/2$) that would be expected for a homogeneous planet whose surface obeys Hapke's law (Hapke, 1981, 1984). We use values of the Hapke parameters $\tilde{\omega}_0$, h, g, and $\bar{\theta}$ derived for Io by Simonelli and Veverka (1986) in both the Voyager narrow-angle camera violet filter ($\lambda \approx 0.42$ μm) and orange filter ($\lambda \approx 0.59$ μm). Each calculated Hapke scan is compared with the corresponding scan predicted by Minnaert's law for various values of the Minnaert limb-darkening parameter k. For a Minnaert scan at a particular k, we arbitrarily choose the value of the reflectance parameter B_0 so that the Minnaert and Hapke scans coincide at the so-called "specular point," the point where the photometric equator and mirror meridian intersect ($\Psi = 0°$, $\omega = \alpha/2$). The violet-filter photometric scans that result from this process are shown in Figs. 1 and 2; orange-filter results are qualitatively similar and are not displayed.

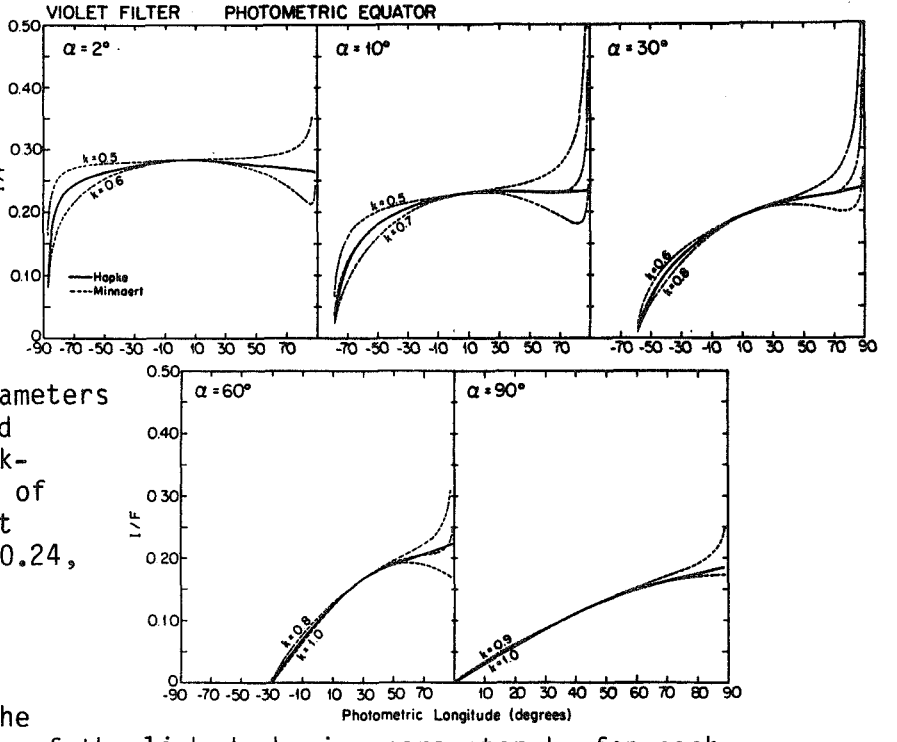

Figure 1. Scans at various phase angles illustrating how the reflectance I/F varies along the photometric equator. The solid curve shown at each phase angle represents a scan predicted by the Hapke function, using values of the Hapke parameters derived by Simonelli and Veverka (1986) from disk-integrated observations of Io in the Voyager violet filter: $\tilde{\omega}_0 = 0.68$, $h = 0.24$, $g = -0.14$, and $\bar{\theta} = 25°$. The dashed curves shown at each phase angle are scans predicted by the Minnaert function for the various indicated values of the limb-darkening parameter k; for each dashed curve, the value of B_0 has been chosen so that the curve coincides with the Hapke scan at the specular point (see text).

It is apparent that the Minnaert law does not match "exactly" Hapke scans at any of the phase angles shown, even $\alpha = 2°$. Yet our plots demonstrate that at least in the case of Io, the Minnaert law is a useful empirical tool. The Minnaert scans deviate most strongly from "real" (Hapke) behavior close to the limb of our hypothetical planet, i.e., near photometric latitude ±90° or photometric longitude +90°. However, as distances along the projected disk of a planet visible to an observer go as the sine of the photometric angles, when compiling photometric information most of the useful data come from areas within ≈ 60° of the sub-observer point. Figure 1 shows that along the photometric equator, the Minnaert description doesn't break down severely until $\omega = \varepsilon > 70°$, which corresponds to $x > 0.94$, where x is a linear scale from x = 0 at the center of the projected disk to x = 1 at the limb, and ε is the emission angle. Thus the Minnaert function breaks down most noticeably at geometries which ordinarily contribute least to observational data sets.

We also note that in the case of Io, the Minnaert description is useful not only at small phase angles, but throughout the range of α considered here. Figs. 1 and 2 suggest that the Minnaert function is as good an approximation at $\alpha = 90°$ as at $\alpha = 2°$; i.e., it seems able to match the Hapke scans to about the same level of approximation at all phase angles.

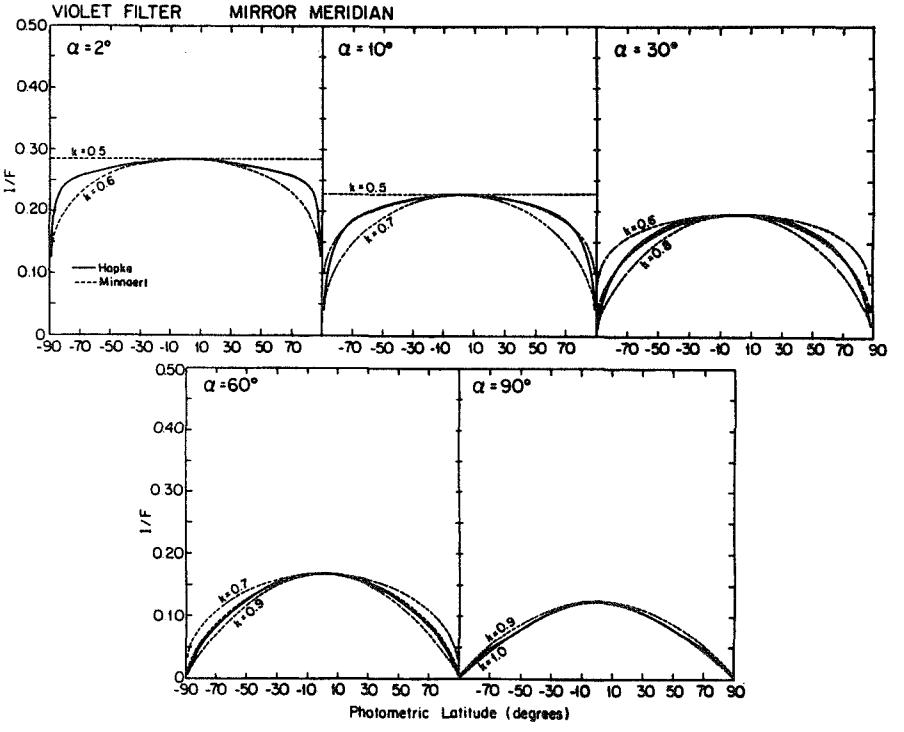

Figure 2. Same as Fig. 1, but for scans along the mirror meridian.

There is only one respect in which the Minnaert approximation worsens at high α: it appears that slightly different values of k are needed to describe scans across the face of a planet in different directions. Specifically, as the phase angle increases, the value of k that best matches behavior along the photometric equator is more likely to differ

from the k that results along the mirror meridian. For example, if we compare the $\alpha = 60°$ scans for the violet filter in Figs. 1 and 2, we find $k \approx 0.9$ along the photometric equator, but $k \approx 0.8$ along the mirror meridian. This variation in k with scan azimuth has already been discussed by Goguen (1981) in another context. It is noteworthy that for Io the effect is not serious for moderate phase angles ($\alpha < 60°$).

In summary, our work with Io data indicates that the empirical Minnaert function, while not a perfect model of real photometric behavior, does provide a very useful parameterization of limb darkening at phase angles out to 90°, and is especially useful near opposition (cf., McEwen and Soderblom, 1984; Clancy and Danielson, 1981). Those who work with the Minnaert law, however, must bear in mind the major limitation inherent in this empirical function: Minnaert parameters are unspecified functions of the phase angle. While $B_0(\alpha)$ for a specific material typically drops with increasing α, and $k(\alpha)$ generally increases toward higher phase angles (a trend seen in Figs. 1 and 2, as well as in Harris, 1961; Goguen, 1981; and McEwen and Soderblom, 1984), the determination of a material's B_0 and k at one α provides no direct information as to the values of these parameters at other phase angles.

This research was supported by NASA Grant NSG 7156.

References

Clancy, R. T., and G. E. Danielson (1981). J. Geophys. Res. 86, 8627-8634.
Goguen, J. D. (1981). Ph.D. dissertation, Cornell University, Ithaca, N.Y.
Hapke, B. (1981). J. Geophys. Res. 86, 3039-3054.
Hapke, B. (1984). Icarus 59, 41-59.
Harris, D. L. (1961). In The Solar System III. Planets and Satellites (G. P. Kuiper and B. M. Middlehurst, Eds.), pp. 272-342. Univ. of Chicago Press, Chicago.
McEwen, A. S., and L. A. Soderblom (1984). NASA Technical Memorandum 86246, pp. 261-262.
Simonelli, D., and J. Veverka (1986). Phase curves of materials on Io: Interpretation in Terms of Hapke's Function. Icarus, in press.

SULFUR-OXYGEN PROCESSES ON IO

Robert M. Nelson, William D. Smythe
Jet Propulsion Laboratory, Pasadena, CA 91109

After many years of research efforts dedicated to interpreting the spectral geometric albedo of Jupiter's satellite Io, the only chemical specie which is generally agreed to exist on Io's surface is, condensed sulfur dioxide (Smythe et al., 1979). Although the evidence for the presence of elemental sulfur is strong, there are several important astronomical observations and laboratory studies which constrain or question the presence of elemental sulfur in widespread areal abundance on the surface. In addition, the presence of sulfur dioxide on Io's surface raises questions regarding the presence of environmentally produced daughter products (if any) which also might be expected on the surface. This laboratory work is directed to understanding sulfur/oxygen processes in the Io environment.

Laboratory studies of irradiated sulfur dioxide frost have found that sulfur trioxide should be formed as a consequence of the irradiation process. We have measured the spectral reflectance of solid sulfur trioxide in the laboratory and we find that it has strong absorption features at 3.37 and 3.70 μm. These features are not present in the spectral geometric albedo of Io. We interpret this as an indication that sulfur trioxide may exist in such limited abundance that it is undetectable in disk averaged spectrophotometry. We suggest that the Near-Infrared Mapping Spectrometer on the Galileo spacecraft should be able to identify condensed sulfur trioxide on Io particularly in regions bordering the sulfur dioxide deposits (Nelson and Smythe, 1986).

The presence of elemental sulfur on Io's surface has been questioned on several grounds most notably the suggested production process (quenched molten sulfur extrusions) and the effect of radiation (most notably x-rays) on some of the allotropes. We have produced mixtures of sulfur allotropes in the laboratory by quenching molten sulfur and we find that the spectra indicate the presence of certain red-colored allotropes which are preserved upon quenching. We find that the color of the sulfur glass produced is redder when the temperature of the original melt is higher (Nelson and Smythe, 1985). This is consistent with the suggestion that Io's spectral geometric albedo can be partly explained by the presence of quenched sulfur glasses.

Preliminary investigations of the effect of x radiation on elemental sulfur indicates that at low temperatures (~100 deg K.), a red-colored allotropes. This would be consistent with the presence of elemental sulfur on Io. Further work in this area remains for a follow-on investigation.

REFERENCES

Nelson, R. M. and W. D. Smythe, (1985). Jupiter's satellite Io: Surface composition based on spectral reflectance of quenched sulfur glasses. EOS, Tr. Am. Geophys. U., 66, p. 947.

Nelson, R. M. and W. D. Smythe, (1986). Spectral reflectance of sulfur trioxide: Implications for Jupiter's satellite Io. Icarus, 66, pp. 181-187.

Nelson, R. M. (1983). Color of irradiated sulfur at low temperature: Implications for Io. Bull. Am. Astron. Soc., 15, p. 851.

Smythe, W. D., R. M. Nelson, D. B. Nash, (1979). Spectral evidence for sulfur dioxide frost or adsorbate on Io's surface. Nature, 280, p. 766.

SOLID SULFUR IN VACUUM: SUBLIMATION EFFECTS ON SURFACE MICRO-TEXTURE, COLOR, AND SPECTRAL REFLECTANCE, AND APPLICATIONS TO PLANETARY SURFACES; D. B. Nash, Jet Propulsion Laboratory, California Institute of Technology, Pasadena, CA

A new form of sulfur that is white at room temperature, and very fluffy in texture, has been found in laboratory experiments on the effects of vacuum sublimation (evaporation) on solid sulfur. This work is an outgrowth of proton sputtering experiments on sulfur directed toward understanding Jovian magnetospheric effects on the surface of Io (Nash, 1985).

Fluffy white sulfur is formed on the surface of solid yellow, tan, or brown sulfur melt freezes in vacuum by differential (fractional) evaporation of two or more sulfur molecular species present in the original sulfur: S_8 ring sulfur is thought to be the dominant sublimation (evaporation) phase lost to the vacuum sink, and polymeric chain sulfur (S_u) the dominant residual phase that remains in place forming the residual fluffy surface layer.

The microscopic structure of the fluffy sulfur layer determined from scanning electron microscope (SEM) images is skeletal with a lacy-like fabric and with filamentary components having a scale size of <1 um. It appears from its relatively organized structure to be dominated by molecular forces rather than adhesive forces between particulate grains such as that described for water/clay sublimate residues by Saunders et al. (1985). In the SEM pictures it resembles cellular sulfur material described by Tuinstra (1967) resulting from dissolving melt-freeze sulfur in liquid CS_2 solvent and obtaining an insoluble polymeric residue. The residual subliming surface becomes very porous (up to about 98% void space) and has a bulk thickness of ~0.5 mm after ~800 hours at 2×10^{-7} torr (~3×10^{-10} atm.)

The color of the evaporating surface changes from the original -- which at room temperature (~300 K) may be yellow, tan, or brown depending on the pre-freeze melt temperature (393-713 K) -- to white with a faint greenish-yellow tint. For fresh sulfur melt-freeze samples evaporating at ~300 K in ~10^{-7} torr vacuum there occur significant spectral, color, and albedo effects in as little as 10 hours, becoming uniformly white within 300 hours, and progressive changes in spectral details continue for at least 1200 hours. Once removed from vacuum conditions the material is stable in form and color with time (for at least several months).

The reflectance spectrum of the original sulfur surface in the UV/VIS (0.35 to 0.70 um) range is greatly modified by formation of the fluffy surface layer: the blue absorption band-edge and shoulder move 0.05 to 0.06 um toward shorter wavelengths resulting in a permanent increase in reflectivity near 0.42 - 0.46 um by as much as 400% or more, and the UV reflectivity below 0.40 um is reduced to about 1/3 its original level to as low as 2%. The new band-edge and shoulder positions are temperature sensitive, as in unmodified sulfur, shifting to shorter wavelengths with decreasing temperature, and returning to their pre-cooled wavelength with temperature recovery; but with fluffy white sulfur the temperature-induced excursion range of the absorption edge is almost entirely within the violet and UV whereas in ordinary sulfur it is mostly in the green and blue wavelengths.

The sublimation (evaporation) rate of sulfur from fresh frozen sulfur melt at initial exposure to high vacuum ($\sim 10^{-7}$ torr) is on the order of 2 x 10^{15} S cm^{-2} sec^{-1} at $\sim$300 K (in agreement with previous measurements by Bradley, 1951), increasing steeply with temperature, decreasing with higher vacuum pressure, and decreasing with vacuum exposure time reaching an equilibrium flux of about 1-4 x 10^{14} S cm^{-2} sec^{-1} after $\sim$1200 hours.

This remarkable form of lacy, fluffy, white sulfur should exist in large quantity on the surface of Jupiter's satellite Io, especially in hotspot regions if there is solid free sulfur there that has solidified from a melt. Its color and spectra will indicate relative crystallization age on a scale of days to months and/or surface temperature distribution history. It suggests that for a sulfur flow surface there could be a class of surface hotspots that have a white-is-hot relationship, an inverse variant of, but not in conflict with, the albedo-vs-temperature relation demonstrated in the Io data by McEwen et al. (1985). The concepts to be developed from this work on fluffy sulfur are expected to be helpful in understanding properties of Io's surface such as composition, adsorbtivity, thermal inertia, polarization, photometry (with solar phase angle), and post-eclipse brightening. The flux of subliming sulfur from hotspots on Io could be a copious and continuous source supplying the Io sulfur torus.

Material with structure similar to that of fluffy sulfur could exist on surfaces of other small (airless) planetary bodies, including comets, that have multiple surface constituents of differing volatility.

References:

Bradley, R. S. (1951). The rate of evaporation and vapour pressure of rhombic sulfur. Proc. Roy. Soc., A205, 553-563.

McEwen, A. S., D. L. Matson, T. V. Johnson, L. A. Soderblom (1985). Volcanic hotspots on Io: Correlation with low-albedo calderas. Submitted to J. Geophys. Res.

Nash, D. B. (1985). Proton irradiation of sulfur: Sputtering yields, spectral reflectance changes, and applications to Io. Bull. Am. Astron. Soc., 17, 921.

Saunders, R. S., F. A. Fanale, T. J. Parker, J. B. Stephens (1985). Properties of filamentary sublimation residues from dispersions of clay in ice. Submitted to Icarus.

Tuinstra, F. (1967). Structural apsects of allotropy of sulfur and the other divalent elements. Uitgerverij Waltman, Delft (The Netherlands). 110 p.

A Preliminary Analysis of the Mariner 10 Color Ratio Map of Mercury

Barry Rava and Bruce Hapke
Dept. of Geology & Planetary Science, Univ. of Pittsburgh

A preliminary geological analysis of the Mariner 10 orange/UV color ratio map of Mercury is given. assuming a basaltic crust. Certain errors in the map are pointed out. The relationships between color and terrain are distinctly non-lunar. Rays and ejecta are bluer than average on Mercury, whereas they are redder on the moon. This fact. along with the lack of the ferrous band in Mercury's spectrral reflectance and smaller albedo contrasts, implies that the crust is low in Fe and Ti. There is no correlation between color boundaries and the smooth plains on Mercury, in contrast the strong correlation between color and maria-highlands contacts on the moon. The smooth plains are not Mercurian analogs of lunar maria, and a lunar-type of second wave of melting did not occur. Ambiguous correlations between color and topography indicate that older, redder materials underlie younger, bluer rocks in many places on the planet, implying that the last stages of volcanism involved low-Fe lavas covering higher-Fe rocks. There is some evidence of late Fe-rich pyroclastic activity.

CHAPTER 7

RADAR APPLICATIONS

A COMPILATION SYSTEM FOR VENUS RADAR MISSION (MAGELLAN)

Sherman S. C. Wu, Francis J. Schafer, and Annie-Elpis Howington,
U.S. Geological Survey, Flagstaff, Arizona 86001

A synthetic aperture radar (SAR) compilation system has been developed for extraction of topographic information of Venus from stereoradar imagery to be obtained from the Magellan mission. The system has been developed for an AS-11AM analytical stereoplotter (Wu et al., 1986). During fiscal year 1986, extensive tests were made on this compilation software by using stereo-images from various radar systems, both spacecraft and airborne (Table 1). Maps were compiled and the precision of planimetry and contour measurement was evaluated. Digital data of some models were also collected for processing orthophoto or perspective views by using the original radar images.

From the Seasat radar images (Wu et al., 1986), a planimetric map was compiled from the New Orleans model and a contour map from the Los Angeles model. Because of strong geometries, i. e., large base-to-height ratios (0.99 and 0.85), 0.9-m and 1.2-m repeatability elevation measurements were obtained from these two models.

A contour map of Mt. Shasta (Fig. 1) was compiled on the AS-11AM analytical stereoplotter from SIR-B stereoradar images (same-side mode). Because the average residual of elevation measurements in this area is about 8 m, the contour interval could have been as small as 25 m. Residuals of elevation measurements vary, however, depending on the combination of look-angles of the pair of stereo-images.

Three stereomodels of the SIR-B images have been compared. Their respective average elevation residuals are 7.3 m, 8.7 m, and 33.9 m, and their respective combinations of look angles are 29.5° and 60.1°, 29.5° and 53.5°, and 53.5° and 60.1°.

The two models of stereoradar images taken by the NASA 102A airborne radar system cover part of Mt. St. Helens. Both models have a repeatability elevation measurement of about 5 m. A contour map was compiled from each model, but the geometry of the model having an opposite-side mode (Fig. 2) is stronger than the one having a same-side mode.

Also tested with the SAR compilation software were two stereomodels of radar images of the vicinity of Spitsbergen taken by the airborne ERIM X-C-L radar system. The models cover the same ground features, but one model is in ground-range geometry and the other is in slant-range geometry. Geometries of both models are compatible. The model in ground-range geometry was used to compile a contour map at a scale of 1:25,000 with a contour interval of 10 m.

As noted above, stereomodeling from radar images has been proven feasible and thus the mathematical concept of the compilation software is the correct approach. All stereomodels tested were, in general, free of parallax and suitable bases for map compilation. During testing, the software was enhanced and modified to obtain more flexibility. Development of the radargrammetry will be continued to improve measurement precision and map compilation for multiple models. Feasibility studies of map compilation from digital radar data will also be considered.

TABLE 1. RADAR IMAGES USED FOR TESTING THE SAR COMPILATION SYSTEM

Vehicle	Spacecraft			Aircraft		
Mission/Radar System	Seasat		SIR-B	NASA 102A		ERIM X-C-L
Site	New Orleans	Los Angeles	Mt. Shasta	Mt. St. Helens		Spitsbergen
Geometry*	S.S.	O.S.	S.S.	O.S.	S.S.	S.S.
Range**	S.R.	S.R.	G.R.	G.R.	G.R.	S.R. & G.R.

Remarks: * S.S.--Same-side mode; O.S.--Opposite-side mode
** S.R.--Slant-range geometry; G.R.--Ground-range geometry

Reference

Wu, S. S. C., Schafer, F. J., and Howington, A. E., 1986, Radargrammetry for the Venus Radar Mapper Mission: Report of Planetary Geology and Geophysics Program-1985, NASA Tech. Memo. 88383, 570-573.

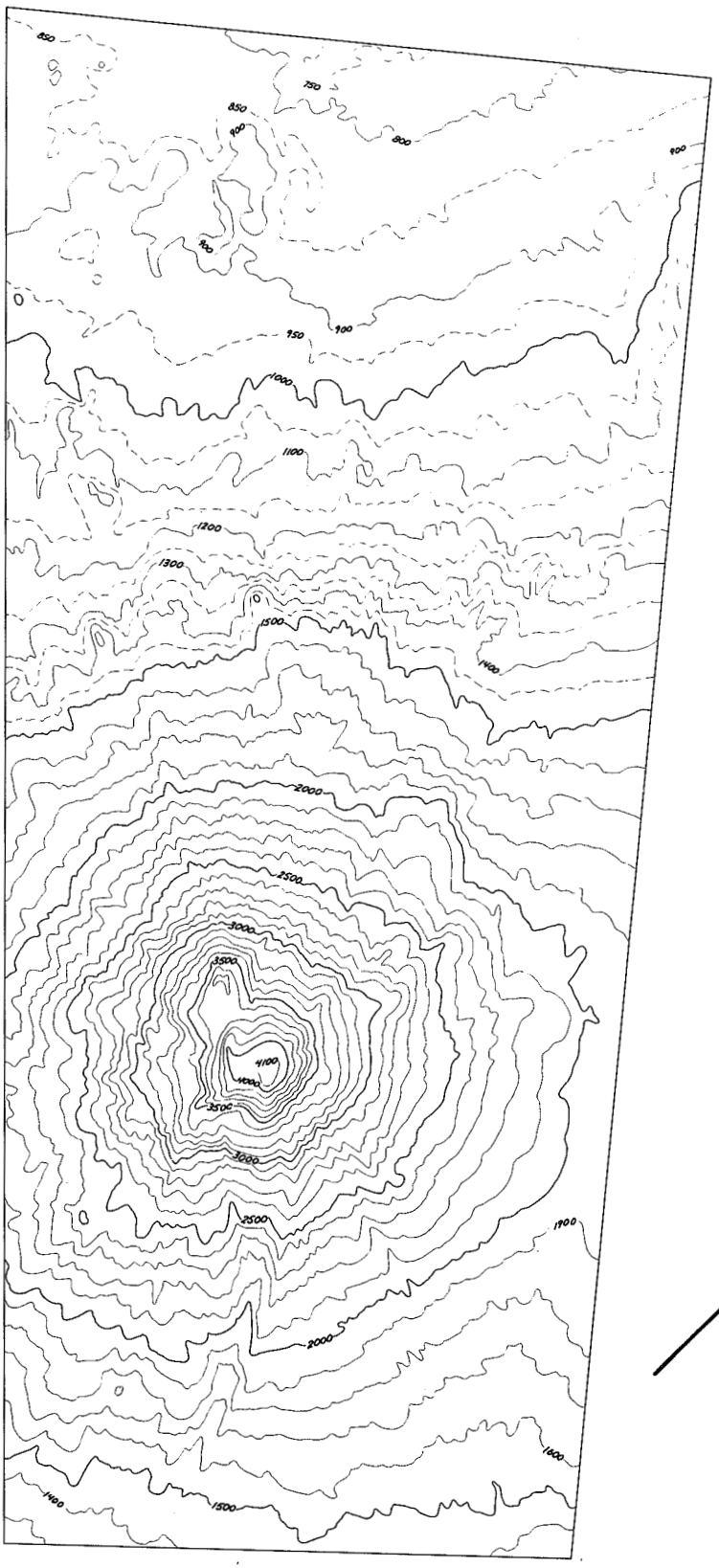

Figure 1. Topographic contour map of Mt. Shasta. Scale 1:200,000. Contour interval 100 m; 50-m intermediate contours in northern part.

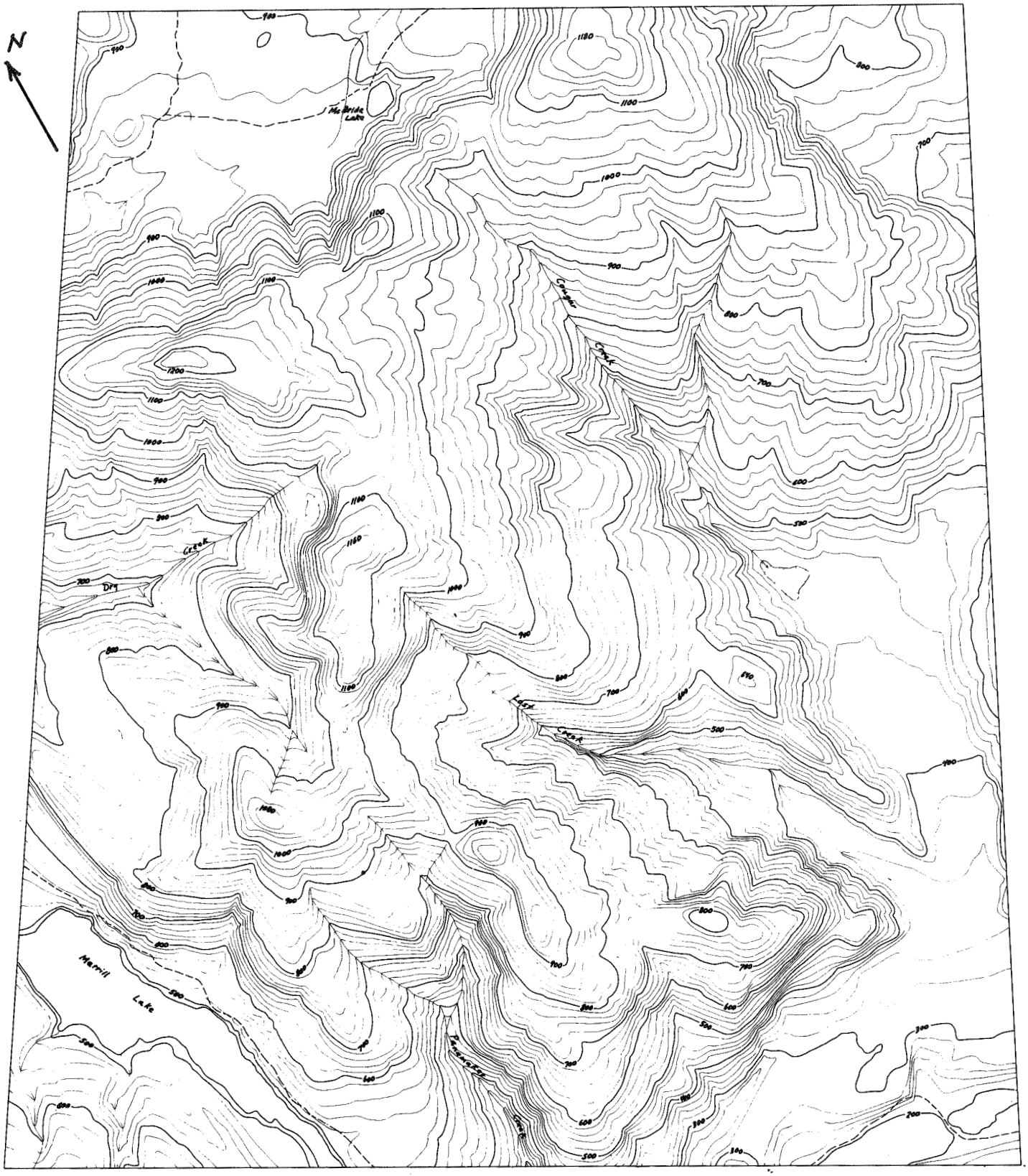

Figure 2. Topographic contour map of part of Mt. St. Helens compiled on the AS-11AM analytical stereoplotter. Scale 1:41,700; contour interval 25 m.

New Very High Resolution Radar Studies of the Moon

Peter J. Mouginis-Mark and Bruce Campbell, Planetary Geosciences, Hawaii Institute of Geophysics, University of Hawaii, Honolulu, Hawaii 96822

As part of an effort to further understand the geologic utility of radar studies of the terrestrial planets, we are currently collaborating with investigators at NEROC Haystack Observatory, MIT and the Jet Propulsion Laboratory in the analysis of existing 3.8 and 70 cm radar images of the moon, and in the acquisition of new data for selected lunar targets. The intent is to obtain multi-polarization radar images at resolutions approaching 75 meters (3.8 cm wavelength) and 400 meters (70 cm wavelength) for the Apollo landing sites (thereby exploiting available ground-truth) or regions covered by the metric camera and geochemical experiments onboard the command modules of Apollos 15, 16 and 17. Similar studies were conducted by Moore and Zisk (1973) immediately following the Apollo Program, but at much lower spatial resolution and without the complete phase history of the radar echo being recorded.

As of Fall 1986, the acquisition of the new data is well underway. Three attempts have so far been made by S. Zisk at Haystack to obtain new images at 3.8 cm wavelength, and preliminary measurements of the leading edge of the moon and the Apollo 17 landing site show that geologically-useful images are likely to be produced by early 1987. 70 cm data have also been obtained by Thompson for Copernicus Crater. Currently, improvements still have to be made to the pointing of the radar antenna, but once the lunar emphemeris is better known and radar tracking has been improved it should be possible to obtain radar images measuring a few thousand square kilometers at the desired sub-kilometer resolution.

In the meantime, we are renewing studies of the 3.8 cm lunar maps produced by Zisk *et al.* (1974) and 70 cm data produced by Thompson (1986). These data were collected in both like- and cross-polarizations, and in the case of the 70 cm data, permit the phase records to be used to assess the scattering properties of the surface in a similar manner to the interpretation of terrestrial quad-polarized radar images (Thompson *et al.*, 1986; Zebker *et al.*, 1986). In particular, we are comparing the distribution of surface units on the moon that show a mismatch between the surface slope implied by like- and cross-polarized scattering data, based on the scattering models of Evans and Hagfors (1964), and Hagfors and Evans (1968). The unusual values of cross-to-like polarization observed for volcanic flows in western Mare Imbrium (Schaber *et al.*, 1975) have been observed in both of our existing data sets and, together with the Apollo landing sites and young craters Copernicus and Tycho, form the basis for targeting of new radar acquisitions for geologically-interesting areas on the moon over the coming months.

REFERENCES: Evans, J.V. and T. Hagfors (1964). On the interpretation of radar reflections from the moon. *Icarus, vol. 3*, p. 151-160. Hagfors, T. and J.V. Evans (1968). Radar studies of the moon. Chapter 5 in: *Radar Astronomy*, (J.V. Evans and T. Hagfors, Eds.), McGraw-Hill, N.Y. Moore, H.J. and S.H., Zisk (1973). Calibration of radar data from Apollo 17 and other mission results. *Apollo 17 Prelim. Sci. Rpt., NASA SP-330*, p. 33-10 to 33-17. Schaber, G.G., T.W. Thompson and S.H. Zisk (1975). Lava flows in Mare Imbrium: An evaluation of anomalously low Earth-based radar reflectivity. *The Moon, vol. 13*, p. 395-423. Thompson, T.W. (1986). High resolution lunar radar map at 70-cm wavelength. Submitted to *Earth, Moon and Planets*. Thompson, T.W., H.A. Zebker and J.J. Van Zyl (1986). Lunar radar polarimetry. *Trans. Amer. Geophys. Union*, in press. Zebker, H.A., J.J. Van Zyl and D.N. Held (1986). Imaging radar polarimetry from wave synthesis. *J. Geophys. Res.*, in press. Zisk, S.H., G.H. Pettengill and G.W. Catuna (1974). High-resolution radar maps of the lunar surface at 3.8 cm wavelength. *The Moon, vol. 10*, p. 17-50.

HIGH RESOLUTION RADAR MAP OF THE MOON

T. W. Thompson, Jet Propulsion Laboratory, Pasadena, CA 91109

Previous radar mappings of the Moon at 70 cm wavelength in the late 1960s by Thompson (1974) have been replaced with a new set of observations conducted between 1981 and 1984 using the 430 MHz radar at the Arecibo Observatory, Puerto Rico. Radar resolution was reduced to 2-5 km radar cell-size and a "beam-sweep", limb-to-limb calibration was conducted. Advances in computer technology provided the principal means of improving lunar radar mapping at this wavelength. These new lunar radar maps are described in greater detail by Thompson (1986).

The antenna beamwidth for the 430 MHz radar at Arecibo is only 10 arc-minutes, about one-third of the angular width of the lunar disk when viewed from Earth. Thus, some 18 separate beam positios were needed to map the entire disk. Twelve of these were placed in an "outer ring" surrounding the center of the disk. To tie the eighteen separate beam positions together, a limb-to-limb, beam swing calibration was conducted. Here the antenna beam was slowly swept across the lunar disk at a rate of 2 arc-minutes per minute. This was repeated north and south of the apparent equator on several different days. This calibration was conducted at somewhat coarser resolution than that for the individual beam positions described above.

Radar observations of the Moon were conducted by transmitting pulses from the main antenna and receiving echoes at an auxiliary antenna located some 11 km NNE of the main antenna. Circular polarization was used to obviate the adverse effects of Faraday rotation in Earth's ionosphere. Post-observation data reduction used the delay-Doppler techniques described by Thompson (1978). Radar echoes from the Moon are separated into time-delay (range) bins and Doppler-frequency bins which provides a two-dimensional separation and eventual mapping to lunar latitude and longitude. Radar echo strengths are also normalized in the mapping by removing predictable variations. This processing removes background noise levels, accounts for antenna gain and scattering area differences across the beam, divides by an average scattering law, and adjusts final map values so their averages on a 5^0 x 5^0 squares agree with the limb-to-limb, beam-sweep calibration described above. The final map is a square array of pixels separated by 0.1^0 in latitude and longitude. Two 1800 by 1800 pixel arrays represent the lunar earthside hemisphere ($+90^0$ in latitude and longitude) in the two radar polarizations. These data have been shipped to the Planetary Data Centers.

The data from these observations is shown in Figure 1, which shows an orthographic projection of the new radar data. The weakest scattering differences in these displays show scattering differences on the order of ten to twenty percent. The largest scattering differences in Figure 1 are those places which saturate as totally white areas have radar echoes ten or more times stronger than the average. Most echo deviations tend to be stronger than the average (whiter in the photographs of Figure 1).

References:

T.W. Thompson, 1974, Atlas of Lunar Radar Maps at 70-cm Wavelength, The Moon, 10, 51-85.

T.W. Thompson, 1979, A Review of Earth-based Radar Mapping of the Moon, The Moon and Planets, 179-198.

T.W. Thompson, 1986, High Resolution Lunar Radar Map at 70-cm Wavelength, accepted for publication in The Earth, Moon, and Planets.

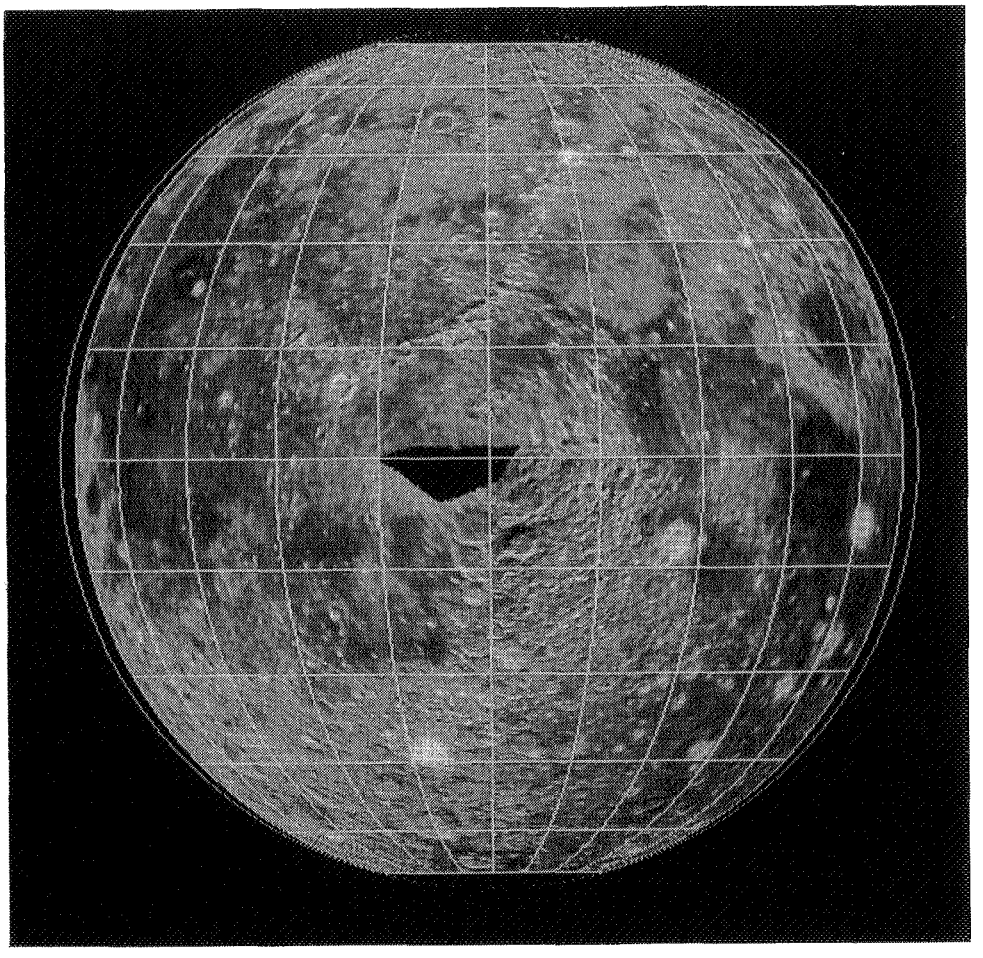

Figure 1. New high resolution radar map of the moon at 70 cm wavelength. North is at the top and grid lines are every 15^{o} in latitude and longitude. Thus, photograph shows "polarized" echoes; the expected polarization from a plane mirror reflection.

LANDFORM IDENTIFICATION - LUNAR RADAR IMAGES

Henry J. Moore, U.S. Geological Survey, Menlo Park, CA 94025
T. W. Thompson, Jet Propulsion Laboratory, Pasadena, CA 91109

Three sets of polarized radar-echo images of the Moon are being examined to establish the relation between radar resolution and landform-identification resolution [1-4]. The wavelengths, radar resolutions (cell sizes), and approximate number of real or apparent landforms for the sets are as follows:

Set #	Wavelength	Cell sizes	Number of landforms
1	3.8 cm [5]	1-2 km	1,553
2	70 cm [6] (high resolution)	2.5-5 km	1,594
3	70 cm [7] (low resolution)	10-20 km	983

The results of the study should be valuable to those planning to acquire or interpret radar images of the Earth or other planetary bodies.

After comparison with lunar maps and photographs, real and apparent landforms on the radar images are grouped into one of seven classes [1-4]: (1) resolved and clearly identified; (2) resolved and would probably be correctly identified; (3) resolved, but interpretation is uncertain; (4) detected, but elements are not resolved; (5) not detected; (6) array of landforms is resolved, but interpretation of the array is uncertain; and (7) radar portrays a fictitious landform.

Data recorded for each real or apparent landform for each set of images includes the following: (1) a name, (2) selenographic coordinates, (3) diameter and relief obtained from lunar maps and photographs, (4) the class, (5) diameter measured on the radar image, (6) background terrain, (7) geologic age, and (8) the Lunar Aeronautical Chart number. A computer program sorts and orders the data by diameter or relief, computes the percent of each class in frequency bins of 100, and computes the geometric mean of the landform diameter or relief for each frequency bin. Calculations are made in frequency steps of 10.

Current results show strong relations between radar resolution and diameter or relief of landforms that are

clearly identified and those that would probably be correctly identified (class 1 + class 2), as shown in table 1. Current results are not depicted; they are similar, but not identical, the those in previous abstracts [e.g. 1, figure 1].

Table 1. Percentage of resolved and identified landforms portrayed in lunar radar images.

Percentage of class 1+2 landforms	Mean diameters of landforms (km) corresponding to the indicated percentage. 3.8 cm	70 cm high	70 cm low
10	5	12	35
20	6	16	56
30	7	25	--
40	9	35	--
50	11	44	--
60	16	--	--
70	20	--	--
80	35	--	--

Percentage of class 1+2 landforms	Mean relief of landforms (km) corresponding to the indicated percentage. 3.8 cm	70 cm high	70 cm low
10	0.5	1.0	2.7
20	0.6	1.7	---
30	0.8	2.6	---
40	1.1	2.8	---
50	1.4	3.1	---
60	2.0	---	---
70	2.2	---	---
80	2.6	---	---

Landforms are not detected (class 5) at all diameters and reliefs, but the percentage of undetected landforms decreases with increasing mean diameter and increasing mean relief. Landforms are simply detected (class 4) at most mean diameters and reliefs. Ambiguous arrays (class 6) portrayed by the radar constitute up to about 16, 22, and 15 percent of the landforms at various diameters and relief values for the 3.8 cm, 70 cm high resolution, and 70 cm low resolution images, respectively. Only a few percent of the landforms portrayed by the radar images at various diameters and relief values are fictitious (class 7).

When data acquisition is complete, the data will be analyzed as functions of angle of incidence (lunar-scattering function) [6], background terrain, and geologic age [7].

Preliminary comparisons of the actual observed crater

size-frequency distributions with those obtained from the radar images show increasing departures with increasing resolution. For the 3.8 cm radar images, the cumulative frequency of craters greater than 22.6 km across agree to within 21 percent of the actual cumulative frequency, and the population indices (slope of the distribution) are similar and near -2. Here, the crater frequencies from the radar image lie below the observed ones. Comparisons for the other radar images are less satisfactory at this time.

References

[1] Moore, H. J. and Thompson, T. W., 1986, Landform identification in lunar radar images: Lunar and Planet. Science XVII, p. 565-566.

[2] Moore, H. J. and Thompson, T. W., 1986, Lunar radar images - landform identification: Repts. Planet. Geol. and Geophys. Prog.--1985, NASA TM 88383, p. 550-552.

[3] Thompson, T. W. and Moore, H. J., 1985, Landform identification in radar images: Lunar and Planet. Science XVI, p. 860-861.

[4] Moore, H. J. and Thompson, T. W., 1985, Landform identification on radar images: Repts. Planet. Geol. and Geophys. Prog.--1984, NASA TM 87563, p. 458-460.

[5] Zisk, S. H., Pettengill, G. W., and Catuna, G. W., 1974, High-resolution radar maps of the lunar surface at 3.8-cm wavelength: The Moon, v.10, p. 17-50.

[6] Thompson, T. W., unpublished data.

[7] Thompson, T. W., 1974, Atlas of lunar radar maps at 70 cm wavelength: The Moon, v.10, p. 51-85.

[8] Hagfors, T., 1970, Remote probing of the Moon by infrared and microwave emissions and by radar: Radio Science, v. 5, p. 189-227.

[9] Wilhelms, D. E., 1980, Stratigraphgy of part of the lunar near side, U. S. Geol. Survey Prof. Paper 1046-A, 71p.

GOLDSTONE RADAR OBSERVATIONS OF MARS: THE 1986 OPPOSITION

T. W. Thompson, Jet Propulsion Laboratory, Pasadena, CA 91109

Radar echoes from the planet Mars were obtained on 27 S-band (wavelength=12.5 cm) and 2 X-band (wavelength = 3.5 cm) tracks using the Goldstone Solar System Radar. These observations took advantage of the favorable 1986 opposition since the earth-Mars distance was 0.40 AU at opposition (the smallest earth-Mars distance since the 1971 and 1973 oppositions) and radar echo strength is proportional to inverse-fourth-power to the distance to the target. Another equally favorable opposition occurs in 1988; these favorable geometries do not reoccur until the next century.

The coverages of the 1986 Goldstone radar observations are summarized in Table 1 and Figure 1; which show the daily start and end point of each observation. The observations were conducted via the cw-spectra techniques described by Harmon et al. (1982 and 1985). A continuous tone was transmitted at Mars and the radar echo was sampled to obtain a Doppler-spread spectrum. Each received event was separated into polarized (opposite sense circular, OC) and depolarized (same sense circular, SC) periods. Also, a minute or two of noise was recorded in each transmit-receive cycle. The total echo time was the round-trip travel-time which was varied from about seven minutes near opposition to over twelve minutes for last runs in October. Thus, about one-third of the total track was devoted to actual echo recording.

The coverage on Mars as shown in Table 1 started at 8^{o} S, travelled toward the equator to 3^{o} S during August, and then migrated south to 14^{o} S for the last run in October. These are new areas for earth-based radars. The data analysis is just getting underway. However, our volatile real-time spectra displays often showed features similar to those observed by Harmon et al. (1982 and 1985).

There was one successful ranging run on 17 October 1986 (the last track). The ground track for this run was similar to the cw observation of 15 October 1986, the Southern-most track in Figure 1. This ranging run had a resolution of 2 microseconds and should yield surface heights accurate to 300 meters.

References:

J. K. Harmon, D. B Campbell, and S. J. Ostro (1982), Dual-Polarization Radar Observations of Mars: Tharsis and Environs, Icarus, 52, 171-187.

J. K. Harmon and S. J. Ostro (1985), Mars: Dual-Polarization Radar Observations with Extended Coverage, Icarus, 62, 110-128.

DOY	DAY-ID	IUTC	LUTC	FREQ				
169	860618	833	1102	S-BAND	LON-LAT =	95.	131.	9- 7S
170	860619	1117	1255	S-BAND	LON-LAT =	126.	150.	9- 0S
174	860623	633	955	S-BAND	LON-LAT =	21.	70.	8-30S
175	860624	619	1225	S-BAND	LON-LAT =	8.	98.	8-22S
177	860626	611	1053	S-BAND	LON-LAT =	349.	57.	8- 5S
186	860705	946	1148	S-BAND	LON-LAT =	321.	351.	6-40S
187	860706	637	1121	S-BAND	LON-LAT =	266.	335.	6-31S
195	860714	452	801	S-BAND	LON-LAT =	169.	215.	5-16S
196	860715	530	930	S-BAND	LON-LAT =	170.	228.	5- 7S
198	860717	430	950	S-BAND	LON-LAT =	137.	215.	4-50S
201	860720	429	959	S-BAND	LON-LAT =	111.	191.	4-26S
202	860721	434	824	S-BAND	LON-LAT =	103.	159.	4-18S
205	860724	410	850	S-BAND	LON-LAT =	70.	139.	3-58S
209	860728	346	807	S-BAND	LON-LAT =	29.	92.	3-36S
216	860804	319	752	S-BAND	LON-LAT =	320.	26.	3-12S
219	860807	302	826	S-BAND	LON-LAT =	288.	7.	3- 8S
221	860809	304	727	S-BAND	LON-LAT =	271.	335.	3- 8S
228	860816	223	626	S-BAND	LON-LAT =	197.	256.	3-21S
237	860825	445	653	S-BAND	LON-LAT =	149.	180.	4- 6S
241	860829	139	704	S-BAND	LON-LAT =	66.	145.	4-35S
244	860901	303	558	S-BAND	LON-LAT =	59.	101.	5- 0S
246	860903	249	634	S-BAND	LON-LAT =	37.	92.	5-19S
250	860907	239	630	S-BAND	LON-LAT =	357.	53.	5-58S
255	860912	430	627	X-BAND	LON-LAT =	337.	5.	6-54S
259	860916	211	643	S-BAND	LON-LAT =	265.	331.	7-41S
260	860917	225	626	X-BAND	LON-LAT =	259.	318.	7-53S
276	861003	420	523	S-BAND	LON-LAT =	135.	150.	11-28S
281	861008	335	600	S-BAND	LON-LAT =	76.	111.	12-40S
285	861012	2335	546	S-BAND	LON-LAT =	329.	59.	13-50S

Table 1: Goldstone Radar Observations of Mars: 1986

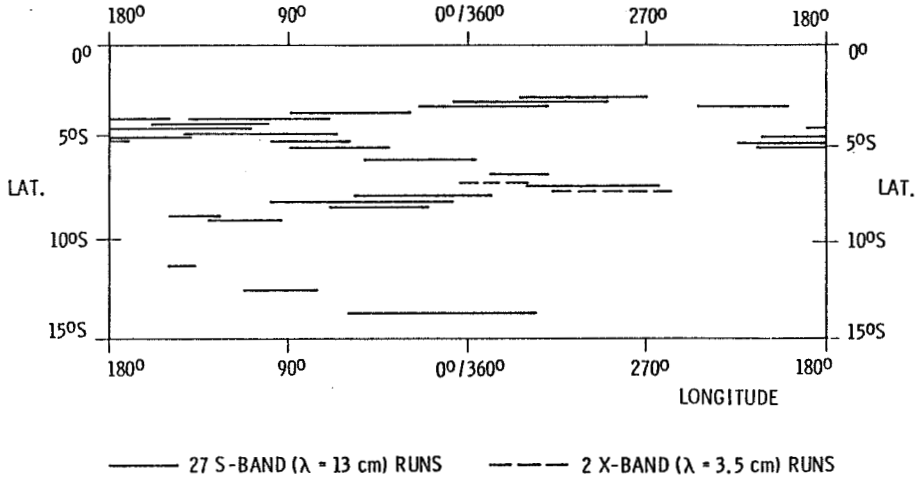

Figure 1: Latitude-Longitude Coverages of 1986 Goldstone Radar Observations of Mars

A DIFFUSE RADAR SCATTERING MODEL FROM MARTIAN SURFACE ROCKS

W. M. Calvin, B. M. Jakosky, Laboratory for Atmospheric and Space Physics, University of Colorado, and P. R. Christensen, Department of Geology, Arizona State University

Remote sensing of Mars has been done with a variety of instrumentation at a variety of wavelengths. Jakosky and Christensen (1986) have shown that many of these data sets can be reconciled with a surface model of bonded fines (or duricrust) which varies widely across the surface and a surface rock distribution which varies less so. Recently, a surface rock distribution map from -60 to +60° latitude has been generated by Christensen (1986). Our objective is to model the diffuse component of radar reflection based on this surface distribution of rocks. The diffuse, rather than specular, scattering is modeled here because the diffuse component arises due to scattering from rocks with sizes on the order of the wavelength of the radar beam. Scattering for radio waves of 12.5 cm wavelength is then indicative of the meter-scale and smaller structure of the surface. The specular term is indicative of large-scale surface undulations and should not be causally related to other surface physical properties. A model of the diffuse component could help us compare various radar and infrared data sets and further constrain the nature of the martian surface.

Based on the images of the Viking Lander sites and radar measurements, diffuse scatterers do not appear to dominate the Martian surface. The scattering particles are irregularly shaped and sized and may reside on top of or within a dielectric discontinuity; this precludes a ready analytical solution to the scattering problem. Therefore, a simplified model of diffuse scattering is undertaken.

Although it has been shown that multiple scattering by subsurface rocks may make a significant contribution to the returned diffuse component in radar scattering (Pollack and Whitehill, 1972), our simplified model assumes that only the rocks on the surface will contribute. It is assumed that the rocks are non-absorbing, so that all power extracted from the beam is scattered (i.e., a single scattering albedo of one). Also, it is assumed that the power is scattered isotropically, and the scattering efficiency, Q, is taken to be one. This latter assumption is consistent with the Mie-scattering calculations of Hansen and Travis (1974) for particles of size parameter 1 to 6. The returned power is normalized to that returned from a smooth planet, so that common factors (e.g., incident power) divide out. The total power returned is then proportional to the projected fractional rock coverage integrated over the visible disk. Integration in one dimension, along lines of constant doppler shift, can be performed to obtain the cross section as a function of doppler shift, in a similar format to actual radar measurements.

There are two principle ways to express the rock distribution of a spherical surface projected onto a disk. Further from the center of the disk the surface rock distribution is viewed at an increasingly oblique angle. If the rocks are sitting on the surface, the projected fractional surface coverage is much higher at the limbs than it is normal to the surface, at disk center. We take the apparent surface distribution to be given by $f=1-\exp(-\tau/\cos i)$, where τ is a parameter used to fit the value of the rock abundance when viewed normal to the surface and i is the angle between the surface normal and the

return beam. The angle i varies from 0 to 90° over the face of the planetary disk, so rock abundances vary from a nominal value (e.g., 10%) at the subradar point (disk center) to 100% at the limbs of the planet. This is called, henceforth, the 'exponential model'. Alternatively, the surface distribution can be modeled as flat rocks imbedded in the surface, the 'cobblestone' model. Here, the surface fraction covered by rocks does not depend on incidence angle, and a planet of uniform coverage is represented by that uniform value (e.g., 10%) everywhere.

Both the cobblestone and exponential models were applied to a planet of uniform fractional rock coverage with values ranging from 5 to 20%. This yielded cross section versus Doppler shift curves which were reasonable in shape, and total cross sections for the planet between 0.010 and 0.080, depending on the rock abundance and model type. These values appeared reasonable in light of the measured diffuse cross sections between 0.049 and 0.092 (Harmon and Ostro, 1985). Finally, we applied the exponential and cobblestone models to the map of rock coverage (Christensen, 1986), and compared the results to the published diffuse radar scattering curves (Harmon and Ostro,1985; Harmon, et al., 1982, hereafter, HO and HCO, respectively).

We found that although neither model fit the measured data, the models gave values that were reasonable. The broad shape of the cobblestone model was in reasonable agreement with the data. The magnitudes of the cross section curves as well as the total cross section as a function of longitude were lower than the values given by HO and HCO by a factor of 2 or 3; but given the general assumptions of the model we did not expect to do better. The total cross section as a function of longitude is also well correlated with the 2.5-cm radio emission curve, which is to be expected because both the surface rock map and the radio emission are correlated to thermal inertia (Jakosky and Christensen, 1986).

The following aspects were in poor agreement with the data. The shape of the exponential model was in serious disagreement with the data due to a large degree of limb enhancement. Also, both models have a convex shape for large doppler shifts whereas HO and HCO results are concave in this region. This disagreement could be due to the effects of diffraction or multiple scattering at highly oblique angles of incidence. Another disagreement was the lack of duplication of small-scale features identified by HO and HCO. The locations of these features, as determined by HCO, did not correspond to any obvious features in the surface rock map. Also, there was no run-to-run correspondence between the magnitudes of the modeled and actual cross section curves. This may indicate the sensitivity of the actual measurements to scattering elements in the subsurface or in the polar region, for which we have no data. Another problem is the lack of uniqueness in the surface map. Twice as many scattering elements of one-half the size would produce the same thermal contrasts, but would have very different radar scattering properties. This implies the surface map derived from thermal contrasts is dependent on the assumed size of the scattering elements.

In an effort to bring the model into better agreement with the actual measurements we are currently examining two possibilities. We plan to vary the surface distribution of rocks in the polar regions to see if some of the features reported by HCO could be accounted for. Also, we plan to vary the surface distribution in the latitude and longitude bands which correspond to

the HCO features to see if a distribution which is consistent with the observed radar scattering as well as the thermal contrasts can be obtained.

REFERENCES

Christensen, P.R., The Spatial Distribution of Rocks on Mars, Icarus, in press, 1986.

Hansen, J.E. and L.D. Travis, Light Scattering in Planetary Atmospheres, Space Sci. Rev. 16, 527-610, 1974.

Harmon, J.K., D.B. Campbell, and S.J. Ostro, Dual-Polarization Radar Observations of Mars: Tharsis and Environs, Icarus 52, 171-187, 1982.

Harmon, J.K. and S.J. Ostro, Mars: Dual-Polarization Radar Observations with Extended Coverage, Icarus 62, 110-128, 1985.

Jakosky, B.M. and P.R. Christensen, Global Duricrust on Mars: Analysis of Remote-Sensing Data, J. Geophys. Res. 91, 3547-3559, 1986.

Pollack, J.B. and L. Whitehill, A Multiple Scattering Model of the Diffuse Component of Lunar Radar Echoes, J. Geophys. Res. 77, 4289-4303, 1972.

MARS: SEASONALLY VARIABLE RADAR REFLECTIVITY

L. E. Roth, R. S. Saunders, and T. W. Thompson
Jet Propulsion Laboratory, Pasadena, CA 91109

Since reflectivity is a quantity characteristic of a given target at a particular viewing geometry, the same (temporally unchanging) target examined by radar at different occasions should have the same reflectivity. Zisk and Mouginis-Mark (1980) noted that the average reflectivities in the Goldstone Mars Data (Downs et al., 1975) increased as the planet's S hemisphere passed from the late spring into early summer. We have examined the same data set and confirmed the presence in the data, of the phenomenon of the apparent seasonal variability of radar reflectivity (Roth et al., 1984; 1985). Objections were raised against our reports. These objections fell into three categories:

(1) Reflectivity variations may be present in the Goldstone Mars data. Their presence must be the result of an instrumental/calibration error.

(2) Reflectivity variations may be present in the Goldstone Mars data. Since there is a two-year interval between the two experiments, the variations must be the result of differences in the data reduction procedures applied first to the 1971 data and then to the 1973 data.

(3) Reflectivity variations are not present in the Goldstone Mars data. The variations were introduced into the analysis through comparing reflectivities obtained during two separate experiments. In other words, what appears to be a seasonally variable reflectivity is, in fact, the result of a joint analysis of two incompatible subsets of the combined data set.

Our work in FY'86 was mostly aimed at answering the listed objections. We have completed the effort aimed at validating the Goldstone (1971, 1973) Mars data set. We have reviewed the procedures followed during both the 1971 and 1973 Goldstone Mars experiments and examined the available records. We present here a summary of the principal findings pertaining to Objections (1) and (3).

System calibrations were a regular feature of each observing run. Included in the calibrations were: (1) Measurements of the system temperature. (2) Measurements of the antenna gain variations vs. elevations. (3) Measurements of the antenna gain variations due to structural modifications. (4) Measurements of the transmitter power. Early in each opposition transmitter calibrations were performed at the start and at the end of each run. Later, when no drifts were observed, the transmitter calibrations were discontinued. (5) Measurements of the additive noise of the microwave links (when links used). (6) Monitoring of the antenna pointing accuracy. Tracks of calibration radio sources were regularly scheduled and the results were folded into the operational procedures. We estimate the resulting total reflectivity calibration error to be less than 5% of the respective absolute values.

After having applied all the known corrections to the radar system sensitivity, global reflectivity averages were computed for each opposition. The results are:

$$\langle R\rangle(1971) = 0.0564$$
$$\langle R\rangle(1973) = 0.0625$$
$$\langle R\rangle(\text{All data}) = 0.0594$$

It is seen that the average reflectivity in the 1973 data (240 deg<Ls<325 deg) is higher than the average reflectivity in the 1971 data (200 deg<Ls<275 deg), in agreement with Zisk and Mouginis-Mark (1980) and Roth et al., (1984; 1985). Note that the ratio

$$\frac{\langle R\rangle(1973)-\langle R\rangle(1971)}{\langle R\rangle(\text{All data})} \times 100$$

is equal to 11%, a value twice that of the estimated calibration error. This discrepancy could be interpreted in the following manner: (1) The difference in the reflectivity averages in the 1971 and 1973 data is being caused by some unknown and unaccounted for instrumental error and calibration drift. This error is of the approximately same magnitude as all the known uncertainties. (2) The difference in the reflectivity averages in the 1971 and 1973 data is being caused by differences in coverage. The overlap is sparse and thus the difference in the mean 1971 and 1973 reflectivities could be caused by differences in coverage. (3) The difference in the reflectivity averages in the 1971 and 1973 data is being caused by changes in the target characteristics. Those changes may be caused by two agents: dust precipitation/removal or thawing of subsurface ice. Modeling exercises indicate that a shifting dust cover is not likely to be a major contributor to the observed reflectivity variations (Zisk and Mouginis-Mark, 1981; Roth et al., 1986a). The liquid-water hypothesis has not been supported by a credible model of the thermal regime in the upper 1 m of the Martian surface. Thus all three interpretations are about equally likely or unlikely, depending on the point of view. The liquid-water hypothesis could, in principle at least, account for the pattern of seasonal variability, whereas the other interpretations could not.

To address Objection (3), we investigated the statistical relationship between reflectivities and the areocentric longitude, Ls, separately for the 1971 and 1973 data (Roth et al., 1986b). The computations were carried out separately for the 1971 data, the 1973 data for the cases when the 1973 scan was taken at a higher solar longitude as the 1971 scan, and for all data combined. Conclusions: (1) Correlation coefficients between the mean reflectivity ratios and the lengths of the temporal separation of overlapping scans are positive for the 1971 Goldstone Mars data. This means that the average reflectivities in the 1971 data tend to increase as the S hemisphere passes from the vernal equinox to the summer soltice. (2) Correlation coefficients between the mean reflectivity ratios and the lengths of the temporal separation of overlapping scans is largely negative for the 1973 Goldstone data. The mean reflectivities in the 1973 data appear to undergo a mild decrease as the S hemisphere enters late summer. At

Crit=0.3 (for the definition of the quantity Crit see Roth et al., 1986b) there is an exception to this general trend. This exception is significant in that it shows that the data set is statistically inhomogeneous. Random removal of a few elements from the sample affects the sample statistics. Thus any conclusions based on purely statistical arguments have to be received with caution. Statistical inhomogeneity of the data deserves further investigation. (3) The apparent seasonal pattern in the behavior of the mean reflectivities is not the result of the joint analysis of the 1971 and 1973 data. This is our most important finding. The seasonal reflectivity variations may or may not be real. However, they are certainly a characteristic property of each individual subset, rather than of the combined (1971, 1973) Goldstone set. (4) Reflectivity variations in the 1971 data are consistent with the hypothetical presence of subsurface moisture passing through a seasonal freeze-thaw cycle. If the correlation coefficient for Crit=0.3 is ignored, reflectivity variations in the 1973 data are also consistent with the liquid water hypothesis, provided we accept a naive, intuitive notion that subsurface moisture in the subequatorial areas freezes after the S hemisphere passes the summer stoltice. (5) Consistency is not equivalent to a proof. Reflectivity variations could only be considered a proof of the existence of the subsurface moisture in the equatorial areas of Mars if the characteristic pattern of seasonal behavior were to be confirmed by further, preferably multifrequency, radar observations.

Downs, G. S., R. M. Goldstein, R. R. Green, G. A. Morris, and P. E. Reichley (1973). Martian topography and surface properties as seen by radar: The 1971 opposition. Icarus 18, 18-21.

Roth, L. E., R. Saunders, and G. Schubert (1984). Radar and the detection of liquid water on Mars (abstract). In Abstracts for Water on Mars Workshop, 63-65. Lunar and Planetary Institute, Houston.

Roth, L. E., R. S. Saunders, and G. Schubert (1985). Mars: Seasonally variable radar reflectivity. Lunar Planet. Sci. XVI, 712-713.

Roth, L. E., R. S. Saunders, and T. W. Thompson (1986a). Radar reflectivity of a variable dust cover. In Abstracts for Dust on Mars Workshop, 59-61. Lunar and Planetary Institute, Houston.

Roth, L. E., R. S. Saunders, G. S. Downs, and G. Schubert (1986b). Mars: Seasonally variable radar reflectivity II. Lunar Planet. Sci. XVII, 730-731.

Zisk, S. H. and P. J. Mouginis-Mark (1980). Anomalous region on Mars: Implications for near-surface water. Nature 288, 735-738.

Zisk, S. H. and P. J. Mouginis-Mark (1981). Alternate models for the Solis Lucas radar anomaly on Mars (abstract). In 3rd Int'l Colloq. Mars, 294-296. Lunar and Planetary Institute, Houston.

MEASUREMENTS OF THE DIELECTRIC CONSTANTS FOR PLANETARY VOLATILES.

Vincent G. Anicich and Wesley T. Huntress, Jr.
Jet Propulsion Laboratory, Pasadena, CA 91109

The model of Titan at present has the surface temperature, pressure, and composition such that there is a possibility of a binary ethane–methane ocean (ref. 1). Proposed experiments for future Titan flybys include microwave mappers. Very little has been measured of the dielectric properties of the small hydrocarbons at these radar frequencies. Nor, is there much known about the loss tangent (imaginary component of the dielectric constant) which relates to the penetration distance of the microwaves into the liquids.

We have set up a laboratory experiment, utilizing a slotted line, to measure the dielectric properties of the hydrocarbons, methane to heptane, from room temperature to −180 C. Temperatures below 25 C are maintained using various ice baths. A large dry box is used to eliminate the condensation of water vapor at these lower temperatures.

The literature reveals very little data on these systems. A substantial study was made into the real part of the dielectric constants of these hydrocarbons using a 1 kHz frequency (refs. 2–6). Besides being so far away from 1.2 GHz, the proposed frequency of the mappers, the measurements were made at both reduced and elevated pressures. The change in pressure has a marked effect on the magnitude of the dielectric constants and therefore these earlier results must be evaluated.

Figure 1 is a graphical summary of our results thus far. We have thus determined that our experimental measurements of the real part of the dielectric constants are accurate to ±0.006 and the imaginary part of the dielectric constants, the loss tangent, of the liquids studied is ≤.001. In order to verify this low of a loss tangent we studied the real part of the dielectric constant of hexane at 25 C as a function of the frequency range of the slotted line system that we have. Figure 2 show these results. The dielectric constant of hexane at room temperature, between 500 MHz and 3 GHz, is constant within our experimental error. The real parts of the dielectric constants measured here are consistent with the those that can be compared to the previous literature after pressure extrapolations.

REFERENCES

1. Lunine, J.I., Stevenson, D. J., and Yung, Y.L., 1983, Ethane Ocean on Titan, Science, 222, p. 1229–1230.
2. G. C. Straty and R. D. Goodwin, 1973, Cryogenics, Dec., p. 712.
3. W. P. Pan, M. H. Mady, and R. C. Miller, 1975, AIChE Journal, 21, p. 283 .
4. R. T. Thompson, Jr. and R. C. Miller, 1980, Adv. Cryog. Eng., 25, p. 698.
5. W. G. S. Scaife and C. G. R. Lyons, 1980, Proc. R. Soc. Lond., A370, p. 193.
6. M. G. Gaikwad, R. Chandkrasekar, S. K. David, and V. G. Alwani, 1980, Phys. Lett., 80A, p. 201.

Figure 1.

Dielectric Constants of Hydrocarbons, @ 1.2 GHz

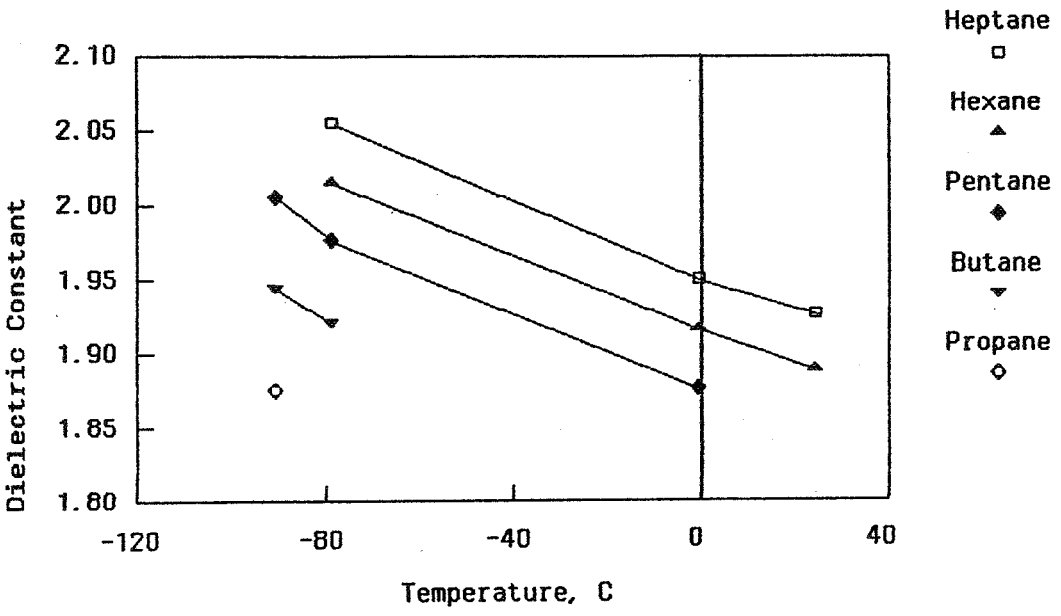

Figure 2.

Dielectric Constant of Hexane, @ 25 C

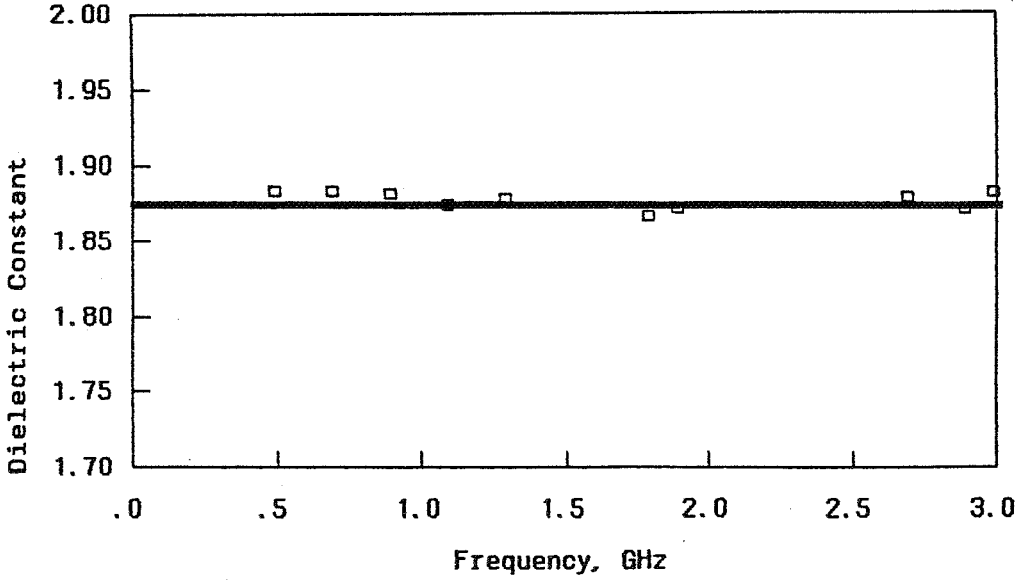

APPLICATION OF NUMERICAL METHODS TO PLANETARY RADIOWAVE SCATTERING

Richard A. Simpson and G. Leonard Tyler
Center for Radar Astronomy
Stanford University, Stanford, CA 94305

Continued advances in computer technology make numerical solution of certain scattering problems feasible. Our work includes investigation of existing techniques to determine those which might be applicable to planetary surface studies, with the goal of improving the interpretation of radar data from Venus, Mars, the moon, and icy satellites.

Numerical scattering models currently require that the surface be approximated by flat, perfectly conducting facets -- as shown in the figure. Each facet is described in some standard way, such as by its unit surface normal and its area. Facet dimensions are limited to fractions (typically one-tenth) of the probing wavelength. The total field is found by simultaneously solving the boundary condition problem on all the facets which make up the approximation to the surface. These equations relate the incident field, the reradiated (scattered) field, and the currents.

Because the complexity of the computation increases rapidly with the number of facets, only relatively simple surfaces have yielded numerical solutions. Somewhat larger structures may be studied if symmetries -- such as about a rotation axis -- are identified, but these are not helpful in the case of randomly rough surfaces. The simple geometrical shapes sometimes have analytical scattering solutions. Comparison of the numerical and analytical results provides insights into the strengths and limitations of both methods.

After experimenting with some smaller numerical codes, we are now examining the Numerical Electrogmatics Code (NEC) developed at the Lawrence Livermore Laboratory. This is one of the most powerful, publicly available codes for scattering analysis in three dimensions. Though not developed for random rough surfaces, it contains elements which may be generalized and which could be valuable in the study of scattering by planetary surfaces.

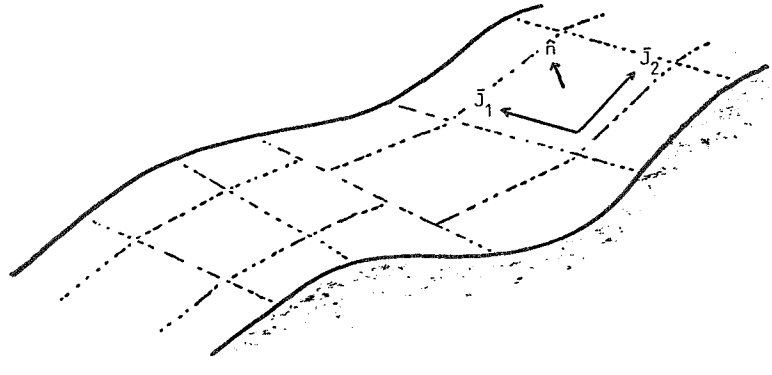

Figure - Gently undulating surface is approximated by facets defined by unit surface normals $\hat{n}$. Orthogonal current components $\bar{J}_1$ and $\bar{J}_2$ link incident and scattered fields through boundary conditions at the surface.

CHAPTER 8

AEOLIAN PROCESSES

BRIGHT SAND/DARK DUST: THE IDENTIFICATION OF ACTIVE SAND SURFACES ON THE EARTH AND MARS

H.G.Blount II[1], *R.Greeley*[1], *P.R.Christensen*[1] *and R. Arvidson*[2], [1]Dept. of Geology, *Arizona State University, Tempe, Arizona, 85287,* [2]*Earth Sciences/ Geology Dept., Washington Univiversity, St. Louis, Mo. 63130*

Aeolian features are common on Mars. Although wind streaks are known to be active features, controversey has arisen regarding the activity of sand sheets and dunes, particularly in the north polar erg. In the absense of *in situ* measurements, remote sensing techniques must be relied upon to address the problem. Field studies and analysis of LANDSAT Thematic Mapper data in the Gran Desierto, Mexico (Blount et al., 1986) may shed light on a technique to distinguish active from inactive (relict) sand surfaces. Active sand bodies are here defined as those with saltation surfaces on which wind-induced ripple marks and/or slipfaces are observable in field outcrop. Inactive sands are those surfaces which do not show evidence of wind movement; sand drapes and fluvial sands being the best examples. Active sand bodies in the study area are consistently brighter (by an average of 20%) at visual and near-infrared wavelengths (0.45-2.35μm) and darker at thermal infrared wavelengths (10.3-12.5μm) than compositionally similar inactive sands. The Gran Desierto study area covers more than 5,500 km^2 and includes major transverse, longitudinal and star dunes.The area is the largest sand sea in North America and has been described in detail by Lancaster et al. (in press). Sands are primarily of quartz composition (80-99%) with varying amounts of amphibole, biotite, carbonate fragments and volcanic detritus as assessory grains.

The reasons for the albedo difference between active and inactive sands are partly explained by a textural analysis of the two terrains. Active surfaces are composed of relatively higher percentages of saltation-sized grains; their higher reflectivity is in agreement with Gerbermann (1979) who found that reflectivity increased directly with weight % sand in sand/silt/clay mixtures. Material in the coarse size fraction (>250μ) is dominated by fragments of amphibole and opaque volcanic lithics (basalt). This size-fraction is generally absent from samples of active sand but makes up as much as 5-10 weight % of many inactive samples. Saltation-sized particles (62.5-250μ) are primarily quartz with minor amphibole and biotite. Active sands are highly unimodal (90-99 wt.%) in this size range. The silt-sized and smaller fraction (<62.5μ) also contains abundant quartz but with relatively more amphibole and aggregated opaque lithics present. Active sands are depleted with respect to inactive sands in both the smallest and largest size fractions present. Inactive sands contain small but conspicuous amounts of coarse sand and silt; the sizes which are dominated by darker materials. It has long been known that minute inclusions of dark material can drastically reduce the reflectance of a mixture (Singer, 1981; Clark, 1983) leading to the conclusion that the apparent darkness of inactive sands is caused by the inclusion of these darker size fractions in small quantities. In the northeastern portion of the Gran Desierto however, darker inactive sands were observed which also lacked a coarse-size fraction; all of the darkening being attributeable to the higher weight percent of darker silt-sized grains. In the TM images, low albedo (at VNIR wavelengths) corresponds to regions of higher silt/clay content. After seiving at one phi intervals both active and inactive samples show a decrease in visual reflectance with particle size. The apparent darkening of these sands with decreasing grain size is apparently contradictory to the characteristic silicate behavior of increasing reflectance with decreasing grain size (Salisbury and Hunt, 1968). While the "normal" situation holds true for the individual components of Gran Desierto sands (primarily quartz and amphibole), it does not describe the mixture of the two end-members. As darker lithic fragments break down to smaller grain sizes, their effective surface area increases in relation to the quartz component. Decreasing grain size then results in a lowering of the overall albedo for the mixture. These results are compatible with laboratory spectral work by Clark (1983), who showed that the overall reflectance in a light/dark mixture (montmorillonite + charcoal) decreases with the particle size of opaques, though the effect was attributed to opaque coatings on otherwise bright grains

rather than the increased surface area of opaques present in smaller particle sizes. Opaque coating have not been observed in the Gran Desierto samples however inactive sand samples always contain quartz/lithic aggregates in their smallest size fraction (<62.5μ). Saltation-size particles of opaques are depleted in both the active and inactive samples. Aeolian sorting may be responsible for this phenomenea, although the presence of lithic opaques in the silt/clay fraction indicates that any saltation-sized fragments are rapidly abraded into smaller-sized grains.

The mixing model of Johnson et al. (1983) has been investigated for tracing the provenance of active and inactive sands based on albedo and spectral variations. If work in other field areas (Kelso Dunes, Ca. and Mohawk Dunes, Az.) confirms that each size fraction indeed possesses a unique reflectivity (assuming constant bulk composition) then a self-mixing model may develop in which each size fraction of the mixture can be considered an independent end-member. It is therefore not simply the weight percent of opaques, but also the weight percent and cross-sectional area of a given size fraction present which will control the total reflectance of a sand/silt mixture. Active sands are found to be brighter than inactive sands, not only because they contain fewer opaques but because the opaques they contain are larger in size and are contributing less to the total sand body radiance.

The Mars Observer (scheduled for launch in 1990) will image the surface at wavelengths from 0.4 to 5.2 μm with the Visual Near-Infrared Mapping Spectrometer (VIMS) and from 6.25 to 50 μm with the Thermal Emission Spectrometer (TES). Portions of these wavelength regions correspond to the Thematic Mapper data which was used to detect albedo differences between active and inactive surfaces. The identification of active sands on Earth, with *a priori* knowledge of bulk composition and grain size distribution, may allow the remote mapping of active sand surfaces on Mars. In conjunction with thermal infrared remote sensing for composition, it may also provide a method for the remote determination of grain size distributiuons within sand/silt mixtures.

REFERENCES:

Blount, H.G.II, Greeley, R. and Christensen, P.R., 1986, Geol. Soc. Amer.Abstr with Prog., v. 18, n. 6

Clark, R.N., 1983, J. Geophys. Res., v. 88, p.10635-10644

Gerbermann, A.H., 1979, Photogrammetric Engr. and Remote Sensing , v. 45, p. 1145-1151

Johnson, P.E., Smith, M.O., Taylor-George, S. and Adams, J.B., 1983, J. Geophys.Res., v.88, p. 3557-3561

Lancaster, N., Greeley, R. and Christensen, P.R., in press, Earth Surface Processes and Landforms

Salisbury, J.W. and Hunt, G.R., 1968, Science, v.161,p.365-366

Singer, R.B., 1981, J. Geophys. Res., v.86, p. 7967-7982

REGIONAL SOURCES AND SINKS OF DUST ON MARS: VIKING OBSERVATIONS OF CERBERUS, SOLIS PLANUM, AND SYRTIS MAJOR

Steven W. Lee, Department of Geology, Arizona State University, Tempe, AZ 85287

Seasonal variability of classical martian albedo features has long been noted by terrestrial observers [1,2]. Spacecraft observations of such features have shown them to be related to aeolian transport of bright dust into and out of regions, primarily in association with major dust storms [cf. 3,4]. Investigation into the amount and direction of dust transport related to variable features can reveal regions which, at present, act as either sources (net erosion of dust from an area) or sinks (net deposition) [5,6].

A study of seasonal variations of albedo features in the Cerberus, Solis Planum, and Syrtis Major regions has been based on Viking Orbiter data obtained over more than one complete martian year. Contour maps of Lambert albedo and single-point thermal inertia have been constructed from the Infrared Thermal Mapper (IRTM) experiment data, and Orbiter images have been used to determine the pattern and variability of regional winds (inferred from wind streak orientations). Coupled with ground-based radar data, these data sets allow the regional sediment transport direction, surface properties (texture, morphology, and roughness), and the implications of the observed seasonal and longer term dust redistribution, to be investigated. The results of this study are outlined below.

Solis Lacus, the most prominent dark albedo feature in Solis Planum, extends over approximately 20° of longitude and 10° of latitude (centered at 25°S, 85°W), and contains and is surrounded by a conspicuous pattern of bright and dark wind streaks. The albedo feature is highly variable in extent and contrast with its surroundings, generally being most distinct during southern spring and summer (minimum Lambert albedo ~0.13) and less distinct during southern fall and winter (minimum albedo ~0.16). The regional thermal inertia values (~8-10 x 10^{-3} cal/cm^2/sec$^{1/2}$/°K) are indicative of a surface covered by particles larger than ~100 μm [7]. A seasonal dust-transport cycle has been proposed to explain these observations: 1) During late southern spring and summer, bright dust is eroded from the surface (possibly ejected by a saltation triggering mechanism) and transported from the region by local dust storms (several were detected by Viking, and have been commonly observed from Earth). Removal of dust over a wide area results in the dark, distinct, Solis Lacus feature. 2) Following cessation of dust-storm activity, sedimentation from the atmospheric dust load occurs over the entire region, decreasing the contrast of the albedo feature with its surroundings. 3) The cycle may be renewed by dust-storm activity the following year. The retention of some albedo features throughout the year, plus the constancy of the regional thermal inertia, requires that the albedo features do not involve erosion or deposition of substantial deposits; cycling of, at most, a few tens of μm of dust is indicated. Differences in time of occurrence, severity, and longevity of dust-storm activity may lead to the observed year-to-year changes in Solis Lacus.

Dramatic seasonal variability is also characteristic of Syrtis Major (~5°S - 25°N, 275° - 300°W). The feature lies on the low-albedo slopes of a volcanic shield [8] (generally darker than ~0.2 in albedo), the darkest area (albedo ~0.1) being closely associated with a mass of dunes located near the crest of the shield. Thermal inertias of ~8 x 10^{-3} cal/cm^2/sec$^{1/2}$/°K, plus the observed dunes, argue strongly for a sandy surface. Syrtis Major increases in albedo immediately following global dust storms, then darkens steadily through the balance of the year until reaching its pre-storm albedo (also confirmed in [9]). The observed trend of bright and dark streaks is in response to winds generally directed upslope and to the west. The dust-transport cycle consistent with these observations is: 1) Enhanced deposition from global dust storms increases the regional albedo. 2) The relatively mobile surface coupled with effective regional winds (possibly reinforced by the global circulation) results in ejection of dust from the surface and net transport to the west during the remainder of the year, yielding a decreased regional albedo. 3) Beginning of another global dust-storm cycle begins the process again. Such a transport cycle provides a

mechanism for significantly enhanced deposition in the neighboring low thermal inertia region, Arabia (as suggested in [10]).

Cerberus is located to the south of the Elysium volcanoes on the gentle slopes (< 0.5°) of Elysium Planitia, extending over about 10° of latitude and 20° of longitude. The feature is generally darker than ~0.2 in albedo, with the eastern portion being darker (minimum albedo of ~0.14) than that to the west (minimum albedo ~0.16). The albedo pattern is closely correlated with the regional thermal inertias, with the darkest areas having inertias of ~10 x 10^{-3} cal/cm^2/sec$^{1/2}$/°K, while the slightly brighter western region exhibits lower inertias of ~8. The entire Cerberus feature is surrounded by brighter (albedos to 0.30), lower inertia (~4) material. The pattern of wind streaks suggests relatively constant effective wind directions from the east, indicating that the gentle topography is not sufficient to significantly alter or enhance the global circulation [5]. Seasonal albedo variations closely mimic those observed in Syrtis Major, although the post-dust-storm darkening is not as pronounced, suggesting that the aeolian environment is less vigorous in Cerberus. The albedo and thermal inertia east-west asymmetry is consistent, however, with coarser material residing in the east and being transported westward by the global winds. Cerberus may therefore be acting as a source of sediment which is transported by saltation rather than in suspension. .

These observations indicate that very different levels of aeolian activity give rise to the noted seasonal variability of these regions: 1) Syrtis Major presents a picture of an extremely active aeolian environment. Deposition occurs only during and immediately following major dust storms, while during the rest of the year regional winds are apparently effective agents of dust ejection and transport. Syrtis Major thus acts as a dust source region through most of the year, possibly supplying the neighboring dust sink region of Arabia. 2) Cerberus may be thought of as a less-vigorous version of Syrtis Major, with definite removal of dust following global storms. A net westward flux of coarser material is evident, possibly encroaching onto surrounding Elysium Planitia. 3) In Solis Lacus, local dust storms result in net removal of dust from the area, while deposition occurs from the atmospheric dust load throughout the remainder of the year. Solis Planum serves as a source region of dust only during the limited period (dust storm season) when regional winds are capable of inducing dust ejection from the surface. Contributions to the global dust load may occur only during major dust storms.

REFERENCES

[1] Slipher, E.C., 1962, *A Photographic History of Mars, 1905-1961*, Northland Press, Flagstaff, AZ.
[2] De Mottoni, G., 1975, *Icarus 25*, 296-332.
[3] Sagan , C. et al., 1973, *J. Geophys. Res. 78*, 4163-4196.
[4] Thomas, P. and J. Veverka, 1979, *J. Geophys. Res. 84*, 8131-8146.
[5] Lee, S.W. et al., 1982, *J. Geophys. Res. 87*, 10025-10041.
[6] Lee, S.W., 1986, submitted to *Icarus*.
[7] Kieffer, H.H., et al., 1977, *J. Geophys. Res. 82*, 4249-4295.
[8] Schaber, G.G., 1982, *J. Geophys. Res. 87*, 9852-9866.
[9] Christensen, P.R., 1986, *Lunar Planet. Sci. Conf. XVII*, 121-122.
[10] Christensen, P.R., 1982, *J. Geophys. Res. 87*, 9985-9998.

HIGH RESOLUTION THERMAL INFRARED MAPPING OF MARTIAN CHANNELS

R.A. Craddock, R. Greeley, and P.R. Christensen, Department of Geology and Center for Meteorite Studies, Arizona State Univesity, Tempe, Arizona 85287.

Morphologic studies [e.g., 1,2] have not yielded a unique interpretation for channel formation [3-7] because of the ambiguity between geomorphologic features and their similarities of one mode of formation with another. For example, teardrop shaped islands, or streamlined hills, have been used in support for all of the channel formation hypotheses and could easily be explained by any of them. Viking Infrared thermal mapper (IRTM) high resolution (2 to 5-km) data have been compiled and compared to Viking Visual imaging subsystem (VIS) data and available 1:5M geologic maps for several martian channels including Dao, Harmakhis, Mangala, Shalbatana, and Simud Valles in an effort to determine the surface characteristics and the processes active during and after the formation of these channels.

Mangala Valles is an approximately 850-km long channel located in the Memnonia quadrangle that cuts through the southern cratered plains from 18.5°S, 149.5°W to Amazonis Planitia at 4.0°S, 150.0°W. Its complicated pattern has been suggested as being the result of several channeling episodes [8]. Channel deposits have been mapped as being approximately 10 to 20-km in width to over 100-km towards the distal portion of the channel [9]. Shalbatana and Simud Valles debouch into Chryse Planitia in the Oxia Palus quadrangle at approximately 10°N, 40°W. Shalbatana Vallis is a sinuous channel with one large tributary and originates in chaotic terrain at 1.0°S, 45.5°W extending NNE for approximately 650-km. Its mapped channel deposits are between 10 to 25-km in width [10]. Simud Vallis originates in Hydroates Chaos at 2.0°N, 36.0°W and may have deposits extending from 20 to over 250-km in width [10] while reaching over 400-km in length. Both Dao and Harmakhis Valles debouch into Hellas Planitia in the Hellas quadrangle. Dao Vallis is a sinuous channel originating in chaotic terrain 33.0°S, 266.0°W and extends for over 500-km to approximately 40.0°S, 275.0°W. Its mapped channel deposits extend from approximately 5 to 50-km in width [11]. Harmakhis Vallis is also sinuous and originates in chaotic terrain closely associated to Reull Vallis at 39.0°S, 265.0°W. Harmakhis Vallis extends for over 450-km and has channel deposits mapped as being 5 to over 40-km wide [11].

This study has involved the use of the highest resolution IRTM data tracks available occurring at ideal conditions (range, 0 to 8,000-km; emission angle, 0° to 60°; time of day, 22 to 2 H; L_s, 0° to 200°). Typically at least two high resolution data tracks occurring at different intervals across the channels' distal extent were examined for each of the above channels; this was needed in an effort to understand the distribution and possibly the mechanism(s) for deposition of material within the channels. Channels such as Huo Hsing, Reull, Samara, and Tiu Valles, among others, have been excluded from this study due to a lack of this optimum data.

Our results show a dominance of aeolian processes active in and around the channels. These processes have left materials thick enough (10's of cm) to mask any genuine channel deposits. High resolution thermal inertia observations taken across the channels' distal extent in various locations compare well with moderate resolution values determined for the corresponding local surrounding regions [12]. A few of the channels (Dao, Harmakhis, and Mangala Valles) showed an increase in thermal inertia with increasing distal extent as observed at Kasei Vallis [13], but these increases were not unique to the area within the channel itself and could be explained as a result of regional trends in grain-size distribution.

Moreover, none of the channels included in this study showed a higher thermal inertia than their surroundings as observed at Ares [13], Ma'adim, and Al-qahira Valles [14]. Results from [13,14] indicate that certain martian channels act as topographic barriers trapping high thermal inertia materials, but instead, our results indicate that very comparable martian channels and their surrounding terrain are blanketed by deposits which are homogeneous in their thermal inertia values. However, optimum IRTM data does not cover the entire martian surface and because local deposits of high thermal inertia material may not be large enough in areal extent or may be in an unfavorable location on the planet, a high resolution data track may not always occur over these deposits. Therefore, aeolian processes may be even more active than the IRTM data tracks can always show. Observations of Ma'adim and Shalbatana Valles illustrate this point.

Ma'adim and Shalbatana Valles are comparable in length (over 900-km versus over 650-km respectively), width (10 to 25-km for both), slope (1/2° to 1° for both), and elevation (from 0 at the distal portion to over 4-km up-channel). They differ in terms of latitude, geologic units, local wind streak patterns, and slightly in the surrounding albedo. Ma'adim Vallis is in the southern hemisphere beginning at 28.0°S, 183.0°W and extending north to 16.0°S, and Shalbatana Vallis is in the northern hemisphere (see above). Ma'adim Vallis is located in hilly and cratered material, which is interpreted as being heavily impacted ancient terrain [15], and Shalbatana is in cratered plateau material, which is interpreted as being heavily impacted lava flows [10]. Local wind streak patterns for Ma'adim Vallis/Aeolis quadrangle are towards the ESE; Shalbatana Vallis/Oxia Palus quadrangle are towards the SSE. Ma'adim is located in a large low albedo region that extends from the Aeolis quadrangle west into Hesperia Planum and further [16,17]. Corresponding wind streak patterns indicate that this low albedo material could move into Ma'adim Vallis and surrounding local craters as suggested in [14,18].

Shalbatana Vallis is approximately 800-km south of a low albedo region situated in northern Chryse and Acidalia Planitias [16, 17]. Based on observed wind streak patterns, we suggest that this low albedo material could move south and remain trapped in Shalbatana Vallis and surrounding large craters. The Oxia Palus quadrangle has dark material centered at 8.0°N, 42.5°W in the junction between Shalbatana Vallis and its tributary, as well as dark material in the south sides of large local craters [19]. However, whether this material is similiar to that observed in Ma'adim and Al-qahira Valles is difficult to determine because the highest resoultion IRTM data tracks do not cover these deposits. The high thermal inertia area reported in nearby Ares Vallis [13] corresponds well to a dark deposit centered a 8.5°N, 22.0°W [20]. This supports the possibility of unobserved high thermal inertia deposits due to the position of the high resolution IRTM data tracks. Our study has also shown that with optimum available data, the mechanism(s) for channel formation will continue to remain ambiguous due to aeolian deposits masking the surface. Future studies should concentrate on the other (i.e., less than optimum) high and additional moderate (30 to 35-km) resolution IRTM data so that the remaining channels may be investigated.

References

[1] Sharp, R.P., and M.C. Malin, 1975, *Geol. Soc. Amer. Bull., 86,* 593-609.
[2] Masursky, H., *et al.,* 1977, *Jour. Geophys. Res., 82,* 4016-4038.
[3] Baker, V.R., and D.J. Milton, 1974, *Icarus, 23,* 27-41.
[4] Cutts, J.A., and K.R. Blasius, 1981, *Jour. Geophys. Res., 86,* 5075-5102.
[5] Lucchitta, B.K., *et al.,* 1981, *Nature, 290,* 759-763.
[6] Nummedal, D., 1978, *NASA TM 79729,* 257-259.
[7] Schonfeld, E., 1976, (abst.), *Eos Trans. AGU, 57,* 948.
[8] Masursky, H., *et al.,* 1986, (abst.), *Lunar Planet. Sci. XVII,* 520-521.
[9] Mutch, T.A. and E.C. Morris, 1979, U.S.G.S., *Map I-1137 (MC-16).*

[10] Wilhelms, D.E., 1976, U.S.G.S., *Map I-895 (MC-11).*
[11] Potter, D.B., 1976, U.S.G.S, *Map I-941 (MC-28).*
[12] Christensen, P.R., 1986, *Jour. Geophys. Res., 91,* 3533-3545.
[13] Christensen, P.R., and H.H. Kieffer, 1979, *Jour. Geophys. Res., 84,* 8233-8238.
[14] Zimbelman, J.R., 1986, (abst.), *Papers Presented to the Symposium on Mars: Evolution of Its Climate and Atmosphere,* 112-114.
[15] Scott, D.H., *et al.,* 1978, U.S.G.S., *Map I-1111 (MC-23).*
[16] Kieffer, H.H., *et al.,* 1977, *Jour. Geophys. Res., 82,* 4249-4291.
[17] U.S.G.S., 1981, *Map I-1343 (MC-11 SW).*
[18] Christensen, P.R., 1983, *Icarus, 56,* 496-518.
[19] U.S.G.S., 1981, *Map I-1343 (MC-11 SW).*
[20] U.S.G.S., 1981, *Map I-1342 (MC-11 SE).*

MARS: MORPHOLOGY OF SOUTHERN HEMISPHERE INTRACRATER DUNEFIELDS.

N. Lancaster and *R. Greeley*, Department of Geology, Arizona State University, Tempe, Arizona 85287.

Although most eolian dunes on Mars occur in the North Polar sand sea (Breed et al., 1979; Tsoar et al., 1979), there are important areas of dunes at mid to high latitudes in the southern hemisphere. At least 75% of these dunes occur within craters (Thomas, 1981; Peterfreund, 1985). In addition to the areas of dunes, many crater floors are mantled by material of probable eolian origins (Thomas, 1981; Christensen, 1983). A large cluster of intracrater dunefields lies in Noachis Terra between latitudes -40 to -48° and longitudes 330-340°, with major dune accumulations in the craters Kaiser, Proctor and Rabe. Dunes in this region were amongst the first to be recognised on Mars (Cutts and Smith 1973; Breed 1977), but have not been studied in detail on Viking Orbiter images.

The size of the dunefields ranges from 40 to 3600 km^2 and varies directly with crater size. Preliminary studies of Viking Oribiter images of intracrater dunefields reveals that they consist of two varieties. The most common type is composed of massed straight to slightly wavy crescentic dunes similar to those described by Breed (1977) and Breed et al. (1979). Dune fields of this type occupy more than 20% of the area of the crater floor, with the dunefield margins often marked by a large "dune wall" or rampart. Dune spacing ranges between 0.7 and 1.2 km. Slipface orientations suggest that dune forming winds were southeasterly. The second type of dune accumulation consists of clusters of large, widely spaced straight or curved ridges, which often intersect to create rectilinear patterns. Dunes are typically spaced 1.6-4 km apart with a mean spacing of 2.42 km. On the margins of some dunefields there are small (0.5-0.9 km spacing) cresentic dunes together with widely spaced barchans. Pyramidally shaped dunes are evident in some examples and many dunes appear to have multiple slip faces which face northwest or south. Dunefields of this type occupy a small proportion (2-10%) of the crater floor.

Terrestrial analogues for dunes in this region which are equivalent to those found in type 1 dunefields have been discussed by Breed (1977). The dunes of the type 2 dunefields appear to be dimensionally similar to large crescentic dunes in the Gran Desierto, Mexico and in central Asian sand seas. Many of the large crescentic dunes in the Gran Desierto are compound forms, with superimposed small dunes on their flanks. Others are complex forms, with reversing or stellate dunes developed on their crests (Lancaster et al., in press). Some of the type 2 dunefields are similar in size and arrangement of dune ridges to those in valleys of the Mojave Desert.

Terrestrial dunes which are analogous to those in the intracrater dunefields have developed in wind regimes in which dominant sand transporting winds are counteracted by seasonal winds from opposed directions. Thomas (1981) has suggested that winds in this region of Mars are strong southeasterly in spring, but southwesterly in winter. In addition, the craters may also generate local winds. In such situations, the existence of apparently complex dune forms may be expected.

Further research is planned to examine the morphology of intracrater dunefields in more detail and to assess their relationship to local geological settings. Wind tunnel modeling of dune-topography interactions will help to interpret the form of dunes developed in areas of complex topography.

References

Breed, C.S. 1977. Terrestrial analogues of the Hellespontus Dunes. *Icarus*, 30: 326-340.

Breed, C.S. Grolier, M.J. and McCauley, J.F. 1979. Morphology and distribution of common 'sand' dunes on Mars: comparison with the Earth. *Journal of Geophysical Research*, 84: 8183-8204.

Christensen, P.R. 1983. Eolian intracrater deposits on Mars: Physical properties and global distribution. *Icarus*, 56: 496-518.

Cutts, J.A. and Smith, R.S.U. 1973. Eolian deposits and dunes on Mars. *Journal of Geophysical Research*, 78: 4139-4154.

Lancaster, N., Greeley, R. and Christensen, P.R. in press. Dunes of the Gran Desierto, Mexico. *Earth Surface Processes and Landforms.*

Peterfreund, A.R. 1985. Contemporary aeolian processes on Mars: local dust storms. Unpublished Ph.D. dissertation, Department of Geology, Arizona State University.

Thomas, P. 1981. North-south asymmetry of eolian features in martian polar regions: analyis based on crater-related wind markers. *Icarus*, 48: 76-90.

Tsoar, H., Greeley, R. and Peterfreund, A.R. 1979. The north Polar sand sea and related wind patterns. *Journal of Geophysical Research*, 84: 8167-8182.

TIMING OF FROST DEPOSITION ON MARTIAN DUNES: A CLUE TO PROPERTIES OF DUNE PARTICLES? P. Thomas, Cornell University.

The nature of the particles in martian dunes has been a source of controversy since the discovery of dune forms on Mars. Their color and high thermal inertias have suggested that the dark dunes are made of medium to coarse grained, minimally weathered basaltic or similar materials. The common association of the dunes with the polar layered deposits, however, has raised questions about whether the dune particles could be agglomerations of much finer particles that can be carried into the polar regions in suspension. It is also not known if the dark material at the surface of dune fields is representative of the bulk of a dune deposit; thick dune fields immediately adjacent to layered deposits are very suspect in this regard. Information on the physical properties of the dunes may be available from the behavior of frost deposition and loss from the dunes. Thomas et al. (1979) found that some dunes at high southern latitudes appeared to be sites of early frost deposition in the fall; James et al. (1979) noted many dunes retained frost late into the spring. We have now mapped the occurrences of dune brightening in the fall and have done the quantitative photometry needed to confirm that the dunes are the sites of early frost deposition.

Early deposition of frost on dark dunes is spectacularly displayed in early fall images by Viking Orbiter 2. Where there are data at the appropriate season, virtually all the dark dunes between 58 and 72°S become bright patches instead of dark areas a few days before the general cap edge passes their locale. The surroundings then brighten rapidly and usually become slightly brighter than the dunes. In the spring, some, but not all, of the dunes remain brighter than their surroundings for several days after passage of the general cap edge to the south.

We have made scans across the dunes in images taken at several different times to determine the time history of the dune albedo. We have estimated atmospheric contributions using optical depth data (F. Jaquin, pers. comm.) and the brightness of shadows in some images. Phase angles are generally over 90° but the viewing geometry does not vary greatly so phase functions are not a major problem. The data show that the dunes brighten very substantially between L_S = 10° and 40°, depending on the latitude. Bright coverings on dunes form outliers 1 to 5° north of the cap edge. Formation of the general cap then sometimes again reverses the contrast of the dune field with the surrounding area (Fig. 1).

Similar data are not available for the north, partly because of the imaging sequences, and partly because of the different distribution of dunes. However, some dunes that are outliers south of the main dunes retain frost throughout the martian year.

Early deposition of frost on dunes, relative to surroundings, could be caused by: (1) More rapid heat loss from dunes; (2) trapping of blown frost; (3) volatiles in the dunes being trapped at the surface in times of cooling atmospheric temperatures. A separate issue is whether the frost is

water or carbon dioxide. More rapid heat loss would imply a lower thermal inertia than the average. Most data on dark martian dunes suggests that they instead have a higher thermal inertia.

The dunes are trapped sediment, thus trapping of blown frost might be expected. However, the excellent correspondence of brightening with the edge of the dunes suggests the presence of dark material is the important characteristic. Additionally, winds in the fall season appear different from those that form the dunes (Thomas et al., 1979).

Water ice trapped in the dunes at depth and at warmer temperatures than the cooling surface might cause deposition of water frost on the surface in an otherwise very dry hemisphere of Mars. It is not clear, however, that the small amount of water that could diffuse to the surface could explain the amount of the albedo change or that it could help explain the extra retention of frost in the spring. The investigation is now concentrating on the amounts of frost necessary to cause the albedo changes and thermal modelling of the regolith.

This work is supported by NASA Grant NAGW-111.

References

Thomas, P., J. Veverka, and R. Campos-Marquetti (1979). Frost streaks in the south polar cap of Mars. J.G.R. 84, 4621-4633.

James, P. B., G. Briggs, J. Barnes, A. Spruck (1979). Seasonal recession of Mars' south polar cap as seen by Viking. J.G.R. 84, 2889-2922.

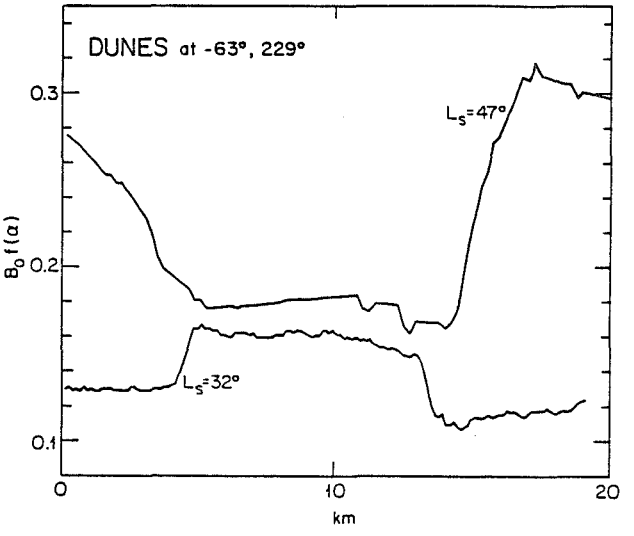

Figure: Reflectance scans across an intra-crater dune field, showing the early fall brightening of the dunes followed by greater brightening of area outside dunes. Data at L_S = 32° are from Viking image 510B76; at L_S = 47°, 545B15. The I/F values have been corrected for atmospheric contribution based on nearby optical depth data, and reduced to $B_0 f(\alpha)$ with a Minnaert k of 0.5. The dunes were 30% darker than surroundings at L_S = 353°. Part of the difference between dunes and surroundings at L_S = 47° is due to shadowing by the dunes.

WIND RIPPLES IN LOW DENSITY ATMOSPHERES

J. S. Miller, J.R. Marshall †, and R. Greeley †, *Department of Mathematics, University of Washington, Seattle, WA 98195, †Department of Geology, Arizona State University, Tempe, AZ 85287.*

The *dynamic pressure* of a fluid, 1/2 ρU^2 (ρ = fluid density, U = fluid velocity) is a primary factor controlling the motion of particles transported in either a liquid or a gas. This quantity is usually varied in experiments by making changes in U. In the Martian Surface Wind Tunnel[1] (MARSWIT), we have examined the effect of varying ρ on particle transport by conducting tests at atmospheric pressures between 1 and 0.004 bar. This study specifically concerns the effect of varying ρ on the character of wind ripples, and elicits information concerning generalized ripple models [2,3] as well as specific geological circumstances for ripple formation such as those prevailing on Mars (atm. press. = 0.0075 bar). In all the MARSWIT experiments, run times were sufficient to procure ripple equilibrium: ripple height and wavelength λ were stable with time. Tests were conducted primarily with 95 μm quartz sand, and for each atmospheric pressure chosen, tests were conducted at two (freestream) wind speeds: 1.1 U_{*t} and 1.5 U_{*t}, where U_{*t} is saltation threshold.

Figure 1 shows the relationship between saltation threshold and atmospheric pressure to be exponential. There is little variation in U_{*t} down to ~0.25 bar, but below this pressure, U_{*t} rises very sharply. Ripples appeared at all pressures tested for both wind speeds. Wavelength data is summarized in Figure 2 from which it is apparent that there are three distinct ripple trends. Trends A and B represent relatively large "ballistic" ripples that show a distinct increase in λ with decreasing atmospheric pressure (for threshold-normalized wind speeds). These are well defined in Figure 3 (oblique photos of the MARSWIT test beds) for 1.5 U_{*t}. The amplitude of these ripples dimishes with decreasing pressure until they are no more than narrow ridges at 0.125 bar and, thereafter, the features disappear. Trend D represents small structures (probably aerodynamic in origin) superimposed on the larger ripples, They were best developed at 1.1 U_{*t} (see Fig. 3) and their wavelengths are more or less independent of atmospheric pressure. Trend C represents laterally discontinuous ripples formed from the coarser fraction of the sand (naturally sorted on the bed by the wind at low pressures), but their relationship to wind speed and pressure is not very clear.

Data analysis is in a preliminary stage, but the MARSWIT data suggests: 1) ballistic ripple wavelength is not at variance with model [2,3] predictions, 2) an atmospheric pressure of ~0.2 bar could represent a discontinuity in ripple behavior, 3) ripple formation on Mars may not be readily predicted by extrapolation of terrestrial observations.

References: 1) Greeley, R., Iversen, J.D., Pollack,. J.B., Udovich, N., White, B.R. (1974), Proc. Roy. Soc. A341, 331-336. 2) Bagnold, R.A. (1941), The Physics of Blown Sand and Desert Dunes, Chapman & Hall, 265, p. 3) Sharp, R.P. (1963), J. Geol., 71, 517-636.

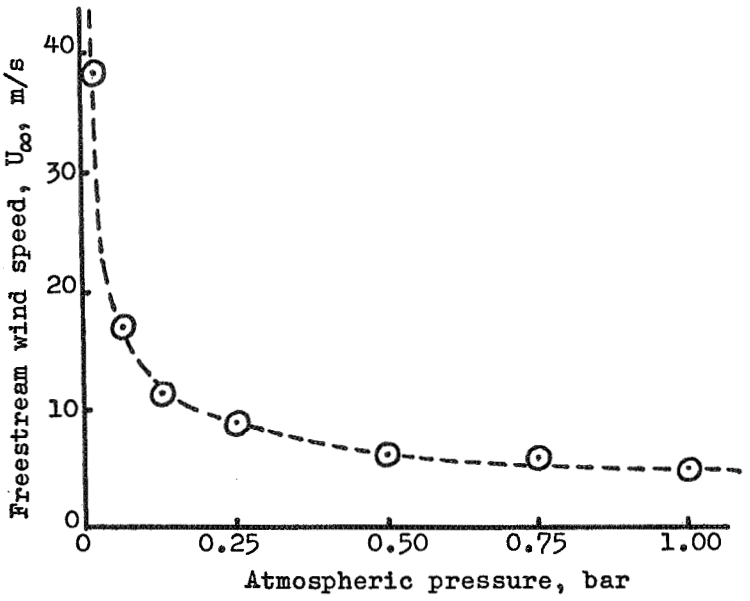

FIGURE 1. Threshold wind speed as a function of atmospheric pressure for 95 μm quartz particles

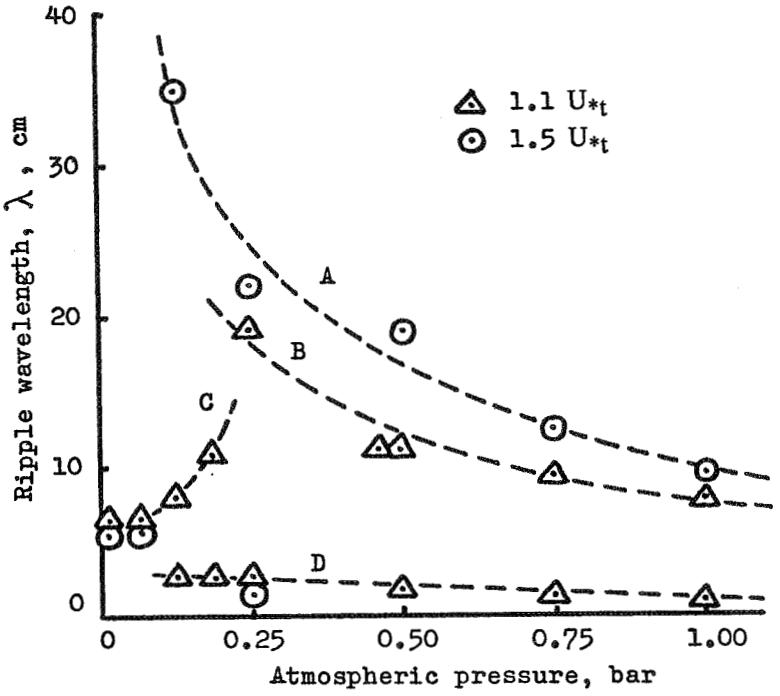

FIGURE 2. Ripple wavelength as a function of atmospheric pressure and wind speed for 95 μm quartz particles

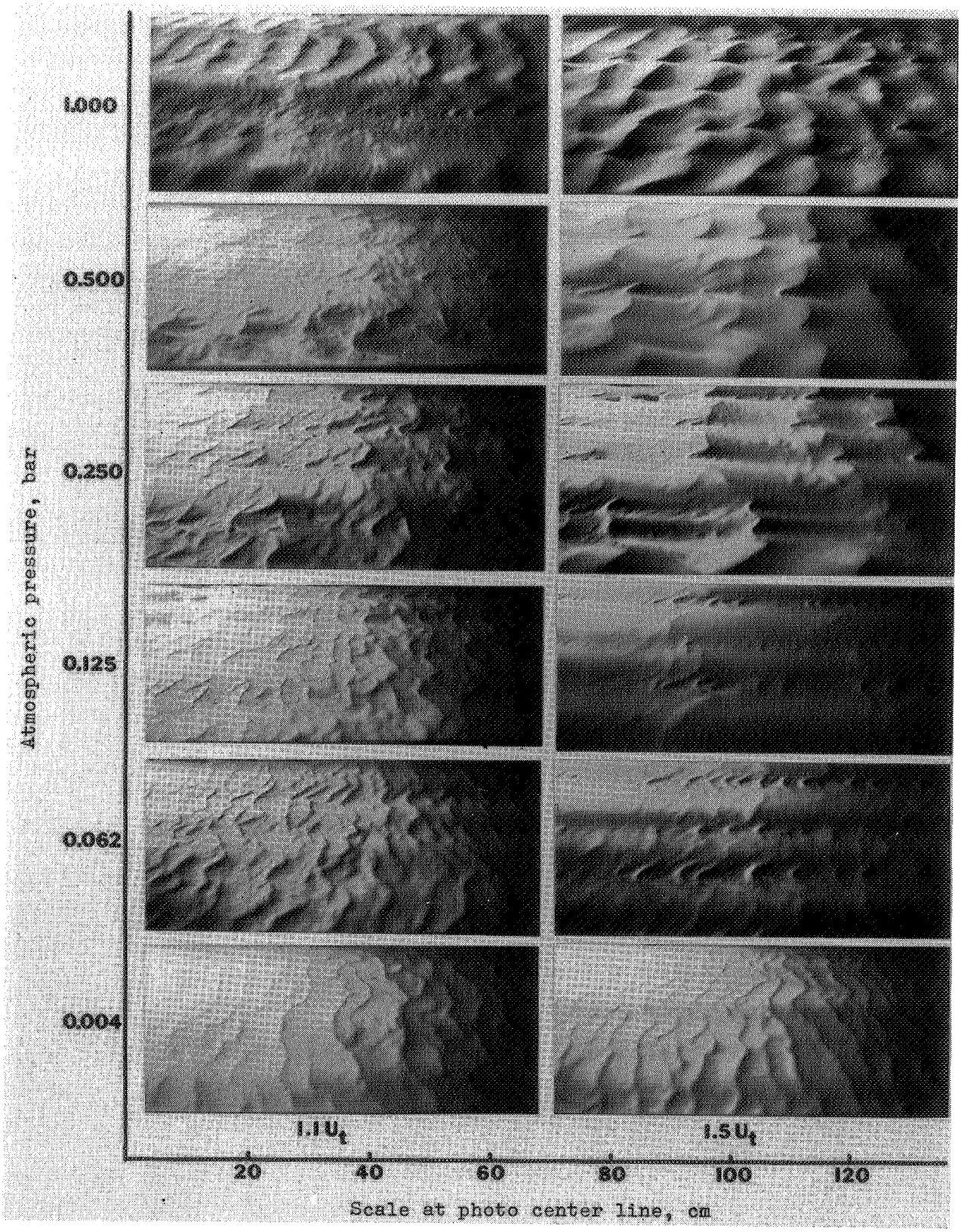

FIGURE 3. Rippled sand surfaces in MARSWIT produced over a range of atmospheric pressures at two wind speeds (oblique photographs). Wind direction is from the left; illumination from upper left.

EOLIAN SALTATION ON MARS

D.J.MacKinnon, USGS, Flagstaff, AZ 86001

At the high wind speeds necessary for saltation on Mars, individual sand grains assume relatively long low angle trajectories compared with those on the Earth. Williams and Greeley [1] argued that saltating grains on Mars do not transmit sufficient momentum to the surface for entrainment of secondary grains, and they concluded that the Martian saltation cloud has a low number density and the sediment flux is weak. I have developed a computer model in order to examine the effects of both the wind field and surface collisions on the Martian saltation cloud; results are summarized here.

Grain trajectories were derived by numerical solution of the exact two-dimensional equations of motion for a spherical sand grain embedded in an arbitrary wind field [2]. The saltating grain collides with an individual surface grain at a randomly chosen point within a collision cross section defined by the colliding grain and the surface grains. The surface grains lie in mutual contact on a horizontal plane. This collision model [3] does not account for entrainment of secondary grains; it focuses only on the primary saltating grain whose behavior dominates the saltation cloud [4]. The horizontal and vertical speeds of a saltating grain just after collison are restored to a fraction of the speeds before collision in proportion to two coefficients of restitution, EN and ET (Figure 1). The vertical wind speed is zero and the horizontal wind speed varies with height according to a logarithmic distribution [5] as scaled by the wind-shear speed.

The horizontal speed versus incidence angle for a single saltating grain just before each of 100 successive, random collisions with a surface of similar-size grains is shown in Figures 1 and 2. The distribution of incidence speeds and angles assumed by one grain in this model characterizes reasonably well the quantitative physical processes in the saltation cloud. Saltating grains (Figure 1a) that transfer small fractions of their horizontal momentum to the surface (ET=0.5) attain higher speeds, rise higher above the surface, and achieve longer trajectories than do saltating grains (Figure 1b) that transfer larger amounts of momentum (ET=0.2); relatively small differences in the coefficients of restitution yield significant differences in the saltation cloud. These conclusions remain valid for wind-shear speeds at the saltation threshold (Figure 2). As shown in Figure 2b, grains can both assume long trajectories and transfer large amounts of momentum to the surface for the rapid development of the saltation cloud. Nevertheless, because the surface-collision parameters of saltating Martian sediments are unknown, the development and effectiveness of the saltation cloud remain uncertain. Surface-collision parameters for spherical sand grains on Mars could be more accurately characterized by scaled laboratory experiments.

References: [1] Williams, S.H., and R. Greeley, 1986, Abs. Lun. Planet. Sci. Conf., 17th, p. 952-953; [2] White, B.R. et al., 1975, NASA TM X-62463, 200 p; [3] MacKinnon, D.J., 1986, NASA TM 88383, p. 254-256, [4] Mitha, S. et al., 1985, Brown bag preprint series in basic and applied sciences, Calif. Inst. Tech., BB-36, 25 p; [5] Bagnold, R., 1941, The physics of blown sand and desert dunes: London, Chapman and Hall, 264 p

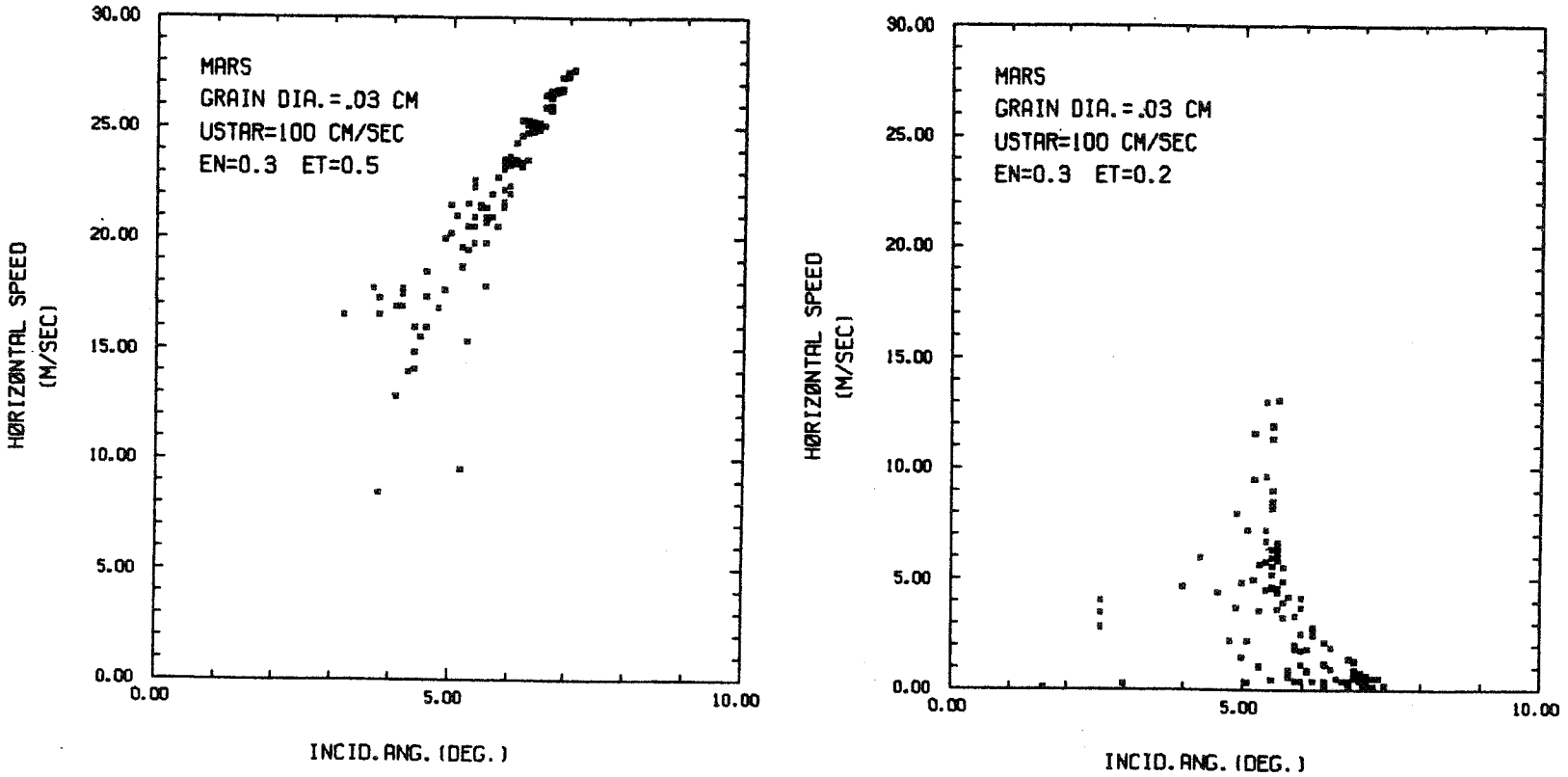

Figure 1 - Horizontal speed vs. incident angle (the angle between the grain trajectory and the horizontal) of a saltating spherical sand grain immediately before 100 successive, random collisions with a surface of similar-size sand grains. Data points are derived for a wind-shear speed (USTAR) less than the saltation threshold for 0.03-cm-diameter sand grains on Mars. EN is the fraction of speed restored along the line of centers between the colliding grain and the surface grain in question; ET is the fraction restored perpendicular to the line of centers. Except for the difference in ET, components of (a) and (b) are the same.

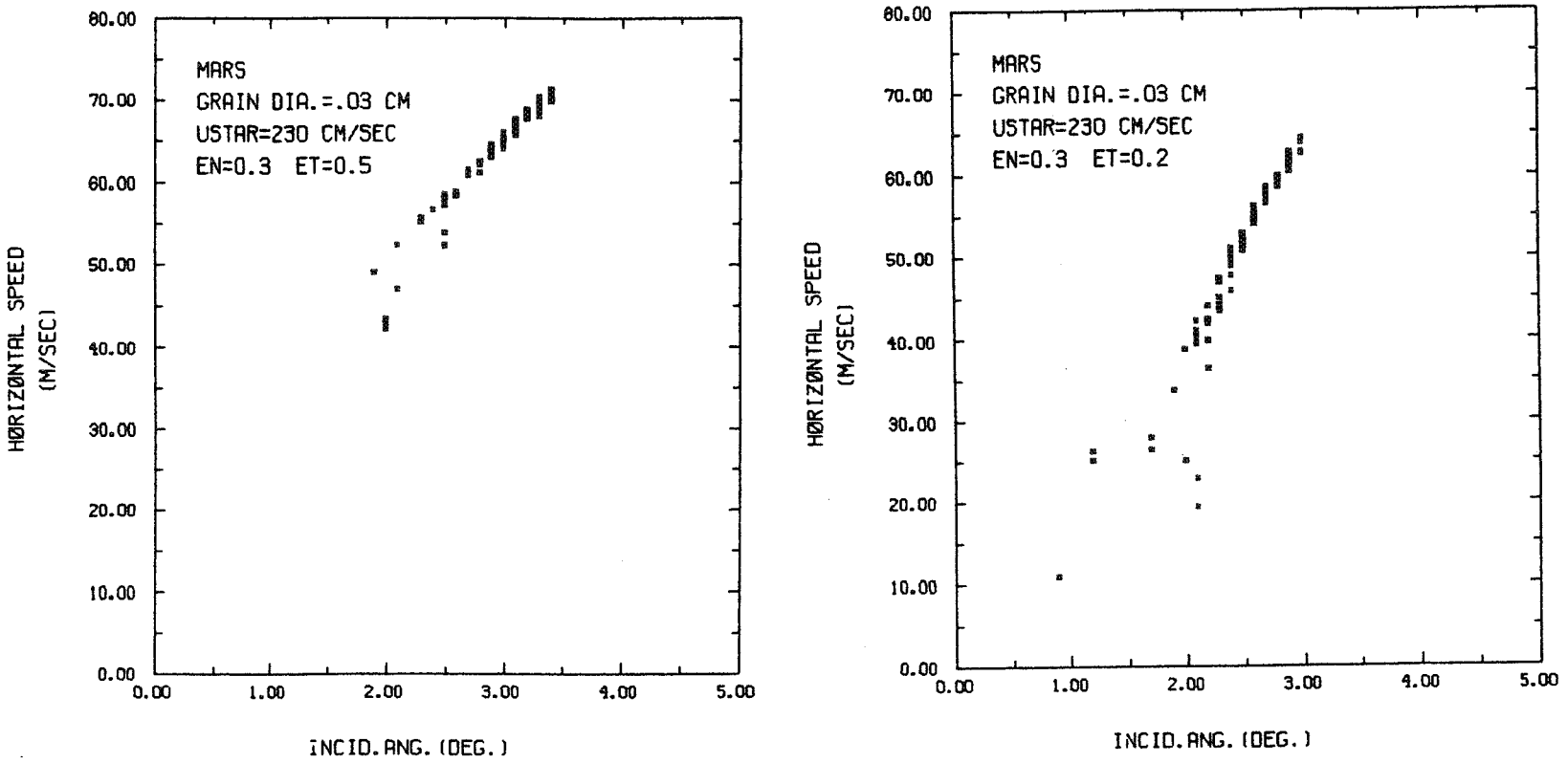

Figure 2 - Same as Figure 1 except that the wind-shear speed (USTAR) is set equal to the threshold wind-shear speed for the saltating grain.

MASS TRANSPORT BY AEOLIAN SALTATION ON EARTH, MARS AND VENUS: THE EFFECTS OF FULL SALTATION CLOUD DEVELOPMENT AND CHOKING.

S. H. Williams and R. Greeley, Department of Geology, Arizona State University, Tempe, Arizona 85287

The purpose of this study is to be able to predict the characteristics of particle motion and the quantity transported by the wind under a variety of planetary environmental conditions. Aeolian transport of surficial material is an important part of the sedimentological cycle, and, on Earth, aeolian activity can strongly affect land utilization and habitability. Consequently, terrestrial aeolian processes have been extensively studied. Numerous expressions for the quantity of material moved in saltation as a function of wind conditions and particle type have been derived (see Greeley and Iversen, 1985, for review). However, these studies do not distinguish between the contribution of particle speed and particle concentration to the overall saltation flux. The wind speed range over which the saltation flux predictions are valid is sensitive to particle concentration, particularly in non-terrestrial cases. At wind speeds near saltation threshold, the predictions do not become accurate until the saltation is fully developed, i.e., when the particle concentration (and with it the particle flux from the surface) is high enough to fully mobilize surface material. At sufficiently high wind speeds, saltation is retarded when the particle concentration reaches a value at which mid-air collisions become common, interfering with the orderly transfer of momentum from wind to particles aloft to surface. This condition has been termed "choking" because too much material is moving in response to the wind stress to allow smooth flow (Williams and Greeley, 1985).

Two wind tunnels were used for this study: an open-circuit, terrestrial environment wind tunnel (ASUWT) and a closed-circuit tunnel capable of operating at venusian atmospheric density (for descriptions, see Greeley et al., 1985 (ASUWT) and Greeley et al., 1984 (VWT)). Particle concentration was determined by measuring particle speed and particle flux at the same height in the saltation cloud. Particle speed was measured using a particle velocimeter modified from a USDA design (Schmidt, 1977). Particle flux was measured using a stack of particle collectors (see Greeley et al., 1985). The mass concentration at the measurement height is the local mass flux, q, divided by the average particle speed, Vp. The particle concentration at that height is the mass concentration divided by the mass of an average particle.

The conditions necessary for full saltation development can be examined in the wind tunnel by measuring the total saltation flux, Q, and the particle speed near the surface. The upward particle flux from a unit surface area, Go, is Q divided by the average saltation pathlength, L. The horizontal momentum available for transfer to the surface is Go x Vp, per unit surface area. If gravitational differences are accounted for, surfaces composed of similar materials should require the same momentum availability for full saltation. Measurements taken at just above saltation threshold in the VWT for quartz particles of 250-300 μm diameter indicate that saltation becomes fully developed when the momentum available is ~3 gm cm/sec per unit surface area. Similar measurements in ASUWT under terrestrial conditions yield a value of ~2 gm/cm sec. If a value of ~1.5 gm/cm sec is considered, the lower value indicating the difficulty of obtaining measurements very near saltation threshold, then the corrosponding minimum saltation flux necessary for full saltation development on Mars is ~0.6 gm/cm sec (Williams and Greeley, 1986). Using the saltation flux equation in White (1979), the wind speed required for full saltation is ~10% above threshold. The presence of rocks on the martian surface further disperses the

saltation cloud by increasing the rebound height of saltating particles. The saltation cloud, therefore, remains poorly developed, with less material in motion than predicted by application of equations derived for terrestrial conditions.

Choking of the saltation cloud due to high particle concentration does not occur on Mars, but can be significant on Earth and it certainly is on Venus. The onset of choking was determined in the ASUWT by observing the change in particle speed at a height of 2 cm as the wind speed increases. As the saltation cloud grows, the particle speed increases but the ratio of particle speed to freestream wind speed decreases, due to the velocimeter becoming relatively lower in the saltation cloud as the cloud thickens. The onset of choking is inferred to occur when the actual particle speed at 2 cm height decreases. This was observed in ASUWT for particles of walnut shell (density ~ 1.1 gm /cc) and quartz of 170-211 μm diameter; larger particles were not observed to display choking behavior. The walnut shell particles showed an actual drop in speed at 2 cm height when the freestream wind speed exceeded ~10.5 m/sec (2.0 x threshold); the quartz particles at wind speeds above ~12.5 m/sec (2.5 x threshold). The critical particle concentrations are ~20 particles/cc for walnut shell and ~10 particles/cc for quartz. The momentum available to the surface is about the same in each case; the difference in critical particle concentration is a reflection of the longer pathlength of the less massive walnut shell. Particle pathlengths on Venus are 1-2 orders of magnitude shorter than on Earth; the "compression" of the particles in saltation into the small volume near the surface causes choking to readily occur.

A summary of saltation behavior is as follows. On Earth, saltation fully develops at near-threshold wind speeds and rarely chokes. On Mars, saltation becomes fully developed only at favorable locations and at wind speeds well above threshold. The martian saltation cloud has an insufficient particle concentration to cause choking, particularly over a partially rocky surface. On Venus, full saltation occurs at wind speeds very near threshold, but saltation flux will increase less rapidly than expected at relatively modest wind speeds due to choking.

REFERENCES

Greeley, R. and J. D. Iversen, 1985, *Wind as a Geologic Process*, Cambridge: Cambridge University Press, 333p.

Greeley, R., J. Iversen, R. Leach, J. Marshall, B. White and S. Williams, 1984, Windblown sand on Venus: Preliminary results of laboratory simulations, *Icarus*, v. 57, p. 112-124.

Greeley, R., S. H. Williams, B. R. White, J. B. Pollack and J. R. Marshall, 1985, Wind abrasion on Earth and Mars, in Woldenberg, M. J. (ed.), *Models in Geomorphology*, Boston: Allen and Unwin, p. 373-422.

Schmidt, R. A., 1977, A system that measures blowing snow, USDA Forest Service Research Paper RM-194, 80 p.

White, B. R., 1979, Soil transport by winds on Mars, *Jour. Geophys. Res.*, v.84, n. B8, p. 4643-4651.

Williams, S. H. and R. Greeley, 1985, Aeolian activity on Venus: The effect of atmospheric density on saltation flux (abs.), Lunar Plan. Sci. Conf. XVI, p. 908-909.

Williams, S. H. and R. Greeley, 1986, Wind erosion on Mars: Impairment by poor saltation cloud development (abs.), Lunar Plan. Sci. Conf. XVII, p. 952-953.

Development of Wind Tunnel Techniques for the Solution of Problems in Planetary Aeolian Processes

Robert Sullivan[1], Jeffrey Lee[2], and Ronald Greeley[1], Departments of [1]Geology and [2]Geography, Arizona State University, Tempe, AZ 85287

Aeolian processes (wind/surface interactions resulting in sediment erosion, transport, and deposition) dominate current surface activity on Mars and are suspected to be active on Venus (Greeley and Iversen, 1985). In the absence of returned comprehensive meteorological data, reliable wind tunnel simulations become necessary for increasing understanding of aeolian processes on other planets. Key to determining the character of any wind/surface interaction is U_* (the wind friction speed). Obtaining U_* values for the surface of Mars, for instance, requires complete velocity-vs.-height wind profiles, but the Viking Lander wind velocity data are only applicable to the spot elevations (1.6 m) of the meteorology booms. An infinite number of wind profile curves can be drawn through each 1.6 m elevation. Determination of the proper wind profile requires the Viking wind velocity data to be coupled with a knowledge of z_o, the surface roughness parameter. The problem can be solved with sufficiently sophisticated wind tunnel simulations of the Viking Lander sites. However, the degree to which scale model wind tunnel experiments accurately reflect field conditions has never been tested directly. The objective of this study is to evaluate wind tunnel experiments in predicting full-scale field results. Such a direct comparison between wind tunnel scale models and full-scale field results can identify working guidelines for a broad range of boundary layer geological modelling applications on Earth, but is especially relevant and critical for the planetary context.

The field study of Kutzbach (1961) is a good candidate for a wind tunnel simulation because the experiment is carefully specified and the results have been utilized in other studies (e.g. Lettau, 1969). Kutzbach (1961) reports wind profiles over a series of roughness elements on a frozen lake and how the wind profile changed as the surface roughness was varied. The approach of the current study is to duplicate Kutzbach's roughness arrays in the wind tunnel at 1/20 and 1/40 scales, and to compare the wind profiles over these scale models to those derived by Kutzbach at full scale in the field. Kutzbach measured U_* and z_o for ten roughness element arrays ranging in basket density from 1 per 48.5 m^2 to 1 per 0.4 m^2. Wind velocities were measured by cup anemometers on a mast located within the basket array close to its downwind end. Depending on the run, six to eleven cup anemometers were arrayed at heights ranging from ten to 340 cm above the ice.

For the wind tunnel simulation, 3/8- and 3/4-inch dowel cut to the proper lengths conveniently produces reasonably accurate 1/40 and 1/20 scale roughness element models. The matrix of runs was as follows: 2 scales (1/40 and 1/20) X 10 arrays (specified by Kutzbach) X 3 tunnel freestream velocities (approx. 9.3, 16.0, and 20.7 m/sec) X 2 repeats for each scale, each array, and each freestream velocity = 120 runs. In practice the number of repeats often exceeded 2 (especially for 9 m/sec freestream runs) to improve overall consistency of the data. The data were collected by a pitot tube rake located within each scaled roughness array in a relative position identical to that of Kutzbach's anemometer mast. Kutzbach, using a fixed number of roughness elements, was forced to decrease his roughness fetch (upwind distance of the roughness array) from 80 m for the low density runs down to 18 m for the high density runs, and discussed the possibility that for the short fetch, high density runs the boundary layer might not have been fully developed. This possibility poses no liability for this study, whose concern is the simulation of real field conditions in a wind tunnel, whether real field conditions are represented by fully developed boundary layers or not. While this represents a severe test of reality for a wind tunnel simulation, it remains relevant, for in nature many surfaces do not possess enough fetch to support a fully turbulent boundary layer.

Kutzbach reduced his field data by using the computer program of Robinson (1961, 1962), which was based on the method outlined by Lettau (1957). In this method the log-law wind profile is assumed correct over the range of heights measured, and values of z_0, U_*, and D (zero-plane displacement) are adjusted until the sum of error squares between the data points and the fitted log curve is a minimum. The method simultaneously finds the best fit log curve and locates the true zero reference level.

However, the same technique is apparently not valid for the reduction of data taken over very rough surfaces in wind tunnels. Several workers (e.g. Kawatani and Meroney, 1970; Mulhearn and Finnegan, 1978; Raupach et al., 1980) have reported a transition zone below 2-3.5 times the height of the roughness elements in which U_* is not constant and the wind log-law is invalid. The data for this study were reduced according to transition zone restrictions specified by Raupach et al. (1980), who used roughness elements very similar in size and shape to those of this study. The zero reference plane was taken to be the floor of the tunnel, and the qualified data were reduced according to

$$U_z = (U_*'/0.4) \ln (z/z_0)$$

where U_z is the velocity at height z and 0.4 is the von Karman constant. Here z_0 represents merely the height at which the average wind velocity = 0, and not necessarily the "effective roughness height" as discussed, for instance, by Greeley and Iversen (1985 pp. 42-43). This simplification expresses the wind profile in a convenient form for future comparison. U_*' represents the modified value of U_* required by the z_0 simplification.

Before comparing the wind tunnel data of this study with the field results obtained by Kutzbach, some comparisons can be made beween the 1/40 scale and 1/20 scale results. These comparisons are summarized in Table 1.

Table 1. Evaluation of scaling relations

		1/40 scale z_0 : 1/20 scale z_0 ratios		
		predicted	actual	std. dev.
Distance scaling only	all velocities	1:2.0	1:3.2	1.3
	9.3 m/sec	1:2.0	1:3.2	1.6
	16.0 m/sec	1:2.0	1:3.3	1.2
	20.7 m/sec	1:2.0	1:3.3	1.7
Distance scaling with Re scaling	20.6 m/sec 1/40: 9.3 m/sec 1/20	1:2 - 1:3.2	1:4.8	2.9
Distance scaling with velocity scaling	9.3 m/sec 1/40: 20.7 m/sec 1/20	1:2.2	1:2.3	1.0

Length scaling alone predicts a 1:2 ratio between values of 1/40 scale z_0 and 1/20 scale z_0, but the actual ratio is found to be 1:3.2. If the data are partitioned by freestream velocity each freestream velocity subset returns essentially the same 1/40 to 1/20 scale z_0 ratio : 1:3.2. Combining length scaling with Reynolds number scaling predicts a lower 1/40 scale:1/20 scale z_0 ratio, although a precise value between 1:2 and 1:3.2 is not indicated. Reynolds numbers (and thus turbulence characteristics) are most closely matched by comparing high freestream smaller scale runs (20.63 m/sec 1/40 scale z_0 results) with low freestream larger scale runs (9.30 m/sec 1/20 scale z_0 results). However, the actual 1/40 scale to 1/20 scale z_0 ratio is found to be 1:4.8 - a relatively less accurate prediction than for length scaling alone. The final prediction to be considered was that of length scaling combined with velocity scaling. Velocity scaling seems appropriate, considering that for the purposes of this study z_0 has been defined as the height where the average velocity = 0. According to velocity scaling the wind should move across the same scale distance - the upwind fetch of an array, for example - in the same time interval at both scales. Thus, comparison of the 1/40 scale 9.29 m/sec freesteam z_0 values with the 1/20

scale 20.65 m/sec freestream z_0 values should yield a 1:2.2 ratio. The actual ratio is found to be 1:2.3. The wind tunnel simulation apparently was performed under a flow regime in which Re scaling is dominated by the effects of simple velocity scaling. The threshold Re below which Re scaling becomes significant was not probed for in this study.

Comparing the wind tunnel data to Kutzbach's field results proved extremely difficult in practice. The main problem lies in differences in data reduction techniques. Kutzbach derived his z_0 and U_* values for each roughness array by applying a log-law fit over his entire height range of data. Raupach et al. (1980) and other workers have shown this to be an invalid procedure for very rough surfaces in the wind tunnel environment. Whether the procedure is invalid for very rough surfaces in the field environment remains unresolved. Test examples showed that the two reduction techniques give widely divergent results when applied to the same data, requiring that a single reduction technique be applied to both raw data sets for a meaningful comparison. Unfortunately, the raw data of Kutzbach (1961) are unavailable, and transfering the raw data from Kutzbach's published figures proved unsatisfactory. (Data points from different runs were often difficult to tell apart, and running even the clearer points through the original Fortran program of Robinson (1961) gave an unsatisfactorily inaccurate reproduction of Kutzbach's results.)

The best comparison that can be made involves reconstructing Kutzbach's best-fit profile curves (from his final results) and re-reducing a set of hypothesized data points from each curve in a manner identical to that used for the wind tunnel data. Dividing the results by 40 and by 20 provides a set of values that can be readily compared with the wind tunnel results. (Unfortunately, Kutzbach's results for the four densest arrays were reduced in a slightly different manner than the others, disabling them from the comparison.) Before a comparison can be made, however, velocity scaling must be taken into account. Kutzbach's reference anemometer wind speeds correspond to a scaled velocity of approximately only 0.3 m/sec in the wind tunnel at 1/20 scale. The trend of results suggests that if it were possible to measure values of z_0 at this freestream, they might range from 1.5 to 2.5 times the z_0 values measured for the same roughness arrays at 16.0 m/sec freestream. In any case the necessary extrapolation is somewhat extended; a factor of 1.1 times the 16.0 m/sec z_0 results turns out to match Kutzbach's field results (divided by 40 and 20) the best.

Although this study suggests that wind tunnel scale models can predict the values of important wind profile parameters measured in the field, the development of more definitive guidelines requires a field experiment designed specifically to be compared in detail with wind tunnel results. Such an experiment is currently in the advanced planning stages.

References

Greeley, R. and J. D. Iversen (1985) *Wind as a Geological Process*, Cambridge University Press, 333 pp.

Kawatani, T., and R. N. Meroney (1970) Turbulence and wind speed characteristics within a model canopy flow field, *Agr. Meteorol., 7*, pp. 143-158.

Kutzbach, J. E. (1961) Investigations of the modification of wind profiles by artificialy controlled surface roughness *in Studies of the Three-Dimensional Structure of the Planetary Boundary Layer*, Ann. Rep., Dept. Meteorol., Univ. Wisc.-Madison, pp. 71-113.

Lettau, H. H. (1957) Computation of Richardson numbers, classification of wind profiles, and determination of roughness parameters *in Exploring the Atmosphere's First Mile, vol. 1*, pp. 328-336.

Lettau, H. H., (1969) Note on aerodynamic roughness-parameter estimation on the basis of roughness-element description, *Jour. Appl. Meteorol., 8*, pp. 828-832.

Mulhearn, P. J. and J. J. Finnigan (1978) Turbulent flow over a very rough, random surface, *Boundary-Layer Meteorol., 18*, pp. 373-397.

Raupach, M. R., Thom, A. S., and I. Edwards (1980) A wind-tunnel study of turbulent flow close to regularly arrayed rough surfaces, *Boundary-Layer Meteorol., 18*, pp. 373-397.

Robinson, S. M. (1961) A method for machine computation of wind profile parameters *in Studies of the Three-Dimensional Structure of the Planetary Boundary Layer*, Ann. Rep., Dept. Meteorol., Univ. Wisc.-Madison, pp. 63-68.

Robinson, S. M. (1962) Computing wind profile parameters, *J. Atmos. Sci., 19*, pp. 189-190.

AEOLIAN ABRASION ON VENUS: PRELIMINARY RESULTS FROM THE VENUS SIMULATOR

J.R. Marshall, R. Greeley, D.W. Tucker, and J.B. Pollack, Dept. of Geology, Arizona State University, Tempe, AZ 85287

The *Venus Simulator* is designed for testing the mechanical effects of aeolian abrasion on rocks and particles at the surface of Venus. The Venus Simulator will impact sand or pebble-size particles with controlled velocity and controlled periodicity against a rock target in a carbon dioxide atmosphere at temperatures up to 770K and pressures up to 114 bar. These extreme conditions are achieved in the pressure vessel depicted in Fig. 1 which has an internal volume of 0.05 m^3. The vessel contains a 7 cm diameter, 75 cm long, tubular furnace which provides an electrically-heated gas reservoir. An abrasion device is inserted through the center of one of the end flanges into the reservoir and is viewed through a 5 cm thick quartz window. Illumination of the device is through a light pipe at the opposite end of the pressure vessel. A gas-pulsing system (Fig. 1a) produces rapid-cycle release of internal pressure and, in so doing, causes gas to be drawn from the reservoir through a 2 cm-long gas gun in the abrasion device. This flow projects particles at a rock target situated directly in the gas stream. Pressure in the vessel is maintained by a gas-intensifier system. The flowing gas is at the same temperature as the impactor and target.

The present test series is examining the role of atmospheric pressure on aeolian abrasion for a constant temperature of 737K. Results from a 20 bar/737K test are depicted in Figure 2. Both the rock target and the impactor were fine-grained basalt. The impactor was a 3 mm diameter angular particle chosen to represent a size of material that is entrainable by the dense venusian atmosphere and potentially abrasive by virtue of its mass. It was projected at the target 10^5 times at a velocity of 0.7 m/s (determined by high-speed video filming). The impactor showed a weight loss of ~1.2 x 10^{-9} gm per impact (calculated from the change in geometry) with the attrition (readily apparent from Fig. 2a & b) occurring only at the edges and corners. The arrow on one of the faces of the particle indicates a spot viewed in the SEM before and after impact and no damage had occurred. The impactor edges developed irregularly-defined surface layers of mechanically "bruised" material (Fig. 2c) and small impact pits with fracture patterns similar to those developed at room temperature. However, stylus profilometry and optical microscopy step-profiling suggested that the target had *gained* material, but further tests are required to substantiate this finding. The surface texture in Figure 2d certainly has the appearance of surface smearing of material, and there were no clearly-defined fracture patterns indicating chipping. Weighing the target before and after the test showed weight loss but was inconclusive because control samples of basalt subjected to the same conditions, except for impact, also lost weight.

It is concluded from these results that particles can incur abrasion at venusian temperatures even with very low impact velocities expected for Venus, but the impacted rocks may present some surprises.

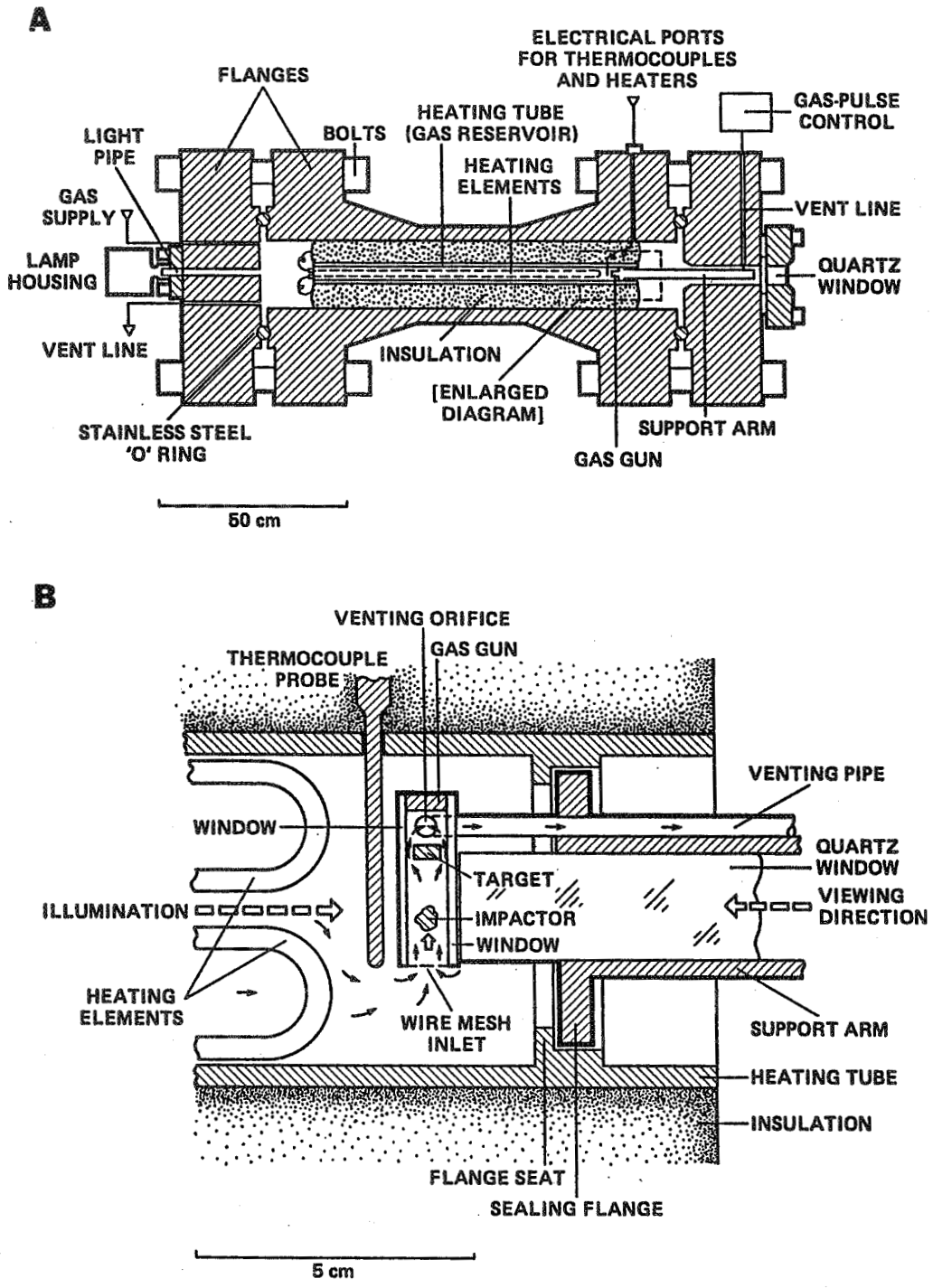

FIGURE 1. VENUS SIMULATOR
A. Pressure vessel sectional view showing internal heating arrangement and position of the gas-gun abrasion device.
B. Abrasion device sectional view (enlargement of area shown in A). Components enclosed by heavy outline form a single unit that is inserted into the pressure vessel through the right-side flange. The impactor rests on a wire mesh at the base of the gas gun until a momentary gas pulse projects it upward against the rock target. Gas flow is induced in the gun by exhausting gas through the venting pipe: gas flows from the reservoir through the mesh and past the target. After each venting pulse, the impactor falls back to the mesh.

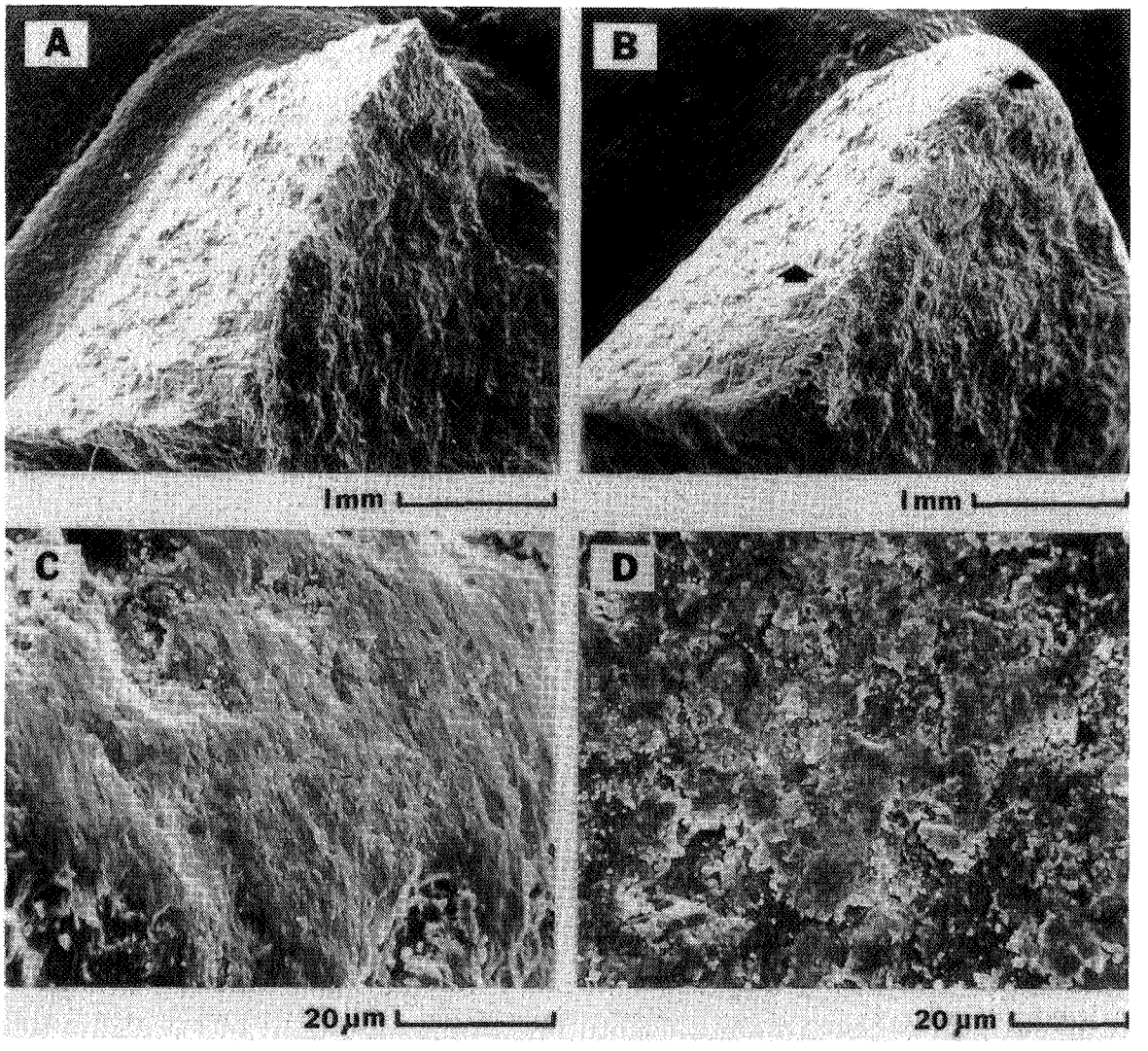

FIGURE 2. IMPACT TEXTURES ON TARGET AND IMPACTOR
A. Impacting particle before abrasion test: note sharp edges and rough fracture faces.
B. Impacting particle after abrasion test: attrition is very apparent -- corners and edges have been subdued. Arrow at top of particle indicates position of area shown in C. Arrow on left face of particle indicates position where impact damage is absent (see text).
C. Corner of impacted particle showing mechanical bruising texture (center of photo) and small impact pits (upper and lower left corners of photo).
D. Impacted target surface showing highly-irregular pattern of surface layer which may be mechanically-bruised target material, or smeared comminution debris transferred from the impactor.

REYNOLDS NUMBER EFFECTS ON SURFACE SHEAR STRESS PATTERNS AROUND ISOLATED HEMISPHERES

J.A. Lee[1] and R. Greeley[2], [1]Department of Geography and [2]Department of Geology, Arizona State University, Tempe, Arizona 85287

Obstacles projecting into the wind stream alter the shear stress on the surface around them, thus altering the erosion, transportation, and deposition of aeolian sediment. This study is concerned with the effect of Reynolds number on the pattern of shear stress on the surface around an isolated hemisphere. An understanding of Reynolds number effects is necessary if wind tunnel results are to be scaled up to natural situations for meaningful applications.

Surface shear stress was measured using the naphthalene sublimation technique outlined by Lee and Greeley (this volume). The hemisphere used is 0.033 m high and was immersed in the lower portion of the 0.13 m boundary layer. Surface shear stress, τ_o, is often presented as the friction velocity, $u*$, where $u* = (\rho_a \tau_o)^{0.5}$ with ρ_a the atmospheric density.

For this study Reynolds number, Re, is defined as

(1) $Re = (u* \ h) / \upsilon$

where h is the hemisphere height and υ is the kinematic viscosity (1.164×10^{-5} m^2 sec^{-1} for the 35 °C air used in the experiments (from Oke, 1978)).

Figure 1 displays the surface shear stress patterns for Re of 1360 to 2977. At the threshold of motion for fine sand this corresponds to object heights of 0.10 to 0.22 m on Earth, 0.76 to 1.67 m on Mars, and 0.024 to 0.053 m on Venus (all values calculated from information in Fig. 3.17 of Greeley and Iversen, 1985).

Over the entire range of Re there is an increase in relative shear stress at all locations except for a small zone immediately downwind of the hemisphere. The highest relative shear stress is immediately in front of the object, presumably caused by reversing flow in the lowest layers of the boundary layer due to fluid impact on the object. (see Baker, 1979, for a more detailed discussion of this phenomenon). The region of low relative shear stress is due to sheltering by the object. Relative shear stress is high behind this region due to increased turbulence, as found by Greeley et al. (1974) for raised rim craters and Greeley (1986) for domical hills.

The most obvious change in the pattern as Reynolds number increases is in the strength of the horseshoe vortex. Figure 1A shows a strong vortex downwind of the edge of the hemisphere. As Re increases, however, the horseshoe vortex decreases in strength. This is likely to be due to an increase in flow separation with Re resulting in the flow tending to wrap around the object at lower wind speeds and flow over it at higher speeds. In Figure 1D a reattachment zone appears from $x = 2h$ to $x = 3.5h$ along the centerline.

In a discussion of air flow around objects Snyder (1972) cites evidence suggesting that for a given object shape there is a minimum Reynolds number above which the flow characteristics are essentially Reynolds number independent. The value of this Reynolds number appears to increase as shapes become more streamlined. Figure 1 shows that for hemispheres this minimum Reynolds number has not been achieved at the wind speeds

used. (For Reynolds number defined by freestream wind speed, u_∞, this corresponds to a range of $(u_\infty h)/\upsilon$ =29515 to 58888.)

This experiment shows that the surface shear stress pattern is strongly affected by Reynolds number, at least within the range of Re used. The strength of the horseshoe vortex decreases with increasing Re. This is presumably due to a decrease in flow around the sides of the hemisphere and an increase in flow over the object as Reynolds number increases.

References

Baker, C.J., 1979, The Laminar Horseshoe Vortex: *Journal of Fluid Mechanics*, v. 95, pt. 2, p. 347-367.

Greeley, Ronald, 1986, Aeolian Landforms:Laboratory Simulations and Field Studies, in, Nickling, W.G., ed., *Aeolian Geomorphology:* Allen and Unwin, New York.

Greeley, R., Iversen, J.D., Pollack, J.B., Udovich, N., and White, B., 1974, Wind Tunnel Studies of Martian Aeolian Processes: *Proceedings of the Royal Society of London, Series A*, v. 341, p. 331-360.

Greeley, R., and Iversen, J.D., 1985, *Wind as a Geological Process on Earth, Mars, Venus and Titan:* Cambridge University Press, Cambridge.

Lee, J.A., and Greeley, R., this volume, Determination of Surface Shear Stress with the Naphthalene Sublimation Technique.

Oke, T. R., 1978, *Boundary Layer Climates:* Methuen and Co., New York.

Snyder, William H., 1972, Similarity Criteria for the Application of Fluid Models to the Study of Air Pollution Meteorology: *Boundary-Layer Meteorology*, v. 3, p. 113-134.

Figure 1. Map views of surface shear stress patterns around a hemisphere. Flow is from negative x/h to positive x/h. Symmetry can be assumed for the patterns. Isolines show relative friction velocity: measured u_* divided by u_* on undisturbed portion of naphthalene surface. Location relative to the hemisphere center is made dimensionless by dividing x and y by object height. '?' indicates area where pattern is not clear with the measurement grid used.

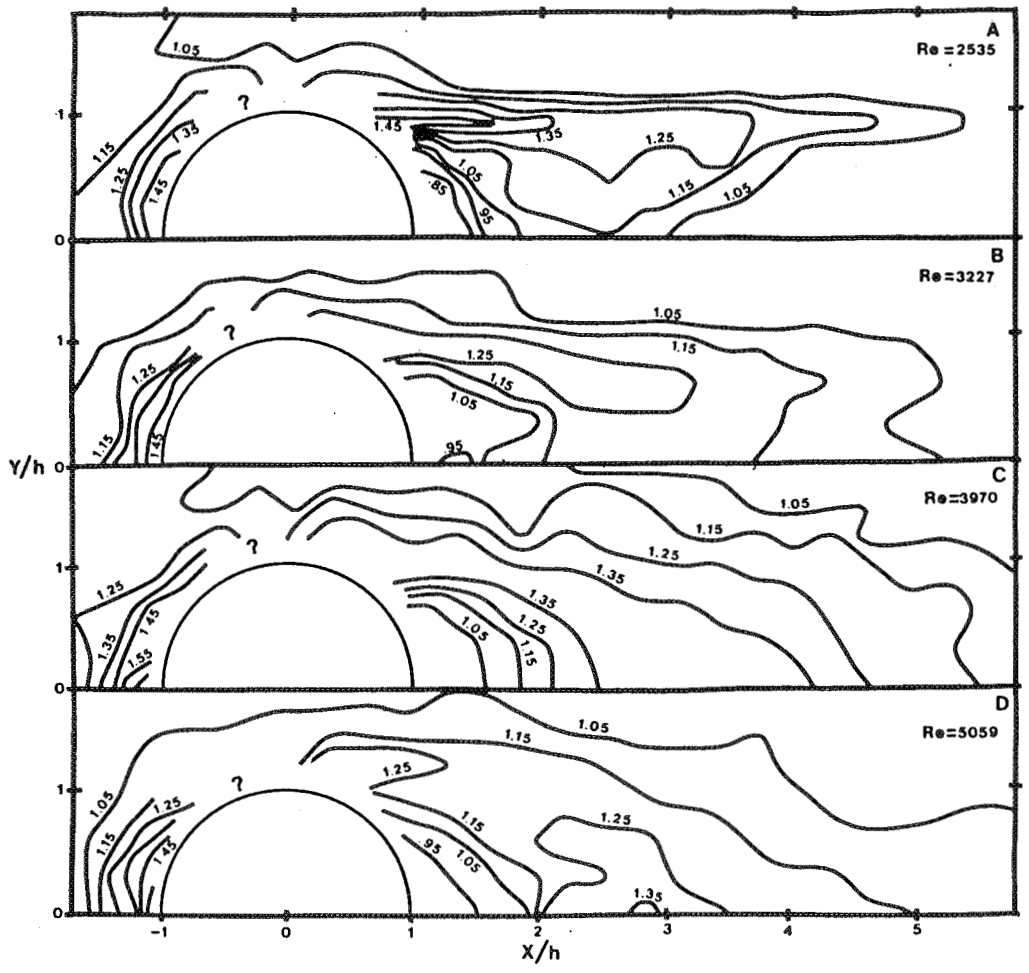

DETERMINATION OF SURFACE SHEAR STRESS WITH THE NAPHTHALENE SUBLIMATION TECHNIQUE

J.A. Lee[1] and R. Greeley[2], [1]Department of Geography and [2]Department of Geology, Arizona State University, Tempe, Arizona 85287

Introduction

Aeolian entrainment and transport are functions of surface shear stress and particle characteristics. Measuring surface shear stress is difficult, however, where logarithmic wind profiles are not found, such as regions around large roughness elements. Presented here is an outline of a method whereby shear stress can be mapped on the surface around an object. The technique involves the sublimation of naphthalene ($C_{10}H_8$) which is a function of surface shear stress and surface temperature.

The naphthalene sublimation technique is based on the assumption that the transfer of momentum, heat and mass are analogous. This assumption is known as the Reynolds analogy (see Kays and Crawford, 1980; Schlichting, 1979). If the Reynolds analogy can be shown to be correct for a given situation, then knowledge of the diffusion of one property allows the determination of the others. The naphthalene sublimation technique was developed for heat transfer studies (see Eckert, 1976) and can be readily applied to the determination of shear stress.

Analytical Framework

The naphthalene mass transfer coefficient, C_{mt}, is defined as

(1) $C_{mt} = q_{ns} / \rho_{ns}$

where q_{ns} is the mass transfer flux of naphthalene from the surface and ρ_{ns} is the density of naphthalene at the surface. Goldstein, et al. (1985) outline a procedure for determinining C_{mt} for naphthalene sublimation experiments.

A value of the heat transfer coefficient allows the calculation of the surface shear stress, τ_s. The Stanton number, St, is a dimensionless term defined as (Schlichting, 1979, p. 708)

(2) $St = C_{mt} / (\rho_a c_p U_\infty)$

where ρ_a is the atmospheric density, c_p is the specific heat of naphthalene and U_∞ is the freestream velocity. The local coefficient of skin friction, c_f, is also dimensionless and is defined as (Schlichting, 1979, p. 143)

(3) $c_f = \tau_s / (0.5\ \rho_a U_\infty^2)$.

If the Reynolds analogy is acceptable, then St can also be expressed as (Schlichting, 1979, p. 708)

(4) $St = 0.5\ c_f$

Combining Equations (2), (3) and (4) and solving for τ_s yields

(5) $\tau_s = (C_{mt} U_\infty) / c_p$

Shear stress is often expressed in terms of the friction velocity, u_*, which is defined as

(6) $u_* = (\tau_s \rho_a)^{0.5}$

Data Acquisition

The naphthalene sublimation technique requires information on the change in surface elevation, surface temperature of the naphthalene and freestream velocity during a wind tunnel run. The measurement surface is obtained by casting naphthalene in an aluminum mold. Surface heights are determined for points on a grid network before and after a wind tunnel run using a linear variable differential transducer mounted on an X,Y positioning device.

Surface temperature is monitored with a thermocouple embedded in the naphthalene with its tip near the surface. Average temperature during the wind tunnel run is used in the analysis.

The naphthalene sublimation technique was tested in the Arizona State University Planetary Geology Wind Tunnel. The tests involved eight wind tunnel runs during which the average sublimation depth (of twenty points) on the naphthalene surface was determined and the wind profile was measured during each run using a boundary layer rake.

The friction velocity was determined both from the naphthalene sublimation technique as described above and the wind profile. The profile data were reduced following a procedure outlined by Lettau (1957) to determine the aerodynamic roughness length, z_0, which was used in the logarithmic wind profile equation (Greeley and Iversen, 1985, p. 42)

(7) $u_* = (0.4\ u_z) / (\ln(z/z_0))$

where u_z is the wind speed at height z

Figure 1 shows the relationship between the two techniques for determining u_*. The naphthalene sublimation technique calculates u_* values one order of magnitude lower than the wind profile technique. This discrepency can be caused by a number of factors. The most likely are 1.) the wind profile is determined on the masonite wind tunnel floor while the naphthalene has a smoother surface, 2.) residue from silicon spray (used in the naphthalene casting) may reduce the sublimation rate, and 3.) the naphthalene surface temperature cannot be measured with a thermocouple; temperature just below the surface is measured.

The linear relationship between the friction velocity values calculated with the two methods (correlation coefficient = 0.99) allows the naphthalene sublimation data to be adjusted (by linear regression) to realistic values for the wind tunnel floor.

Conclusion

The naphthalene sublimation technique as outlined here is a reasonably accurate method for determining surface shear stress. Its most useful application is in determining the spatial variation of shear stress around objects where numerous point values are needed.

Acknowledgement

Dr. M.K. Chyu (Arizona State University Department of Mechanical and Aerorspace Engineering) provided invaluable advice on the naphthalene sublimation technique.

References

Eckert, E.G.R., 1976, Analogies to Heat Transfer Processes, in, Eckert, E.G.R., and Goldstein, R.J., eds., *Measurements in Heat Transfer,* Second Edition, McGraw-Hill Book Company, New York, p. 397-423

Goldstein, R.J., Chyu, M.K., and Hain, R.C., 1985, Measurement of Local Mass Transfer on a Surface in the Region of the Base of a Protruding Cylinder with a Controlled Data Acquisition System: *International Journal of Heat and Mass Transfer,* v. 28, p. 977-985.

Greeley, R., and Iversen, J.D., 1985, *Wind as a Geological Process on Earth, Mars, Venus and Titan*:: Cambridge University Press, Cambridge.

Kays, W.M., and Crawford, M.E., 1980, *Convective Heat and Mass Transfer,* Second Edition: McGraw-Hill Book Company, New York.

Lettau, H.H., 1957, Computation of Richardson Numbers, Classification of Wind Profiles, and Determination of Roughness Parameters, in Lettau, H.H., and Davidson, B., eds., *Exploring the Atmosphere's First Mile,* v. 1: Pergamon Press, New York p. 328-336.

Schlichting, H., 1979, *Boundary-Layer Theory,* Seventh Edition: McGraw-Hill Book Company, New York.

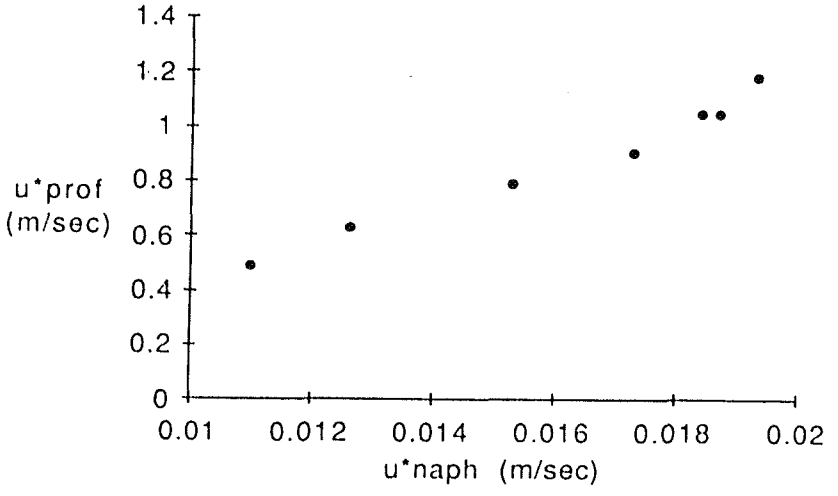

Figure 1. Friction velocity determined from naphthalene sublimation ($u_{*\,naph}$) and wind profile ($u_{*\,prof}$) during the same wind tunnel run.

CHAPTER 9

FLUVIAL PROCESSES

GROUNDWATER SAPPING CHANNELS: SUMMARY OF EFFECTS OF EXPERIMENTS WITH VARIED STRATIGRAPHY

Kochel, R. Craig and Simmons, David W., Department of Geology,
Southern Illinois University, Carbondale, IL 62901

Experiments in our recirculating flume sapping box have modelled valley formation by groundwater sapping processes in a number of settings. We have examined the effects of the following parameters on sapping channel morphology: 1) surface slope; 2) stratigraphic variations in permeability cohesion and dip; and 3) structure - joints and dikes.

Figure 1 illustrates the variety of designs used to simulate the gently-dipping strata and joints characteristic of the Colorado Plateau. Run 3 can be viewed as a control because it used uncemented, homogeneous sediment. Runs 8 - 11 were designed to observe the effect of joints in a variety of stratigraphic settings. Joints were constructed by excavating the fine sand in linear troughs and backfilling with coarser, more permeable sand. Runs 27 and 28 investigated the effects of varying cohesion. Cohesion was varied by mixing different amounts of cement (between 0.5 and 5% cement) or loess in the fine sand and by using sediments of varying grain size.

Slope of the sediment surface and the slope of the internal stratigraphy were varied between runs to determine the effect of slope upon the rate of sapping. In particular, we were interested in how slope affects the rate of sapping channel development and sapping channel morphology. Initial experiments using homogeneous sediment (Run 3) indicated that there existed a threshold slope of about 9^{o} below which no sapping channels formed. Below this critical slope, a seepage face formed, but channel incision failed to occur because sediments were not entrained. This slope value is probably diagnostic of the fine sand used in these experiments. Experiments with initial slopes above 11^{o} experienced significant slumping at the expense of channel formation.

The effects of slope in experiments with layered stratigraphy appear to be more complex. Variations in the dip of strata seem to be more important in channel development than surface slope. Runs 14 and 27 contained layered strata with markedly different surface and dip slopes. The 9^{o} surface slope of Run 14 should have resulted in rapid channel formation. However, only small channels formed directly above the toe of the coarse layer. Slumping occurred downslope from this point. The stratigraphy in Run 14 was parallel to the surface slope and no layering was exposed on the seepage face. Most of the groundwater discharge through the coarse layer either flowed along the flume floor to induce slumping or emerged directly above the toe of the coarse layer, taking the shortest route through the fine layer. The surface slope of Run 27 was only 3^{o}, well below the threshold of transport seen in homogeneous fine sand, but experienced significant channel development. Channels developed because the coarse, permeable layer was exposed on the face of a low scarp at the toeslope.

The depth of the sapping canyons also appeared to have been directly related to the thickness of the sediment in the upper strata. In situations where there was a more permeable upper layer (weakly cemented) over a less permeable base (strong cement or loess mixture), the basal layer acted as a base level control on incision. Width of the sapping channels varied considerably with the thickness of the strata and cohesion. Cohesion limited the rate of lateral cutting by retarding the rate of channel wall slumping, resulting in narrower valleys.

Laity and Malin (1985) drew attention to the role of structure in controlling the pattern of channel networks developed by sapping in the Navajo Sandstone of the Colorado Plateau. They noted that on a regional scale tributaries to the Escalante River were asymmetrically distributed on opposite sides of the channel. Structural features such as joints and faults create zones of increased permeability in consolidated rocks which are preferred paths for groundwater flow. Runs 8 - 11 were designed to observe the effect of joints upon the development of sapping channels. In general, main channel trends followed joint patterns and tributaries developed parallel to joints. Our experiments with linear zones of increased permeability suggest that if significant joints are present, sapping valleys will preferentially extend along these avenues of increased groundwater discharge. The degree of influence joints will have upon channel location probably depends upon the relative differences between the permeabilities of the joints and the host rock. As this difference becomes greater, the influence of jointing should become more pronounced.

We are currently experimenting with the development of channels by the combination of groundwater sapping and rainfall runoff processes. Channels formed in Run 28 were established first by sapping and then supplementd by periodic rainfall. The resulting channels exhibited a tapering head area more indicative of runoff valleys and was also characterized by more bifurcation than valleys produced only by sapping. However, close inspection revealed a distinctive scalloped morphology of alcoves developed along the channel walls.

We noticed the importance of groundwater piracy in the evolution of channel networks during most of the sapping experiments. Subsurface piracy was commonplace in all types of stratigraphic settings and regardless of the presence of joints. Between 3 and 6 channels typically formed at regularly-spaced positions across the seepage face during the initial few hours of sapping runs. During the course of a run, one or two of these channels extended headward more rapidly until it captured groundwater from surrounding areas that would have flowed into neighboring channels. Once dominance of a given channel began, the process became self-enhancing and the disparity between development of neighboring channels became even more apparent. Eventually, the pirated channels became inactive and channel evolution was terminated.

Groundwater piracy was best developed during several runs 7 and 18 where conditions were established to mimic the intersection of channels with

subsurface high-level aquifers in experiments designed to simulate channel development on Hawaii (Kochel and Piper 1985). Head regions of the first channels that reach the high-level aquifers widened dramatically and grew at the expense of neighboring channels that were pirated. This process is probably responsible for the light-bulb shaped valleys typical of sapping valleys on the Hawaiian Islands.

These kinds of modelling experiments are particularly good for: 1) testing concepts; 2) developing a suite of distinctive morphologies and morphometries indicative of sapping; 3) helping to relate process to morphology; and 4) providing data necessary to assess the relative importance of runoff, sapping, and mass wasting processes on channel development. The observations from the flume systems can be used to help interpret features observed in terrestrial and Martian settings where sapping processes are through to have played an important role in the development of valley networks.

References

Kochel, R.C., Howard, A.D., and McLane, C., 1985, Channel networks developed by groundwater sapping in fine-grained sediments: Analogs to some Martian valleys: in Woldenberg, M., ed., Models in Geomorphology; Allen & Unwin, Boston, p. 313-341.

Kochel, R.C., and Piper, J.F., 1985, Morphology of large valleys in Hawaii: Evidence for groundwater sapping and comparisons to Mars: 17th Lunar Planet, Sci. Conf., Houston, p. 424-425.

Laity, J.E., and Malin, M.C., 1985, Sapping processes and the development of theater-headed valley networks on the Colorado Plateau: Geol. Soc. Amer. v. 96, p. 203-217.

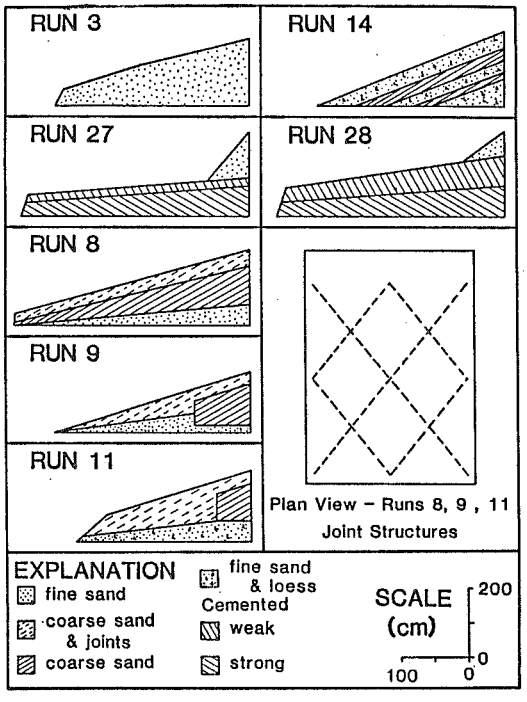

Fig. 1. Schematic of stratigraphic styles used in sapping experiments.

FLUVIAL VALLEYS ON MARTIAN VOLCANOES

Victor R. Baker, Department of Geosciences and Department of Planetary Sciences, University of Arizona, Tucson, Arizona 85721; and Virginia C. Gulick, Department of Geosciences, University of Arizona, Tucson, Arizona 85721

Channels and valleys have been known on the Martian volcanoes since their discovery by the Mariner 9 mission. Their analysis has generally centered on interpretation of possible origins by fluvial, lava, or viscous flows (debris, lahar, etc.). As summarized by Baker (1982), fluvial and related degradational processes (sapping) produce landforms strikingly similar to those observed on some Martian volcanoes. However, the possible fluvial dissection of Martian volcanoes has received scant attention in comparison to that afforded outflow, runoff, and fretted channels (Mars Channel Working Group, 1983).

Valley and/or channel forms on Martian volcanoes have not received a systematic investigation, and some confusion has been generated by studies with a local perspective. For example, Milton (1973) interpreted a single high-resolution Mariner 9 picture from the northwest flank of Alba Patera as displaying dendritic fluvial gullies. Carr and others (1977) used Viking imagery of the whole region to demonstrate an origin by lava tube and channel formation. However, in a preliminary mapping study of the Alba channels/valleys, we find that fluvial valleys may also occur with lava channels. The fluvial valleys occur in networks with remarkably high magnitudes for Mars (Table 1). They are well integrated and concentrated on the northern flank of the volcano, in areas where lava flow morphology is subdued. Nearby areas with prominent lava flow fronts and ridges show classic lava channel and tube morphologies.

We have initiated photo interpretive, mapping, and morphometric studies of three Martian volcanoes: Ceraunius Tholus, Hecates Tholus, and Alba Patera. Ceraunius is drained by radial valleys, interpreted as fluvial in origin by Sharp and Malin (1975). Reimers and Komar (1979) summarized evidence that the valleys (or channels) of both Ceraunius and Hecates were not formed by lava erosion, lava tube collapse, or tectonic fracturing. Some lava channels and collapsed tubes exist, but we have found that, as on Alba Patera, these have distributary patterns and discontinuous, irregular surface morphologies. Fluvial valleys, in contrast, are continuous and display tributary development. Some have prominent fan deposits at their mouths, indicating sediment transport and deposition. Fans are especially prominent on the western flank of Hecates, where valleys appear to have reached an advanced state, perhaps by enlargement through sapping.

Preliminary morphometric results (Table 1) indicate that, for these three volcanoes, valley junction angles increase with decreasing slope. Drainage densities are quite variable, apparently reflecting complex interactions in the landscape-forming factors described above.

Five other Martian volcanoes are characterized by prominent valley systems: Uranius Tholus, Uranius Patera, Apollinaris Patera, Hadriaca Patera, and Tyrrhena. Many of these valleys, on preliminary investigation, appear to have formed or were extensively modified by lava erosional activity. Tyrrhena has been interpreted as having a history of pyroclastic activity (Greeley and Spudis, 1981). Its radial system of troughs resembles valleys formed by sapping (Baker, 1982, p. 75-77).

Ages of the Martian volcanoes have recently been reinterpreted in studies in progress by R.G. Strom, N. Barlow, and associates. The new data indicate that Ceraunius Tholus, Uranius Tholus, Apollinaris Patera, Tyrrhena Patera, and Hecates Tholus all date from the period of heavy bombardment. Hadriaca Patera and Uranius Patera date from the terminal heavy bombardment, and Alba Patera is post heavy bombardment. This refined dating provides a time sequence in which to evaluate the degradational forms.

An anomaly has appeared from our initial study: fluvial valleys seem to be present on some Martian volcanoes, but not on others of the same age. The Hawaiian analogy (Gulick and Baker, 1986) may provide some answers here. For example, ash mantling of Hecates (Mouginis-Mark and others, 1982) may have contributed to drainage initiation, as it does on Mauna Kea and Kohala in Hawaii. Volcanic surfaces characterized only by high permeability lava flows may have persisted without fluvial dissection.

Table 1. Morphometry of Valleys/Channels on Martian Volcanoes

Volcano	Average Slope*	Drainage Density (km/km^2)	Magnitude	Junction Angles θ_1	θ_2	$\theta_1+\theta_2$
Ceraunius Tholus	10-12°	0.5-1.1	5+	29	2	28
Hecates Tholus	3-5°	0.6-2.3	10+	25	7	33
Alba Patera	<1°	0.3-1.1	34+	33	7	41

*Reimers and Komar (1979)

REFERENCES

Baker, V.R., 1982, The Channels of Mars: University of Texas Press, Austin, Texas, 198 p.

Carr, M.H., Greeley, R., Blasius, K.R., Guest, J.E., and Murray, J.B., 1977, Some Martian volcanic features as viewed from the Viking orbiters: Journal of Geophysical Research, v. 82, p. 3985-4015.

Greeley, R., and Spudis, P.D., 1981, Volcanism on Mars: Rev. Geophys. Space Phys., v. 19, p. 13-41.

Gulick, V.C., and Baker, V.R., 1986, Evolution of valley networks on Mars: The Hawaiian analog: Geological Society of America Abstracts with Programs, v. 18, no. 6, p. 623.

Mars Channel Working Group (V.R. Baker, chairman), 1983, Channels and valleys on Mars: Geological Society of America Bulletin, v. 94, p. 1035-1054.

Milton, D.J., 1973, Water and processes of degradation in the Martian landscape: Journal of Geophysical Research, v. 78, p. 4037-4047.

Mouginis-Mark, P.J., Wilson, L., and Head, J.W., 1982, Explosive volcanism on Hecates Tholus, Mars: Investigation of eruption conditions: Journal of Geophysical Research, v. 87, p. 9890-9904.

Reimers, C.E., and Komar, P.D., 1979, Evidence for explosive volcanic density currents on certain Martian volcanoes: Icarus, v. 39, p. 88-110.

Sharp, R.P., and Malin, M.C., 1975, Channels on Mars: Geological Society of America, v. 86, p. 593-609.

VALLEY DEVELOPMENT ON HAWAIIAN VOLCANOES

Victor R. Baker, Department of Geosciences and Department of Planetary Sciences, University of Arizona, Tucson, Arizona 85721; and Virginia C. Gulick, Department of Geosciences, University of Arizona, Tucson, Arizona 85721

Work in progress on Hawaiian drainage evolution (Baker, 1986; Baker and Kochel, 1984; Kochel and Baker, in press; Gulick and Baker, 1986) indicates an important potential for understanding drainage development on Mars. Similar to Mars (Baker and Partridge, 1986), the Hawaiian valleys were initiated by surface runoff, subsequently enlarged by groundwater sapping, and eventually stabilized as aquifers were depleted.

We have used quantitative geomorphic measurements to evaluate the following factors in Hawaiian drainage evolution: (1) climate, (2) stream processes (surface runoff versus groundwater sapping), and (3) time. In comparing regions of similar climate, drainage density shows a general increase with the age of the volcanic island (Table 1). With age and climate held constant, sapping dominated valleys, in contrast to runoff-dominated valleys, display the following: (1) lower drainage densities, (2) higher ratios of valley floor width to valley height (V_f ratios), and (3) more positive profile concavities (Table 2). Some anomalies in drainage density development with time were idenitifed: (1) unusually high values on the windward side of Mauna Kea and Kohala, where low permeability ash deposits mantle relatively young, high permeability basalt flows; (2) low values on Oahu because of the dominance of sapping processes; (3) low values on Kahoolawe, Lanai, and Nihau, probably because of rainshadow effects.

Studies of stream junction angles (Table 3) indicate increasing junction angles with time on the drier leeward sides of the major islands. However, relatively low values occur on the dry side of Oahu. On the windward sides of the major islands, sapping processes and associated slope changes result in variable junction angles.

The quantitative geomorphic studies and earlier field work (Baker, 1980, 1982) yielded important insights for Martian geomorphology. The importance of ash mantling in controlling infiltration on Hawaii also seems to apply to Mars. Some valleys, such as Kaupo and Keanae on Maui, evolve from lava surfaces, enlarge by groundwater sapping, and later become conduits for lava flows and lahars (Baker, 1982). Some valleys on Martian volcanoes seem to have similar experiences of multiple flow processes.

The Hawaiian valleys also have implications for the valley networks of the Martian heavily cratered terrains. Baker and Partridge (1986) found evidence for two types of valleys in this area: (a) slightly older, more dense networks on higher, probably relict land surfaces, and (b) younger, less dense networks of deeply incised valleys that seem to have grown headward at the expense of type (a) valleys. It is hypothesized that these relationships indicate an evolutionary sequence similar

to that observed in the Hawaiian volcanoes. High-density surface-water ravines formed initially because of low-permeability rock types, appropriate climate, adequate relief, or some combination of these factors. With time, some valleys deepened sufficiently to tap ground-water flow in deeper, more permeable rock types. These valleys then enlarged by headward growth at the expense of the older networks. The latter were isolated as relict, degraded components of the landscape. The entire system ceased functioning and was "frozen" in its approximate present configuration at the termination of the heavy bombardment on Mars.

Table 1. Drainage densities (km/km^2) for Hawaiian Study Sites

	Hawaii	Maui	Molokai	Oahu	Kahoolawe	Lanai	Nihau
humid areas	0.3-7.0	1.2-3.5	2.4-5.5	1.7-5.1	---	---	---
dry areas	0.2-1.1	1.2-2.4	1.2-4.0	1.0-4.0	1.4-3.9	0.9-3.5	1.8-2.9

Table 2. Properties of Drainage Networks

	Drainage Density (km/km^2)	V_f Ratio	Profile Concavity
Sapping-Dominated	0.7-2.0	0.8-3.2	positive
Runoff-Dominated	2.1-3.2	0.1-0.8	negative

Table 3. Junction Angles of Hawaiian Valleys and Channels

	Humid Study Sites			Dry Study Sites		
Volcano/Island	θ_1	θ_2	$\theta_1+\theta_2$	θ_1	θ_2	$\theta_1+\theta_2$
Mauna Loa	34	11	45	--	--	--
Mauna Kea	34	5	40	--	--	--
Kohala	38	11	49	33	14	47
Maui	41	19	60	44	15	58
Molokai	38	10	52	49	17	64
Oahu	41	16	57	37	21	57

θ_1, θ_2, and $(\theta_1+\theta_2)$ are mean values.

REFERENCES

Baker, V.R., 1980, Degradation of volcanic landforms on Mars and Earth: N.A.S.A. Technical Memorandum 82385, p. 234-235.

Baker, V.R., 1982, The Channels of Mars: University of Texas Press, Austin, Texas, 198 p.

Baker, V.R., 1986, Evolution of valleys dissecting volcanoes on Mars and Earth: N.A.S.A. Tech. Memorandum 88383, p. 414-416.

Baker, V.R., and Kochel, R.C., 1984, Valley network development by spring sapping: Geological Society of America Abstracts with Programs, v. 16, no. 6, p. 435.

Baker, V.R., and Partridge, J.B., 1986, Small Martian valleys: pristine and degraded morphology: Journal of Geophysical Research, v. 91, p. 3561-3572.

Gulick, V.C., and Baker, V.R., 1986, Evolution of valley networks on Mars: The Hawaiian analog: Geological Society of America Abstracts with Programs, v. 18, no. 6, p. 623.

Kochel, R.C., and Baker, V.R., in press, Groundwater sapping and the geomorphic development of large Hawaiian valleys, in Higgins, C.G., and Coates, D.R., editors, Groundwater Geomorphology: Geological Society of America Special Paper.

THE APPLICATION OF FLOW COMPETENCE EVALUATIONS TO THE ASSESSMENT OF FLOOD-FLOW VELOCITIES AND STRESSES

Paul D. Komar, College of Oceanography, Oregon State University, Corvallis, OR 97331.

The concept of flow competence is generally employed to evaluate the velocities, discharges and bottom stresses of river floods inferred from the size of the largest sediment particles transported (Baker and Ritter, 1975; Costa, 1983). Flow competence has become an important tool for evaluating the hydraulics of exceptional floods on Earth, including those which eroded the Channeled Scabland of eastern Washington (Baker, 1973), and has potential for similar evaluations of the floods which carved the outflow channels on Mars.

For the most part, flow-competence evaluations have been empirical, based on data compiled from a variety of sources including major terrestrial floods caused by natural processes or dam failures. Costa (1983) provides a recent compilation of this data, yielding relationships equivalent to

$$\tau_c = 26.6\, D^{1.21}$$

and

$$u_c = 57\, D^{0.46}$$

respectively for the flood bed stress (τ_c) and velocity (u_c) as a function of the diameter D of the maximum-size gravel or boulders transported (units of the relationships are in the cgs system). Data used in support of these empirical equations include diameters ranging 1 to 500 cm.

Such flow-competence relationships would appear to provide a straight-forward assessment of flood-flow stresses and velocities based on the maximum size of gravel and boulders transported.

However, a re-examination of the data base and comparisons with measurements of selective entrainment and transport of gravel in rivers open to question such evaluations (Komar, in press). It is found that the competence data and empirical relationships trend counter to those obtained for selective entrainment, indicating that the competence evaluations are affected by varying degrees of selective size entrainment as well as by limits to the availability of extreme particle sizes. In many instances the empirical competence equations greatly over-estimate the hydraulics of flood flows, and it is suggested that the better established selective entrainment equations be used instead for competence evaluations as well. For gravels and coarser materials, these can be expressed as the dimensionless relationship

$$\theta_{ti} = 0.045\,(D_i/D_{50})^{-0.7}$$

for the Shields θ_{ti} for the entrainment of a clast of individual diameter D_i from a deposit of mixed sizes having a D_{50} median diameter. The 0.045 and -0.7 coefficients are empirical, based on several data sets such as those of Milhous (1973) and Carling (1973). In the application to flow-competence evaluations, D_i is the maximum size material transported, generally much larger than D_{50}. The relationship indicates that the Shields θ_{ti} for such extreme sizes will be reduced below the 0.045 value given by the standard Shields curve as revised by Miller et al. (1977), a curve which applies to deposits of uniform grain sizes. This results because the larger grains within a deposit of mixed sizes are more exposed to the flow and have smaller pivoting angles, factors which ease their ability to be entrained by the flow. This can be demonstrated through analyses of the forces acting on the grain during entrainment by pivoting, rolling or sliding, an approach which focuses more on the physical processes than the above purely empirical relationships. However, those derived equations require further testing by flume and field measurements before being applied to flow-competence evaluations. Such tests are now underway.

REFERENCES:

Baker, V.R. (1973) Paleohydrology and sedimentology of Lake Missoula flooding in eastern Washington: *Geol. Society of America Special Paper* 14, 79 p.

Baker, V.R., and D.F. Ritter (1975) Competence of rivers to transport coarse bedload material: *Geol. Society of America Bull.*, v. 86, p. 975-978.

Carling, P.A. (1983) Threshold of coarse sediment transport in broad and narrow natural streams: *Earth Surface Processes*, v. 8, p. 1-18.

Costa, J.E. (1983) Paleohydraulic reconstruction of flash-flood peaks from boulder deposits in the Colorado Front Range: *Geol. Society of America Bull.*, v. 94, p. 986-1004.

Komar, P.D. (in press) Selective grain entrainment by a current from a bed of mixed sizes: A reanalysis: *Jour. Sedimentary Petrology* .

Komar, P.D. (in press) Selective gravel entrainment and the evaluation of flow competence: *Sedimentology* .

Milhous, R.T. (1973) Sediment transport in a gravel-bottomed stream: Unpublished Ph.D. thesis, Oregon State University, Corvallis, 232 p.

Miller, M.C., I.N. McCave, and P.D. Komar (1977) Threshold of sediment motion in unidirectional currents: *Sedimentology* , v. 24, p. 507-528.

POSSIBLE ORIGIN OF SOME CHANNELS ON ALBA PATERA, MARS

S. E. Postawko and P. Mouginis-Mark, Planetary Geosciences Div.,
Hawaii Inst. Geophysics, Univ. Hawaii, Honolulu, HI 96822

Several alternative models have been proposed for the origin and mode of formation of channels and valley networks on martian volcanoes, notably Hecates Tholus, Ceraunius Tholus, Alba Patera. Early interpretations of Mariner 9 and Viking images suggested that these features on Alba were lava channels (Carr *et al.*, 1977), while those on Ceraunius Tholus were interpreted as fluvial (Sharp and Malin, 1975) or volcanic debris channels (Reimers and Komar, 1979). Subsequent mapping of Tyrrehna Patera (Greeley and Spudis, 1981) and Hecates Tholus (Mouginis-Mark *et al.*, 1982) has suggested that pyroclastic activity may have characterized eruptions on these volcanoes, and that at least for Hecates the channels were probably formed by fluvial erosion of unconsolidated ash deposits on the flanks of the volcano. As part of a continuing program to better understand the eruptive history of the young volcanic centers on Mars, we have identified numerous channels on the flanks of Alba Patera that resemble the channels on Hecates. As a result, we are exploring the possibility that some of the small channels on the flanks of Alba Patera may be fluvial in origin, and are examining potential water sources and modes of formation.

There are several ways in which these Alba channels could have been formed by fluvial action. One way is by direct rainfall, with the water coming either from degassing of the magma, or being driven out of the regolith due to volcanic heating. Alternatively, this water may have been deposited within the shallow regolith as ice or snow and then melted by intrusives to form channels.

The exposed portion of Alba Patera was evidently formed at a time when any early, dense, warm atmosphere on Mars had disappeared (if such an atmosphere ever did indeed exist) (Cattermole, 1986a). Therefore, it is inferred that the channels formed under climatic conditions similar to those at present-day Alba, with an atmospheric surface pressure of ~6mb and annual average surface temperatures between 180 - 220K (Kieffer *et al.*, 1977). Very little water vapor (a mass mixing ratio on the order of 10^{-4}) is required to saturate the atmosphere at this pressure and temperature range, and even less at greater altitudes in the atmosphere. Since the atmosphere of Mars is, in general, close to saturation on a daily basis (Davies, 1979), the addition of water vapor from degassing magma or evaporation/sublimation of subsurface water/ice due to intrusive heating may well have resulted in precipitation in the vicinity of Alba Patera. This depends, in part, on the release rate of water vapor to the atmosphere, the temperature of the gas, and how the gas is distributed through the atmosphere. Assessing the likelihood of precipitation, of any kind, playing a role in the formation of some of the channels seen on the flanks of Alba Patera is a primary goal of our current research.

Studies of lava flows on Alba Patera indicate the production of large volumes of lava during a given eruption (Cattermole, 1986b; Pieri *et al.*, 1986); meaning either very high rates of effusion for a relatively short period of time, or eruptions of long duration with lower effusion rates. In either case, if the magma initially contained water, then large volumes of lava may have exsolved a sufficient amount of water vapor (Greeley, 1986) to supersaturate the atmosphere. However, Wilson and Head (1983) have shown that even a very low (~0.01 wt.%) volatile content in martian magmas is sufficient to disrupt the magma and result in explosive eruptions. As yet, no evidence of explosive volcanism on Alba Patera has been detected. This does not eliminate the possibility of *very* low volatile magmas releasing some water to the atmosphere, although whether these could provide

enough to carve channels is still under investigation.

Another possible source of water is the martian regolith. Calculations by Fanale *et al.* (1986) have shown that subsurface ice is stable at the latitude of Alba Patera, even for present-day climatic conditions. Heating in the vicinity of the volcano may have been enough to drive substantial amounts of water out of the ground and into the atmosphere.

Calculations are presently under way to determine probable amounts and rate of release of water by magmatic outgassing of low volatile magmas, and by warming of the regolith. To date, we have examined the effects of volcanic gases (CO_2, H_2O, and SO_2) on the paleoclimate of Mars, and their ability to warm the atmosphere a sufficient amount to permit surface flow of water or brines (Postawko and Kuhn, 1986). From these calculations, it does not appear that pure water could be released to flow on the martian surface unless local heating by intrusives raised the local temperature of the regolith. Currently, our efforts are therefore focused on the distribution of the vapor through the atmosphere during and immediately after a volcanic eruption. Water released within a volcanic cloud will likely rise quite high in the atmosphere (Wilson and Head, 1983), and may be dispersed before saturation occurs. It is also possible that precipitation may originate from so high up that snow/rain would sublimate/evaporate before reaching the ground. Water released from the regolith may more easily saturate the lower atmosphere, and thus be a more likely source for any water which may have cut channels.

REFERENCES: M.H. Carr *et al.* (1977). *J. Geophys. Res., vol. 82*, p. 3985-4015. P. Cattermole (1986a), *Lunar Planet. Sci. XVII*, p. 107-108. P. Cattermole (1986b). *Lunar Planet. Sci XVII*, p. 105-106. D. Davies (1979), *J. Geophys. Res., vol. 84*, p. 8335-8340. F. Fanale *et al.* (1986), *Icarus, vol. 67*, 1-18. R. Greeley (1986). *Symp. on MECA, LPI Contr. 599*, p. 26-28. R. Greeley and P. Spudis (1981). *Revs. Geophys. & Space Phys. vol. 13*, p. 13-41. H. Kieffer *et al.* (1977), *J. Geophys. Res., vol. 82*, 4249-4291. K.B. Krauskopf (1979), *Introduction to Geochemistry* McGraw-Hill, New York. P.J. Mouginis-Mark *et al.* (1982). *J. Geophys. Res., vol. 87*, p. 9890-9904. D. Pieri *et al.* (1986). *Rpts. Plan. Geol. Prog. 1985. NASA TM 88328*, p. 318-319. S. Postawko and W.R. Kuhn (1986). *Proc. Lunar Planet. Sci. Conf. 16th, J. Geophys. Res., vol. 91*, p. D431-D438. C.E. Reimers and P.D. Komar (1979). *Icarus, vol. 39*, p. 88-110. R.P. Sharp and M.C. Malin (1975). *Geol. Soc. Amer. Bull., vol. 86*, p. 593-609. L. Wilson and J.W. Head (1983), *Nature, vol. 302*, p. 663-669.

NON-EQUILIBRIUM FREEZING OF WATER-ICE IN SANDY BASALTIC REGOLITHS AND IMPLICATIONS FOR FLUIDIZED DEBRIS FLOWS ON MARS. J. L. Gooding, SN2/ Planetary Materials Branch, NASA/Johnson Space Center, Houston, TX 77058

Introduction. Many geomorphic features on Mars have been attributed to Earth-analogous, cold-climate processes involving movement of water- or ice-lubricated debris. Clearly, knowledge of the behavior of water in regolith materials under Martian conditions is essential to understanding the postulated geomorphic processes. Pertinent laboratory data have been reported by D. M. Anderson and collaborators [e.g., 1-2]) but have been based mostly on experiments with ultrafine-grained samples of clay minerals or their admixtures. New experiments have been performed with sand-sized samples of natural "basaltic" regoliths in order to further elucidate how water/regolith interactions depend upon grain size and mineralogy. The new data reveal important contrasts with data for clay-mineral substrates and suggest that the microphysics of water/mineral interactions might affect Martian geomorphic processes in ways that have not been fully appreciated.

Ice-Formation Experiments. Sand- and silt-sized fractions of two soils from the summit region of Mauna Kea, Hawaii [3] were used as Mars-analogous regolith materials. Makanaka glacial outwash consisted of relatively little-weathered lithic and mineral fragments of basalts whereas Puu Poliahu weathered tephra consisted largely of palagonitized pyroclastic debris [3,4]. Using previously described equipment and methods [5], differential scanning calorimetry (DSC) was used to measure temperatures of water/ice phase transitions as wet slurries of individual soil fractions were cooled or heated at controlled rates under a carbon dioxide atmosphere. Freezing and melting of ice was studied as a function of water/soil mass ratio, soil particle size, and thermal-cycle rate. Comparison tests were done under the same conditions with U. S. Geological Survey standard rock powders PCC-1 (peridotite) and BHVO-1 (basalt), and with powdered Lithology A (olivine-pyroxene-maskelynite) of the shergottite meteorite, EETA79001.

Freezing and melting temperatures of water-ice in the soils were only weakly dependent on particle size over the silt- and sand-sized intervals. Freezing points were essentially independent of water/soil mass ratio but varied inversely with cooling rate. Melting points varied directly with heating rate (Fig. 1). For both the soils and the comparison rocks, though, freezing occurred at temperatures > 6 K below the equilibrium freezing point of pure bulk water (Fig. 2). Depressed freezing points were not controlled by salts in the samples (salt contents were negligible) but were a consequence of the difficulty with which water-ice nucleates on igneous minerals and noncrystalline weathering products. Olivine, pyroxene, plagioclase, and glass (mafic or felsic) are all poor nucleators of water-ice [5]. Although crystalline clay minerals are good nucleators of water-ice [1,5], the mineraloids palagonite and allophane are demonstrably poor nucleators [5]. Therefore, even at slow cooling rates, water mixed with either fresh or palagonitized basalts or closely related materials can survive metastably at temperatures significantly below 273 K.

Implications for Martian Geomorphology. Lifetimes of outburst floods with low sediment/water ratios would probably be controlled by discharge rates and degree of cover by ice bridges [6,7], rather than by the microphysical phenomena reported here. However, in any process that might form a water-based slurry (high sediment/water ratio) on Mars, undercooling of water should be an important factor in determining the longevity and efficacy of the slurry as an agent of geomorphic change. Degree of

undercooling should be a strong function of the mineralogy of the sediment. Debris flows composed of fresh igneous materials or poorly crystalline weathering products (e.g., palagonite) should support greater degrees of undercooling and, therefore, greater dynamic lifetimes, than should debris flows composed of crystalline weathering products such as smectites. Photogeologic studies of debris flows on Mars might profit from greater attention to possible correlations between styles and distances of debris-flow movements and the lithologic characters of local regolith materials.

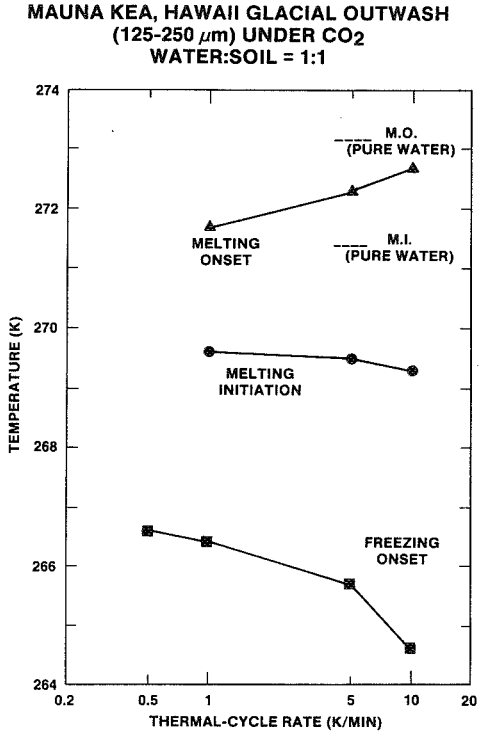

Figure 1. Phase-transition temperatures of water, as a function of heating and cooling rate, in slurries prepared from Mauna Kea glacial outwash soil.

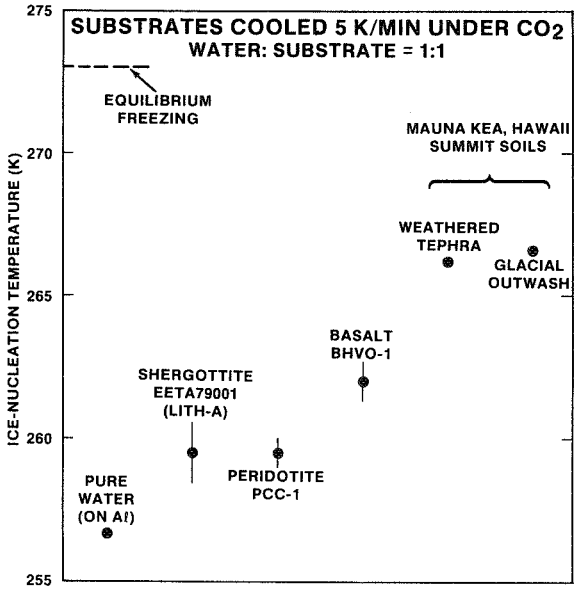

Figure 2. Freezing temperatures for wet slurries of silt-sized "basaltic" materials. Error bars represent standard deviations of replicate measurements.

References:

[1] Anderson D. M. (1968) Israel J. Chem., 6, 349-355.
[2] Banin A. and D. M. Anderson (1975) Nature, 255, 261-262.
[3] Japp J. M. and J. L. Gooding (1980) Rept. Planet. Geol. Program - 1980, NASA Tech. Memo. 82385, 212-214.
[4] Porter S. C. (1979) Geol. Soc. Amer. Bull., Part II, 90, 908-1093.
[5] Gooding J. L. (1986) Icarus, 66, 56-74.
[6] Carr M. H. (1979) J. Geophys. Res., 84, 2995-3007.
[7] Wallace D. and C. Sagan (1979) Icarus, 39, 385-400.

VOLATILE RESERVOIRS BELOW THE SURFACE OF THE ELYSIUM REGION OF MARS: GEOMORPHIC EVIDENCE

Eric H Christiansen, Brigham Young University, Provo, Utah, 84602
Jennifer A. Hopler, University of Iowa, Iowa City, Iowa 52242.

The Elysium volcanic province contains a variety of geomorphic evidence for the existence of large volatile reservoirs of subsurface volatiles. Study of these landforms yields insight into the distribution and size of these reservoirs and how they interact with the surface environment and will ultimately place constraints on the geometry, constitution, origin, time of formation, and temporal evolution of these important components of the martian crust. Three principal types of landforms appear to be related to subsurface volatile reservoirs in the Elysium region of Mars : 1) small outflow channels; 2) large lahars; and 3) vast expanses of knobby terranes around the margins of the Elysium dome.

Outflow Channels.

The most obvious expressions of the presence of a subsurface volatile reservoir in this region are two relatively small outflow channels (1). Located southwest of Elysium Mons, both channel systems arise and cut across a broad expanse of older plains dotted by irregular mesas and smaller knobs (knobby plains).

The anastomose **Hebrus Valles** system of channels is 250 km long and emerges full-strength from an elongate depression. The source depression is 10 km across and has narrow finger-like projections. Individual sinuous channels are less than 100 m deep and about 1 km wide; a braided reach is about 10 km wide. Streamlined bedforms are abundant in the middle reach. The channels become narrower and shallower downslope. Hebrus Valles terminate as a series of narrow distributaries. No sedimentary deposits are obviously related to the development of the channels. Hebrus Valles are similar to other small martian outflow channels and appear to result from fluvial erosion following the outbreak of a confined aquifer.

Hephaestus Fossae are a connected series of linear valley segments which branch and cross downslope but have high junction angles. Locally, the valley pattern is polygonal. Hephaestus Fossae are parallel to Hebrus Valles but are considerably deeper and longer (600 km). The rectilinear pattern of the valleys has suggested to some that the fossae are tectonic in origin. However, unlike graben systems, Hephaestus Fossae originate in an isolated depression similar to the source of Hebrus Valles. Two sinuous, apparently fluvial, channels also arise from this depression. We suggest that, Hephaestus Fossae are also of fluvial origin and resulted from catastrophic flooding and draining of water from beneath the surface. Hephaestus Fossae channels appear to have cut through the knobby plains unit which overlies polygonal terrane like that exposed at the NW end of the fossae in Adamus Labyrinthus (4). Downcutting to, or subsurface flow at this unconformity produced a channel pattern that was controlled by the polygonal troughs beneath the younger knobby plains materials. Hebrus Valles channels did not excavate this deposit and hence show more typical outflow features.

Mega-lahars.

Photogeologic studies of the Elysium volcanic province provide examples of the interaction of magmatism and subsurface volatile reservoirs to produce distinctive landforms (2, 5). Three sets of volcanic debris flows or lahars issue from the northwest-trending system of fractures that localized the three major volcanic constructs in the Elysium province. The deposits are lobate in plan and have steep well-defined snouts. Evidence that these mass flow deposits were wet slurries and not lava or ash flows includes: 1) the intimate association of channels with their surfaces--these channels are sinuous, form anastomose distributary patterns, and have streamlined features on their floors. These characteristics are consistent with the flow of water across the deposits. 2) discrete channels issue from the base of the lobate masses suggesting draining of water from initially wet sediments; 3) short reticulate systems of sinuous valleys cut portions of the deposits' margins and look like seepage channels (3); and 4) numerous irregular depressions mark other areas of the flows and have clearly developed from a formerly smooth and more extensive deposit. These pits may be created by the removal of volatiles by sublimation or seepage.

We have postulated that the lahars resulted from the melting of ground ice and liquefaction of subsurface materials (2). The Elysium volcanoes are the most reasonable sources of heat. This is consistent with the stratigraphic evidence that lavas and lahars were nearly contemporaneous. The contact of magma with liquid water may have resulted in hydromagmatic explosions which can produce large quantities of easily mobilized fine-grained material (7). The intersection of this fluid reservoir with the regional fracture system led to the rapid expulsion of a muddy slurry down the steep western slope of the province. These sedimentary deposits extend nearly 1000 km down the regional slope to the northwest and cover 10^6 km^2. The deposits are less than 200 m thick near their sources and are probably much thinner on average. The total volume of the lahars may then be approximately 10^5 km^3. Taking a value of 30% water by volume--a figure typical of terrestrial lahars and non-volcanic debris flows (6)--implies that over 10^4 km^3 of water were involved.

Knobby Terranes.

Knobby terrane provinces have relatively smooth surfaces with variable proportions of knobs and flat-topped mesas. Broadly similar knobby terranes cover approximately 3 million km^2 in the Elysium region. The knobs and mesas appear to be erosional remnants of a formerly thicker deposit. The polygonal terrane of Adamus Labyrinthus underlies the knobby terrane in the Amenthes quadrangle. In southern Amenthes quadrangle, the knobby terranes have developed at the expense of an extensive plateau marked by irregular depressions and pits. Layering is visible in the walls of these ragged depressions. Erosional stripping of the knobby deposit has exhumed large impact craters. North of the volcano Hecates Tholus, knobby terranes developed at the expense of lava plains that partially bury the undegraded precursor of the knobby terranes. Here, large lava-capped blocks give way to smaller mesas which grade northward into smaller knobs. Even farther north the knobby terranes disappear and reveal underlying polygonal terrane. The knobby terranes' precursor

appears to have developed in middle martian history. It overlies the polygonal terranes of Adamus Labyrinthus which are post-Lunae Planum in age (4) and is in turn buried by Elysium lavas and lahars. The knobby plains are also cut by the two large outflow channels noted above and numerous small seepage channels on the western flanks of the Elysium dome. However, evidence for fluvial erosion is not extensive and the volume missing from the knobby plains precursor must have been either stripped away by eolian processes or it may represent the sublimation of water that had been sequestered in the layered deposits. The spatial coincidence of the knobby plains with other water-related landforms lends credence to the latter hypothesis. The degradation of the knobby plains precursor appears to have occurred mostly before Elysium volcanism because vast tracts of smooth lava plains bury knobby terrane; but at least in the small region north of Hecates, knob development appears to have persisted until the later stages of Elysium volcanism. Assuming that most of the missing volume represents removal of volatiles, and ignoring the extent of the knobby plains that must underlie the Elysium volcanic province, the amount of water lost from this region may be approximately 10^5 km^3.

Implications for Sub-Surface Volatile Reservoirs at the Surface of Mars.

The evidence provided by these landforms is internally consistent with the presence of a large relatively shallow volatile reservoir in the Elysium region of Mars. If the geologic features described above are reliable indicators of subsurface volatiles, they imply that:

- volatile reservoirs lie relatively close to the surface and underlie millions of km^2 in this region.
- their is no apparent latitudinal variation in the depth or thickness of the volatile reservoirs.
- the precursors of the knobby terranes are or were important volatile reservoirs.
- volatiles may be lost in a variety of ways from these reservoirs.
- volatiles were incorporated in an easily eroded surficial deposit in the middle history of Mars. The ultimate origin of the water in this reservoir is uncertain. A model to explain the preferential entrapment of volatiles into the region's surface materials may be required.

References.

(1) Christiansen, EH (1985) Geol Soc America Abstr Prog. 17, p. 545.
(2) Christiansen, EH, and Ryan, MP (1984) Geol Soc America Abstr Prog. 16, p. 470.
(3) Higgins, CG (1984) in RG LaFleur, Groundwater as a geomorphic agent, Allen and Unwin, p. 18-58.
(4) McGill, GE (1986) Geophys Res Lett 13, p. 705-708.
(5) Mouginis-Mark, PJ (1985) Icarus 64, p. 265-284.
(6) Pierson, TC (1985) Geol Soc America Bull 96, p. 1056-1069.
(7) Sheridan, MF, and Wohletz, KH (1983) J Volcanol Geotherm Res 17, p. 1-29.

EVIDENCE FOR GLACIATION IN ELYSIUM

Duwayne M. Anderson
Texas A&M University

Evidence for the existence of permafrost and the surface modification due to frost effects and the presence of ice on Mars dates from early observations by Otterman and Bronner (1), Leighton and Murray (2), Anderson et al. (3), Baranov (4) and Anderson and Gatto (5). The Viking landers I and II confirmed the presence of water in the regolith and the periodic occurrance of frost at the surface of Mars, Bieman et al. (6), Anderson (7). Observations from the Viking Orbiters I and II demonstrated the presence of atmospheric water at various concentrations in the atmosphere of the planet (Farmer et al. [8]) and also provided a means of documenting the accumulation and sublimation of frost and ice in the two polar caps and at several other locations on the planet. Later analysis of the Viking Orbiter imagery produced evidence suggesting the former presence of ice sheets that could have played a part in shaping the surface of Mars (Lucchitta et al. [9]). Similarities have been pointed out between a number of streamlined Martian channel features and similar streamlined landforms created by antarctic ice sheet movements.

A study of Viking Orbiter imagery of Granicus Valles and the surrounding terrain in Elysium has produced further evidence of glaciation on Mars. Granicus Valles is located in the Northern hemisphere between 25 degrees and 40 degrees latitude and 220 degrees to 240 degrees longitude. It extends from the Elysium fossae near Elysium Mons to Utopia planitia, the plains where Viking Lander II is located. Granicus Valles has been characterized as an outflow channel (Malin [10], Carr [11]). It is approximately 1100 km long, about 10 km wide at the source, with distributory branches that cover an area approximately 300 km wide. Three distinctly different geological units are involved (Mouginis-Mark [12], Christiansen and Greeley, [13]). Part of the region is characterized as a Complex Vent Area. It is one of the main volcanic centers in Elysium. Another has been referred to as Modified Lava Plain by Christiansen and Greeley (13), and Compound Lava Plains and Erosional Plains by Mouginis-Mark (12). A portion of it was earlier referred to as Channeled Plain by Christiansen and Greeley (13).

Volcanism has played an important role in developing the landscapes of the Elysium region. Two features that strongly resemble terrestrial moberg ridges have been found. These features are ridge shaped, serrated mountains, very similar to the moberg ridges described by Allen (14). Terrestrial moberg ridges form as a result of subglacial, fissure eruptions. The only apparent difference between those observed on earth and these two Martian counterparts is scale; the Martian features are much larger. Because the

size of a moberg ridge is limited by the thickness of ice above the erupting fissure lava, the greater height of the Martian ridges implies a thicker ice sheet. The height of the moberg ridge near Granicus Valles is estimated to be about 2.6 km. The ground surface surrounding both Martian moberg ridges appears to have two distinct levels; it is lowest at the base of the ridges, rising to a level near the top of the ridges at a distance. A possible explanation is that subsidence occurred during formation of the Martian moberg ridges due to the melting of ground ice near the eruption area while at a distance most of the ground ice in the permafrost is still present and the original elevation has been preserved. Meltwater during and following eruptions might have been suddenly released during subglacial volcanism into Granicus Valles in one case and into Hrad Valles in the other. Fluvial erosion thus could have played a role in shaping both.

Crater size-frequency plots indicate differences in the ages of surfaces from one region to another, ranging from one to three billion years. The presence of a thick ice sheet together with underlying permafrost could help to explain this. A thick mantle of ice would have intercepted and contained many meteoric impacts, shielding the underlying regolith. Subsequent removal of this ice by sublimation or melting would then expose a relatively unmarked surface to subsequent meteoric bombardment. These surfaces, from crater size-frequency plots, would always appear younger than the surrounding, continuously exposed terrains.

Many of the volcanic edifices in Elysium appear to have uncommonly steep slopes at their bases. Many are quite large and probably stood above the hypothetical, pre-existing ice sheet. Volcanic flows and ejecta cascading down slope would have come to rest on the surrounding ice. Later disappearance of the ice would result in the subsidence and redeposition of these materials, helping to explain the abnormally steep basal slopes now evident.

References

1. Otterman, J. and Bronner, F.E. (1966), Martian Wave of Darkening: A Frost Phenomenon?, Science, 153, pp. 56-59.
2. Leighton, R. B. and Murray, B. C. (1966). Behavior of Carbon Dioxide and Other Volatiles on Mars, Science, 153, pp. 136-144.
3. Anderson, D. M., Gaffney, E. S., and Low, P. F. (1967). Frost Phenomena on Mars, Science, 155, pp.319-322.
4. Baranov, I. Ya. (1959). Geographical Distribution of Seasonally Frozen Ground and Permafrost,

Principles of Geocrynology, Part 1. V. A. Obruchev Institute of Permafrost Studies, Academy of Science, U.S.S.R.

5. Anderson, D. M., Gatto, L. W., and Ugolini, F. (1973). An Examination of Mariner 6 and 7 Imagery for Evidence of Permafrost Terrain on Mars. PERMAFROST: The North American Contribution to the Second International Conference, Yakutsk, Siberia. National Academy of Sciences, pp. 499-508.
6. Bieman, K., et al. (1976). Search for Organic and Volatile Inorganic Compounds in Two Surface Samples From the Chryse Planitia Region of Mars. Science, 194, pp.72-76.
7. Anderson, D. M. (1978). Water in the Martian Regolith. Comparative Planetology, Academic Press, Inc., pp. 219-224.
8. Farmer, C. B., et al. (1977). Mars: Water Vapor Observations From the Viking Orbiters. J. Geophys. Res., 82, pp. 4225-4248.
9. Lucchitta, B. K., Anderson, D. M., and Shoji, H. (1981). Did Ice Streams Carve Martian Outflow Channels? Proc. Third Coll. on Planetary Water, Niagara Falls, New York, Nature, 290/5809, pp.759-763.
10. Malin, M. C. (1976). Age of Martian Channels. J. Geophys. Res., 81, pp. 4825-4845.
11. Carr, M. H. (1981). The Surface of Mars, Yale University Press, New Haven.
12. Mouginis-Mark, P. J., et al. (1984). Elysium Planitia, Mars: Regional Geology, Volcanology, and Evidence for Volcano-Ground Ice Interactions. Earth, Moon, Planets, 30, pp. 149-173.
13. Christiansen, E. H., and Greeley, R. (1981). Mega-lahars(?) in the Elysium Region, Mars, (abstract). Lunar Planet. Sci. XII, pp. 138-140.
14. Allen, C. C. (1979). Volcano-Ice Interactions on Mars. J. Geophys. Res., 84, pp. 8048-8059.

WATER AND ICE ON MARS: EVIDENCE FROM VALLES MARINERIS*

B. K. Lucchitta, U.S. Geological Survey, Flagstaff, Arizona 86001

An important contribution to the volatile history of Mars comes from a detailed study of Valles Marineris, where excellent stereoimages and a three-dimensional view of the upper Martian crust permit unusual insights: the subsurface in the equatorial region of Mars below about 1 km depth was not desiccated until relatively recently, even though desiccation is predicted by models of the equilibrium between water in the ground and in the atmosphere [1].

The evidence that ground water and ice existed until relatively recently or still exist in the equatorial area comes from observations of landslides [2,3], wall rock [4], and dark volcanic vents [5,6]. Several observations suggest that landslides were lubricated by water. Three young slides generated an outwash fan and gave rise to a channel that has several bends and extends on a gradient of 4 m/km for a total distance of 250 km from its source [7]. Also, the material in this channel was capable of erosion at considerable distance from its source; it breached a bedrock ridge, carved flutes in the lower channel, and eroded its banks. Doughnut-shaped hills within this channel resemble moraines containing kettle holes, which on Earth are formed by the melting of blocks of ice.

Some landslides have lobes that angle backward from the main debris mass and flow downhill, others give rise to small sinuous valleys, and many small landslides are surrounded by levees like terrestrial mudflows. These observations also suggest that the landslide deposits contained fluids. A small channel debouches from a tributary canyon to Valles Marineris; apparently water discharged from the canyon walls, if canyon tributaries were indeed formed by sapping [9].

Valles Marineris landslides are different in efficiency from large catastrophic landslides on Earth. Whereas terrestrial landslides increase in efficiency (distance traveled) with increasing weight [9], the large landslides in Valles Marineris retain the same efficiency regardless of weight [3]. One explanation for the difference might be that the Martian slides are lubricated by water, whereas most large terrestrial slides are dry-rock avalanches [10].

A comparison of landslide speeds also suggests that the Martian slides contained water. Among large catastrophic landslides on Earth, only the Huascaran slide [11] matches the Martian ones in speed [3]; the Huascaran slide contained much water and ice. Because all landslides in Valles Marineris are released from wall rock, some layers within the walls that are 7-10 km high must have contained these lubricating materials.

A relatively young, level deposit embaying eroded layered beds occurs in the lowest area of the central troughs of Valles Marineris [12]. The deposit looks like a dry lake bed or alluvial flat, which suggests that wet debris contributed to its formation. The wet debris was apparently derived from landslides or wall rock.

That Valles Marineris wall rock contained water or ice is further suggested by its difference from the interior layered deposits. Landslides having flow lobes that extend far out onto the chasma floors debouch only from wall rock or erosional remnants of wall rock. No such landslides come from the layered deposits, even where the layered deposits are as high and steep as the wall rock. Apparently, landslides formed from the wall materials flowed easily; those from the interior deposits generally did not [13].

Faults and fault zones in Valles Marineris also shed light on the problem of water content in the walls. Contrary to what is commonly seen on Earth, many fault zones in Valles Marineris are more resistant to erosion than the country rock. Spurs projecting into Valles Marineris developed along faults [4], and all the median ridges of wall rock paralleling chasma walls or separating chasmata from each other occur where faults and fracture zones are densely spaced. Apparently faults were lithified or intruded by dikes and thus are more resistant to erosion than the country rock. Conversely, the observation implies that the country rock is weaker relative to the faults. Such weak country rock would be consistent with wall rock composed of breccia [10] that is weakly cemented by ice near the free faces and is charged with water at some depth.

Another argument supports the idea that the wall rock contained water and ice. Dark deposits interpreted as volcanic-vent material [5,6] occur only at elevations lower than 6 km above Martian datum. The highest deposits are 3 km below the rim of adjacent plateau surfaces. This 6-km elevation appears to be the maximum height reached by extruding magmas and can be used to calculate relative densities of magma and wall-rock columns [14,15]. It appears that the material in the column of combined solid crust and mantle rock underlying the plateau must have been less dense than the material in the liquid magma column. Upper crustal rock composed of loosely consolidated breccia mixed with water or ice might fulfill such a requirement.

Because the main evidence for water and ice in the wall rock comes from landslides, their time of emplacement is important. The landslides in Valles Marineris date from the time of late eruptions on the Tharsis volcanoes [2] and thus were emplaced after the major activity on Martian outflow channels. Therefore, the concept of ground saturated by water and ice in the equatorial region is consistent with Carr's [16] hypothesis that confined aquifers developed in this region and gave rise to outflow channels. The concept also agrees with the presence of rampart craters in the equatorial area.

None of the above observations conclusively demonstrate that water or ice existed in the wall rock of Valles Marineris, but altogether the evidence is highly suggestive. Any models addressing the exchange of water with the atmosphere in the equatorial region of Mars must therefore take into account that, below a depth of about 1 km, this region was not entirely desiccated, at least until the time of landslide formation.

References

1) Fanale F. R. (1976) Icarus, 28, p. 179-202.
2) Lucchitta B. K. (1979) J. Geophys. Res., 84, p. 8097-8113.
3) Lucchitta B. K., Kaufman K. L., and Tosline D. J. (1981) NASA TM 84211, p. 326-328.
4) Lucchitta B. K. (1981) NASA TM 84211, p. 419-421.
5) Lucchitta B. K. (1985) Lunar Planet. Sci. XVI, p. 503-504.
6) Lucchitta B. K. (1986) Lunar Planet. Sci. XVII, p. 496-497.
7) Lucchitta B. K. (1984) Workshop on Water on Mars, Nov. 30-Dec. 1, 1984, p. 45-47.
8) Pieri David (1980) Science, 210, p. 895-897.
9) Scheidegger A. E. (1973) Rock Mechanics, 5, p. 231-236.
10) Hsü K. J. (1975) Geol. Soc. Am. Bull., 86, p. 129-140.

11) Plafker George and Erickson G. E. (1978) Rock slides and avalanches, Barry Voight, ed., Elsevier, Amsterdam, p. 277-314.
12) Lucchitta B. K. and Ferguson H. M. (1983) Proc. Lunar Planet. Sci. Conf. 13th, Part 2, 88, Supplement, p. A553-A568.
13) Lucchitta B. K. (1982) Repts. Planet. Geol. Prog.-1982: NASA TM 85127, p. 233-234.
14) Eaton J. P. and Murata K. J. (1960) Science, 132, p. 925-938.
15) Vogt P. R. (1974) Earth and Planet. Sci. Letts., 23, p. 337-348.
16) Carr M. H. (1979) J. Geophys. Res., 84, p. 2995-3007.

*(Published in Symposium on Mars: Evolution of Its Climate and Atmosphere, July 17-19, 1986, p. 59-61.)

FORMATION OF THE LAYERED DEPOSITS IN THE VALLES MARINERIS, MARS

Susan S. Nedell, NASA Ames Research Center, Moffett Field, CA 94035, and Steven W. Squyres, Cornell University, Ithaca, NY 14853.

Thick sequences of layered deposits are found in the Valles Marineris, Mars [1-3]. They exhibit fine, nearly horizontal layering, and are present as isolated plateaus of what may once have been more extensive deposits. Individual sequences of layered deposits are as thick as 5 km. We have argued previously that the morphology of the deposits is most consistent with origin in standing bodies of water [3]. The rhythmic nature of the layering, their lateral continuity, horizontality, great thickness, and stratigraphic relationships with other units in the canyons all appear most consistent with deposition in a quiet aqueous environment. If standing bodies of water existed for any significant period of time in the Valles Marineris, they were almost certainly ice-covered. Here, we examine in detail the conditions necessary for the existence of ice-covered martian paleolakes, and consider mechanisms for sediment deposition in them.

Ground water has been very important in shaping the martian surface. There is ample evidence that the martian regolith is highly porous and permeable, and that it at one time contained large amounts of water [4]. If a large tectonic depression such as the Valles Marineris cut deep into an aquifer system in the martian regolith, it would be natural for the canyons to become partially filled with water. As long as the subsurface aquifer system remains charged, water in the lakes could be replenished readily by seepage from the canyon walls.

It is unlikely that the martian atmosphere was thick enough to have sustained mean annual temperatures above freezing after the earliest epoch of martian history. Any standing water bodies would be expected to have a perennial ice cover. Perennially ice-covered lakes presently exist in the Dry Valleys of Antarctica. There the mean annual temperature is also well below freezing, and the ice on the lakes has reached an equilibrium thickness [5]. As ice is lost from the upper surface of the lake by ablation, new ice forms at the lower surface, releasing latent heat as it does. This heat is the dominant term in the energy balance equation that gives the equilibrium ice thickness. Water in the lake is replenished in Antarctica by surface flow; on Mars this could be accomplished by ground water seepage. The rate of ablation exerts a strong influence on the equilibrium ice thickness, and on Mars it is poorly known. Based on reasonable estimates of ablation rates, the equilibrium thickness of ice on martian lakes under the present climate might be 65 to 650 m [5]. The depth of possible lakes is very poorly constrained, and could have ranged from very shallow depths to more than 5 km deep.

There are three ways that sediment could enter an ice-covered lake: down through the ice cover, up from the lake bottom, or in from the lake margins. We now consider each of these possibilities in turn.

Four processes that could have transported sediment downward through an ice cover are considered: (a) solar energy warmed individual particles, allowing them to melt through the ice; (b) sediment worked its way downward through vertical melt channels; (c) a layer of sediment deposited on the ice was thick enough to cause the ice layer to founder, dumping the sediment into the lake; and (d) a layer of sediment deposited on the ice cover led to a Rayleigh-Taylor instability, and sediment diapirs penetrated downward through the ice layer.

Simple energy calculations show that solar warming is inadequate to melt moderate-sized grains downward through the 5-meter ice cover of typical Antarctic lakes [6]. It is therefore expected to be wholly inadequate on Mars, where the surface temperature and solar flux are still lower, and the equilibrium ice thickness may be one or two orders of magnitude greater.

Migration through vertical melt channels appears to be the primary sedimentation mechanism in some Antarctic lakes [7]. Melt channels form when the ice thickness is less than about 3 m. In order for this process to have operated on Mars, surface temperatures and ablation rates must have been high enough to thin the ice to only a few meters, and liquid must have been stable at the surface for periods during the summer. Neither condition is likely to have been met, as there is no evidence that the martian climate at the time of layer deposition was substantially warmer than it is at the present.

Foundering of the ice cover could have occurred if enough debris was loaded onto the ice surface so that the overall density of the ice-sediment layer became greater than that of the liquid below. As sediment accumulated on the ice surface, the ice layer would thicken continuously, since freezing at the lower surface of the ice would no longer be balanced by ablation from the upper surface. We have calculated, for a given thickness of the sediment layer to be dumped into the lake, how rapidly sediment must be piled onto the ice surface for foundering to occur. We take ice surface temperatures of 210 to 240 K, bulk sediment densities of 1.5 to 2.5 g cm^{-3}, and sediment layer thicknesses of 75 to 150 m (the thicknesses of a light layer and a light/dark couplet, respectively, measured in Candor Chasma). Sedimentation rates of 0.4 to 15 mm yr^{-1} are required, and will lead to foundering at ice thicknesses ranging from 0.5 to 2.8 km. A weakness of the foundering hypothesis is that the ice would not undergo substantial melting during the foundering event, and could subsequently reform as a continuous cover and continue to thicken. However, these calculations neglect the effect of a geothermal heat flow. If the geothermal heat flow had an Earth-like value, the equilibrium thickness of even a sediment-covered ice layer might be no more than $\sim$ 2 km. Foundering could then occur repeatedly, taking place each time the sediment thickness exceeded the critical value. For an equilibrium ice thickness of 2 km, continuous sedimentation and repetitive foundering with a bulk sediment density of 2.0 g cm^{-3} would produce a sequence of layers each 140 m thick.

Even if foundering did not take place, it is likely that a thick layer of sediment that accumulated on the ice surface would penetrate the ice via a Rayleigh-Taylor instability. The configuration of dense sediment over less dense ice would favor diapiric upwelling of the ice and sinking of the sediment. We consider the flow to be dominated by the rheology of the ice, and take an upper sediment layer 75 to 150 m thick. For an ice temperature near freezing, the instability will grow in tens of years. For a temperature of 210 K, the growth time is of the order of 10^4 yr. Therefore, if a sediment layer thick enough to form one of the observed layers accumulated on an ice cover, it would probably penetrate it rapidly.

The limiting factor for sediment deposition by foundering or Rayleigh-Taylor instability is the ability to accumulate substantial amounts of sediment on the ice surface. Global dust storms could conceivably be the source for the sediment, but there are significant problems with this hypothesis. The present martian climate produces net deposition of dust at the poles, and this process would have to be somehow reversed. Furthermore, sediment would have also presumably accumulated on the surrounding uplands as well as in the Valles Marineris. None is presently observed there. This difficulty could be overcome if there were repeated periods of deposition and erosion near the equator. Sediment built up on the uplands would be swept away during erosional episodes, while debris deposited on the ice would be trapped by foundering or Rayleigh-Taylor instability, and preserved. Without a clearly plausible mechanism for massive, repeated sedimentation at low latitudes, however, origin of the deposits by downward migration through an ice cover remains speculative at best.

Volcanic material that originated beneath the lake might also be a source for the layered deposits. There are several arguments against formation of the deposits by subaerial vulcanism. One would expect that accumulations of ash-fall debris would be widespread, yet there are no

layered deposits on the uplands surrounding the Valles Marineris. The nature of the layering also does not support an ash-flow origin. Typical large terrestrial ash flows form aprons of individual flows that taper away from central vents. Smaller and more abundant flows would produce irregular layering. In addition to there being no unambiguous volcanic calderas, the layered deposits are characterized by fairly uniform layer thicknesses that extend laterally for at least many tens of kilometers. These arguments would be largely overcome if the vulcanism were subaqueous. Volcanic constructs may have been destroyed by slumping of material off cones as they were forming, or masked by floating pumice that eventually became waterlogged and sank to the lake bottom. Volcanic eruptions in water also would distribute effusive material much more easily. Even at fairly great depths, it is likely that explosive vulcanism could occur on Mars. On Earth, eruptions change from effusive to explosive activity, due to magma vessiculation, at water depths of 300 m for basaltic magma [8], and 500 m for silicic magma [9]. The corresponding water depths for explosive eruptions on Mars are about 800 m and 1300 m, respectively. Although there is no direct evidence for it, the process of subaqueous explosive vulcanism is an attractive mechanism for explaining some aspects of the layered deposits.

Finally, the nearby canyon walls are an obvious source of sediment for the layered deposits. It is likely that the Valles Marineris formed as tectonic grabens, some of which were substantially enlarged by removal of interstitial ground ice and collapse of the canyon walls. In a lacustrine environment, sediment would have been transported from the canyon walls into the deeper portions of the canyons by gravity flows, and deposited in nearly horizontal layers. This mechanism presents some geometric complications, and may not be able to account for all of the deposits. The material from the collapsing canyon wall is sufficient to fill the depressions that formed only partially, yet the present deposits rise nearly to the level of the canyon rims in places. This problem could be alleviated if plateaus of layered deposits had cores of undisturbed canyon wall material, or if material were also added by volcanic eruptions or sediment transport downward through the ice.

We conclude that there are several geologically feasible mechanisms that could have led to formation of thick deposits in ice-covered paleolakes in the Valles Marineris. Present data are insufficient to choose conclusively among the various possibilities. Several types of data from the Mars Observer mission will be useful in further characterizing the deposits and clarifying the process of their origin. The deposits should be considered important targets for a future Mars sample return mission.

References: [1] McCauley, J.F., *USGS Misc. Inv. Ser. Map I-897* (1978); [2] Lucchitta, B.K., *NASA Tech. Memo. 85127*, 233 (1982); [3] Nedell, S.S., and Squyres, in *Workshop on Water on Mars*, 56 (1984); [4] Carr, M.H., *J. Geophys. Res.* **84**, 2995 (1979); [5] McKay, C.P., *et al.*, *Nature* **313**, 561 (1985); [6] Simmons, G.M., *et al.*, *U.S. Antarc. Jour.* (1985); [7] Nedell, S.S., submitted to *Sedimentology*; [8] Sigurdsson, H., *Geol. Assoc. Can., Short Course Notes* **2**, 294 (1982); [9] Moore, E.C., and Schilling, J.G., *Contrib. Min. Petrol.* **41**, 105 (1973).

GEOMORPHIC EVIDENCE FOR ANCIENT SEAS IN WEST DEUTERONILUS MENSAE, MARS - I: REGIONAL GEOMORPHOLOGY

by

Timothy J. Parker, Dale M. Schneeberger, David C. Pieri, and R. Stephen Saunders

Jet Propulsion Laboratory, California Institute of Technology, Pasadena, CA

Deuteronilus Mensae lies at the western end of a swath of fretted terrain greater than 500km wide and 3000km long comprising the boundary between the northern lowland plains of Mars and the topographically higher and more heavily cratered southern highland terrain from 30° to 50° latitude, 280° to 350° longitude. We will concentrate on the fretted terrain morphology within a specific region in west Deuteronilus Mensae (44° to 50° latitude, 342° to 347° longitude, figure 1).

The fretted terrain in west Deuteronilus Mensae consists of extensive cratered upland "penninsulas" or isolated plateaus cut by long, finger-like canyons typically 10 to to 20km wide and upwards of 300km long. The longest of these canyons trend roughly north-south to north-northeast in much of the region depicted in figure 1, which may reflect some local structural and/or topographic control. Along the east side of figure 1, and throughout much of Deuteronilus Mensae, the lowland dissection of the cratered upland also exhibits some circular and arcuate trends that might indicate preferential degradation of buried large impact structures (1). This particular example of martian fretted terrain presents a relationship to the lowland/upland boundary which is unique in that the gross fretted terrain morphology, rather than defining the lowland/upland boundary as is the case for most martian fretted terrains, is in fact present on both sides of the boundary (though it is highly degraded on the north side).

At least three geomorphic zones roughly parallel to the lowland/upland boundary, suggestive of increasing modification northward, can be recognized on the fretted terrain of the region. These zones appear to be equivalent to what Weiss et al. (2) interpreted as stratigraphic units. For convenience of description we have identified these zones, from southern highlands to northern plains, as "A", "B", and "C".

The southern-most zone (zone "A") consists of sharply defined fretted terrain. The highland plateau surfaces generally appear brighter and more varied in albedo and texture than do those of the middle zone immediately to the north (Zone "B"). They are separated from the canyon floors by escarpments ranging from 262m (±32m) near the plateau surface contact with zone"B", to greater than 650m (±32m) toward the south edge of figure 1. (All shadow measurements for the canyon walls were measured from Viking Orbiter image 673B43, which covers this same region at a resolution of 204 m/pixel with a sun elevation of 9°). The canyon floors of zone "A" are comprised of smooth plains partially to completely buried by relatively bright debris aprons from the canyon walls. These debris aprons occur as sharply defined, gently sloping surfaces that are either concentric to isolated plateau outliers or parallel to canyon walls and are typically less than 10km wide. They occur at the bases of all fret escarpments within zone "A" except those within about 50km of the contact with zone "B" on the plateau surface. The contact between zones "A" and "B" is a well defined irregular line running east-west across the cratered upland surface and plateau outliers. This contact can be readily traced across the highland surface for several hundred kilometers, both to the southwest and east of the area shown in figure 1. On the lowland surface it is less easily recognized, particularly to the east, where the plateau outliers are more scattered.

The middle zone (zone "B") consists of well defined fretted terrain in which the plateau surfaces appear smoother, with a somewhat darker and much less varied albedo surface than those of zone "A". The canyon walls in zone "B" range in height from less than 64m (±32m) just north of the degraded 10km crater at D in figure 1, to as high as 163m (±32m) north of the plateau surface contact between zones "A" and "B". North of the crater at D, the canyon wall slopes approach that of the sun elevation, so heights cannot be determined reliably by shadow measurements. The canyon floors of zone "B" are comprised of smooth plains similar to those of zone "A", but lack the prominent debris aprons. Instead, much of the canyon floors adjacent to the escarpments either lack debris aprons entirely at this scale or, at best, exhibit poorly defined or subdued debris aprons expressed as narrow features (a few km or less wide) intermediate in slope between those of the canyon wall and floor.

The northern-most zone (zone "C") consists of rounded or "softened" fretted terrain. The plateau and canyon surfaces consist of light and dark "striped" terrain within about 50km of the contact with zone "B", and mottled terrain beyond about 50km from the contact with zone "B". Slope inflections at plateau/canyon margins within zone "C" are very subdued. On the plateau and upland surface, the contact between zones "B" and "C" is expressed as a moderately well defined line separating the smooth, relatively uniform albedo surface of zone "B" from the striped or mottled surface of zone "C". Within the fret canyons, the contact between zones "B" and "C" is somewhat sharper than it is on the plateau surface and is expressed as smooth arcs or lobes with their concave sides facing zone "C" (at E, figure 1). The plateau/lowland morphology typical of the fretted terrain, though

apparently highly subdued, is visible in this region as far north as 51° latitude, more than 200km north of the contact between zones "B" and "C" - approximately coincident with the usual position given for the boundary between the northern plains and the southern highlands (3,4).

Weiss et al. (2) interpreted the zones as surface exposures of successively lower stratigraphic units. In their model, these units are nearly horizontal layers intersecting the northward-dipping plateau surface. However, at least two problems with a stratigraphic interpretation for the zoning become apparent in the 200m/pixel images of figure 1. Such problems become even more apparent upon examination of very high resolution images (see footprints for these images on map, figure 1) of the region (5): (A) The northern limit of the occurrence of prominent debris aprons associated with zone "A" exhibits an apparently topograpically conformal offset to the south with respect to the plateau surface contact between zones "A" and "B". If the debris aprons are associated with the wasting of an upper "A" stratigraphic unit, they should occur as far north as the plateau surface contact between zones "A" and "B". Also, the gradual decrease in height of the canyon walls to the north might expectedly produce progressively narrower debris aprons to the north. Further, if they are comprised of material from all three units, one might expect them to be found associated with escarpments in zones "B" and "C" as well. (B) The smooth, lobate contact between zones "B" and "C" (at F, figure 1) embays an old, degraded crater about 15km in diameter. A stratigraphic contact would have been disrupted by the formation of the crater.

Another, though provocative mechanism by which topographically conformal zone contacts might be produced on the fretted terrain is by successively lower levels of standing water associated with episodes of catastrophic outflow channel development elsewhere along the lowland/upland boundary. If the zone boundaries represent old shorelines, the above problems can be addressed: (A) The absence of prominent debris aprons in zones "B" and "C" could be due to reworking or complete removal of the debris by rising and falling water levels. The southward offset of the contacts between zones "A" and "B" and between zones "B" and "C" could be due to successive episodes of embayment of the canyons. (B) Embayment of the 15km degraded crater by the contact between zones "B" and "C" easily fits the expected behavior of a shoreline.

In addition to providing reasonable explanations for the above problems, successive levels of standing water within the northern lowlands might be useful in addressing some other fretted terrain problems. (A) Removal of debris (likely to be comprised of a wide range of grain sizes) wasted and/or sapped from the canyon walls in a near shore lacustrine environment would be efficient and could produce the smooth canyon floor surface without affecting the plateau surface (as might be expected of eolian processes). It also provides a very effective way of maintaining the steep cliffs by focusing erosion (through wave action) at the bases of the cliffs and, at the same time, preventing the accumulation of talus deposits.

References:

(1) Sharp, R. P., 1973, Mars: Fretted and chaotic terrains: Journ. Geophys. Res., Vol. 78, p. 4073-4083.

(2) Weiss, D., Fagan, J. J., Steiner, J., and Franke, O. L., 1981, Preliminary obsevations of the detailed stratigraphy across the highland-lowlands boundary: Reports of the Planetary Geology Program - 1981, NASA Tech. Memo. 84211, p. 422-425.

(3) Lucchita, B. K., 1978, Geologic map of the Ismenius Lacus Quadrangle of Mars: USGS Map I-1065, Atlas of Mars, 1:5,000,000 Geologic Series.

(4) Scott, D. H., and Carr, M. H., 1978, Geologic map of Mars: USGS Map I-1083, Atlas of Mars, 1:25,000,000 Geologic Series.

(5) Parker, T. J., Schneeberger, D. M., Pieri, D. C., and Saunders, R. S., Geomorphic evidence for ancient seas in west Deuteronilus Mensae, Mars - II: From very high resolution Viking Orbiter images: This volume.

Figure 1: Geomorphic Map of West Deuteronilus Mensae, Mars. Viking Orbiter Images: 675B34,59.

GEOMORPHIC MAP OF
WEST DEUTERONILUS MENSAE, MARS
Explanation
Zone A
Zone B
Zone C
Scale (kilometers)

GEOMORPHIC EVIDENCE FOR ANCIENT SEAS IN WEST DEUTERONILUS MENSAE, MARS - II: FROM VERY HIGH RESOLUTION VIKING ORBITER IMAGES

by

Timothy J. Parker, Dale M. Schneeberger, David C. Pieri, and R. Stephen Saunders

Jet Propulsion Laboratory, California Institute of Technology, Pasadena, CA

Very high resolution (10m/pixel or better) Viking Orbiter images of the martian surface, though rare, make it possible to examine specific areas at image scales approaching those of high altitude terrestrial aerial photographs. Of the approximately 1300 total Viking images in this range, probably less than 500 of them are clear enough to be very useful for studies of the martian surface. Twenty three clear very high resolution images (458B41-51, 61-72; at 9m/pixel) lie within west Deuteronilus Mensae (see 1 figure 1, for location). This discussion will deal with the northernmost images (458B61-72) which constitute an almost unbroken mosaic of the west wall of a long finger-like fret canyon (figure 1).

In the very high resolution images, morphological details on the plateau surface within zone "B" (1), not detectable at low resolution, make it possible to divide the zone into two distinct subzones separated by an east-west escarpment (at D, figure 1). South of this escarpment, the plateau surface is characterized by its smooth texture at small scales and relatively uniform albedo. The plateau surface north of this escarpment has a more mottled appearance. The most notable characteristic of this subzone is the presence of well defined polygons several tens of meters to as much as 200m to 300m across (2). These are best expressed on the plateau surface from about 2km north of the escarpment at D to within 20km of the top of figure 1. Individual polygons are separated by well-defined cracks that are typically a few tens of meters or less wide and appear filled with relatively bright material. The canyon floor south of the contact between zones "B" and "C" is characterized by the presence of polygons similar to but somewhat larger than those on the plateau surface.

The canyon floor north of the contact between zones "B" and "C" consists of two principal morphologic styles. Much of it consists of a relatively uniform albedo, smooth plains surface, broken by a system of narrow, sharp wrinkle ridges. The remainder of the canyon floor consists of a system of bright, low relief mounds. Their contacts with the surrounding plains are usually quite sharp. Individual mounds are typically ovate to elongate with a rounded, irregular outline. The ovate mounds are up to 300m across. The elongate mounds may be 300m wide by as much as 3km long and occur as disconnected, subparallel arcs concave northward. It is this system of subparallel arcs which gives the southernmost portion of zone "C" its "striped" appearance in lower resolution images (1, figure 1).

One of the more interesting aspects of this set of images is the presence of at least three, and possibly four parallel, and apparently topographically conformal benches on the canyon wall. These benches become progressively less sharply defined from lowest to highest (numbered 1 through 4), and are traceable for many tens of kilometers along the canyon wall. Only the lowest of these, bench 1, can be seen in the lower resolution images as the contact between zones "B" and "C". Each bench occurs progressively higher up the wall when traced from south to north. Benches 2, 3, and 4 each in turn disappear at the top of the escarpment. Bench 2 intersects the top of the escarpment in the vicinity of the fresh 800m crater near the top of figure 1. Bench 3 intersects the cliff top just south of the 10km degraded crater in figure 1. Bench 4, less readily traceable than the other three benches, appears to coincide with the base of the east-west escarpment on the plateau surface. Bench 1, though it cannot be seen intersecting the cliff top, is the only one of the four that intersects the canyon floor in the very high resolution images.

The contact between zones "B" and "C" on the canyon floor and along part of the canyon wall is well represented in the very high resolution images. On the canyon floor, it consists of a parallel system of alternating low ridges and swales about 1km wide (E, figure 1) crossing the canyon floor. These describe smooth parallel arcs, concave northward. At its west end, the southernmost of the arcs, a low positive relief feature, grades into bench 1 at the base of the canyon wall. From here northward, it occurs at successively higher positions on the canyon wall until, at the top of figure 1, it appears to be about midway up the wall.

Shading across the benches suggests that the steepest slope elements occur immediately above the benches, with the profile between benches being convex upward. This is opposite what might be expected of most stratigraphic benches. The most common profile for a cliff comprised of layers of varying resistance to erosion is concave upward for the slope profile between benches. In such an example, the steepest slope element lies immediately below the bench (since the more resistant layers tend to be cliff formers). Sapping interfaces within a cliff might produce profiles similar to those in west Deuteronilus Mensae. In this case, sapping above a permeability boundary results in more rapid erosion immediately above the boundary than below. Sapping, however, does not adequately explain the change in the contact between zones "B" and "C" from a bench to a series

of arcuate ridges and swales across the canyon floor.

A series of strandlines, each lower and younger than the previous one could explain all the above aspects. Wave action against a sloped surface (in this case the canyon wall) could produce the observed profiles. Wave energy is focused on the slope at the shorezone, producing a cliff on the slope immediately above. If successively lower "high stands" are separated by enough time, the lowest, youngest strandline should be the best preserved and the highest the least preserved. The series of ridges and swales at the contact between zones "B" and "C" are similar in scale and plan to terrestrial beach ridges on a very gentle slope.

REFERENCES:

(1) Parker, T. J., Schneeberger, D. M., Pieri, D. C., and Saunders, R. S., Geomorphic evidence for ancient seas in west Deuteronilus Mensae, Mars - I: Regional Geomorphology: This volume.

(2) Lucchita, B. K., 1984, Small-scale polygons on Mars: Reports of the Planetary Geology Program - 1983, NASA TM 86246, p. 205-207.

Figure 1: Very high resolution photomosaic of part of west Deuteronilus Mensae, Mars. Viking Orbiter images: 458861-72. Regional slope is downward to the north. Brief unit descriptions: (Pp), Polygonally patterned plains; (Ps), Smooth Plains; (Psp), "Splotchy" smooth plains; (S), Bright, low mounds (splotches); (B), Blocky material; (Cs), Canyon wall and/or cliff slopes; (Ds), "Debris" slopes; (Ce), Crater ejecta blankets; (H), Hilly material; (C), Craters - C4 freshest, C1 most degraded.

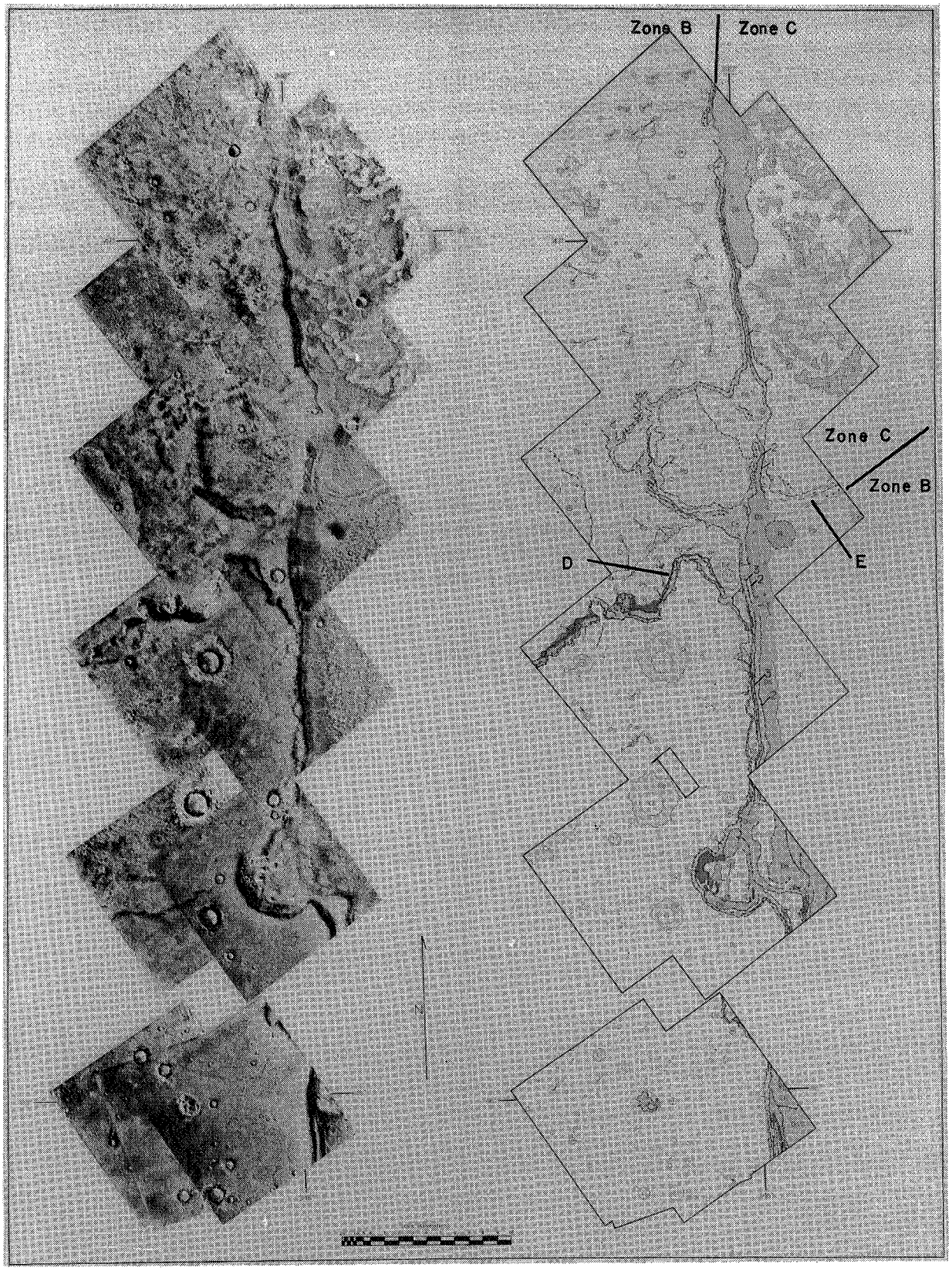
Zone B
Zone C
Zone C
Zone B
D
E

CHAPTER 10

VOLCANIC PROCESSES AND LANDFORMS

EXPLOSIVE VOLCANIC DEPOSITS ON MARS: PRELIMINARY INVESTIGATIONS

D.A. Crown, L.A. Leshin, and R. Greeley, Department of Geology, Arizona State University, Tempe, Arizona 85287

The existence of explosive volcanism and the identification of related eruptive products on Mars have been the subject of much controversy. Most research regarding martian volcanism has centered around basaltic volcanism. Terrestrial analog studies, photogeologic investigations, Viking Lander chemical analyses, and remote sensing information all indicate the presence of basaltic volcanism on both regional and local scales [1]. Small-scale explosive volcanism is indicated by possible cinder cones [2-4] and "pseudo craters" resembling those in Iceland [5]. A possible ash-fall deposit associated with Hecates Tholus has been proposed [6], and volcanic density currents have been suggested to explain features surrounding volcanoes in the Tharsis region [7]. The possibility of explosive volcanism on a larger scale was implied by Malin's [8] comparison of the Elysium region of Mars and the Tibesti region on Earth. Other investigators have considered the existence of rhyolitic lava flows [9] and silicic domes [10], but the occurrence of silicic volcanism, which is commonly explosive in nature on the Earth, has received little support [11]. Large-scale explosive volcanism was suggested to account for the basal scarp [12] and aureole deposits [13] of Olympus Mons, as well as deposits covering $> 10^6$ km^2 in the Amazonis, Memnonia, and Aeolis regions [14,15]. The deposits in Amazonis Planitia were proposed to be pyroclastics on the basis of similarities (such as complementary joint sets and thick flow sheets) to ignimbrites in the Pancake Range of Central Nevada [15], but the morphology observed on Mars may not be definitive of ignimbrites, and the deposits have also been suggested to be of a non-volcanic polar origin [16] and mantling deposits of an aeolian origin [17]. The formation of the martian highland paterae, which are distinguished by low, broad forms, radial channels, lobate ridges, and central caldera complexes [18], has been attributed to explosive volcanism. Originally, Potter [19] suggested that the highland paterae were formed by eruptions of extremely fluid basaltic lava, but Pike [20] noted the morphometric correlation of the highland paterae with large ash sheets on Earth. Greeley and Spudis [1] proposed that the highland paterae were formed by phreatomagmatic eruptions in an early period of martian history.

Two investigations have been undertaken to examine possible large-scale explosive volcanic deposits on Mars. The first includes an analysis of Viking Infrared Thermal Mapper (IRTM) data covering the vast deposits in the Amazonis, Memnonia, and Aeolis regions. These "postulated ignimbrites" have been mapped by Scott and Tanaka [15], and at least five high-resolution nighttime IRTM data tracks cross the deposits. Preliminary analysis of the data covering Amazonis Planitia show that local features (such as yardangs) have anomalous thermal inertias but the "ignimbrites" as a whole do not consistently have significantly different thermal inertias from their surroundings. However, this does not necessarily discount the existence of ignimbrites, as local features and apparent mantling by a fine layer of dust can dominate thermal inertias [21]. Further investigation including examination of lower resolution data is needed to provide a complete characterization of these deposits using IRTM data and to ascertain whether they possess a discernable thermal signature.

Preliminary photogeologic and IRTM studies of the large and small highland paterae [22] have also begun. Two high-resolution nighttime tracks trending NW-SE cross Apollinaris Patera, which is located adjacent to the lowland-highland scarp (9°S, 186°W). In both the northern and southern regions of Apollinaris Patera thermal inertias are

significantly greater than those observed in the surrounding areas. The thermal signature of Apollinaris Patera is more prominent on its southern flanks; within the southernmost of the two tracks thermal inertias increase from ~ 3.0 - 3.5 in the region surrounding Apollinaris Patera to a high of greater than 6.0 (x 10^{-3} cal cm^{-2} $sec^{-1/2}/K^{-1}$) on the volcano and within the northern track from ~ 1.9 to a high of 3.4. Lower thermal inertias on the northern flanks of Apollinaris Patera are consistent with the regional trend reflecting the transition from the cratered uplands to the smooth plains [21] and also with observations of less morphologic detail on the northern flanks suggesting more thoroughly mantled surfaces. Continued analysis of IRTM data covering the large and small highland paterae will determine if the paterae possess distinctive thermal signatures.

The purpose of IRTM studies of postulated martian explosive volcanic deposits is to determine the physical properties of the proposed ignimbrites. If volcanic deposits are exposed at the surface, high thermal inertias, as are observed for Apollinaris Patera, should be present. However, the thermal signature of the paterae, for instance, may not be the result of a primary volcanic surface. If a distinctive thermal signature is observed, it may be only an indirect reflection of the volcanic deposits. Nevertheless, this would allow a characterization (by albedo, thermal inertia, and rock abundance [23]) of the material controlling the thermal properties of the paterae and should provide important information for the consideration of explosive volcanism on Mars.

Although many investigators have considered explosive volcanism on Mars, currently much of the evidence for extensive deposits is tenuous, and the occurrence of large-scale explosive volcanism remains controversial. The present studies are intended to address the question in more detail with the aid of new and previously unused sources of information. The implications of explosive volcanism are critical to understanding the evolution of the martian surface. In combination with the examination of possible martian explosive volcanic deposits, this investigation will also include a remote sensing analysis and a field examination of a selected terrestrial analog. Due to their morphologic similarities, ignimbrites in the Central Andes are presently the best candidates as analogs for the martian highland paterae.

References

[1] Greeley, R., and Spudis, P.D., 1981, *Rev. Geophys. Space Phys., 19*, 13-41.
[2] West, M., 1974, *Icarus, 21*, 1-11.
[3] Mouginis-Mark, P.J., 1981, *Proc. Lunar Planet. Sci. Conf., 12th*, 1431-1447.
[4] Lucchitta, B.K., 1985, *Lunar Planet. Sci. Conf., XVI*, 503-504.
[5] Frey, H., and Jarosewich, M., 1982, *J. Geophys. Res., 87*, 9867-9879.
[6] Mouginis-Mark, P.J., Wilson, L., and Head, J.W., 1982, *J. Geophys. Res.,87*, 9890-9904.
[7] Reimers, C.E., and Komar, P.D., 1979, *Icarus, 39*, 88-100.
[8] Malin, M.C., 1977, *Geol. Soc. Am. Bull., 88*, 908-919.
[9] Fink. J., 1980, *Geology, 8*, 250-254.
[10] Plescia, J.B., 1981, *Icarus, 45*, 586-601.
[11] Francis, P.W., and Wood, C.A., 1982, *J. Geophys. Res., 87*, 9881-9889.
[12] King, J.S., and Riehle, J.R., 1974, *Icarus, 23*, 300-317.
[13] Morris, E.C., 1980, *NASA TM-82385*, 252-254.
[14] Scott, D.H., and Tanaka, K., 1980, *NASA TM-82385*, 255-257.
[15] Scott, D.H., and Tanaka, K., 1982, *J. Geophys. Res., 87*, 1179-1190.

[16] Schultz, P.H., and Lutz-Garihan, A.B., 1981, *Lunar Planet. Sci. Conf., XII,* 946-948.
[17] Greeley, R., Williams, S.H., White, B.R., Pollack, J.B., and Marshall, J.R., 1985, in *Models in Geomorphology*, ed. M.J. Woldenberg, Allen & Unwin, Boston, 373-422.
[18] Plescia, J.B., and Saunders, R.S., 1979, *Proc. Lunar Planet. Sci. Conf., 10th,* 2841-2859.
[19] Potter, D., 1976, *U.S. Geol. Survey Misc. Geol. Inv. Map I-941.*
[20] Pike, R.J., 1978, *Proc. Lunar Planet. Sci. Conf., 9th,* 3239-3273.
[21] Zimbelman, J.R., and Leshin, L.A., 1986, submitted to *Proc. Lunar Planet. Sci. Conf., 17th.*
[22] Albin, E.F., 1986, Master's Thesis (unpublished), Arizona State University, 84 pp.
[23] Christensen, P.R., 1982, *J. Geophys. Res., 87,* 9985-9998.

PSEUDOCRATERS AS INDICATORS OF GROUND ICE ON MARS

Herbert Frey, Geophysics Branch, Goddard Space Flight Center, Greenbelt, MD 20771

In the search for reliable indicators of the past location of surface or near surface volatiles on Mars, pseudocraters (if they exist) would be of direct but limited use. We have previously suggested that the thousands of small (subkilometer) pitted cones which dot portions of the plains-forming units in northern Mars may be volcano-ice analogs of Icelandic pseudocraters (1,2), which on Earth form where lava flows over water or water-saturated ground (3). The steam explosion caused by this interaction is only marginally less efficient if (as is likely on Mars) ice is the volatile(4). Positive identification of martian pseudocraters would therefore be strong indication of past occurrence of ice at or near the surface of Mars.

The basis for suggesting that the small cones on Mars are pseudocraters includes: (a) small size, (b) abundant but patchy distribution on what appear to be volcanic plains, (c) presence of other features suggestive of surface or subsurface ice. (d) morphological similarities to Icelandic pseduocraters, and (e) the similarity in distribution of crater/cone diameter ratios to Icelandic pseudocraters(2). This last morphometric parameter may be the most important, since other possible small terrestrial volcanic analogs have very different crater/cone diameter ratio distributions(2). In a survey of the available high resolution Viking Orbiter imagery, abundant fields of possible pseudocraters were found in SE Acidalia Planitia, S Utopia-Elysium, W Isidis Planitia and, perhaps, near Hellas (2,5,6). However, only a small fraction of the plains-forming units imaged at high resolution (range $\leq$ 2000 km) were found to contain the small cones: of some 12,200 images searched we found subkilometer cones with central pits on less than 350 (<3%). This low discovery rate, combined with the limited high resoluiton imagery, restrict martian pseudocraters as global indicators of surface or subsurface ice.

There are only minor morphological differences between the subkilometer cones found in Acidalia and those found in Utopia-Elysium-Isidis; more striking is the variation in background terrain on which the cones are found. In Acidalia the cones are found on smooth plains of both uniform and mottled appearance but also on widespread fractured and subdued fractured plains (2,7). The fractured plains are of interest because they may themselves be indicators of ground ice(8). All the plains-forming units on which cones have been found also contain rampart craters, but there are regional differences in the size distributions of these craters which may be interesting (see below). In Acidalia there are general trends in the dimensional and distributional characteristics of the cones which seem to depend on background terrain: the younger plains (which are smooth, not fractured) have a higher density of cones, but the average cone diameter is lower (<700 m) than on the fractured plains (>700 m). Cones on subdued fractured plains (9), which are under-populated in impact craters at the smallest diameters and have soft, incomplete or interrupted fracture patterns, have the largest mean diameters observed and also the highest percentage of widest central craters. Preferential obscuration of small cones and decrease in the observed cone base diameter due to blanketing by dust seems likely (7).

This demonstrates another problem with using pseudocraters as indicators of ground ice on Mars: because of their small size they are easily removed or obscured by a variety of erosional processes.

Pseudocraters do have one important contribution to make to the study of the distribution of volatiles in the martian crust. Because of the way they form, they indicate the presence of only surface (or very near surface) ice over which relatively thin lava flows have been emplaced. If the lava flow is too thick, cones will not form as the work required to lift the overlying molten rock becomes greater than that available from the explosion. Likewise, if the ice is buried too deeply beneath an insulating layer, the heat from the lava flow may dissipate before sufficient volatilization of the buried ice occurs(4). Therefore the size of pseudocraters and their spatial density depends on a combination of lava flow thickness and temperature, depth to the ice layer and fraction of ice in mixed layers (soil and ice). Dense concentrations are favored by relatively thin flows over abundant ice close to the surface; more wide-spread groupings may indicate variations in flow thickness and/or the depth to the (top of the) ice layer.

It would be interesting to compare the spatial density of possible martian pseudocraters with the size frequency distribution of rampart craters (10,11,12,13). Not only could such comparisons help to define the thickness of the ice layer(14), but comparison of rampart and non-rampart crater populations with a varying density of pseudocraters could place temporal constraints on the longevity of the ice-rich layer. For example: in Utopia Planitia where widely scattered small cones occur, rampart craters are rare for diameters < 3 km, but for $D > 5$ km almost all craters have this structure. Perhaps the small craters formed largely after the near-surface ice vanished. By contrast the rampart craters found in the fractured plains in Acidalia occur at very small diameters in the regions where small cones exist.

Despite the sampling problem, the latitudinal distribution of martian pseudocraters and its comparison with other ice-related features is of interest. In Acidalia Planitia most of the small cones lie at latitudes greater than 38°N, ranging up to 50°N. We find no convincing evidence for such features below ~35°N; however, there is very little high resolution imagery available. No small pitted ones are found in Chryse between 20 and 30°N, even though good imagery does exist (15,2). By contrast small cones are found as low as 10°N latitude in Isidis. These are unusual in their spatial distribution, however, being very densely grouped and often occuring in long chains(2). If these are also pseudocraters, then at the time they formed surface or near surface ice must have existed at this low latitude in eastern Mars.

References:

1. Frey, H. et al., J. Geophys. Res. 84, 8075 (1979).
2. Frey H. and M. Jarosewich, J. Geophys. Res. 87, 9867 (1982).
3. Thorarinsson, S., Bull. Volcanol. Ser. 2, 14, 3 (1953).
4. Rocha, D., unpublished manuscript (1979).
5. Frey, H. and M. Jarosewich, Lunar Planet. Sci. XII, 297 (1981).
6. Frey, H. et al., Lunar Planet. Sci. XII, 300 (1981).
7. Frey, H. and A.M. Semeniuk, Lunar Planet. Sci. XV, 272 (1984).

8. Carr, M.H. and G.G. Schaber, J. Geophys. Res. 82, 4039 (1977).
9. Guest, J.E. et al., J. Geophys. Res. 82, 4111 (1977).
10. Johansen, L.A., NASA TM 80339, 123 (1979).
11. Allen, C.C., Icarus 39, 111 (1979).
12. Carr, M.H. et al., J. Geophys. Res. 82, 4055 (1977).
13. Mouginis-Mark, P.J., J. Geophys. Res. 84, 8011 (1979).
14. Barlow, N.G., B.A.A.S. 17, 735 (1985).
15. Greeley, R. et al., J. Geophys. Res. 82, 4093 (1977).

ERUPTIVE HISTORY OF THE ELYSIUM VOLCANIC PROVINCE OF MARS

Kenneth L. Tanaka and David H. Scott, U.S. Geological Survey, Flagstaff, AZ

New geologic mapping of the Elysium volcanic province at 1:2,000,000 scale and crater counts provide a basis for describing its overall eruptive history. (We counted craters larger than 2 km in diameter to achieve optimal consistency; accurate counting of smaller craters is adversely affected by apparent variations in density due to secondaries, volcanic pits, image quality, and erosion.) The following stages are described in order of their relative age; they are also distinguished by eruption style and location.

Stage 1: Central volcanism at Hecates and Albor Tholi

These volcanoes are embayed by lava flows from Elysium Mons. This relation, as well as crater densities (Table 1), supports an Upper Hesperian surface age [1]. We have no evidence to determine when these volcanoes became active. Their steep slopes indicate that they are composed of once-viscous lava or interbedded lava and pyroclastic material [2,3]; no lava-flow scarps were identified.

Stage 2: Shield and complex volcanism at Elysium Mons and Elysium Fossae

The vast majority of exposed lava flows in the region were extruded from Elysium Mons and nearby fissures. The flows overlie Lower Hesperian ridged plains material in eastern and southwestern Elysium Planitia and polygonally grooved material west of the Elysium rise [4]. The extent of the flows is more clearly defined on Viking than on Mariner 9 images [5], but in some areas, such as northeast of Hecates Tholus, the flows and smooth plains material appear to intergrade. We divided the area of the unit into 27 5° x 5° sections each covering 65,000 to 75,000 km^2. The average count (Table 1) indicates that the flows are lowermost Amazonian, and variance in the counts allows placement of many of the flows in the Upper Hesperian. Individual counts range from N(2)=278±61 to 508±84 (craters >2 km diameter per 10^6 km^2), and only three areas have crater densities whose standard-deviation limits do not overlap with the standard-deviation limits of the average count. Elysium Mons itself has a crater density of about N(2)=350, which corresponds to a slightly younger stratigraphic position than indicated by previous N(1) counts [3,6]. Because of the uniformity in crater densities and the fair to poor quality of images in some areas, we could not distinguish flow sequences of different periods in most cases. One exception is south of Eddie crater, where its ejecta have prevented the burial of precrater flows by younger flows.

The morphology of the flows of this Elysium sequence is about the same as those of the widespread flow units (members 1 to 5) of the Tharsis Montes Formation [7], which are Late Hesperian to Middle Amazonian in age [1]. The generally large volumes, lengths, and thicknesses of the flows indicate that they result from high rates of eruption of low- to moderate-viscosity lava. Thickness of the flow sequence is a few hundred meters in distal areas, where they partly bury impact craters several to tens of kilometers in diameter that were formed on older surfaces [8]; near Elysium Mons, where such impact craters are apparently completely buried, flows are perhaps more than a kilometer thick.

The flows mostly originated from the northwest-trending fractures of Elysium Fossae and fractures circumferential to Elysium Mons. Some fractures, perhaps where eruption rates were particularly high [9], developed into sinuous rilles or depressions. These features are mostly found west of

Elysium Mons, along with small domes, eroded flows, and crenulated ridges. The ridges and some of the domes may be eruptive features of high-viscosity lava. Other domes have summit craters and resemble cinder cones. These domes, as well as the eroded flows, may be composed of pyroclastic material resulting from the interaction of ground ice with erupting magma.

High up on Elysium Mons, lava flows are shorter, narrower, and less common than those in lower areas. Their smaller size indicates that they were erupted at lower extrusion rates. They resemble flows that are common high on Olympus Mons and Tharsis Montes. Also found on Elysium Mons are sinuous ridges that generally trend downslope; they are prominent on the north flank of the shield. Other sinuous ridges interfinger with flows south of Elysium Mons and west of Albor Tholus. Their origin is uncertain, for they resemble neither wrinkle ridges (of structural origin), nor ridges (of lava-flow or debris-flow origin) having collapse pits and channels on their crests. Perhaps the sinous ridges formed by eruption, flow, and erosion of pyroclastic material.

Also apparently associated with this stage of volcanism are vast eroded and channelized flows in Utopia Planitia [10]. Their origins have been ascribed to debris flow [11] and pyroclastic flow [10] caused by volcano-ice interactions.

Stage 3: Rille volcanism at Elysium Fossae and Utopia Planitia

After an apparent hiatus in volcanic activity, several large rilles of northwesternmost Elysium Fossae extruded lavas that flowed northwestward into Utopia Planitia. Morphologies of these flows range from voluminous sheet flows to thin, narrow flood lavas. Crater counts (Table 1) are approximate because the flows are not clearly distinguishable from older flows, and areas proximal to the rilles have fewer craters. Also, age relations with Utopia flows are unclear; some of the thicker Utopia flows originating from Elysium Fossae appear coeval with the lava flows. These Utopia flows themselves may have a volcanic origin related to this period of activity. Given these relations and the crater counts, we tentatively place these lavas and Utopia flows in the Lower and Middle Amazonian Series.

Stage 4: Flood-lava and pyroclastic eruptions at Hecates Tholus and Elysium Mons

A virtually uncratered area west of the summit of Hecates Tholus was postulated to be mantled by a pyroclastic air-fall deposit [12]. The lack of craters suggests an Upper Amazonian position. Similarly, on Elysium Mons, an oblong area 60 x 90 km surrounding the summit caldera and extending to the north and west appears to be mantled by a thin, low-albedo deposit (on images taken at low sun-incidence angles). The edge of the deposit is composed of fingerlike extensions radiating downslope. We speculate that this deposit is composed either of thin pyroclastic flows or air-fall deposits that have subsequently moved downslope along talus chutes.

On the west flank of Elysium Mons are several patches of sparsely cratered, very young flood lavas. Although they resemble the flows described by [9], we distinguish three separate areas, two of which occur outside the area mapped by [9]. Similarly, most of the youngest flows of Olympus Mons and Tharsis Montes appear to be thin flood lavas. Very young lavas also have been postulated to make up smooth plains in the southern part of the Elysium region [13]; however, we believe that this area is mostly covered by channel material [10,14].

Discussion

Tectonic and channeling activity in the Elysium region is intimately associated with volcanism [9,10,14]. Recent work [8,15] indicates that isostatic uplift of Tharsis, loading by Elysium Mons, and flexural uplift of the Elysium rise produced the stresses responsible for the fracturing and wrinkle-ridge formation in the region. Coeval faulting and channel formation almost certainly occurred in the pertinent areas in Stages 2 to 4. Older faults east of the lava flows [8] and channels on Hecates Tholus may be coeval with Stage 1. Also, these stages show that the viscosity of erupted magma has decreased over the eruptive history of Elysium, as it has at Tharsis, perhaps indicating that the magma originated from progressively deeper sources.

REFERENCES CITED

[1] Tanaka, K.L. (in press) PLPSC 17.
[2] Malin, M.C. (1977) GSA Bull., v. 88, p. 908.
[3] Plescia, J.B. and Saunders, R.S. (1979) PLPSC 10, p. 2841.
[4] Downs, G.S. and others (1982) JGR, v. 87, p. 9747.
[5] Scott, D.H. and Allingham, J.W. (1976) USGS Misc. Inv. Ser. Map I-935.
[6] Neukum, G. and Hiller, K. (1981) JGR, v. 86, p. 3097.
[7] Scott, D.H. and Tanaka, K.L. (in press) USGS Misc. Inv. Ser. Map I-1802A.
[8] Plescia, J.B. (1986) LPSC 17 (abstracts), p. 672.
[9] Mouginis-Mark, P.J. and others (1984) Earth Moon Planets, v. 30, p. 149.
[10] Tanaka, K.L. and Scott, D.H. (1986) NASA TM 88383, p. 403.
[11] Christiansen, E.H. and Greeley, R. (1981) LPSC 11 (abstracts), p. 138.
[12] Mouginis-Mark, P.J. and others (1982) JGR, v. 87, p. 9890.
[13] Plescia, J.B. (this volume).
[14] Tanaka, K.L. and Scott, D.H. (1986) LPSC 17 (abstracts), p. 865.
[15] Hall, J.L. and others (1986) JGR, v. 91, p. 11377-11392.

Table 1.
Crater Densities and Stratigraphic Positions of Elysium Volcanic Units

Unit	Crater density N(x) = no. > x km diam./10^6 km^2	Stratigraphic series
Hecates Tholus mantle	no fresh craters observed [12]	Upper Amazonian
Elysium Mons mantle	few kilometer-size craters	Upper Amazonian
Elysium flood lavas	few kilometer-size craters	Upper Amazonian
Elysium Fossae--Utopia Planitia flows	N(2) = about 100-200	Lower Amazonian-Middle Amazonian
Elysium Mons flows		
all	N(2) = 378±15	Upper Hesperian-
shield	N(1) = 2350±153 [3]	Lower Amazonian
	N(1) = 1800-4800 [6]	
	N(2) = about 350	
Albor Tholus	N(1) = 1500±263 [3]	Upper Hesperian
Hecates Tholus	N(1) = 1800±351 [3]	Upper Hesperian
	N(1) = 1300-15,000 [6]	

Note: Stratigraphic series determined by crater counts and stratigraphic relations (see text).

LATE-STAGE FLOOD LAVAS IN THE ELYSIUM REGION, MARS J.B. Plescia, U.S. Geological Survey, 2255 N. Gemini Drive, Flagstaff, AZ 86001

In the southeastern part of the Elysium region, centered near lat 5° N., between long 180° and 210°, and adjacent to the Cerberus Rupes fractures, is a unit that exhibits little texture and a generally low albedo and that has a very low crater frequency (Figure 1). This unit has been mapped as "smooth plains material" and interpreted as an eolian deposit on the basis of Mariner 9 images (Scott and Allingham, 1976). More recently, Scott and Tanaka (1986) mapped the unit as material deposited during a channeling episode. Here, however, I interpret the smooth plains unit as being a volcanic deposit composed of low-viscosity lava flows: both flood lavas and individual flows.

In images that have resolutions of 200-300 m/pixel, the unit is characterized by a smooth texture and albedo patterns suggestive of flowage in an easterly to northeasterly direction. In higher resolution images (30-40 m/pixel), the large-scale albedo patterns in some locations are recognized to be lava flows having well-defined lobate margins. This surface represents the youngest widespread unit in the Elysium region and one of the youngest volcanic units on the planet (Table 1).

The plains formed by these young volcanics are locally interrupted by inselbergs of knobby material and by kapukas of a brighter material. The brighter material typically lies adjacent to dark, narrow channels or forms teardrop-shaped islands within the channels. In the high-resolution images, the brighter material is seen to be an older, more cratered unit that has been channelized, the channels being filled with a dark, smooth material — the volcanic flows.

The volcanics flowed through preexisting channels eastward and northeastward into and across the knobby terrain east and west of Orcus Patera and continued to the north into western Amazonis Planitia (Figure 1). East of Orcus Patera, the volcanics flowed through well-defined channels whereas west of Orcus Patera, it moved through a myriad of narrow channels. This region is mapped in Figure 1 as Volcanic plains, mixed (vpm) because individual flows cannot be differentiated from older units at this scale.

The volcanics apparently have a source around Cerberus Rupes as indicated by the flow pattern, and several vents have been recognized in the southwestern part of the region (Figure 1). The vents are poorly resolved but appear to be low shields having a central vent surrounded by radial flows. All of the vents occur in areas where the lavas are thin, as indicated by the degree of exposure of preplains craters and the frequency of inselbergs. These vents may reflect either a late-stage eruptive style or one specific to this area. Elsewhere, where such vents have not been observed, the lavas may have erupted through fissures ultimately buried by the eruptions. Although centrally located, Cerberus Rupes can not be confidently considered a vent because flows have not been observed to originate along it. In addition, Earth-based radar-topography profiles across Cerberus Rupes suggest that it is a series of normal faults having several hundred meters of displacement; hence it is probably a late-stage tectonic feature.

Tanaka and Scott (1986) studied this same region and came to a different conclusion regarding the nature of the smooth, young material. They recognized the channeling aspects of the region, but attributed the origin of

the unit directly to the channeling episode; hence they interpreted the young age of the unit as indicative of a major late-stage fluvial episode. In contrast, I interpret these plains to be volcanic flows which locally fill preexisting channels. Thus, the channels represent an older, probably unrelated event. The source region for the channeling fluid is unknown; perhaps it is now buried by the volcanic plains, or perhaps it lies to the south beneath material interpreted to be ash flow and ignimbrite material (Malin, 1979; Scott and Tanaka, 1982).

This volcanic unit is important for several reasons. Its presence indicates that in Elysium, unlike in Tharsis, plains volcanism continued or resumed after shield building ended. Additionally, this late-stage volcanism was of sufficent volume and low viscosity that it covered a wide area. The lack of topography, even in high resolution, and the distance the flows traveled suggest the material had a very low viscosity. Only at its distal end, in Amazonis, are flow features and lobate fronts well developed. This material further indicates that there was sufficent heat in the upper mantle to generate considerable quantities of "basaltic" lava at a high eruption rate late in Martian history.

REFERENCES: Malin, M.C., 1979, Mars: Evidence of indurated deposits of fine materials: NASA Conf. Pub. 2072, p. 54; Scott, D.H., and Tanaka, K.L., 1982, Ignimbrites of Amazonis Planitia region of Mars: J. Geophys. Res., v. 87, p. 1179-1190; Scott, D.H., and Allingham, J.W., 1976, Geologic map of the Elysium quadrangle of Mars: U.S.G.S. Misc. Inv. Series Map I-935; Tanaka, K.L., and Scott, D.H., 1986, The youngest channel system on Mars: Abstracts Lunar and Planet. Sci. Conf. 17th, p. 865-866.

TABLE 1
CRATER FREQUENCIES

	FREQUENCY OF CRATERS $\geq$ D / 10^6 km^2 DIAMETER			
TERRAIN	**1 km**	**2 km**	**5 km**	**10 km**
Knobby terrain (kt)	2780±275	1580±205	790±145	390±100
Ridged plains (rp)	2730±190	780±100	252± 60	80± 30
Elyisum plains (Epu)	1420± 74	440± 40	90± 20	35± 10
Volcanic plains (vp)	90± 15	23± 8	5± 4	3± 3

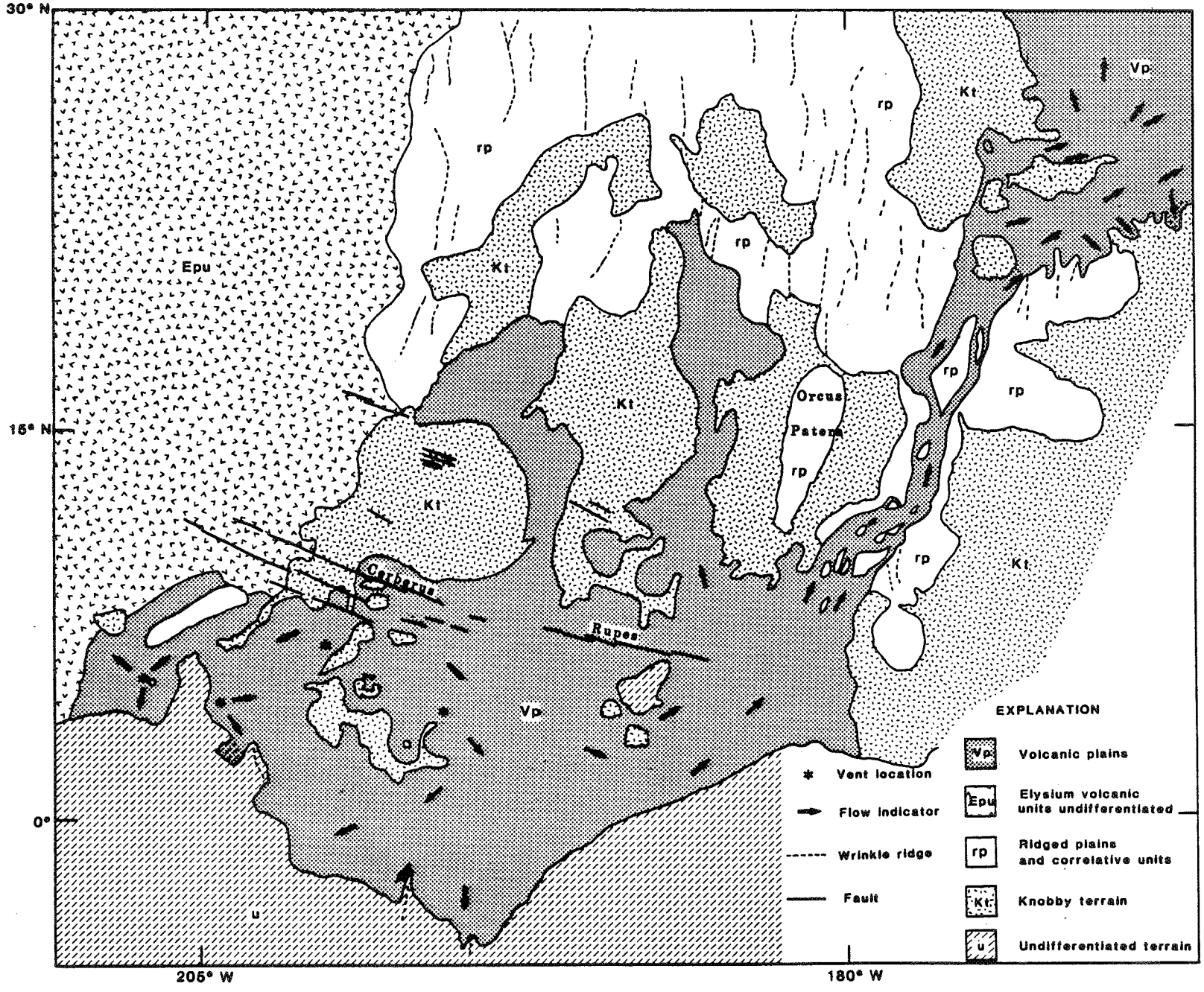

FIGURE 1. Geologic map of southeastern Elysium Region, Mars.

Relative Ages Of Lava Flows At Alba Patera, Mars

by
Dale M. Schneeberger and David C. Pieri
Jet Propulsion Laboratory, California Institute Of Technology, Pasadena, CA

Many large lava flows on the flanks of Alba Patera are astonishing in their volume and length (11). They are enormous by terrestrial standards ranging from 60 kilometers to over 500 kilometers in length. As a suite, these flows suggest tremendously voluminous and sustained eruptions, and provide dimensional boundary conditions typically a factor of 100 larger than terrestrial flows (2). One of the most striking features associated with Alba Patera is the large, radially oriented lava flows that exhibit a variety of flow morphologies. These include sheet flows, tube-fed and tube-channel flows, and undifferentiated flows (3,4,5,7).

Three groups of flows were studied; flows on the norhtwest flank, southeast flank, and the intracaldera region. Flow F4 is part of a system of complex flows located on the northwest flank of Alba Patera. The two sheet flows (F5 and F6) on the southeast flank appear to be less complex as compared to those on the northwest flank but resembles the lobate flow morphology of flow F4. Within the confines of the concentric fracture/graben system lies the central caldera complex with its intracaldera flows. Six flows (F7 to F12) were identified here and, although their dimensions are considerably smaller, they continue to exhibit lobate morphology.

Two general models have been proposed (10,14) relating observed crater densities to absolute age using crater diameters of either >1 Km or >4 Km. A review of the literature uncovers that a number of crater densities and absolute ages have been reported for Alba Patera (9,12). Within the framework of these models their data suggests a maximum absolute age for the Alba shield of 3.8-3.5 bybp (1,9,10) down to a minimum age of 2.6-1.0 bybp (1,9,14). Plescia and Saunders (1979) (12) have suggested that a transition in the types and loci of cone building volcanism occurred from about 2.0 to 1.5 bybp beginning at the time of major activity at Alba Patera (12). In contrast, Neukum and Wise (1976)(10) believe that by 3.0 bybp the major tectonic/volcanic disturbances were winding down and that by 2.5 bybp the activity was essentially over. These differences remain unresolved.

The above cited ages are for regional studies of the entire Alba shield whereas our work concerned itself with attempting to deduce the ages of the individual flows. Plotting of cumulative size-frequency distribution curves of the flows shows a general clustering of the data, except for flows F6 and F7 which are noticeably shifted vertically from the rest (Figure 1). The apparent clustering of most of the flows is an artifact of the overlapping of confidence intervals as determined from an assumed Poisson distribution (8,13,15) of the data. Crater density data was also plotted using crater diameters binned in $\sqrt{2}$ intervals (15). These data show a clustering of the flows similar to the cumulative curves with flows F6 and F7 being somewhat distinct from the rest (Figure 2).

Crater diameters measured for the flows on the flanks and intracaldera region ranged from about 100 meters to 2.82 kilometers. However, the majority measured (387 out of 411) are less than 1 kilometer in diameter. The use of a 1 kilometer datum for the determination of both relative and absolute ages has been widely used in the literature (3,6,10,13). Using this datum, two widely separated ages were determined from the cumulative size-frequency plots (Fig 1). Plotting this data against the Neukum and Wise (1976) (10) curve yielded an absolute age range of 3.9-3.3 bybp while plotting the same data against the Soderblom et al. (1974) (13) curve yielded a range of 0.8-0.1 bybp (Fig 3). Craters numbers, independent of size-frequency plots, suggest an absolute age range between 1.3 and 0.4 bybp after calibrating the data to fit the derived martian absolute age curve (for craters >4 Km) by Soderblom et al. (1974) (17).

A relative age sequence can be deduced from size-frequency distribution plots. Cumulative size-frequency distribution curves suggest that flows F6 and F7 are distinct from the apparent clustering of the other flows. The remaining flows (F4, F5, F8, F9, F10, F11, and F12) have plots that are very close with considerable overlap of their confidence intervals. It seems unlikely that any confident separation of relative ages for these flows is possible.

Like the cumulative curves above, the data arranged in $\sqrt{2}$ diameter bins to produce size-frequency distribution curves shows that flows F6 and F7 appear distinct from the others with flow F7 being the oldest. Again, a similar clustering of flows into an intermediate group is suggested. Flows F8, F11, and F12 appear to be lost in the noise typical for the smaller crater diameters less than 1 Km,

although somewhat better separated than in the cumulative curves. If the vertical displacements of curves are real, the suggested relative ages of the flows is F7 (oldest), followed by flows F10, F9, F5, F4 as intermediate, and flow F6 as the youngest. The relative age positions of flows F8, F11, and F12 remain, for the most part, undetermined.

Relative ages based on crater numbers, for craters ≥1 km intercept, suggest a sequence, oldest to youngest, of F7, F4, F10, F9, F5, and F6. Flows F8, F9, F11, and F12 are undetermined because they lack craters ≥ 1 km diameter. The smaller diameter crater numbers, of probable secondary origin, show a somewhat different sequence than above. Both data sets agree that flow F7 is the oldest and F6 the youngest. In contrast, however, the latter suggests that flow F4 is younger than both flows F10 and F9. Additionally, it allows for the placement of two of the three previously undetermined flows (F8, F11) on either side of flow F4, older and younger, respectively. The relative age of flow F12 still remains undetermined. Since two possible age sequences are suggested, depending on which data set is accepted as representative, a relative age sequence based on both data sets can be made so long as the larger diameter (≥ 1Km) data is given more weight. Thus a possible sequence, from oldest to youngest, is F7, F4, F10, F9, F8, F11, F5 and F6. Perhaps flow F12 is the youngest of all as it has the least number of craters. However, since there are no craters in either size bin, judgement as to its age will not be attempted.

Source vents, as a rule, are not clearly defined on the flanks of Alba Patera. However, some estimation of vent sequence can be made. The data suggests that the earliest vent activity was from the northeast part of the caldera complex producing flow F7. This area appears to have had recurring activity at later times as well to produce flows F10 and F9. The southeastern part of the caldra complex also became active producing lavas that fed flow F5. Perhaps simultaneous with this activity (within the scope of crater ages), lavas erupted from vents or fissures of unknown location on the northwest flank to produce flow F4. It is possible that the northwest flank flows may have erupted from a lateral vent on the patera's flank at or near the present ring fracture zone. Finally, the southeast part of the caldera became active once again to produce flow F6 (or possibly F5). Flows F8, F11 and F12 were erupted from the northern half of the caldera most likely sometime after the effusion of flow F7 but before or simultaneously with flows F10, F9 and F5. This suggests that the vents and/or fissures associated with the effusion of lavas from northern half and southeast portions of the caldera complex were perhaps operating within a relatively narrow geologic time frame. Unfortunately, high resolution delineation of vent activity beyond a rudimentary relative sequence is not possible with current crater density analysis techniques.

In summary, the lava flows discussed above probably were erupted as group during the same major volcanic episode as suggested by the close grouping of the data. Absolute ages are poorly constrained for both the individual flows and shield, due in part to disagreement as to which absolute age curve is representative for Mars. A relative age sequence is implied but lacks percision due to the closeness of the size-frequency curves. Regardless, it appears that the final stages in Alba's volcanic history were anything but quiet.

REFERENCES

(1) Basaltic Volcanism Study Project (1981) New York, Pergammon Press, 1286p.
(2) Bologa, S. M., and Pieri, D. C. (1985) NASA TM-87563, p. 245-247
(3) Carr, M. H. (1981) The Surface Of Mars: New Haven, Yale University Press, 232 p.
(4) Carr, M. H., et al. (1977) Jour. Geophys. Res., V. 82, p. 3985-4015
(5) Carr, M. H., and Greeley, Ronald (1980) NASA SP-403
(6) Dial, A. L. (1978) NASA TM 79729, p. 179-181
(7) Greeley, Ronald, and Spudis, P. D. (1981) Rev. Geophys. Space Phys. 19, p. 13-41
(8) Hartmann, W. K. (1973) Jour. Geophys. Res., V. 78, p. 4096-4116
(9) Hiller, Konrad, and Neukum, Gerhard (1980) NASA Tech. Memo. 81776, p. 119-121
(10) Neukum, G., and Wise, D. U. (1976) Science, V. 194, No. 4272, p. 1381-1387
(11) Pieri, D. C., et al. (1986) NASA TM 88383, p. 318-320
(12) Plescia, J. B., and Saunders, R. S. (1979) Proceedings, LPSC-X, p. 2841-2859
(13) Soderblom, L. A. et al. (1974) Icarus 22, p. 239-263
(14) Soderblom, L. A. (1977) in Roddy, D. J., Pepin, R. O., and Merrill, R. B., eds., Impact and Exploration Cratering: Pergamon Press, New York, p. 629-633
(15) Woronow, A., et al. (1978) NASA TM 79730, 20 p.

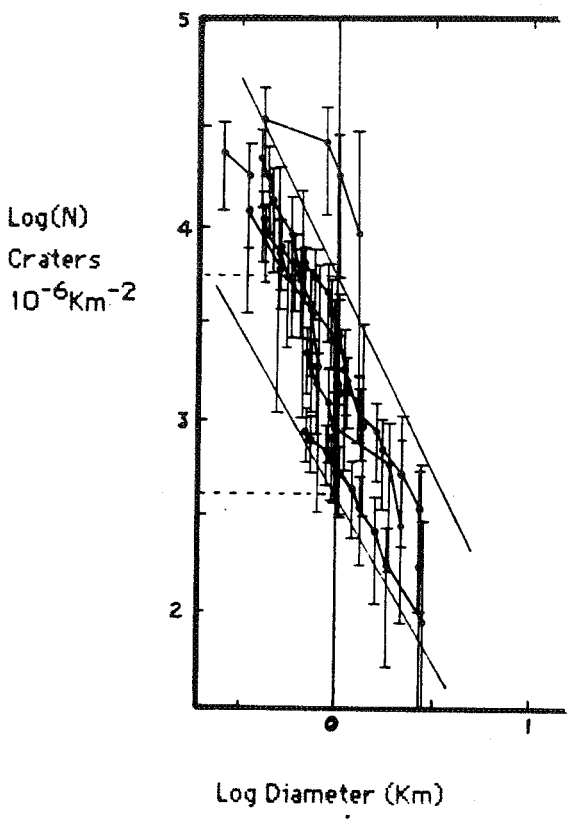

Figure 1.

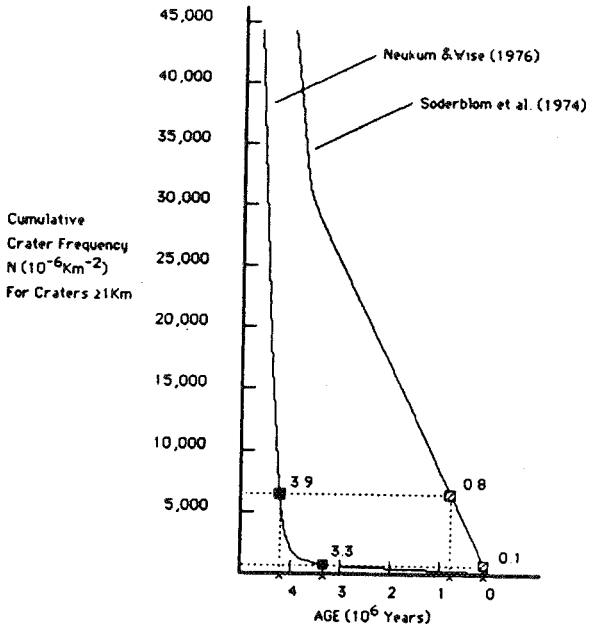

Figure 3.

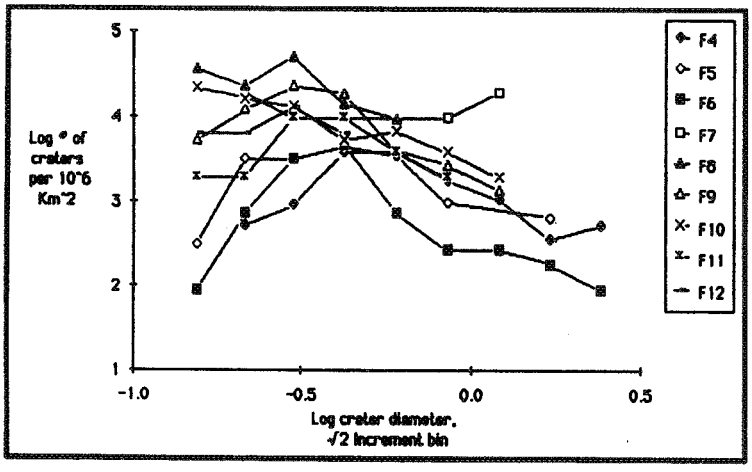

Figure 2.

MARTIAN VOLCANISM: FESTOON-LIKE RIDGES ON TERRESTRIAL BASALT FLOWS AND IMPLICATIONS FOR MARS

E. Theilig and R. Greeley, Dept. of Geology, Arizona State University, Tempe, Arizona, 85287

Determination of lava flow compositions on Mars is a significant problem with major implications for the thermal history and differentiation of the planet. Silica content within a magma is one of the factors controlling rheological properties of a flow. Thus, one of the major focuses within martian volcanology has been to estimate the composition of a lava flow based on rheological properties determined from flow morphology. One method, derived by Fink and Fletcher [1] and Fink [2], which has been used is the analysis of regularly spaced, arcuate, festoon-like ridges oriented perpendicular to flow direction. Their model relates ridge height and spacing to lava rheology, thickness of the flow's thermal boundary, and applied stresses and allows the viscosity of the interior of the flow at the time of ridge formation to be estimated. Festoon ridges on martian lava flows are similar in size to those on terrestrial silicic flows and previously have been compared to rhyolitic, dacitic [2-4], and trachytic [5] flows. In this study we use the Fink and Fletcher [1] and Fink [2] model to assess and compare flow rheology for two terrestrial basalt flows and one martian flow with previous studies.

Lava flows selected for this study include the Lakagigar and Barthardalshraun flows, Iceland and a flow west of Arsia Mons on Mars, located at 3°S, 138.2°W. The Lakagigar flow [6], more commonly referred to as Laki, contains festoon ridges which occur locally but which are dominant where the flow spreads out on a coastal plain. Festoon ridges on the Barthardalshraun lava flow, Iceland are located in an area of the flow which ponded in a valley ~ 80 km from the vent [7]. On the martian flow west of Arsia Mons, festoon ridges occur across large flow lobes [4]. Values of ridge spacing and height used for this study are shown in Table 1. Statistical analyses of the data indicate that a dominant spacing exists for the flows included in the study [8]. This suggests that a strong folding instability existed, thus the model of ridge growth should be applicable to these flows.

Fink and Fletcher [1] and Fink [2] considered festoon-like ridges to be folds resulting from compression of a fluid in which viscosity decreases with depth. Regular ridge spacing indicates a folding instability which places constraints on dimensionless parameters expressing the ratio of surface to interior viscosity, the ratio of gravitational stress to compressive stress, and ridge spacing [2]. Based on these constraints, minimum interior viscosity at the time of ridge formation can be estimated from ridge height and spacing, determined either in the field or from image data [2,3,5]. The dimensionless groups used for this analysis are:

$$R = \eta_o / \eta_i \quad (1)$$

$$\ln R > 30\ h/d \quad (2)$$

$$\dot{\epsilon}\,\eta_i > \rho g h / (0.08\ R \ln R) \quad (3)$$

where R is the ratio between the exterior viscosity (η_o) and interior viscosity (η_i), h is the thickness of the thermal boundary layer approximated by ridge height, d is the average ridge spacing, $\dot{\epsilon}$ is the strain rate, ρ is lava density, and g is the gravitational acceleration. To estimate the minimum interior viscosity, strain rate can be approximated from finite strain and an assumption of ridge growth time.

Results are shown in Table 2 and compared with previous studies. Estimated viscosities for the Icelandic flows are high ($5x10^6$ - $8x10^{11}$ Pa s) for terrestrial basalts which typically range from 10^2 - 10^4 Pa s [9]. Higher than normal viscosity can be obtained, however, by decreasing temperature, increasing solid content in the magma, or decreasing gas content, all of which are related. In the cooled, terminal areas of basaltic flows on Mount Etna, viscosities reached 10^8 - 10^{10} Pa s as the flow halted [10]; and for a basalt flow on Mauna Loa, viscosity was estimated at 10^7 Pa s at the toe [11]. Cigolini et al. [12] determined viscosities of ~ 10^7 Pa s from both field measurements and experimental results for basaltic andesite flows on Arenal Volcano, Costa Rica. They attributed the high viscosity values to a high crystal content in the magma and low effusion temperatures. Thus the viscosities for the Icelandic flows indicated by the formation of festoon ridges are not unreasonable for mafic magmas. The dominant location of these ridges on the terminal lobes of the Laki flow and in the ponded section of the Barthardalshraun flow suggest that cooling was a significant factor in increasing the viscosity in these flows.

The minimum interior viscosity values are comparable to those for a trachyte flow on Hualalai, Hawaii ($7.6x10^8$ - $7.6x10^{10}$ Pa s), a flow on Ascraeus Mons ($1.1x10^8$ - $1.1x10^{10}$ Pa s) [5], a dacite flow in Chile (> $4.6x10^8$ Pa s), and some ridges in Arcadia Planitia (10^8 Pa s) [2]. The similarity in results (Table 2) probably reflects a requirement for lavas to have high viscosities before this size ridge will form. Because basalt may have a high viscosity under specific conditions ridge height and spacing may not represent compositional variations. Thus, caution should be used in applying this model to obtain rough estimates of composition.

Based on the morphologic similarities between the martian flows and the Icelandic flows and knowledge of the emplacement of the terrestrial flows, the flows west of Arsia Mons are considered to have been emplaced as large sheet flows from basaltic flood-style eruptions. Festoon ridges represent folding of the surface crust in the last stages of emplacement when viscosities would be high due to cooling. Alternatively, the lava may have had a high crystallinity or was erupted at low temperatures. In addition, increased compressive stress behind halted flow fronts or in ponded areas may have contributed to ridge formation.

REFERENCES

[1] Fink, J. H., and R. C. Fletcher, Ropy pahoehoe: Surface folding of a viscous fluid, *J. Volcanol. Geotherm. Res., 4*, 151-170, 1978.

[2] Fink, J., Surface folding and viscosity of rhyolite flows, *Geology, 8*, 250-254, 1980.

[3] Fink J. H., Possible rhyolite flows in the Arcadia Planitia region of Mars: Evidence from surface ridge geometry (abstract), in *Lunar and Planet. Sci. XI*, 285-287, Lunar and Planetary Institute, Houston, 1980.

[4] Schaber, G. G., Radar, visual and thermal characteristics of Mars: Rough planar surfaces, *Icarus, 42*, 159-184, 1980.

[5] Zimbelman, J. R., Estimates of rheologic properties for flows on the Martian volcano Ascraeus Mons, *J. Geophys. Res., 90*, D157-D162, 1985.

[6] Thorarinsson, S., The Lakagigar eruption of 1783, *Bull. Volcanol., Ser. 2, 33*, 910-927, 1970.

[7] Greeley, R., and H. Sigurdsson, Pristine morphology of a quasi-flood basalt flow: The Bardardalshraun of Trolladyngja, Iceland (abstract), in Reports Planetary Geology Program 1980, *NASA TM 82385*, 245-246, 1980.

[8] Theilig, E., and R. Greeley, Lava flows on Mars: Analysis of small surface features and comparisons with terrestrial analogs, *J. Geophys. Res.*, 1986, in press.
[9] Basaltic Volcanism Study Project, Basaltic volcanism on the terrestrial planets, 1286 pp. Pergamon Press, Inc, New York, 1981.
[10] Walker, G. P. L., Thickness and viscosity of Etnean lavas, *Nature, 213*, 484-485, 1967.
[11] Moore, H. J., Preliminary estimates of the rheological properties of the 1984 Mauna Loa lavas, *U.S. Geol. Surv. Prof. Paper 1350*, 1986, in press.
[12] Cigolini, C., A. Borgia, and L. Casertano, Inter-crater activity, aa-block lava, viscosity and flow dynamics: Arenal Volcano, Costa Rica, *J. Volcanol. Geotherm. Res., 20*, 155-176, 1984.

Table 1. Ridge Geometry Data Used in Calculations.

Study Area	Values Used in Calculations		Ridge Spacing					
	Height (m)	Spacing (m)	Range (m)	Number of Samples	Median (m)	Mean (m)	Standard Deviation	Dispersion
West Arsia Mons	12	90	30-194	120	89.0	91.7	29.7	0.3
Laki Flow								
Interior	1	10	7-23	56	13.1	12.9	4.3	0.3
	2	10						
	2	15						
Margin	2	16.5	9-37	65	16.4	16.8	5.3	0.3
Barthardalshraun Flow	5	100	–	–	–	–	–	–

Table 2. Estimates of Interior Viscosity for Martian and Terrestrial Lava Flows

Study Area	Height (m)	Spacing (m)	$\dot{\epsilon}\eta$	Interior Viscosity (Pa s) 1 Hour	1 Week
West Arsia Mons	12	90	6.5 E3	1 E8	2 E10
Laki Flow					
Interior	1	10	5.1 E3	1 E8	2 E10
	2	10	2.5 E2	5 E6	9 E8
Margin	2	16.5	4.4 E3	1 E8	2 E10
Barthardalshraun Flow	5	100	2.3 E5	5 E9	8 E11
Chao Flow (Dacite)*	30	100		5 E8	
Arcadia Planitia*	100	750		1 E8	1 E9
Hualalai (Trachyte)†	15	150		8 E8	8 E10
Ascraeus Mons†	15	120		1 E8	1 E10

* [2] †[5] "E" Indicates the exponent in powers of 10.

STUDIES OF FLUID INSTABILITIES IN FLOWS OF LAVA AND DEBRIS

Jonathan H. Fink, Geology Department, Arizona State University, Tempe, AZ 85287

Introduction

Estimating the rheology of lava flows is an essential tool for the remote determination of flow compositions on other planets and is also a component in the evaluation of many volcanic hazards. For flows whose emplacement is not observed, indirect methods must be used to assess such physical parameters as viscosity, yield strength, density, and volatile content. Most studies of this type have assumed that the geometry of large scale morphological features on the flow surface reflects the bulk rheology of the active lava. One class of lava surface structures that is particularly well-suited to this sort of interpretation includes those periodic features that result from fluid instabilities.

At least two instabilities have been identified and utilized in lava flow studies: surface folding and gravity instability. Both lead to the development of regularly spaced structures on the surfaces of lava flows. The geometry of surface folds, first analyzed by Fink and Fletcher (1978), has been used by Fink (1980a), Fink et al. (1983), Zimbelman (1985), Head and Wilson (1986), and others to estimate the rheology of lava flows on other planets. Fink and Fletcher's (1978) analysis assumed that lava flows have a temperature-dependent newtonian rheology, and that the lava's viscosity decreased exponentially inward from the upper flow surface.

The presence of a gravity or Taylor instability was proposed by Fink (1980b) to explain certain regularly spaced domal outcrops of low density pumice on the surfaces of silicic lava flows. Subsequent investigations (Fink, 1983; Fink and Manley, 1986; Manley and Fink, submitted) have attempted to relate the density inversion to the distribution and migration of volatiles within actively advancing flows. Such studies provide possible criteria for the identification of silicic lava flows on high resolution images of other planets, since diapirism results in flow surfaces with very high albedo contrasts, and the associated concentrations of volatiles may lead to formation of large craters and other explosive features on the surface of a silicic flow. These models are also important for hazards studies since the presence of volatiles in silicic magmas is considered a major factor in the inception of explosive volcanism.

Analyses of surface folding

Surface folding (Biot, 1960; Fink and Fletcher, 1978) produces regularly spaced ridges that range from cm-scale ropes on pahoehoe basalt flows to 100-m-scale lava ogives seen on rhyolite flows. Analysis shows that ridge spacings depend on the thickness of the cooling crust, magnitude of the compressive stress, and weight of the lava. Ridges can only form when the ratio between surface and interior lava viscosities lies in a restricted range: if the crust is too stiff (cool), the surface deforms by fracture rather than flow; if too soft (hot), ridges form but are not retained.

The application of this model to extra-terrestrial lava flows has been attempted by numerous investigators. One of the main drawbacks of the model has been that it requires estimating the thickness of a flow's thermal boundary layer (crust). Previous planetary applications have required assumptions about the strain rates and times of formation associated with large ridges (formation times have been assumed to be between 1 day and one week), and about how the crustal thickness relates to the amplitude of the ridges (crust thickness was generally assumed equal to ridge amplitude).

A lower bound on strain rates was obtained from observations of the active 1984 Mauna Loa basalt flow. During this eruption, surface ridges with wavelengths ranging from 10-30 m and amplitudes of 1-2 meters were seen to form relatively abruptly at positions that migrated upstream as part of an overall change in aa surface characteristics described by Lipman, Banks, and Rhodes (1986). Ridges were seen to form behind flow constrictions over a period of less than a day. The observed wavelengths and amplitudes correspond to strains of between about 0.003 and 0.080. If these occurred over periods of less than a day, the minimum strain rates would be between 10^{-7} and 10^{-8} sec^{-1}, which are considerably less than those used in earlier calculations. Lower strain rate estimates in turn lead to higher calculated viscosity values.

Analyses of Taylor instability in lava flows

Recent drilling investigations in rhyolite flows (Eichelberger et al., 1985; Goff et al., 1986) have provided new information about their volatile distributions, and now allow more accurate specification of boundary conditions for the gravity instability model. Fink's original linear analysis (1980b) assumed newtonian rheology, an absence of slope-induced shear stresses, a rigid upper flow surface, and a two-dimensional perturbation of the unstable interface. The new drill data have motivated a more rigorous and generalized analysis of the Taylor instability in lava flows.

The new formulation allows for three dimensional disturbances, the effect of a mean shear flow on the instability, and a deformable free upper surface. This analysis allows determination of whether transverse ridge formation is favored over other possible orientations, assessment of the deformation of the free surface relative to that of the unstable internal interface, and use of the viscosity ratio to help determine the state of volatiles within the buoyant layer.

Results of the new analyses (Baum et al., in review) include calculations of preferred wavelength and growth rates as functions of buoyant and dense layer thicknesses and viscosities. In general, diapir spacing increases in proportion to the thickness of the buoyant layer and to the viscosity of the dense layer. The measured thicknesses of buoyant and dense layers in three different drill cores and in two well-dissected rhyolite flows in Arizona allow the relative viscosities of the layers to be determined. It was found that the presence of regularly spaced, dark, pumiceous diapirs on the surface of terrestrial silicic flows reflects a local concentration of volatiles of from 3 to 6 times the average values. Recognition of such diapiric structures in conjunction with unusually large surface ridges on martian or venusian flows would suggest more evolved lavas than have previously been identified. Such features are currently being sought in high resolution Viking images.

Surface folding on debris flows

Not all terrestrial flows that preserve regularly spaced ridges are lavas. Debris flows, landslides, mudflows, and other sorts of mass movements may all develop surface folds in response to flow parallel compression. As part of a study of the Chaos Jumbles debris avalanche deposit at Lassen National Park, an analysis of surface folding instabilities on plastic materials was conducted (Eppler, Fink and Fletcher, 1987). The main differences between the rheological model used for debris avalanches and for lava flows were (1) the debris was assumed to have an isothermal, power-law rheology with a finite yield strength, rather than a temperature-dependent newtonian rheology; and (2) the debris was assumed to move primarily by slip over a frictionless basal surface rather than by continuous flowage.

A surprising result of the analysis was that the spacing of ridges was proportional to the total thickness of the flow, rather than to the crustal thickness alone. The ratio of ridge spacing to flow thickness ranged from 1.4 to 2.8 for all reasonable rheologic values. These two endmembers correspond to relatively low and high values of debris strength. Hence, by measuring the spacing of ridges on a debris flow, it may be possible to estimate its thickness (and volume) to within a factor of two. For the case of Chaos Jumbles, volume estimates based on ridge spacing were consistent with volume estimates based on the size of the collapse scar left behind by the falling debris. Application of this model to the interpretation of landslide deposits on Mars is currently in progress.

References

Baum, B., Fink, J., Krantz, W., and Dickinson, R., Rayleigh-Taylor instability in rhyolite flows. JGR (submitted)

Biot, M., 1960, J. Franklin Inst., *270*: 190-201.

Eichelberger, J., Lysne, P., Miller, C., Younker, L., 1985, EOS,*66*: 186-187.

Eppler, D., Fink, J. and Fletcher, R., 1987, Rheology and kinematics of the Chaos Jumbles debris avalanche deposit, Lassen National Park, CA. JGR (in press).

Fink, J. and Fletcher, R., 1978, J. Volcanol. Geotherm. Res., *4*: 151-170.

Fink, J., 1980a, Geology, *8*: 250-254.

Fink, J., 1980b, Tectonophysics, *66*: 147-166.

Fink, J., Park, S., and Greeley, R., 1983, Icarus, *56*: 38-50.

Fink, J., 1983, Geol. Soc. America Bull., *94*, 362-380.

Fink, J. and Manley, C., 1987, in Fink, J., editor, G.S.A. Special Paper 212, (in press).

Goff, F., Rowley, J., Gardner, J., Hawkins, W., Goff, S., Charles, R., Wachs, D., Maassen, L., and Heiken, G., 1986, JGR, *91*: 1742-1752.

Head, J. and Wilson, L., 1986, JGR, *91*: 9407-9446.

Lipman, P., Banks, N., and Rhodes, J., 1986, Nature, *317*: 604-607.

Manley, C. and Fink, J., Internal textures of rhyolite flows as revealed by research drilling. Geology (submitted).

Zimbelman, J., 1985, Proc. Lunar Planet. Sci. Conf., *16*: D157-D162.

LONG, PAIRED A'A/PAHOEHOE FLOWS OF MAUNA LOA: VOLCANOLOGICAL SIGNIFICANCE, AND INSIGHTS THEY PROVIDE INTO VOLCANO PLUMBING SYSTEMS

Scott K. Rowland & George P.L. Walker, Hawaii Institute of Geophysics,
2525 Correa Rd., Honolulu, Hawaii 96822

Martian lava flows of Olympus Mons and the Tharsis volcanoes are an order of magnitude longer, wider, and more voluminous than any single lava flows on Earth (cf. Carr, 1981). The long lava flows of Mauna Loa, Hawaii have been cited as Earth's closest analogs to the large Martian flows (Carr, 1981). It is therefore important to understand the flow mechanisms and characteristics of the Mauna Loa flows and to make use of these in attempts to gain insights into Martian eruptive processes.

A number of workers (Walker, 1973; Malin, 1980) have made attempts to find regular relationships between flow characteristics such as flow thickness, length, and area with physical controls of lava flows such as underlying gradient and average eruption rate. Assumptions regarding lava rheology can then be made if a quantitative method of analyzing the found relationships exists.

The careful mapping of selected Mauna Loa flows has revealed the unexpected relationships that lavas with very different flow mechanisms can have very similar volumes, areas, and lengths. The division of Hawaiian lavas into pahoehoe and a'a (cf. Macdonald, 1953) is a fundamental one and is useful for many reasons. The common down-flow change from pahoehoe to a'a due to degassing, cooling, and shearing (Emerson, 1926; Peterson & Tilling, 1980) is well established; what is not so well known is that flows having similar lengths (up to 47 km) and volumes (up to 200 x 10^6 m^3) can consist of pahoehoe or a'a in their entirety.

Our mapping has revealed the existence of several paired lavas, each consisting of an earlier a'a member and a later pahoehoe member erupted in the same eruption, the two members of a pair having similar lengths and volumes and, so far as we know, identical initial viscosities and chemical compositions.

The 1859 and 1880-81 lavas of Mauna Loa are particularly striking examples of paired a'a/pahoehoe flows. Historical accounts allow us to piece together the characteristics of the eruptions, which we can then relate with features of the eruptive products analyzed in the field and in air photos. An important relationship which we find for these two eruptions is the close correlation of erupted lava type with discharge rate; channel-fed a'a formed at a time of high discharge rate and tube-fed pahoehoe formed at a time of low discharge rate. Eruptive style is also closely related to discharge rate; high gas-driven fountaining accompanied the high discharge-rate activity, and little or no fountaining accompanied the low discharge-rate activity. A similar relationship was noted on Kilauea during the Mauna Ulu series of eruptions (Swanson, 1973; Swanson et.al., 1979), and is at present being demonstrated by the 1983-1986 Puu O'o and "C-fissure" (Ulrich et.al., 1986) activity.

At a time of high discharge, lava is strongly channelized and the high flow velocity precludes the roofing-over of significant lengths of the main channels. The loss of heat from open channels is very rapid, and a significant viscosity increase occurs in the channelized lava. Because of lateral velocity gradients, any portion of chilled lava crust is subjected to a torque due to traction by the underlying lava, and because of this torque adjacent portions of skin tend to be torn apart. If the underlying lava is too viscous to well up and heal the tears, then the torn-apart portions of skin become rubble fragments (Macdonald, 1953) and the lava flow becomes a'a.

In contrast, at a time of low discharge, flowage of the lava through tubes under the surface crust is favored. A labyrinth of small single-flow-unit tubes forms, and coalescence or enlargement of these causes master tubes to develop. Heat is very efficiently

conserved in tubes and lava can travel far from the vent without cooling significantly (Swanson, 1973). These eruption conditions favor the extreme subdivision of the lava into flow units, and these units are individually so thin that flowage has almost ceased by the time that the lava viscosity has reached a value appropriate (in rapidly flowing lava) to the formation of an a'a surface. A'a does not therefore form and the lava is predominantly pahoehoe right to its distal limits.

Close monitoring of Kilauea summit tilt during the current (1983-1986) eruptive activity gives an insight into factors relating to the drastically different eruptive characters. In the time prior to each episode of high discharge and high fountaining at Pu'u O'o, the summit reservoir swelled (Wolfe et.al., 1987). The periodicity of eruptive episodes is recorded as a saw-tooth pattern on a tilt angle vs. time diagram (cf. Eaton & Murata, 1960), due to the slow inflation followed by rapid deflation accompanying eruption. This pattern is interpreted to indicate that magma is stored in a summit reservoir between eruptive episodes (Wolfe et.al., 1987). In contrast, during eruptive periods of low or no fountaining (episode 35-B and the current activity), associated with pahoehoe production, little systematic variation in the tilt record is shown; magma is not being stored in the summit chamber and output at the vent equals input from the mantle (Heliker et.al., 1985; Ulrich et.al., 1987).

By analogy, temporal information regarding the 1859 and 1880-81 eruptions of Mauna Loa allows us to constrain volumes of Mauna Loa summit magma chambers as well as supply rates to the chamber. The values are approximately 200 x 10^6 m^3 and 7 m^3/sec respectively. Dzurisin et.al. (1984, fig. 7) estimate the volume of Kilauea's chamber as ranging between 50 and 200 x 10^6 m^3. Estimates of the supply rate to Kilauea's summit chamber range from 2.7 to 3.5 m^3/sec (Ulrich et.al., 1986 ; Swanson, 1972; Dzurisin et.al., 1984). Analysis of total area covered by a'a and tube-fed pahoehoe on Mauna Loa by Lockwood & Lipman (1985) indicates that prior to 750 y ago, pahoehoe was the dominant eruptive product while since then, a'a has dominated. This may indicate that since 750 y ago, magma has been stored between eruptions in a summit chamber.

Consider now the reasons for the differences in discharge rate during single eruptions as well as for the episodic behavior of Kilauea between 1983 and 1986, that produced a paired assemblage of a'a and pahoehoe. Three possibilities are considered. One, the primary control for the episodic activity was partial blockage of the conduit (between magma chamber and vent) between eruptive episodes. Eventually (by July, 1986) the conduit attained thermal equilibrium, and continuous unimpeded magma flow became possible. Two, the primary control for the episodic activity was the accumulation of gas bubbles in the magma within the upper part of the magma chamber, and its depletion lower down. Each eruptive episode released gas-rich magma, and was then terminated because the underlying gas-poor magma lacked sufficient bouyancy to rise to the surface. Since then, steady state conditions have been attained, and the magma emerges continuously with a uniform and moderate content of bubbles. Three, high effusion-rate lava is is erupted when strain release on a swelled magma chamber is the mechanism which drives magma upward to shallow levels, where gas bubble expansion rapidly takes place. The later pahoehoe uses the same conduit to reach the surface at a much lower velocity by means of gas bubble-induced bouyancy.

The relevance of this work to the Martian volcanoes is that two fundamentally different kinds of long lava flows can be distinguished on Hawaiian volcanoes. The two kinds may have identical initial viscosities, chemical compositions, flow lengths, and flow volumes, but their flow mechanisms and thermal energy budgets are radically different. One travels a distance set by the discharge rate as envisaged by Walker (1973) and Wadge, (1978), and the other travels a distance set mainly by the eruption duration and ground slope. In the Mauna Loa lavas, yield strength becomes an important flow-morphology control only in the distal parts of a'a lavas. The occurrence of

paired flows on Mauna Loa yields insights into the internal plumbing systems of the volcano, and it is significant that all of the volume of the a'a flow must be stored in a magma chamber before eruption, while none of the volume of the pahoehoe needs to be so stored. We are confident that it should be possible to distinguish between the two kinds of flows on images of Martian volcanoes and hence start to aquire an improved understanding of these huge structures.

BIBLIOGRAPHY

Carr, M.C., 1981, **The Surface of Mars**, Yale University Press, New Haven & London, 232pp.

Dzurisin, D., Koyanagi, R.Y., and English, T.T., 1984, Magma supply and storage at Kilauea volcano, Hawaii, 1956-1983. J. Volcanol. Geotherm. Res., **21**: pp. 177-206.

Eaton, J.P., and Murata, K.J., 1960, How volcanoes grow. Science, **132**: pp. 925-938.

Emerson, O.H., 1926, The formation of a'a and pahoehoe. Am. J. Sci., ser. 5, **5**: pp. 109-114.

Heliker, C., Hoffmann, J., Rowland, S., Greenland, P., and Reason, M., 1985, Fissure activity near Pu'u O'o, Kilauea volcano, Hawaii. Eos, **66**: p. 851.

Lockwood, J.P., and Lipman, P.W., 1985, Holocene eruptive history of Mauna Loa volcano, Hawaii. Eos, **66**: p. 1132.

Macdonald, G.A., 1953, Pahoehoe, a'a, and block lava. Am. J. Sci., **251**: pp. 169-191.

Malin, M.C., 1980, Lengths of Hawaiian lava flows. Geology, **8**: pp. 306-308.

Peterson, D.W., and Tilling, R.I., 1980, Transition of basaltic lava from pahoehoe to a'a, Kilauea volcano, Hawaii: field observations and key factors. J. Volcanol. Geotherm. Res., **7**: pp. 271-293.

Swanson, D.A., 1972, Magma supply rate at Kilauea volcano, 1952-1971. Science, **175**: pp. 169-170.

Swanson, D.A., 1973, Pahoehoe flows from the 1969-71 Mauna Ulu eruption, Kilauea volcano, Hawaii. Geol. Soc. America Bull., **84**: pp. 615-626.

Swanson, D.A., Duffield, W.A., Jackson, D.B., and Peterson, D.W., 1979, Chronological narrative of the 1969-71 Mauna Ulu eruption of Kilauea volcano, Hawaii. U.S. Geol. Surv. Prof. Pap. **1056**: 55pp.

Ulrich, G., Heliker, C., Greenland, P., Koyanagi, R., and Griggs, J., 1986, Geology section in H.V.O. Bulletin for July, 1986.

Ulrich, G.E., Wolfe, E.W., Heliker, C.C., and Neal, C.A., 1987, Pu'u O'o IV: Evolution of a plumbing system. in "Hawaii symposium on how volcanoes work" abstract volume.

Wadge, G., 1978, Effusion and the shape of a'a lava flow fields on Mount Etna, Geology, **6**: pp. 503-506.

Walker, G.P.L., 1973, Lengths of lava flows, Philos. Trans. Roy Soc. A, **274**: pp. 107-118.

Wolfe, E.W., Garcia, M.O., Jackson, D.B., Koyanagi, R.Y., Neal, C.A., and Okamura, A.T., 1987, The Pu'u O'o eruption of Kilauea volcano, episodes 1-20, January 1983-June 1984. U.S. Geol. Soc. Prof. Pap. **1350**.

THE 1984 MAUNA LOA ERUPTION AND PLANETARY GEOLOGY

Henry J. Moore, U.S. Geological Survey, Menlo Park, CA., 94025

In planetary geology, lava flows on the Moon and Mars are commonly treated as relatively simple systems. The purpose of this abstract is to illustrate some of the complexities of actual lava flows using the main flow system of the 1984 Mauna Loa eruption. The outline, brief narrative, and results below are based on a number of sources [1,2,3].

This flow system developed in four distinct stages that overlap in time: (1) rapid advance of a narrow aa sheet, (2) development of a channel within the aa sheet that conducted lava from the vents to the lower reaches, (3) formation of blockages and obstructions in the channel that produced overflows, levees, and lava ponds on the aa sheet, and (4) waning stages during which the lava channels drained and the distal parts of the flow thinned and spread. Blockages, obstructions, and overflows progressed upstream with time. There were also significant variations in the lava flowing in the channel from the vent toward the toe: (1) densities of samples from the flowing lava increased from less than 530 to more than 2,400 kg/m^3, (2) tempertures of the most fluid lava decreased from 1140°C to as low as 1086°C, (3) concentrations and sizes of warm to incandescent objects increased, (4) apparent viscosity increased dramatically, (5) the rheology changed, and (6) the volume flow rates decreased.

On the afternoon of March 25, lava was issuing from fissure vents at the 2850-m elevation that became the principal sources of lava for the remainder of the eruption. Three southerly flow lobes fed by the vents stagnated by March 27, but the main flow was fed at a fairly constant volume-flow rate (560 m^3/s). Constant-volume flow rates were sustained from March 30 to April 7; after April 7, flow rates declined. The main flow (flow 1) advanced rapidly as a narrow aa sheet, elliptical in profile, to the 910-m level, 25 km from the vents. The sheet flow evolved into (1) a channel zone within the sheet flow below the vents, (2) a transition zone farther downstream, and (3) a dispersed-flow zone led by the advancing toe. The lava channel had developed in the sheet flow by March 29. Also on March 29, obstructions and blockages near the 1740-m level caused a channel overflow or breakout that cut off the lava supply to flow 1 so that it moved about another km in a day. Lava from this breakout gave rise to flow 1A, which advanced rapidly along a course sub-parallel to and north of flow 1. A series of overflows that progressed upstream beginning April 3 produced levees and lava ponds that were superposed on the aa sheet. Blockages and collapse of lava-pond walls gave rise to surges, ebbs, and small overflows that reduced the lava supply to flow 1A. On April 5, a breakout occurred at about the 1980-m level and cut off the lava supply to flow 1A, which stopped

about 27 km from the vents. The April 5 breakout gave rise to flow 1B, which moved toward the northeast. Repeated channel blockages and overflows continued progressively upstream from April 5 to April 8. On April 7, lava production at the vent began to dwindle; subsequently, the flow system stagnated, vent activity ceased, and the channels drained.

The appearance of lava during the eruption correlated with changes in the apparent viscosity of the flow. At the vents and 3 km away, the flow was composed of sparse cinders and clinkers in a matrix of molten lava confined in a channel 20 m wide. Flow was laminar and steady; velocities were 15 m/s (vents) and 5.3 m/s (3 km from vents). At 9 km from the vents, the flow was composed of dark cinders and clinkers, and incandescent clots in molten lava. At 15 km from the vents, the flow resembled a slowly moving mass of debris confined in a rubbly, leveed channel 57 m wide; the flow included warm to incandescent fragments that were block size and smaller, and molten lava. Movement occurred by displacement of discrete, intact units with boundaries that paralleled the crests of the levees. Flow was laminar but unsteady, with surges and ebbs; velocities ranged from 0.1 to 0.3 m/s.

Apparent viscosities of the lava were calculated from observed velocities, assumed densities based on samples from the flowing lava, and flow dimensions along the main flow. On a given day, apparent viscosities increased downstream. On April 2, they were about 10^2 Pa·s at the vents, 10^3 Pa·s at 3 km from the vents, 10^5 Pa·s at 15 km from the vents, and near 10^7 Pa·s at the toe. These increases in apparent viscosity were probably related to (1) increases in the concentrations of solid debris, crystals, and plastic clots, (2) reductions in gas and bubble contents, (3) decreases in temperatures, and (4) decreases in stresses and shear rates.

Flow laws probably varied along the length of the flow from Newtonian, through Bingham, to pseudoplastic fluids [e.g. 4]. Other fluid models may also apply [5]. Estimated stresses and shear rates for the lava compare favorably with laboratory data at similar temperatures (1120-1140°C) [4].

Volume-flow rates at the vents on April 3 were near 560 m^3/s, about 12 times higher than at 15 km downstream. Mass-flow rates, calculated with the densities assumed in calculations of apparent viscosities, indicated a mass loss along the flow that could not be accounted for by the observations, ponding, overflows, or gas loss. With certain assumptions, conservation of mass requires a lava density at the vents about 220 kg/m^3, implying a mass-flow rate near 1.2×10^5 kg/s. If these masses were deposited with an average bulk density of 2,200 kg/m^3, the volume-flow rate would appear to be 56 m^3/s.

The implications of the above results to planetary geology are clear. Volume-flow rates during an eruption depend, in part, on the volatile content of the lava. These differ from the volume-flow rates calculated from post-eruption flow

dimensions and the duration of the eruption [6,7] and from those using models that assume a constant density [8,9]. Mass-flow rates might be more appropriate because the masses of volatiles in lavas are usually small, but variable and sometimes unknown densities impose severe restrictions on mass estimates. Lava flows cannot necessarily be modeled as simple flow units because they may develop in time-dependent stages. All rheological properties probably vary with time.

Despite these complications, planetary geologists should persist in their endeavors to understand lava flows on Earth and other planetary bodies [8,9,10,11,12].

REFERENCES CITED

[1]Lockwood, J.P., Banks, N.G., English, T.T., Greenland, L.P., Jackson, D.B., Johnson, D.J., Koyanagi, R.Y., McGee, K.A., Okamura, A.T., and Rhodes, J.M., 1985, The 1984 eruption of Mauna Loa Volcano, Hawaii: Trans. Amer. Geophys. Union (EOS), v. 66. no. 16, p. 169-171.

[2]Lipman, P.W., and Banks, N.G., in press, Aa flow dynamics, Mauna Loa 1984, chapter 57 in Decker, R.W., Wright, T.L., and Stauffer, P.H. eds., Volcanism in Hawaii: U.S. Geol. Survey Prof. Paper 1350.

[3]Moore, H.J., in press, Preliminary estimates of the rheological properties of the 1984 Mauna Loa lava, chapter 58 in Decker, R.W., Wright, T.L., and Stauffer, P.H., eds., Volcanism in Hawaii: U.S. Geol. Survey Prof. Paper 1350.

[4]Shaw, H.R., 1969, Rheology of basalt in the melting range: Journal of Petrology, v. 3, no. 3, p. 510-535.

[5]McBirney, A. R. and Murase, T., 1984, Rheological properties of magmas: Annual Review Earth and Planetary Science, v. 12, p. 337-357.

[6]Walker, G.P.L., 1967, Lengths of lava flows: Phil. Trans. Royal Soc. of London, Series A, v. 274, p. 107-118.

[7]Malin, M.C., 1980, Lengths of Hawaiian lava flows: Geology, v. 8, p. 306-308.

[8]Hulme, Geoffrey, and Fielder, Gilbert, 1977, Effusion rates and rheology of lunar lavas: Phil. Trans. Royal Soc. of London, Series A, v. 285, p. 227-234.

[9]Zimbelman, J. R., 1985, Estimates of rheological properties of flows on the martian volcano Ascraeus Mons: Jour. Geophys. Res., v. 90, Suppl., Part I, p. D157-D162.

[10]Wilson, Lionel, and Head, J.W., III, 1983, A comparison of volcanic eruption processes on Earth, Moon, Mars, Io, and Venus: Nature, v. 302, p. 663-669.

[11]Baloga, S.M., and Pieri, D.C., 1986, Time-dependent profiles of lava flows: Jour. Geophys. Res., v. 91. no. B9, p. 9543-9552.

[12]Fink, J. H. and Zimbleman, J. R., 1986, Rheology of the 1983 Royal Gardens basalt flows, Kilauea, Volcano, Hawaii: Bull. Volcan., v. 48, p. 87-96.

CALCULATED VISCOSITY-DISTANCE DEPENDENCE FOR SOME ACTIVELY FLOWING LAVAS

David Pieri, Jet Propulsion Laboratory, Pasadena, CA 91109

The importance of viscosity as a gauge of the various energy and momentum dissipation regimes of lava flows has been realized for a long time. Nevertheless, despite its central role in lava dynamics and kinematics, it remains among the most difficult of flow physical properties to measure in situ during an eruption. Viscosity measurements on active flows are traditionally fraught with local uncertainties due to small-scale anomalies in the flow, as well as with global systematic errors [e.g., 1,2,3]. In addition, the act of making the measurement affects the perceived viscosity. Finally, the presence and evolution of volatiles within the flow during emplacement strongly affects physical properties of the flow, including viscosity. As a result, a posteriori laboratory viscosity measurements made on remelted, nearly volatile-free samples are usually at strong variance with channel-dimension based estimates (e.g., using the Jeffrey's equation) and in-flow field measurements (e.g., using penetrometers or viscometers) made during lava flow emplacement. Thus, only a few systematic studies have been carried out on the viscosity of flows during their emplacement [2,3,4,5,6,7].

Attempts at reconstructing the actual emplacement viscosities of lava flows from their solidified topographic form are difficult. Work in Hawaii by Fink and Zimbelman [8] involved highly detailed topographic surveys of a recent flow from the Puu'Oo vent of Kilauea coupled to reconstructions of emplacement viscosity using a variety of models. They were able to infer a general increase of viscosity with increasing distance from the vent. Recent theoretical work [9] derives characteristic one-dimensional topographic profiles for lava flows based on spatially variable viscosity for both steady-state and time-variable effusion rates. Given the overall topographic profiles coupled to measurements of effusion rate as a function of time, general classes of viscosity-distance functions can be discerned for terrestrial flows. For planetary lava flows, the solution of such boundary-value problems are key to the deciphering of parameters such as initial lava viscosity and initial eruption temperatures [9]. In particular, the estimation of a cessation viscosity (i.e., the viscosity above which a flow cannot move) at the flow front, is a crucial boundary condition on calculations of initial vent parameters and for inferences of flow composition. Thus it would be useful to estimate effective flow viscosities during emplacement as a function of distance and time.

Where data are available on the position of an advancing flow front as a function of time, it is possible to calculate the effective viscosity of the front as a function of distance from the vent, under the assumptions of a steady-state regime (e.g., constant effusion rate, constant source depth, constant initial viscosity). Specifically, the admissible location of the advancing flow front is given by Baloga and Pieri ([9]; equation (9), p. 9544) as

$$\frac{dL}{dt} = \left[\frac{g \sin\theta \ (Q_o/W)^2}{3\nu(L)} \right]^{1/3} \qquad (1)$$

Equation (1) provides an alternative to the usual Jeffreys' method of viscosity determination in that if the flow front velocity, slope (θ), average effusion rate (Q_o), an width (W) are known, the aggregate viscosity $\left(\nu(L)\right)$ of the flow-front as a function of distance can be calculated. It is precisely this "aggregate viscosity" which reflects the kinematic and dynamic conditions at the distal end of the flow, and which is the key to the interpretation of revealing parameters such as "topographic form factors" [10] for planetary flows.

As an application and test of equation (1), relevant parameters from five recent flows on Mauna Loa and Kilauea [11, 12] were utilized to infer the dynamic structure of their aggregate flow-front viscosity as they advanced, up to cessation. Representative results of these calculations are shown in Figures 1 and 2. Instantaneous velocities were determined from least-square fits to the flow position versus time data. Viscosities were calculated using a measured average effusion rate, a measured initial flow depth and viscosity, and observed width as a function of distance from the vent.

The observed form of the viscosity-distance relation for the five active Hawaiian flows examined appears to be exponential, with a rapid increase just before the flows stopped, as one would expect. Cessation viscosities appear to be on the order of 10^{11}–10^{13} stokes, which is consistent with field estimates of that parameter from another Hawaiian flow (H. Moore, personal communication). Similar calculations (Figure 3) using the traditional Jeffreys' equation (i.e., not taking into account changes in flow width) for the same flows, produce cessation viscosities which appear to be systematically low and do not show the same characteristic viscosity increase corresponding to the stopping of the flow.

An exponential viscosity-distance dependence has been inferred for flows thickening exponentially with downflow distance (e.g., many Hawaiian flows and long flows at Alba Patera, Mars). Results shown here are consistent with such inferences and additionally provide a key boundary condition for modelling the behavior of flow fronts.

REFERENCES

[1] Shaw, H. R., T. Wright, D. L. Peck, and R. Okamura (1968). The viscosity of basaltic magma: An analysis of field measurements in Makaopuhi lava lake, Hawaii, Am. J. Sci., 266, pp. 255-264.

[2] Gauthier, F. Field and laboratory studies of the rheology of Mt. Etna lava, Philos. Trans. R. Soc. London, Ser. A, 274, pp. 83-98.

[3] Pinkerton, H., and R. S. J. Sparks (1978). Field measurements of the rheology of lava, Nature, 276, pp. 383-385.

[4] Minikami, T., (1951). On the temperature and viscosity of the fresh lava extruded in the 1951 Oo-sima eruption, Bull. Earthquake Res. Inst. Univ. Tokyo, 29, pp. 487-498.

[5] Walker, G. P. L., (1967). Thickness and viscosity of Etnean lavas, Nature, 213, pp. 484-485.

[6] Booth, B. and S. Self (1973). Rheological features of the 1971 Mt. Etna lavas, Philos. Trans. R. Soc. London, Ser. A., 274, pp. 99-106.

[7] Borgia, A., S. Linneman, D. Spencer, L. Morales, and L. Andre, (1983). Dynamics of the flow fronts, Arenal volcano, Costa Rica, J. Volcanol. Geotherm. Res., 19, pp. 303-329.

[8] Fink, J. and J. Zimbelman, (1986). Morphology and rheology of the Roy-al Gardens basalt flows, Kilauea volcano, in Bougan ed., Reports of Planetary Geology and Geophysics Program 1985, pp. 427-429.

[9] Baloga, S. M. and D. C. Pieri (1986). Time dependent profiles of lava flows, Jour. Geophys. Res., 91, pp. 9543-9552.

[10] Baloga, S. M. and D. C. Pieri (1986). The validity of the Jeffreys' equation for the lava flows at Alba Patera, S. J. Bougan ed. op cit. pp. 291-293.

[11] Wolfe, E. W., C. A. Neal, N. B. Banks, and T. J. Duggan (1985). Geol. Observations and chronology of eruptive events during the first 20 episodes of the Puu' Oo eruption, Jan. 3, 1983 – June 8, 1984 (unpublished manuscript).

[12] Lockwood, J. P., N. G. Banks, T. T. English, L. P. Greenland, D. B. Jackson, D. J. Johnson, R. Y. Koyanagi, K. A. McGee, A. T. Okamura, and J. M. Rhodes (1985). The 1984 eruption of Mauna Loa volcano, Hawaii, EOS, 66, pp. 169-171.

VISCOSITY-DISTANCE RELATIONS FOR TWO HAWAIIAN LAVA FLOWS

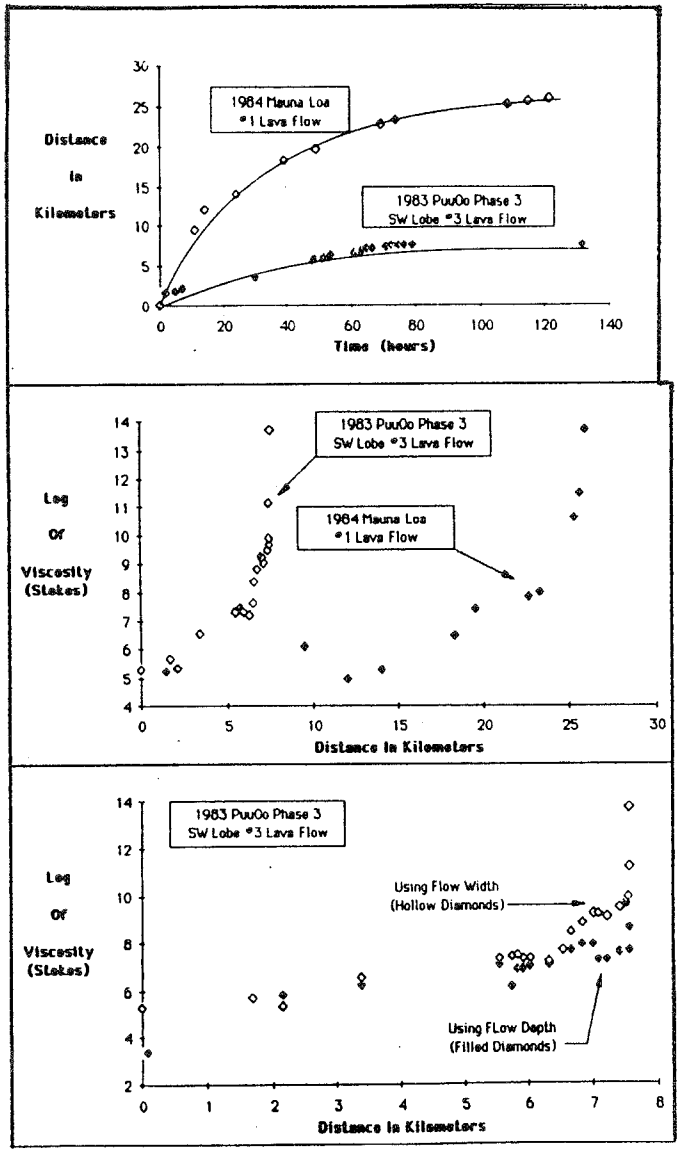

Figure 1. Distance versus time data [11, 12] for two representative Hawaiian lava flows: the 1984 Mauna Loa #1 Flow and the 1983 Puu' Oo vent Phase 3 (SW Lobe #3) Flow of Kilauea. The solid lines shown represent best-fit arbitrary least sqaures regressions on the data. Velocity values for the flow were calculated by taking derivatives of the best-fit curves. (Effusion rates for the two flows differed by an order of magnitude [11, 12].)

Figure 2. Viscosity versus distance for the same two flows. Here, both viscosities are calculated using equation (1). Note the strong similarity in forms of the two viscosity-distance curves. These viscosities represent the effective viscosity of the flow front as a function of distance from the vent for an observed average eruption rate. Also note the strong viscosity increase at cessation.

Figure 3. Viscosity calculated (as in Figure 2) using equation (1): (Hollow diamonds), versus viscosity calculated using the standard Jeffreys' formulation ((i.e., $\nu = g\ (\sin\theta)\ gh^2/3\upsilon$): filled diamonds). Note the systematic difference between the two calculated curves and the lack of sensitivity in the Jeffreys' calculation to flow cessation.

TOWARD A MODEL FOR LEVEED LAVA FLOWS

Stephen Baloga, Jet Propulsion Laboratory, Pasadena, CA 91109

Many lava flows have two distinct volumetric components during emplacement. First, there is a component actively flowing in accordance with Newtonian or other constitutive relations. Second, there may be an inactive, stationary component that is no longer participating in the forward movement of the flow. Such passive components may take the form of flow-confining levees, solidified lateral margins, overspills, plating, small ponds and sidestreams, or a lava tube. To describe the conservation of flow volume for the active component, the governing equation is taken as,

$$w \frac{\partial h}{\partial t} + \frac{\partial Q}{\partial x} = -\lambda w h \qquad (1)$$

where $h = h(x,t)$ is the depth of the flow, $w = w(x)$ is the width, $Q = Q(x,t)$ is the local flowrate, x and t represent the distance from the source and time, and λ is a rate constant for the volumetric loss to levees or other stationary constructs. "Global" volume conservation is described by,

$$\int_0^t Q(t')\, dt' = \int_0^{L(t)} w(x)\, h(x,\, t)\, dx + \lambda \int_0^t \int_0^{L(t')} w(x')\, h(x',t')\, dx'\, dt'$$

$$\text{Discharge} \quad = \quad \text{Active} \quad + \quad \text{Passive} \qquad (2)$$

where $Q(t) = Q(0,t)$ is the effusion rate and $L(t)$ is the length of the flow. Eqs. (1) and (2) with $\lambda=0$ have been studied by Baloga and Pieri [1986] and Baloga [1986]. Eq. (2) accounts for the entire discharge by distributing it dynamically between the active and passive components. From eq. (2), the active volume of the flow, $V(t)$, is given by,

$$V(t) = \int_0^{L(t)} w(x)\, h(x,\, t)\, dx = \int_0^t e^{-\lambda(t-t')}\, Q(t')\, dt' \qquad (3)$$

The growth of the stationary volume fraction is determined solely by the effusion rate and the rate constant. Because $h(x,t)$ must satisfy eq. (1), we have in eq. (3) a key relationship between levee production, time-dependent source behavior, the advance of the flow front, and viscous changes along the flow path. Studies of these interactions are in progress.

To illustrate some of the consequences of eq. (1) alone, we will choose a highly specialized flowrate,

$$Q(x) = \frac{g \sin \Theta\, h(x)^3 w(x)}{3 \nu\, (x)}, \qquad (4)$$

where g is gravity, Θ is the slope and ν is the viscosity, and use data from the 1951 eruption of the Mihara volcano in Japan [Minikami, 1951]. Figure 1 shows the relevant geometrical data for this flow and appropriately fitted lines. Although the width and depth of the flow increase appreciably downstream, the product of the flow width and the slope measurements are

approximately constant. The theoretical formalism simplifies considerably if w(x) sin Θ is taken as its average value, <w sin Θ>. In Figure 1, the average is indicated by the dashed line. From eqs. (1) and (4), with the boundary condition h(0) = ho,

$$h(x) = ho \left[\frac{\nu(x)}{\nu o}\right]^{1/3} \left[1 - \frac{2\lambda\ \nu o^{2/3}}{h_o^2 g\ \langle w \sin \Theta\rangle} \int_o^x \nu(x')^{1/3} w(x')\ dx\right]^{1/2} \quad (5)$$

This solution indicates that the flowdepth is affected by both the local viscosity and its cumulative behavior along the path of the flow. Because depth and width variables are, unlike viscosity, more amenable to direct measurement while the flow is active, a more useful result is obtained by inverting eq. (5) for the viscosity in terms of the depth and width. One can show that,

$$\frac{\nu(x)}{\nu o} = \left[\frac{h(x)}{ho}\right]^3 \left[1 - \frac{\lambda}{Qo} \int_o^x h(x')\ w(x')dx'\right]^{-1} \quad (6)$$

where $Qo = g\langle w \sin \Theta\rangle\ ho^3 / 3\ \nu o$. This interesting result shows that the viscosity has a simple power law dependence on the local depth of the flow unless significant flowrate losses are occurring. Estimated lava viscosities were computed by Minikami using a form of the Jeffreys' equation [Williams and McBirney, 1979]. The particular formula used by Minikami does not account for changes in width or flowrate losses, but does have a slope dependence. Minikami also attempted to correct the viscosity estimates for effects from the sides of the channel. His values are shown in Figure 2, where a constant lava density of 2.5 gm/cm^3 has been assumed. Figure 2 also shows results computed from eq. (6) using identical parameters and the linear fits to the depth and width data. When $\lambda = 0$, the volumetric flowrate is conserved in the channel and the computed viscosities are significantly higher than the conventional Jeffreys' equation results. Even for a small λ, the effect of a small flowrate loss eventually accumulates and produces a significant discrepancy between methods of estimation. The flowrate can also be recast directly in terms of depth and width measurements without resorting to intermediate viscosity computations. Eqs. (4)-(6) imply,

$$\frac{Q(x)}{Qo} = \left[1 - \frac{2\ \lambda}{3\ Qo} \int_o^x h(x')\ w(x')\ dx' \left\{1 - \frac{\lambda}{Qo} \int_o^{x'} h(x'')\ w(x'')\ dx''\right\}^{-1/3}\right]^{3/2} \quad (7)$$

In principle, measurement of the flowrate and the flow geometry, i.e., both sides of eq. (7), provides a mechanism for testing the validity of the theory. Flowrates computed from the Mihara flow data are shown in Figure 3. Although a flowrate loss seems clearly evident, Minikami discusses a variety of errors that could easily account for the flowrate variations depicted. Figure 3 also shows typical results from eq. (7), illustrating the form of the flowrate loss associated with linear fits to the flow depth and width data. There is enough uncertainty in the data to preclude these results from being considered as actual improvements over Minikami's analysis. Efforts are underway to apply eqs. (1) and (2) to lava flows at Alba Patera, Mars, where high resolution Viking images clearly indicate the presence of levees and other passive components and dimensional data has been compiled

[Pieri et al., 1986]. A model that describes the emplacement of leveed lava flows is expected to provide interesting inferences about the nature of the eruptions and possibly the compositions involved.

REFERENCES

Baloga, S. M., 1986, On a kinematic wave model for lava flows, submitted to Jour. Geophys. Res.

Baloga, S. M. and Pieri, D. C., 1986, Time-dependent profiles of lava flows, Jour. Geophys. Res., 91, pp. 9543-9522.

Minikami, T., 1951, On the temperature and viscosity of the fresh lava extruded in the 1951 Oo-sima eruption, Bull. Earthq. Res. Inst., 29, pp. 487-498.

Pieri, D. C., Schneeberger, D., Baloga, S., Saunders, S., 1986, Dimensions of lava flows at Alba Patera, Mars, NASA TM 88383.

Williams H. and McBirney, A. R., 1979, Volcanology, Feeman, Cooper & Co., San Francisco, 379 pp.

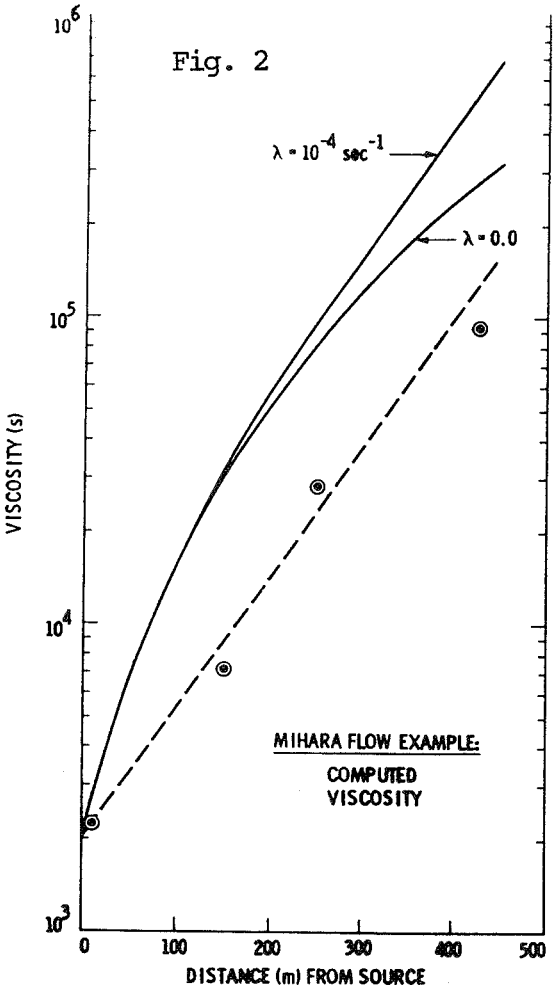

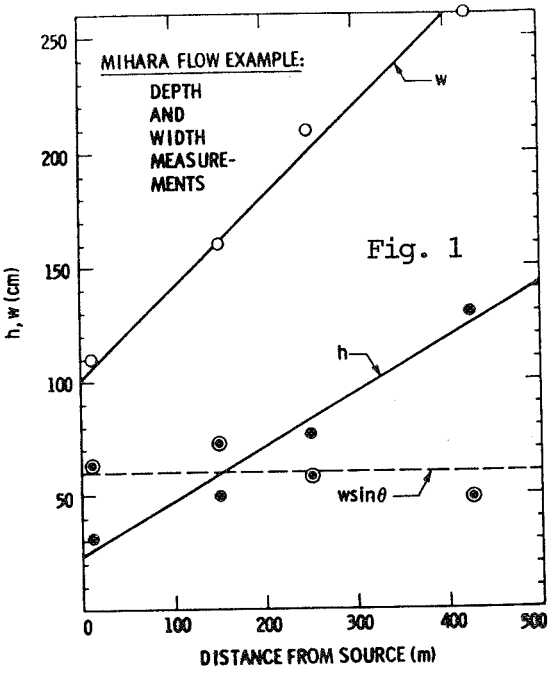

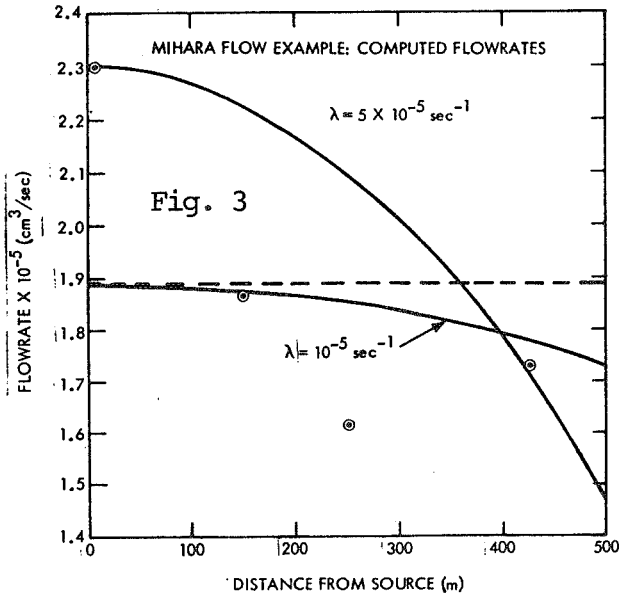

STUDIES OF VESICLE DISTRIBUTION PATTERNS IN HAWAIIAN LAVAS

George P.L. Walker
Hawaii Institute of Geophysics
Honolulu, HI 96822

Basaltic lava flows are generally vesicular, many of them highly so, and the broader facts relating to vesicle distribution have long been established; few detailed studies have however yet been made with a view to determining how and when vesicles form in the cooling history of the lava, explaining vesicle shape and size distributions, and gaining enough understanding to employ vesicles as a geological tool. Various avenues of approach exist by which one may seek to gain a better understanding of these ubiquitous structures and make a start towards developing a general theory, and three such avenues have recently been explored.

One avenue involves the study of pipe vesicles; these are a well known feature of lava flows and are narrow (3-15 mm) pipes which occur near the base of many pahoehoe flow units. They have often been attributed to the rise of steam into a lava where it flows over marshy ground. A new interpretation is that they develop at a time when the cooling lava has acquired a yield strength of a few tens of N m^{-2} and is almost static; bubbles a few cm wide are big enough to rise through such lava, but complete closure behind the rising bubbles is prevented by the yield strength, and each pipe therefore survives as a bubble trace. Larger but related features are vesicle cylinders, in which parcels of relatively low-viscosity melt plus bubbles rise diapirically through the lava. These structures have an origin broadly similar to that of pipe vesicles

A totally unexpected feature of pipe vesicles is their confinement, at the studied Hawaiian localities, to lavas on depositional slopes of 4° or less. They are thus sensitive paleoslope indicators of great potential when studying the paleogeography of lava accumulations. The proposed explanation is that a pipe vesicle survives only if the bubble of which it is a trace rises fairly steeply through the lava: that is, if the lateral lava flow rate is comparable with or less than the bubble ascent-rate. This condition is best realized if the lava stands on a horizontal or near-horizontal surface. Pipe vesicles and vesicle cylinders thus enable us to document the rheological condition and relative flow velocity of lava at a late stage in its cooling history.

Another avenue of approach is that presented by the distinctive "spongy pahoehoe" facies of lava that is common in distal locations on Hawaiian volcanoes. Spongy pahoehoe is characterized by a high content and rather uniform distribution of vesicles having a high degree of sphericity. The vesicle size systematically increases inward to reach a maximum in the center of the lava flow-unit. The bilateral symmetry of vesicle distribution and size above and below the horizontal median plane indicates that the vesicles formed in near-static lava, and their rise was prevented by the yield strength which the lava at that time possessed. Earlier, olivine crystals where present had settled through the same lava at a time when it lacked a yield strength. The vesicles in spongy pahoehoe thus belong to a generation formed late in the cooling history of the

lava, and probably represent gas released by crystallization of the lava.

Various relationships show that early-formed vesicles were eliminated by flowage from spongy pahoehoe before the present vesicle population developed. Application of this idea of vesicle elimination by flowage explains one outstanding feature of some aa lavas, namely, the fact that vesicles are almost totally absent from distal-type aa. These studies of vesicles thus enable us to investigate the gas budget in lava flows.

A third avenue of approach is that of the study of gas blisters in lava. Gas blisters are voids, which can be as much as tens of meters wide, where the lava split along a vesicle-rich layer and the roof was up-arched by gas pressure. It has proved possible to distinguish gas blisters from lava tubes (which have similar dimensions), and among blisters to distinguish between those related to early-formed vesicles, and those related to late-generation vesicles.

One unexpected feature is that the distribution of gas blisters and tubes has utility when assessing how much erosion of a volcano has occurred. This is because they are rather transient features which soon either become infilled or collapse when the load of lava overburden exceeds about 30 meters. In the case of the Koolau volcano on Oahu, the presence of gas blisters and tubes establishes that the well-known cuestas above Honolulu and Waikiki are remnants of the original volcano surface, from which only a negligible amount of rock has been eroded.

These studies of vesicles are not yet finished. Vesicles hold great promise as a means of assessing the changing rheological condition of lava, they are sensitive indicators of the times and amounts of gas loss, and they have utility as paleoslope, lava facies, and erosion-depth indicators. A start has now been made to realize their potential.

CRUSTAL AND SUBCRUSTAL NODULES IN EJECTA FROM KILBOURNE HOLE MAAR, NEW MEXICO.

J.L. Whitford-Stark, Department of Geology, Sul Ross State University, Alpine Texas 79832.

Nodules retrieved from the ejecta of volcanic craters serve as the source of two major items of information. The first is in providing details of the geochemistry and mineralogy of the Earth's interior by supplying samples of materials that cannot be obtained by existing drilling techniques. The other is in providing information regarding the process which led to their transport from the Earth's interior to the surface.

Kilbourne Hole is one of several maars located in southeast New Mexico (Hoffer, 1976). It is elongate, approximately 3 km long and 2.5 km wide and nearly 100 m deep. The age of the maar is not well constrained. A basalt underlying the maar ejecta has yielded K-Ar whole rock ages of 141 ± 75,000 years and 103,000 ± 84,000 years. The remains of a ground sloth found in a fumarole of the nearby younger Aden lava cone are dated at 11,000 years (De Hon, 1965). The xenoliths are found within the eruptive breccia which immediately overlies the Afton Basalt flow. The breccia ranges in thickness from 15.25 m thick on the northern rim of the crater and is thin to absent on the southern rim.

The primary purpose of the present study was to examine the morphology of the nodules in an attempt to place some constraints on the process that brought them to the surface. The spinel-lherzolites and garnet-granulites from Kilbourne Hole have been the object of several geochemical studies (Padovani and Carter, 1977; Basaltic Volcanism Study Project, 1980; Irving, 1980; Padovani and Hart, 1981; Feigenson, 1986). It is not unfair to assume that the authors of those articles, and other unnamed persons, have removed a quantity of the "better" and probably larger nodules from the maar. At the other extreme, the small (less than 2 cm diameter) nodules are invariably totally enclosed by a rind of alkali basalt and are not obvious until the rock is broken open. Once the rock is broken, it is then difficult (in the field) to determine the dimensions of the nodules. The study was therefore somewhat biased in that it ignores the small nodules and is probably underrepresentative of the bigger nodules.

The primary targets for the present analysis were the spinel-lherzolite nodules since these are readily identifiable because of their color contrast with the enclosing lava and because they invariably still have a protective enveloping basaltic rind. This olivine and pyroxene phenocrystic and vesicular rind varies from less than 1 mm to about 1 cm in thickness and forms a sharp contact with the enclosed nodule.

Figure 1 presents a summary of the axial length data for over 250 nodules collected at Kilbourne Hole. Although some nodules were recovered with lengths in excess of 25 cm, the majority have long axes of about 8 cm. This distribution appears to be similar to that obtained at other maars by McGetchin and Ulrich (1973). A feature which emerged from this study is that the nodules are not circular. A straight line fit through the

data on figure 1 results in an approximate value of short axis equals 0.6 times the long axis length. This observation is important since departures from sphericity of the nodules result in changes in its drag coefficient (e.g., Komar and Reimers, 1978) - a parameter involved in the calculation of minimum flow rates.

A second feature to emerge from the study is the wide range in size of the nodules from less than 1 cm to in excess of 25 cm. The majority (68%) of the nodules, however, have long axes between 5 and 10 cm in length. Further study is needed to determine if these values reflect the initial sizes of the nodules at their point of origin, sorting and collisional effects on the way to the surface, or sorting effects within the ejecta blanket.

Dimensional and density data for representative samples of the nodules plus their basaltic rinds are presented in table 1.

Rock Type	Weight (grms)	Volume (cm^3)	Density (kg/m^3)
Pyroxenite	1786	570	3133
Spinel-lherzolite	609.5	198	3078
Gneiss	7200	2935	2453

Table 1:

References:

Basaltic Volcanism Study Project, 1980, Basaltic Volcanism on the Terrestrial Planets, Pergamon Press, N.Y. 1289 pp.

De Hon, R. 1965, Maare of La Mesa. New Mexico Geol. Soc. Guide Book, 15th Field Conf. p.204-209.

Feigenson, M.D., 1986, Continental alkali basalts as mixtures of kimberlite and depleted mantle: evidence from Kilbourne Hole Maar, New Mexico. Geophys. Res. Letters 13, 965-968.

Hoffer, J.M., 1976, Geology of the Potrillo Basalt Field, South-Central New Mexico. New Mexico Bur. Mines & Min. Res. Circular 149, 30 p.

Irving, A.J., 1980, Petrology and geochemistry of composite ultramafic xenoliths in alkali basalts and implications for magmatic processes withinn the mantle. Amer. J. Sci. 280-A, 389-426.

Komar, P.D., and Reimer, C.E., 1978, Grain shape effects on settling rates. J. of Geol. 86, 193-209.

McGetchin, T.R., and Ullrich, G.W., 1973, Xenoliths in maars and diatremes with inferences for the Moon, Mars, and Venus. J. Geophys. Res. 78, 1833-1853.

Padovani, E.R., and Carter, J.L., 1977, Non-equilibrium partial fusion due to decompression and thermal effects in crustal xenoliths. State of Oregon Dept. of Geol. & Min. Ind. Bulletin 96, Magma Genesis. p.43-57.

Padovani, E.R. and Hart, S.R., 1981, Geochemical constraints on the evolution of the lower crust beneath the Rio Grande Rift. Conf. on the Process of Planetary Rifting. Lunar and Planetary Institute, Houston, TX. p. 149-152.

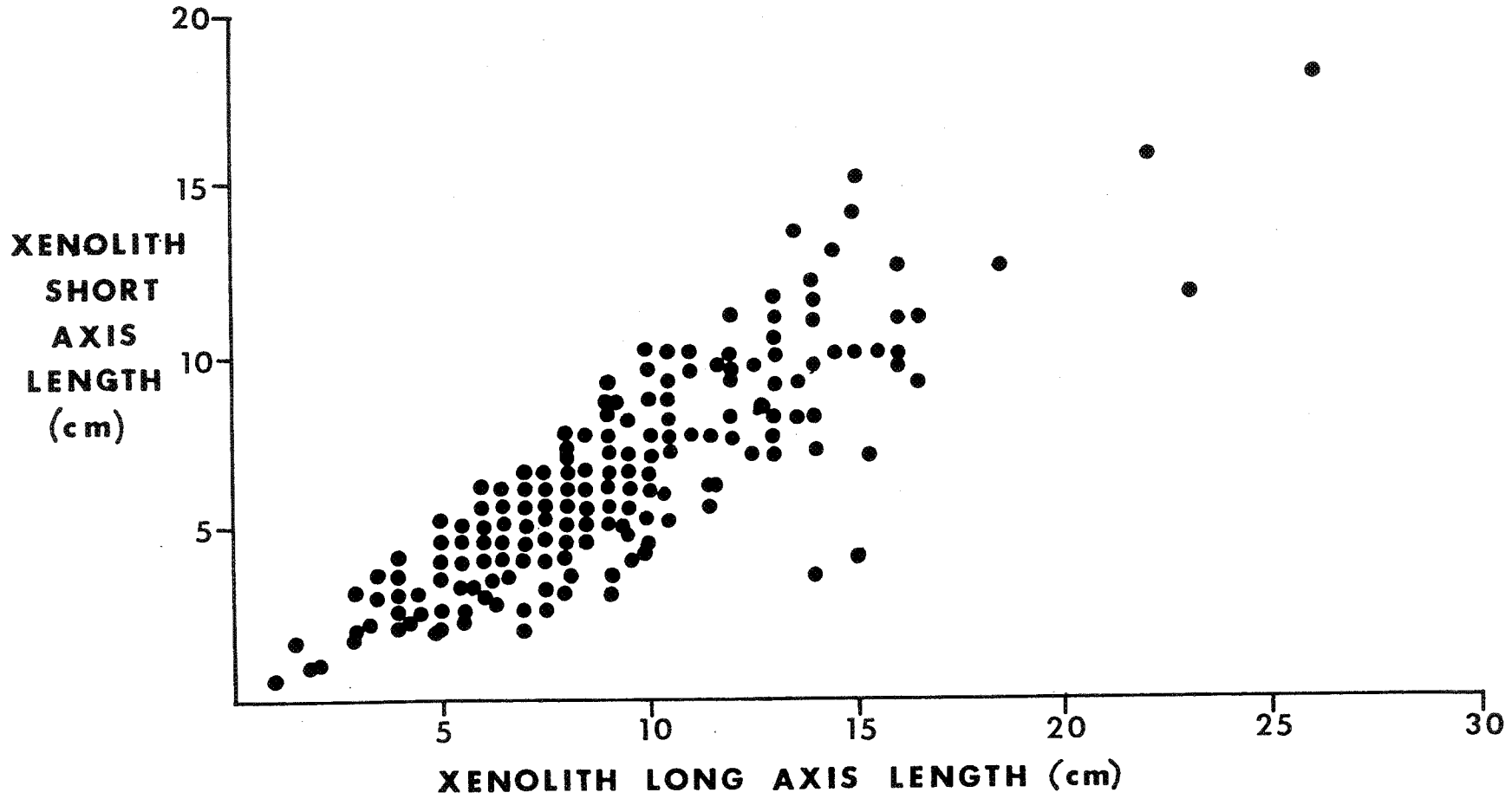

Figure 1: Axial lengths of nodules from Kilbourne Hole maar, New Mexico.

GEOLOGY OF THE MOHON MOUNTAIN VOLCANIC FIELD, YAVAPAI AND MOHAVE COUNTIES, ARIZONA: A PRELIMINARY REPORT

Ardyth M. Simmons and John S. King, Department of Geological Sciences, State University of New York at Buffalo, 4240 Ridge Lea, Amherst, New York 14226

The Mohon Mountains form the center of a volcanic field which covers a 500 km^2 area of west-central Arizona. The field consists of scattered plugs, domes, and flows that surround a central silicic complex. Mohon Mountain is the highest peak in the central vent area. It rises to an elevation of 2273 m, with 909 m of local relief above the surrounding plateau basalts and volcaniclastic covered plains.

The Mohon Mountains are located in the southern transition zone between the Basin and Range and Colorado Plateau provinces. This 100 km wide arc exhibits structural, volcanic, and petrologic characteristics of both provinces. The Mohon Mountains are bounded on the north by the Aquarius Mountains caldera. Basalts at the base of the Aquarius pile were dated by K-Ar methods at 24 m.y. (Fuis, 1974). To the west the Mohons are bounded by Precambrian granites and granodiorites of the Aquarius Cliffs. These are upwarped to the west and form a sharp boundary with downdropped Basin and Range structures along the north-south trending Big Sandy graben. To the south the Mohons are bounded by undated plateau basalts of Goodwin Mesa. The Mohon volcanic field extends eastward past Mount Hope, a rhyodacite dome that has been K-Ar dated at 8.0 ± 0.5 m.y. (Simmons, 1986). The field is bounded on the east by the basalt-capped Juniper Mountains, which include the farthest eastward exposures of Paleozoic strata in the transition zone.

The age of volcanism in the Mohon Mountains can be constrained by relationships found in Gonzales Wash in the northwestern portion of the Mohon field. Exposed in this canyon tributary of Trout Creek is 30 m of Peach Springs Tuff, a widespread ignimbrite unit with a mean K-Ar age of 18.2 m.y. (Glazner et al., 1986). The Peach Springs Tuff overlies breccias which were derived from the Aquarius Mountains to the north. It is covered by Mohon basalts and breccias. Based on the stratigraphic relationships in Gonzales Wash, the younger age of overlying Mount Hope flows to the east, and a generally younging northeastward trend of volcanics on the southern edge of the Colorado Plateau (Arney et al., 1980), the age of Mohon volcanism can be narrowed to between 18 and 9 m.y. (Mid Miocene). The Gonzales Wash section shows a conformable contact between the Peach Springs Tuff and overlying basalts so that the period of time between deposition of the Peach Springs Tuff and Mohon-derived basalts may have been geologically brief.

The Mohon Mountain vent complex was highly explosive. The 152 km^2 area of the central eruption is composed almost exclusively of tuff breccia conglomerates. Ridges are usually

capped by more resistant flow remnants. Blocks in the breccias are of two types. A plagioclase phenocryst-rich assemblage dominates to the north and west, whereas a vitric, hornblende-rich and plagioclase-poor assemblage dominates to the south and east. Both may be found in any given region, however, and they do not show a consistent stratigraphic relationship, although statistically hornblende breccia overlies plagioclase breccia. This suggests that the two types were produced by a number of pulses from the same vent or from nearby vents that tapped different portions of a magma chamber, with hornblende breccia erupting dominantly during later stages. The flow remnants mimic underlying breccia blocks in composition.

The central vent complex of Mohon Mountain is subcircular and is breached on its southern flanks by two explosively produced basins which are together believed to be the erosional remnants of the vent area. The basins are bridged by low ridges which preserve resistant plugs that were part of the internal portion of the vent. Mohon Mountain is rimmed on the north and west by peripheral endogenous domes at Black Butte, Walker Mountain, and Palomino Peak. Two other explosive vents at the southern border of Mohon Mountain produced rhyodacitic and dacitic flows and tuff breccias at Pilot Knob and Red Canyon. These domes and explosive vents are younger and produced smaller volumes of lava than those of Mohon Mountain. Before and after eruption at Mohon Mountain, tholeiitic plateau basalts were extruded from fissures in the southwestern and southeastern portions of the field, giving evidence that production of both basaltic and silicic magmas occurred throughout the period of active volcanism. Following eruption at the peripheral domes and explosive vents, alkalic megacryst-bearing basalts and basaltic andesites were extruded through numerous northwest-trending dikes and cinder cones. The last stage of activity was the eruption of ash flow tuffs from the Mount Hope vent to the east, followed by growth of the Mount Hope dome. A north-south trending graben 4.4 km wide borders the eastern flank of Mount Hope and was probably active during the final stage of activity.

Chemistries of the Mohon volcanics appear to be more similar to those found along the southern margin of the Colorado Plateau than to those in the Basin and Range. Basin and Range volcanics are characterized by bimodal assemblages of alkalic basalts and high-silica rhyolites (Suneson and Lucchitta, 1983). Most Colorado Plateau margin volcanics have chemistries mildly alkaline in basalts to calc-alkaline in more silicic rocks (Wenrich-Verbeek, 1979), although some tholeiites occur along the Plateau margin in Arizona (Simmons, 1986).

Chemical diversity in basalts may be characteristic of tectonically transitional regimes. Variation of tholeiitic and alkalic basalt, reflecting magma generation over a large depth range in the mantle, occurs in marginal areas between structural provinces. This suggests that the bounding discontinuities between provinces may extend through the crust and affect the entire lithospheric plate to influence magma generation at upper mantle depths (Lipman and Moench, 1972).

Field mapping has produced a preliminary picture of Mohon Mountain as a composite volcano, in which pyroclastic ash and larger tephra erupted alternately with flows of rhyodacite and dacite. An analog study which uses imagery of lunar and martian features will compare the overall shape of the vent complex, including its breached southern flank and satellite vents, to similar landforms found on Mars and the moon which are believed to have formed by similar processes. Ash flow sheets were hypothesized to comprise the outer slopes of Olympus Mons (King and Riehle, 1974), suggesting that explosive eruptions which are more volatile-rich than those which produce basalt flows are not confined to terrestrial settings but may also be found on bodies such as Mars, which have a thicker crust and deeper magma source in the mantle. The analog study will explore further evidence for explosive eruptions on Mars and the moon.

REFERENCES

Arney, B.H., Goff, F.E., and Eddy, A.C., 1980, Volcanic rocks of the Colorado Plateau transition zone, northern Arizona: Geol. Soc. Am. Abstr. Prog. 12, p. 266.

Fuis, G., 1974, The geology and mechanics of formation of the Fort Rock Dome, Yavapai County, Arizona: Ph.D., California Inst. of Technology, University microfilms. Ann Arbor, 274 p.

Glazner, A.F., Nielson, J.E., Howard, K.A., and Miller, D.M., 1986, Correlation of the Peach Springs Tuff, a large-volume Miocene ignimbrite sheet in California and Arizona: Geology 14, p. 840-843.

King, J.S., and Riehle, J.R., 1974, A proposed origin of the Olympus Mons escarpment: Icarus 23, p. 300-317.

Lipman, P.W., and Moench, R.H., 1972, Basalts of the Mount Taylor volcanic field, New Mexico: Geol. Soc. Am. Bull. 83, p. 1335-1344.

Simmons, A.M., 1986, The geology of Mount Hope, a volcanic dome in the Colorado Plateau-Basin and Range transition zone, Arizona: unpublished M.A. thesis, SUNY at Buffalo, 156 p.

Suneson, Neil, and Lucchitta, Ivo, 1983, Origin of bimodal volcanism, southern Basin and Range province, west-central Arizona: Geol. Soc. Am. Bull. 94, p. 1005-1019.

Wenrich-Verbeek, K., 1979, The petrogenesis and trace element chemistry of intermediate lavas from Humphrey's Peak, San Francisco volcanic field, Arizona: Tectonophysics 61, p. 103-129.

THE GEOLOGY OF PINE AND CRATER BUTTES: TWO BASALTIC CONSTRUCTS ON THE FAR EASTERN SNAKE RIVER PLAIN

Paul F. Mazierski and John S. King, Department of Geological Sciences, State University of New York at Buffalo, 4240 Ridge Lea Road, Amherst, NY 14226

Pine and Crater Buttes are two basaltic volcanic centers of the Mud Lake volcanic area which lie approximately 9 km west of the Island Park caldera complex on the Eastern Snake River Plain (ESRP). The Mud Lake volcanic area consists of extensive pahoehoe lava flows derived from a variety of local vents which vary both in structure and chemical composition. The types of vents in this region include low relief basaltic shields, spatter and cinder cones, as well as more silicic rich tuff cones (Stearns, 1938, 1926). No detailed investigations of this area have ever been conducted so the purpose of this study was to develop and describe the emplacement history and petrochemical evolution of the volcanics associated with Pine Butte, Crater Butte and other nearby vents.

The area around Pine and Crater Buttes exhibits features characteristic of basaltic "plains" type volcanism (Greeley, 1976) in which flows have been erupted from numerous local vents associated with a northwest trending rift zone. All the observed vents are small coalescing shields produced by accumulation of tube and channel-fed flows of relatively high volumes. East of the area the rift zone is a tensional crack while within the vent area where it is visible it is marked by abundant elongate spatter ramparts and spatter cones. The spatter ramparts are typically less than a meter high while the spatter cones often attain heights of over 4 meters. The spatter cones have developed around small vents where local concentration of activity along the rift set has occurred. Spatter composing the ramparts and cones consists of welded blebs of magma, ejected in a semi-fluid state.

Four major vents were identified in the study area (Figure 1) and their associated eruptive products were mapped. All of the vents show a marked physical elongation or linear orientation coincident with the observed rift set. Flows from these vents moved predominantly southwest illustrating the generally southern slope of the Snake River Plain (Greeley, 1977).

Pine Butte is an elongated low shield with two collapse pits, Pine Butte East and Pine Butte West, at its summit. Pine Butte East is approximately .28 km wide and the base of its summit crater is at an elevation of 6435 m. A distance of only 259 m separates the two craters implying that the two vents are genetically related and, for the most part, contemporaneous in age although activity did not cease at both centers simultaneously. A lack of any significant in situ exposures in the crater wall and the highly degraded character of the lava tubes and channels from the summit indicate that Pine Butte East is the older of the two craters. Pine Butte West is an elongate collapse pit approximately .26 km in width and .43 km in length with its summit crater at an elevation of 6298 m. The final eruptive activity occurred at Pine Butte West with tube

emplacement of flows to the west and southwest, away from the topographically higher Pine Butte East.

Crater Butte consists of several coalescing smaller vents including Little and Big Craters. Little Crater is an oval shaped depression which lies just east of Pine Butte along the rift set. Several major lava tube/channel systems emanate from Little Crater and can be traced for many kilometers from the source area. Exposures in the walls of collapsed tubes and channels reveal the presence of at least four eruptive episodes. Each flow exhibits a similar stratigraphy which, from top to bottom, consists of 1) a sequence of thin, gas-rich layers with abundant pahoehoe toes and small distributary tubes, 2) a fine grained massive section with vesicular flow banding, 3) a nonvesicular massive section with accumulation of olivine and plagioclase phenocrysts, and 4) a thin, undulating vesicular section at the base. Distributary tubes from the main systems, varying in size from a few tens of centimeters to a few meters in diameter, are extremely numerous and therefore played an important role in flow emplacement. The youngest eruptive episode from Little Crater represents the most recent activity of any of the major vents in this area. Big Crater is about 1 km farther east along the rift from Little Crater. Big Crater is a deep collapse/explosion pit which has a single major tube/channel system which extends over 13 km to the southeast. The 55 m deep summit pit is a result of explosive activity late in the vent's history and post-eruption collapse following withdrawal of magma from beneath the vent. Big Crater's explosive nature is manifested by the presence of a tephra ring on the southwest rim of the crater.

Planetary exploration has revealed the importance of volcanic processes in the genesis and modification of extraterrestrial surfaces. Interpretation of surface features has identified plains-type basaltic volcanism in various mare regions of the Moon and the volcanic provinces of Mars (Greeley and Schultz, 1977). Plains-type basaltic terrains are differentiated from flood basalts and shield basalts by the presence of lava tubes and channels (sinuous rilles), rift zones, and low-profile shields. Portions of the Orientale Basin including Lacus Veris and Lacus Autumni, the upper parts of Mare Imbrium, Oceanus Procellarum and many of the smaller lunar maria have been proposed as areas of plains basaltic activity (Greeley, 1976) by the presence of small, low relief constructs and a marked abundance of sinuous rilles relative to other mare regions. Small shields, often associated with rilles, have also been identified in the southeastern part of Chryse Planitia of Mars (Greeley et al, 1977) and the Marius Hills of the Moon (Greeley, 1971). Identification of these areas with features that appear analogous to those observed in the Pine Butte area suggests similar styles of eruption and mode of emplacement. Such terrestrial analogies serve as a method to interpret the evolution of volcanic planetary surfaces on the inner planets.

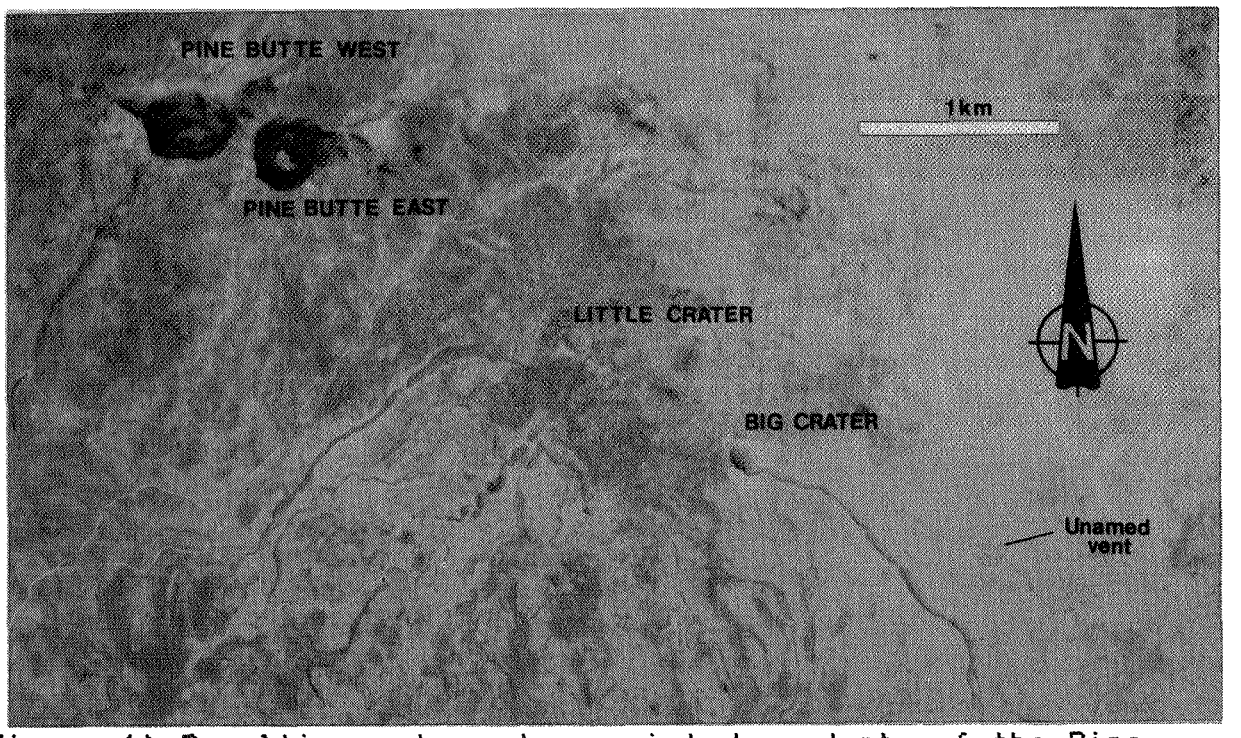

Figure 1) Basaltic vents and associated products of the Pine Butte and Crater Butte area.

REFERENCES CITED

Greeley, R., 1971, Lava Tubes and Channels in the Lunar Marius Hills, The Moon, v. 3, p. 289-314.

Greeley, R., 1976, Modes of Emplacement of Basaltic Terrains and an Analysis of Mare Volcanism in the Orientale Basin: Proc. Lunar Sci. Conf. 7th, p. 2747-2759.

Greeley, R., 1977, Basaltic "plains" volcanism, p.24-44 in Greeley, R. and J.S. King, ed., Volcanism of the Eastern Snake River Plain, Idaho: A Comparative Planetary Geology Guidebook: Prepared for the National Aeronautics and Space Administration, Washington, D.C.

Greeley, R., and P.H. Schultz, 1977, Possible Planetary Analogs to Snake River Plain Features, p. 233-251 in Greeley, R. and J.S. King, ed., Volcanism of the Eastern Snake River Plain, Idaho: A Comparative Planetary Geology Guidebook: Prepared for the National Aeronautics and Space Administration, Washington, D.C.

Greeley, R., et al, 1977, Geology of Chryse Planitia: J. Geophys. Res., v. 82, p. 4093-4109.

Stearns, H.T., 1926, Volcanism in the Mud Lake Area, Idaho: Amer. Jour. Sci., v. 11, n. 64, p. 353-363.

Stearns, H.T., 1938, Geology and Water Resources of the Mud Lake Region, Idaho: Geol. Survey Water-Supply Paper 818, 125 p.

THE GEOLOGY OF PICACHO BUTTE, A SILICIC VOLCANIC DOME IN NORTHWEST ARIZONA

Andrew P. Kisiel and John S. King, Department of Geological Sciences, State University of New York at Buffalo, 4240 Ridge Lea Road , Amherst, N.Y. 14226

Picacho Butte is a prominent physiographic feature located in Yavapai County in northwestern Arizona along the southern margin of the Colorado Plateau approximately 96 kilometers west of Flagstaff, Arizona. Picacho Butte has a local relief of 381 meters, rising to a maximum elevation of 2185 meters above sea level (fig. 1).

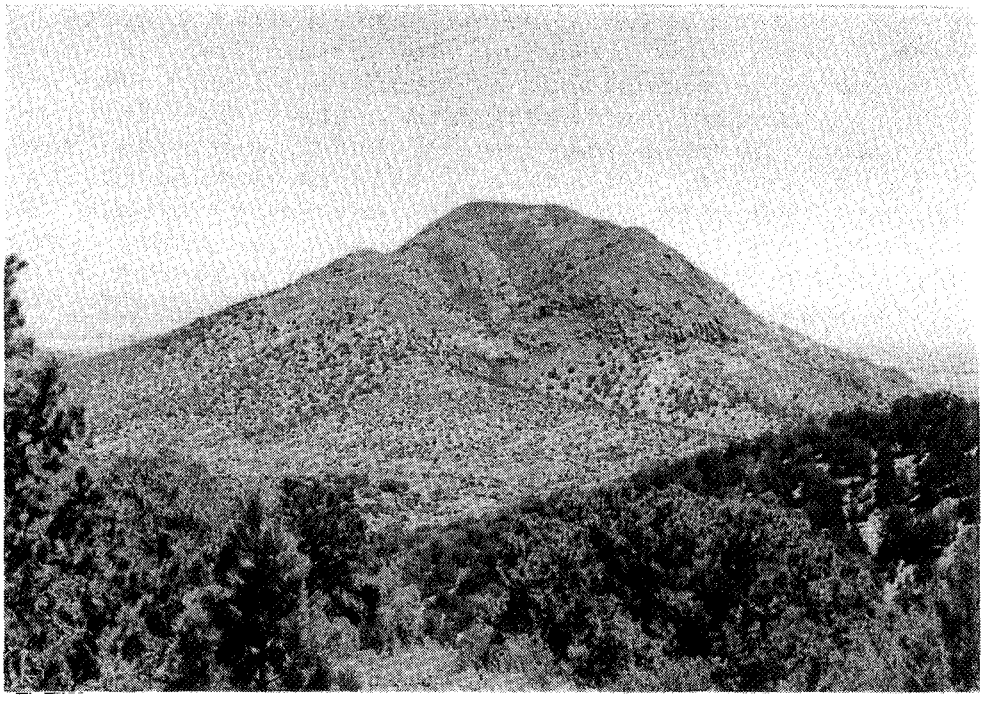

Figure 1. View of Picacho Butte to the east from 1.8 km away.

The purpose of this investigation was to determine the geologic history of Picacho Butte and vicinity through careful mapping of a 38 square kilometer area surrounding the peak. A detailed analysis of the geochemistry and petrology will aid in the development of a petrogenetic model for the area. The relationship of Picacho Butte to regional volcanism in Arizona, and more specifically to nearby volcanic centers can thus be established. Furthermore, in conjuction with this study a search will be made for possible planetary analogs exibiting photogeologic characteristics similar to those in northern Arizona.

Picacho Butte may be the oldest silicic center in the Mount Floyd volcanic field. A K-Ar age obtained by Goff and others (1983) shows Picacho Butte to be 9.8 ± 0.6 m.y. old. Mount Floyd, approximately 19 km north of Picacho Butte is 2.7 ± 0.7 m.y. old (Nealey, 1980). An apparent northward progression of silicic volcanism in the Mount Floyd volcanic field (Nealey, 1980) may be structurally controlled by zones of weakness in the lower crust, associated with a northeast and northwest lineament system traversing the Colorado Plateau (Eastwood, 1974). Faults may have been instrumental in the linear spatial relationship between some silicic centers on the southern Colorado Plateau.

Picacho Butte is a circular dome, less than two kilometers in area which has been extensively eroded. Erosion has exposed the core of the volcano, revealing a dike complex on the western side. The dike complex is comprised of pink and lavender brecciated hornblende rhyodacite flows. The dome is covered by a veneer of colluvium, shed by the volcano. Contacts between the dome and the surrounding strata are thus difficult to determine. Relatively well preserved cinder cones in the vicinity compared to the more severely eroded Picacho Butte suggests that the silicic dome is older than the surrounding basalt flows. Furthermore, no evidence exsists of silicic units overlying basalts in the map area.

Mapping indicates that the volcanic rocks are bimodal, like many late Cenozoic fields associated with the extensional tectonic regime prevelant during this time (Christiansen and Lipman, 1972). The rocks consist of olivine basalts and hornblende rhyodacites. They were classified on the basis of field relationships, color, texture, phenocryst and xenolith contents. The dome is composed of pale pink to dark pink and gray to lavender flow banded hornblende rhyodacites. Elongate hornblende needles are often aligned parallel to the flow banding. The flow banded rhyodacites contain abundant anhedral phenocrysts of plagioclase up to 3mm in diameter, as well as phenocrysts of quartz and biotite. Massive gray, lavender and pink flow breccia is found in the lower sections of the dome. The flow banded rock often grades into the massive flow breccia. Flow structures and flow folding are characteristic of the Picacho Butte silicic lavas. The rhyodacites are glassy in areas, particularly in the massive flow breccia units. The summit contains some gray and pink non-banded rhyodacites.

The dominant volcanic rocks in the area are basalts in the form of massive and vesicular flows. These basalts overlie the Pennsylvanian-Permian Supai Formation. Cinder cones, bombs and radiating dikes also occur. An eroded vent in the northwestern part of the map area has three vertical dikes intersecting an eroded exposed lava lake. The flows are typically fine to

medium grained gray to black olivine basalts with variable amounts of black clinopyroxene and extremely fine grained plagioclase phenocrysts. Flows north of Picacho Butte contain rounded xenoliths of felsic, mafic and ultramafic composition in variable amounts. In some flows they are locally abundant while in others they are rare. A basalt flow to the south of Picacho Butte older than those immediately to the north contained abundant quartz.

References Cited

Christiansen, R.L. and Lipman, P.W., 1972, Cenozoic volcanism and plate-tectonic evolution of the western United States. II.Late Cenozoic: Royal Society of London Philosophical Transactions, ser. A, v. 271, p.249-284.

Eastwood, R.L., 1974, Cenozoic volcanism and tectonism of the southern Colorado Plateau, in Geology of northern Arizona, in Pt. 1 - Regional Studies, Geological Society of America Rocky Mountain Section Meetings, p. 236-256.

Goff, F.E., Eddy, A.C. and Arney, B.,1983, Reconnaissance geologic strip map from Kingman to south of Bill Williams Mountain, Arizona: LA 9202-MAP, Los Alamos, New Mexico.

Nealey, L.D., 1980, Geology of Mount Floyd and vicinity, Coconino County, Arizona: M.S. thesis, Northern Arizona University, Flagstaff, Arizona, 144 p.

CHAPTER 11

CRATERING PROCESSES AND CHRONOLOGIES

Computer Simulations of 10-km-Diameter Asteroid Impacts into Oceanic and Continental Sites--Preliminary Results on Atmospheric Passage, Cratering, and Ejecta Dynamics

Roddy, D.J., U.S. Geological Survey, Flagstaff, Ariz.; Schuster, S.H., Rosenblatt, Martin, Grant, L.B., Hassig, P.J., and Kreyenhagen, K.N. California Research and Technology, Chatsworth, Calif.

The effects created by large asteroids and comets impacting on the Earth have generated increasing interest in a number of scientific disciplines, ranging from cratering mechanics to biological research. An intriguing idea raised in 1980 by Alvarez and co-workers and now discussed by many others is that a number of large impacts formed giant craters on the Earth and have ejected sufficient material into the atmosphere to cause major global atmospheric and biologic changes [1]. In an effort to quantify certain aspects of such impact events, we are working on a series of analytical calculations of large-scale cratering events for both oceanic and continental sites in order to examine their effects on the target media and atmosphere.

The first of our analytical studies that have been completed consists of computer simulations of the dynamics of (a) the passage of a 10-km-diameter asteroid moving at 20 km/sec through the Earth's atmosphere, and (b) the impact-cratering events in both oceanic and continental environments. The asteroid was modeled as a spherical body moving vertically downward, and the physical properties and equations of state of the asteroid, ocean, crust, and mantle were selected to represent generalized but realistic terrestrial conditions. The asteroid composition was modeled as a single generic silicate (quartz). The geologic layering was defined on the basis of V_p and V_s seismic data, and densities and thermal gradients were modeled for the target rocks. The passage of the asteroid through the atmosphere was simulated with the multiphase DICE computer code, and the impact-cratering events were simulated with the CRALE2 computer code. Both codes were chosen because of their extensive testing and calibration against a wide range of high-explosive and nuclear-explosion data.

Calculation of the dynamics associated with the passage of the asteroid through the atmosphere showed strong effects on the surrounding air mass throughout a calculational time of 30 s. During its descent, the asteroid generated a strong shock wave of hot compressed air that initially formed a narrow, conical bow wave extending back along the trajectory. After impact, this mass of shocked air expanded rapidly for tens of kilometers as a strongly heated, low-density region behind the outward-moving shock front in the air. Peak air pressures in front of the asteroid were about 0.5 Kb at 10-km altitude and reached 200 Kb at the time of impact. A large heated mass of low-density air that had peak temperatures of nearly 20,000 K formed adjacent to the uplifting crater rim and moved rapidly out from the impact area; surface fires could be expected at greater ranges if combustible materials were present. By 10 s, the low-density air still had temperatures of several thousand degrees kelvin, and extended outward in excess of 30 km and upward more than 30 km. At ranges of 200 km, the peak air velocity was estimated to be as high as 50 m/s. Calculations to 30 s showed that the air shock fronts and most of the following shocked air mass preceded the

formation of the crater, ejecta, and rim uplift in time and location and did not interact. Uplifted rim and target material were later ejected into the shock-heated, low-density air immediately above the forming crater and would interact only in this region of the expanding atmosphere.

The calculations of the impact-cratering events showed equally dramatic effects on the oceanic and continental environments throughout a calculational interval of 120 s. Early in both impact sequences, the asteroid penetrated and compressed the ocean and sedimentary rocks to about a 2-km thickness. By 10 s in both calculations, the asteroid was largely vaporized and the transient craters were about 30 km deep and about 40 km across; the oceanic impact had penetrated into mantle material that had residual temperatures of about 400 °C. At this time, transient rim uplift of ocean and crustal material exceeded 20 km in height above the original ocean level. Peak axial overpressures were about 4 Mb at the surface, 2 Mb at a depth of 5 km, 1 Mb at a depth of 10 km, and 0.25 Mb at a depth of 40 km. Increasingly strong rebound of the deeper rocks occurred after about 30 s, and the transient craters ceased to deepen below about 40 km in mantle material at about 450 °C. The transient oceanic diameter, about 60 km across at 30 s, continued to expand at a slower rate for the next 90 s. The transient rim crest of ocean and crust rose to a maximum of about 40 km at 30 s into the event. At 60 s, the transient rim stood at least 35 km above the original ocean level and was moving outward at velocities as great as 0.5 km/s. At 120 s, the transient oceanic diameter was about 105 km and the transient continental diameter was about 85 km. The massive rebound of the subcrater floor crust and mantle that started at about 30 s continued to the end of the calculational times and exhibited major inward flow and uplift. Central uplift structures are indicated in both cratering calculations. The transient rim crests were initially above the original impact surfaces, but late-stage relaxation is expected to lower the rims and produce major slump terraces and inward-dipping layers.

At 120 s, the target materials that surrounded the crater floors and walls were responding largely to gravitational relaxation, but still had material velocities ranging from 5 to 50 m/s. The final transient-crater motions, coupled with certain explosion and impact-crater analogs, lead us to tentatively estimate that the final oceanic crater will have a diameter on the order of 120 to 150 km and a depth of less than 10 km, coupled with central uplift and/or multiring uplift structures; the final continental crater is tentatively estimated to have a diameter of about 100 to 120 km and a depth of less than 10 km. More than 7×10^4 km^3 (10^{14} metric tons) of target material was ejected (no mantle) and would have formed a massive ejecta blanket surrounding the cratered areas. If scaling holds from other large explosion and impact-crater field data, more than 70% of the ejecta should lie within three crater diameters of the impact points. The remaining ejecta, including most of the asteroid material, would reside both at different altitudes in the atmosphere as high as the ionosphere and at extended ground ranges. The uplifted hot crustal/mantle rocks would cover about 15×10^3 km^2 of the inner-crater floor and, depending on their volatile content, may degas violently and add ash to the atmosphere that

potentially could exceed the ejecta contributions. Other cratering processes that require additional study include such effects as late-stage crater relaxations, ejecta/atmosphere interactions, ejecta distributions in atmosphere, return flow of ocean, tsunamis, long-term induced volcanism, and numerous other late-stage effects.

Reference

[1] Alvarez, L.W. Alvarez, W., Asaro, F., and Michel, H.V., 1980, Extraterrestrial cause for the Cretaceous-Tertiary extinction: Science, v. 208, p. 1095-1108.

IMPACTS OF HEMISPHERICAL GRANULAR TARGETS: IMPLICATIONS FOR GLOBAL IMPACTS. P.H. Schultz, Dept. of Geological Sciences, Brown University, Providence, RI 02912, D.E. Gault, Murphys Center of Planetology, P.O. Box 833, Murphys, CA 95247 and D. Crawford, Dept. of Physics, Brown University, Providence, RI 02912.

Introduction: As impact excavation diameters subtend a nontrivial fraction of a planetary body, both the excavation process and ejecta emplacement may depart from the classical description of impacts into a planar surface. Hemispherical particulate targets were impacted at the NASA-Ames Vertical Gun Range in order to trace the evolution of the ejecta curtain and to document the effects of slope and surface curvature on crater shape and cratering efficiency.

Experiments: The cratering process in low-strength granular sand targets have been extensively studied over the last two decades. Unfortunately such targets have such little strength that hemispherical surfaces are difficult to construct without a bonding agent that results in spallation and an ejecta curtain with only a few large fragments. Compacted pumice has been used successfully for a variety of studies (1,2) and possesses sufficient shear strength to maintain steep slopes while behaving as a reasonably low-strength particulate material upon impact. Hemispherical targets were constructed by compressing pumice with a mold on a pumice base. The pumice base minimized unwanted effects produced by shock reflections from materials with contrasting strength. Both 0.318 cm and 0.635 cm velocities aluminum spheres impacted the hemispheres with 1.9-2.3 km/s. In addition, a ledge was created in two experiments in order to examine the effects of slope on the ejecta plume.

Results: Four significant findings can be cited. First, the ejecta plume maintains an angle of about 45^{o} from the local surface during most of crater excavation. Consequently, the ejecta plume appears to decrease with respect to the horizontal on a curved surface or changes dramatically as it crosses a stepped surface. Second, the ejecta curtain after excavation maintains an approximate constant angle with respect to the horizontal. As a result, the ejecta curtain meets the surface at increasingly steeper angles away from the point of impact (Figure 1). Third, cratering efficiency (displaced mass/projecticle mass) in a hemispherical target is greater than a plane-surface crater but approximately matches the plane surface case if the displaced mass above the chord from rim-to-rim (apparent rim) is ignored. Fourth, the diameter/depth ratio referenced to the pre-impact curved surface is greater than the ratio for planar surface impact.

Discussion: The uniformly downward-directed gravity vector in the experiment is unlike the radially inward vector for a planetary body. Previous experiments at high (3) and low (4) gravitational fields suggest that the gravity vector does not modify the cratering flow field but only limits crater growth. Consequently, the experiments may have a direct bearing on excavation and shape and efficiency of craters whose diameters subtend a significant fraction of planetary curvature. Moreover, it is believed that during excavation, the ejection angle (and therefore plume angle) near the surface is approximately constant. The experiments indicate that the ejecta curtain after excavation meets the curved surface

at increasing angles, and the effect of a radially inward gravity vector can be examined by theoretically modeling the ejecta curtain under laboratory and planetary conditions. The cratering flowfield follows the approach in (5) where ejection velocity decreases a $(X/R)^{-3}$ with X/R representing the fractional stage of growth of a crater with final apparent radius, R. Additionally, the crater is assumed to grow as $(X/R)^4$ over most of its late stages. Although such a model does not provide an accurate description throughout the entire growth of a crater, it suffices for comparing the contrasting laboratory and planetary gravitational fields. Figure 2 reveals that the effect of the inward-direct g-field increases the angle between the surface and ejecta curtain. For the Moon, the ejecta curtain becomes vertical at a distance of nearly 1200 km for a relatively small crater (D< 200km). A basin-size impact (D~600km) requires shifting the curve laterally, thereby preserving the constant ejection angle, with respect to the surface, and results in a vertical ejecta curtain at a distance of about 1400 km.

Implications: The experiments suggest that basin-size impacts or large craters on small bodies may be shallower than their counterparts on a planar surface but may have displaced a larger relative mass. Moreover, the increased ejecta curtain angle with distance may result in a change in ejecta emplacement style with distance. Although the ejecta curtain is vertical, ejecta within the curtain impact the surface at 45° and the time between first and last arrival within the curtain increases. This increased interaction time as the ejecta curtain density decreases should result in a more chaotic style of emplacement, perhaps accounting for the transition in ejecta facies surrounding the Imbrium basin noted in (6).

(1) Schultz, P.H. and Gault, D.E. (1985) J. Geophys. Res., 90, 3701-3732. (2) Schultz, P.H. and Gault, D.E. (1984) Lunar and Planetary Science XV, 732-733. (3) Schmidt, R.M. (1984) Lunar and Planetary Science XV, 722-723. (4) Gault, D.E. and Wedekind, J. (1977) In Impact and Explosion Cratering (Roddy et al., eds), p. 1231-1244, Pergamon, NY. (5) Schultz, P.H. and Gault, D.E. (1979) J. Geophys. Res. 84, 7669-7687. (6) Spudis, P.D. (1985) Workshop Apollo 15, Lunar and Planetary Institute, Houston, TX.

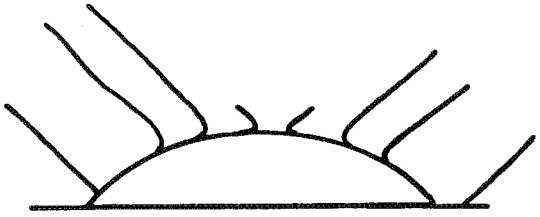

Figure 1. Evolution of ejecta curtain at 2.5, 62, 125, and 188 ms for a 2.3 km/s impact into a hemispherical target of compacted pumice with a diameter of 37 cm.

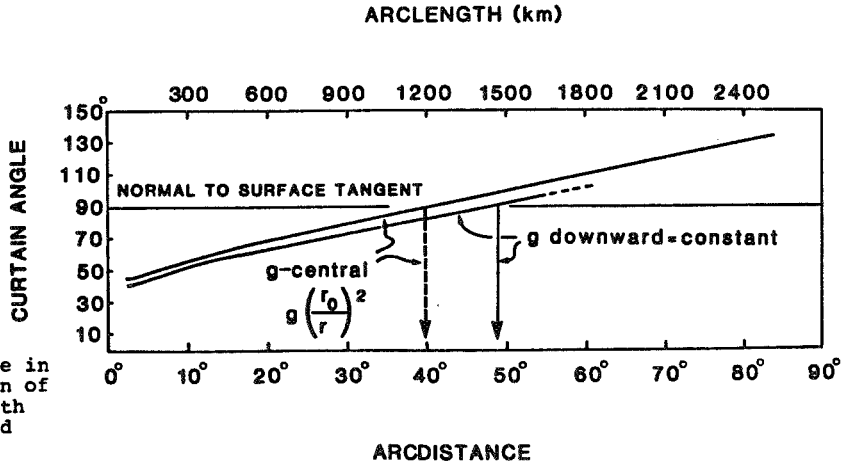

Figure 2. Comparison of the change in ejecta curtain angle as a function of arcdistance (degrees) and arclength (Moon) for planar (g downward) and planetary (g inward) cases.

IMPACT VAPORIZATION: LATE TIME PHENOMENA FROM EXPERIMENTS P.H. Schultz, Dept. of Geological Sciences, Brown University, Providence, RI 02912, D.E. Gault, Murphys Center of Planetology, P.O Box 833, Murphys, CA 95247.

Previous experiments revealed an increase in impact vaporization for volatile-rich targets (dry-ice) with decreasing impact angle and increasing atmospheric pressure as documented by high frame-rate (35,000 fps) images of the self-luminous ionized vapor cloud. These experiments have continued at the NASA-Ames Vertical Gun Range in order to investigate the following processes: (a) effect of vaporization on late-time ejecta dynamics; (b) atmospheric response revealed by quarter-space experiments with airflow indicators; and (c) the effect of impact vaporization on cratering efficiency, crater aspect ratio, and ejecta emplacement. Aluminum (0.635 cm-diameter) spherical projectiles and lexan cylinders (.31 x .31 cm) impacted into a 1 cm layer of dry-ice powder overlying a granular substrate with velocities from 2.3 to 6.3 km/s.

Ejecta Curtain Evolution: Vertical impacts into dry-ice powder overlying No. 24 sand under near-vacuum conditions (5 mm Hg) produced no observable self-luminous ionized cloud at 35,000 fps (1). Slower framing rates (5800 fps) have revealed, however, a blue vertical spike within the first 0.17 ms of a 5.8 km/s impact that was not previously visible. An ionized blue vapor cloud subsequently rose at 800 m/s while expanding at 300 m/s. This ionized cloud disappeared after 0.34 ms, evolving into a non-luminous expanding cloud preceding the ejecta curtain and scouring the pre-impact surface. The ejecta curtain behind the expanding cloud formed the classical funnel-shaped profile although the curtain angle at early stages was less than 30^{o}. At lower impact velocities (1.8 km/s), a spherically expanding non-luminous cloud rose above the impact. For both events, the early-time expanding cloud had no obvious effect on late-time curtain development, which was indistinguishable from a nominal impact under vacuum conditions.

Under atmospheric conditions (700 mm Hg, Argon), a 5.9 km/s (launch velocity) into dry-ice produced a brilliant self-luminous ejecta cloud that became opaque after 1.6 ms. The rising ionized ball observed at 35,000 fps was invisible due to exposure saturation and slow frame rate. The ejecta curtain was distinctly more distorted (convex-outward) than the curtain for impacts into No. 24 sand without the dry-ice layer. Late-time curtain evolution, as under vacuum conditions, did not reflect the early-time interactions.

Atmospheric Response: A plexiglass sheet adjacent to the projected impact point revealed the interior of the growing ejecta curtain. Flexible black and white yarn spaced 10 cm apart and 5 cm apart on either side of the impact point provided a record of the airshock passage and the airflow behind the advancing ejecta curtain. These experiments used 0.31 x 0.31 cm lexan cylinders impacting pumice with and without dry-ice at about 5.0 km/s (launch velocity) under 395 mm Hg of Argon.

Without dry-ice, passage of the airshock was detected by the tracers and dissipated rapidly prior to the growth of the ejecta curtain. Movement of the airflow tracers revealed the vertical airflow behind the outward-moving ejecta curtain inferred in previous studies (2). Barocells also recorded

the decrease in atmospheric pressure immediately behind the advancing ejecta curtain. With dry-ice powder, a very different response was recorded. A hemispherically expanding "bubble" inside the ejecta curtain expanded at 120 m/s above the crater. The self-luminous projectile wake moving downward, also at 120 m/s, disappeared as it encountered the bubble.

Ejecta Emplacement: Late-time curtain evolution was not modified by early-time impact-vaporization. This observation was further confirmed by the nominal distribution of ejecta for impacts into sand. An impact into dry-ice on pumice under 0.25 P_o produced the previously reported continguous rampart, which is a response to late-time airflow produced by the advancing ejecta curtain (2).

Cratering Efficiency and Crater Shape: The presence of a near-surface layer of dry-ice did not affect cratering efficiency or the crater aspect ratio under vacuum conditions for vertical impacts into dry-ice. Although cratering efficiency for impacts into pumice was relatively unaffected, the diameter-to-depth ratio increased to 12. The presence of an atmosphere significantly reduces cratering efficiency for impacts into compacted pumice (3), and only by 30% for impacts into No. 24 sand. Impact vaporization, however, raises these values to nominal vacuum conditions. The aspect ratio for impacts into sand and pumice were increased, relative to values without dry-ice. The most significant effect occurred for oblique impact (15^o) into sand under vacuum conditions. Efficiency was more than double the value of an impact into sand without dry-ice, and the aspect ratio increases from about 4.3 (without dry-ice) to 5.3 (with dry-ice). These results are consistent with the previous observations from the high frame-rate photographs (35,000 fps) that indicated little vaporization for vertical impacts in a vacuum but increased vaporization for oblique impacts or impacts under atmospheric conditions. To this observation should be added the apparent decoupling between vapor and crater growth under vacuum conditions (the vapor phase rising rapidly above the event).

Concluding Remarks: While simple airflow produced by the outward movement of the ejecta curtain can be scaled to large dimensions (4), the interaction between an impact-vaporized component and the ejecta curtain is more complicated. The goal of these experiments was to examine such interaction in a real system involving crater growth, ejection of material, two-phased mixtures of gas and dust, and strong pressure gradients. The results will be complemented by theoretical studies at laboratory scales in order to separate the various parameters for planetary-scale processes. These experiments prompt, however, the following conclusions that mayhave relevance at broader scales. First, under near-vacuum or low atmospheric pressures, an expanding vapor cloud scours the surrounding surface in advance of arriving ejecta. Second, the effect of early-time vaporization is relatively unimportant at late-times. Third, the overpressure created within the crater cavity by significant vaporization (oblique impacts, atmospheric conditions) results in increased cratering efficiency and larger aspect ratios.

References: (1) Schultz, P.H. and Gault, D.E. (1985) Lunar and Planetary Science XVI, 740-741, Houston; (2) Schultz, P.H. and Gault, D.E. (1984) Lunar and Planetary Science XV, p. 732-733, Houston; (3) Schultz, P.H. and Gault, D.E. (1983) Lunar and Planetary Science XIII, p. 694-695, Houston; (4) Schultz, P.H. and Gault, D.E. (1981) in Geol. Soc. Amer. Sp. Paper 190, p. 153-174.

OBLIQUE IMPACT: PROJECTILE RICHOCHET, CONCOMITANT EJECTA, AND MOMENTUM TRANSFER: Donald E. Gault, Murphys Center of Planetology, Box 833, Murphys, CA 95247 and Peter H. Schultz, Dept. Geolog. Sciences, Brown University, Providence, R.I. 02912

Experimental studies of oblique impact (1) indicate that projectile ricochet occurs for trajectory angles less than 30 and that the ricocheted projectile (fragments), accompanied by some target material, are ejected at velocities that are a large fraction of the impact velocity. Because the probability of occurrence of oblique impacts less than 30° on a planetary body is about one out of every four impact events, oblique impacts would seem to be a potential mechanism to provide a source of meteorites from even the largest atmosphere-free planetary bodies (Ceres, Moon, Mars?).

Because the amount of "richocheted" target material cannot be determined from results in (1), additional experiments in the Ames Vertical Gun have been undertaken toward that purpose using pendulums, one to measure momentum of the richocheted projectile and concomitant target ejecta, and a second to measure the momentum transfered from projectile to target. Witness plates downrange from the point of impact provide a basin for estimating the velocities of the projectile fragment(s). The current results are limited to targets of #24 sand, aluminum and pyrex spheres, with velocities ranging from Vi = 1 - 8 km/s and impact angles from 7.5° to 45°. Pendulum motions are recorded on high frame-rate video (200 fps) and movie (400 fps) cameras.

The current results indicate that for increasing angle of impact the mass of "ricocheted" target material also increases but the ejection velocity decreases. For impact at 7.5° the aluminum projectile fragments ricocheted with a mean velocity of 0.82 Vi and were accompanied with target material in excess of 0.27 of the projectile mass. At 15° and 30° angles, velocity and target mass fractions are 0.55 and >0.65, and 0.2 and >2.0, respectively. Target masses with pyrex projectiles may be even greater. These preliminary results support oblique impacts as a source of meteoritic material, but the physical condition (i.e. shock state) of the ejecta remains an uncertainty that must be addressed before any final conclusions can be reached.

The momentum transfer efficiency, as noted in (2,3) is significantly less than the 50 - 100% commonly believed. For aluminum spheres the efficiency decreases with increasing velocity and increases with increasing impact angle; from 12% at 1 km/s to 8% at 6 km/s for 15° impacts; from 27% at 2.3 km/s to 17% at 5.3 km/s for 30°; and 34% at 5.5 km/s for 45°. An intriguing observation is that after impact (<10 ms) there is consistently a very small uprange displacement of the target pendulum before the initiation of the large, final downrange movement that occurs during the time for completing crater formation (<100 ms). It is speculated that the uprange motion is triggered by the momentum transfered during the time interval of projectile impact and richochet which is then cancelled by a much larger down-range momentum component during crater formation and the return of the main mass of ejecta to the target surface. This suggests that for oblique impacts for which most or all ejecta escapes from the planetary body the momentum

transfer is negative (i.e., uprange direction) and would tend to cause the body to rotate "against" the direction of the trajectory of the impacting projectile. Further experiments are required to clarify these results and to examine any effects of curvature of the target surface.

(1) Gault, D.E. and Wedekind, J.A. (1978) Proc. Lunar Planet. Sci. Conf., 9th, p. 3843-3875. (2) Davis, D.R. and Weidenschilling, S.J. (1982) Lunar and Planet. Sci. XIII, P. 740-741. (3) Schultz, P.H. and Gault, D.E. (1986) Lunar and Planet. Sci. XVII, p. 781-782.

MOMENTUM TRANSFER FROM OBLIQUE IMPACTS. P.H. Schultz, Dept. of Geological Sciences, Brown University, Providence, RI 02912, D.E. Gault, Murphys Center of Planetology, P.O. Box 833, Murphys, CA 95247.

Background: The transfer of momentum during an impact and the fraction of impactor momentum that can change the angular momentum of a planetary body affects the spin rates of asteroids and comets as well as the evolution of angular momentum for larger planetary bodies (Earth-Moon, Venus?). Most existing data describe momentum transfer from impacts into brittle material, thereby resulting in large spall fragments (1,2,3). This may not be an appropriate model since asteroid surfaces probably have a regolith and since sufficiently large events result in shock comminution prior to excavation. Consequently, use of granular targets provide a better analogy for large events. Moreover, recent experiments revealing significant vaporization at low impact angles (4) would lead to the prediction of a momentum component in the opposite sense, i.e. uprange. A completely satisfactory experiment would be in a low gravity environment where the effect of momentum imparted by ejecta impacting the surface can be removed or controlled from momentum transfer during impact (5). Nevertheless, preliminary estimates can be made using a ballistic pendulum. Such experiments were initiated at the NASA-Ames Vertical Gun Range in order to examine momentum transfer due to impact vaporization for oblique impacts, but during calibration, intriguing new results have been obtained for non-volatile targets.

The impact experiments involved a physical (compound) pendulum using a small sand-filled target free to swing on a platform suspended by four wires. The targets consisted of No. 24 sand and dry-ice blocks/powder; the projectiles included aluminum, lexan, pyrex, and pyrex clusters. Impact velocities ranged from 1 to 8 km/s with impact angles from 15 to 45°. An apron surrounding the pendulum (but not attached) decreased the effects of momentum added by the deposition of ejecta. Successive mylar diaphragms minimized any possible effect of muzzle blast. A high frame-rate (200 fps) video camera system provided both vertical and side real-time views and was complemented by a higher resolution film record at 400 fps.

Results: Initial analysis reveals that the measured efficiency of momentum transfer (target-momentum/impactor-momentum) for 15° impacts is typically below 12% at hypervelocities (> 4km/s), a value significantly lower than the 50% - 100% commonly cited (2,6). This surprisingly low efficiency is largely the result of the impactor ricocheted downrange as previously documented (8,9). Aluminum witness plates positioned downrange from the point of impact recorded both the dispersion and angle of ricocheted fragments and are currently undergoing analysis in order to determine the total energy lost by this process.

Momentum transfer efficiency (k) appears to decrease with increasing velocity: from 12% at 3 km/s to less than 8% at 6 km/s from 0.635 cm-diameter aluminum spheres. Preliminary data further indicate that the value of k increases with impact angle: about twofold from 15° to 30°. This trend is consistent with the observation that less projectile material is ricocheted downrange with increasing impact angle. There also may be projectile size and density effects where decreasing projectile size and density increases k; however, additional experiments are necessary.

Finally, easily volatized target material appears to increase downrange momentum transfer although this effect may yet be due to other factors. Momentum transfer typically is initiated prior to completion of crater formation (100 ms) and, therefore, before ejecta emplacement. However, there consistently appears to be a very small uprange component immediately (<10 ms) after impact.

Discussion and Implications: The preliminary results indicate that momentum from oblique impacts is very inefficient: decreasing with increasing impact velocity and perhaps size; increasing with decreasing density; and increasing with increasing impact angle (from horizontal). At face value, such results minimize the effect of momentum transfer by grazing impacts; the more probable impact angles of 30^{o} would have a greater effect, contrary to the commonly held impression. The process of momentum transfer, however, may involve two opposing components. Although the asymmetric distribution of ejecta during emplacement imparts momentum downrange, the ejection process should result in an initial momentum component uprange prior to emplacement. A small uprange motion has been tentatively identified, but the inertia of the ballistic pendulum is relatively large. The dominating effect of subsequent ejecta emplacement can mask this brief uprange component. On planetary bodies where the near-rim ejecta are retained (small bodies or large events on large bodies), momentum transfer is likely to be less than 10%. It is conceivable, however, that momentum transfer for small objects may not only be less than 10% but even in a negative sense. Consequently, until these competing responses have been defined, we must approach applications with caution.

Further experiments are necessary in order to confirm the observed preliminary trends and to test the limits of application. Ongoing complementary studies of ejecta distribution for oblique impacts (9) may help to resolve the competing roles of ejection and ejecta emplacement. Controlled experiments under a low-g environment, however, would permit evaluating the effects in absence of ejecta emplacement and more subtle phenomena damped by pendulum systems yet relevant to producing angular momentum in planetary objects.

References: (1) Gault, D.E. and Heitowit, E.D. (1963) Proc. of Sixth Hypervelocity Symposium, 2, pp. 419-456, Firestone Rubber Company, Cleveland, Ohio. (2) Davis, D.R. et al. (1979), in Asteroids (T. Gehrels, ed.) U. Arizona, Tucson, p. 528-557. (3) Davis, D.R. and Weidenschilling (1982) Lunar and Planetary Science XIII, p. 142-143. (4) Schultz, P.H. and Gault, D.E. (1985) Lunar and Planetary Science XIII, p. 740-741. (5) Schultz, P.H. and Gault, D.E. (1985) in NASA Workshop on Space Station Planetology Experiments, p. 68-69, LPI Houston. (6) Harris, A.W. (1977) Icarus 40, 168-174. (7) Gault, D.E. and Wedekind, J. (1978) Proc. Lunar Planet. Sci. Conf. 9th, 3843-3875. (8) Hartmann, W.K. (1981) Lunar and Planetary Science XII, p. 398-400. (9) Davis, D.R. (1985) personal communication.

EXPERIMENTAL STUDIES OF COLLISION AND FRAGMENTATION PHENOMENA

William K. Hartmann, D.R. Davis, S.J. Weidenschilling
Planetary Science Institute, Tucson, Arizona

Current work on this project is focusing on reduction and publication of an extensive data set collected in experiments over several years at Ames Research Center and PSI. Eileen Ryan, graduate student in geology, is assisting in the data reduction program, which involves measurements from our films and computer data reduction.

Hartmann has been assembling data sets from his experiments on catastrophic fragmentation of various materials, including basalt, other igneous rock, ice, and weak dirt clods. Measurements were made on the size of the largest fragments surviving after targets were struck at various velocities, energies, and projectile sizes. Early studies suggested that for target and projectile of the same material, half the impact energy went into each body. Assuming the energy density (joules/kg) from this result, we find an excellent correlation between the energy density and the size of the largest fragment scaled to original target mass. This result is shown in Figure 1, a computer plot newly derived from our data for ice. Hartmann pioneered such plots (WKH, Icarus 33, 50, 1978), which have recently been widely used to study fragmentation phenomena (see report of workshop on catastrophic disruption, Mem. Soc. Astr. Italiana 57, 1986, ed. D. Davis et al.). Such data sets will be important in studying solar system collision regimes, from small particle collisions in rings to collisions between large asteroids.

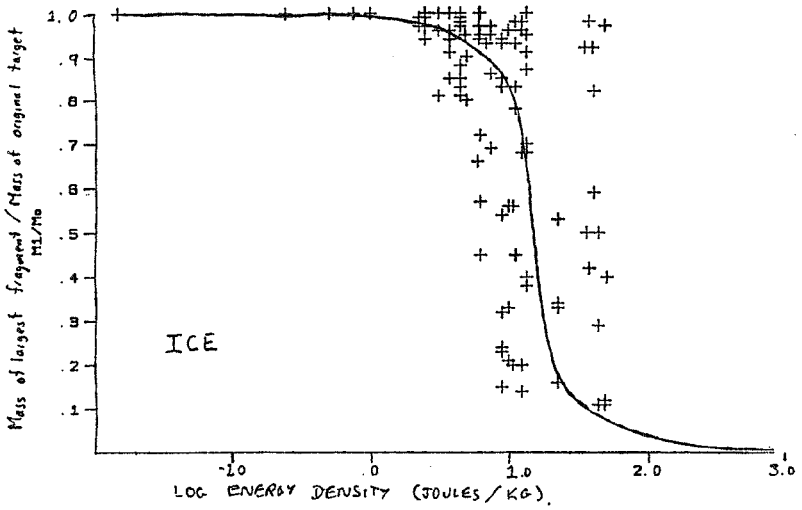

Figure 1. Plot of experimental data on collisional energy density vs. mass of largest surviving fragment (scaled to original target mass). Solid curve shows transition from rebound and chipping regime (upper left, negligible mass loss) to catastrophic pulverization (lower right, largest fragments less than a few percent of original mass).

Weidenschilling and Davis have continued to gather and reduce data on oblique impacts. Preliminary results were presented at LPSC 1986 (SJW and DRD, Lunar Planet. Sci. XVII, 931). The data indicate a power-law distribution of ejecta mass vs. velocity, with a slope that is independent of azimuth, and does not vary with impact angle from normal impacts to at least 75° from vertical. Thus, a single relation can characterize ejecta velocities for the vast majority of impacts on solar system bodies. The total ejecta mass and the azimuthal distribution vary with impact angle. The degree of asymmetry in the ejecta blanket depends on impact velocity; in principle, this might be a means of distinguishing low-speed and high-speed impacting populations. The measured ejecta distributions refer to the low-velocity component that forms the continuous blanket out to $\leq$ 10 crater radii; the higher-velocity ejecta cannot be collected due to the limited size of the AVGR chamber. The net transverse momentum of the recovered ejecta accounts for $\leq$ 5% of the projectile's momentum. Earlier studies with a ballistic pendulum (DRD and SJW, Lunar Planet. Sci. XIII, 142, 1982) indicated only a tens of % of transverse momentum imparted to the target. It seems probable that most of the incident transverse momentum is carried off by a small fraction of the ejecta mass that forms a high-velocity "jet." To study this phenomenon, SJW performed a series of shots in 1986 with paper "witness sheets" downrange to record the angular distribution of high-speed ejecta. These impacts were also filmed with two high-speed Nova cameras; one viewing crossrange, and the other using a mirror to provide an effective view directly downrange. These data are still being analyzed.

In order to improve models of coagulation of dust aggregates in the solar nebula (SJW, Icarus 60, 553, 1984), SJW developed an apparatus for drop tests of fragile "projectiles." A dust charge is released from a spherical container by a solenoid. In vacuo, the cohesion of dust yields a coherent dust-ball impactor. Preliminary tests of this apparatus have demonstrated its feasibility, and will be used to plan protocols for imaging and ejecta collection in future experiments.

Davis and Weidenschilling continued to collect and analyze experimental data on collisional catastrophic disruption at the Ames Vertical Gun Range. Results of this program were presented at LPSC XVII, p. 156, 1986 and at the Pisa Workshop on Catastrophic Disruption, 1985. Our experimental program is designed to obtain data on the outcome of catastrophic collisions, particularly on the fragmental size and velocity distribution for a wide range of impact conditions. Of great importance is the velocities of fragments which determine whether or not ejecta can escape the gravitational binding of the larger, target body. Our goal is to construct an experimental database on the impact conditions that result in catastrophic disruption for a variety of solar system materials (e.g. silicate rocks, ices, iron-nickel bodies, etc.) and physical condition (e.g., coherent uniform bodies, weakly consolidated bodies, regolith covered cores, differentiated bodies, etc.), and to determine the fragment mass and velocity distributions for the collisional outcomes.

We have carried out impact experiments using targets of basalt, conglomerate rocks, ice-sand mixtures and concrete. Most of our shots have been using concrete mortar targets which are thought to be a reasonable analogue of silicate rocks found in the solar system. Mortar allows the strength of the target to be readily controlled over more than an order of magnitude and also permits construction of target bodies having different physical properties in their interior, i.e. simulated differentiated bodies.

The mortar targets were found to have a different disruption mode than do the basalt spheres used by Fujiwara (Fujiwara et al., Icarus 41, 277, 1977). The mortar spheres break up into sector or conical-shaped fragments, rather than spallation breakup leading to core-type disruption characteristic of the way basalt spheres fail in high-speed (~2-3 km/s) impacts. On the other hand, Matsui et al., LPSC XIII, 475, 1982, found that basalt targets broke up into sector-like fragments by low velocity impacts (tens to hundreds of m/s). The different types of failure may be due to the differences in the rise time of the stress pulse (Melosh, Geology 13, 144, 1985). Further work is in progress to understand both the origin and implications for different failure modes of material at different impact speeds.

Velocities of individual fragments have been determined from high-speed camera films of the disruption event. These fragments compose 60-70% of the mass of the target body for the barely catastrophic shots -- hence the bulk of the mass of a marginally disrupted target travels at speeds around 5 m/s for impact speeds ~1-2.5 km/s. Thus the mean ejecta speed is around 1% of the collision speed for the majority of the mass of the target body. There is also a trend toward higher fragment speeds with increasing collisional energy density: barely catastrophic impacts have the lowest mean fragment speed (~5 m/s), while a super-catastrophic impact, produces mean fragment velocities around 13 m/s.

We now compare our results on ejecta velocities with those found by Fujiwara and Tsukamoto Icarus 44, 142 (1980) and Waza et al, JGR 90, 1995 (1983). Fujiwara and Tsukamoto found that the bulk of the target mass (70-80%) travels at less than twice the antipodal fragment speed which varies from ~5 m/s to ~9 m/s between barely catastrophic and very catastrophic collisional outcomes. The impact speed was 2.5 km/sec. These results are not inconsistent with our results for similar impact speeds.

Waza et al (1983) measured fragment speeds for low velocity (tens to hundreds of m/s) impacts of both steel and basalt projectiles into basalt targets and found significantly higher fragment speeds for basalt fragments than those reported by Fujiwara and Tsukomoto -- typically 20-30 m/s for the bulk of the target mass. These fragment speeds are significantly higher than those found for the concrete targets, which is of interest since the failure mode of the concrete sphere is more like that for the low speed impacts on basalt targets than for the high speed ones.

Centrifuge Impact Cratering Experiments: Scaling Laws for Non-Porous Targets

Robert M. Schmidt Boeing Aerospace Co., M/S 3H-47, P. O. Box 3999, Seattle WA 98124.

A geotechnical centrifuge has been used to investigate large-body impacts onto planetary surfaces. At elevated gravity, it is possible to match various dimensionless similarity parameters which have been shown to govern large-scale impacts. Observations of crater growth and target flow fields have provided detailed and critical tests of a complete and unified scaling theory for impact cratering. Current work is directed toward the determination of scaling estimates for non-porous targets. Scaling estimates for large-scale cratering in rock proposed previously by others have assumed that the crater radius is proportional to powers of the impactor energy and gravity, with no additional dependence on impact velocity. The energy exponent is typically reported to be 0.28 to 0.29 while estimates of the gravity exponent range from 0.11 to 0.17. The size scaling laws determined from ongoing centrifuge experiments differ from earlier ones in three respects. First, a distinct dependence of impact velocity is recognized, even for constant impactor energy. The effects of velocity are smallest for nonporous targets, which approach (but do not reach) the asymptotic case of pure energy scaling. The porosity of materials like dry sand result in velocity-dependent energy losses. Hence, the velocity dependence is greatest for these materials. Second, the present energy exponent for low-porosity targets, like competent rock, is lower than earlier estimates. Although the difference might appear to be small (the present estimate is 0.26 versus the values of 0.28-0.29 mentioned above), the effect of this difference can be significant when extrapolating many orders of magnitude in energy up to kilometer-sized craters. Third, the gravity exponent is recognized here as being related to both the energy and the velocity exponents.

IMPACT CRATER SCALING LAWS

K.A. Holsapple, University of Washington
Seattle, WA 98195
November, 1986

Impact craters are numerous on planetary bodies and furnish important information about the composition and past histories of those bodies. The interpretation of that information requires knowledge about the fundamental apects of impact cratering mechanics. Since the typical conditions of impacts are at a size scale and velocity far in excess of experimental capabilities direct simulations are precluded. For that reason, one must either rely on extrapolations from experiments of relatively slow impacts of very small bodies, using physically based scaling laws, or must study the actual cases of interest using numerical code solutions of the fundamental physical laws that govern these processes.

This is a progress report on research on impact cratering scaling laws, on numerical studies that were designed to investigate those laws, and on various applications of the scaling laws developed by the author and his colleagues.

Previous work has showed that the basis for all common cratering scaling laws is that the impactor radius a, velocity U and mass density δ occur in those scaling laws as a single combined measure of the form $aU^{\mu}\delta^{\nu}$, where the exponents μ and ν vary between different scaling laws. This single measure has been termed a coupling parameter, since it measures the coupling of the energy and momentum of the impact into the planetary body. [1] Previous applications of the theory and scaling laws based on this coupling parameter have been reported. [2-7]

Recent theoretical studies [6] have exposed the reason that such a single measure can be used to characterize the impact: the important phenomena that give the final obserable crater occur at a distance from the impact point that is fairly large compared to the impactor size itself. As a consequence, those phenomena are the same as would occur for the deposition of the finite impactor energy and momentum at a single point; and are therefore governed by a "point source" solution. Point-source solutions of various types that are related to various impact conditions exist and have been studied and extended in this research. One of the more important is for a point source in an ideally porous material, since that model represents fairly well the mechanical behaviours of common soil-like materials. Those solutions, as well as others, have been reported in [8].

The assumption that a point-source approximation can be used to measure an impact, together with appropriate assumptions as to the mechanisms that absorb the energy and momentum of the impactor allows one to generate specific scaling laws, for all aspects of the cratering processes that occur sufficiently far from the impactor so that the assumption is in fact valid. The recent paper [8] presents a large number of scaling results derived in this way. These include not only results for the final crater size, but also for dynamic phenomena such as crater growth histories and formation times. A different paper [9] looks at the application to the volume of melt that occurs at sufficiently high impact velocities.

Recent code calculations of impacts into porous half-space targets have also been studied to obtain confirmation of the scaling forms and to obtain specific numerical exponents of those forms. Those calculations are also reported in [8].

REFERENCES

1. Holsapple, K.A., "Coupling parameters in cratering mechanics", EOS Trans. AGU 62, p. 949, 1981.

2. Holsapple, K.A. and K.R. Housen, "Scaling considerations for cratering in ice", Lunar Planet. Sci. XV, 1985.

3. Holsapple, K.A. and K.R. Housen, "Scaling laws for the catastrophic collisions of asteroids", in Memorie della Societa Astronomica Italiana, 57, No. 1, pp. 65-86, 1986.

4. Holsapple, K.A., "On the existence and implications of coupling parameters in cratering mechanics", Lunar Planet. Sci. XIV, p. 319, 1983.

5. Holsapple, K.A. and K.R. Housen, "Cratering estimates for ice", in preparation.

6. Holsapple, K.A. and R.M. Schmidt, "Point-source solutions and coupling parameters in cratering mechanics", in press, J. Geophys. Res., 1986.

7. Schmidt, R.M. and K.A. Holsapple, "Explosively generated water waves", EOS (Trans. AGU) 65, p. 221, 1984.

8. Holsapple, K.A., "The scaling of impact phenomena", in press, J. Impact Engr. 5, 1987.

9. Bjorkman, M.D. and K.A. Holsapple, "Velocity scaling impact melt volume", in press, J. Impact Engr. 5, 1987.

EXPERIMENTAL EVIDENCE FOR NON-PROPORTIONAL GROWTH OF LARGE CRATERS P.H. Schultz, Dept. of Geological Sciences, Brown University, Box 1846, Providence, RI 02912 and D.E. Gault, Murphys Center of Planetology, Box 833, Murphys, CA 95247.

INTRODUCTION: The role of gravity in modifying the excavation cavity of large craters can be documented in the terrestrial geologic record (1,2) and observations of lunar craters (3,4). The terrestrial record also exhibits craters with flattened profiles and geologic cross-sections (5,6) that have prompted hypotheses for low-density impactors (7) or unusual impact conditions, e.g. atmospheric break-up or a shallow-sea environment (8,9). Others have proposed shallow basin excavation due to lunar internal structure (10). Evidence from laboratory impact experiments is indicating, however, that increasing crater aspect ratios (diameter:depth) also can result from increasing both velocity and projectile size without invoking unusual impactor conditions. If this trend continues to planetary-scale dimensions, then the shallowness of 100km-diameter craters may result not only from post-formation collapse but also from a modification of the cratering flow field during excavation.

EXPERIMENTAL RESULTS: An extensive data base of experimental impact cratering has been analyzed for a variety of impactors (aluminum, pyrex, lexan, lead, iron, clustered pyrex, etc.) and impact velocities (0.05 - 8km/s) for low strength targets (sand and compacted pumice). These data indicate a change in cratering efficiency that appears to be related to the onset of projectile deformation or rupture (11,12). For constant projectile size, this transition is accompanied by an increase in crater diameter relative to undeformed projectiles and net increase in diameter/depth (D/d). The aspect ratio for low-velocity impact ($v<1.3$km/s) decreases slightly with increasing velocity but increases markedly for high-velocity impacts ($v>2$kms). For constant impact velocity, D/d increases with projectile radius (r) for 0.159-0.635cm radii aluminum spheres. Smaller projectiles ($r<0.2$cm), however, exhibit a reversal in this relationship for velocities greater than 3km/s: craters become deeper with increasing size. Combining these results, we find that $D/d \propto \alpha \log(r) - \beta \log(v)$ for larger projectiles larger projectiles (>.2cm) undergoing deformation at impact where $\alpha \simeq \beta \simeq 0.05$. The same relationship is found for aluminum wafers where the characteristic projectile dimension is the thickness (/2) rather than the radius. Small, high-velocity impactors, however, have $\alpha \simeq -0.04$ to -0.1 and $\beta \simeq -0.09$.

When all projectile types and sizes are considered, we find two contrasting relationships between crater aspect ratio and impactor parameters (r,v and density, δ_p). The transition occurs at a critical value of $\eta_c = (\delta_t/\delta_p)(r/v)$, which depends on target material: for sand, $\log \eta_c \simeq -4$; for compacted pumice, it is -6. If $\eta < \eta_c$, we find that $\log D/d \propto \lambda \log (\delta_t/\delta_p)(v^2/r)$ where $\lambda \simeq +0.1$. The gravity-scaled scaling parameter described in (13) can be used in place of r/v^2, but subsequent analyses suggest that gravity does not alter the cratering flow field, only the limiting diameter. The physical significance of the observed relationship may be related to the energy transfer rate to the target, which to first order can be expressed as v/t or v(v/r) if v/r is proportional to the time for projectile penetration. Higher rates of energy transfer result in proportionally shallower craters. For $\log \eta > \log \eta_c$, the aspect ratio depends simply on the time (r/v) for projectile penetration and target/projectile density contrast provided that projectile deformation occurs upon impact. Undeformed projectiles result in small aspect ratios. Long penetration times, whether the result of large hypervelocity or small low velocity impacts produce shallow craters. This point can be illustrated (Figure 1) by hypervelocity impacts by debris clusters with large radii or low velocity impacts by easily deformed projectiles (plastic or lexan). It should be remembered that these results apply to low-strength targets where gravity-dominated scaling relations apply. Both sand and compacted pumice targets indicate $\log D/d \propto 0.28 \log (\delta_t/\delta_p) \cdot (r/v)$. At extremely low impact velocities

(<0.1km/s) and no projectile deformation, a different relationship between aspect ratio and impactor/target parameters appears to be present.

MPLICATIONS: Most laboratory experiments permit a wide range in impact velocities (.05-7km/s) but only a narrow range in projectile sizes (0.159-0.318cm) over the same velocity range. Consequently subtle but important effects of projectile size at planetary scales are easily masked. On the Moon, the situation is reversed: projectile sizes can range over many orders of magnitude with the most probable impact velocities confined to less than an order of magnitude. If a typical lunar impact velocity of 15km/s is assumed, then π_c indicates a corresponding projectile diameter of 3m. The requirement that gravity-controlled scaling exists requires that either the crater is formed completely in low strength material (regolith) or at large enough scales (>2km) where gravity controls crater growth. At small scales, the Ranger and SIV-B impacts of the lunar surface have values of $\pi > \pi_c$ and were formed largely within the regolith. If the relation between crater aspect ratio and impactor parameters for small but high-velocity impacts were adopted, a small deep crater would be predicted. The alternative relation for predicts a shallow crater with a central mound, as is observed (15). If D/d = 5 for a 5km-diameter crater, then the gravity-limited transient cavity aspect ratio for a 100km-diameter crater is predicted to be about 12. The importance of post-cratering rim collapse (plastic flow and slumping), however, may be lessened but cannot be ignored.

References: (1) Dence, M.R., Grieve, R.A.F., and Robertson, P.B. (1977) in *Impact and Explosion Cratering*, p. 247-275, Pergamon, NY (2) Grieve, R.A.F., Robertson, P.B., and Dence, M.R., (1981) in *Multi-Ring Basins*, p. 37-57, Pergamon, NY. (3) Quaide, W.L., Gault, D.E., and Schmidt, R.A. (1965) in *New York Acad. Sci. Ann., 123*, p. 563-572. (4) Pike, R.J. (1980) *U.S. Geol. Survey Prof. Paper 1046-C* 77 p. (5) Roddy, D.J. (1968) in *Shock Metamorphism of Natural Materials*, p. 31-32, Mono Book Corp., Baltimore, MD. (6) Wilshire, H.G., Offield, T.W., Howard, K.A., and Cummings, D. (1972), *U.S. Geol. Survey Prof. Paper* 599-H, 42 p. (7) Roddy, D.J. (1977) in *Impact and Explosion Cratering*, p. 277-308, Pergamon, NY. (8) Melosh, H.J. (1981) in *Multi-ring Basins*, p. 29-35, Pergamon, NY (9) Gault, D.E. and Sonnett, C. P. (1982) *Geol. Soc. Spec. Paper 190*, p. 69-92. (10) Wilhelms, D. *et al.* (1977) in *Impact and Explosion Cratering*, p. 539-562, Pergamon, NY (11) Gault, D.E. and Wedekind, J. (1977) in *Imapct and Explosion Cratering*, p. 1231-1244, Pergamon, NY (12) Schultz, P.H. and Gault, D.E. (1985), *J. Geophys. Res., 90*, p. 3701-3732. (13) Schmidt, R.M. and Holsapple, K.A. (1980), *J. Geophys. Res, 85*, 235-252. (14) Whitaker, E.A. (1972) *Apollo 16 Prelim. Sci. Report. NASA SP-315*, 29.39-29.45.

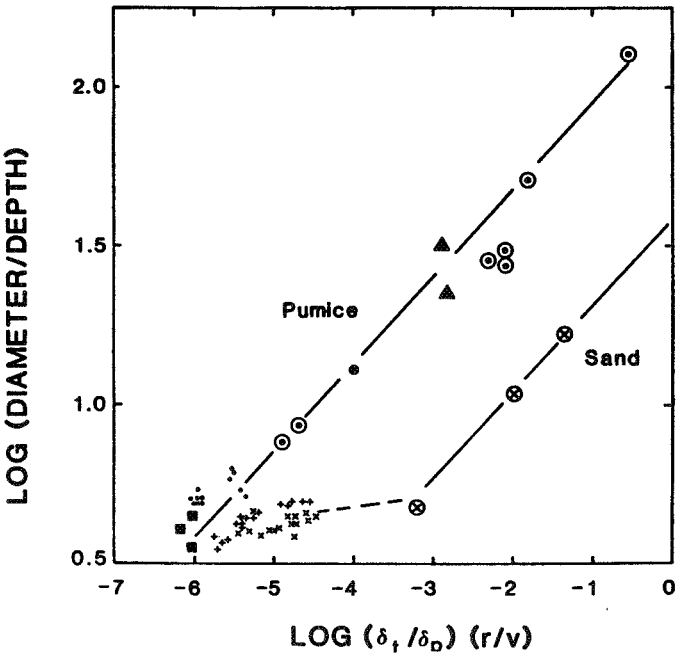

Figure 1. Data indicating the increase in D/d for increasing penetration times and δ_t/δ_p. Symbols for sand targets are: ⊗ clustered impacts; + 1.27cm diameter aluminum spheres; and x 2cm diameter lexan cylinders. Symbols for pumice targets are: ⊙ clustered impact; ▲ hollow nylon; • easily deformed plastic; ■ 0.635cm aluminum spheres. Dots indicate data for aluminum spheres impacting lead and glass shot targets.

Centrifuge Impact Cratering Experiments: Scaling Laws for Non-Porous Targets

Robert M. Schmidt Boeing Aerospace Co., M/S 3H-47, P. O. Box 3999, Seattle WA 98124.

This work is a continuation of an ongoing program whose objective is to perform experiments and to develop scaling relationships for large-body impacts onto planetary surfaces. The development of the centrifuge technique has been pioneered by the present investigator and is used to provide experimental data for actual target materials of interest. With both powder and gas guns mounted on the rotor arm, it is possible to match various dimensionless similarity parameters, which have been shown to govern the behavior of large-scale impacts. Current work (Schmidt and Housen, 1986: Schmidt et al. 1985,1986) is directed toward the determination of scaling estimates for non-porous targets. The results are presented here in summary form.

The table below lists our scaling estimates in two forms. The upper part of the table gives the results in the nondimensional form shown in the accompanying figures. Note that the equation for time of formation, expressed in terms of crater volume and gravity, is independent of material type. As can be shown with the coupling parameter theory given by Holsapple and Schmidt (1986), the crater volume "accounts" for variations in target and impactor properties. The lower part of the table shows the same scaling laws in a dimensional form (with cgs units) in terms of the impactor energy and velocity, and gravity. In constructing these scaling laws, the density ratio was assumed to be constant, because in most cases there were insufficient data to determine the dependence on density. The lower part of the table was calculated with the target density appropriate for each material and a nominal impactor density (δ) of 3 gm/cm^3. Crater dimensions in all cases refer to the apparent crater.

V=crater volume
R=crater radius
T=crater formation time
ρ=target density
Y=target strength
g=gravity
a=impactor radius
U=impactor velocity
E=impactor energy
t=time

	Dry Sand	Wet Sand	Water
Crater Volume	$\Pi_V = 0.24\Pi_2^{-0.51}$	$\Pi_V = 0.2\Pi_2^{-0.65}$	$\Pi_V = 2.1\ \Pi_2^{-0.65}$
Crater Radius	$\Pi_R = 0.84\ \Pi_2^{-0.17}$	$\Pi_R = 0.8\Pi_2^{-0.22}$	$\Pi_R = 0.94\Pi_2^{-0.22}$
Volume vs Time	$\Pi_V = 0.16\ \Pi_t^{0.86}$	$\Pi_V = 0.25\ \Pi_t^{1.07}$	$\Pi_V = 1.1\ \Pi_t^{1.07}$
Time of Formation	$\Pi_T = 1.9\Pi_2^{-0.58}$	$\Pi_T = 1.6\Pi_2^{-0.61}$	$\Pi_T = 2.3\Pi_2^{-0.61}$
	$T = 0.8\,V^{1/6}\,g^{1/2}$		

$\Pi_V = \rho V/m$
$\Pi_R = R\,(\rho/m)^{1/3}$
$\Pi_2 = 3.22ga/U^2$
$\Pi_t = Ut/a$
$\Pi_T = UT/a$

	Dry Sand	Wet Sand	Water
Volume	$V=0.20E^{0.83}U^{-0.64}g^{-0.51}$	$V=0.13E^{0.78}U^{-0.27}g^{-0.65}$	$V=2.9E^{0.78}U^{-0.27}g^{-0.65}$
Radius	$R=0.77E^{0.28}U^{-0.21}g^{-0.17}$	$R=0.70E^{0.26}U^{-0.09}g^{-0.22}$	$R=1.1E^{0.26}U^{-0.09}g^{-0.22}$
Vol vs t	$V=0.29E^{0.71}U^{-0.57}t^{0.86}$	$V=0.21E^{0.64}U^{-0.22}t^{1.07}$	$V=1.9E^{0.64}U^{-0.22}t^{1.07}$
Form. Time	$T=0.74E^{0.14}U^{-0.12}g^{-0.58}$	$T=0.62E^{0.13}U^{-0.04}g^{-0.61}$	$T=0.89E^{0.13}U^{-0.04}g^{-0.61}$

The slopes of the lines in the two figures below are based on a value of μ=0.4 for dry sand and μ=0.55 for water and wet sand. Also note that the effective size scale for the wet sand shots was not large enough to put them fully in the gravity regime. Thus, the proposed scaling estimate was constructed as an asymptote to the data, with a slope calculated from a value of μ=0.55. The estimate is significantly above the dry sand line because of better coupling in the (nonporous) wet sand, but below the line for water targets. The wet sand line is regarded as a current best-estimate for rocky materials, and differs from our earlier estimate (Schmidt and Holsapple, 1982) where the slope was calculated based on a value of μ more appropriate to porous materials.

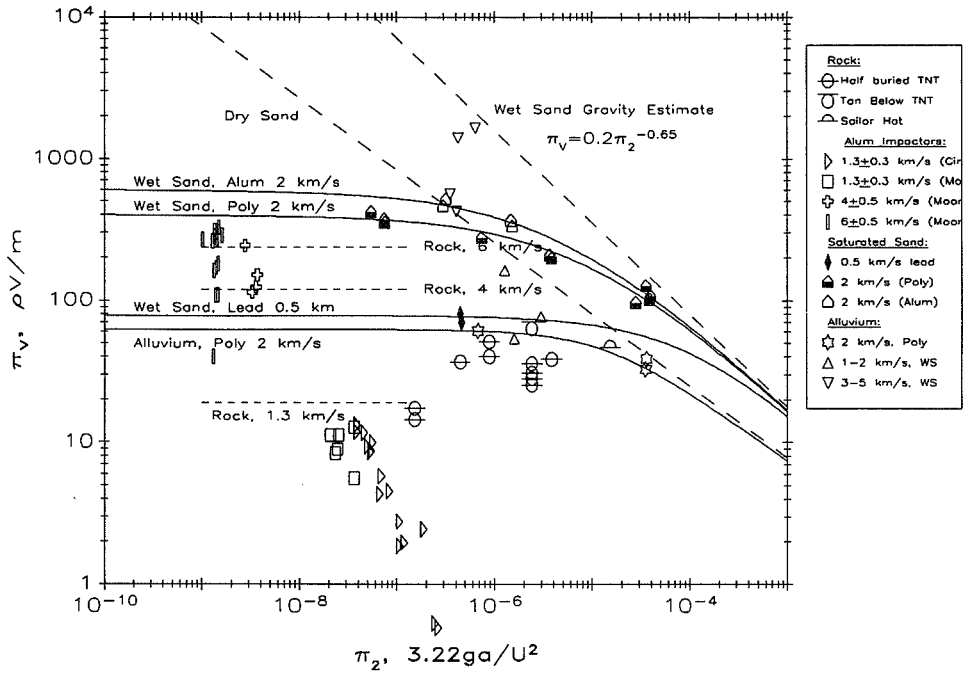

Cratering efficiency for impacts and explosions in dry sand, alluvium, wet sand, and rock. The dashed line (labeled Wet Sand Gravity Estimate) is proposed as a current best estimate for large-scale cratering in rock.

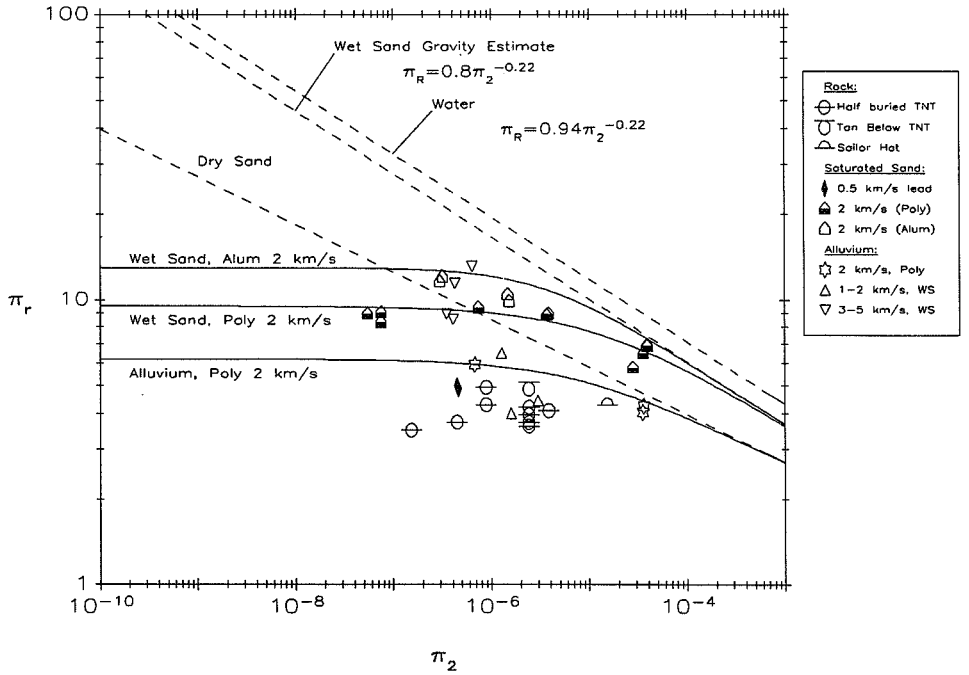

Scaled crater radius results for impacts and explosions in various materials. The dashed line (labeled Wet Sand Gravity Estimate) is proposed as a current best estimate for large-scale cratering in rock.

Scaling estimates for large-scale cratering in rock proposed previously by others have assumed that the crater radius is proportional to powers of the impactor energy and gravity, with no additional dependence on impact velocity. The energy exponent is typically reported to be 0.28 to 0.29 while estimates of the gravity exponent range from 0.11 to 0.17. The size scaling laws proposed here differ from earlier ones in three respects. First, a distinct dependence of impact velocity is recognized, even for constant impactor energy. The effects of velocity are smallest for nonporous targets, which approach (but do not reach) the asymptotic case of pure energy scaling. The porosity of materials like dry sand result in velocity-dependent energy losses. Hence, the velocity dependence is greatest for these materials. Second, the present energy exponent for low-porosity targets, like competent rock, is lower than earlier estimates. Although the difference might appear to be small (the present estimate is 0.26 versus the values of 0.28-0.29 mentioned above), the effect of this difference can be significant when extrapolating many orders of magnitude in energy up to kilometer-sized craters. Third, the gravity exponent is recognized here as being related to both the energy and the velocity exponents. As shown in the table below, these exponents are all determined by the single scaling exponent, μ, as defined by a coupling parameter of the form $C = aU^{\mu}\delta^{\nu}$

	Strength Regime	Gravity Regime
Crater Volume	$\frac{\rho V}{m} \propto (\frac{\rho}{\delta})^{1-3\nu} (\frac{Y}{\rho U^2})^{\frac{-3\mu}{2}}$	$\frac{\rho V}{m} \propto (\frac{\rho}{\delta})^{\frac{2+\mu-6\nu}{2+\mu}} (\frac{ga}{U^2})^{\frac{-3\mu}{2+\mu}}$
Formation Time	$\frac{UT}{a} \propto (\frac{\rho}{\delta})^{-\nu} (\frac{Y}{\rho U^2})^{\frac{-(1+\mu)}{2}}$	$\frac{UT}{a} \propto (\frac{\rho}{\delta})^{\frac{-\nu}{2+\mu}} (\frac{ga}{U^2})^{\frac{-(1+\mu)}{2+\mu}}$
Growth of the Transient Crater	$\frac{\rho V}{m} (\frac{\rho}{\delta})^{3\nu-1} (\frac{Y}{\rho U^2})^{\frac{-3\mu}{2}} = F [\frac{Ut}{a} (\frac{\rho}{\delta})^{\nu} (\frac{Y}{\rho U^2})^{\frac{1+\mu}{2}}]$	$\frac{\rho V}{m} (\frac{\rho}{\delta})^{\frac{6\nu-\mu-2}{2+\mu}} (\frac{ga}{U^2})^{\frac{3\mu}{2+\mu}} = F [\frac{Ut}{a} (\frac{\rho}{\delta})^{\frac{\nu}{2+\mu}} (\frac{ga}{U^2})^{\frac{1+\mu}{2+\mu}}]$
	Prior to the onset of strength or gravity effects	
	$\frac{\rho V}{m} \propto (\frac{\rho}{\delta})^{\frac{1+\mu-3\nu}{1+\mu}} (\frac{Ut}{a})^{\frac{3\mu}{1+\mu}}$	

As mentioned above, the wet-sand result is assumed to be a current best-estimate for large-scale cratering in rock. We stress however that this approximation is tentative until a better understanding is achieved of the dominant material properties which govern cratering in the gravity regime (e.g. density and friction angle). Once the role of density and friction angle are understood, reasonable analogues of rock might be constructed for which laboratory experiments can be performed in the gravity regime.

Holsapple K. A. and Schmidt R. M. (1986) Point-source solutions and coupling parameters in cratering mechanics. *J. Geophys. Res.* (in press).

Schmidt R. M. and Holsapple K. A. (1982) Estimates of crater size for large-body impact: Gravity scaling results. *Geological Society of America Special Paper 190*, 93-102.

Schmidt R. M. and Housen K. R. (1986) Some recent advances in the scaling of impact and explosion cratering. *Proceedings of the 1986 Hypervelocity Impact Symposium.* Pergamon Press.

Schmidt R. M., Housen K. R., and Webbeking V. T. (1985) Growth of water cavities over a range of 10^6 in time (abstract). *EOS (Trans. Amer. Geophys. U.)* **66**, 947.

Schmidt R. M., Wauchope C. R. and Watson H. E. (1986) Experimental investigation of crater formation dynamics. In *Lunar Planetary Science XVII*, 766-767.

IMPACT AND CRATERING PROCESSES ON ASTEROIDS, SATELLITES, AND PLANETS

Clark R. Chapman, Donald R. Davis, and Stuart J. Weidenschilling
Planetary Science Institute

We have developed and applied a new model for scaling the outcome of catastrophic collisions from laboratory-scale experiments to large bodies where gravitational binding is dominant. This algorithm includes a pressure-dependent impact strength (see Davis et al, Icarus 62, 1985 for definition of terms) which predicts that large asteroids behave as intrinsically strong objects due to compressive loading of overburden throughout their interiors. For small bodies (< few kilometers diameter), where the gravitational loading is negligible, this model assumes that the impact strength is independent of size. There was considerable discussion of scaling laws for disruption at the August 1985 workshop in Pisa where Dr. Davis presented these results (see Davis, Mem. Soc. Astron. Ital. Vol. 57, No. 1, 1986). The pressure strengthening impact strength model was viewed as physically quite plausible; however, it was argued that the impact strength should decrease with increasing size in the size range where gravitational compression is negligible.

Numerical simulations of asteroid collisional evolution, which investigate possible initial assteroid mass distributions at the time their collisional speeds were pumped up to 5 km/s, are also described by Davis et al (Icarus 62, 1985). Successful candidate intial populations must satisfy three constraints: (a) they must evolve to the present observed size distribution, (b) Vesta must not be shattered in order to preserve its observed nearly-homogeneous basaltic crust, and (c) there must be enough collisional evolution to produce at least the observed number of Hirayama families. We considered various hypothetical initial population distributions, and found that a very steep size distribution, containing very few large bodies but numerous small bodies totalling only several times the current belt mass, best satisfied all constraints. This result implies that the asteroid region already was depleted in mass relative to the terrestrial planet region by the time velocities were stirred up to ~5 km/s.

We also calculate the number of asteroids that are formed by different mechanisms, e.g. unshattered original survivors, gravitationally bound rubble piles, fragments from the collisional disruption of larger bodies, etc. We then relate these distributions to statistical properties of the observed asteroid population that may be influenced by asteroid physical states. For example, intermediate size asteroids (100-200 km diameter) are the sizes at which gravitationally bound rubble piles should be most abundant. This is also the size range at which Zappala et al. (Icarus 59, 261, 1984) found observational evidence for large amplitude lightcurves among rapidly rotating asteroids. One interpretation is that the gravitationally bound rubble piles relax to quasi-equilibrium shapes. Other relationships between observable properties and the calculated physical state are being investigated.

The idea that rotational properties of asteroids constrain their physical nature and collisional history has been stimulated by demonstrations

that the mean spin period varies with size and taxonomic class (Farinella et al. Astron. Astrophys. 104, 159, 1981; Dermott et al., Icarus 57, 14 1984). These studies show that intermediate-sized asteroids ($20 < D < 200$ km) rotate more slowly, on average, than do smaller and larger ones. Dobrovolskis and Burns (Icarus 57, 464, 1984) interpret this as due to "angular momentum drain" (i.e., braking by preferential escape of impact ejecta in the direction of rotation). While this mechanism is qualitatively plausible, many quantitative details remain to be worked out. Their formalism treats all impacts as crater-forming events, with ejecta derived from the surface at the impact point. From the observed size distribution, it is known that most of the mass and angular momentum impacting an asteroid is delivered in the few largest events that occur in its lifetime. Moreover, our collisional simulations show that most asteroids smaller than ~150 km either have been shattered by major impacts on a much larger scale than crater-forming events, or are fragments from the disruption of larger parent bodies. Thus, it may be premature to draw quantitative conclusions as to asteroid properties and collisional history based on this model. Still, we note that Farinella et al. conclude that the observed angular momenta of large asteroids is compatible with only a moderate depletion, about a factor of five, of the original mass of the belt, in substantial agreement with our own results based on the observed size distribution.

It is accepted by most workers that Hirayama families are formed by major asteroid collisions. The collision shatters and disrupts both target and projectile producing fragments moving at velocities which enable them to escape their mutual gravitational binding and to follow their own orbits about the sun. Even the small mass belt favored by Davis et al. (1985) for the initial asteroid belt would have resulted in catastrophic disruption of around 150 bodies larger than 100 km size over solar system history. Yet there are nowhere near that number of Hirayama families that make sense geochemically. Hirayama families, if created by catastrophic disruption, may have a lifetime considerably shorter than the age of the solar system. There was catastrophic disruption of 10-12 bodies larger than 100 km in size in the last billion years according to the favored scenario of Davis et al. (1985). This number is in reasonably good agreement with the ten families having parent bodies $\gtrsim$ 90 km in size described by Gradie et al. (in Asteroids, T. Gehrels, ed., p. 359, 1979). This suggests that Hirayama families, if of collisional origin, might be recognizable only for times much less than the age of the solar system.

Dr. Chapman gave a presentation at the Pisa workshop on several issues in which observational properties of asteroids (chiefly those relating to composition) have a bearing on collisional evolution. Although a major focus of Chapman's discussion (see Chapman, Mem. Soc. Astron. Ital. Vol. 57, No. 1, 1986) was Hirayama families, he also pointed out a major problem with the identification of S- and M-type asteroids as the collisionally stripped cores of differentiated parent bodies, if collisional evolution has been modest. In addition, olivine-rich asteroids (which should be observed in abundance as fragments of the mantle material of these parent bodies) are, in fact, extremely rare in the belt.

Chapman has been examining databases on the compositions of Hirayama family members to see if they "make sense" as collisional products. Using

the 8-color survey, augmented by other spectrophotometric and radiometric databases, Chapman has been investigating whether members of 60 families (as assigned by Williams and by Kozai) show compositional distributions different from the "background" expected at the family's semi-major axis (based on the Gradie/Tedesco/Bell plots of distributions of taxonomic classes with a). He has also addressed the question of whether families that do seem to be significant in that sense make cosmochemical sense, according to adopted models for parent-body interiors. Tentative conclusions are that 45 of the 60 families are "not real", by Chapman's criteria. Half are due simply to poor statistics. But many are random collections like the background, perhaps grouped by unknown dynamical processes (or separated into apparent groups by unknown dynamical gaps). Kozai's families, in particular, seem to be too large and lacking in reality. Eleven of the 60 families studied are "real". Half of these are of homogeneous composition, implying the break-up of an undifferentiated parent body; several of these families are the well-known populous families (e.g. Themis, Koronis). The other half are problems, in the sense that they do not seem to make cosmochemical sense (these include Eos, Nysa, Ceres, and Budrosa). Preliminary results were presented at the autumn 1986 meeting of the Meteoritical Society; a paper is in preparation.

Drs. Chapman, Weidenschilling, and Davis, in response to referee's comments, have revised their manuscript prepared in collaboration with M. Leake, about the cratering history of the planet Mercury. They suggest an alternative history of Mercury possibly involving a population of intra-Mercurian bodies ("vulcanoids"); revised results were presented at the Mercury Conference held in Tucson, Arizona in August, 1986.

Chapman and McKinnon's lengthy chapter on cratering of planetary satellites for the Natural Satellites book has now appeared. It contains a thorough review of cratering physics, with particular application to icy satellites, prepared chiefly by McKinnon. It also contains Chapman's critical review of cratering statistics on the various planetary satellites, as well as on the terrestrial bodies. The authors apply crater-scaling relationships developed in the first part of the chapter in order to make inferences about the projectile populations responsible for cratering the planets and satellites throughout ancient and modern epochs. Chapman and McKinnon conclude that there are 4 (possibly 5) distinct projectile populations implied by the observed crater distributions. However, no good links have been found connectin different source populations either spatially (e.g. comets for the late heavy bombardment and more recent cratering in the inner solar system with the Ganymede/Callisto population in the outer solar system) or temporally, (comets for both the present cratering rate and the earlier heavy bombardment in the inner solar system). With no physical or temporal connection betwen the inner and outer solar system, there is no basis for estimating -- even crudely -- the cratering chronologies for the satellites of Jupiter and Saturn. More recently, Chapman and McKinnon, have been investigating the connections between their scenario and the crater populations of the Uranian satellites, recently imaged by Voyager (see McKinnon and Chapman, Eos Vol. 66, No. 46, 1985).

CRATER PRODUCTION ON VENUS AND EARTH BY ASTEROID AND COMET IMPACT

Eugene M. Shoemaker and Ruth F. Wolfe, U.S. Geological Survey, Flagstaff, AZ 86001

Observations of the impact-crater record on the surface of Venus obtained by means of the Venera 15 and 16 spacecraft (Ivanov et al., 1986; Basilevsky et al., in press) have stimulated renewed interest in the cratering rate on Venus (e.g., Schaber et al., in press). Accordingly, we have carried out new calculations of the collision probabilities of asteroids and comets with Venus based on the orbits of the known Venus-crossing asteroids and comets. For comparison, we recalculated asteroid and comet collision probabilities and cratering rates on the Earth and Moon and normalized the estimated cratering rates on Venus to those of the Earth.

Of 71 Earth-crossing asteroids discovered through October 1986 (one more than reported by Shoemaker and Shoemaker, this volume), 48 currently pass perihelion inside Earth's orbit and 24 pass perihelion inside the orbit of Venus. For these objects, approximate collision probabilities with Earth and Venus can be calculated by means of Opik's (1951) equations. Because we use the mean orbital elements of the Earth and Venus in these equations, collision probabilities with the Earth can also be calculated for three additional asteroids that pass perihelion inside the mean aphelion of Earth's orbit.

We are primarily concerned here with calculating the relative collision and cratering rates on Venus and Earth; use of the Opik collision probabilities is expected to yield a satisfactory preliminary estimate of the relative cratering rates from asteroid impact on the two planets. Although Opik's equations lead to significant errors for the collision probabilities of individual asteroids (Shoemaker et al., 1979), the average probability of collision with Earth calculated from Opik's equations for 22 asteroids is only 13% greater than the average obtained by much more rigorous methods. We have neglected the contribution to the total impact rate on Earth of Earth-crossing Amors and the contribution to the impact rate on Venus of an analogous set of asteroids that have part-time overlap with the orbit of Venus. Collision probabilities for these objects can only be obtained by methods based on secular perturbation theory; these much more difficult calculations have been deferred for future study. The part-time overlapping objects contribute only about 25% of the total impact rate; for purposes of this preliminary investigation, we have assumed that the proportion of their contribution to the total impact rate is the same on Earth and Venus.

Cratering rates (number of craters per unit area per unit time) have been derived from collision probabilities by methods described by Shoemaker and Wolfe (1982). Uncertainties about the total population of impactors and their physical properties do not affect our results, as we report only relative cratering efficiencies and relative cratering rates (Table 1). We have assumed that the distribution of physical properties is the same for Venus- and Earth-crossing impactors.

The new mean collision probability with Earth calculated from 48 Apollo and Aten asteroids is 80% higher than the mean collision probability found by Shoemaker et al. (1979) for 22 Apollos and Atens. This increase is due chiefly to the discovery of several asteroids having unusually high collision probabilities with Earth. Half of the

total probability of collision with Earth is contributed by 12% of the asteroids in the observed sample of Earth crossers. Because the distribution of collision probabilities is strongly skewed, it is critically important to continue surveys for planet-crossing asteroids in order to obtain reliable estimates of both absolute and relative cratering rates on the terrestrial planets.

The relative asteroid cratering rate shown in Table 1 for Venus (≈0.9 times the cratering rate on Earth) is strictly applicable only to craters large enough for the shielding effect of the Venusian atmosphere to be considered negligible. A correction should be applied to account for an undiscovered class of Venus-crossing asteroids whose orbits are entirely inside the orbit of the Earth. These asteroids are expected to have been captured by repeated encounters with Venus, just as Aten asteroids have been captured in small orbits by combined encounters with Earth and Venus. In the case of Earth, Atens account for 27% of the total estimated asteroid impact-cratering rate. A similar but probably somewhat smaller contribution to the cratering rate on Venus can be expected from the undiscovered class of Venus-crossing asteroids. We tentatively estimate the total asteroid impact-cratering rate on Venus at 1.0 to 1.1 times the rate on Earth.

The relative rates of crater production by comet impact were evaluated from the orbits of long period comets listed by Marsden (1986). Calculations were made for all Earth- and Venus-crossing comets having periods greater than 20 years. The crater production on Earth and on Venus by impact of comets having shorter periods is sufficiently small to be neglected. Orbits are available from Marsden's catalog for a total of 400 long period Earth-crossing comets; 255 of these comets are also Venus crossers. The relative comet impact-cratering rate on Venus, calculated by the methods described by Shoemaker and Wolfe (1982), is 1.14 times the rate on Earth (Table 1). Again, this rate applies only to craters large enough that the shielding effect of the Venusian atmosphere can be considered negligible. Probably few, if any, craters smaller than about 100 km in diameter have been formed by comet impact on Venus (cf. Melosh, 1981; Ivanov et al., 1986; Basilevsky et al., in press).

References

Basilevsky, A.T., Ivanov, B.A., Burba, G.A., Chernaya, I.M., Kryuchkov, V.P., Nikolaeva, O.V., Campbell, D.B., and Ronca, L.B., in press: Proc. 17th Lunar and Planet. Sci. Conf., Jour. Geophys. Res.

Ivanov, B.A., Basilevsky, A.T., Kryuchkov, V.P., and Chernaya, I.M., 1986: Proc. Lunar and Planet. Sci. Conf., Jour. Gephys. Res., v. 91, p. D413-430.

Marsden, B.G., 1986, Catalogue of cometary orbits: International Astronomical Union, Cambridge, Massachusetts, 102 p.

Melosh, H.J., 1981: in Multi-ring basins (P.H. Schultz and R.B. Merrill, Eds.): Proc. Lunar Planet. Sci., 12A, p. 29-35.

Opik, E.J., 1951: Proc. Roy. Irish Academy, Sect. A, v. 54, p. 165-199.

Schaber, G.G., Shoemaker, E.M., and Kozak, R.C., in press: Astronomichesky Vestnik and Solar System Research.

Shoemaker, E.M., and Shoemaker, C.S.: Reports of the NASA Planetary Geology Program, 1986, National Aeronautics and Space Administration Tech. Memo., this volume.

Shoemaker, E.M., Williams, J.G., Helin, E.F., and Wolfe, R.F., 1979: in Asteroids (T. Gehrels, Ed.): Univ. Arizona Press, Tucson, Arizona, p. 253-282.
Shoemaker, E.M., and Wolfe, R.F., 1982: in The satellites of Jupiter (D. Morrison, Ed.): Univ. Arizona Press, Tucson, Arizona, p. 277-339.

Table 1. Crater production on Earth, Venus, and the Moon by impact of asteroids and long period comets

	N	P	A_2 km^2	V km/sec	D	R
Asteroid Impact Craters						
Earth	1.00	0.635×10^{-8}	0.509×10^{9}	17.5	1.00	1.00
Venus	0.48	0.788×10^{-8}	0.460×10^{9}	21.1	1.14	0.88
Moon	1.00	0.241×10^{-9}	0.380×10^{8}	16.1	0.82* 1.07+	0.77* 1.37+
Comet Impact Craters						
Earth	1.000	0.308×10^{-8}	0.509×10^{9}	57.7	1.00	1.00
Venus	0.638	0.414×10^{-8}	0.460×10^{9}	64.3	1.09	1.14
Moon	1.000	0.214×10^{-9}	0.380×10^{8}	57.6	0.98* 1.27+	0.89* 1.58+

N = Number of impactors overlapping orbit of planet normalized to number overlapping orbit of Earth.
P = Mean probability of collision per year per asteroid or mean probability of collision per perihelion passage per comet.
A = Surface area of planet or the Moon.
V = Root mean square impact velocity weighted according to probability of collision (atmospheric retardation neglected).
D = Weighted mean diameter of crater produced by impactor of a given mass normalized to diameter of crater produced on Earth. D is applicable only at diameters greater than the threshold below which the planetary atmospheres shield the surfaces from crater production.
R = Crater-production rate per unit surface area normalized to crater production rate on Earth. R is applicable only at diameters greater than the threshold below which the planetary atmospheres shield the surfaces from crater production.
* Values of D and R calculated for lunar craters smaller than threshold diameter for crater collapse (generally less than 20 km).
\+ Values of D and R calculated for lunar craters larger than threshold diameter for crater collapse (generally greater than 20 km).

THE SURFACE AGE OF VENUS: APPLYING THE TERRESTRIAL CRATERING RATE [1]

Gerald G. Schaber, Eugene M. Shoemaker, and Richard C. Kozak;
U.S. Geological Survey, Flagstaff, AZ 86001 USA

The population of Venusian craters having suspected impact-crater morphology has been reported from 115 X 10^6 km^2 of the northern hemisphere of the planet [2, 3]. They estimated the average age of the surface to be approximately 1 b.y. (±0.5 b.y.) on the basis of lunar crater-production curves [4,5] corrected for Venus. Such an old average age is somewhat difficult to reconcile with the similarity in size and mass of Venus and Earth and with Earth's high heat flow and crustal resurfacing rate.

The average crater age of Venus's northern hemisphere may be less than 250 m.y. if we assume equivalence between the recent terrestrial cratering rate and that on Venus for craters ⩾20 km in diameter. For craters larger than this threshold size, below which crater production is significantly affected by the Venusian atmosphere, there are fairly strong observational grounds for concluding that such an equivalence in cratering rates on Venus and Earth may exist. One could argue that the lunar crater-production curves corrected for Venus may be inappropriate for the Venusian surface. The recent cratering rate on Earth, as estimated from astronomical observations of asteroids and determined directly from the terrestrial cratering record, is a factor of about 2 to 3 greater than the equivalent estimated average lunar cratering rate over the last 3.3 b.y. [6,7]. Grieve [7] speculated that this higher cratering rate has been in effect for about the last 1 b.y. Also, Shoemaker [8] noted that the ⩾10-km-diameter cratering record in Phanerozoic rocks of the central United States is indistinguishable from that predicted from astronomical observations of present Earth-crossing asteroids. Thus, it seems reasonable to base the estimate of the cratering rate on Venus for the last 0.5 b.y. on the terrestrial cratering record (e.g., the North American and European cratons), where the record of large (⩾20-km-diameter), dated craters is thought to be most complete.

As of October 1986, 48 asteroids had been discovered that currently pass perihelion inside Earth's orbit; 24 of these asteroids also pass perihelion inside the orbit of Venus. Even though only half of these observed Earth-crossing asteroids overlap the orbit of Venus, the average collision probability per unit surface area per asteroid is 37% higher on Venus than on Earth, the average collision velocity (neglecting atmospheric retardation) is 21% higher on Venus, and the surface gravity is 9.5% lower on Venus. Taking all of these factors into account but neglecting the screening effects of the Venusian atmosphere, the calculated ratio of the rate of crater production by asteroid impact on Venus to the rate on Earth is about 0.9 [9]. After correction for the contribution from the undiscovered class of Venus-crossers on very small orbits, the crater production rate by asteroid impact on Venus is estimated to be 1.0 to 1.1 times the rate on Earth.

In the absence of an atmosphere, the production rate of craters by comet impact would be about 15% higher than the production rate of comet impact craters on Earth [9]. However, the atmosphere of Venus may effectively shield the surface from production of cometary impact craters smaller than about 100 km in diameter. Indeed, it is possible that none of the craters so far observed on Venus were produced by

cometary impact. A major unresolved question in applying either the terrestrial or lunar cratering record to Venus, therefore, is the fraction of terrestrial and lunar craters produced by cometary impact. Recent work suggests that as many as half of the observed terrestrial impact craters could have been produced by comet showers [10]; a smaller fraction, probably about 10% to 20%, has been produced by the background flux of comets [11, 12].

Given the probable role of the dense Venusian atmosphere in reducing the observed number of craters less than about 20 km in diameter [2,3,13], we considered only craters whose diameters are ⩾20 km, ⩾50 km, ⩾100 km, and ⩾140 km in diameter. The production of craters ⩾20 over the past 1 b.y. on the North American and European cratons has been estimated by Grieve [7] to be $5.4 \pm 2.7 \times 10^{-15}$ km^{-2} yr^{-1}. This production rate agrees well with that based on astronomical observations of Earth-crossing asteroids [8] and thus was used in the calculation of the Venus crater-retention ages listed in table 1.

For craters larger than 50 km in diameter, the progressively younger Venusian ages reflect the fact that the cumulative size-frequency distribution of Venusian craters is significantly steeper than that of lunar craters. This steepness might be explained as the consequence of nearly complete shielding of the observed surface from comet impacts. Observations of the magnitude-frequency distribution of discovered Earth-crossing asteroids indicate that their size distribution is much steeper than the average size distribution of the projectiles that produced the postmare lunar craters [14]. Most impact craters on the Moon and Earth larger than 50 km in diameter probably have been produced by comet impact. However, the size distribution of Earth-crossing asteroids, by itself, probably is too steep to account for the distribution of Venusian craters. Two possibilities seem likely: (1) some of the Venusian craters greater than 50 km in diameter have been produced by comets, or (2) shielding by the atmosphere has very substantially reduced the production by asteroids of craters in the diameter range of 20-50 km. In either case, the age based on craters ⩾50 km in diameter may be closest to the true age (Table 1).

Given the present uncertainties in the role of both active and inactive comet nuclei in the cratering history of Earth, we conclude that the average age of the observed surface in the northern hemisphere of Venus could be as great as the 450-m.y. mean age of the Earth's crust (oceanic and continental [15]). The surface of Venus might be even older, but no evidence from the crater observations supports an age as great as 1 b.y: if the age of the observed Venusian surface were 1 b.y., it probably should bear the impact scars of a half dozen or more large comet nuclei that penetrated the atmosphere and formed craters well over 100 km in diameter.

In future studies we hope to provide more quantitative constraints on the present crater-production rates and on the cratering history of Venus. Venera 15/16 mapped only about 25% of Venus, the remaining 75% may tell us a completely different story.

Acknowledgments: Funding for this research was furnished to the U.S. Geological Survey by the National Aeronautics and Space Administration (Planetary Geology/Geophysics Program) under contract W-15,814 and the NASA Magellan Radar Investigation Group under contract WO-8777.

References: [1] Schaber, G.G., Shoemaker, E.M., and Kozak, R.C., Astronomichesky Vestnik and Solar System Res.- in press. [2] Ivanov,

B.A., et al., 1986, Proc. Lunar and Planet. Sci. Conf., J. Geophys. Res., 91, D413-430. [3] Basilevsky, A.T., et al., Proc. 16th Lunar and Planet. Sci. Conf., J. Geophys. Res. in press. [4] Basaltic Volcanism on the Terrestial Planets (BVTP), 1981, Pergamon, 1050-1127. [5] Hartmann, W.K., Izv. Acad. Nauk SSSR Ser. Geologicheskaya (in Russian), in press. [6] Wetherill, G.W., and Shoemaker, E.M., 1982, in Geological implications of impacts of large asteroids and comets on the Earth (L.T. Silver and P.H. Schultz, Eds.) Geol. Soc. Am. Spec. Pap. 190, 1-13. [7] Grieve, R.A.F., 1984, Proc. 14th Lunar Planet. Sci. Conf., J. Geophys. Res, 89, B403-B408. [8] Shoemaker, E.M., 1983, Ann. Rev. Earth Sci., 11, 461-494. [9] Shoemaker, E.M. and Wolfe, R.F.- this volume. [10] Shoemaker, E.M., and Wolfe, R.F., in The galaxy and the Solar System (M. Matthews et al., Eds.), Univ. Arizona Press, Tucson, in press. [11] Shoemaker, E.M., and Wolfe, R.F., 1982, in The satellites of Jupiter (D. Morrison, Ed.), Univ. Arizona Press, Tucson, Arizona, 277-339. [12] Weissman, P.R., 1982, Geol. Soc. Am. Spec. Pap. 190, 15-24. [13] Melosh, H.J., 1981, in Multi-ring basins (P.H. Schultz and R.B. Merrill, Eds.), Proc. Lunar Planet. Sci., 12A, 29-35. [14] Shoemaker, E.M., and Shoemaker, C.S., -this volume. [15] Cogley, J.G., 1984, Amer. Geophys. Union, 22, 101-122.

TABLE 1. CRATER-RETENTION AGES ON VENUS DERIVED FROM USE OF CRATERING RATES ON THE TERRESTRIAL CRATONS

CRATER DIAMETER [1] >D	NUMBER OF CRATERS [2] / (RATE) (AREA)	AGE (m.y.)	VARIANCE [3]	STANDARD DEVIATION
>20 km	$\frac{98}{(5.4 \times 10^{-15} \pm 2.7\ km^{-2}\ yr^{-1})\ (1.15 \times 10^{8}\ km^{2})}$	158 ± 81	x(0.25 + 0.01)	x(0.51)
>50 km	$\frac{20}{(1.0 \times 10^{-15} \pm 0.50\ km^{-2}\ yr^{-1})\ (1.15 \times 10^{8}\ km^{2})}$	174 ± 95	x(0.25 + 0.05)	x(0.55)
>100 km	$\frac{3}{(0.28 \times 10^{-15} \pm 0.14\ km^{-2}\ yr^{-1})\ (1.15 \times 10^{8}\ km^{2})}$	94 ± 71	x(0.25 + 0.333)	x(0.76)
>140 km	$\frac{1}{(0.15 \times 10^{-15} \pm 0.075\ km^{-2}\ yr^{-1})\ (1.15 \times 10^{8}\ km^{2})}$	54 + 65 - 54	x(0.25 + 1.0)	x(1.12)

[1] >20-km-diameter crater-production rate ($5.4 \pm 2.7 \times 10^{-15}\ km^{-2}\ yr^{-1}$) after [7]. >50, >100, and >140-km-diameter crater-production rates derived from >20-km production rate as $\frac{>D}{>20} = (X^{-1.84})\ (5.4 \times 10^{-15}\ km^{-2}\ yr^{-1})$, assuming crater index of 1.84 [8].

[2] Number of craters on Venus above a given diameter (D) taken from [1,2] amd B.A. Ivanov (personal communication, August 1986, Moscow)

[3] Estimated variance of the age is calculated as the $\sum$ of the variance of the cratering rate and the variance of the crater count (number of craters).

A STATISTICAL STUDY OF MERCURIAN CRATER CLASSES APPLIED TO THE EMPLACEMENT OF THE INTERCRATER PLAINS

Alex Woronow and Karen Love, University of Houston, Houston, TX 77004

Studies of crater classes have been few in number and disappointing in value. Perhaps this stems from the difficulties in statistically treating a nonstationary, multivariate data set, or from the propensity to treat all crater data phenomenologically rather than statistically. In either case, recent statistical innovations (Aitchison, 1982) afford a new opportunity to reconsider the value of crater classes.

Two principal processes have been invoked for emplacement of the intercrater plains: 1) basin ejecta and autochthonous surface materials reworked by that ejecta or 2) volcanic flows. Previous studies directed at discriminating among these two plausible origins have used two broad approaches: analysis of crater population statistics, and assessment of diagnostic landforms. For several reasons, neither approach has substantiated the origin of the plains units nor persuaded many to alter their initial view point. Therefore, we undertook a new approach: the multivariate statistical analysis of crater-class. The results of the analysis constrain the formative process of the intercrater plains units to have affected craters on both terrains in a similar manner. Any emplacement process brief in temporal extent (compared to the period of late heavy bombardment), such as emplacement of ejecta from a single event or a brief period of extensive volcanism, violates this constraint.

In order to apply standard crater statistical methodologies to the comparison of the two terrains, class by class and crater size by crater size, one must achieve good counting statistics. That is, the number of craters in a given class in a given diameter interval should be as large as possible so that sampling errors (that are equal to the square root of the number of craters counted) are as small as possible. In order to achieve this one must include large expanses of each terrain type in the study. But if the different areas have not experienced the emplacement process in a substantially identical manner, then combining areas may blur the signature of the process beyond recognition. Therefore, one would ideally like to sample small regions to obtain a homogeneous crater population, but large regions to obtain adequate sampling statistics. Faced with this problem, the most common approach has been to amalgamate the data from different regions and simply hope that heterogeneities would not frustrate the analysis. But amalgamation of samples clearly has traps in terms of both diluting the homogeneity of the signatures and reproducing locations of terrain boundaries.

The densely cratered terrains of Mercury occur in widely separated, poorly defined patches that are not constrained to constitute a

homogeneous data set. However, each area has only a relatively small number of craters. This data set begs for a new multivariate approach to the statistical treatment of craters.

We have classified craters in eleven regions of densely cratered plains and eleven regions of intercrater plains into four classes based on their degree of filling (from 1 = pristine to 4 = totally filled). The percentage of craters in each class in each region was then recorded, thus eliminating the problem of nonstationarity--but introducing the problem of induced correlations. Induced correlations arise in percentage data because as the percentage of craters in one class increases, the percentage in at least one other class must decrease--without the necessary intervention of any geologic process. This is commonly alluded to as King's law: "Some of it plus the rest of it equals all of it."

By standard statistical analyses, the correlation matrix (below) formed from percentage data seems to indicate a very significant (beyond the 1% level) negative correlation between class 2 and class 4 craters. A simple story could be constructed to account for this--a tale that makes excellent geologic sense, but, in fact, is no more than hand flailing if not supported by the statistical attributes of the data. In fact, when the algorithm suggested by Aitchison (1982) and implemented by Woronow and Butler (1986) is applied, this correlation is found to lack significance--no significant correlations (at the 5% level) exist in these data. Additional tests of the data divided into diameter intervals and terrain types also reveal no significant correlations. This implies that the crater classes on both terrains responded equally to, or independently of, the emplacement of the intercrater plains.

Among the processes that satisfy this substantial constraint would be a protracted period of volcanic emplacement spanning much of the period of late heavy bombardment, with the craters on both terrains being affected in a similar manner (although not necessarily to the same degree) on both terrains and in all areas studied here. Alternatively, the filling process could be linked to the impact bombardment itself so that craters would progress through the classes in proportion to the cumulative intensity of the bombardment on both surfaces. Processes that cannot account for the emplacement of the intercrater plains include short pulses of emplacement of volcanic deposits or of basin ejecta.

Aitchison, J. (1982). The statistical analysis of compositional data sets. J. Roy. Statis. Soc., **B44**, 139-177.

Woronow, A. and Butler, J.C. (1986). Complete subcompositional independence testing of closed data. Comp. & Geosci. 12, 267-280.

Correlation Matrix for Percentage Data

	CLASS II	CLASS III	CLASS IV	TOTAL
CLASS I	-0.11	-0.39	-0.20	-0.09
CLASS II		-0.25	-0.63	-0.13
CLASS III			-0.37	-0.25
CLASS IV				-0.04

STUDIES OF EARLY INTENSE CRATERING AND POSSIBLE SATURATION EFFECTS

William K. Hartmann
Planetary Science Institute, Tucson, Arizona

Crater counts on Rhea were completed, to be compared and combined with independent counts by Steve Squyres; the material is now being integrated into a study of cratering on Rhea and other Saturn satellites by Squyres, Lissauer, and Hartmann. Special attention is being paid to lighting and other effects on the apparent changes in crater density from one region to another.

In my 1984 Icarus paper, "Does Crater Saturation Equilibrium Occur in the Solar System," I proposed that a common steady state density has been reached on a number of different planets' and moons' surfaces, at a number of different crater-diameter-scales. This crater density is given (within a factor 2 or 3) by the equation

$$\log N_{HC} = 1.83 \log D_{km} - 1.33$$

where N_{HC} = crater density in heavily cratered regions (craters/km^2)

expressed as craters in $\sqrt{2}$ logarithmic increments of diameter.
and D_{km} = crater diameter in km.

I proposed in that paper that a further test of the concept could be made by seeing if sub-hectometer-scale lunar craters, which are widely regarded as being saturated, in order to explain the regolith, match this curve. This is a sensitive test, because at scales from about 2 km down to a few hundred m, these craters fall on a steeply ascending curve with slope near -3, rather than the slope of -1.83 found in the equation above. Therefore, if they fit the saturation curve, we will find a dramatic "roll-over" from the steep branch to the flatter -1.83 branch described by the equation. My preliminary results indicate that this roll-over is found. One example is shown in Figure 1, where the craters in Mare Cognitum are shown down to diameters of a meter. Segment A is the under-saturated set of large primary impacts formed in the last 3-1/2 billion years. Segment B is the steep secondary branch. It can be seen that B rolls over sharply at about 300 m to segment C, which falls along the curve described by the equation.

This result is unexpected according to those who assert that there is no saturation, and it has profound implications for re-interpretation of Voyager results on outer planet satellites, where the Voyager team interpreted all surfaces as being not saturated. This new result raises the possibility of saturation and, therefore, changes in their estimates of crater origin.

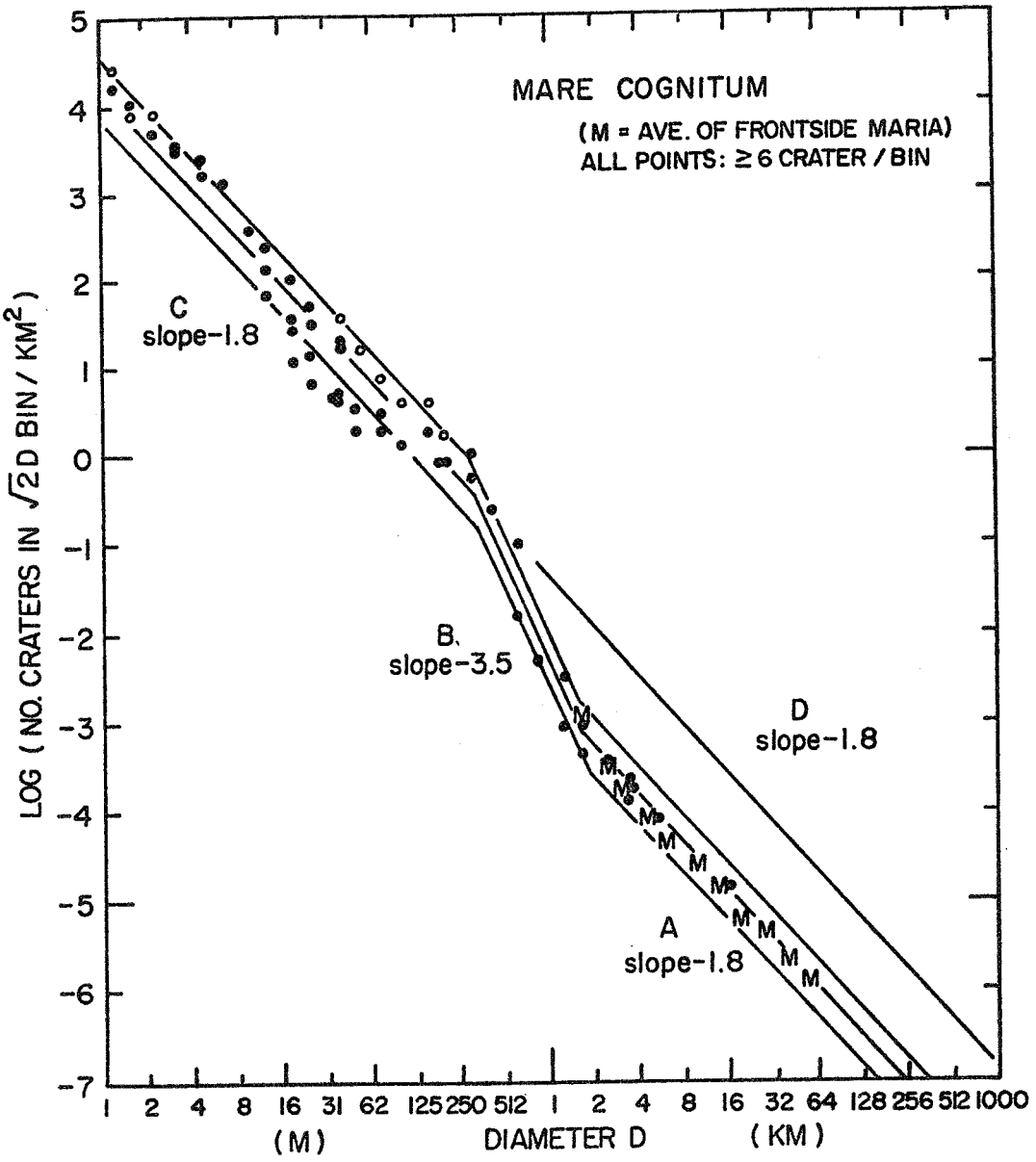

Figure 1: Crater counts in Mare Cognitum. Segment C offers evidence for saturation equilibrium as discussed in text.

REVISION OF THE MARTIAN RELATIVE AGE CHRONOLOGY. Nadine G. Barlow, Lunar and Planetary Laboratory, University of Arizona, Tucson, Arizona 85721.

A number of martian chronologies, both absolute and relative, exist in the literature. These histories are derived primarily from Mariner 9 images of small (<10-km diameter) craters in localized regions of the planet. The higher quality Viking Orbiter images have not been in a convenient format for global mapping until recently when the USGS 1:2M photomosaic series was completed. Thus, no planet-wide chronologic studies have been developed from this more recent data.

Using the Viking 1:2M photomosaic series, I have divided the surface of Mars into approximately 25 generalized geologic units and a number of localized regions. All craters ≥8-km in diameter were mapped and classified by a variety of properties. The crater size/frequency distribution curves were determined for each of these units. The relative plotting technique was used since the shapes and positions of the distribution curves on this type of plot give information on the relationship of the terrain to the period of heavy bombardment (see Barlow and Strom, 1986, for further discussion of this technique).

It was found that approximately 60% of the martian surface dates from the period of heavy bombardment. Areas within the southern highlands which show no erosion by lava flows ("pure uplands") are the oldest regions on the planet. Jovis Tholus, Uranius Tholus, Tyrrhena Patera, Ulysses Patera, and Ceraunius Tholus also formed early in martian history, contrary to what is commonly believed (volcanic data is from a study by Katz and Strom, 1984). The time of the Hellas and Argyre impacts was determined from the crater information on the rims of these basins. They are found to be similar in age to the intercrater plains in the southern highlands, Hellas being slightly older than the intercrater plains and Argyre slightly younger. Tharsis Tholus, Hecates Mons, Albor Tholus, and Apollinaris Patera are approximately contemporaneous with the formation of Argyre as are the various fractured and dissected highlands regions. The fractured highlands south of the present-day Tharsis Province probably indicate that the Tharsis Bulge was beginning to form around this time. The volcanic plains south-southwest of the Hellas Basin formed long after the impact creating the Hellas Basin.

The use of the relative plotting technique has solved the controversy over the age of the ridged plains. These plains definitely show a heavy bombardment-type distribution curve, but the lower crater density relative to the highlands indicates that these regions formed near the end of heavy bombardment. Lunae Planum, Hesperia Planum, Syrtis

Major Planitia, Sinai Planum, and Chryse Planitia all fall into this category. The floors of the Hellas and Argyre Basins as well as the volcanic constructs of Hadriaca Patera, Biblis Patera, and Uranius Patera also formed near the end of heavy bombardment.

The remaining 40% of the martian surface has formed since the end of heavy bombardment and is located primarily in the northern hemisphere. The northern plains was divided into several localized regions and it was found that a variety of formation ages exist for these plains units. The post-heavy bombardment period can be divided into older, intermediate, and younger sections based on crater densities. The older division contains the general units of plains and mottled plains, the local units of Utopia Planitia, Solis Planum, Isidis Planitia, Elysium Planitia, Syria Planum, and Vastitas Borealis, the Elysium Mons volcano, and the chaotic terrain and fractured plains surrounding Tharsis. The intermediate period saw the formation of the equatorial layered deposits, Amazonis Planitia, Mare Acidalium, Arcadia Planitia, Alba Patera, the latest episode of resurfacing by the outflow channels, and the beginning of Valles Marineris. The most recent period of martian history includes the formation of the polar layered deposits, Tharsis plains, Olympus Mons, and the floor of Valles Marineris.

This study has provided a more detailed chronology than currently exists in the literature and has created some changes to the currently accepted geological evolutionary sequence of Mars. The period of heavy bombardment, although dominated by impact processes, experienced many forms of volcanic activity and at least one episode of intense fracturing. Most small volcanic constructs and the ridged plains regions are found to date form this early period, contrary to common belief. The fracturing and dissection of the highlands helps to provide further constraints on the timing of events such as the formation of the hemispheric dichotomy and the formation of the Tharsis Bulge. The northern plains are found to consist of a number of differently aged regions. Plains units bordering each other can be vastly different in age, as demonstrated by Sinai Planum and Solis Planum. The difference in age between the chaotic terrain and the outflow channels together with differences in the distribution curves among craters of various erosional states found on the channels supports the theory of episodic periods of flooding (Neukum and Hiller, 1981).

Mars has experienced a very active geologic history, with two identifiable periods of peak activity (Figure 1). The first gentle peak corresponds to the formation of the extensive intercrater plains in the highlands. The second peak is sharper and is due to the recent formation of the

northern plains. This revised relative chrnology will help provide constraints on the various geologic and thermal evolutionary models proposed for Mars.

References:
Barlow, N.G. and R.G. Strom (1986). Reports of the Planetary Geology and Geophysics Program--1985, NASA TM88383, 211-213.

Katz, L.T. and R.G. Strom (1984). Personal Communication.

Neukum, G. and K. Hiller (1981). J. Geophys. Res., 86, 3096-3121.

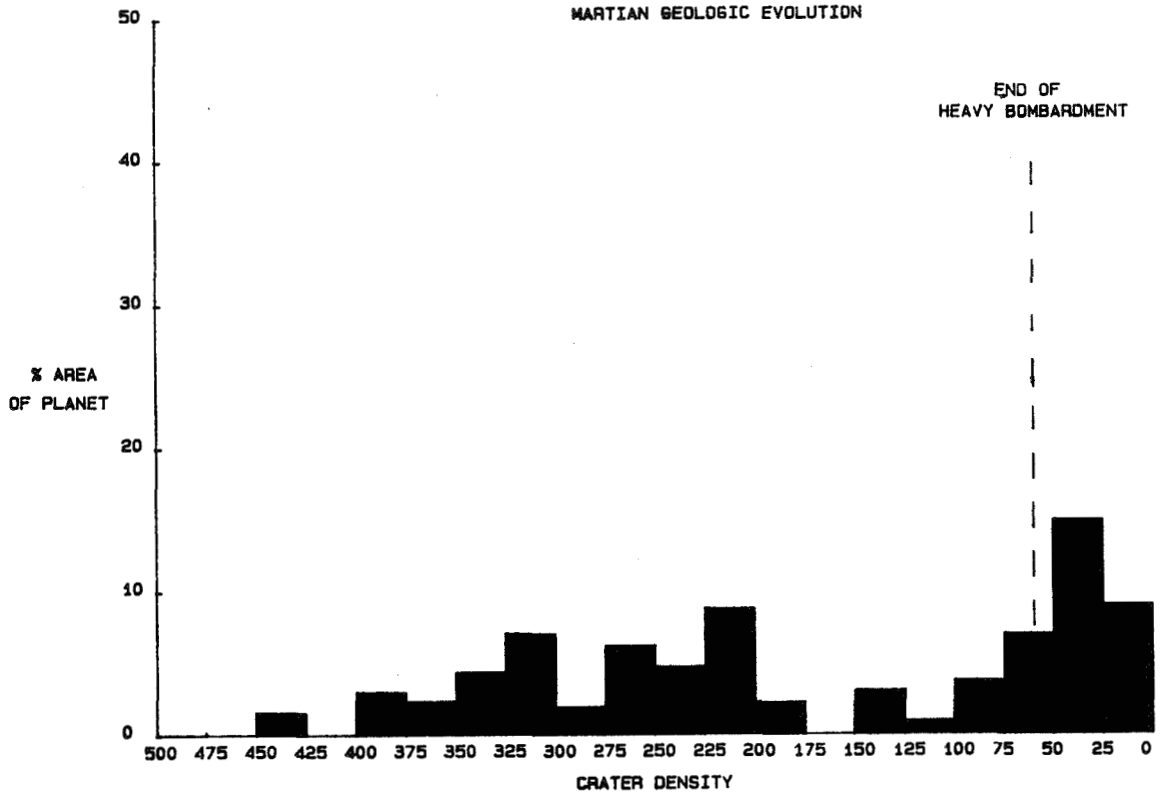

Figure 1: Histogram of the percentage of the martian surface displaying a particular range in crater density. This graph provides an indication of the minimum level of geologic activity at any particular point in martian history. Crater density is defined as the number of craters ≥8-km diameter/10^6 km^2.

EARLY CHANGES IN GRADATION STYLES AND RATES ON MARS P. H. Schultz and D. Britt, Brown University, Dept. of Geological Sciences, Box 1846, Providence, RI 02912

INTRODUCTION: The history of an active surface-atmosphere exchange of volatiles on Mars is recorded in the ancient cratered terrains. Large impact basins and craters provide a means to document this process and any changes in style with time. Two large impact basins (Isidis and Argyre) produced large well-defined geologic units and terrains, thereby allowing reliable crater statistics and dentification of time-dependent processes prior to most well-perserved volcanic events. Moreover, the collective impact basin record permits calibration of ancient gradation rates.

APPROACH: The wide annulus of massifs and knobs of Isidis and Argyre provided sufficiently large areas for meaningful crater statistics of large (>30km diameter) craters. Counts were made over adjacent and nested areas in order to test consistency and to derive relative ages of each basin. Within the Isidis annulus, characteristic terrains provided counting areas for dating contrasting surface process: channeled hummocky terrain, etched terrains, and intermassif channeled plains. The channeled hummocky terrain contains a high channel density (length/area) of narrow valley networks cutting both primary Isidis features and old craters. The etched terrains represent a broad region outside the inner high-relief massifs of southwestern Isidis where numerous irregular plateaus, mesas, and relict craters indicate a different style of erosion. The intermassif channeled plains occur along the inner mountainous ring. Shallow meandering channels form a large integrated drainage system that is linked to numerous smaller intermountain basins ("ponds"). These ponds and interconnected tributaries extend beyond the primary inner massif ring through broad canyons.

The Argyre basin presents a dramatic contrast in channel development. Deeply incised, narrow valleys exist but emerge along the scarp or are highly localized. Intermassif plains contain subtle curvilinear channels but the high density networks and furrowed massifs typical for Isidis are missing (1,2). To the south, long curvilinear channels and canyons follow heavily degraded basin structure and topography from beyond the Argyre scarp to the interior where narrow ridges appear to replace the original channel course. Narrow-valleys on ejecta facies superposing Argyre are isolated and unlike the systems within Isidis. Crater statistics have been obtained for the knobby terrain inside the scarp where larger post-terrain craters could not be buried by plains.

Figure 1 and Table I summarizes selected data from this study and permits comparison with other published crater counts of major volcanic events (3). Both the Isidis and Argyre crater distributions contrast with distributions derived for the oldest plains units examined here and elsewhere (4). A rapid fall-off in the number of craters smaller than 20km in diameter may reflect a different production population, enlargement of craters by erosion (¬25%), or a basin secondary crater population (10-50km in diameter). Each possibility is being explored in more detail but we tentatively believe that the distribution curves are indicating active gradational processes since the formation of Isidis and Argyre. The observed crater distribution of Sinai Planum has been used as a "standard" in order to correct for crater loss of ancient terrains and to extend data from small counting areas. These counts have been normalized to $10km/10^6km^2$ in order to minimize the amount of extrapolations from either ancient or recent terrains.

DISCUSSION: The change in narrow-valley-network (nvn) drainage density within well-defined drainage basins and the change in style with time is shown in Figure 1. As discussed previously (2,5), a rapid change is indicated after the Argyre impact. This can be documented not only by comparison between Isidis and Argyre but also by old impact craters. Four conclusions emerge. First, the interior massif/knobby annulus of Argyre does not appear to be a pristine basin surface but a modified terrain dating from early volcanic plains emplacement. The terrain is similar to but later than the knobby terrains of Elysium, which may be related to an ancient

modified basin (6). Second, much later channel development is observed within the Isidis intermassif region. These channels form a long, relatively mature and integrated system. Third, both the etched terrains within Isidis and the nearby volcanic plains of Syrtis Major Planitia date from approximately the same period. Fourth, late-stage (comparable in age to Syrtis Major Planitia) unintegrated run-off channel systems occur within the mantled ejecta facies of old impact craters or are localized in certain deposits/terrains.

These results provide quantitative data for the change in gradation with time on Mars. Prior to the Argyre impact, the formation of narrow valley networks within Isidis resulted in removal of 75% of the crater smaller than 3km in diameter and 30% of craters smaller than 10km and/or 10-25% enlargement of larger craters. The size distribution of large martian impact basins in the ancient cratered terrains suggests broader scale losses during earlier epochs, rather than an absence of basin-forming impactors. The knobby terrain of the Elysium region and the nearby fretted terrain margins developed after the formation of Argyre, at about the time of the earliest volcanic constructs were formed. This process, and presumably the formation of the martian "dichotemy" appears to reflect on erosional event (rather than, or in addition to a tectonic process). The knobby terrains within Argyre may preserve a similar process nearly simultaneous with early volcanic plains emplacement (Sinai Planum). The etched terrains that apparently are associated with the emplacement of Syrtis Major Planitia of southern Isidis may represent an arrested analog for this process. Narrow-valley network formation apparently had ceased except as highly localized occurrences reflecting geothermal activity or emergent springs. The dramatic change in broad-scale gradation rates and style from pre-Argyre to Tharsis times suggest a change from atmosphere-surface exchange to principally surface/subsurface volatile loss including water and perhaps trapped carbonates (7).

References: (1) Schultz, P.H. and Rogers, J. (1982) *Conf. on Planetary Volatiles*, LPI Contrib. 488, p. 97-98. (2) Schultz, P.H. *et al.* (1984), LPI Tech Report 85-03 (S. Clifford, ed), p. 82-84. (3) Plescia, J.B. and Saunders, R.S. (1979) *Proc. Lunar Planet. Sci. Conf. 10th*, p. 2841-2859. (4) Neukum, G. and Wise, D. (1976) *Conf. on Evolution of the Martian Atmosphere*, Lunar and Planetary Institute, Houston. (6) Schultz, P.H. (1984) *Lunar and Planetary Science XV*, p. 728-729, Lunar and Planetary Institute, Houston. (7) Kahn, R. (1985) *Icarus, 62*, 175-190.

Feature/Unit[+]	Log N(>10Km)/10^6km^2*	Channel Density (km/km^2)	Channel Style
Hellas (B)	3.1		valley networks
Isidis (B)	3.0	10^{-1}	valley networks
Uranius Tholus (V)	2.9		channeled
Argyre (B)	2.68	$<2x10^{-2}$	localized networks
Ulysses Patera (V)	2.62		
Nepenthes Mensae (KT)	2.29		
Elysium Knobby terrain	2.29		
Tharsis Tholus (V)	2.25		
Argyre-massif annulus (KT)	1.98		run-off;emergent
Apollonaris Patera (V)	1.95		channeled
Uranius Patera (V)	1.95		
Tyrrhena Patera	1.93		channeled
Sinae Planum (VP)	1.90		
Syrtis Major Dy (C)	1.85	$2x10^{-2}$	isolated run-off
Hesperia Planum (VP)	1.83		
Cerulli	1.83		isolated run-off
Isidis-intermassif (ChP)	1.75		integrated run-off
Syrtis Major Planitia	1.75		
Peridier (C)	1.71	$<2x10^{-2}$	isolated run-off
Lunae Planum (VP)	1.55		
Holden (C)	1.55		

+ B = basin; C = impact crater; V = volcanic construct; KT = knobby terrain; VP = volcanic plain; ChP = channeled plains.

* adjusted using crater statistics for Sinae Planum

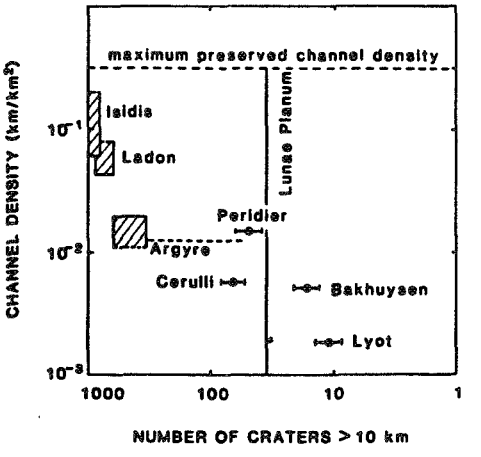

Figure 1. Production rate of narrow valley formation on selected basins and craters indicated by channel density (length/area) and superposed crater density (number > 10km/10^6km^2).

CRATERING AND OBLITERATION HISTORY OF THE SOUTH POLAR REGION OF MARS

J.J. Plaut, R.E. Arvidson, E.A. Guinness, and R. Kahn, McDonnell Center for the Space Sciences, Department of Earth and Planetary Sciences, Washington University, St. Louis, MO 63130.

The diverse assemblage of geological units in the south polar region of Mars implies a complex geological history, with exogenic processes strongly modulated by climatic phenomena. In this study results are presented from a comprehensive analysis of crater size frequency distributions compiled from Viking Orbiter images of south polar terrains. Depositional histories for the various terrain units are modelled based on deviations of cumulative crater size frequency plots from an assumed production function. Stratigraphic and morphologic data obtained from visual examination of Viking images are also used, primarily to corroborate inferences concerning ages and obliteration histories derived from the crater data.

The model used for crater production and obliteration is adopted from [1]. We assume a cratering history consisting of an early exponentially decaying rate along with a long-lived steady rate. The amount of obliteration needed to remove a crater of a certain size is assumed to be equivalent to crater depth. These assumptions are incorporated into an algorithm which generates a model cumulative size frequency distribution curve for a given obliteration history and surface age. Actual crater abundance data are then compared with the model curves to select a best-fitting obliteration history.

Application of this model to south polar cratered terrain indicates that an intense depositional episode occurred on this unit during the ending phase of heavy bombardment. We infer a depositional rate of 2.2 +/- 0.4 km/Ga for a period of about 0.5 Ga. A roughly concurrent episode, but with a higher deposition rate and of shorter duration, is recognized in counts done for equatorial cratered terrain. Following this episode the polar cratered terrain appears to have continued to accumulate material at a rate of 0.08 +/- 0.01 km/Ga, while the equatorial areas show crater production only.

In parts of the south polar region, a plains unit with a crater production surface and a model age of 3.5 Ga overlies the cratered terrain. Pitted terrain materials with a thickness up to 1km [2] overlie the plains unit in places. The plains and pitted terrain units are found in similar latitudes as the polar layered terrain, but in the hemisphere on the opposite side of the pole. The plateau surfaces of the pitted terrain have crater production populations also, with a model age of 3.3 Ga, suggesting that erosion has been limited to pit excavation and that obliteration rates have been insignificant. The end of deposition of pitted terrain debris implied by the model age of 3.3 Ga coincides with the end of the inferred depositional episode on the cratered terrain.

Study of high resolution images of a large portion ($\sim 3 \times 10^5$ km^2) of south polar layered terrain yields a dozen features strongly resembling impact craters. The craters range in size from 1km to 5km. The cumulative size frequency distribution for this set of craters implies that the surface that recorded the impacts was in place no later than several hundred million years ago. This crater age is at least an order of magnitude greater than estimates in previous studies [3]. Although statistics are poor due to the small number of craters, the log-log cumulative size frequency distribution is best fit to a slope of -1.3, suggesting that the surface is undergoing some obliteration (the assumed production slope is -2). An obliteration rate of 2.5 km/Ga is implied for a steady state obliteration model.

The continuing deposition on polar cratered terrain noted above appears limited to the areas surrounding the layered terrain. The pitted terrain plateaus and the plains unit, which lie at greater distances from the layered terrain, evidently have not accumulated significant amounts of material since their formation. We suggest that the continuing deposition represents redistribution of layered terrain debris on the cratered terrain. The spatial association, as well as the clearly erosional morphology of the layered terrain support this argument.

A model geological history thus emerges for the south polar region. Formation of the cratered terrain was followed by an intense obliterative episode, of possibly global extent. Polar plains formation occurred toward the end of this episode, and massive poleward transport of debris resulted in emplacement of pitted terrain material on top of the plains. A period of erosion preceded emplacement of layered terrain, evidenced by the unconformable contact between already eroded pits and overlying layered terrain. The timing of initiation of layered terrain accumulation is difficult to constrain, but crater data certainly suggest that much of the deposit was in place by several hundred million years ago. A change from an early (>3.5 Ga) dense atmosphere to one that is thinner and more strongly modulated by orbital variations is consistent with our results. However, the excavation of pits within the pitted terrain and the lack of obliteration on high latitude plains and pitted terrain plateaus also require explanation. We are pursuing a variety of models to explain these observations.

REFERENCES

[1] Phillips, R. and M. Malin, (1980), *Science, 210,* p.185-188.
[2] Guinness, E. et al., (1986), *NASA Tech. Memo. 88383,* p.245-247.

Martian Rampart Craters: Morphologic Clues for the Physical State of the Target at Time of Impact.

Peter J. Mouginis-Mark, Planetary Geosciences, Hawaii Institute of Geophysics, University of Hawaii, Honolulu, Hawaii 96822

From the return of the first Viking Orbiter images of martian impact craters it was evident that the morphology of the ejecta blankets surrounding these craters was different from their lunar and mercurian counterparts insofar as much of the ejecta appeared to have been emplaced by surface flow (Carr *et al.*, 1977). Over the last ten years, considerable debate has focused on the possible cause(s) for this ejecta fluidization and flow. Possible forms that the fluidizing medium may have taken include water ice or liquid water within the target material (Carr *et al.*, 1977; Boyce, 1979; Johansen, 1979) or atmospheric gases interacting with suitable particle sizes within the ejecta curtain (Carr *et al.*, 1977; Schultz and Gault, 1979; Schultz, 1986). Indeed, Schultz (1986) draws attention to the fact that the fluidized ejecta facies only indicate fluid-like emplacement, and laboratory experiments (Schultz and Gault, 1981, 1984) have shown that rampart-bordered ejecta facies and ejecta flow lobes can develop without the presence of water.

A ground water system has been proposed for Mars on a global scale (Carr, 1979; Clifford, 1986), and it is believed likely that such a system would influence the occurrence and physical state of impact crater ejecta. A major difficulty in correlating these inferences about ground volatile content with the observed properties of crater ejecta blankets lies in knowing the extent to which the ground water system (the deep megaregolith) was filled. Many of the large outflow channels seen on Mars may have formed through the eruption of ground water under pressure from the megaregolith beneath the permafrost, which is estimated to have been about 1 km thick (Carr, 1979). Carr (1986) concluded that the megaregolith below this permafrost layer, planetwide, might contain no less than the equivalent of a water layer 350 meters thick, while Clifford's (1986) calculations of outgassed H_2O on Mars would suggest that if more than a few percent of the quantity of water required to saturate the pore volume of the cryosphere were present, then a sub-permafrost water system of substantial proportions would result. After saturation of the pore volume of the cryosphere, the equivalent of an additional 100 meters of H_2O inventory would be sufficient to create an acquifer nearly 4.3 km deep. This small volume of water is all that is required to produce this acquifer because the predicted pore volume at depth is very low (Clifford, 1986). It is further predicted that much of the water originally at depths of less than 1 km would remain *in situ* for most of martian history (Fanale *et al.*, 1986), thus constituting a possible method for fluidizing impact crater ejecta.

Because of the importance that the presence of liquid water, liquid brines, or ground ice close to the surface would hold in global models of volatile abundance and physical state (e.g., Fanale and Jakosky, 1982; Fanale *et al.*, 1986), more precise observational information is needed to help constrain these theoretical models of volatile distribution and state. One approach to identifying both the former presence (or absence) and physical state of subsurface volatiles in the martian past comes from their inferred influence in controlling the morphology of rampart craters and crater ejecta blankets. Key testable morphologic indicators are thought to be the identification (or lack thereof) of melt water channels and small-scale topography on the surface and edges of the ejecta blankets, and the degree of stability of the parent crater walls (Mouginis-Mark, 1986). Diagnostic features are likely to be physically small in size (probably less than a kilometer in extent) and so have not previously been considered either in global studies of rampart craters (e.g. Johansen, 1979; Horner and Greeley, 1986) or cratering models (e.g., Schultz and Gault, 1984; Schultz, 1986). The current research therefore attempts to describe morphologic features seen in very high resolution (8 to 17 meters per pixel) Viking Orbiter images of crater ejecta blankets and interiors, in order to constrain the most likely target properties at the time of crater formation.

The Viking Orbiter image data set contains approximately 400 frames at a spatial resolution of better than 10 meters per pixel, and 2,200 frames at a resolution of better than 20 meters per pixel, for which the atmosphere was either clear or only slightly obscured (J. Zimbelman, pers. comm. 1986). A search is being conducted of all these images and so far has revealed several examples of both interior and exterior features of impact craters that bear on the nature of the ejecta fluidizing medium. Preliminary observations and speculations on the physical state of the martian regolith at the time of crater formation are as follows:

1) The ejecta lobes retain much of the small-scale structure that was produced during ejecta deposition. Radial striations, pressure ridges and the sharp distal ramparts are all well preserved on craters ranging in size from 4.5-26 km in diameter. The general absence of remobilized materials as a consequence of water sapping from the emplaced ejecta suggests that the lobes possessed appreciable mechanical strength at the time of their emplacement and that the liquid water content of the flows was very low. No evidence to support the proposal by Woronow (1981) that the ejecta contained 16 to 72% water has been found.

2) For two ejecta deposits within the basin Schiaparelli that have been partially eroded, it is evident that large blocks were transported within the ejecta flow, and that some of these blocks were most likely ice-rich. Subsequent melting or ablation of this ice has led to collapse of the ejecta deposit in isolated places to form features similar to terrestrial kettle holes.

3) The same eroded ejecta blankets reveal that flow striations extend through the thickness of the ejecta deposit, rather than simply being superficial features. This would imply that the ejecta flow was non-turbulent, akin to poorly fluidized terrestrial pyroclastic flows.

4) Most of the crater interiors studied to date reveal few signs of melt water release or the abnormal amounts of slumping that would be expected if the rim material were water-rich.

5) Rare examples of surface flow can be found both on the ejecta deposits and crater inner walls. In the case of a small crater southwest of Bakhuysen, it is believed that this surface flow was made possible due to the formation of this small crater on the ejecta blanket of Bakhuysen. For the crater Cerulli, no obvious explanation for the unusually volatile-rich wall material presents itself, but it is clear that extensive surface flow, expressed by numerous small channels on the wall and continuous ejecta blanket, took place following the formation of the crater.

It should be remembered that only a very small number of craters, all in a narrow latitude band (predominately in the southern hemisphere) have been included in this investigation, primarily due to the sparse coverage of the high resolution Viking Orbiter images. Individually, the above observations do not argue convincingly for a single set of properties for the target material or the derived ejecta; small volumes of liquid water, larger volumes of ice, or purely atmospheric effects could all be used to explain ejecta fluidization. Taken together, however, it is believed that the observational data supports the notion that ice, rather than water or atmospheric effects, dominated both the emplacement process and the mode of ejecta fluidization for the majority of rampart craters studied here. By implication, ice must have been present in the target rocks in significant amounts (a few to perhaps 10 volume percent?) at the time of impact. The surface channels (both on the ejecta blankets and within craters) and kettle holes argue against atmospheric effects dominating ejecta fluidization, while the stability of small-scale topography and only the rare occurrence of surface channels indicates that liquid

water was not commonly associated with the ejecta.

As a topic for future investigation, numerical models need to be developed to determine the effects of different volumetric amounts of ice that would have to be entrained within the ejecta to produce the observed morphologies. At the present time the high mechanical strength of ejecta lobes, as demonstrated by up to several tens to hundreds of meters of relief on the lobes and ramparts, would suggest that the volumetric amount of ice that was incorporated within the ejecta was quite low. Quantitative estimates for the volume of ground ice are needed, but currently estimates appear consistent with the regolith/atmosphere models proposed for Mars and can explain the observed landform morphology.

Clearly, however, the observations presented here only pertain to a very small number of fresh craters that by chance were imaged at very high resolution by the Viking Orbiters. While these craters provide an insight into the physical state of the target material for these random areas, image resolution is inadequate to draw firm conclusions on volatile state for most of Mars. As a result, it is concluded that the identification of small-scale features diagnostic of water sapping and ejecta remobilization on crater ejecta blankets constitutes one of the many interesting experiments that could be conducted with the sub-meter resolution camera planned as part of NASA's Mars Observer Mission.

REFERENCES Boyce, J.M. (1979). A method for measuring heat flow in the martian crust using impact crater morphology (Abstract). *Rpts. Plan. Geol. Prog. 1978-1979*, **NASA TM-80339**, p. 114-118. Carr, M.H. (1979). Formation of martian flood features by release of water from confined aquifers. *J. Geophys. Res.*, **vol. 84**, p. 2995-3007. Carr, M.H. (1986). Mars: A water-rich planet (Abstract). *Symposium on Mars: Evolution of its climate and atmosphere* **LPI Contr. #599**, p. 9-11. Carr, M.H., L.S. Crumpler, J.A. Cutts, R. Greeley, J.E. Guest and H. Masursky (1977). Martian impact craters and emplacement of ejecta by surface flow. *J. Geophys. Res.*, **vol. 82**, p. 4055-4065. Clifford, S.M. (1986). Mars: Crustal pore volume, cryosphere depth, and the global occurrence of groundwater (Abs.). *Symposium on Mars: Evolution of its climate and atmosphere*, **LPI Contr. 599**, p.18-20. Fanale, F.P. and B.M. Jakosky (1982). Regolith-atmosphere exchange of water and carbon dioxide on Mars: Effects on atmospheric history and climate change. *Planet. Space Sci.* **vol. 30**, p. 819-831. Fanale, F.P., J.R. Salvail, A.P. Zent and S.E. Postawko (1986). Global distribution and migration of subsurface ice on Mars. *Icarus*, **vol. 67**, p. 1-18. Horner, V.M. and R. Greeley (1986). Effects of elevation and plains thicknesses on martian crater ejecta morphologies on the ridged plains (Abstract). *Rpts. Plan. Geol. and Geophys. Prog. 1985*, **NASA TM-88383** p. 446-448. Howard, K.A. and H.G. Wilshire (1975) Flows of impact melt at lunar craters. *Jour. Research U.S. Geol. Survey*, **vol. 3**, p. 237-251. Johansen (1979). The latitude dependence of martian splosh cratering and its relationship to water (Abstract). *Rpt. Plan. Geol. Prog. 1978-79*, **NASA TM-80339**, p. 123-125. Mouginis-Mark, P.J. (1986). Ice or liquid water in the martian regolith? Morphologic indicators from rampart craters (Abstract). *Symposium on Mars: Evolution of its climate and atmosphere*. **LPI Contr. #599**, p. 67-69. Schultz, P.H. (1986). Crater ejecta morphology and the presence of water on Mars (Abstract). *Symposium on Mars: Evolution of its climate and atmosphere*. **LPI Contr. # 599**. p. 95-97. Schultz, P.H. and D.E. Gault (1979). Atmospheric effects on martian ejecta emplacement. *J. Geophys. Res.* **vol. 84**, p. 7669-7687. Schultz, P.H. and D.E. Gault (1981). Ejecta emplacement and atmospheric pressure: Laboratory experiments (Abstract). *Third International Colloq. on Mars*, **LPI Contr. 441** p. 226-228. Schultz, P.H. and D.E. Gault (1984). On the formation of contiguous ramparts around martian impact craters (Abstract). *Lunar Planet. Sci.* **XV**, p. 732-733. Woronow, A. (1981). Preflow stresses in martian rampart ejecta blankets: A means of estimating the water content. *Icarus*, **vol. 45**, p. 320-330.

CRATER EJECTA MORPHOLOGY AND THE PRESENCE OF WATER ON MARS; P. H. Schultz, Brown University, Department of Geological Sciences, Providence, Rhode Island 02912

Introduction: Various approaches have been used to establish the presence of buried ice or water on Mars. A popular and frequently referenced diagnosic indicator has been the multi-lobed or rampart-bordered martian ejecta facies (1,2,3 among others). The implicit premise has been that fluidized ejecta facies indicates the presence of water; in fact, fluidized ejecta only indicate fluid-like emplacement. Laboratory experiments (4,5) have shown that rampart-bordered ejecta facies and ejecta flow lobes can develop without the presence of water. These results do not disprove the notion that subsurface water/ice exists but reveal the non-uniqueness in interpretations owing to a variety of controlling variables. The purpose of this contribution is to review the possible effects of projectile, target, and environment on the cratering process.

Atmospheric Effects: Laboratory experiments performed at the NASA-Ames Vertical Gun Range (AVGR) have documented the effects of an atmosphere on ejecta emplacement at small scales. For vertical impacts into compacted pumice, a systematic change in ejecta morphologies is observed with increasing atmospheric pressure (4,5): vacuum-like ($P_0 < 0.05\ P_0$); contiguous rampart (0.1-0.3 P_0); multiple flow lobe (0.3-0.6 P_0); and radially scoured (0.7-1.0 P_0). These changes are accompanied by an increasingly distorted ejecta curtain and the development of a basal ejecta flow.

Further studies reveal the effects of atmospheric density impact velocity, and *in-situ* ejecta size. Reduced atmospheric density (He) still results in rampart-bordered ejecta facies in the appropriate pressure range (0.1-0.3 P_0) without significant distortion of the ejecta curtain. Impact velocity (from 0.03 km/s to 6.5 km/s) has little effect on ejecta morphology; therefore, ejecta curtain modification and the distinctive ejecta patterns reflect late-stage processes, decoupled from early-time impact velocity effects. An important variable, however, is the average *in-situ* grain size in the target. A shift in the modal grain size from 50 μ to 100μ also changes the onset of characteristic ejecta patterns to larger atmospheric pressures. A modest amount of fine-grained material (20% pumice) with coarser grained No. 24 sand, however, results in rampart-bordered ejecta facies at 1 P_0.

This brief summary indicates that Mars-like ejecta facies can be produced in the laboratory without the presence of water and principally depends on atmospheric pressure and ejecta size. The dynamic process responsible for the ejecta patterns has been revealed through stereo-photography and 1/4-space experiments wherein airflow patterns are revealed by splitting the evolving ejecta curtain in half. As summarized elsewhere (5,6), the outward movement of the wall of ejecta creates a partial vacuum within the crater cavity. At late-stages, this pressure difference results in a toroidal airflow that pursues the ejecta curtain. With increased atmospheric pressure, the relatively simple toroidal circulation breaks into tongues of air-ejecta. The process can be successfully scaled to much broader scales if the Froude number similitude is preserved and the Reynolds number is high enough (6).

Atmospheric pressure appears to establish the toroidal winds; air drag establishes limits on the size of ejecta that can be entrained. The latter effect requires that the combination of ejecta size, ejecta velocity, and drag coefficient must be properly simulated between the laboratory and martian conditions (8). If an impact-generated airflow is established but the ejection velocity is too low or ejecta size is too large, then ejecta emplacement will not be modified significantly. Such considerations indicate that at present atmospheric conditions, martian craters 5 km in diameter with a sufficient fraction (20%) of ejecta smaller than a few centimeters should result in craters with contiguous ramparts. Small craters do not result in sufficiently high ejecta velocities nor excavate (generate) sufficiently fine-grained ejecta. Larger craters or impacts into finer grained

substrates will result in multi-lobed or even radial facies. As crater size increases, however, the effects of atmosphere scale height and secondary cratering reduce the role of the atmosphere (6).

Effects of Volatiles: The possible effect of high water content on ejecta emplacement has been studied in the laboratory both directly (9) and indirectly (10). A difficulty in directly equating the presence of water with fluid-like ejecta flow is the fate of ballistic water in the martian atmosphere. The low velocities (cm/s) for near-rim ejecta in the laboratory preserve the splosh-like behavior, whereas the high-velocities (50 m/s) for ejecta around a 5 km-diameter martian crater result in aerodynamic dispersal and atomization. During ballistic ejection, the distinction between drag-decelerated ejecta and drag-decelerated atomized water becomes less apparent. During emplacement, the inner near-rim lobe may reveal the effects of decreased viscosity due to the presence of water, whereas the outer facies records a more complex behavior reflecting atmospheric interactions and air entrainment (8,11).

Recent laboratory experiments have explored the possible effects of impact-induced vaporization by using powdered dry-ice on the surface at the point of impact (7,12). High-frame-rate photography (8,000-35,000 fps) reveals enhanced vaporization and ionization in the presence of an atmosphere or for oblique impacts. Early-time (< 10% completion) modification of the ejecta curtain does not persist to late time, and contiguous ramparts are produced. This is primarily because impact-induced vapor is jetted vertically and expands. The expanding vapor cloud scours the pre-impact surface well in advance of the ejecta plume. Although decoupled from the plume, the presence of the dry-ice resulted in a decreased ejection angle during the early stages of crater growth. Burial of the dry-ice has little effect on ejecta emplacement and does not result in a two component curtain as suggested in (13).

Discussion: For a given size crater between 5 and 20 km in diameter, a relatively contiguous rampart-bordered ejecta facies is believed to reflect the presence of relatively coarse ejecta sizes. Multiple rampart-bordered ejecta lobes around craters of the same given size reflect an increased fraction of smaller ejecta. Strong radial grooves indicate an even greater contribution by smaller ejecta. This sequence from contiguous rampart to multiple rampart to radial grooves reflects the increased entrainment of ejecta in the recovery airflow pattern created by the advancing ejecta curtain. The different emplacement styles correspond to a factor of 10-20 in ejecta size. Transitions from one ejecta emplacement style to another also can be produced by different atmospheric pressure, thereby perhaps accounting for craters of identical size but different ejecta morphologies only 50 km apart on the same geologic unit. It is important to note that the possible range in atmospheric pressures due to time variations (factor of 5) or to elevation (factor of 7) is small compared with the potential range range in target-controlled ejecta sizes. Because the effect of such variations is reflected in shifts in ejecta emplacement styles with crater size, a given region still may exhibit the same range in ejecta morphologies. Ejecta size is controlled by *in-situ* particle size and impact-induced comminution. The former control reflects local geologic history; the latter reflects processes including effects of impact velocity, total impact energy, and target-entrapped volatiles.

This discussion suggests that contradictions in interpreting martian crater ejecta morphologies reflect oversimplifying the process as a singular consequence of buried water. It seems entirely possible that most ejecta facies could be produced without the presence of liquid water. However, the combination of extraordinary ejecta fluidity, absence of secondaries, and high ejection angles all would point to the combined effects of atmosphere and fluid-rich substrates (11). Moreover, recent experiments revealing the broad scour zone associated with rapid vapor expansion may account for numerous craters in the circum-polar regions with subtle radial grooving extending 10 crater radii away with faint

distal ramparts. Thus certain crater ejecta morphologies may yet provide fundamental clues for the presence of unbound water.

References: 1) Johansen, L.A. (1979) NASA TM 80339, 123-125; 2) Masursky, H. (1982) In the *The New Solar System* (J.K. Beatty, *et al.*, eds), p. 90; 3) Horner, V.M. and Greeley, R. (1986) *Lunar and Planetary Science XVII*, 358-359, LPI, Houston; 4) Schultz, P.H. and Gault, D.E. (1981) *Third International Colloq. on Mars, LPI Contrib. 441*, p. 226-228; 5) Schultz, P.H. and Gault, D.E. (1984) *Lunar and Planetary Science XV*, 732-733, LPI, Houston; 6) Schultz, P.H. and Gault, D.E. (1982) *Geol. Soc. Sp. Paper 190* (L.T. Silver and P.H. Schultz, eds), p. 153-174; 7) Schultz, P.H. and Gault, D.E. (1986) *Lunar and Planetary Science XVII*, 779-780, LPI, Houston; 8) Schultz, P.H. and Gault, D.E. (1979) *J. Geophys. Res. 84*, 7669-7687; 10) Wohletz, K. and Sheridan, M. (1983) *Icarus 56*, 15-37; 11) Schultz, P.H. and Singer, S. (1980) *Proc. Lunar and Planetary Science XI*, 2243-2259; 12) Schultz, P.H. and Gault, D.E. (1985) *Lunar and Planetary Science XVI*, 740-741, LPI, Houston; 13) Mouginis-Mark, P. (1981) *Icarus 45*, 60-76.

THERMAL INERTIA CHARACTERISTICS OF THE MARTIAN CRATER CURIE

V. M. Horner and J. R. Zimbelman , Dept. of Geology, Arizona State University, Tempe, AZ, 85287 and Lunar and Planetary Institute, 3303 NASA Rd. One, Houston, TX 77058.

Thermal inertia characteristics have been determined for the martian crater Curie from high resolution groundtracks of Viking Thermal Infrared Mapper (IRTM) data. Curie is located at 28.8° lat, 4.8° long. It is ~120 km in diameter and has an extensive, but somewhat degraded, ejecta blanket. Flow features near the southeastern edge of the ejecta indicate that at least part of the Curie ejecta was emplaced in a manner similar to the ejecta of rampart craters. Curie straddles a boundary between the ridged plains (Hr) and the cratered highlands (Npl_1), as mapped by (1).

Five high resolution IRTM groundtracks which cross Curie provide coverage of the crater wall, rim and ejecta (fig. 1). They were all obtained between $L_S = 347°$ and $L_S = 6°$, within an hour of local midnight. Emission angles are <40°. Where the groundtracks overlap, the placement of thermal inertia contours agree to within ~0.2 x 10^{-3} cal cm^{-2} $sec^{-1/2}$ K^{-1}. The highest thermal inertia values for Curie are obtained for the inner crater wall. Thermal inertia decreases to lowest values just beyond the crater rim, then increases by ~0.5 x 10^{-3} cal cm^{-2} $sec^{-1/2}$ K^{-1} within the rest of the ejecta unit. The main ejecta unit has lower thermal inertias than the surrounding terrain by ~0.5 x 10^{-3} cal cm^{-2} $sec^{-1/2}$ K^{-1}. Thus, ejecta near the crater rim is ~1 x 10^{-3} cal cm^{-2} $sec^{-1/2}$ K^{-1} lower than the surrounding terrain.

Average particle sizes for different units can be derived from thermal inertias. Using the Kieffer et al. model (2), the following average particle sizes are obtained: ridged plains west of Curie = 0.16-0.25 mm, main ejecta unit = 0.13-0.16 mm, near-rim ejecta = 0.10 mm, crater rim = ~0.3 mm, inner crater wall = ~0.4 mm, and the ridged plains east of Curie = 0.13-0.20 mm. Note, however, that the model assumes a uniform distribution of one particle size. If the calculated particle sizes reflect actual ejecta sizes on Mars, then Curie ejecta should have been eroded beyond detectability, since grain sizes of ~0.16 mm are the most easily moved by wind on Mars (3). However, larger blocks are almost certainly incorporated into the thermal inertia signatures; as these would tend to increase thermal inertia values, it can be implied from our observations that the Curie ejecta generally consists of smaller particles and blocks than those within the surrounding terrain.

These observations are consistent with those of Schultz and Mendell (4) for the thermal inertia signatures of lunar crater ejecta. They found that ejecta within a crater radius of the rim of large lunar craters have lower thermal inertia values than the surrounding region. They proposed that the comminution of ejecta particles during emplacement, and their fragmentation upon impact, result in a greater proportion of fine ejecta for large lunar craters than might be expected from scaling the observed ejecta sizes of small explosion craters. This high proportion of smaller particles within the ejecta deposit would result in thermal inertia values lower than those of the surrounding terrain.

Our observations of Curie ejecta might be explained by a similar model. The comminution of ejecta during emplacement and the fragmentation of ejecta upon impact could also result in a large amount of fines for large martian craters. Increased brecciation of ejecta during impact from the vaporization of volatiles within the target material (5,6) may be an additional factor that contributes to the decrease in the average size of ejecta for martian craters.

Block abundances of the region can be obtained from brightness temperatures at different IRTM wavelengths, using a method first developed by Christensen (7). Emissivity-corrected

spectral differences are used to obtain the abundance of hypothetical blocks with a thermal inertia of 30 x 10^{-3} cal cm^{-2} $sec^{-1/2}$ K^{-1} and an albedo of 0.10. We found that the inner walls and floor of Curie have slightly lower block abundances, on the average, than its surroundings even though their thermal inertias are the highest in the region. These results are similar to recent observations of the dark streak of the crater Pettit, which also has high thermal inertias (6-7 x 10^{-3} cal cm^{-2} $sec^{-1/2}$ K^{-1}) but no difference in block abundance from its surroundings (8). Although no dark material can be seen on the crater walls, the floor of Curie has a region near the central peak which is covered with dark material (fig 1A, unit Ad), and other regions of the floor appear to be darkened by similar materials. Dark 'splotches' within craters have been interpreted as coarse, possible sand-sized material with an anomalously high thermal inertia resulting from its low emissivity (9). Some of the dark material on the floor of the crater may also have been deposited on the crater walls in amounts sufficient to change the brightness temperature, but insufficient for visual detection.

Within the study region there appears to be a general southeastern trend towards lower thermal inertia values (figure 1 b). This trend may be related to the proximity of the Arabia region, which is mainly to the south and east of Curie. Arabia has an extremely low thermal inertia, and is considered to be an area of dust accumulation (7,9). Curie is in a region where the overall thermal inertias change over relatively short distances radial to Arabia (7). Therefore, the observed general decrease in thermal inertia may represent increasing regional dust accumulation in the direction of Arabia. It should be noted that any accumulation of aeolian fines would reduce both the values of thermal inertia throughout the region, as well as the magnitudes of the differences in thermal inertia between the crater rim, the ejecta, and the area surrounding Curie. As only a few centimeters of dust are required to completely obscure the thermal inertia signatures of underlying materials (10), the thermal inertia characteristics of the Curie region may help to provide constraints on the distribution and rates of dust deposition near Arabia.

REFERENCES:

1) Scott, D. and K. Tanaka, 1986, *1:15M Geologic Map of the Western Region of Mars*, USGS, in press.
2) Kieffer, H. H. *et al.*, 1973, *J. Geophys. Res.* **78**, 4291-4312.
3) Greeley, R., *et al.*, 1976, *Geophys. Res. Lett.* **3**, 417-420.
4) Schultz, P. H. and W. Mendell, 1978, *Proc. Lunar Planet. Sci. Conf. 9th*, 2857-2883.
5) Schultz, P. H. and D. E. Gault, 1979, *J. Geophys. Res.* **84**, 7669-7687.
6) Wohletz, K. and M. Sheridan, 1983, *Icarus* **56**, 15-37.
7) Christensen, P. R., 1982, *J. Geophys. Res.* **87**, 9985-9998.
8) Zimbelman, J. R., 1986, *Icarus* **66**, 83-93.
9) Zimbelman, J. R. and H. H. Kieffer, 1979, *J. Geophys. Res* **84**, 8239-8251.
10) Jakosky, B. M., 1979, *J. Geophys. Res.* **84**, 8252-8262.
11) Witbeck, N. E. and J. R. Underwood, Jr., 1984, *Map I-1614*, USGS.

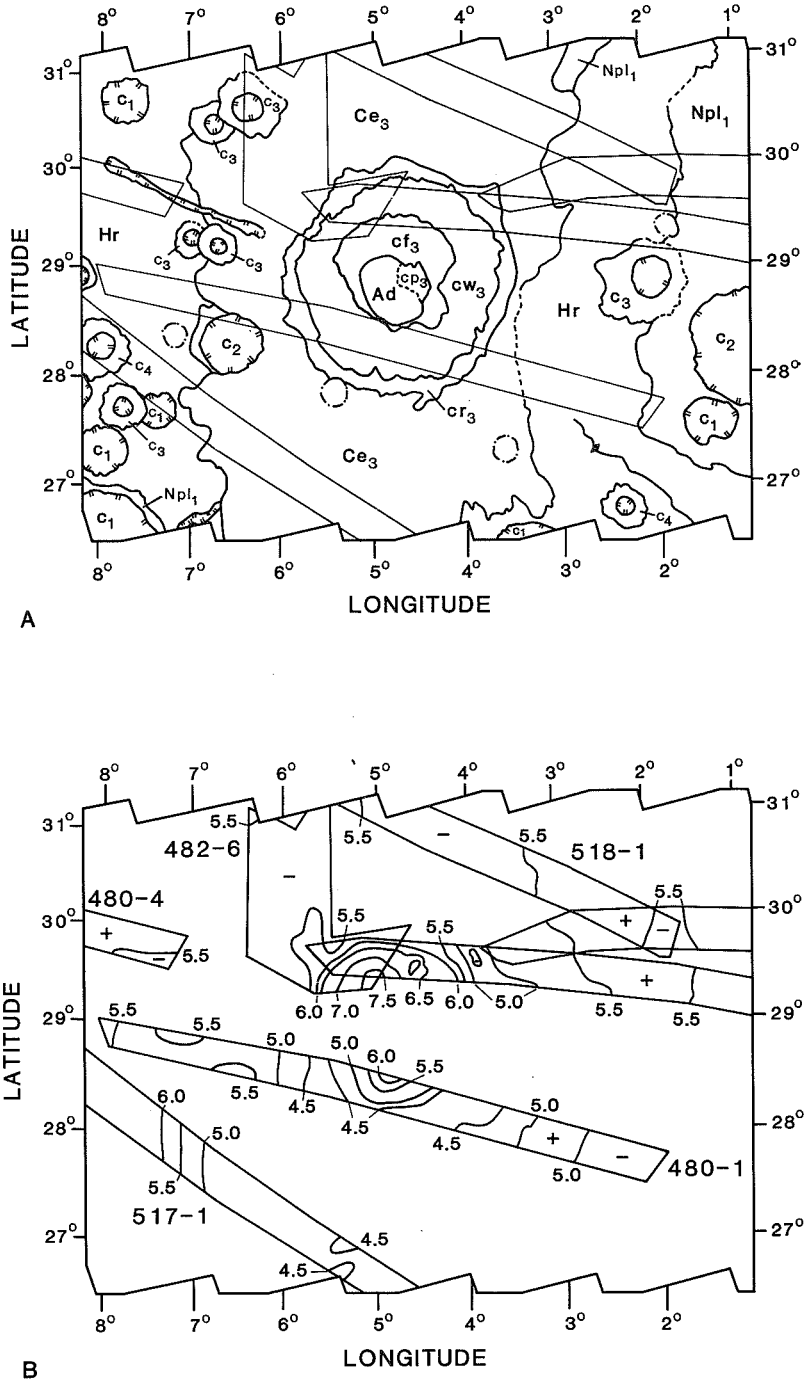

Figure 1 - High resolution Viking IRTM coverage of the crater Curie. Typical resolution ~25 km^2, and represents a combination of surface area viewed by each detector and the camera motion along the groundtrack during the integration time. A) Relationship between groundtracks and regional geology; B) Contours of thermal inertia within groundtracks. Geologic units adapted from (1,11). Thermal inertia values are x 10^{-3} cal cm^{-2} $sec^{-1/2}$ K^{-1}.

Dome Craters on Ganymede

J. M. Moore and M. C. Malin, Department of Geology, Arizona State University, Tempe, Arizona, 85287

Voyager observations reveal impact craters on Ganymede that are characterized by the presence of broad, high albedo, topographic domes situated within a central pit (Fig. 1). Although elsewhere termed Type II penepalimpsests[1], they are referred to here by the descriptive term "dome craters." Fifty-seven craters with central domes have been identified in images covering ~50% of the surface of Ganymede at resolutions between 0.5 to 3.0 km per picture element. Owing to limitations in resolution, and viewing and illumination angles, the features identified in this study are most likely a subset of dome craters on Ganymede. The sample appears to be sufficiently large to infer statistically meaningful trends.

Dome craters appear to fall into two distinct populations on plots of the ratio of dome diameter to crater rim diameter (Fig. 2). Large-dome craters have dome to crater diameter ratios of 0.25 to 0.56 (mean 0.33) while small-dome craters have dome to crater diameter ratios of 0.05 to 0.19 (mean 0.10). Large-dome crater rim diameters range from 30 km to 185 km (mean 96 km), while small-dome craters diameters begin at 52 km and increase to 108 km (mean 81 km). Large domes have diameters from 10 km to 50 km (mean 31 km) while small-dome diameters range from 3 km to 20 km (mean 9 km).

Large-dome craters preferentially occur on dark terrain. Of the twenty samples in this class, fifteen (75%) are on dark terrain, three (15%) occur on light terrain, and two (10%) occur on the border between the two terrains. Small-dome craters tend to occur on light terrain. Of a sample of thirty-four, twenty-two (65%) occur on light terrain, four (12%) on dark terrain, and eight (23%) on the border. No latitudinal or longitudinal trend in dome crater distribution could be identified.

The two "classes" of dome craters are morphologically distinct from one another. In general, large-dome craters (Fig. 1a) show little relief and their constituent landforms appear subdued with respect to fresh craters. They display the generic morphology widely described as "viscously relaxed"[1,2,3,4], or hypothesized to have formed as a consequence of the presence of sub-surface liquid(s) at the time of impact[5,6]. The physical attributes of small-dome craters (Fig. 1b) are more sharply defined, a characteristic they share with young impact craters of comparable size observed elsewhere in the solar system. Although their morphology may generally resemble fresh craters of similar size on the terrestrial planets, it should be noted that the small-dome craters display less relief[1,2,3].

Both types of dome craters exhibit central pits in which the dome is located. This is not surprising as virtually all craters on Ganymede > 20 km in diameter have a central pit[1], and the smallest crater with a dome has a rim diameter of 30 km.

As it is difficult to produce domes by impact and/or erosional processes[7,8], an endogenic origin for the domes is reasonably inferred. Several hypotheses for their origin have been proposed. Squyres[9] has suggested that two large domes situated in the center of impact features > 100 km in diameter were formed either by

H_2O liquid volcanism and/or isostatic upwarping of a thinned ice crust. Croft[6,10] suggested that icy target material, uplifted within a complex crater during formation will melt if the bolide velocity is sufficiently high. In this scenario, newly formed complex craters will have a "melt lake" within a central pit rather than a central peak, and the dome is formed by the subsequent freezing and expansion of this lake. Malin[7,11] proposed that the domes may be the tips of diapirs.

The diapir hypothesis, while as speculative as the other hypothesis, appears most consistent with contemporary models of Ganymedian internal and thermal evolution. Kirk and Stevenson[12] have investigated the potential for diapirism in the lithosphere of Ganymede and have found that the likelihood of its occurrence is great over a wide range of values for lithospheric physical properties. If the domes are the tips of diapirs, it would explain the relief and the albedo displayed by these features. A diapir, once exposed to the surface, would cool and become more viscous. The ice in the dome would be able to maintain relief comparable to that of the crater in which it formed.

It is hypothesized that perturbation of a low density layer underlying a "viscously relaxing" impact crater initiated diapir formation. The diapir rose to penetrate the surface at the center of the crater, forming a dome. Provided that the high albedo material covering approximately half of Ganymede is the same material that forms the domes, two alternative hypotheses may be posed to explain the partition of dome sizes between dome craters on light and dark terrain. Both hypotheses assume that the reduction in size reflects a reduction in supply: small domes may have formed after the emplacement of light terrain had depleted the available source material, or they may have formed after cooling had reduced the thickness (and volume) of the source region. In both scenarios, large-dome craters formed at a time when the light material source region was voluminous and relatively untapped. A global disturbance of the source then resulted in creation of light terrain, presumably by effusion. Subsequent, local disturbances of the reduced amount of light material remaining at depth produced smaller domes. The present observations cannot distinguish between depletion of the source zone by effusion and "depletion" by thinning as a consequence of other factors, such as increased strength of its outer portions owing to cooling following light terrain formation.

REFERENCES

1. Passey, Q. R. and E. M. Shoemaker (1982) in Satellites of Jupiter, D. Morrison, ed., p.p. 379-434, University of Arizona Press, Tucson. 2. Smith, B. A., et. al. (1979) Science, 204, 951-972. 3. Smith, B. A., et al. (1979) Science, 206, 927-950. 4. Shoemaker, E. M., et. al. (1982) in Satellites in Jupiter, D. Morrison, ed., p.p. 435-520, University of Arizona Press, Tucson. 5. Greeley, R., et. al. (1982) in Satellites in Jupiter, D. Morrison, ed., p.p. 340-378, University of Arizona Press, Tucson. 6. Croft, S. K. (1983) J. Geophys. Res., 88, B71-B89. 7. Malin, M. C. (1978) Proc. Lunar. Sci. Conf. 9th, 3395-3409. 8. Malin, M. C. (1980), NASA TM-82385, p. 67. 9. Squyres, S. W. (1980) Icarus, 44, 472-480. 10. Croft, S. K. (1980) IAU Coll. 57. The Satellites of Jupiter (abstract 6-16). 11. Malin (1980) IAU Coll. 57. The Satellites of Jupiter (abstract 6-3). 12. Kirk, R. L. and D. J. Stevenson (1986) Thermal evolution of a differentiated Ganymede and implications for surface features, submitted to Icarus.

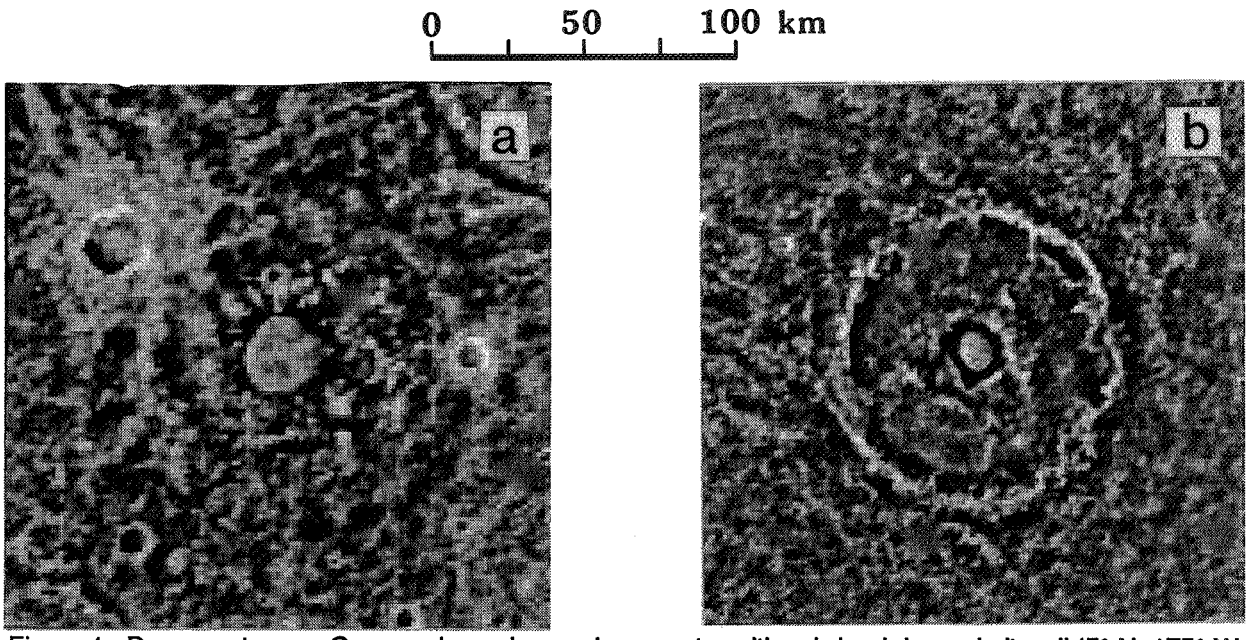

Figure 1. Dome craters on Ganymede: a. Large-dome crater with subdued rim and pit wall (5° N, 175° W, image FDS 20635.49). b. Small-dome crater. Note morphological freshness and surrounding field of secondary craters (13° S, 140° W, image FDS 20637.23).

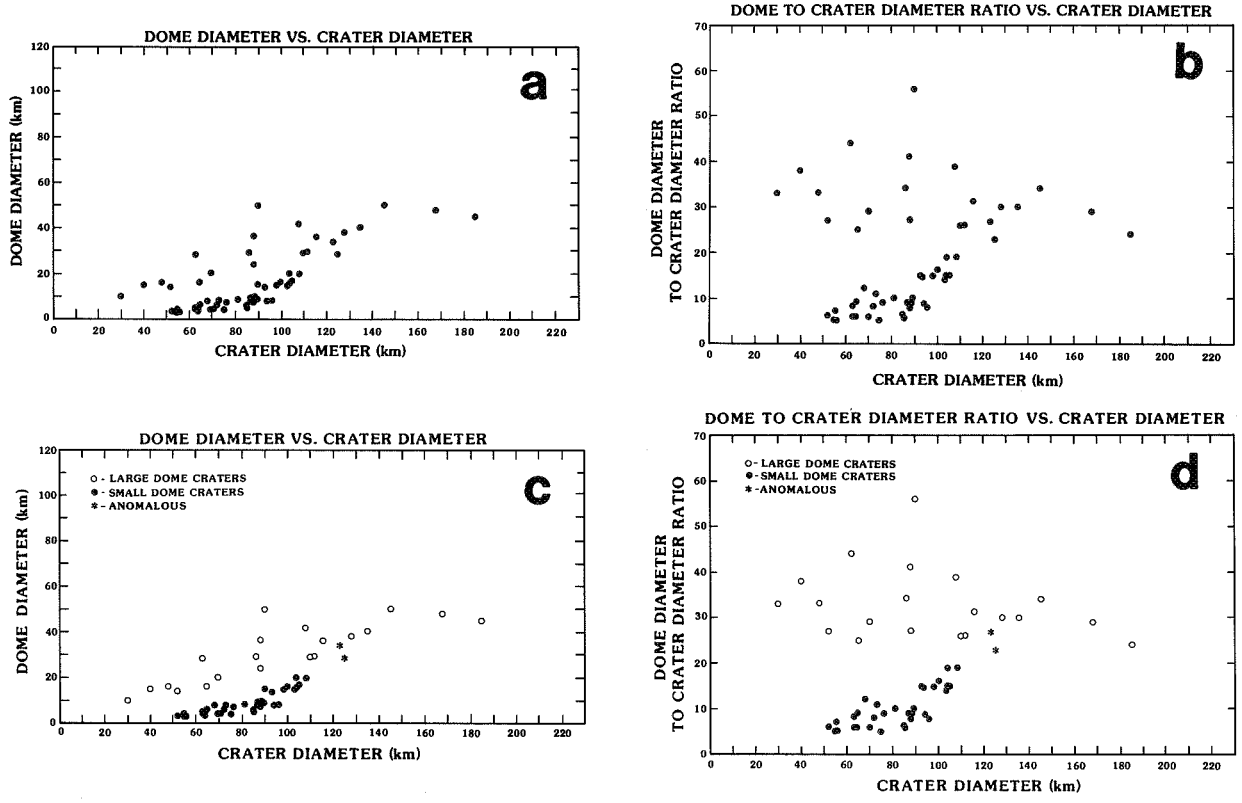

Figure 2. a. A plot of dome diamter versus crater rim diameter of all 57 recognized dome craters. b. A plot of the ratio of dome diameter to crater rim diameter versus crater rim diameter. c. Same as plot (a) with different dome crater types marked. d. Same as plot (b) with different types marked.

NON-NEWTONIAN ICE RHEOLOGY AND THE RETENTION OF CRATERS ON GANYMEDE

Paul J. Thomas and Gerald Schubert*

Theoretical Studies Branch, NASA Ames Research Center, Moffett Field CA 94035.

*Department of Earth and Space Sciences, University of California, Los Angeles, CA 90024.

Recent laboratory data (Durham *et al.*, 1983; Kirby *et al.*, 1985) reveals that H_2O ice has a strongly non- Newtonian (power-law) rheology at temperatures appropriate to the near-surface regions of the Galilean satellites *i.e.* that

$$\dot{\epsilon} = A \exp(-Q/RT)\tau^n \tag{1}$$

where $\dot{\epsilon}$ is strain-rate, τ is effective stress and $A = 2.51 \times 10^{-26} Pa^{-3.7} s^{-1}$, $Q = 27\ kJ\ mole^{-1}$ and $n = 3.7$ for $158\ K < T < 195\ K$. Numerical calculations incorporating this rheological law indicate that crater relaxation in a non-Newtonian rheology has significantly different characteristics to viscous relaxation in a Newtonian medium (Thomas and Schubert, 1986). These arise principally by virtue of the fact that viscosity η varies as $\eta \sim \tau^{1-n}$. Thus high stresses are associated with low viscosities, which permit relatively rapid relaxation flow. However, once the initial stress is reduced, viscosity increases and relaxation flow becomes markedly slower. Consequences of this phenomenon observed for numerical simulations of crater relaxation include the formation of a high-stress, low-viscosity region immediately below the center of the crater; a relatively rapid relaxation rate intially, followed by a marked slowing of the relaxation flow as stresses decrease (and viscosities increase) and, concomitantly, much greater differences between relaxation timescales for small *vs.* large craters than would be expected for a Newtonian medium.

Calculations carried out for craters of varying sizes in a medium with constant temperature $T = 173\ K$ yield values for the crater relaxation time t_e (defined as the time required for the crater depth to become $1/e$ of its original value) that appear to be too small to account for the observed retention of craters on Ganymede and the other icy satellites. Typical values were $t_e \approx 10^2 y$ for craters with a diameter of $D = 300\ km$ and $t_e \approx 10^5 y$ for $D = 50\ km$. Although the rate of crater relaxation at times greater than t_e is much slower than the initial rate, as mentioned above, as many as 10^6 e-folding times are available to reduce the remaining topography. Such a calculation is thus seriously in conflict with the observed crater population of the surfaces of the icy satellites.

In an attempt to reconcile this conflict, we consider possible explanations for the much slower relaxation rate of craters on the icy satellites. It is possible that an admixture of silicates in the surface ice regions of the icy satellites may raise the viscosity to some extent. However, even a silicate volume fraction of the order of 0.6, implausible for the icy satellites, whose surfaces seem to be predominantely ice, only increases the viscosity (and thus the relaxation time) by at most two orders of magnitude (Friedson and Stevenson, 1983).

A rheological transition to a Newtonian law (where $n = 1$) will not occur unless the the Newtonian rheology permits a greater strain-rate for a given stress than the non-Newtonian rheology. One cannot thus increase viscosity by appealing to a rheological transition mechanism. In fact, the critical stress τ_c below which a

Newtonian rheology is dominant, given currently accepted values for Newtonian ice viscosity laws ($Q = 57.7\ kJ\ mole^{-1}$) and ($A = 9.06 \times 10^{-15} Pa^{-1} s^{-1}$) (Reynolds and Cassen, 1979) is of the order of 10 Pa, many orders of magnitude less than the stresses associated with even small craters.

It may be argued that the grain size of the ice in the upper layers of the icy satellites is unknown, and this may render inapplicable the experimental results of Kirby *et al.* (1986). While the creep of polycrytalline ice is sensitive to the grain size at temperatures close to the melting point (Baker, 1978; Goodman *et al.*, 1981), it is probably of less importance at low temperatures (S.H. Kirby, personal communication, 1986). In any event, this effect alone is not likely to be responsible for the orders of magnitude increase required in viscosity.

A solution to the problem can be achieved by accounting for temperature variations in the surface regions of the icy satellites, and utilizing more recent experimental data (Kirby *et al.*, 1986). This data, the product of an over 200% increase in experimental runs at low temperature, yields $n = 4.8$, $A = 2.10 \times 10^{-33} Pa^{-4.8} s^{-1}$ and $Q = 29\ kJ\ mole^{-1}$. The significantly higher value of n is observed to enhance the non-Newtonian phenomena associated with crater relaxation and mentioned above.

To incorporate the effects of a temperature gradient, we take the case of Ganymede ($T_{surface} = 120K$) and assume a temperature gradient $dT/dz = 1\ K\ km^{-1}$, consistent, for the present day Ganymede, with global thermal models (Schubert *et al.*, 1981). These models predict the onset of convective motion at a depth where $T \approx 0.6\ T_m = 164K$. The adiabatic temperature gradient for the icy satellites is small, and thus we assume that the convecting region is isothermal, with $T = T_m$. Thus the maximum temperature determining the viscosity for crater relaxation is 164 K, although higher temperatures may be appropriate to the early history of Ganymede. We further assume that the dominant viscosity is that determined by the temperature T_a at a depth $z = D/2$ (which lies in the center of the relaxation flow region (Thomas, 1986)) and a typical stress τ_a determined from numerical analysis of craterform stresses (Thomas and Schubert, 1986). We can thus construct estimates of relaxation times for various craters as follows:

$D(km)$	$T_a(K)$	$\tau_a(MPa)$	$\eta(\tau)(Pas)$	$t_e(y)$
300	164	1.00	5.76×10^{19}	5.10×10^{4}
250	164	0.83	1.17×10^{20}	1.24×10^{5}
200	164	0.67	2.64×10^{20}	3.50×10^{5}
150	164	0.50	8.02×10^{20}	1.42×10^{6}
100	164	0.33	3.89×10^{21}	1.03×10^{7}
75	157.5	0.25	2.69×10^{22}	9.52×10^{7}
50	145	0.17	∞	∞
25	132.5	0.08	∞	∞
10	125	0.03	∞	∞

Kirby *et al.* (1986) did not observe viscous behavior for $T < 158\ K$, and thus viscous relaxation is not expected for the craters of smallest sizes. Relaxation times are calculated for the $D = 75\ km$ crater, a borderline case for which viscous relaxation may occur.

These results are in good qualitative agreement with observations of the surface of Ganymede: they account for the paucity of well-preserved large ($D > 100\ km$) craters without requiring any *ad hoc* mechanisms such as impact melt-lubrication (Croft, 1983) or acoustic fluidization (Melosh, 1979) while allowing for the long-term retention of smaller craters. Further research will concentrate on the quantitative comparison of calculated relaxation times to the observed population of craters on Ganymede.

References

Baker, R.W. (1978).*J. Glaciol.*, **21**, 485-500.

Croft, S.K. (1983).*A proposed origin for palimpsests and anomalous pit craters on Ganymede and Callisto*, J. Geophys. Res., **88**, 71-89.

Durham, W.B., H.C. Heard and S.H. Kirby (1983).*Experimental deformation of polycrystalline H_2O ice at high pressure and low temperature: preliminary results*, J. Geophys. Res., **88**, 377-392.

Friedson, A.J. and D.J. Stevenson (1983).*Viscosity of Rock-Ice mixtures and Applications to the Evolution of Icy Satellites*, Icarus, **56**, 1-14.

Goodman, D.J., H.J. Frost and M.F. Ashby (1981).*The plasticity of polycrystalline ice*, Phil. Mag. A, **43**, 665-695.

Kirby, S.H., W.B. Durham and H.C. Heard (1985).*Rheologies of H_2O ices I_h, II and III at high pressures: a progress report*, in *Ices in the Solar System*, J. Klinger *et al. (eds.)*, Reidel.

Kirby, S.H., W.B. Durham, M.L. Beeman, H.C. Heard and M.A. Daley (1986).*Inelastic properties of ice I_h at low temperatures and high pressures*, Journal de Physique, (in press).

Melosh, H.J. (1979).*Acoustic fluidization, a new geologic process?*, J. Geophys. Res., **84**, 7513-7520.

Reynolds, R.T. and P.M. Cassen (1979).*On the internal structure of the major satellites of the outer planets*, Geophys. Res. Lett., **6**, 121-124.

Schubert, G., D.J. Stevenson and K. Ellsworth (1983).*Internal structures of the Galilean satellites*, Icarus, **47**, 46-59.

Thomas, P.J. (1986).*Finite element models of non-Newtonian crater relaxation on the icy satellites*, Ph.D dissertation, Monash University, Australia.

Thomas, P.J. and G. Schubert (1986).*Finite Element models of non-Newtonian crater relaxation*, J. Geophys. Res., (in press).

EJECTA TYPES ON GANYMEDE AND CALLISTO

V. M. Horner and R. Greeley, Department of Geology, Arizona State University, Tempe, Arizona 85287

Ejecta types on Ganymede and Callisto have been identified from Voyager 1 and 2 images. Image resolutions used in this study range from ~0.6 to ~4 km/pxl, which allowed us to survey almost all of the mappable surface of the two satellites.

Seven ejecta classes have been identified on Voyager images of Ganymede on the basis of albedo pattern and type of terminus. Type G1 is pedestal ejecta, as described by Horner and Greeley (1). The distinctive characteristic of this ejecta class is the sharp, convex terminus. The albedo of the ejecta appears to be slightly higher than the surrounding terrain, yet underlying topography can be discerned. At terrain boundaries, the ejecta is sometimes truncated, with a diffuse deposit appearing beyond the boundary at about the same distance as an extrapolated pedestal ejecta boundary (2). Type G2 ejecta has a uniformly high albedo, with a sharp outer albedo boundary. Type G3 has a moderate to high, mottled albedo and a gradational terminus. Type G4 is similar to type G3, except that it is an outer ejecta unit. Inner ejecta classes are predominately types G1 and G2. Type G5 ejecta is identified only by changes in surface texture circumferential to the crater and a gradational terminus. Type G6 is similar to G5 except for a sharp ejecta boundary. Type G7 represents low albedo ejecta discussed previously by Schenk and McKinnon (3).

The effects of different terrains on ejecta characteristics were investigated for the most populated ejecta types - G1, G2, G3, and G4. Using power law regression calculations to the equation (ejecta diameter) = 10^a x (crater diameter)^b, it was observed that neither of the coefficients changed significantly for any ejecta type between the grooved and dark terrains. Thus, ejecta extent is apparently unaffected by terrain units. Type G3 is observed more often on the cratered terrain, and pedestal ejecta (G1) is more prevalent within the grooved terrain. However, contrary to a previous study (5) craters with pedestal ejecta are present in significant numbers in the cratered terrain, representing ~15% of all craters with measurable ejecta within that unit.

Pedestal ejecta may be more common on Ganymede than originally thought. At high sun angles, ejecta with a uniformly high albedo and a sharp terminus can be identified in Voyager images. For this ejecta type (G2), the ratios of ejecta diameter to crater diameter are similar to those for pedestal crater ejecta, and are significantly lower than those for ejecta with a moderately high albedo and a gradational terminus (figure 1). It therefore seems plausible that at high sun angles, pedestal crater ejecta may appear as a uniformly bright annulus with a sharp albedo edge. If ejecta type G2 represents pedestal crater ejecta observed at high sun angles, the percentage of pedestal ejecta to other ejecta types on the cratered terrain increases to ~33%.

On the basis of the power law regression calculations, crater ejecta on Ganymede can be divided into two classes; ejecta types with $a \leq 0.40$ and $b \leq 0.96$, and those with $a > 0.40$ and $b \geq 1.00$. When the data are plotted logarithmically (figure 1; table 1), ejecta types of the first major class - types G1, G2, and G6 - are tightly clustered along the best fit curve to the data. Ejecta diameters for classes with $a > 0.4$ and $b \geq 1.00$ - types G3, G4, G7, - show more variation with respect to crater diameter, although power law fits are also valid for these data. Ejecta type G5 fits neither catagory. Because of its appearance, and as it is observed predominately near the terminator, this class could represent G2 ejecta which is eroded enough to be observable only at very low sun

angles. Statistical line fits for the most populated ejecta types are shown in figure 1. Slopes for these classes are all within ±0.05 of the value b=1.01 derived for post-Orientale lunar craters (6).

Two major ejecta types have been identified on Callisto: both have counterparts on Ganymede. Type C1 has a uniformly high albedo and a sharp terminus. On Ganymede, this ejecta type (G2) may represent pedestal crater ejecta (G1) seen at moderate to high sun angles, but no pedestal craters have yet been positively identified on Callisto. Type C2 is has a gradational terminus and a moderate albedo: it is similar to ganymedean ejecta types G3 and G4. As on Ganymede, Type C2 ejecta is generally more extensive than Type C1 ejecta, although the differences are not as great (figure 1, table 1). The calculated values of coefficients a and b are quite different for the callistoan ejecta types compared to those on Ganymede. As plots of the best statistical fits to these data are similar to those of the two major ejecta groups on Ganymede, the coefficient values may be partly the result of the small number of craters with measurable ejecta identified thus far on Callisto. No craters with dark rays or ejecta similar to those on Ganymede have been observed on Callisto; however, the low surface albedo would render them almost unidentifiable.

The similarity in ejecta types on Ganymede and Callisto may indicate similarities in the near-surface environment of the two satellites, with different ejecta types representing several possible conditions for the impact environment. Although the hypothesis that pedestal formation requires target viscosities lower than the cratered terrain (5) is intriguing, the identification of ejecta types G1 (1) and G2 on the cratered terrain of Ganymede, as well as the discovery of an ejecta type on Callisto (C1) similar to type G2 on Ganymede, indicate that this hypothesis is untenable. Ejecta with a gradational boundary may indicate transport ballistically and/or by vapor expansion (7). Morphological studies indicate that pedestal crater ejecta, and by extension, ejecta with a high albedo and sharp terminus, may be a more dense, ground-hugging mixture of vapor, ice and silicate fragments (1,2). However, whether these conditions result from different projectile characteristics or target properties, such as layering (8), is still undetermined.

REFERENCES

1) Horner, V. M. and R. Greeley, 1982, *Icarus* **51**, 549-562.
2) Horner, V. M. and R. Greeley, 1983, *NASA TM 86246*, 94-96.
3) Schenk, P. M. and W. B. McKinnon, 1985, *J. Geophys. Res.* **90**, C775-C783.
4) Conca, J., 1981, *Proc. Lunar Planet. Sci. Conf. 12th*, 1599-1606.
5) Forni, O. *et al.*, 1986, *Earth, Moon, and Planets* **34**, 177-188.
6) Moore, H. J. et al., 1974, *Proc. Lunar Planet. Sci. Conf. 5th*, 71-100.
7) Chapman, C. and W. B. McKinnon, in *Natural Satellites*, in press.
8) Hartmann, W. K., 1980, *Icarus* **44**, 441-453.

TABLE 1 - Results of power law least squares fit to the equation (ejecta diameter) = 10^a x (crater diameter)^b for ejecta classes on Ganymede and Callisto, where N is the number of craters, and R^2 is the correlation coefficient. Ejecta types are defined in the text.

	N	a	b	R^2
		GANYMEDE		
Type G1	207	0.32±0.02	0.96±0.02	0.95
Type G2	84	0.38±0.02	0.92±0.02	0.97
Type G3	93	0.50±0.04	1.00±0.03	0.92
Type G4	108	0.50±0.05	1.05±0.04	0.88
Type G5	22	0.29±0.12	1.02±0.07	0.91
Type G6	98	0.40±0.03	0.91±0.02	0.95
		CALLISTO		
Type C1	28	0.54±0.07	0.80±0.05	0.91
Type C2	18	0.33±0.14	1.04±0.09	0.89

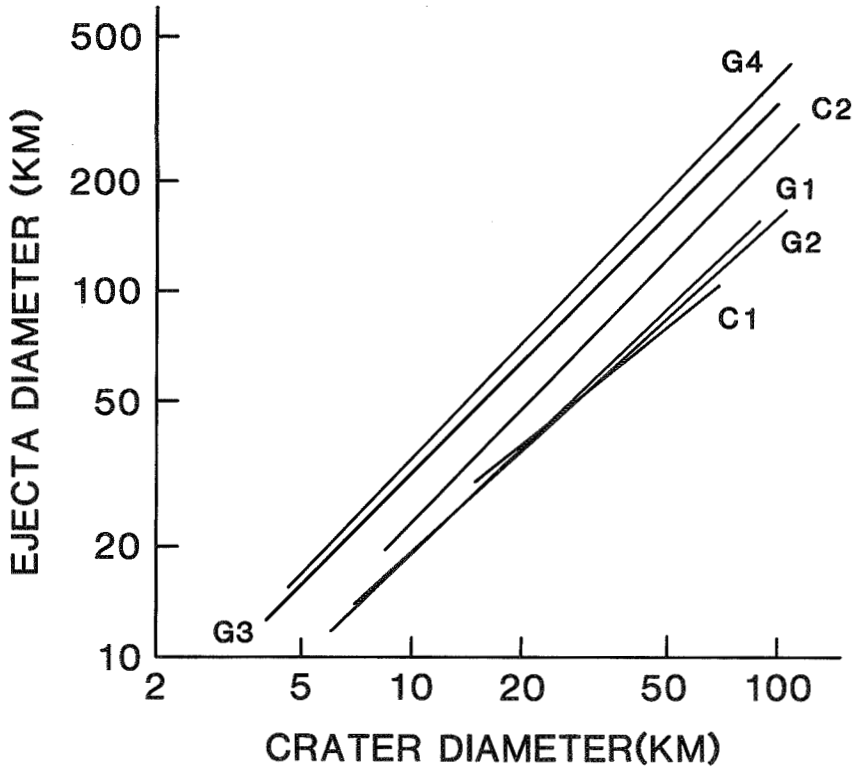

Figure 1 - Ejecta diameter as a function of crater diameter for related ejecta types on Ganymede and Callisto. See text for details.

SHATTER CONES IN ILLINOIS: EVIDENCE FOR METEORITIC IMPACTS AT GLASFORD AND DES PLAINES; John F. McHone*, Michael L. Sargent**, and W. John Nelson**, *Geology PSF, Arizona State Univ., Tempe AZ 85287, ** Illinois State Geological Survey, 615 E. Peabody, Champaign, IL 61820

Shatter cone fragments have been recovered from rock cores at two previously suspected, but heretofore unverified, impact structures in Illinois. Both sites are buried features known from geophysical surveys and drill holes.

The Glasford Structure (4 km dia., Lat. 40°36.1' N; Long. 089°47.1' W) is a domal feature centered about 16 km WSW of Peoria, Illinois. Deep wells reveal a normal sequence of about 350 m of undisturbed Quaternary and Paleozoic strata overlying more than 400 m (depth of penetration) of intensely disturbed and brecciated sedimentary rocks (Buschbach and Ryan, 1963). Oldest undisturbed rocks are an anomalously thick, atypical, originally flat (now slightly domed) shale of Cincinnatian (upper Ordovician) Maquoketa Group which are in abrupt contact with randomly oriented cm-scale breccia clasts of similar appearance. Deeper rocks are mostly chaotic blocks of severely brecciated dolomites with some lower units of autochtonous sandstone breccia and strongly contorted shales. Rare but well-developed shatter cones occur in fractured blocks of unidentified massive brittle dolomite and also as dolomite clasts within breccia veins bounded by fractured and contorted sandstones.

The Des Plaines Disturbance (8 km dia., Lat. 42°02.7'N; Long. 087°52.4'W) underlies the Chicago suburb of Des Plaines (Emrich and Bergstrom, 1962). A central core of brecciated Champlainian (middle Ordovician) St. Peter Sandstone is uplifted more than 250 m above normal elevation. Individual quartz grains commonly have well-developed percussion fractures, strain lamellae, and occasional sets of crystallographically oriented planar microfractures. Shales of the Maquoketa Group surround this central uplift in moderately to steeply tilted beds in which numerous faults cause repeated sections and layers of severe fracturing. Occasional beds of brittle dolomite contain distinct, weakly developed shatter cones between layers of otherwise thoroughly crushed shales.

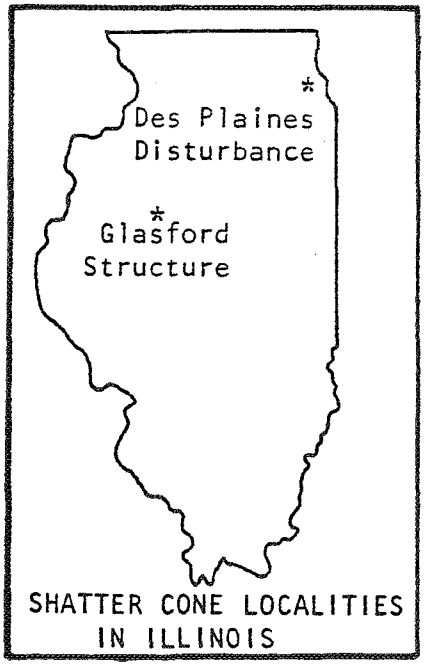

SHATTER CONE LOCALITIES IN ILLINOIS

Shatter cones are accepted widely as field criteria of meteoritic impact (Dietz, 1960). Detection of these shock indicators in both the Glasford Structure and the Des Plaines Disturbance upgrades these sites in Earth's inventory of known and suspected impact structures from possible impact sites with compatible structure and morphology to probable impact structures which possess also evidence of shock metamorphism.

References: Buschbach and Ryan, Bull. Am. Assoc. Petrol. Geol., v. 47, no. 12, p. 2015-2022, (1963); Dietz, Science, v. 131, p. 50-58 (1960); Emrich and Bergstrom, Geol. Soc. Am. Bull., v. 73, p. 959-968, (1962).

Search for, and study of, Paleozoic impact ejecta: progress made during the past year.

William F. Read NASA grant NAGW 638 Nov. 14, 1986

When I reported at this time last year, nodule-like objects which I believe to be impact bombs had been found in Middle Ordovician rocks of sotheastern Wisconsin and northern Illinois. In northern Illinois, rock fragments containing oolith-like spherules, which I believe to be solidified impact droplets, and numerous large bubble-holes, had been found at the same stratigraphic level. Samples of drill-cuttings had been obtained from the Illinois Geological Survey in the hope that similar spherules may be recognizable in them.

The spherule-bearing rock is described in an article recently published in Meteoritics. A (several-times-revised) manuscript on the nodules is nearing completion and will be submitted for publication to the Journal of Geology. There has been no opportunity for work on the drill-cuttings.

Also in last year's report, mention was made of the discovery of bomb-type nodules in Lower Ordovician rocks of southeastern Wisconsin. At that time they were known only from two quarry exposures. They have since been found, at the same stratigraphic level, in other quarries.

During the past year, bomb-type nodules associated with droplet-type spherules have been found in Lower Ordovician rocks of central Pennsylvania. Droplet-type spherules have been found to be associated with the bomb-type nodules previously discovered in Lower and Middle Ordovician rocks

of southeastern Wisconsin. Spherule-bearing rock containing large bubble holes has been found in Lower Ordovician rocks of southwestern Wisconsin. Thin-section and other laboratory work on samples from these finds is just getting under way.

In my opinion, the discoveries noted above suffice to show that impact ejecta are widespread in marine sediments of Ordovician age and are likely to be widespread also in marine sediments of other ages. Unfortunately there is little indication so far that they have been accepted as valid by the concerned scientific community. This is evident from the negative reviews my manuscripts have generally received when submitted for publication, and, more recently, by the discontinuation of funding by NASA. The only way to correct this situation, as I see it, is to keep on working with or without funding and to report at meetings and publish in journals whenever possible.

CHAPTER 12

STRUCTURE, TECTONICS, AND STRATIGRAPHY

COMMENTS ON THE TECTONISM OF VENUS

R.C. Kozak and G.G. Schaber, U.S. Geological Survey, Flagstaff, AZ 86001

Preliminary tectonic mapping of Venus from Venera 15/16 images shows unquestionable evidence of at least limited horizontal tectonism. Gravity-induced spreading and/or sliding has been suggested as the mechanism which caused the motion of Laima Tessera (fig. 1) [1,2]; the downslope movement of the Laima terrane was probably induced by a rifting event along Sigrun Fossae.

However, the majority of tectonic features on Venus have no similar relation to topography. In fact, many axes of disruption interconnect, and cross sharp topographic boundaries at large angles (commonly near 90°), thereby discounting gravity as the driving force. One type of disruption zone, interpreted as extensional, is chain-like series of paterae, such as one that follows a NNW-trending topographic low near 0°E, 50°N. The morphology and tectonic setting of these paterae chains outwardly resemble models of propagating rifts [3]. These and other types of extensional zones (EZ's) that include Bezlea and Hera Dorsa, Sigrun Fossae, fractures north of Kamari Dorsa, and two branches roughly paralleling Lasdonna and Aranyani Chasmata (fig. 1) form part of a regional network. The network is difficult to follow beyond its east end, near Allat Dorsa; however, south of Bezlea/Hera Dorsa, beyond the Venera coverage, Pioneer Venus altimetry indicates that this system of EZ's may continue as far south as westernmost Aphrodite Terra, probably linking with the near-equatorial rift system [4]. Arecibo images of the southern hemisphere (near 325°E) also suggest the presence of EZ's, further implying a global distribution and a closer analogy to multi-plate tectonism than to single-plate tectonism. The idea that EZ's reflect deep crustal movements, therefore suggesting that mantle drag is at work, is bolstered by their tendency to coincide with relative lows even where they cross lowlands -- a situation inconducive to gravity tectonism. Quantitative analysis of stress fields within the EZ's may be derivable from "arachnoids" [5] which are interpreted as volcanoes whose radial dikes conformed to the differential stress field associated with the extension.

Compressional zones (CZ's), unlike EZ's, tend to be discontinuous, and, whereas EZ's cross tectonic and topographic boundaries at various angles, many CZ's on Venus are subparallel to these boundaries. Many of the large fold belts (Itzpapalotl Tessera; Semuni, Kamari, and other dorsa) occur at, and parallel to, the boundary between tesserae and adjacent plains, which is similar to the tendency of Earth's mobile belts to make a shallow angle with continental-oceanic crust boundaries [6]. If this analogy is carried one step further, the quiltwork appearance of Fortuna Tessera is reminiscent of the accretionary growth model for continents [7]. Also, many major tectonic features intersect at, or trace out, ~120° angles, a common angle of intersection for rift systems and junctions on multi-plate Earth. In the study area, EZ's and CZ's tend to occur in pairs at ~60° angles to one another (Sigrun Fossae and Ausra Dorsa, for example), but the significance of this is unclear at present.

Strike-slip faulting is curiously lacking from our mapping, possibly due to the steep incidence angle of the radar, which is far from optimal for detecting faults of small throw. A probable right-lateral fault occurs in western Clotho Tessera. Possible shear zones include the southwest terminus of Fortuna Tessera, and the southwest boundary of Itzpapalotl Tessera. The chasmata of Laima Tessera may also delineate zones of relative displacement; these chasmata are similar in many respects to oceanic fracture zones (R.

Kozak, work in prgress).

A chronology of horizontal crustal movements, and hence the analysis of Venus' thermal development, is largely dependent on understanding the crater-form features. The Venera SAR and altimeter resolutions are insufficient to permit accurate distinction between impact and volcano-tectonic craters based solely on morphometry [8,9]. Therefore ancillary data must be used to achieve an accurate analysis of Venus' tectonic history: data such as morphologic details, geologic associations, chronostratigraphic position, and distribution. This type of approach was used to argue a volcanic origin for Cleopatra Patera [10]. Based on similar arguments, several other craters (15-100 km in diameter) previously suggested as impact [11; Ivanov, B.A., personal comm.] may not be; Zhilova, Koidula, Potanina, Josefina, Jadwiga, Gloria, Tsvetayeva, and Dashkova, for example. Also, there is an unusual density of volcano-tectonic depressions and impact-like craters within the EZ's where they cross the low plains. Depressions are gradational from broad shallow paterae to sharp-rimmed impact-like craters, including some paterae with central peaks. This suggests that some of the impact-like craters may be endogenic. It is unlikely that the EZ craters are remnants of an older population of impact craters, as at least one segment of the EZ network disrupts, and is therefore younger than, tessera conspicuously void of craters. Other surfaces also exhibit unusual size-density distributions of craters: craters on Lakshmi Planum are unusually small (19 km mean diameter) and limited in size (σ = 7.2 km) for an area with such a relatively high crater density. Likewise, the mean diameter of craters on fold belts is 33 km (σ = 11 km), and on large volcanic constructs is 73 km (σ = 32 km). The few craters available so far for counting make these comparisons very preliminary and subject to further testing; but even if the number of these craters that are volcanic is only a small fraction of the total, impact crater densities within small tectonic regions are nonetheless so low that their use for relative dating will be of marginal use on Venus, requiring a heavy reliance on careful image interpretation.

Regardless of their uncertain origin, the craters still could hold the answer to whether, and to what extent, crustal shuffling is occurring on Venus. Recent interpretation of about 150 of the craters as impact features may translate to a ~750-m.y. mean surface age for Venus [5,11,12]. However, such age determinations are sensitive to estimates of the asteroid flux rate, selection of an appropriate crater-production curve, and the relative contribution of comets to the cratering record, all of which are currently in dispute; Schaber et al. (this volume) suggest a mean surface age possibly as low as ~100 m.y. The older age would vindicate models that suggest tectonism on Venus shut down about 500 m.y. ago, wheras the younger age would clearly imply ongoing resurfacing -- a view implied by our mapping.

REFERENCES

[1]Kozak, R.C., and Schaber, G.G., 1986, Abs. 17th LPSC: 444-445. [2]Sukhanov, A.L., 1986, Geotektonika, 1986(4): 60-76. [3]Bosworth, W., 1985, Nature, 316: 625-627. [4]Schaber, G.G., 1982, Geoph. Res. Ltrs., 9(5): 499-502. [5]Barsukov, V.L., et al., 1984, Geokhimiya, 12: 1811-1820. [6]Gastil, G., 1960, 21st Int. Geol. Cong., Norden, pt.9: 162-169. [7]Wilson, J.T., 1959, Am. Sci., 47: 1-24. [8]Pike, R.J., 1974, Earth Plan. Sci. Letrs., 22: 245-255. [9]BVSP, 1981, Basaltic Volcanism on the Terrestrial Planets, 745; Pergamon, 1286 p.[10]Schaber, G.G., et al., 1986, Abs. 17th LPSC: 762-763. [11]Ivanov, B.A., et al., 1986, Jour. Geophys. Res., 91(B4): D413-430. [12]Bazilevskiy, A.T., et al., 1986, Doklady Akademii Nauk CCCP, 282(3): 671-674.

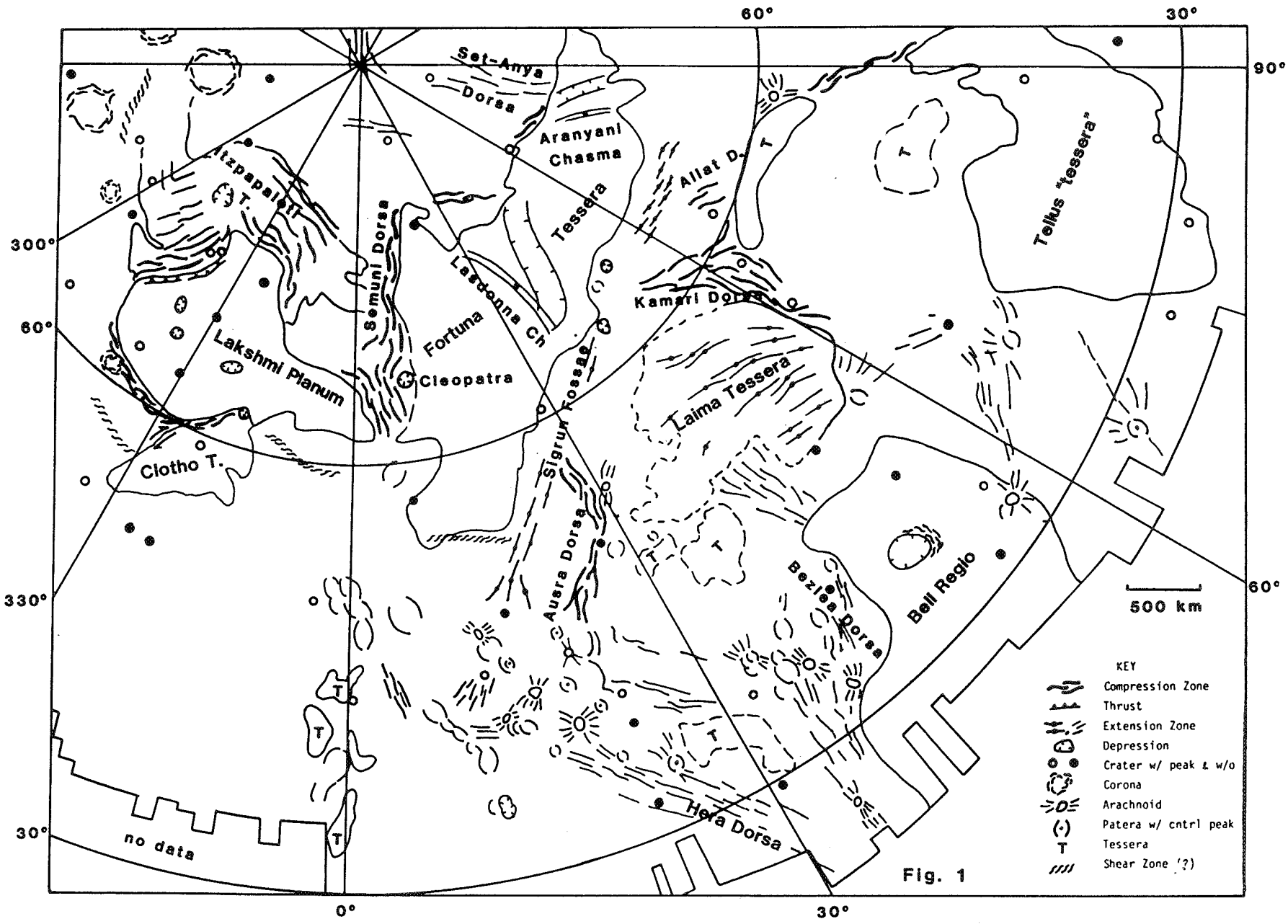
60°
30°
90°
300°
60°
330°
30°
0°
30°
60°
Set-Anya
Dorsa
Aranyani
Chasma
Tessera
Allat D.
Telius "tessera"
Itzpapalotl
T.
Semuni Dorsa
Lastdonna Ch
Kamari Dorsa
Lakshmi Planum
Fortuna
Cleopatra
Laima Tessera
Clotho T.
Sigrun Fossae
Ausra Dorsa
Bezlea Dorsa
Bell Regio
Hera Dorsa
no data
T
500 km
KEY
Compression Zone
Thrust
Extension Zone
Depression
Crater w/ peak & w/o
Corona
Arachnoid
Patera w/ cntrl peak
Tessera
Shear Zone (?)

Fig. 1

LITHOSPHERIC STRUCTURE ON VENUS FROM TECTONIC MODELLING OF COMPRESSIONAL FEATURES

W. B. Banerdt and M. P. Golombek, Jet Propulsion Laboratory, California Institute of Technology, Pasadena, CA 91109

Introduction. Spacecraft and Earth-based radar imagery of Venus, along with low resolution altimetry, have revealed a wide variety of landforms, many of which appear to be of tectonic origin. Features with a presumed tectonic origin tend to have broadly linear trends and characteristic widths or spacings within a group. The widths and spacings generally fall into one of two groups: one with a scale of 15-25 km, and the other with a scale of 100-300 km, with both sizes of features sometimes occurring in the same location.

Inasmuch as the detailed characteristics of surface deformation depend on the mechanical properties of the shallow interior, these tectonic features may be used to constrain models of Venus's lithosphere [e.g. 1,2,3]. In previous studies we used extensional models that incorporated realistic rheologies in order to constrain lithospheric structure [2,4]. Here we consider lithospheric modelling from the standpoint of compressional deformation. In this abstract we will review features of presumed compressional tectonic origin and present a model for compressional folding based on lithospheric strength envelopes that include the effects of both brittle and ductile yielding as well as finite elastic strength. Model predictions are then compared with the widths and spacings of observed tectonic features and we conclude that the results are consistent with a thin crust overlying a relatively stronger mantle, with thermal gradients probably in the range of 10-15^{o}/km.

Observations. Earth-based radar images of Ishtar Terra at 2 km resolution have revealed regions of high backscatter that are characterized by sets of linear bands of greater and lesser backscatter striking generally parallel to the long axes of the Maxwell, Akna, and Freyja mountain ranges [5]. These features have characteristic spacings between individual bands of 15-20 km [1]. Subsequent Venera data have shown that the bands correspond to subparallel ridges and grooves [6]. On the basis of its close correlation with mountainous topography and the continuity, regular spacing, and detailed morphology of the bands a compressional tectonic origin for the banded terrain is considered likely [1,5,7]. Venera mapping of the northern plains and Atalanta Planitia has also revealed ridge belts, which appear to be of tectonic origin [6]. These belts are several hundred to a thousand km long and up to 150 km wide, and trend roughly north-south with a mean spacing of 200-300 km [3]. The belts are composed of subparallel ridges and troughs that are continuous for 100-200 km along the strike of the belt and that are each 10-15 km wide [6], giving a mean spacing of about 25 km. The morphological similarity of these ridges to those surrounding Lakshmi Planum suggests that they are the result of compressional deformation [7].

The features discussed above are characterized by their continuity, linearity, and characteristic spacings and subparallel strikes within a group. These traits imply that the stress field and mechanical properties involved in their formation were relatively homogeneous, suggesting that simple deformational models may yield some insight into the structure of

the lithosphere. It can also be seen that these features tend to fall into two groups: one with characteristic wavelengths (i.e. spacings) of about 15-25 km and the other with characteristic wavelengths of approximately 100-300 km. In addition, the ridge belts have both scales of deformation superimposed on one another, an observation for which any successful model must account.

Folding Model. When an elastic layer overlying an inviscid fluid is subjected to a sufficiently large compressive edge load it will deform by buckling with a dominant wavelength that depends primarily on the elastic properties and thickness of the layer. This simple model has been applied to Venus [1] in an attempt to use the observed spacing in the banded terrain to constrain the structure of the lithosphere. A layer thickness of the order of a few kilometers was derived, in good agreement with estimates of the elastic lithosphere thickness based on thermal arguments. However the critical stress required to induce the buckling instability was greater than 500 MPa, in excess of the yield strength of rocks. This discrepancy is even larger if it is assumed that the ridge belts of the northern plains formed by a compressional instability of an elastic plate, although again the plate thickness (about 25 km) is reasonable on thermal grounds if an olivine-rich lithosphere is assumed.

The problem of unreasonably high critical buckling stresses can be eliminated if a more realistic model is used that incorporates both frictional and ductile yielding of the lithosphere [e.g. 8]. A model incorporating such a rheology has been developed by McAdoo and Sandwell [9] in a study of periodic undulations observed in the topography and geoid of the northern Indian Ocean. They linearized the moment-curvature equation for small moments and found that the onset of folding is described quite well by the classical buckling equations with the plate thickness given by the "elastic core" of the lithosphere, the depth interval for which the yield stress is not exceeded and the material behaves elastically. The folding instability occurs well before the yield strength of the lithosphere is reached. Applying this model to Venus, we find that the critical buckling stress is less than 100 MPa for typical crustal materials and a few hundred MPa for dunite. Thus the basic physical objection of unreasonably high stress levels for lithospheric folding is removed.

Folding wavelengths as a function of thermal gradient for various materials are shown in Figure 1. The bottom four curves represent the deformation of a 10 km thick crust, while the top two curves show the behavior of a dunite mantle with and without such a crust. The two pairs of horizontal dashed lines denote the two ranges of wavelengths observed, as discussed above. The curve for dunite under a 10 km crust assumes that mantle deformations are decoupled from those in the crustal layer by a ductile lower crust (which is a natural consequence of the high surface temperature and the assumed range of thermal gradients), while the "no crust" curve is equivalent to assuming a crust thin enough so that ductile flow within it does not contribute significantly to the extensional strain. Thicker crusts have no significant effect on the crustal material curves and result in dunite curves with somewhat shorter wavelengths at a given gradient.

For the shorter wavelength features an anorthositic crust implies relatively low thermal gradients of 5-15^{o}/km, while a more likely basaltic

composition gives higher gradients of 10-28°/km. The longer wavelength features put tighter bounds on the gradient, requiring 9-14°/km to satisfy observations.

Conclusions. These results imply that a thin (~10 km) crust overlying a stronger mantle with thermal gradients of the order of 10-15°/km is required in the northern plains of Venus if the observed features formed by elastic buckling of the lithosphere. The banded terrain in Ishtar Terra is consistent with a thicker crust and either a basaltic composition with higher gradients (10-30°/km) or a more ductile composition such as anorthosite with a thermal gradient similar to that found for the northern plains.

REFERENCES: [1] Solomon & Head (1984) JGR 89, 6885; [2] Banerdt & Golombek (1985) Repts. PGP, 363; [3] Zuber (1986) LPSC XVII, 979; [4] Banerdt & Golombek (1985) Proc. Heat Detach. Conf., 2; [5] Campbell et al. (1983) Science 221, 664; [6] Barsukov et al. (1986) Proc. LPSC 16, JGR 91, D378; [7] Basilevsky et al. (1986) Proc. LPSC 16, JGR 91, D399; [8] Brace & Kohlstedt (1980) JGR 85, 6248; [9] McAdoo & Sandwell (1985) JGR 90, 8563; [10] Byerlee (1978) PAGeoph 116, 615; [11] Goetze (1978) Phil. Trans. RSL A288, 99; [12] Shelton & Tullis (1981) EOS 62, 396; [13] Hansen & Carter (1982) EOS 63, 437.

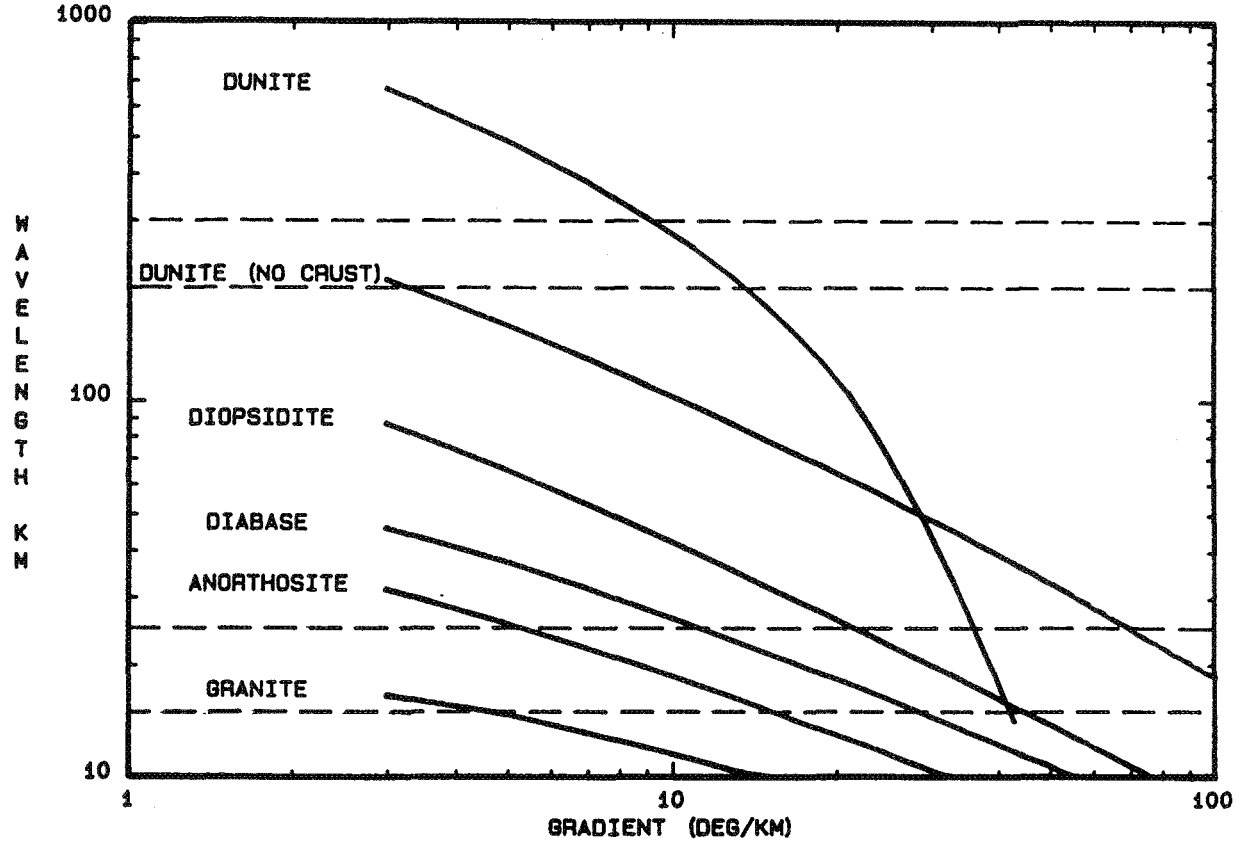

Figure 1. Characteristic folding wavelength versus thermal gradient for a number of geologic materials. A surface temperature of 720°K and a crustal thickness of 10 km (except for the "no crust" curve) is assumed. The frictional law from [10] is used along with flow laws from [11-13].

VENUSIAN TECTONICS: CONVECTIVE COUPLING TO THE LITHOSPHERE?

R.J. Phillips, Dept. of Geological Sciences, SMU, Dallas, TX 75275

The relationship between the dominant global heat loss mechanism and planetary size has motivated the search for tectonic style on Venus. Prior to the American and Soviet mapping missions of the past eight years, it was thought that terrestrial style plate tectonics was operative on Venus because this planet is approximately the size of the Earth and is conjectured to have about the same heat source content per unit mass [e.g., *Phillips and Malin*, 1984]. However, surface topography mapped by the altimeter on the Pioneer Venus spacecraft did not show any physiographic expression of terrestrial style spreading ridges, trenches, volcanic arcs or transform faults, although the horizontal resolution was questionable for detection of at least some of these features [*Masursky et al.*, 1980; *Phillips et al.*, 1981; *Solomon and Head*, 1982; *Phillips and Malin*, 1983,1984]. The Venera 15 and 16 radar missions mapped the northern latitudes of Venus at 1 to 2 km resolution [*Barsukov et al.*, 1986] and showed that there are significant geographic areas of deformation seemingly created by large horizontal stresses [*Basilevsky et al.*, 1986]. These same high resolution images show no evidence for plate tectonic features [*Barsukov et al.*, 1986; *Basilevsky et al.*, 1986]. Thus a fundamental problem for venusian tectonics is the origin of large horizontal stresses near the surface in the apparent absence of plate tectonics. There have been a number of studies of venusian tectonics that, *given the existence* of (large) horizontal stresses or strain-rates in an elastic or viscous lithosphere, have predicted the *style* of deformation. Tectonic studies have modeled these terrains as extensional rifts, horsts and graben, imbricate normal faults, and necking or folding instabilities [*Solomon and Head*, 1984; *Zuber*, 1986; *Banerdt and Golombek*, 1986; *Parmentier*, 1986]. The interest here is in the development of viable models for the *creation* of large horizontal stress in the venusian lithosphere, from which the tectonic deformation presumably follows. *Basilevsky et al.* [1986] have suggested "drag of the lithospheric by asthenospheric currents or gravity-induced spreading of surface material over upwellings" as alternative means to plate tectonics for producing horizontal deformation.

The first of these processes, mechanically described as convective stress coupling into an elastic or viscous lithosphere, has been examined in a preliminary fashion. Spectral Green's function solutions have been obtained for stresses in thick elastic and viscous lithospheres overlying Newtonian interiors with an exponential depth dependence of viscosity, and a specified surface-density distribution driving the flow in the fluid [*Phillips*, 1986]. It is found for long wavelengths and for a rigid elastic/fluid boundary condition that horizontal normal stresses in an elastic lid are either purely tensional or purely compressional, are controlled by the vertical shear stress gradient in the lid, and are directly proportional to the depth of the density disturbance in the underlying fluid.

These theoretical solutions combined with information on the depth and strength of density anomalies in the venusian interior inferred by analyses of long wavelength gravity data [*Phillips and Malin*, 1983; *Sjogren et al.*, 1984; *Reagan*, 1986] and topography [e.g., *Bills and Kobrick*, 1985] suggest that stresses in excess of 100 MPa would be generated in a 10-km-thick [*Solomon and Head*, 1984] elastic lid. These results, if they apply to specific regions of Venus, would imply that the topography in these areas is dynamically maintained and the subsurface density anomalies are associated with viscous flow. These stress levels would be greatly diminished, however, if a low viscosity channel (LVC) or positive viscosity gradient occurs beneath the lid. This would uncouple the flow stresses. The great apparent depth of compensation of topographic features argues against this [see *Robinson et al.*, 1986] as does actual admittance spectrum modeling [*Kiefer et al.*, 1986], thus supporting the importance of the coupling mechanism. If there is no elastic lid, stresses will also be very high near the surface, providing also that the same conditions on viscosity gradient hold.

It is often stated, but yet to be demonstrated, that a LVC is a requirement for terrestrial seafloor spreading. The implication is that the lack of coupling of the oceanic lithosphere to the underlying mantle allows the domination of the necessary driving forces (ridge push, slab pull?). This leads to the following hypothesis regarding the difference in venusian and terrestrial tectonics: *The tectonic styles of Earth and Venus are determined by the presence and absence of a LVC, respectively.* If this hypothesis is correct, then the uncoupled nature of the oceanic lithosphere results in the direct focusing of convective effects only at the ridges, while on Venus mantle convection can be strongly coupled over large regions, leading to broad zones of intense deformation. Whether or not this concept might have application to the Archean Earth depends on when the terrestrial mantle became hydrated.

REFERENCES

Banerdt, W.B., and M.P. Golombek, Lithospheric modeling of Venus, *Lunar and Planet. Sci. XVII*, LPI, Houston, 22-23, 1986.

Barsukov, V.L., and 29 other authors, The geology and geomorphology of the Venus surface as revealed by the radar images obtained by Veneras 15 and 16, *Proc. 16th Lunar and Planet. Sci. Conf., Part 2, J. Geophys. Res.*, *91*, D378-D398, 1986.

Basilevsky, A.T., A.A. Pronin, L.B. Ronca, V.P. Kryuchkov, A.L. Sukhanov, and M.S. Markov, Styles of tectonic deformations on Venus: Analysis of Venera 15 and 16 data, *Proc. 16th Lunar and Planet. Sci. Conf., Part 2, J. Geophys. Res.*, *91*, D399-D411, 1986.

Bills, B.G., and M. Kobrick, Venus topography: A harmonic analysis, *J. Geophys. Res.*, *90*, 827-836, 1985.

Kiefer, W.S., M.A. Richards, B.H. Hager, and B.G. Bills, A dynamic model of Venus's gravity field, *Geophys. Res. Lett.*, *13*, 14-17, 1986.

Masursky, H., E. Eliason, P.G. Ford, G.E. McGill, G.H. Pettengill, G.G. Schaber, and G. Schubert, Pioneer Venus radar results: Geology from images and altimetry, *J. Geophys. Res.*, *85*, 8232-8260, 1980.

Parmentier, E.M., Topography due to horizontal stresses in a ductile lithosphere of variable thickness: Application to Venus, *Lunar and Planet. Sci. XVII*, LPI, Houston, 648-649, 1986.

Phillips, R.J., A mechanism for tectonic deformation on Venus, *Geophys. Res. Lett.*, *13*, 1141-1144, 1986.

Phillips, R.J., and M.C. Malin, The interior of Venus and tectonic implications, in *Venus*, edited by D. M. Hunten, L. Colin, T. M. Donahue, and V. I. Moroz, pp. 159-214, Univ. of Arizona Press, Tucson, 1983.

Phillips, R.J., and M.C. Malin, Tectonics of Venus, *Ann. Rev. Earth. Planet. Sci.*, *12*, 411-443, 1984.

Phillips, R.J., W.M. Kaula, G.E. McGill, and M.C. Malin, Tectonics and evolution of Venus, *Science*, *212*, 879-887, 1981.

Reagan, M.T., Investigation of the extent of isostatic equilibrium and depth of compensation on Venus (abs.), *EOS*, *67*, 299, 1986.

Robinson, E.M., B. Parsons, and S.F. Daly, The effect of a shallow low viscosity zone on the apparent compensation of mid-plate swells, *Earth Planet. Sci. Lett.*, in press, 1986.

Sjogren, W.L., B.G. Bills, and N.A. Mottinger, Venus: Ishtar gravity anomaly, *Geophys. Res. Lett.*, *11*, 489-491, 1984.

Solomon, S.C., and J.W. Head, Mechanisms for lithospheric heat transport on Venus: Implications for tectonic style and volcanism, *J. Geophys. Res.*, *87*, 9236-9246, 1982.

Solomon, S.C., and J.W. Head, Venus banded terrain: Tectonic models for band formation and their relationship to lithospheric thermal structure, *J. Geophys. Res.*, *89*, 6885-6897, 1984.

Zuber, M.T., Constraints on the lithospheric structure of Venus from mechanical models and tectonic surface features, in press *Proc. Lunar Planet. Sci. Conf. XVII*, *J. Geophys. Res.*, 1986.

BILATERAL SYMMETRY ACROSS APHRODITE TERRA

L. S. Crumpler and J. W. Head, Department of Geological Sciences, Brown University, Providence, RI 02912, and D. B. Campbell, NAIC Arecibo Observatory, Arecibo, PR 00612.

Introduction

There are three main highland areas on Venus: Beta Regio, Ishtar Terra and Aphrodite Terra (1). Aphrodite Terra is the least known and the least mapped of these three areas, yet existing analyses of Aphrodite Terra based on available Pioneer-Venus orbiter data (1) suggest that it may be the site of extensive rifting (2, 3). Some of the highest resolution (30 km) PV data (SAR) included most of the western half of Aphrodite Terra. Recent analyses of the SAR data together with Arecibo range-doppler topographic profiling (10 x 100 km horizontal and 10 m vertical resolution) across parts of Aphrodite (4), further characterized the nature of possible tectonic processes in the equatorial highlands. The results of that study (4) indicated the existence of distinct topographic and radar morphologic linear discontinuities across the nearly east-west strike of Aphrodite Terra. Another prominent set of linear features is distinctly parallel to and orthogonal to the ground tracks of the PV spacecraft and are not included because of the possibility that they are artifacts. Study of the northwest trending cross-strike discontinuities (CSD's) and the nature of topographic and morphologic features along their strike suggest the presence of bilateral topographic and morphologic symmetry about the long axis of Aphrodite Terra.

Data Analysis

Data covering the Aphrodite region are limited and include PV altimetry, PV imagery (SAR) and Arecibo altimetric profiling. Venera 15/16 coverage is all above approximately 30 degrees north (5), whereas most of the features discussed here lie within 30 degrees of the equator. Arecibo high-resolution imaging (6) covers the hemisphere antipodal to Aphrodite and only Arecibo altimetry has been obtained of Aphrodite.

In order to further understand the nature of the CSD's identified earlier (4), the PV topographic and PV radar image characteristics of CSD's were examined along their strike and compared to the existing high-resolution Arecibo altimetric profiles which cross the strike of the CSD's. Seven of the most distinct CSD's were chosen showing strong linear topographic signatures in PV topography and steep radar backscatter gradients in SAR images. These CSD's are located in Figure 1 on a PV-based topographic contour map of western Aphrodite. As noted previously (4) CSD's mark distinct transitions of discontinuities in the large (thousands of kilometers) and intermediate (hundreds of kilometers) scale structure of Aphrodite Terra including distinct linear right offsets in regional morphologic boundaries of the plateau-like highlands responsible for the segmented shape of Aphrodite.

Examination of the topographic profiles across Aphrodite Terra, adjacent and parallel to the CSD's (Fig. 2), illustrates that the general character of topography across the highlands parallel to the CSD's differs significantly from that seen in profiles along the strike of the highlands and across the strike of the CSD's. When examined parallel to the CSD trends, the dominant characteristic of topography is a strong bilateral symmetry (Fig. 2a-d) which is not apparent in topographic profiles along other directions, including those profiles differing only slightly from the dominant CSD orientation (Fig. 2e). In addition to a broad symmetrical bell-shaped curvature or convexity of the highlands and the surrounding lowlands, there is also a finer-scaled symmetry in which peaks and troughs on one flank have similar or conjugate features on the opposite flank. Conjugate topographic features occur at the same distance from the center of regional bell-shaped symmetry.

Axes of symmetry defined by many adjacent profiles parallel to and between adjacent CSD's generally fall along lines striking about N70E; this is approximately parallel to the ridge and valley structure of Ovda Regio. The centers of symmetry of two adjacent profiles constructed parallel to and separated by a prominent CSD generally do not align on single lines as do those between two prominent CSD's. The axes of symmetry so defined have distinct right lateral offsets and are at least partly responsible for the large-scale segmented appearance of Aphrodite Terra.

In addition to the bilateral symmetry visible in topographic profiles, conjugate landforms are visible on PV altimetric maps. A linear ridge (x-y) 3000 km NW of the Ovda Regio axis of symmetry, as defined in profiles, is mirrored in the linear ridge (x'-y') 3000 km SE of Ovda Regio. A more striking example of mirrored or conjugate topography is an arcuate trough 3500 km NW of Thetis Regio which is similar in size and map shape to the arcuate Artemis Chasma 3500 km SE of Thetis Regio. The east and west extents of both arcuate troughs are tangent to the trend of the same east and west CSD's outlining distinct elements of Thetis Regio.

Conclusions

Cross-strike discontinuities (CSD's) in Aphrodite Terra reported previously (4) define the boundaries of distinct topographic and morphologic offsets of Aphrodite Terra. Topographic profiles constructed from PV altimetry data parallel to these CSD's show extreme bilateral symmetry on both regional (thousands of kilometers) and local (hundreds of kilometers) scales. The existence of a mirror image or conjugate of the arcuate Artemis Chasma illustrates the scale, extent and degree of bilateral symmetry across Aphrodite Terra.

We find the symmetric cross-strike profiles of Aphrodite, the conjugate minor topographic features and the offset axes of topographic symmetry to be broadly comparable to terrestrial oceanic thermal topography, topographically symmetric crustal spreading (7, 8) and transform faults. We conclude that these structures may represent evidence for crustal spreading on Venus. Other processes that may form the observed bilateral symmetry, evident on a scale of thousands of kilometers, include: 1) distributed rifting across a regional thermal uplift; 2) crustal traction and folding over bilaterally symmetric mantle plumes; and 3) global-scale block rotation between latitudinal strike-slip faults (9, 10). We are presently investigating the relationship of CSD's to tectonic features in mid and high latitudes, and the east-west extent of symmetry, in order to clarify which of these, or other possible mechanisms, are responsible for the topographic and morphologic bilateral symmetry across Aphrodite Terra.

References

1. Pettengill, G. et al., 1980, Pioneer Venus radar results: Altimetry and surface properties, J. Geophys. Res., 85, 8261-8270.
2. Schaber, G.G., 1982, Venus: Limited extension and volcanism along zones of lithospheric weakness, Geophys. Res. Lett., 9, 499-502.
3. McGill, G. et al., 1982, Topography, surface properties and tectonic evolution, in Venus (D.M. Hunten, L. Colin, T.M. Donahue and V.I. Moroz, eds.), Univ. of Arizona Press, Tucson, AZ, 690-730.
4. Crumpler, L.S. et al., 1986, Cross-strike discontinuities in western Aphrodite Terra, Venus, Lunar Planet. Sci. Conf. XVII, 1029-1030.
5. Barsukov, V.L. et al., 1986, The geology and geomorphology of the Venus surface as revealed by the radar images obtained by Venera 15 and 16, Proc. Lunar Planet. Sci. Conf. XVI, J. Geophys. Res., 91, D378-D398.
6. Campbell, D.B. and Burns, B.A., 1980, Earth-based radar imagery of Venus, J. Geophys. Res., 85, 8271-8281.
7. Lewis, B.T.R., 1979, Periodicities in volume and in longitudinal magma flow on the east Pacific rise at 23 degrees N, Geophys. Res. Lett., 6, 753-756.
8. Brozena, J.M., 1986, Temporal and spatial variability of sea floor spreading process in the northern South Atlantic, J. Geophys. Res., 91, 497-510.
9. Garfunkel, Z. and Ron, H., 1985, Block rotation and deformation by strike-slip faults, 2, the properties of a type of macroscopic discontinuous deformation, J. Geophys. Res., 90, 8589-8602.
10. Cowan, D.S. et al., 1986, Bookshelf tectonics: Rotated crustal blocks within the Sovanco fracture zone, Geophys. Res. Lett., 13, 995-998.

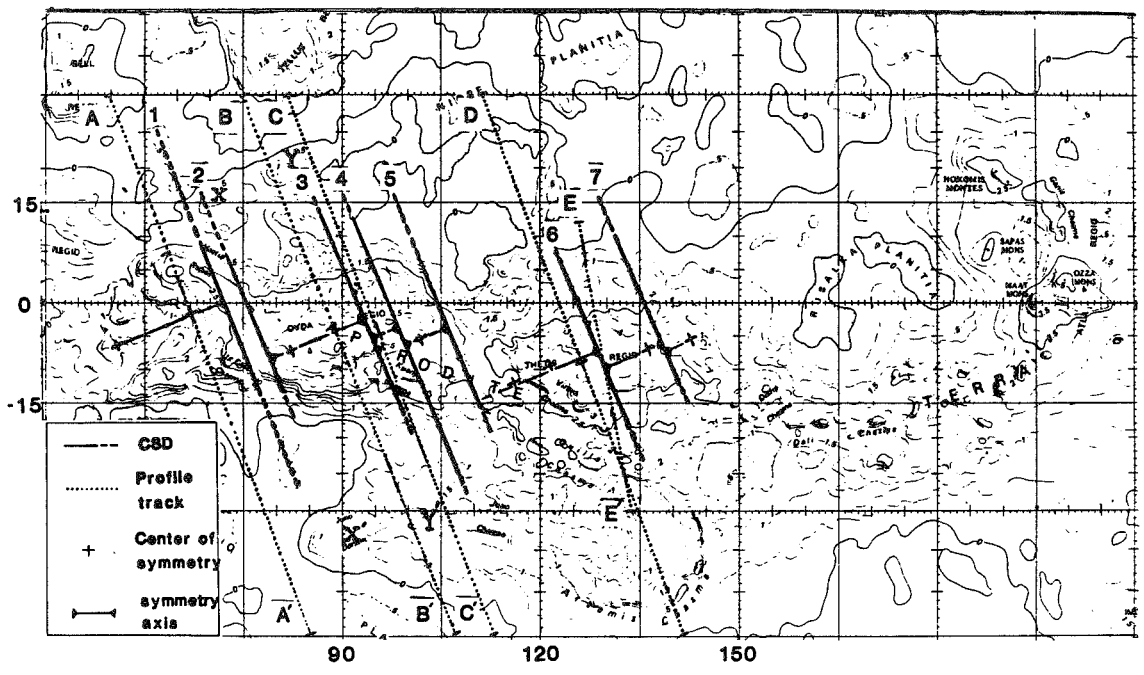

Figure 1

Fig. 1. Location of main cross-strike discontinuities, profiles of Figure 2, and axes of symmetry.

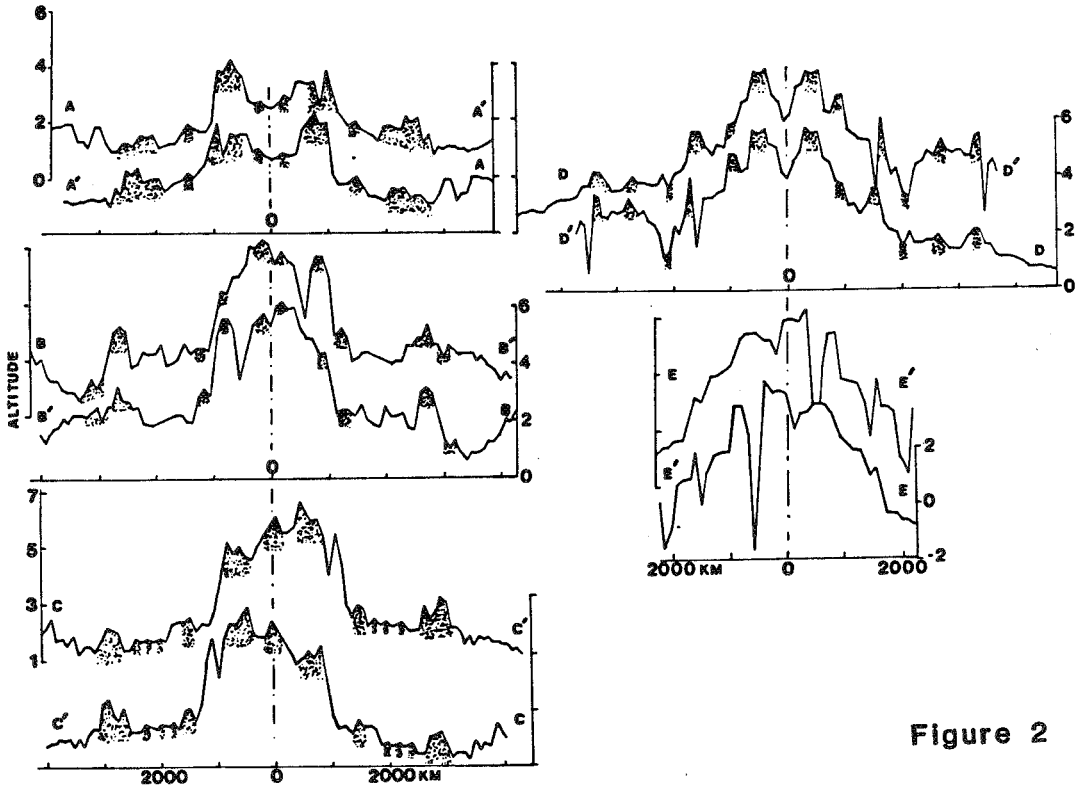

Figure 2

Fig. 2. Altimetry profiles across Aphrodite Terra and parallel to CSD trends. PV raw data.

SECULAR COOLING OF EARTH AS A SOURCE OF INTRAPLATE STRESS

Sean C. Solomon, Department of Earth, Atmospheric, and Planetary Sciences, Massachusetts Institute of Technology, Cambridge, MA 02139

Introduction. The once popular idea that changes in planetary volume play an important role in terrestrial orogeny and tectonics [1,2] was generally discarded with the acceptance of plate tectonics. It is nonetheless likely that the Earth has been steadily cooling over the last 3-4 billion years [e.g., 3,4], and the global contraction that accompanied such cooling would have led to a secular decrease in the radius of curvature of the plates. We explore here the implications of this global cooling and contraction for the intraplate stress field and the evolution of continental plates.

Procedure. We make used of the formulation of Turcotte [5] and McKinnon [6] for stress in a thin, spherical, elastic cap on an expanding or contracting planetary body. The formulation is based on conservation of cap area and the assumption that the radial or polar ($\sigma_{\theta\theta}$) horizontal stress is zero at the cap boundary. The latter assumption is quite reasonable for lithospheric plates subjected to episodic stress release by earthquakes at their boundaries. Extensional stress is predicted in the interior of a plate on a contracting Earth (opposite to the effect of contraction on a body with a globally continuous lithosphere), with a time rate of stress accumulation approximately proportional to the plate area and to the rate dR/dt of global contraction [5,6]. The quantity dR/dt may be obtained from a thermal history model and an estimate of the radial dependence of the coefficient of volumetric thermal expansion. The effects of radial migrations of phase boundaries involving changes in specific volume can also be incorporated.

Rate of Global Contraction. As a simple first approximation, consider that $dR/dt \cong R\,\alpha/3\,dT/dt$ where α is the mean coefficient of thermal expansion in the Earth and T is a characteristic temperature. From the estimated eruption temperatures of Archaean komatiites, Sleep [7] has estimated that $dT/dt \cong -100$ K/b.y. for the last 3 b.y. With $\alpha = 3 \times 10^{-5}$ K^{-1}, this gives $dR/dt \cong -6$ km/b.y. (Table 1). Comparable results are given by thermal history models, making use of the approximation $q - q_{ss} \cong 4/3\,\pi R^3 \rho C_p\,dT/dt$, where q is the mean global heat flux, q_{ss} is the steady-state value of q (if heat loss equaled heat production), and ρ and C_p are density and specific heat, respectively. Thermal history models differ in how mantle convective heat transport is parameterized, principally in whether whole-mantle or layered convection systems predominate [e.g., 3,4]. These differences yield variations in q/q_{ss} ranging from about 1.1 to 2, with values toward the upper end of this range yielding estimates for dT/dt most consistent with the estimate from the eruption temperatures of mantle-derived magmas [7].

Effects of Phase Boundary Migrations. As the mantle cools, temperature dependent phase boundaries will move radially outward or inward, depending on whether the Clapeyron slope dP/dT is respectively positive or negative. The resulting change in the volume of mantle changing phase is equivalent to a change in R. We show in Table 1 estimates for dR/dt due to a rate of global cooling dT/dt of 100 K/b.y. and consequent migration of the olivine-β phase boundary, the β–γ (spinel) phase boundary, and the reaction γ-$(Mg, Fe)_2SiO_4 \rightarrow (Mg, Fe)SiO_3$ (perovskite) + (Mg, Fe)O. The specific volumes are from Lees et al. [8], and the Clapeyron slopes are taken to be 35 bar/K [9], 55 bar/K [9], and -20 bar/K [10], respectively. The effect on the rate of global contraction may be seen to be an order of magnitude less than for whole-Earth cooling, and the contributions of these phaase boundaries partially concel each other because of the mix of signs of the Clapeyron slopes.

Also shown in Table 1 is an estimate of the contribution to dR/dt from inner core solidification, under the assumption that solid Fe at inner core pressures is in the ε phase [11] and that the rate of increase in inner core volume has been constant for 4 b.y. This effect is much smaller than the others considered and may be neglected.

Rates of Stress and Strain. For the overall rate of global contraction given in Table 1, a circular plate of radius R would experience a secular increase in the rate of extensional membrane stress and strain in the plate interior [5,6] of 120 bar/b.y. and 3×10^{-21} s^{-1}, respectively. Neither one of these rates is particularly large, but it is of interest to compare them with other sources of steady change in membrane stress and to consider the conditions under which these estimates might be raised.

Another source of membrane stress is the change in the ellipticity e of the Earth's figure accompanying tidal despinning. From first order hydrostatic theory, $\dot{e}/e = 2\dot{\Omega}/\Omega$, where Ω is the spin rate. From the paleontological record of growth in corals and bivalves, Lambeck [12] gives $\dot{\Omega} = -5 \times 10^{-22}$ s^{-2} since the mid-Paleozoic, which yields $\dot{e} = -1.4 \times 10^{-3}$/b.y., equivalent to changes in mean radius of curvature dR/dt of -9 km/b.y. at the poles and +9 km/b.y. at the equator. The rate of change of radius of curvature of a large plate due to change in spin rate is thus comparable to that due to global cooling.

Membrane stress also accumulates as plates change latitude on an ellipsoidal Earth [5]. For a circular plate with radius R moving from the pole to the equator at 1 cm/yr latitudinal velocity, the central interior is subjected to increasing extension at the rate 1 kbar/b.y. [5]. This effect can thus yield locally larger stress than the stress due to global contraction or despinning, but only if the poleward component of plate motions are rapid or are sustained for a long interval of geological time.

Several effects might increase the importance of global cooling and contraction for the intraplate stress field. The stress level increases with the area of a plate and with its longevity, and thus would be maximum for a long-lived "supercontinent" plate such as Pangaea. The rate of stress build-up would also be increased during periods of accelerated plate cooling; such periods have been suggested on the basis of documented intervals of rapid seafloor spreading [13] and convective thermal history models.

Conclusions. Global cooling of the Earth can be an important contributor to the state of stress in the interiors of large continental plates. Global contraction in the geologic past should have led to extension in plate interiors, and may have contributed to the formation of intracontinental rifts and to the break-up of supercontinents.

Table 1. Contributions to Global Contraction

Whole Earth Cooling	dR/dt
dT/dt = -100 K/b.y.	-6 km/b.y.
Mantle Phase Changes (assuming same cooling rate)	
$\alpha \rightarrow \beta$ -$(Mg, Fe)_2SiO_4$	-0.5 km/b.y.
$\beta \rightarrow \gamma$ -$(Mg, Fe)_2SiO_4$	-0.3 km/b.y.
$\gamma \rightarrow$ pv + mw	0.4 km/b.y.
Inner Core Solidification	-0.05 km/b.y.

References. [1] H. Jeffreys, *The Earth,* Cambridge, 1929; [2] J. T. Wilson, in *The Earth as a Planet*, Chicago, 1954; [3] D. McKenzie and F. M. Richter, *J. Geophys. Res., 86*, 11667, 1981; [4] W. R. Peltier and G. T. Jarvis, *Phys. Earth Planet. Inter., 29*, 281, 1982; [5] D. L. Turcotte, *Geophys. J. Roy. Astron. Soc., 36*, 33, 1974; [6] W. B. McKinnon, *Proc. Lunar Planet. Sci., 12B*, 1585,1981; [7] N. H. Sleep, *J. Geol., 87*, 671, 1979; [8] A. C. Lees, M. S. T. Bukowinski and R. Jeanloz, *J. Geophys. Res., 88,* 8145, 1983; [9] K. Suito, in *High-Pressure Research*, Academic, 1977; [10] E. Ito and H. Yamada, in *High-Pressure Research in Geophysics*, Reidel, 1982; [11] L. Liu, *Geophys. J. Roy. Astron. Soc., 43*, 697, 1975; [12] K. Lambeck, *The Earth's Variable Rotation,* Cambridge, 1980; [13] D. L. Turcotte and K. Burke, *Earth Planet. Sci. Lett., 41*, 341, 1978.

A TEST OF THE HYPOTHESIS THAT IMPACT-INDUCED FRACTURES ARE PREFERRED SITES FOR LATER TECTONIC ACTIVITY

Sean C. Solomon and Elizabeth D. Duxbury, Department of Earth, Atmospheric, and Planetary Sciences, Massachusetts Institute of Technology, Cambridge, MA 02139

Introduction. Because impact cratering has been such an important process on the solid objects of the solar system and because the cratering event is generally accompanied by faulting in adjacent terrain, impact-induced faults are nearly ubiquitous over large areas on the terrestrial planets. The suggestion has frequently been made in the planetary geology literature that these fault systems, particularly those associated with the largest impact features [e.g., 1,2] are preferred sites for later deformation in response to lithospheric stresses generated by other processes. Much of the evidence in support of this view is circumstantial, such as a perceived clustering of orientations of tectonic features either radial or concentric to the crater or basin in question.

An opportunity exists to test this suggestion more directly on Earth. The terrestrial continents contain more than 100 known or probable impact craters [3], with associated geological structures mapped to varying levels of detail. Prima facie evidence for reactivation of crater-induced faults would be the occurrence of earthquakes on these faults in response to the intraplate stress field. Either an alignment of epicenters with mapped fault traces or fault plane solutions indicating slip on a plane approximately coincident with that inferred for a crater-induced fault would be sufficient to demonstrate such an association. As a first step toward testing this hypothesis on Earth, we have examined published catalogs of earthquakes for evidence of seismic activity near terrestrial impact craters.

Procedure. We began with Grieve's [3] list of 25 probable impact craters with diameter D greater than or equal to 20 km. We then searched standard seismicity catalogs [4-6] for earthquakes having epicenters in the vicinity of each crater, taking care to compare the rate of activity around each crater with the background seismicity in the region. The earthquake catalogs have magnitude thresholds that vary spatially and with time; these must be taken into account when interpreting the results. Local or microearthquakes studies have also been performed with temporary seismic stations near a few craters; the findings from such surveys are also incorporated.

Crater-Earthquake Associations. The 25 craters with D > 20 km are all located in the stable interiors of continents, distant from plate boundaries [3]. The lithosphere in the vicinity of these craters is nonetheless subject to the intraplate stresses generated by plate tectonic forces [7], topographic and density variations [8], and the effects of vertical loading and unloading [9].

For 8 craters with D = 25 to 40 km (Araguainha Dome, Clearwater Lake West and East, Slate Is., Mistastin, Kamensk, Steen River, and St. Martin), the standard earthquake catalogs [4-6] list no earthquakes within 2° in latitude or longitude of the crater. For an additional 10 craters with D = 20 to 100 km (Popigai, Puchezh-Katunki, Kara, Carswell, Manson, Teague, Boltysh, Strangways, Gosses Bluff, and Haughton), fewer than 5 earthquakes have occurred within 2°-3° in latitude or longitude in the last two decades [4], rates of seismicity that are comparable to or below background levels. It should be noted, however, that the magnitude threshold for regions near craters in the Soviet Union is generally higher than for North America or Australia.

Five craters with D = 23 to 140 km (Sudbury, Manicouagan, Siljan, Ries, and Rochechouart) have seen one to several earthquakes occur within two crater radii of the crater center during the last 20 years [4]. These earthquakes are relatively small ($m_b < 5$), however, and the level of seismic activity in the vicinity of the crater is not noticeably higher than the regional background level.

Two large terrestrial craters are associated with high levels of recent seismic activity. During the last 20 years, several thousand small to moderate earthquakes occurred within one to two crater radii from the center of the Vredefort structure (D = 140 km) in South Africa [4,10]. All or nearly all of these earthquakes, however, are rock bursts resulting from deep level gold mining operations in the Witwatersrand [10].

Finally, the Charlevoix impact structure ($D \cong 50$ km) is centrally located in La Malbaie seismic zone in Quebec, one of the most seismically active areas of North America east of the Rocky Mountains [11]. Modern seismicity is concentrated near the conjunction of the St. Lawrence rift system and the 360-m.y.-old crater [12]. Earthquake epicenters [13] and focal mechanisms obtained from first motion and surface wave studies [14], however, indicate that it is the NE-striking, moderately to steeply dipping, rift-related faults that are slipping rather than those created by the impact. The coincidence of the zone of most intense activity with the impact/rift intersection has led to the suggestion that the impact has somehow "weakened" the older fault systems of the rift [e.g., 11,13], but this suggestion is not testable with the seismic data available.

Conclusion. Modern intraplate seismicity does not show any general correlation with fault structures associated with the largest terrestrial impact craters. For the two craters with higher than normal levels of nearby seismic activity, other

factors appear to control earthquake occurrence. We conclude that terrestrial analogs offer little support for the hypothesis that impact-induced fractures remain preferred sites for the release of lithospheric stress long after the impact event.

References. [1] R. Mason, J. E. Guest, and G. N. Cooke, *Proc. Geol. Assoc., 87,* 161, 1976; [2] P. H. Schultz and H. Glicken, *J. Geophys. Res., 84,* 8033, 1979; [3] R. A. F. Grieve, Geol. Soc. Amer. Spec. Pap. 190, 25, 1982; [4] *Bulletin of the nternational Seismological Centre, 1-20,* 1964-83; [5] J. P. Rothe, *The Seismicity of the Earth 1953-1965*, UNESCO, 1969; [6] B. Gutenberg and C. F. Richter, *Seismicity of the Earth,* Princeton Univ. Press, 1954; [7] R. M. Richardson, S. C. Solomon, and N. H. Sleep, *Rev. Geophys. Space Phys., 17,* 981, 1979; [8] L. Fleitout and C. Froidevaux, *Tectonics, 1,* 21, 1982; [9] W. F. Haxby and D. L. Turcotte, *Geology, 4,* 181, 1976; [10] J. D. Fairhead and R. W. Girdler, *Geophys. J. Roy. Astron. Soc., 24,* 271, 1971; [11] A. E. Stevens, *Bull. Seismol. Soc. Amer., 70,* 529, 1980; [12] J. Rondot, *J. Geophys. Res., 76,* 5414, 1971; [13] F. M. Anglin, *Bull. Seismol. Soc. Amer., 74,* 595, 1984; [14] H. S. Hasegawa and R. J. Wetmiller, *Earthquake Notes, 51* (4), 23, 1980.

PHYSIOGRAPHIC CONSTRAINTS ON THE ORIGIN OF LUNAR WRINKLE RIDGES

M. P. Golombek and B. J. Franklin (Jet Propulsion Laboratory, Caltech, Pasadena, CA 91109)

Wrinkle ridges are linear asymmetric topographic highs with considerable morphologic complexity that are commonly found on the lunar maria and the smooth plains of Mars and Mercury. The origin of planetary wrinkle ridges has been a much argued and debated topic in the literature. Early ideas suggested that wrinkle ridges resulted from volcanic intrusion and extrusion of high viscosity lavas (e.g. Quaide, 1965; Strom, 1972; Scott, 1973); these early ideas were countered with suggestions that wrinkle ridges formed from tectonic processes involving folding and faulting (e.g. Ronca, 1965; Bryan, 1973; Howard and Muehlberger, 1973; Muehlberger, 1974; Maxwell et al., 1975; Lucchitta, 1976, 1977; Sharpton and Head, 1982). Combined volcanic and tectonic mechanisms have also been suggested (e.g. Colton et al., 1972; Young et al., 1973). The identification and analysis of a number of morphologically similar structures on the earth has helped in the recent interpretation of wrinkle ridges as thrust faults that deform surface rocks (Plescia and Golombek, 1986). Nevertheless, in the literature there remains the uncertainty of the dominant role of thrusting versus folding in the formation of planetary wrinkle ridges. In this abstract, we present the detailed physiographic analysis of lunar wrinkle ridges in an effort to help distinguish the dominant deformation mechanism. Our results agree with the findings of the earth analog study (Plescia and Golombek, 1986) and support the hypothesis that wrinkle ridges form from thrust faults that deform surface rocks.

We have completed a comprehensive survey of the entire collection of high-resolution topographic data, Lunar Topographic Orthophoto Maps, that cover wrinkle ridges. These maps are at a nominal scale of 1:250,000 with 100 m contours; supplemental maps are at scales of 1:50,000 and 1:10,000 with 20 and 10 m contours, respectively. Identification of ridges was made on Lunar Orbiter and Apollo photographs. A total of 76 topographic profiles were constructed across suitable ridges on the supplemental high resolution topographic maps.

These profiles reveal that wrinkle ridges are composed of three physiographic elements. 1) Broad rise - a linear or convex upward, gentle slope that rises from an essentially flat mare surface toward the center of the ridge. The slope is so gentle that the broad rise is rarely visible on images of the lunar surface. 2) Superposed hill or arch - generally narrower and steeper in slope than the broad rise and located toward the center of the ridge. Because it has steeper slopes it is the physiographic element identifiable in images as the "ridge" of wrinkle ridges. 3) Crenulation - complex, narrow, low-relief wrinkles or crumples in the surface that are found at various locations across the structure, although they are preferentially found near the high point of the ridge. These wrinkles are quite visible, especially in low-sun angle images, and make up the "wrinkle" of wrinkle ridges. They can be paired or braided. All ridges investigated have a broad rise on one or both sides. Almost all ridges have superposed hills, and most have crenulations.

In addition to these previously noted elements (e.g. Strom, 1972; Maxwell et al., 1975; Lucchitta, 1977), every topographic profile across a wrinkle ridge shows a regional elevation change. That is, the elevation of

the mare surface on one side of the ridge is always different from that on the other side. As a result, wrinkle ridges accommodate a vertical structural offset between structural units or blocks of the mare that are at different elevations.

The 76 profiles fell into 7 basic profile types (illustrated in Fig. 1), based on the presence and arrangement of the 3 elements, ridge asymmetry and asymmetry of the regional elevation change. The number of physiographic forms found underscores the complexity and diversity of wrinkle ridges. In an effort to quantify the contribution of the different elements of wrinkle ridges to the overall structural form, a group of 31 representative profiles was selected from the total for statistical analysis. The selection was made to mimimize the bias in the profiles created by the oversampling of particular ridges covered by high-resolution topographic maps. The following quantities (shown in Fig. 1) were measured from the profiles: regional elevation change (5-280 m), maximum relief (80-500 m), maximum broad rise height (25-300 m), maximum superposed hill height (25-410 m), steep face height (55-410 m), total ridge width (2.5-41 km), total broad rise width (1-35 km), and superposed hill width (1-29 km). Two-axis graphs of various combinations of these data reveal that a number of these quantities appear related through linear regression analysis. The most significant correlation (correlation coefficient of 0.77) is found between the total ridge width and maximum relief, indicating that wider ridges have greater relief. The maximum relief also relates to the height of the steep face (0.75 correlation coefficient), indicating that most of the maximum relief is accommodated by the steep face when it exists. The total ridge width has a correlation coefficient of 0.72 with the total broad rise width, indicating that most of the width of a ridge is taken up by the broad rises. Finally, the width and height of the superposed hill have a correlation coefficient of 0.71, showing that wider hills are also higher. These relationships suggest a continuity in form between small and large wrinkle ridges, regardless of the differences in the particular form of the ridge (i.e. the 7 types identified earlier). The simplest explanation is that continuing development of wrinkle ridges results in both wider and higher ridges and is suggestive that large ridges have experienced more deformation and shortening than smaller ridges.

Wrinkle ridges are complex structural features that exhibit a significant variability in the presence and arrangement of a few morphologic and physiographic elements. Our comprehensive analysis of the topographic profiles of lunar wrinkle ridges reveals that all ridges for which there exists high-quality topographic data have a change in regional elevation across the structure. This regional elevation change requires a fault beneath the ridge to accommodate the change in mare surface elevation. It is important to point out that simple fold mechanisms for wrinkle ridges cannot readily explain this regional elevation change. The relationship between ridge width and maximum relief suggests a tectonic process that progressively develops wider structures having greater structural relief and greater shortening. The similarity in morphology between planetary wrinkle ridges and analogous structures identified on earth (Plescia and Golombek, 1986) suggests that the faults are low-angle thrust faults that produce subsidiary folds near the surface. For lunar wrinkle ridges the thrust fault is required to dip beneath the high side of the change in regional elevation to produce the greater elevation of that

mare block. This, in turn, suggests that the faults near the surface have an opposite vergence from the main fault at depth where wrinkle ridges change asymmetry along strike but have the same regional elevation offset, assuming that the asymmetry is created by the dip of the fault near the surface as is the case for the earth analogs (Plescia and Golombek, 1986). We expect that this detailed physiographic analysis will help provide data-constrained estimates of tectonic shortening across these complex structures.

References

Bryan (1973) Proc. Lun. Sci. Conf. 4th, 93-106. Colton et al. (1972) Apollo 16 Prelim. Sci. Rep., NASA SP-315, 29/90-29/93. Howard & Muehlberger (1973) Apollo 17 Prelim. Sci. Rep., NASA SP-330, 31/22-31-25. Lucchitta (1976) Proc. Lun. Sci. Conf. 7th, 2761-2782. Lucchitta (1977) Proc. Lun. Sci. Conf. 8th, 2961-2703. Maxwell et al. (1975) Geol. Soc. Am. Bull. 86, 1273-1278. Muehlberger (1974) Proc. Lun. Sci. Conf. 5th, 101-110. Plescia & Golombek (1986) Geol. Soc. Am., in press. Quaide (1965) Icarus 4, 374-389. Ronca (1965) Icarus 4, 390-395. Scott (1973) Apollo 17 Prelim. Sci. Rep., NASA SP-330, 31/25-31/28. Sharpton & Head (1982) J. Geophys. Res. 87, 10,986-10,998. Strom (1972) in The Moon, IAU Symp. 47, 187-215. Young et al. (1973) Apollo 17 Prelim. Sci. Rep., NASA SP-330, 31/1-31/11.

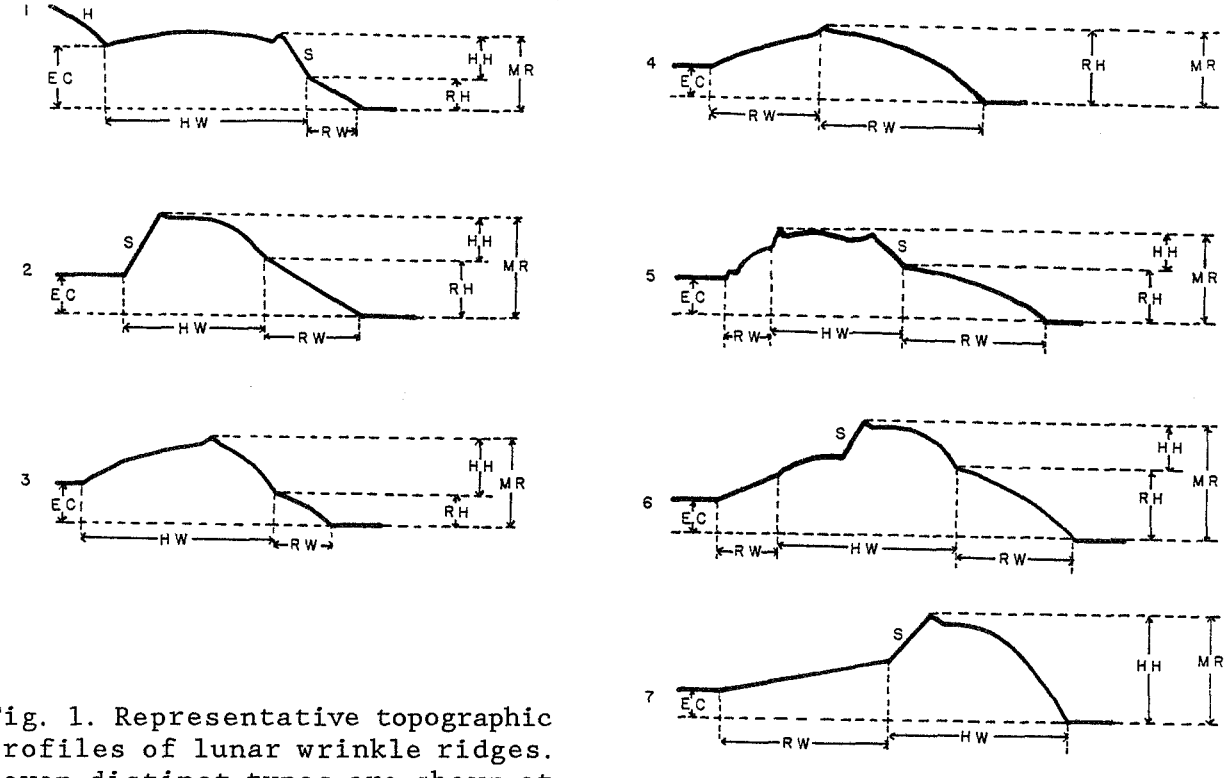

Fig. 1. Representative topographic profiles of lunar wrinkle ridges. Seven distinct types are shown at 10 times verticalexaggeration. Physiographic elements measured in this study are: RW-broad rise width, HW-superposed hill width, RH-broad rise height, HH-superposed hill height, MR-maximum relief, EC-regional elevation change, S-scarp height. Type 1 backs up against highlands (H).

LITHOSPHERIC LOADING AND TECTONICS OF THE LUNAR IRREGULAR MARIA

J. Lynn Hall and Sean C. Solomon, Dept. of Earth, Atmospheric, and Planetary Sciences, Massachusetts Institute of Technology, Cambridge, MA 02139

Introduction. Many of the tectonic features associated with the circular maria are the result of stresses generated by loading of the lunar lithosphere by mare basalt units [1]. In this paper we test the hypothesis that the irregular lunar maria share with the circular maria the processes leading to the formation of associated graben and mare ridge systems. We apply a formulation of the lithospheric flexure problem that accounts for the variable distribution of basalt loads for the irregular maria. On the basis of the tectonic structures and geologic history of each of the major irregular maria, as well as models for the distribution of mare basalt for each region, we compare the predicted stress fields with the distribution of tectonic features for a range of assumed values of the thickness of the elastic lithosphere. We then compare the best fitting values for lithospheric thickness beneath the irregular maria with those previously inferred for the circular maria [1].

Procedure. To model the stress field induced by lithospheric loading, we employ the theory [2] for flexure of a thin elastic shell overlying an inviscid fluid interior. The stresses due to an arbitrary surface load are approximated by summing the solutions for stress from a set of disk loads [2]. The load models are based on estimates of mare basalt thickness derived from a simultaneous inversion of nearside gravity and topographic data [3]; the contributions of mantle relief and mare basalt load are separated by assuming that basin topography was isostatically compensated prior to mare fill and that subsidence in response to mare loading may be neglected. These asssumptions lead to minimum values for the calculated mare basalt thicknesses [4]. Where appropriate, geological estimates of mare basalt thickness [5,6] are also employed for comparative models.

Fecunditatis. Mare Fecunditatis occupies an irregularly shaped depression 600 km by 900 km in dimension; the main northern part is generally held to be the site of a degraded impact basin [7]. Graben are found primarily adjacent to the northwestern mare margin, with some additional extensional features to the southeast; mare ridges occur throughout the northern section of the mare [8]. Lithospheric loading models provide a good fit to the distribution and orientation of extensional features surrounding Mare Fecunditatis, as long as the stress fields contributed by the nearby Nectaris and Crisium mascons are taken into account. The best fit of the area of maximum extensional stress difference to the observed locations of graben is for values of the thickness T of the elastic lithosphere between 40 and 75 km. The best-fitting value of T for the area of maximum compressive stress difference is somewhat greater, 50 to 100 km, consistent with lithospheric cooling between the times of graben formation [9] and of formation of mare ridges following emplacement of the youngest mare basalt lavas [10].

Tranquillitatis. Tranquillitatis is one of the oldest identified basins on the lunar nearside [7] and contains mare units that are among the oldest on the Moon [10]. Extensional features are concentrated to the western side, where basalt thicknesses are greatest [3,5]; mare ridges are located throughout, but are most concentrated in the Lamont region [8]. The best fit of the area of maximum extensional stress to the locations of observed graben is for T = 30 to 60 km. A lithospheric thickness of 60 to 150 km is implied by the distribution of mare ridges. Whether an episode of ridge formation postdating graben formation in fact occurred in Tranquillitatis is not clear from available age relationships [9,10].

Nubium. Located near the southern end of Oceanus Procellarum, Mare Nubium occupies an ancient basin [7]. A few isolated extensional features are present, as are several sets of mare ridges [8]. The best fit of the areas of maximum extensional stress to the observed graben positions is for T = 30 to 75 km. The corresponding best value at the time of formation of mare ridges postdating the youngest mare units [10] is 50 to 150 km.

Procellarum. Oceanus Procellarum, the largest lunar mare, has had a complex volcanic history [11]. A series of graben are located in the uplands to the west of the mare, and numerous ridges are located throughout the mare. The thickness of mare basalt exceeds 1 km along an axis trending NW from Mare Humorum. In constructing load models, we have divided Procellarum into separate western (including Grimaldi) and eastern segments; this division is an oversimplification to the loading history but has some correspondence in the surface mare units [11]. In western Procellarum, the best fit of extensional stresses at the time of graben formation is for T less than 25-35 km; the lithospheric thickness beneath eastern Procellarum at this time is indeterminate. The best match of predicted stress differences to the distribution of ridges is for T = 25-75 km beneath Procellarum and perhaps a slightly greater thickness (50-100 km) beneath the eastern portion.

Discussion and Conclusion. In general, most tectonic features in the vicinity of the irregular maria can be explained as the result of vocanic loading and flexure of the lunar lithosphere. The inferred values of the thickness of the elastic lithosphere at the time of formation of lunar graben 3.6-3.8 b.y. ago [9] and at the time of cessation of mare volcanism compare well with estimates of contemporaneous thicknesses beneath nearby circular maria (Figure 1). The thickness of the lunar lithosphere apparently varied smoothly in space and time, with the lowest values indicated for the west-central nearside. One possible source of the heterogeneous thermal gradients implied by the thinner lithosphere in this region is residual impact heat remaining from the formation of the large Procellarum basin [12].

References. [1] S. C. Solomon and J. W. Head, *Rev. Geophys. Space Phys., 18,* 107, 1980; [2] J. F. Brotchie, *Mod. Geol., 3,* 15, 1971; [3] S. R. Bratt et al., *J. Geophys. Res., 90,* 3049, 1985; [4] C. H. Thurber and S. C. Solomon, *Proc. Lunar Planet. Sci. Conf., 9,* 3481, 1978; [5] R. A. DeHon and J. D. Waskom, *Proc. Lunar Planet Sci. Conf., 10,* 2935, 1979; [7] D. E. Stuart-Alexander and K. A. Howard, *Icarus, 12,* 440, 1970; [8] D. H. Scott et al., *Proc. Lunar Sci. Conf., 6,* 2531, 1975; [9] B. K. Lucchitta and J. A. Watkins, *Proc. Lunar Planet Sci. Conf., 9,* 3459, 1978; [10] J. M. Boyce, *Proc. Lunar Sci. Conf., 7,* 2717, 1976; [11] J. L. Whitford-Stark and J. W. Head, *J. Geophys. Res ., 85,* 6579, 1980; [12] D. E. Wilhelms, *Lunar Planet. Sci., 14,* 845, 1983.

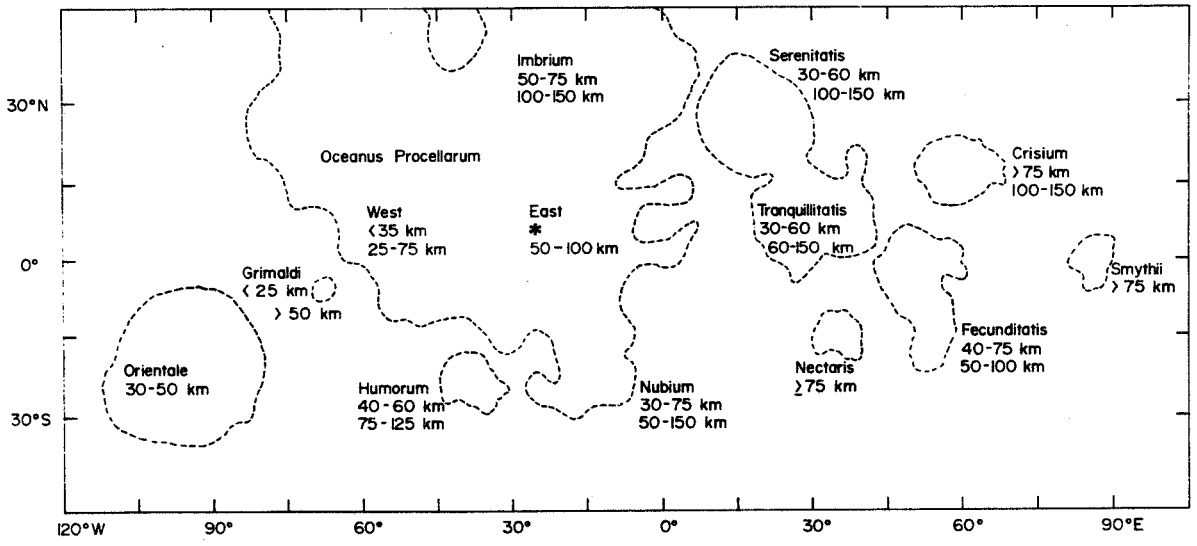

Figure 1. Summary of determination of the thickness T of the elastic lithosphere on the Moon from mare tectonic features. For each load, the upper figure gives T in km at the time of graben formation 3.6-3.8 b.y. ago [9]; the lower figure gives T at a later stage in mare flooding when mare ridge formation and subsidence were continuing but rille formation had ceased.

CHARACTERISTIC STRUCTURES OF THE HIGHLAND BOUNDARY ON MARS: EVIDENCE AGAINST A SINGLE MEGA-IMPACT EVENT?

Ann Marie Semeniuk[1], and Herbert Frey . Astronomy Program, Univ. of Maryland, College Park, MD 20742. [2]Geophysics Branch, NASA/Goddard Space Flight Center, Greenbelt, MD 20771

Wilhelms and Squyres(1) have suggested that an early mega-impact event might explain the fundamental crustal dichotomy on Mars. Detailed morphological mapping of the structures which characterize the boundary between the cratered highlands and northern plains does not support this idea: the distribution of these features along and especially away from the boundary is more consistent with a larger number of smaller but overlapping impacts.

We have assembled a data base for the study of the highland boundary through quantitative mapping (including crater counts) based on the 1:2 M controlled photomosaics (2,3,4). Whole and partial craters larger than 10 km in diameter, knobby terrain, detached plateaus and intervening plains-forming units have been identified wherever they occur on Mars between +65 and -45° latitude. We find evidence for occurrences of possibly old cratered terrain (or its remanants) at high latitudes well north of the current or likely former location of the proposed Borealis Basin(1) rim which are difficult to reconcile with an impact structure of the proposed size and location. In a low resolution map showing the fractional area(2,3) occupied by impact craters, knobby terrain and/or detached plateaus, the overlap produced by combinations of these features is obvious along the highland boundary in eastern Mars. Significant occurrences are also found along the western margin of Mareotis-Tempe, in the outflow channels and chaotic terrain south of Chryse, and in the knobby terrain unit in Elysium-Amazonis. This last area is particularly difficult to understand in terms of a mega-impact event.

The Elysium-Amazonis knobby terrain block is high standing and in many places consists of incomplete large crater rims thinly covered by younger plains. The unit lies on the more gently sloping eastern flank of the high Elysium volcanic complex, at an elevation of 0 to 3 km above reference(5) or perhaps lower(6). While this elevation is in part due to the proximity to Elysium, it is unlikely that it would be lowered by removal of that major structure (off-loading of the Elysium volcanic pile might even cause the crust to rebound). The large partial craters outlined by much of the knobby terrain have a size frequency distribution similar to that of the cratered highlands further south. Schultz(7) has suggested a large impact basin near the Elysium volcanic constructs. This evidence favors the interpretation that this block, which represents as much as 10% of the area of the proposed Borealis Basin, is a relic of old cratered highlands thinly veiled by plains-forming units(8,9). The northermost portion of this unit lies near the proposed center of th mega-impact (50°N, 190°W); the southernmost portion lies only 500 km from the proposed basin rim in Aeolis.

Detailed mapping of landforms found along the highland boundary does not support the idea that the northern third of Mars is a single large impact basin. Widely scattered occurrences of knobby terrain and occassional detached plateaus are found throughout the high latitude portions of the northern lowlands. Irregular distribution of knobby terrain of

different scales parallel to the present highland boundary west of the Isidis Basin become much less obvious to the east, departing from the parallel orientation and instead striking northeast. While some of these may represent units younger than the highland boundary(10), there is implication of possible structural control not dominated by the Borealis Basin rim. The major "holes" in the distribution of high latitude knobs and detached plateaus occur in the two lowest parts of Vastitas Borealis, at 230°W north of Utopia Planitia and at 30°W north of Acidalia Planitia. The first of these lies adjacent to the proposed center of the mega-impact; the second straddles the proposed basin rim. Although the topography in these regions is suspect(6), these "holes" are the only two portions of the high latitude plains lower than 2 km below reference (i.e., as deep as the Chryse Basin). At higher elevations some evidence for possibly old terrain usually exists.

As described elsewhere(11), evidence for a continuous circular highland boundary is lacking, especially in western Mars. It is not obvious this lack is due to subsequent geologic events. The occurrence of possibly old terrain at relatively high elevations in the northern lowlands, especially close to the proposed basin center, the lack of convincing topographic expression of the basin(9), and the patchy distribution of both elevations and landforms north of the highland boundary all are more easily understood in terms of multiple overlapping impacts of more moderate size.

References

1. Wilhelms, D.E. and S.W. Squyres, Nature 309, 138 (1984).
2. Semeniuk, A.M. and H.V. Frey, Lunar Planet Sci. XV, 748 (1984).
3. Frey, H. and A.M. Semeniuk, Lunar Planet Sci. XVI, 252 (1984).
4. Semeniuk, A.M. and H.V. Frey, EOS Trans. Am. Geophys. Un. 66,400 (1985).
5. Scott, D.H. and M.H. Carr, Geol. Maps Mars (1978).
6. Downs, G.S. et al., J. Geophys. Res. 87, 9747 (1982).
7. Schultz, P.H., Lunar Planet Sci. XV, 728 (1984).
8. Scott, D.H. and J.W. Allingham, Geol. Map Elysium Quad. Map I-935 (1976).
9. Morris, E.C. and S.E. Dwornik, Geol. Map Amazonis Quad. Map I-1049 (1978)
10. Mouginis-Mark, P.J. et al., Earth Moon Planets 30, 149 (1984).
11. Frey, H. et al., Lunar Planet Sci. XVII, 241, (1986).

THE MARTIAN CRUSTAL DICHOTOMY: PRODUCT OF ACCRETION AND NOT A SPECIFIC EVENT?

Herbert Frey, Goddard Space Flight Center, Greenbelt, MD 20771, R.A. Schultz, Dept. Geosciences, Purdue University, W. Lafayette, IN 47906 and T.A. Maxwell, NASM, Smithsonian Inst., Washington, DC 20560

Attempts to explain the fundamental crustal dichotomy on Mars range from purely endogenic to extreme exogenic processes (1,2) but to date no satisfactory theory has evolved which is generally accepted. What is accepted is (a) the dichotomy is an ancient feature of the martain crust, and (b) the boundary between the cratered highlands and northern plains which marks the dichotomy in parts of Mars has undergone significant and variable modification during the observable parts of martian history. Fundamental uncertainties remain, including: (a) the true present and former extent of the boundary (i.e., is it global?), (b) the nature of the crustal materials underlying the northern part of the dichotomy (is the dichotomy both topographic and compositional?), (c) the nature and duration of the formative process(es?), and (d) the relation between the establishment of the crustal dichotomy and the overall internal and crustal evolution of Mars. These are important questions because crustal dichotomies are a common feature among the terrestrial planets.

Wilhelms and Squyres (2) call on a single mega-impact event, essentially an instantaneous rearrangement of the crustal structure (topography and lithospheric thickness). Wise et al. (1) prefer an internal mechanism: a period of vigorous convection subcrustally erodes the northern one third of Mars, causing foundering and isostatic lowering of that part of Mars. This major tectonic rearrangement of the lithosphere is also considered an "event" in martian history, ending by crater ages 50,000 to 100,000. In this paper we review the evidence for each of these two extreme theories, conclude there is little to recommend or require either, and suggest an alternative: the formation of the crustal dichotomy on Mars was not a specific tectonic "event" but a by-product of the accretionary process and therefore a primordial characteristic of the martian crust, predating the oldest recognizeable landforms.

The Mega-Imapact Hypothesis: Because it is a well-defined process, the formation of the martian crustal dichotomy through a 7700 km diameter impact (2) is more easily examined that the less precisely defined alternative (1). Exceptions to the impact hypothesis are several. The described small circle suggested as the basin rim is incomplete and better described as a semi-circular arc covering less than 180° of longitude. Circularity in any case is a necessary but not sufficient condition to demonstrate impact. The basin "rim" is highly variable in expression and character and its location in western Mars is inferred from presumption of circularity and continuity. Even where well displayed, features used to define the rim vary along its length by more than might be expected for a single impact, even allowing for likely variation in the subsequent erosional processes which have clearly modified the boundary (3,4,5,6). Massifs used to define the rim in many cases have been ascribed to other smaller basins (7,8,9). There is a lack of both concentric and in particular radial structures over the entire circumference that might be expected for such a large impact. Detailed mapping of detached plateaus and knobby terrain along and away from the presumed rim (10,11) does not support the statement that all the old cratered terrain lies outside the suggested basin. Outcrops north of Olympus Mons and in particu-

lar the highstanding old subsurface characterized by the knobby terrain in Elysium-Amazonis (12,13,14) which lies near the center of the basin are difficult to reconcile with an impact basin structure. Topographically the basin has rim-like gradients only along its southernmost portion in Amenthes-Aeolis; elsewhere the slope from cratered highlands into the northern plains is much more gradual and lacks rim-like character.

Subcrustal Erosion and Underplating: The Wise et al. (1) model lacks quantitative detail which could be tested. Calculations of the amount of surface crustal material that would have to be removed from the north and deposited in the cratered terrain are presented and found inadequate (15), but no similar volumetric calculations are provided for the favored subcrustal erosion and subsequent underplating. It is not explained how lower density crustal blocks are preserved in the higher density and hotter mantle for the time period between the lowering of the northern third of Mars and the later isostatic rise of Tharsis. It is not easy to understand why such surviving blocks would preferentially collect in one or two locations (pre-Tharsis and pre-Elysium?) rather than being uniformly distributed over the remaining two thirds of the martian lithosphere. The duration of the vigorous convection required by this mechanism is not specified and the stability of the simple convective pattern pictured may also be questioned. Vigorous convection may in fact never have been part of martian history: thermal models suggest a more moderate episode of core formation which raises the global temperatures on Mars by only 200°C (16,17). If pieces of old, unfoundered crust exist in the northern third of Mars (11,12) then ad hoc preservation mechanisms must be invoked or pre-existing lithospheric heterogeneity undermined the effectiveness of the subcrustal erosion.

An Alternative to the "Single Event" Approach: The geophysical difficulties associated with the subcrustal erosion theory and the evidence against the single mega-impact model require that alternatives to account for the martian crustal dichotomy be considered. There is no requirement that the modification to the martian lithosphere be due to a single "event" and in fact there is little available evidence to recommend such one-shot scenarios. Perhaps more useful would be considering the cumulative effects of multiple smaller scale events. Impacts are appealing because of their ability to drastically alter (locally) the lithospheric structure. Because the single giant impact hypothesis seems inconsistent with the observational evidence, we raise the question of whether or not the crustal dichotomy on Mars could be due to the combined effects of many more moderately-sized impacts such as might occur at the tail end of the accretionary process.

Recognition of ancient impact basins is hampered by the processes associated with the formation and evolution of basins (7,18). Despite this, new basins continue to be found on Mars (8,9). If the Chryse Basin (7) is taken as the largest currently accepted impact structure on Mars and a D^{-2} scaling is used to estimate the number of smaller impact basins that could exist on the planet, then an estimate of the number of "missing" or undiscovered basins can be made: 7 with diameters larger than 1000 km, 32 larger than 500 km and 155 larger than 250 km. The combined area of these exceeds that of the suggested Borealis Basin. If these structures were all in the northern hemisphere of Mars (which is unlikely), the overlap expected to occur between them would still allow large portions of the ancient cratered terrain to remain as isolated islands between basins. In particular large blocks such as the Elysium-Amazonis knobby terrain unit might survive. The patchy distribution

of possible old crust in the northern plains (11,12) as well as the topographic irregularities found there are more easily understood in terms of multiple overlapping impacts than with a single giant impact.

Multiple impacts could be expected to produce drastic and long-lived effects in the martian lithosphere which in sum might be far more effective at establishing and maintaining a crustal (lithospheric) dichotomy than either of the two single event theories. Large impacts will thin the lithosphere both mechanically and thermally (19,20,21). The depth-diameter relation for very large impacts is not known, but it is likely to be a shallow function. Therefore overlapping large impacts could produce a greater total mechanical thinning (locally) than might be accomplished by a single giant impact, especially away from the presumed center of such a mega-impact. Detailed thermal histories for large scale impacts are still few, but most show enhancement of the thermal gradients below the basin for several hundred million years after impact (19,22). During late stage accretion overlapping impacts could occur within this period. Volcanism in such areas might be accelerated and the establishment of a deep-seated thermal anomaly is not unreasonable. It has been suggested that impact basins play a role in the development of both Elysium and Tharsis (8): we suggest that multiple overlapping impacts may offer the best opportunity for development of a longlived volcanic complex through maximum thinning of the lithosphere and localization of thermal effects.

Given the efficiency of major impacts (especially overlapping impacts) for thinning the lithosphere and localizing volcanism and the expected high rate of such impacts during the final accretionary sweep-up, it seems likely that a crustal dichotomy may will have been primordial, a primary characteristic of the martian crust.

References:

1. Wise, D.U. et al. (1979) Icarus 38, 456.
2. Wilhelms, D.E. and S.W. Squyres (1984) Nature 309, 138.
3. Squyres, S.W. (1978) Icarus 34, 600.
4. Lucchitta, B.K. (1984) Proc. Lunar Planet. Sci. Conf. 14th, 409.
5. Semeniuk, A.M. and H.V. Frey (1984) Lunar Planet. Sci. XV, 748.
6. Maxwell, T.A. et al. (1984) Geol. Soc. Am. Abstracts w/Prog. 16 586.
7. Schultz, P.J. et al.(1982) J. Geophys. Res. 87, 9803.
8. Schultz, P.J. (1984) Lunar Planet. Sci. XV, 728.
9. Stam, M. et al. (1984) Lunar Planet. Sci. XV, 818,
10. Semeniuk, A.M. and H.V. Frey (1985) EOS Trans. Am Geophys. Un. 66, 400.
11. Frey H,V and A.M. Semeniuk (1985) NASA TM 87563, p. 347.
12. Frey, H.V. and Semeniuk (1986) Lunar Planet. Sci. XVII, 796.
13. Scott D.H. and J.W. Allingham (1976) Geol. Map Elysium Quad., Map I-935.
14. Morris, E.C. and S.E. Dwornik (1978) Geo. Geol. Map Amazonis Qad., Map I-1049.
15. Wise, D.U. et al. (1979) J. Geophys. Res. 84, 7934.
16. Toksoz, M.N. and A.T. Hsui (1978) Icarus 34, 537.
17. Solomon, S.C. (1979) Phys. Earth Planet. Inter. 19, 168.
18. Malin, M.C. (1976) Proc. Lunar Planet. Sci. Conf. 7th, 3589.
19. Frey, H.(1980) Precamb. Res. 10, 195.
20. Grieve, R.A.F. (1980) Precamb Res. 10, 217,
21. Solomon S.C. et al. (1982) J. Geophys. Res. 87, 3975.
22. Grieve, R.A.F. and E. M. Parmentier (1984) Lunar Planet. Sci. XV, 326.

IMPLICATIONS OF VIKING COLOR DATA FOR EVOLUTION OF THE AMENTHES REGION, MARS

Ted A. Maxwell, Center for Earth and Planetary Studies, National Air and Space Museum, Smithsonian Institution, Washington, D.C. 20560

In the eastern hemisphere of Mars, where the hemispheric dichotomy is not overlain by relatively recent flows from the Tharsis volcanoes, the Mars cratered terrain boundary (CTB) now exists as highly fractured terrain juxtaposed with the smooth plains of the northern hemisphere. Based on Mariner 9 topopgraphy, the southern cratered terrain in the Amenthes region (0-30°N, 225-270°W) is approximately 3-4 km above the northern plains, and the transition zone is marked by both broad plateaus and knobby terrain. In the Amenthes Southeast quadrangle, in particular, the continuum between large detached plateaus, smaller smooth topped plateaus and knobby hills can be seen. Knobby terrain, though, is not restricted to areas adjacent to the boundary, and extends some 1000 km to the north where isolated knobs can be mapped. To define the previous position and evolution of the boundary, the distribution of cratered terrain, characteristic landforms (knobby terrain and detached plateaus) have been mapped (1), as well as structural features across the boundary. Structural mapping (2) has indicated that the few graben that are present are oriented parallel to the boundary in the eastern hemisphere, and the the orientation of elongate knobs and detached plateaus also are parallel to the CTB. These results imply that the evolution of the CTB has involved normal faulting through extension perpendicular to the boundary.

If the knobby terrain is truly remnant of the ancient cratered terrain, then the far northerly occurrence of the knobs implies that at least part of the northern plains may be underlain by ancient terrain. In order to look at possible compositional variations to test this hypothesis, we have investigated the global color set compiled by the mars consortium (3). The application of this data to geologic interpretation of the boundary has been initially confined to the Amenthes quadrangle in an attempt to limit the numerous problems inherent in the data. Limitations of the Viking II approach color have been enumerated in (4), and include 1) time - the data is a "snapshot" of the northern hemisphere summer, 2) condensates - found to be a major subset of units defined in (4), 3) aeolian blanketing - subdues bedrock (?) reflectance, 4) redundancy in filter bandwidths, and 5) mixing of surface compositions without adequate ground truth. The two most serious problems for the present study are atmospheric contributions that increase with latitude, and the high correlation among the three color bands. Previous attempts to reduce the correlation among the three colors (red = .59 $\pm$ .05 microns, green = .53 $\pm$ .05 and violet = .45 $\pm$ .03) used ratios of the data and included albedo and thermal inertia (5). In that study, covariance among the three color ratios remained high, and most of the color variations were expressed by the red/violet ratio, consistent with (4).

To characterize units in the Amenthes quadrangle previously defined on the basis of high spatial resolution photogeologic mapping, the three

colors of the Viking II approach data were used at the original (1/4 degree) resolution. The data for this quadrangle do not differ significantly from the entire data set in that all three colors are highlycorrelated. As is true for areas studied in (4) and (5), most of the variance in the original Mars data set is carried by the red and violet channels. Reduction of the correlation among the three colores was done by a principal components analysis (see (5) for description). The three eigenvectors for the original data indicate that the first component is controlled equally by the three color channels, and accounts for 94% of the variance in the original data. The second component is controlled by the red and violet channels (4.86% of the variance), and the third by the green (1.11% of the variance). Before transformation of the data back to color space, the principal component images were normalized. The resulting data set showed correlation values of 0.50 (red to green), 0.26 (violet to red) and 0.88 (violet to green).

The decorrelated image data (in which reflectance values differ from the original data) were then subjected to an unsupervised classification, starting with the maximum number of data clusters present (n= 19), and interactively reducing the number by comparison of classified image with the geologic mapping results. The final classification resulted in definition of 13 units, 4 of which were related to atmospheric variations north of 10 - 15° N. In the southern part of the quadrangle, the classified units show areas of possible mixing (the "checkerboard-type" of (4) and (6)) between cratered terrain and smooth plains. Despite the problems inherent in the color data, some geologically meaningful correlations between surface units and the decorrelated color data suggest that in the Amenthes region, knobby terrain protruding through the plains units may be remnants of ancient cratered terrain extending northward beneath the more youthful smooth plains.

Using higher resolution individual Viking frames, we have identified two spectral types of plateaus in the Amenthes-Aeolis regions. The morphologic characteristics of these plateaus do not differ, but spectrally, one group is similar to the cratered terrain, whereas the other is intermediate between the cratered terrain and smooth plains. Such compositional indications are being used to map the extent of scarp retreat of the CTB, and to infer its former position.

References:
(1) Semeniuk, A. and Frey, H. (1984) Lunar and Planetary Science XV, p. 748-749, LPI, Houston.
(2) Maxwell, T. and Barnett, S. (1984) Lunar and Planetary Science XV, p. 521-522, LPI, Houston.
(3) Soderblom, L. et al. (1978) Icarus, v. 34, p. 446-464.
(4) McCord, T. et al. (1982) JGR, v. 87, p. 10,129-10,148.
(5) Arvidson, R. et al. (1982) JGR, v. 87, 10,149-10,157.
(6) Singer, R. et al. (1984) Lunar and Planetary Science XV, p. 794-795.

TIMING OF ANCIENT EXTENSIONAL TECTONIC FEATURES ON MARS R. Wichman and P.H. Schultz, Dept. of Geological Sciences, Brown University, Providence, RI 02912.

Introduction: Although numerous studies have delineated the Tharsis and post-Tharsis volcanic/tectonic history on Mars (e.g., 1,2,3), only a few attempts (2,4,5) have examined the earlier epochs. This is not an easy task since unambiguous crater ages for pre-Tharsis and early Tharsis units are difficult to determine owing to a variety of active surface processes. Ancient tectonic features, however, have a sufficiently large superposed crater population that should permit relative dating. Tanaka (6) proposed a technique for crater counting along linear features analagous to areal crater density. A modification of this approach has been tested and applied to a variety of ancient tectonic features.

Approach: Tanaka (6) previously reported a method for determining the areal density for narrow elongate or linear areas. This method creates an envelope around the feature for any overlapping crater of radius R. The derived areal density depends on the mean diameter in any given size bin, which is controlled by the bounding diameter and crater production function. Our modification uses a discrete unbinned count where an observed arithmetic mean is calculated without an assumption about crater production. This expression has been successfully tested for arbitrary lines drawn through martian plains units with different crater ages.

Discussion: Figure 1 shows two global projections centered on Tharsis and Hellas. Our primary interest focuses on early and pre-Tharsis tectonic features where crater statistics are more reliable. Four broad tectonic systems are considered: Hellas, Isidis, Argyre, and Tharsis. Within the Hellas system, the older tectonic activity (or at least the earliest cessation of activity) is associated with a concentric system of broad troughs (H2,H3) 1900 km to the west and northwest of the center of Hellas. This system predates most easily identified volcanic constructs in this hemisphere. A significantly younger concentric system occurs farther west from Hellas (2400 km) at about the same distance and time as Tyrrhena Patera. Hesperia Planum was emplaced in the same concentric zone at a significantly later time. The Isidis system is first marked by the development of the Isidis scarp. It is likely that scarp actually dates from the time of basin formation but erosional processes result in a slightly younger crater age. Amenthes Rupes (AR) is part of a system of Isidis-radial scarps and plains-filled troughs dating from the earliest period. The Isidis concentric grabens were formed later: at about the same time as Tyrrhena Patera, all of which appear to be part of a Hellas-radial pattern (5). In the opposite hemisphere, ancient graben systems date from about the same time as the oldest Hellas concentric troughs and the Isidis-radial trough. These features are loosely grouped as part of the Tharsis system but occur more than 90° from Tharsis. Grabens crossing the Elysium knobby terrains apparently began prior to the development of this knobby relief and the fretted margins east of Isidis--a date consistent with the preservation of some of these structures. Mareotis Fossae and the distant troughs north of Argyre are contemporary with the development of the knobby terrains. The generally recognized ancient Tharsis-radial grabens of Alba, Tempe, and Tantalus are younger structures contemporary with the older volcanic patera and Bosporos Rupes, which is part of the Argyre system. Later Tharsis grabens appear to be contemporary with the development of the oldest ridged plains and volcanic shields.

Finer time resolutions are not yet possible. Nevertheless, four groupings of the data on a global scale may be emerging. The earliest epoch is related to the Hellas and Isidis basins with an ancient parallel system in the Elysium region (log N > 700 where N5=cumulative number of craters larger than 5 km per $10^6 km^2$). A second epoch is expressed by basin radial/concentric systems, patera construction in the Hellas hemisphere, earliest Tharsis radial/concentric patterns in the opposite hemisphere, and the development of fretted/knobby terrains of Elysium (log N5 = 350 to 700). This epoch was followed by more extensive radial/subradial grabens in the Tharsis hemisphere and the emplacement of the older ridged volcanic plains (log N5 = 175 to 350). Extensive volcanic shield development and later plains occurred in the next epoch (log N5 = 100-175. Future studies will examine whether or not these are gradational epochs and will attempt to refine/test these preliminary results.

References: (1) Plescia, J.B. and Saunders, R.S. (1982) J. Geophys. Res., 87, p. 9775-9791; (2) Wise, D.U., Golombek, M.P., McGill, G.E. (1979) Icarus, 38, p. 456-472; (3) Carr, M.H. (1981) The Surface of Mars (Yale Univ. Press, New Haven 1981), p. 202; (4) Wise, D.W., Golombek, M.P., McGill, G.E. (1979) J. Geophys. Res, 84, p. 7934-7939; (5) Schultz, P.H. (1984) Lunar and Planet. Sci. XV, p. 728-729; (6) Tanaka, K.L. (1982) NASA TM 85127, p. 123-124.

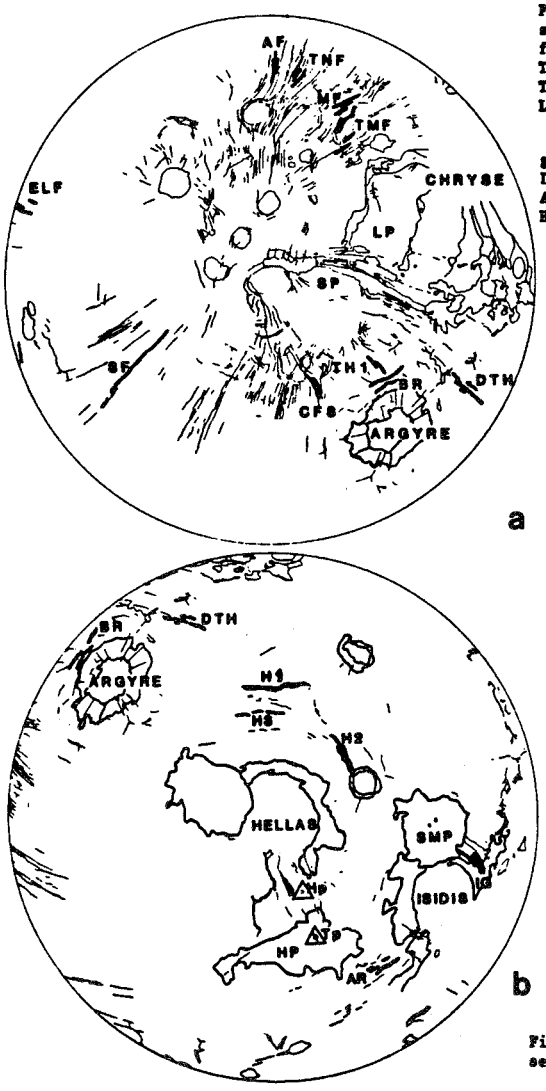

FIGURE 1. Tharsis-centered Lambert projection (Fig. 1a) of tectonic and selected geologic features showing dated fractures systems. ELF=Elysium fractures, AF=Alba Fossae, TNF=Tantalus Fossae, MF=Mareotis Fossae, TMF=Tempe Fossae, DTH=Distant Tharsis Fracture, BR=Bosporos Rupes, TH1=Recent Tharsis fracture, CFS=Claritas Fossae South, SF=Sirenum Fossae, LP=Lunae Planum, SP=Sinai Planum.

Hellas-centered Lambert projection (Fig. 1b) of tectonic and selected geologic features showing dated fracture systems. BR=Bosporos Rupes, DTH=Distant Tharsis Fractures; H1, H2, H3=Hellas concentric systems 1,2,3; AR=Amenthes Rupes, IG=Isidis concentric system. SMP=Syrtis Major Planitia, HP=Hesperia Planum, Tp=Tyrrhena Patera, Hp=Hadriaca Patera.

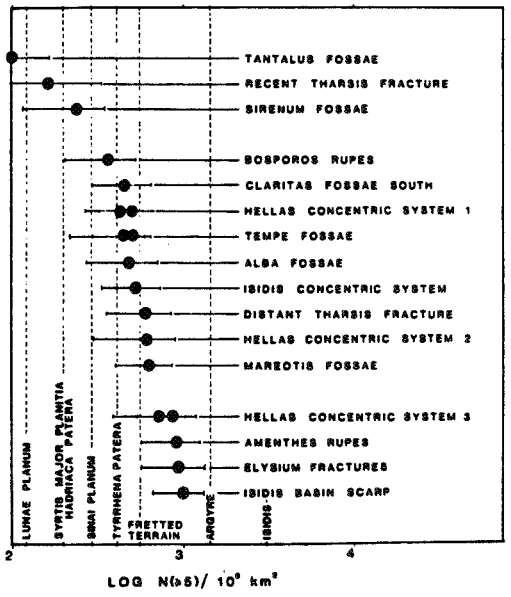

Figure 2. Age plot of dated fracture systems in areal crater density with seven volcanic and impact reference dates.

STRESS HISTORY OF THE THARSIS REGION, MARS

Robert A. Francis, Department of Geology and Geography
University of Massachusetts, Amherst, MA 01003

The Tharsis topographic rise of Mars is roughly 5,000 km wide and 10 km high and is believed to have originated more than 3.5 by ago (Carr, 1984). Within its boundaries lie the four largest volcanoes on the planet. It is also the locus of a series of fracture traces which extend over approximately a hemisphere.

The events that led to the formation of the Tharsis region continue to generate debate. Three geophysical models for the formation of Tharsis are now in general contention and each of these models has been used to predict a characteristic stress-field. These models are: the volcanic construct model (Solomon and Head, 1982; Willemann and Turcotte, 1982), the isostatic compensation model (Sleep and Phillips, 1985; Banerdt et al., 1982), and the lithospheric uplift model (Banerdt et al., 1982). Each of these models has been used by its proponents to predict some of the features observed in the Tharsis region but none accurately accounts for all of the fracture features observed. This is due, in part, to the use of fractures which are too young to be directly related to the origin of Tharsis. To constrain the origin of Tharsis, as opposed to its later history, one should look for the oldest fractures related to Tharsis and compare these to the predictions made by the models.

In this study, the old terrains in and around the Tharsis rise have been mapped from 1:2,000,000 scale photomosaics. This mapping has revealed 175 old fracture features not previously used for stress history studies of Tharsis. These fracture features are scarps, block faulted regions, or grabens. When plotted stereographically, these features reveal systematic orientations with respect to Tharsis, either radial or concentric. These plots show that the tectonic center of the Tharsis region shifted from a very old position at 19° S, 107° W to a younger (but still relatively old) position at 8° S, 104° W. The latter position agrees with the starting position of Plescia and Saunders (1982) who used the young grabens to define a shift from 8° S, 100° W towards the present topographic center of Tharsis.

As a result of this work the Tharsis stress history has been expanded to include (oldest to youngest):

1) A radial system of grabens centered at 19° S, 107° W, oriented as predicted by the isostatic compensation model of Sleep and Phillips (1985).
2) A concentric system of scarps centered at 8° S, 104° W, too far from its center to be associated with the predictions of any present model.
3) A radial system of grabens centered at 8° S, 100° W, originating possibly as a response to volcanic loading such as predicted by Turcotte and Willemann (1982).
4) A radial system of grabens centered near present topographic center of Tharsis, with the same origins as stage 3.

Systems 3 and 4, the dominant grabens of the Tharsis region, have been the subjects of many past studies (Schultz, 1985; Plescia and Saunders, 1982; Wise, Golombek, and McGill, 1979). The features found in this study not only indicate a migration of tectonic activity in the Tharsis region, but the differing fracture patterns also demonstrate changes in the processes responsible for the Tharsis region.

References cited

Banerdt, W. B., R. J. Phillips, N. H. Sleep, and R. S. Saunders, Thick shell tectonics on one-plate planets: Applications to Mars, J. Geophys. Res., 87, 9723-9733, 1982.

Carr, M. H., The Geology of the Terrestrial Planets, NASA SP-469, U. S. Govt. Printing Office, pp 207-263, 1984.

Plescia, J. B., and R. S. Saunders, Tectonic history of the Tharsis region, Mars, J. Geophys. Res., 87, 9775-9792, 1982.

Schultz, R. A., Assessment of global and regional tectonic models for faulting in the ancient terrains of Mars, J. Geophys. Res., 90, 7849-7860, 1985.

Sleep, N. H., and R. J. Phillips, Gravity and lithospheric stress on the terrestrial planets with reference to the Tharsis region of Mars, J. Geophys. Res., 90, 4469-4489, 1985.

Solomon, S. C., and J. W. Head, Evolution of the Tharsis Province of Mars: The importance of Heterogeneous lithospheric thickness and volcanic construction, J. Geophys. Res., 87, 9755-9774, 1982.

Willemann, R. J. and D. L. Turcotte, the role of lithospheric stress in the support of the Tharsis rise, J. Geophys. Res., 87, 9793-9801, 1982.

Wise, D. U., M. P. Golombek, and G. E. McGill, Tharsis province of Mars: Geologic sequence, geometry, and a deformation mechanism, Icarus, 38, 456-472, 1979.

HISTORY AND MORPHOLOGY OF FAULTING IN THE NOCTIS LABYRINTHUS-CLARITAS FOSSAE REGION OF MARS

Kenneth L. Tanaka and Philip A. Davis, U.S. Geological Survey, Flagstaff, AZ

The topographically high areas cut by Noctis Labyrinthus, Noctis Fossae, and Claritas Fossae [1] were subjected to only minor resurfacing during and following local tectonic activity. Principal resurfacing materials consist of lava flows from Syria Planum and Tharsis Montes [2]. Thus, these areas preserve much of the fault record produced by tectonism in this region. Although recent geologic maps of the area have been produced from Viking images [2,3], the only detailed fault histories available until now were described from Mariner 9 images [4,5]. Much of the faulting in the Tharsis tectonic province was centered in Syria Planum [6,7]; therefore, understanding the fault history in this region is critical to understanding the stress history and tectonism of Tharsis as a whole.

Our preliminary mapping of fault patterns in the Noctis Labyrinthus-Claritas Fossae region of Mars reveals several distinct stages and morphologies of faulting. The regional fault history (from oldest to youngest) is as follows:

(1) Broad, mostly east-trending grabens cut into older fractured terrain and basement material [2] of southern Claritas Fossae. The graben-bounding scarps became degraded and were embayed by smooth deposits.

(2) Long, narrow grabens oriented radial to Syria Planum form dense, parallel-to-fanning areas of faults in Noctis Fossae and throughout Claritas Fossae (Fig. 1). Although much of the faulting preceded resurfacing from Syria Planum, some later faults cut low, smooth areas of the Noctis area and flows of the lower member of the Syria Planum Formation [2] south of Syria Planum (south-central part of area in Fig. 1). A few east-trending faults are radial to and lie west of Syria Planum.

(3) Concentric fractures formed mainly north and west of Syria Planum (Fig. 2) and appear more pristine, wider, and deeper than local radial fractures of the previous stage. They are dense at the north and west edges of Syria Planum, and some cut the upper member of the Syria Planum Formation in southwestern Syria Planum.

(4) Collapse pits, pit-crater chains, rilles, and deep grabens characterize the deformation that collectively describes Noctis Labyrinthus (Fig. 3). The orientations of these features are controlled mainly by the preexisting radial and concentric fault systems; additionally, some tangential, WNW- to NNW-trending faults and collapse features were produced. This activity was most significant north and east of Syria Planum, particularly at the west end of Valles Marineris. Sinuous rilles that may have been sites of lava extrusion formed on Syria Planum.

(5) Arcuate, scallop-shaped and linear NNW-trending faults developed along the east side of the Claritas rise and in southern and western Syria Planum, cutting circumferential faults of Syria Planum and the upper member of the Syria Planum Formation; northwest-trending faults in the Noctis area cut across the collapse depressions of the previous stage (Fig. 4).

Although this fault history generally agrees with that of [4,5] on a local basis, their regional syntheses of the fault patterns and their tectonic inferences differ from those presented here. The fault history ascertained above forms the basis upon which we set forth the following style and timing of the tectonic history of the region, given stress-field predictions based on geophysical models [8-10] and the stratigraphic positions of the faults and the materials they cut or underlie [11]:

Early to Middle Noachian Epochs: North-south extension produced east-trending grabens in southern Claritas Fossae; faults scarps were eroded and embayed.
Late Noachian to Late Hesperian Epochs (stage 1): Isostatic uplift centered in Syria Planum produced radial fractures (Fig. 1).
Late Hesperian Epoch (stage 2): Flexural loading of northern Syria Planum caused subsidence and concentric fracturing (Fig. 2).
Late Hesperian Epoch (stage 3): Uplift of the Noctis area north and east of Syria Planum initiated collapse that may have been intensified by subsurface withdrawal of magma and volatiles (Fig. 3).
Early Amazonian Epoch: Lowering of the eastern flank of the Claritas rise produced NNW-trending grabens and normal faults (perhaps related to uplift of the Claritas rise [12]); northwest-trending faults in the Noctis area may be related to this tectonism.

The structures corresponding to these tectonic episodes appear to have, in most cases, distinctive overall morphologies. They differ in shape (e.g., grabens vs. pit-crater chains), spacing (between faults and between graben-bounding faults), vertical throw, fault-scarp slope angle, continuity (lengthy vs. segmented), and so forth. With the aid of photoclinometry to measure the vertical dimension, we intend to quantify such parameters so that the relation of fault style and morphology to tectonic and resurfacing history can be further analyzed.

REFERENCES CITED

[1] Wu, S.S.C. and others (1986) NASA Tech. Mem. 88383, p. 614-617.
[2] Scott, D.H. and Tanaka, K.L. (in press) USGS Misc. Inv. Ser. Map I-1802A.
[3] Scott, D.H. and Tanaka, K.L. (1981) USGS Misc. Inv. Ser. Map I-1277.
[4] Masursky, H. and others (1978) USGS Misc. Inv. Ser. Map I-896.
[5] Masson, P. (1980) Moon Planets, v. 122, p. 211-219.
[6] Wise, D.V. and others (1979) Icarus, v. 38, p. 456-472.
[7] Plescia, J.B. and Saunders, R.S. (1982) JGR, v. 87, p. 9775-9791.
[8] Banerdt, W.B. and others (1982) JGR, v. 87, p. 9723-9733.
[9] Solomon, S.C. and Head, J.W. (1982) JGR, v. 87, p. 9755-9774.
[10] Comer, R.P. and others (1985) Rev. Geophys., v. 23, p. 61-92.
[11] Tanaka, K.L. (in press) JGR, Proc. Lunar Planet. Sci. Conf. 17th.
[12] Plescia, J.B. and others (1980) NASA Tech. Mem. 81776, p. 68-70.

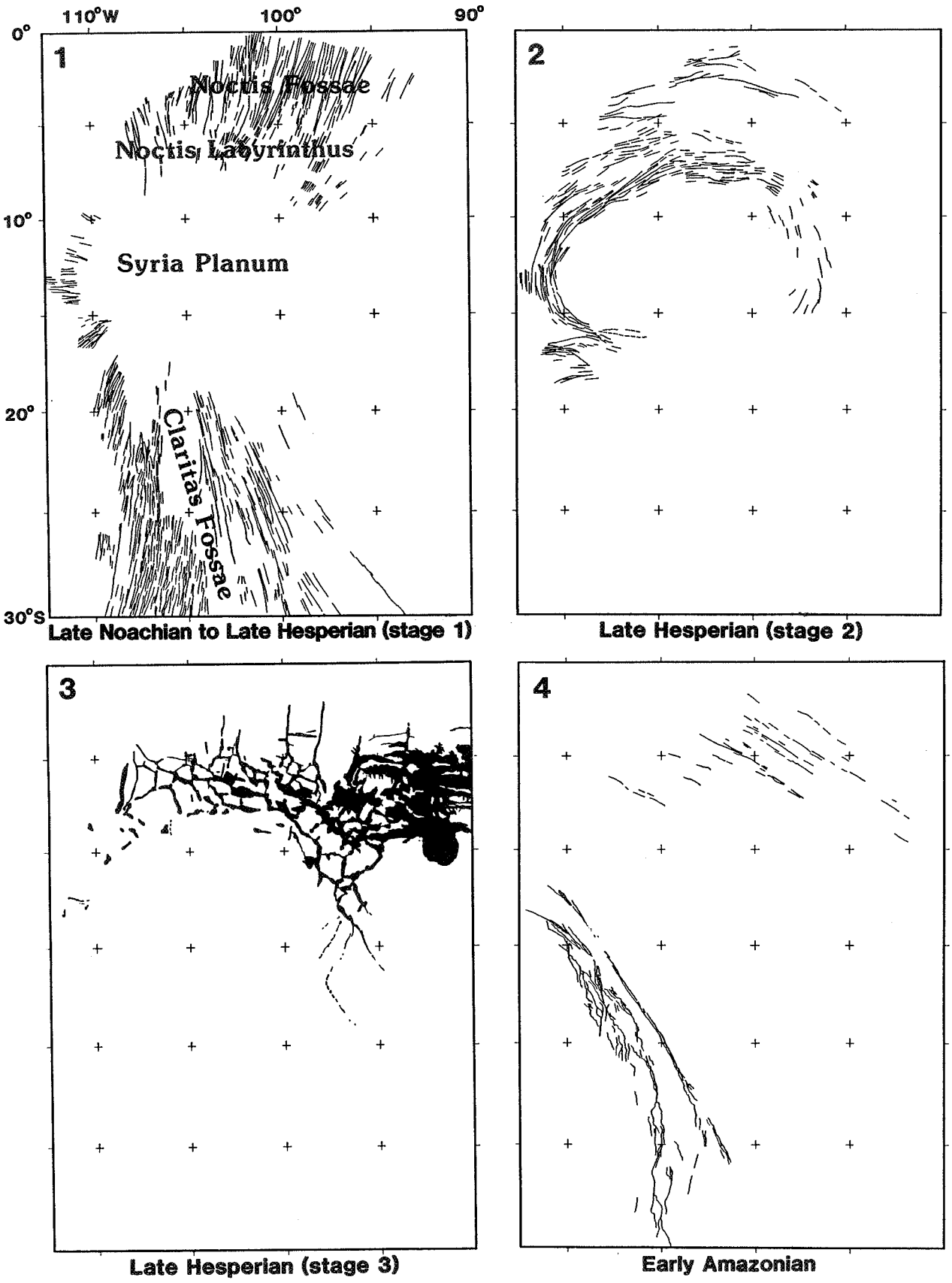

Figs. 1-4. Progressive structural development of the Noctis Labyrinthus-Claritas Fossae region of Mars.

THIN AND THICK-SKINNED DEFORMATION IN THE THARSIS REGION OF MARS.

Thomas R. Watters, National Air and Space Museum, Smithsonian Institution, Washington, D.C. 20560

The ridge system of the Tharsis Plateau is a dominant structural form only equaled by the radial fracture system. The structural interpretation of the ridges are: 1) folds formed by regional or local compressional stress [Watters and Maxwell, 1983; Watters and Maxwell, 1985a]; 2) the surface manifestation of reverse or thrust faults [Plescia and Golombek, 1986]; or 3) folds with thrust faulting developing as a result of fold geometry [Watters and Maxwell, 1985b]. Watters and Maxwell [1986] suggest that the compressional events that generated the ridges occurred after the emplacement of the ridged plains volcanic units, but before the episode of faulting that generated the majority of the observed ridge-fault crosscutting relationships on the ridged plains [Watters and Maxwell, 1983] and that it did not continue beyond the emplacement of the Syria Planum Formation or the basal units of the Tharsis Montes Formation.

Models for the origin of the regional stresses involving a combination of isostatic uplift and flexural loading have been proposed by Banerdt et al. [1982] and Sleep and Phillips [1985]. One important aspect of these models is that the stresses are calculated for the surface of a spherical lithosphere. This requires that stress be transmitted through the lithosphere to the free surface. If the Tharsis ridges are the result of compressional stress from isostatic uplift then they are the result of full lithospheric compression involving deformation of the basement as well as surface units.

Compressional deformation of terrestrial oceanic lithosphere has been observed in the interior of the Indo-Australian plate. Topographic undulations observed seismically and with Seasat altimeter profiles have been interpreted as lithospheric folds, resulting from horizontal compression associated with continental collision. These features have an average or dominant wavelength of 200 km and amplitudes that approach 3 km. The thickness of the lithosphere in the region of the folds is estimated to be 40-50 km [McAdoo and Sandwell, 1985]. The ratio of the dominant wavelength to the deformed plate thickness (L_d/T) for these lithospheric folds is about 4. The L_d/T of the lithospheric folds are within the range of L_d/T of folds in sedimentary rocks reported by Currie et al. [1962] and the open folds of the Appalachians of Pennsylvania. The wavelength to thickness ratio for these folds range from > 2 to < 40 (indicated on figure 1).

The significance of the L_d/T ratio in characterizing folds is found in plate bending theory, and the relationship of ratio to the bending moment is largely a function of the rheology. The solution to the differential equation for the buckling of a plate resting on a weaker substrate is a sinusoidal deflection curve, and thus, the plate buckles in the shape of a sine wave. However, this need not be the form of the final structure. Deformation may begin with the development of low amplitude deflections where the anticlines serve as sites of 1) localized deformation resulting from cataclastic flow; or 2) fault nucleation and

gross fracturing (i.e. thrust faults). These mechanisms will result in non-sinusoidally shaped, but regularly spaced structures.

The relationship of L_d/T can be used to estimate the wavelength of deformation for a known plate thickness or the plate thickness for an observed wavelength. The lithospheric thickness on Mars has been estimated to be between 100 to 400 km [see Banerdt et al., 1982]. Assuming a lithospheric thickness of 100 km, a L_d/T of 4, and solving for L_d:

$$L_d = 4T \qquad (1)$$

lithospheric folds in the Tharsis region would have a dominant wavelength of 400 km. Roth et al. [1980], using radar altimetry data, generated a three-dimensional reconstruction of the topography covering a portion of the Coprates region (figure 2). This topography indicates the presence of three parallel N-S trending undulations in SE Coprates spaced at roughly 400 km with amplitudes approaching 3 km. These features may be analogous to the topographic undulations observed in the interior of the Indo-Australian plate. If the long wavelength, low amplitude features in Coprates are interpreted to be lithospheric folds, then applying equation (1), the thickness of the deformed lithosphere is on the order of 100 km. These long wavelength ridges may be the result of full lithospheric compression resulting from the lithospheric stresses predicted in the models by Banerdt et al. [1982] and Sleep and Phillips [1985].

The wavelength predicted by equation (1) can also be compared with measured spacings of compressional ridges on volcanic plains units. Regularly spaced ridges in SW Coprates are generally NE trending with an average spacing of approximately 60 km. Compressional features with spacings of 60 km would involve a deformed layer with a thickness of approximately 15 km. This suggests that the plains ridges in SW Coprates are the result of thin-skinned deformation of the upper 15 km of the crust. Thus, it appears that there are two distinct levels of compressional deformation in the Tharsis region.

References

Banerdt, W.B., R.J. Phillips, N.H. Sleep, and R.S. Saunders, J. Geophys. Res. 87, 9723-9733, 1982.

Currie, J.B., H.W. Patnode and R.P. Trump, Geol. Soc. Amer. Bull. 73, 655-674, 1962.

McAdoo, D.C. and D.R. Sandwell, J. Geophys. Res. 90, 8563-8569, 1985.

Plescia, J.B. and M.P. Golombek, Geol. Soc. Amer. Bull. 90, 1289-1299, 1986.

Roth, L.E., G.S. Downs, R.S. Saunders, and G. Schubert, Icarus 41, 287-316, 1980.

Sleep, N.H. and R.J. Phillips, J. Geophys. Res. 90, 4469-4489, 1985.

Watters, T.R. and T.A. Maxwell, Icarus 56, 278-298, 1983.

Watters, T.R. and T.A. Maxwell, Lunar and Planet. Sci. XVI, 897-898, 1985a.

Watters, T.R. and T.A. Maxwell, Reports of Planetary Geology Program, 1984, NASA Tech. Mem. 87563, 479-481, 1985b.

Watters, T.R. and T.A. Maxwell, J. Geophys. Res. 91, 8113-8125, 1986.

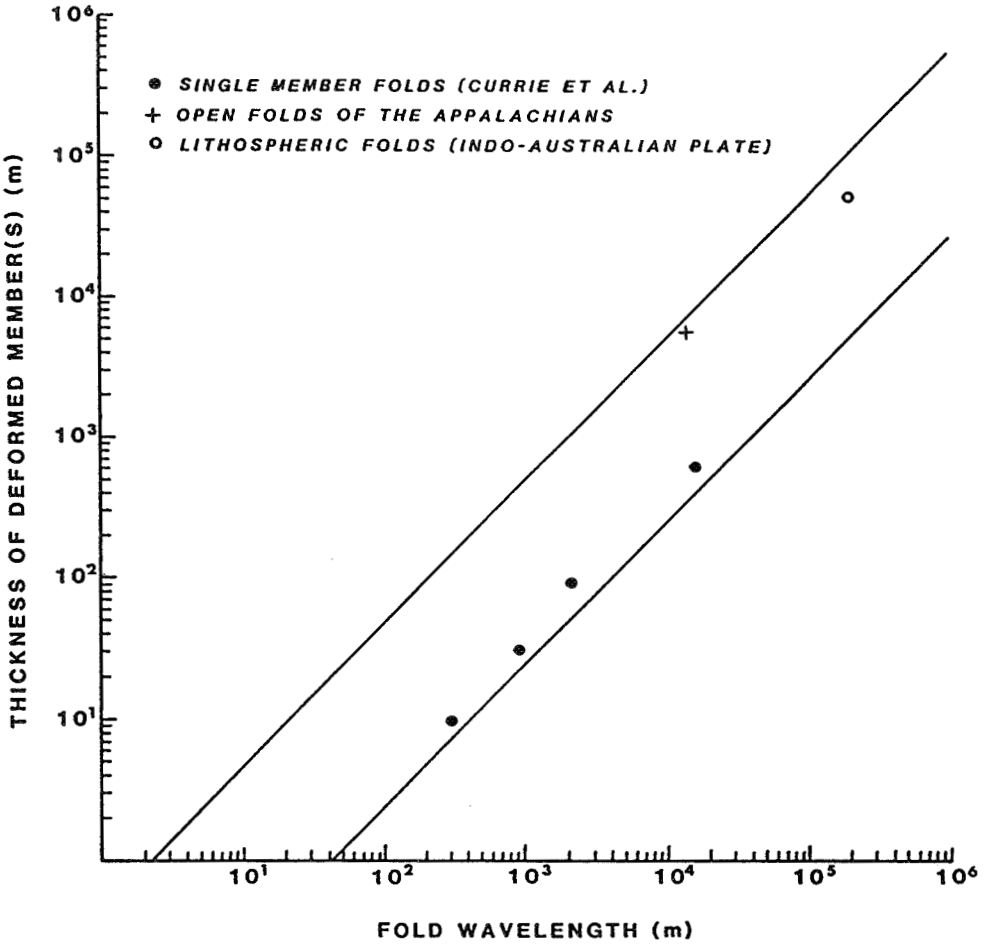

FIGURE 1.

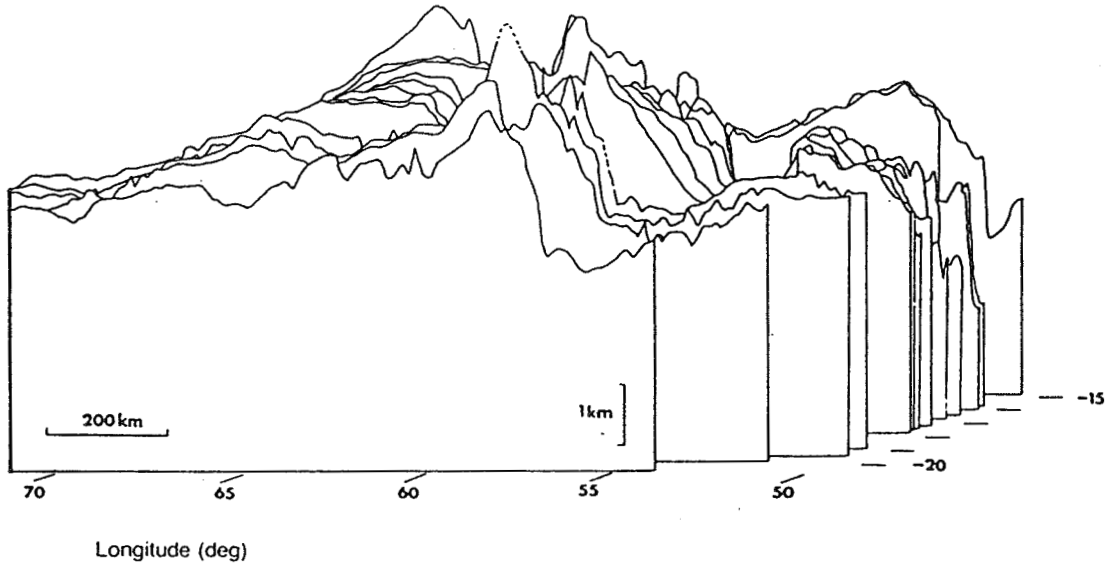

FIGURE 2.

FLEXURALLY-RESISTED UPLIFT OF THE THARSIS PROVINCE, MARS

R.J. Phillips, Dept. of Geological Sciences, SMU, Dallas, TX 75275, and
N.H. Sleep, Dept. of Geology and Geophysics, Stanford University, Stanford, CA 94305

The tectonic style of Mars is dominated by vertical motion, perhaps more than any of the terrestrial planets. The imprint of this tectonic activity has left a surface widely faulted even though younger volcanism has masked the expression of tectonism in many places. Geological activity associated with the Tharsis and, to a lesser extent, Elysium provinces is responsible for a significant portion of this faulting [*Banerdt et al.*, 1982; *Willemann and Turcotte*, 1982; *Sleep and Phillips*, 1985; *Hall et al.*, 1986] while the origins of the remaining features are enigmatic in many cases. The origin and evolution of the Tharsis and Elysium provinces, in terms of their great elevation, volcanic activity, and tectonic style, has sparked intense debate over the last fifteen years in the planetary geosciences community. Central to these discussions are the relative roles of structural uplift and volcanic construction in the creation of immense topographic relief. For example, *Phillips et al.* [1973] and *Plescia and Saunders* [1980] have argued that the presence of very old and cratered terrain high on the Tharsis rise, in the vicinity of Claritas Fossae, points to structural uplift of an ancient crust. *Solomon and Head* [1982] have pointed out, however, that there is no reason that this terrain could not be of volcanic origin and thus part of the constructional mechanism.

Uplift of Tharsis, if it occurred, could have taken place by some combination of buoyancy forces associated with lateral mass loss and with intrusion into the crust. By the term "flexurally-resisted uplift" (or simply "flexural uplift") we mean that flexural strains that occurred in the elastic lithosphere during uplift could not be accommodated and flexural faulting resulted. Mechanical models for Tharsis that involve flexural stresses in the lithosphere resulting from uplift have been rejected by *Solomon and Head* [1982], *Willeman and Turcotte* [1982] and *Banerdt et al.* [1982] on the basis that the tectonic pattern from the resulting stress pattern is not observed. Conversely, *Hall et al.* [1986] find tectonic evidence for flexural uplift stresses in the Elysium Province and speculate that the same process must have occurred for Tharsis but that the scale was very small or the evidence has been obliterated by subsequent volcanism and faulting.

Flexural uplift would plausibly have been an early phase in the evolution of Tharsis. Tectonic evidence, if it exists, might be found in the oldest geological units in the region, namely those associated with Claritas Fossae. Flexural uplift would produce circumferential faults or graben in the vicinity of Claritas Fossae that would lie along small circles centered on Tharsis. Examination of images and derived geological maps [e.g., *Masursky et al.* [1978] of this region reveals a distribution of extensional structures that can be classed as "circumferential." These features are confined to the two oldest units in the region: "cratered plateau material" and "old fractured plains material." The first of these

units is the oldest of the two, and the graben show relatively more extension in this unit. It is clear that Claritas Fossae, which was first cited as evidence for structural uplift of Tharsis because of its age and elevation [*Phillips et al.*, 1973], also shows clear tectonic evidence for uplift. Thus we conclude that flexurally-resisted uplift could have played an important role in the early history of Tharsis.

Flexurally uplift can be incorporated into a model for the evolution of Tharsis. From earlier studies [*Banerdt et al.*, 1982; *Sleep and Phillips*, 1979; 1985] we have concluded that Tharsis was in an isostatic state over much of its history. The view is adopted that flexural *loading* of Tharsis occurred relatively late in its history. We wish to describe a model that in its present state is consistent with the present-day topography and gravity fields, but one that follows from an isostatic configuration for which we do not know specifically the boundary conditions that were operative at the time. *Sleep and Phillips* [1985] examined two specific models for Tharsis. In simple terms, for reasonable depths of compensation there is no two-element isostatic model that will satisfy both the gravity and topography data [*Phillips and Saunders*, 1975]. What we will call Model I of *Sleep and Phillips* [1985] circumvents this problem by adding a second load besides topography, positive relief on the crust/mantle boundary. Both loads are compensated by Pratt density variations in the upper mantle; this is the model first described by *Sleep and Phillips* [1979]. Model II satisfies the boundary conditions by being superisostatic. This is essentially the model of *Phillips and Saunders* [1975] with partial compensation at the crust/mantle boundary, except that the excess load is supported flexurally.

Model II comes closest to describing our preferred model in its present geological state, and it can be described in terms of evolution from an earlier isostatic condition. Some 20 km of excess crustal thickness beneath Tharsis in this model [*Sleep and Phillips*, 1985, Fig. 10] can be interpreted in terms of crustal thickening by the magmatic products of partial melting. This could in fact be a dominant mechanism for crustal uplift, as described in the model of *McKenzie* [1984]. An evolutionary sequence is as follows: (1) Partial melting of a mantle source region gives rise to crustal intrusion and underplating because of the nature of early melts (denser than upper crust, less dense than mantle). (2) This leads to buoyant uplift of the crust. The overlying elastic lithosphere flexurally resists the uplift and tectonically fails. (3) Further uplift is supported isostatically as is extrusive volcanism, which commences as the partial melt products evolve to a lower density and reach the surface. Continued growth of Tharsis leads to faulting associated with isostatic stresses. Early extrusive volcanism is pyroclastic, which leads to further uplift. (4) As intrusions cool, a combination of membrane stress support and a thickening lithosphere eventually lead to flexural loads and the creation of the radial fractures on the periphery of Tharsis.

Further testing of this model will include considerations of the thermal evolution of Tharsis.

REFERENCES

Banerdt, W. B., R. J. Phillips, N. H. Sleep, and R. S. Saunders, Thick shell tectonics on one-plate planets: Applications to Mars, *J. Geophys. Res, 87*, 9723-9733, 1982.

Hall, J. L., S. C. Solomon, and J. W. Head, Elysium region, Mars: Tests of lithospheric loading models for the formation of tectonic features, *J. Geophys. Res., 91*, 11377-11392, 1986.

Masursky, H., A. L. Dial, Jr., and M. H. Strobell, Geologic map of the Phoenicis Lacus Quadrangle of Mars, U.S. Geol. Survey, Atlas of Mars 1:5,000,000 Geol. Series, Map I-896 MC-17, 1978.

McKenzie, D., A possible mechanism for epeirogenic uplift, *Nature; 307*, 616-618, 1984.

Phillips, R. J., and R. S. Saunders, The isostatic state of Martian topography, *J. Geophys. Res., 80*, 2893-2898, 1975.

Phillips, R. J., R. S. Saunders, and J. E. Conel, Mars: Crustal structure inferred from Bouguer gravity anomalies, *J. Geophys. Res., 78*, 4815-4820, 1973.

Plescia, J. B., and R. S. Saunders, Estimation of the thickness of the Tharsis lava flows and implications for the nature of the topography of the Tharsis plateau, *Proc. Lunar Planet. Sci. Conf. 11th*, 2423-2436, 1980.

Sleep, N. H., and R. J. Phillips, An isostatic model for the Tharsis province, Mars, *Geophys. Res. Lett., 6*, 803-806, 1979.

Sleep, N. H., and R. J. Phillips, Gravity and lithospheric stress on the terrestrial planets with reference to the Tharsis region of Mars, *J. Geophys. Res., 90*, 4469-4489, 1985.

Solomon, S. C., and J. W. Head, Evolution of the Tharsis province of Mars: The importance of heterogeneous lithospheric thickness and volcanic construction, *J. Geophys. Res., 87*, 9755-9774, 1982.

Willemann, R. J., and D. L. Turcotte, The role of lithospheric stress in the support of the Tharsis rise, *J. Geophys. Res., 87*, 9793-9801, 1982.

TECTONIC DOMAINS IN THE EASTERN HEMISPHERE OF MARS

Ted A. Maxwell and C. E. Leff, Center for Earth and Planetary Studies, National Air and Space Museum, Smithsonian Institution, Washington, D. C. 20560

The definition of boundaries of discrete structural provinces on the surface of Mars has previously been made by the assumptions of circular or radial symmetry (in the case of the Tharsis plateau), by artificial quadrangle boundaries for regional studies, or simply by regional geographical features. Much of the planetary structural mapping has been presented in a line or spot format in existing consortium data. We are presently generating methods to convert the detailed maps of tectonic features to a format that can be used with standard image processing techniques. In this manner such data can be more readily compared to age and other attributes deduced from geologic mapping, gravity results, and topography. The 24 photomosaics covering the eastern hemisphere of Mars have already been examined for four types of structural features: erosional remnants, ridges, graben, and scarps. When digitized, each feature was flagged according to feature type, azimuth and length. These values were stored as text files on a quad-by-quad basis for each quad studied.

To exploit the speed and flexibility of image processing techniques and to remove artifical limits imposed by quadrangle boundaries, we have now reorganized the data by feature type rather than by quad, and converted the data from text to image format. For instance, ridge data for each quad were combined into one dataset,and were then grouped according to 1/4° bins to be compatible with the Mars Consortium format. The number of data points in the bin, the vector mean azimuth and the vector mean length were calculated for each 1/4° bins. When coded as gray tones according to their magnitude and written as image files, these calculated values provided three channels of image data for each type of structural feature. Now in a form analogous to the BGR triplet of conventional imaging data, the tectonic data can be manipulated and compared with other available data.

The development of this method for treating structural features was prompted by the need to sort these data by topography and geologic map unit in the eastern hemisphere. Our initial studies of this re-formatted data looked for the distribution of azimuths for each feature and the relationships to topography, geology and age. Graben (n=807) revealed a strong azimuthal trend of 0°-40° and 120°-130°, but only at lower elevations north of the CTB. Similarly, erosional remnants (n=522) showed less-defined azimuthal concentrations, but also occurred only at low elevations. These directional and topographic preferences became clear only in combination with additional geological data.

One ultimate goal of using this technique is the ability to use the vast array of image processing statistics on encoded versions of the tectonic features. For example, a principal components analysis on two

images of ridge and graben azimuths would immediately indicate the degree of correlation between the two features, and displaying the first principal component image would provide a view of the geographic region with the highest degree of correlation. However, in our initial attempts at such analyses, we ran into the problem of aliasing in that each 1/4° geographic bin may not contain features (especially in 1/4° format), and the statistics were highly skewed towards 0-values.

To address this problem, the data were re-sampled into 1° bins, so that the coarser resolution would show longer wavelength trends, and would also facilitate statistical comparison of tectonic features by increasing the fraction of the image array actually containing data. The large geographical extent of the data set should help to separate Tharsis tectonic controls from more localized controls of eastern hemisphere tectonic regimes. Preliminary results indicate that the orientation of compressional features is particularly sensitive to topography in the eastern hemisphere, where trends north of the boundary at low elevations are consistent with Tharsis-related compressional stress, whereas those at high elevations suggest a NW-SE global-scale fabric. In contrast, the orientations of grabens are not related to topographic setting; NW trends to dominate in both the ancient cratered terrain and in the smooth plains, and are probably due to later periods of extension as well as retreat of the CTB scarp. Both geographic setting and orientation of graben correlate more closely with the orientation of graben than with other features. Consequently we believe that this technique is well suited to regional tectonic problems on Mars, and will aid in distinguishing domains not geographically constrained by artificial boundaries.

AGE OF FRACTURING AND MESA DEVELOPMENT IN THE ELYSIUM AREA, NORTHERN MARTIAN PLAINS

George E. McGill, Center for Earth and Planetary Studies, National Air and Space Museum, Smithsonian Institution, Washington, DC 20560 (on leave, University of Massachusetts, Amherst 01003)

One of the fundamental questions of martian crustal history is the origin of the crustal dichotomy between northern plains and southern highlands (cf. Wise et al., 1979; Wilhelms and Squyres, 1984). Hypotheses for the origin of this dichotomy may be constrained by global-scale, geophysical considerations, or by detailed geological studies of the genesis and relative ages of materials and landforms in the northern plains of Mars and along the boundary between the plains and the highlands. This abstract summarizes progress on one aspect of a long-range geological study intended to constrain hypotheses for the dichotomy by tracing the history of the northern plains from the most recent events backward -- essentially the same approach used to understand old events in Earth history.

Both the giant impact and the mantle convection models for the crustal dichotomy imply a major coeval fracturing event. As has been known for some time (Scott, 1978; Hiller and Neukum, 1978; Maxwell et al., 1984), the present dichotomy boundary lies well south of its original position, at least in some places. Nevertheless, there is severe fracturing of this present dichotomy boundary in many places. The specific objectives of this portion of the study are to determine the age(s) of fracturing along the present dichotomy boundary, and to determine when the abundant knobs and mesas scattered over much of the northern plains were formed or emplaced.

The work summarized here includes detailed mapping of portions of Elysium Mons and adjacent plains using 1:500,000 USGS MTM quadrangles, and crater dating of materials, surfaces, and fracturing events. For the crater dating, the production curve of Neukum (1983) has been used in order to state all ages in terms of cumulative number of craters greater than 1 km in diameter per million square kilometers. Neukum's 1983 curve fits the crater plots better than his earlier curve (Neukum and Hiller, 1981), and produces ages for older surfaces more in line with those reported by other workers.

Careful mapping of the northern boundary region between Elysium Mons and adjacent plains indicates that there is no consistently mappable contact between the lava flows of Elysium Mons and the plateau material faulted into the spectacular fretted terrain along its north edge, nor between this plateau material and the material capping the mesas immediately to the north of the fretted terrain. Furthermore, no consistently mappable contact can be defined between plateau and mesa caprock and the materials within the troughs of the fretted terrain. The youngest Elysium lavas occur as clearly defined lobate flows, two or three of which are obviously cut by faults of the fretted terrain. These relationships imply that the plateau and mesa caprocks are lavas related to Elysium Mons volcanism, and that the faulting responsible for the fretted terrain is younger than these flows. A crater count on

the northern flank of Elysium Mons, immediately upslope from the fretted terrain, yields a 1-km crater age of 3,800. This is a composite age, because it is obvious that the flows on the flank of Elysium Mons are not all the same age. Because the youngest, lobate flows cover only a small part of the counting area, and because they are too thin to obliterate the craters used to date the surface (>1.5 km in diameter), the crater age obtained is a good estimate of the age of the older and smoother surface beneath the young flow lobes; it is this surface that is apparently continuous with the fretted plateau surface and the caprock of the mesas to the north. Clearly, the faulting responsible for the formation of the fretted terrain must be younger than this surface, and thus must be younger than crater age 3,800. Because some of the youngest flow lobes are cut by faults, this faulting could be significantly younger than 3,800.

North of the fretted terrain is a complex plains surface with at least three mappable material units intimately interspersed, and with numerous mesas scattered about. A small proportion of the plains consists of a smooth-surfaced material that occupies topographic lows and that appears much younger than the other types of plains materials. The other plains materials appear to be the same age, and the crater age for these is 2,900.

The scattered mesas on the northern plains were in place as discrete, isolated landforms before the intervening plains units formed. Wherever the relationships are resolvable on the images, the mesas are older than the craters used to define the 2,900 age: ejecta rest on top of mesas, and mesas interfere with the flow of ejecta from splosh craters. In the east-central part of the MTM 35212 1:500,000 quadrangle are curious, winding ridges that lie in shallow, broad depressions between what appear to be simple flood flows. Here, the mesas are concentrated in these depressions, commonly occuring in sinuous lines connected by ridges. Commonly, the winding ridges appear to pass beneath mesas, but locally they clearly cut them. In places, winding ridges can be seen to change along trend into open fractures, and these clearly cut mesas. The age implications are that the mesas are older than both the winding ridges and the flood lavas that are the local surface unit of the plains. It seems likely that the depressions between the young flood flows represent topographically high, unflooded places on the underlying surface. These highs may well represent the residual elevations left from the erosion of the older plateau surface now represented only by the surviving mesas. This peculiar topography suggests that the original "plateau" may not have been continuous, but may instead have consisted of discrete lobes with low areas between them.

Two interesting results are emerging from this study:

1) The plateau in the Elysium area that now survives as fretted terrain and isolated mesas was genetically linked to volcanism from the Elysium Mons area. This plateau was faulted and eroded into fretted terrain and isolated mesas during a very short time interval following its formation (later than crater age 3,800 and before crater age 2,900).

2) Most of the isolated topographic features projecting through the plains north of Elysium Mons (and apparently elsewehere in the northern plains as well) are better described as knobs than as mesas. In places, these knobs can be shown to represent remnants of ancient highland crust (McCauley et al., 1972; Carr et al., 1973; McGill, 1986); thus they are clearly different from mesas, and they need not be due to the major erosional event between crater ages 3,800 and 2,900 that appears responsible for the development of mesas. This in addition to evidence cited above for a lobate rather than continuous original distribution of the "plateau" precursor to the mesas indicates that the volume of material removed from the northern plains during erosion between crater ages 3,800 and 2,900 may be more manageable than once feared; in fact, most of it may not have been removed at all, but may lie beneath the young lava flows now covering the plains surface between the mesas. It should be noted that these results stem primarily from work in the Elysium area; their validity for other parts of the northern plains remains to be demonstrated. Finally, the possible elimination of the "volume problem" for late erosion in the northern plains area does not solve the even greater volume problem inherent in the low elevation of the northern third of Mars.

References

Carr, M.H. et al., Jour. Geophys. Res., 78, 4031-4036, 1973.
Hiller, K., and Neukum, G., NASA Tech. Mem. 79729, 91-93, 1978.
Maxwell, T.A. et al., Geol. Soc. America, Abs. with Prog., 16, 586, 1984.
McCauley, J.F. et al., Icarus, 17, 289-327, 1972.
McGill, G.E., Geophys. Res. Letts., 13, 705-708, 1986.
Neukum, G., Habilitationsschrift, 1983.
Neukum, G., and Hiller, K., Jour. Geophys. Res., 86, 3097-3121, 1981.
Scott, D.H., Icarus, 34, 479-485, 1978.
Wilhelms, D.E., and Squyres, S.W., Nature, 309, 138-140, 1984.
Wise, D.U. et al., Icarus, 38, 456-472, 1979.

GEOMETRY AND RELATIVE AGE OF LARGE PATTERNED FRACTURES IN SOUTHERN ACIDALIA PLANITIA, MARS

Murray C. Borrello, Department of Geology and Geography
University of Massachusetts, Amherst, MA 01003

Extraordinary patterned fractures occur in Elysium, Utopia and Acidalia Planitiae of Mars. Theories as to their origin range from permafrost patterning to tectonic fracturing (reviewed by Pechmann, 1980). Recent studies indicate the patterned fractures may be a surface reflection of rough, buried terrane in which fracturing occurs as a result of differential compaction (McGill, 1986).

The patterned terrane in the southern portion of the Acidalia region (MC4-SE, MC4-SC) is being studied to determine its age relative to other terranes and events, and to constrain models for the origin of the fractures. Fracturing in this area occurs between 5 and 25 degrees west longitude and 37 and 50 degrees north latitude. Many fracture patterns are roughly polygonal, with polygons ranging in size from approximately 11 to 32 kilometers in diameter. Fracture traces range from the limit of resolution (10's of meters) to 35 kilometers in length.

Two types of fracture patterns occur in the Acidalia region: straight-sided and circular.

Straight-sided fracture patterns occur near 12 degrees west longitude, 41 degrees north latitude and are extremely well exposed (Fig. 1). These features are roughly polygonal, and the fractures are graben-like in appearance. Curved-sided and circular fracture patterns occur near 17 degrees west longitude, 45 degrees north latitude and appear more subdued due to a thin cover of younger material (Fig. 2).

The area included in MC4-SE subquadrangle contains six distinct geomorphic and structural domains:

Domain 1 is distinct because of its curved to circular fractures and abundance of younger cover material. Also prevalent are features interpreted as volcanic landforms. These include flat-topped hills, domes, flows and cinder cones (Allen, 1979; Greeley and Spudis 1981; Scott 1982; Frey and Jarosewich, 1982). These volcanic landforms appear to be superposed on the fractures and in some cases lie over fracture traces undisturbed indicating they are younger.

Domain 2 exhibits well-developed, straight-sided, roughly polygonal fracturing. There is partial burial of the fractures near the center of the area, probably by ejecta from a nearby impact centered at 15 degrees west longitude, 42 degrees north latitude. Cinder cones are present and appear to be superposed on fracture traces.

The boundary between domains 1 and 2 is marked by a fairly abrupt change in the degree of exposure of the fractures. Domain 1 has subdued to completely buried fractures, while domain 2 has little to no cover over the fractures.

South of domains 1 and 2 is modified southern highland terrane (domain 6) which grades northward into a dissected, hummocky terrane (domain 5). This terrane appears in many erosional states from large blocks (44 km by 30 km) to small knobs and ridges. These knobs and ridges appear superposed on and unaffected by the fractures in domain 2 and are, therefore, interpreted as younger.

Domains 3 and 4 exhibit most of the main features discussed except the features mentioned are partially to completely buried.

On a broad scale, then, what is seen are progressively younger terranes northward from the modified southern highlands to the buried circular fractures. The window of fractured terrane in domain 2 provides evidence of structural activity in older terrane below the northern cover material and, therefore, gives clues to the origin of the fracture patterns themselves. It is important to keep in mind that although the circular fractures in domain 1 are covered by relatively younger plains materials, there is no evidence to indicate the fractures were active after the deposition of this younger material.

The fractures making up the patterned terrane appear to be among the oldest features in the Acidalia region. An age sequence has been constructed based on cross-cutting relationships and superposition:

Youngest	Volcanism; cinder cones and other volcanic landforms
	Dissection of hummocky terrane
	Deposition of hummocky terrane material
	Patterned fracturing in fracture terrane
	Deposition of fractured terrane material
	Modification of southern highland material
Oldest	Deposition of southern highland terrane

REFERENCES

1. Allen, C.C. (1979) J. Geophys. Res., 84, 8040-8059.
2. Frey, H. and Jarosewich (1982) J. Geophys. Res., 87, 9867-9879.
3. Greeley, R. and P. Spudis (1981) Rev. Geophys. and Space Phys., 19, 13-41.
4. McGill, G.E. (1986) Geophys. Res. Letters, 13, 705-708.
5. Pechmann, J.C. (1980) Icarus, 42, 185-210.
6. Scott, D.H. (1982) J. Geophys. Res., 87, 9837-9852.

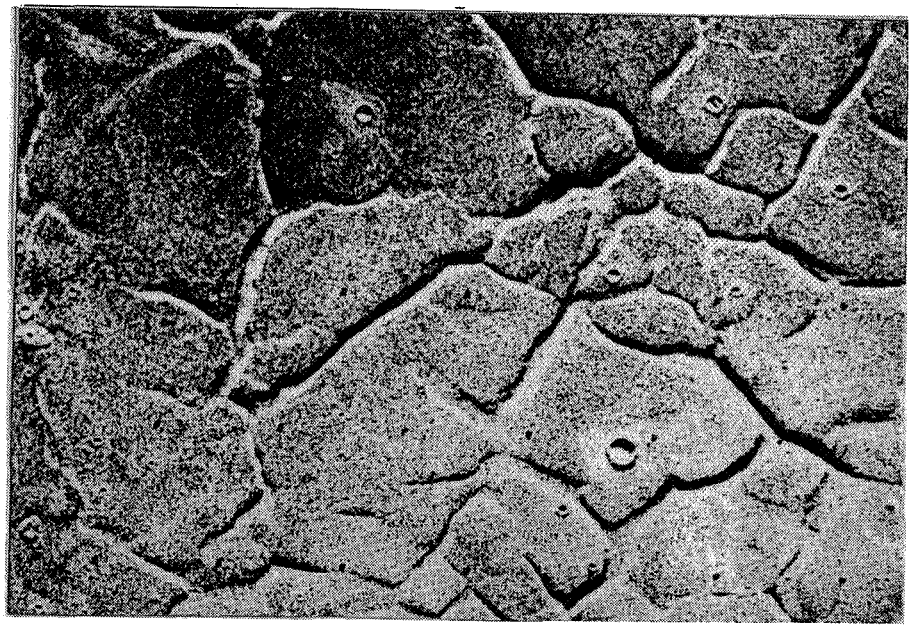

Figure 1. Well-exposed, roughly polygonal straight-sided fractures. Picture width is approximately 40 km.

Figure 2. Circular fracture patterns. Note the subdued nature of these fractures in comparison with those in Figure 1. Picture width is approximately 55 km.

ORIGIN OF FRACTURES, MARTIAN POLYGONAL TERRAIN

L. Scott Hills, Department of Geology and Geography
University of Massachusetts, Amherst, MA 01003

It has been proposed that the origin of the polygonally fractured terrain on Mars is due to stress caused by differential settlement of material deposited over an irregular base topography (McGill, 1986). The eventual goal of this study is to evaluate this proposal by construction of mathematical models for this process. These models will attempt to determine what combinations of base topography, covering material composition and depositional rate would cause the fractures observed. Because fracture formation would largely be a function of generated stress, the first step in modeling is calculation of stresses created during settlement.

A preliminary 2-dimensional model was constructed using as a base topography the cross-section of a crater 5 km in diameter and 900 meters deep (Pike, 1980). This size crater was chosen since average fracture spacings are reported at 4-5 km. The cover material selected was a fine-grained clastic. Possible source areas in the region surrounding the polygonal terrain support a choice of water saturated sediment or pyroclastics as the covering material. The Terzaghi theory for one-dimensional consolidation of saturated clay (Terzaghi, 1925) is a conventional method for treatment of the magnitude of settlement under applied loads. An average clay was chosen with material properties: density of 2.6 gm/cc, liquid limit of 80%, and initial void ratio of 0.5 (Rieke & Chilingarian, 1974). To evaluate stress induced during the settlement process an elastic beam bending model was used (Gere & Timoshenko, 1984; Turcotte & Schubert, 1982). A Poisson's ratio of 0.4 was used along with a range of values for the elastic modulus.

To evaluate consolidation and bending, as they occur together, the cover material was modeled in two parts. The lower part is the fill material, extending from the underlying topography up to the level of topographic highs. The upper part is the layer material extending from the fill material to the ground surface. A force balance is considered to have occurred during the depositional process. After deposition of the lower, fill material further consolidation is caused by a load exerted by the upper, layer material. Conversely, the load available for bending in this upper material is controlled by how much has gone into consolidating the lower material. The balance point between these two processes was found numerically for a range of upper layer thicknesses by calculating deflections and redistributing loads until a balance was reached.

The results of running this model are contained in the table showing maximum tensional surface stresses, which occur at topographic highs. Stress is actually underestimated for a number of reasons. These include further settlement in the fill material due to its self-weight after being covered by the layer material, tensional stress due to extension of the layer material, and also surface tension caused by shrinkage due to desiccation of the material.

Table of surface stress due to bending

Elastic Modulus	Thickness of covering layer 300 meters	500 meters	1000 meters
10 MPa	3.5 MPa	4.2 MPa	5.7 MPa
20 MPa	5.1 MPa	6.3 MPa	8.3 MPa
50 MPa	8.3 MPa	10.4 MPa	13.9 MPa
100 MPa	12.2 MPa	15.2 MPa	20.8 MPa
500 MPa	29.3 MPa	37.3 MPa	46.4 MPa

The stresses shown in the table above are large enough to exceed both the tensile and the shear strength of the soil for near surface conditions, making fracture creation by this process a reasonable possibility. Model refinements in progress include a nonelastic, time dependent depositional model, use of a pyroclastic cover material, and evaluation over a wider range of initial conditions including 3-dimensional base topography.

References cited

Gere, J.M., and S.P. Timoshenko, Mechanics of Materials. Boston, PWS Publishers, 1984.

McGill, G.E., The giant polygons of Utopia, northern martian plains, Geophys. Res. Letts., 13, 1986.

Pike, R.J., Control of crater morphology by gravity and target type: Mars, Earth, Moon, Proc. Lunar Planet. Sci. Conf. 11th, 2159-2189, 1980.

Rieke, H.H., and G.V. Chilingarian, Compaction of Argillaceous Sediments. New York, Elsevier Publ Co, 1974.

Terzaghi, K., Erdbaumeckanik auf bodenphysikalischer Grundlage. Leipzig, Deuticke, 1925.

Turcotte, D.L. and G. Schubert, Geodynamics. New York, John Wiley & Sons, 1982.

THE EFFECT OF OVERBURDEN THICKNESS ON TENSION FRACTURE PATTERNS ABOVE AN UPLIFTING DOME

H. PRANGER II
Department of Earth Resources, Colorado State University, Ft. Collins, Colorado 80523

Four experiments demonstrate that tension-fracture patterns above an uplifting dome depend on the thickness of the overburden layer being deformed. Four layers of increasing thicknesses (4.92 cm, 6.92 cm, 9.05 cm, and 11.12 cm) of a very fine sand (85%) and silt-clay (15%) mixture were updomed by slowly inflating a 1.22 m-diameter circular rubber pillow. The upper 2 cm of each layer was wetted and air dried to make it brittle and susceptible to fracture. The fractures that formed during these experiments exhibited a continuum of patterns from dominantly arcuate to dominantly radial as the overburden thickness increased. However, fracture density remained constant in each case for a given amount of surface deformation.

Features common to each experiment are (Fig. 1): 1) radial fractures at the edge of the dome; 2) arcuate fractures on the flanks of the dome and 3) a central zone where randomly oriented fractures result from tension in all directions. The outer radial fractures lengthened and the arcuate fractures formed nearer to the center of the dome as overburden thickness increased.

The spatial distribution of fractures changed drastically during the experiment. The highest fracture density was located near the perimeter of the dome in the thin layers (Fig. 1A, B), but it occurred nearer the center of the dome in the thicker layers (Fig. 1C, D). The surface deformation pattern explains this distribution. The strain is greatest near the perimeter with a thin overburden (Fig. 1A, B), but it is more uniformly distributed with a relatively thick overburden (Fig. 1B, C).

Salt domes on Earth and the Tharsis bulge of Mars provide excellent examples of radial faults due to updoming. Arcuate fracture patterns are associated with calderas and ring dikes. Playa lake fissures, the grabens of the Labyrinthus Noctis on Mars and many mudcracks often display a random orientation similar to the central zone of each experiment. These simple experiments show that distinctly different tension fracture patterns on domes depend on overburden thickness and strain distribution (Fig. 1).

Figure 1. Fracture patterns (left) and maps showing surface deformation in millimeters (right). Overburden thickness above the pillow is as follows: A) 4.92 cm, B) 6.92 cm, C) 9.05 cm, D) 11.12 cm.

A

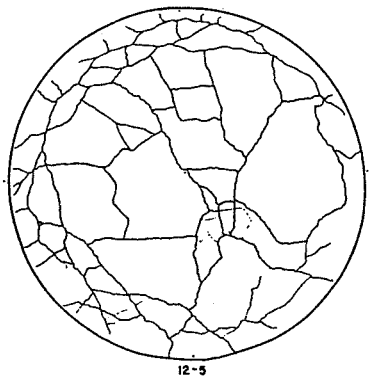
12-5

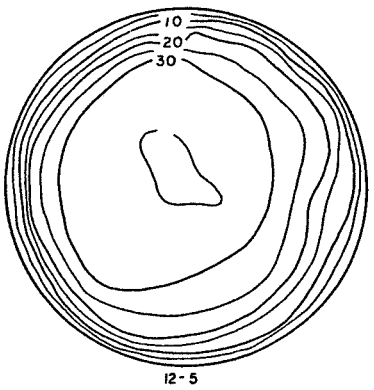
10
20
30
12-5

B

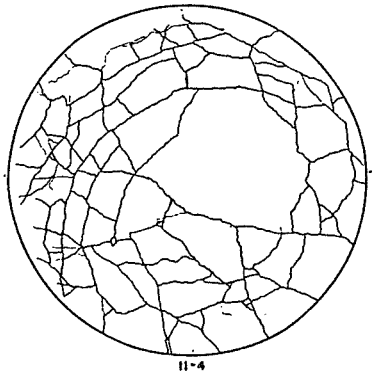
11-4

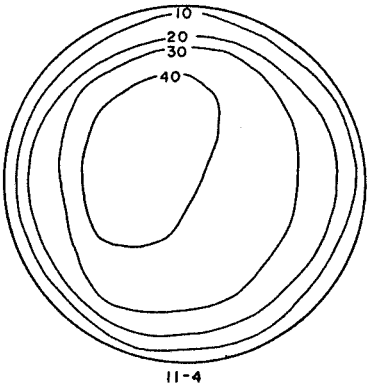
10
20
30
40
11-4

C

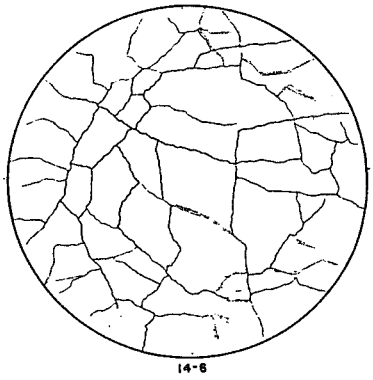
14-6

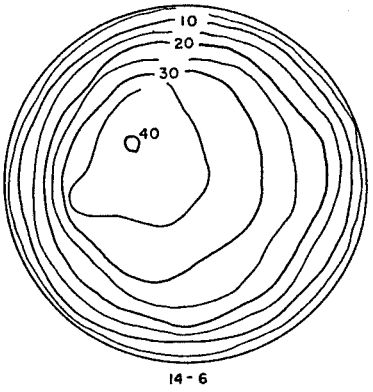
10
20
30
O40
14-6

D

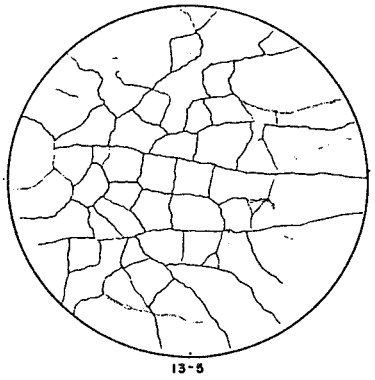
13-5

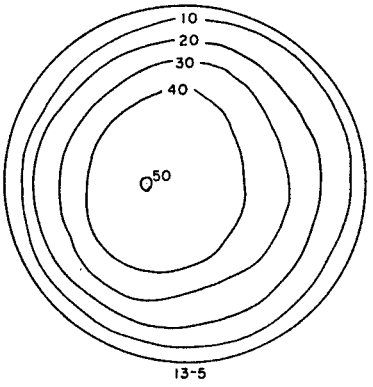
10
20
30
40
O50
13-5

NATURAL FRACTURE SYSTEMS ON PLANETARY SURFACES: GENETIC CLASSIFICATION AND PATTERN RANDOMNESS

Lisa A. Rossbacher, Department of Geological Sciences, California State Polytechnic University, Pomona, CA 91768

One method for classifying natural fracture systems is by fracture genesis. This approach involves the physics of the formation process, and it has been used most frequently in attempts to predict subsurface fractures and petroleum reservoir productivity (Stearns and Friedman, 1972; Nelson, 1979). This classification system can also be applied to larger fracture systems on any planetary surface.

This process-based system for classification of natural fractures was originally proposed by Stearns and Friedman (1972) and later modified by Nelson (1979):

Classification of Natural Fractures

1. Tectonic
2. Regional
3. Contractional
   a. Desiccation
   b. Syneresis (chemical dewatering of clays)
   c. Thermal contraction (including lava cooling)
   d. Mineral phase changes
4. Surface related
   a. Unloading
   b. Weathering (including freeze-thaw activity)

One problem in applying this classification system to planetary surfaces is that it was developed for relatively small-scale fractures that would influence porosity, particularly as observed in a core sample (Stearns and Friedman, 1972). Planetary studies also require consideration of large-scale fractures. Nevertheless, this systems offers some valuable perspective on fracture systems of any size.

Terrestrial studies of fracture patterns have generally concentrated on just 3 of the categories listed above: desiccation, lava cooling, and freeze-thaw, which is a subset of the weathering category in the system listed here. Relatively few data are available in the literature for fracture patterns generated by unloading, syneresis, and mineral phase changes. An additional consideration in applying this classification to large-scale features is that "regional" fractures are typically generated either by tectonism, which is a separate category, or by regional desiccation and lowering of the groundwater table, which should fall under the contractional/desiccation category. Thus, the classification system may require further

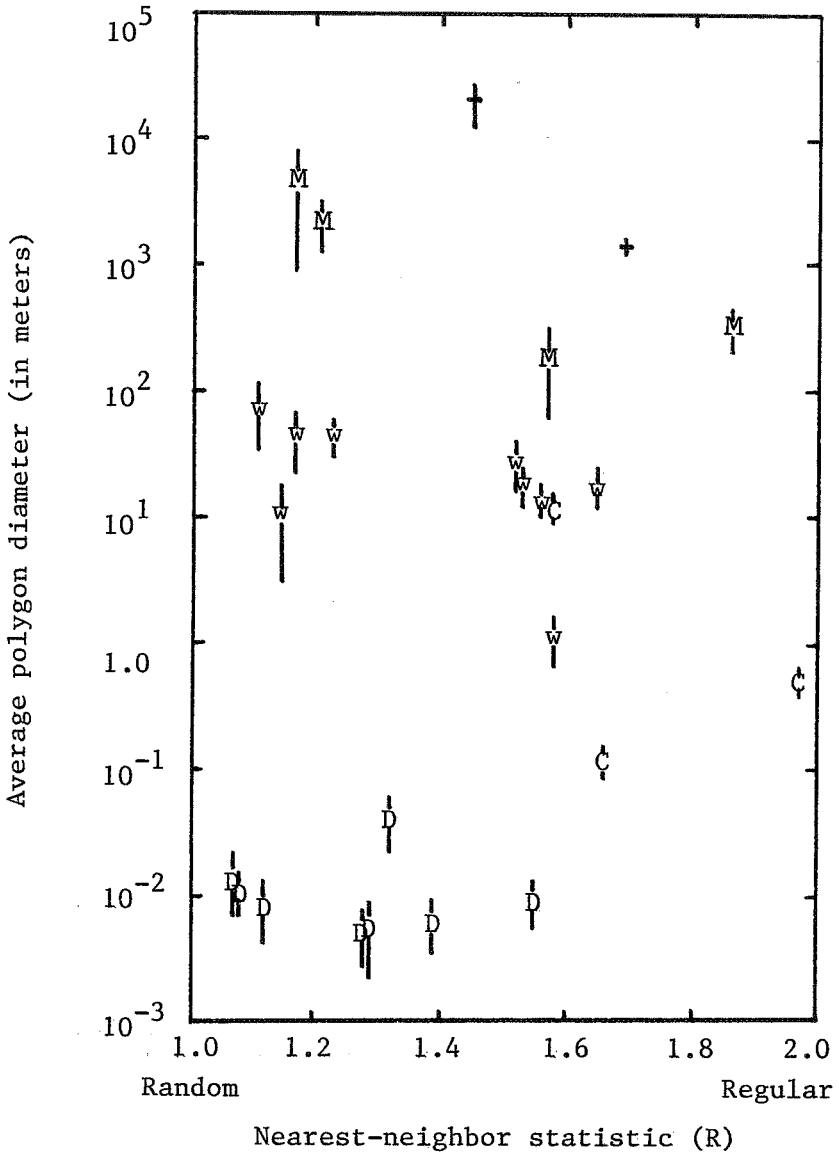

Fig. 1. The morphology of fracture patterns, as described by polygon diameter and nearest-neighbor analysis, supports the genetic classification system for natural fractures (+ = tectonic; D = desiccation; C = thermal contraction; w = weathering; M = Martian fractures - no genesis inferred). Data from Rossbacher (1985, 1986a, 1986b, 1986c).

modification to make it clearly reflect genetic processes.

Two approaches to quantifying the morphology of the fracture system are measuring polygon diameter and determining the randomness of the pattern itself. The latter can be calculated by applying nearest-neighbor analysis, which yields the R-statistic (Rossbacher, 1985, 1986b).

The R-statistic can be plotted against average polygon diameter for the various categories of natural fracture systems (Fig. 1). Although Figure 1 does not include sufficient measurements within several categories to allow definite conclusions, the data do support several tentative interpretations: 1) The genetic classification system for natural fractures does seem to describe specific relationships between polygon size and pattern randomness. 2) The fracture patterns observed on the surface of Mars do not clearly fall into any of the other categories for terrestrial features. This suggests that either the Martian fractures formed by yet another process or the physics of the fracturing processes are sufficiently different on Mars that the morphology of the Martian landforms cannot be directly compared with their terrestrial analogs. If size and pattern randomness are controlled by the mechanism of formation, as suggested by the data presented here, then it may be possible to infer fracture origin from the morphology, at least for terrestrial examples. The parameters controlling the physics of the process need to be better understood in order to apply similar interpretations to Martian fracture patterns.

References Cited

Nelson, R.A., 1979, Natural fracture systems: Description and classification: AAPG Bulletin, v. 63, p. 2214-2232.

Rossbacher, L.A., 1985, Quantitative analysis of Martian polygonal ground, in Lunar and Planetary Science XVI: Houston, LPI, p. 710-711.

Rossbacher, L.A., 1986a, Ground patterns on Earth and Mars, in Lunar and Planetary Science XVII: Houston, LPI, p. 726-727.

Rossbacher, L.A., 1986b, Nearest-neighbour analysis: A technique for quantitative evaluation of polygonal ground patterns: Geografiska Annaler, v. 68A, p. 101-105.

Rossbacher, L.A., 1986c, Size and randomness of ground patterns for Earth and Mars: Implications for origin and modification: Reports of Planetary Geology and Geophysics Program - 1985, NASA Technical Memorandum.

Stearns, D.W., and M. Friedman, 1972, Reservoirs in fractured rocks, in Stratigraphic oil and gas field classification, exploration methods, and case histories: AAPG Memoir 16, p. 82-106.

CURVILINEAR RIDGES AND RELATED FEATURES IN SOUTHWEST CYDONIA MENSAE, MARS

by
Timothy J. Parker, Dale M. Schneeberger, David C. Pieri, and R. Stephen Saunders
Jet Propulsion Laboratory, California Institute of Technology, Pasadena, CA

Figure 1 depicts a region in southwest Cydonia Mensae (32° lat., 17° lon.) just northwest of the lowland/upland boundary escarpment. The dominant morphologic features in the region are the clusters of large massifs and plateau outliers (Pl), knobby material (K), and smooth lowland plains (Ps). Surrounding the clusters and linking many isolated knobs is a system of curvilinear ridges and arcuate terrain boundaries which tend to separate the massifs and knobs from the smooth plains.

Curvilinear ridges are arcuate to nearly linear ridges that are smoother in plan than wrinkle ridges and show no apparent correlation with regional structural grain. They are typically 5-10km long but can range from as little as 2 or 3km to greater than 50km long. The widths vary from about 100m to as much as 2km. Ridge crests usually appear sharp to somewhat rounded. Changes in symmetry and width occur gradually along strike. Wrinkle ridge crests, in contrast, are often irregular, en echelon, and abruptly cross from one side of the ridge to the other along strike. Curvilinear ridges are most numerous within 100km of the lowland/upland boundary escarpment and are associated with massifs and knobby terrain. When enclosing clusters of massifs, they tend to do so with their concave sides facing the open plains.

Arcuate terrain boundaries are defined as arcuate boundaries between units of different apparent albedo or arcuate breaks in slope. When an arcuate terrain boundary separates units of different albedo, the unit with the lightest albedo is typically on the concave side of the boundary. There are two types of arcuate slope breaks: (A) The most common occur as low escarpments cut into adjacent topographically higher terrain by the lowland plains. In this case, the escarpment faces the concave (plainward) side of the arc. (B) Less commonly, they exhibit a low, sharp escarpment suggestive of a thin onlapping of the adjacent topographically higher material by the lowland plains material. In this case, the escarpment is on the convex side of the arc and faces upslope, away from the lowland plains. Arcuate breaks in slope may or may not be associated with an albedo change. All three of the above elements may occur along a single arcuate terrain boundary. Arcuate terrain boundaries display a plan and distribution relative to topography similar to the curvilinear ridges and may grade into them (figure 2). Those that are found downslope from the curvilinear ridges tend to be traceable over the longest distances (as much as 200km or more). Arcuate terrain boundaries, like the curvilinear ridges, are most common within 100km or so of the lowland/upland boundary.

Several terrestrial and lunar processes can produce ridge forms: (A) Volcanic ridge forms include intrusive dikes. Volcanic dikes intruding into a since-removed surface deposit have been suggested (1,2) as a possible explanation for the sinuous ridges in Argyre Basin (3), which share some morphological similarities with the curvilinear ridges of southwest Cydonia, though at a larger scale. Such ridges should exhibit some sort of structural control to their distribution, however. (B) At least two glacially derived terrestrial features - eskers and moraines - may be of similar scale and morphology to the martian curvilinear ridges. Both types of features require the presence of an extensive ice sheet within the northern plains and movement of material toward its margin. Movement of the ice over the now-exposed plains would likely have produced drumlin-like forms and other scour features. (C) Longitudinal dunes or sand ridges are common in the vast desert regions of Africa and Australia. Individual ridges are similar morphologically to those found on Mars. Terrestrial sand ridges, however, occur in parallel sets oriented with the dominant winds. The curvilinear ridges on Mars do not occur parallel to one another as a rule, and show no preferred alignment with local wind patterns. (D) Lacustrine and coastal ridge forms - spits, bars, and coastal barriers - may provide the best analogs for the curvilinear ridges. They are of similar scale to the curvilinear ridges and exhibit similar distributions relative to topography. Spits and bars form by longshore transport of sediment. Most bars form parallel to the coast, tending to close off re-entrants, or bays, or link offshore islands to the mainland or to one another. Spits are bars connected to the coast at one end. Their length, width and direction relative to the shore are dependent upon a number of interrelated factors: source, amount, and duration of sediment supply; strength, duration, and direction of the dominant swell; tidal range and currents (oceanic); and depth and slope of the lake or sea bottom (4,5). While most terrestrial spits are only a few kilometers long, some are known that are as much as 90km long (6). In terrestrial coastal regions with a gently sloping bottom profile and an abundant sediment supply, such as along the east coast of North America, large barrier islands have formed as a result of sea level rise since the last glaciation (7). Coastal barrier systems can be thousands of kilometers long.

The arcuate terrain boundaries have two possible analogs: (A) Lunar mare flow fronts result from the interaction of vast volcanic floods and pre-existing terrain. One of the most striking features associated with the lunar maria are long, sinuous scarps which have been interpreted as flow fronts (8). Where individual flow fronts

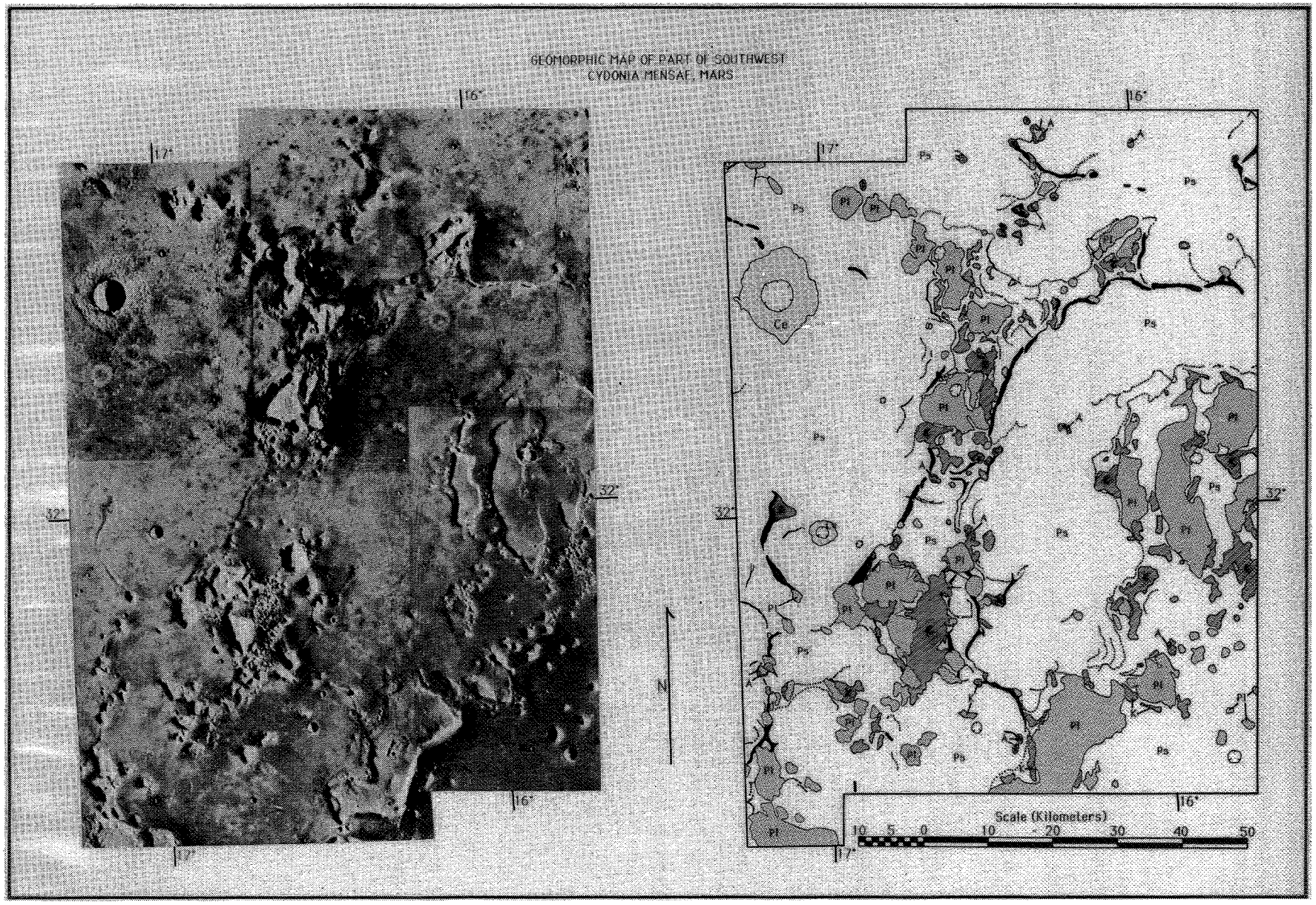

Figure 1: Principle geomorphic elements of part of Cydonia Mensae. (Pl), Plateau outliers and large massifs; (K), Knobby material; (A), flat-topped massif-encircling debris aprons; (Ps), Smooth plains; (Ce), Crater ejecta blanket; Curvilinear ridges indicated by solid black; Arcuate terrain boundaries indicated by dotted lines.

are not recognizable in the lunar maria, the flood lavas onlap pre-existing terrain in a topographically conformal fashion. This type of terrain boundary is also found in many places on Mars, but it is distinct from the morphology of the arcuate terrain boundaries found within the northern lowlands. Although onlapping of elevated terrain by lowland plains might be expected of lunar mare-type flood lavas, those boundaries exhibiting an escarpment cut into the elevated terrain would require the unlikely erosion of the elevated material by the lavas. (B) Terrestrial shorelines on gently sloping terrain can produce similar morphologies that might be visible at medium to high resolution Viking Orbiter image scales. These include such features as beach ridges and cuspate and zetaform shorelines. Beach ridges are constructional features that may be several meters in height, tens of meters in width, and hundreds of meters to kilometers in length (9). The cuspate or zetaform plan of many coastlines, which may have both constructional and erosional elements, is a result of wave refraction and is a function of the dominant swell direction, the bottom topography, and the resistance of the coastal material to wave erosion.

References:

(1) Carr, M.H., 1984, Mars: in Geology of the Terrestrial Planets, Carr, M. H., ed., NASA SP-469, p. 207-263.
(2) Carr, M. H., 1981, The Surface of Mars: Yale University Press, New Haven and London, 232 p.
(3) Parker, T. J., Pieri, D. C., and Saunders, R. S., 1986, Morphology and distribution of sinuous ridges in central and southern Argyre: Reports of the Planetary Geology Program - 1985, NASA TM 88383, p. 468-470.
(4) Gilbert, G. K., 1890, Lake Bonneville: U.S. Geol. Survey Mon., Vol. 1, 438 p.
(5) Evans, O. F., 1942, The origin of spits, bars, and related structures: Journal of Geology, Vol., p. 846-866.
(6) Zenkovich, V. P., 1967, Processes of Coastal Development: (Steers, J. A., ed.) Interscience Publ., John Wiley and Sons, New York, 738 p.
(7) Bloom, A. L., 1978, Geomorphology-A Systematic Analysis Of Late Cenozoic Landforms: Prentice-Hall, Inc., New Jersey, 510 p.
(8) Basaltic Volcanism Study Project, 1981, Basaltic Volcanism On The Terrestrial Planets: Pergamon Press, Inc., New York, 1286 p.
(9) Reineck, H. E., and Singh, I. B., 1980, Depositional Sedimentary Environments, with Reference to Terrigenous Clastics: Springer-Verlag, Berlin, Heidelberg, New York, 549p.

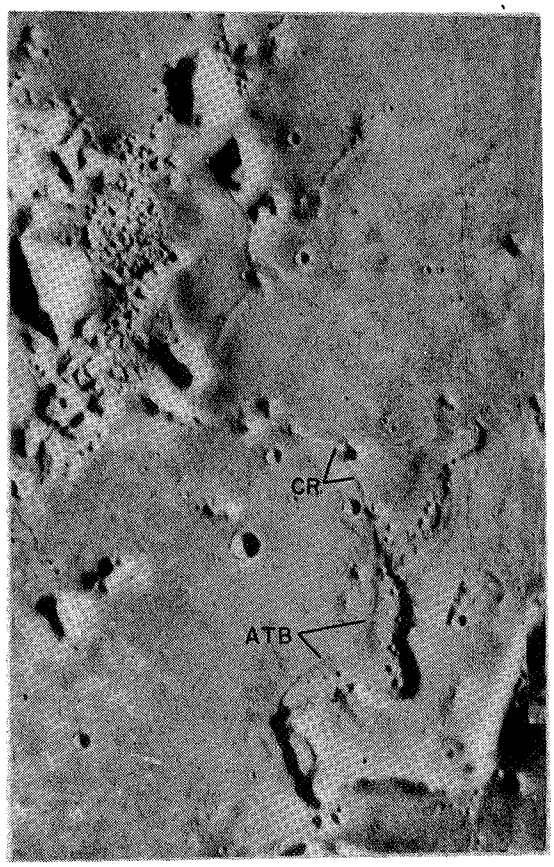

Figure 2: Magnified view of area along south edge of figure 1. Arcuate break in slope (ATB; erosional?) at base of plateau remnant at lower right grades smoothly into curvilinear ridge (CR; constructional?). Other arcuate terrain boundaries and curvilinear ridges can also be seen in this view. A cluster of large massifs and knobby material can be seen at upper left.

LOCAL-SCALE STRATIGRAPHY OF GROOVED TERRAIN ON GANYMEDE

Scott L. Murchie, James W. Head, and Paul Helfenstein, Department of Geological Sciences, Brown University, Providence, RI 02912, and Jeffrey B. Plescia, U.S. Geological Survey, Flagstaff, AZ 86001.

The surface of Ganymede is divided into two major units, dark terrain cut by arcuate and subradial furrows, and light terrain consisting largely of areas with pervasive U-shaped grooves (grooved terrain) (1,2). The grooved terrain may be subdivided on the basis of pervasive morphology of groove domains into four terrain types (3): (*a*) elongate bands of parallel grooves (*groove lanes*); (*b*) polygonal domains of parallel grooves (*grooved polygons*); (*c*) polygonal domains of two orthogonal groove sets (*reticulate terrain*); and (*d*) polygons having two to several complexly cross-cutting groove sets (*complex grooved terrain*). Reticulate terrain is frequently dark and not extensively resurfaced, and grades to a more hummocky terrain type. The other three grooved terrain types have almost universally been resurfaced by light material during their emplacement (1,2,3,4,5).

The sequence of events during grooved terrain emplacement has been investigated by Lucchitta (4), who suggested that reticulate terrain is an intermediate stage in the conversion of dark terrain into light grooved terrain. Golombek and Allison (6) proposed that groove lanes dissect older dark terrain into polygonal blocks that are later resurfaced and fractured to form grooved polygons. In this study, we attempt to integrate observed geologic and tectonic patterns to better constrain the relative ages and styles of emplacement of grooved terrain types. A revised model of grooved terrain emplacement is proposed and is tested using detailed geologic mapping and measurement of crater-density.

Important spatial and temporal tectonic patterns in grooved terrain include (*a*) structural control of grooves, whose orientations are closely related to the regional orientations of older, arcuate and radial furrows (3), (*b*) the correspondence of global groove lane orientations with the pattern predicted for reactivated tidal despinning fractures (7), (*c*) similar sizes and shapes of nearby polygons of different terrain types, and (*d*) evidence for emplacement of light terrain as shallowly resurfaced downdropped blocks (4,8). Narrow dark troughs are observed to widen into groove lanes, and exhibit a longitudinal sequence of (*a*) initial trough formation, (*b*) patchy discontinuous resurfacing, and (*c*) extensive resurfacing and pervasive groove formation, interpreted here to imply a sequence of initial extension followed by ice volcanism. The groove lanes are similar in plan to continental rifts, and Murchie *et al.* (9) proposed that they are passive rifts driven by global expansion. Concentration of grooved polygons and reticulate terrain between closely spaced groove lanes suggests that polygonal blocks were deformed where the lithosphere had been thinned, as it may be on earth (10), between closely spaced rifts. This hypothesis is consistent with the inference of Grimm and Squyres (11) that lithospheric thinning occurred during the emplacement of grooved terrain. One further very significant tectonic pattern is that groove lanes defining the margins of reticulate and grooved polygons also bury and cross-cut grooves within the polygons. This relationship implies that many groove lanes developed by reactivation of older structures (grooves or normal faults), that had earlier confined fracturing and the lateral extent of light material emplacement within the deformed polygons.

On the basis of the patterns listed above, we propose the following generalized sequence of events during grooved terrain formation: *stage 1*, dissection of the lithosphere by incipient rifts following preexisting, throughgoing zones of weakness (furrows, relict despinning fractures), accompanied by thinning and probably deformation of intervening blocks as stress is concentrated there; *stage 2*, extensive resurfacing and continued deformation of the polygons; and *stage 3*, repeated reactivation of the throughgoing zones of weakness, which are

deformed preferentially as the lithosphere thickens.

Three areas were investigated in detail to test this model. Results in each case were similar, so only the results from the area of central Uruk Sulcus (5°S-12°N, 145°-160°W, Voyager 2 image 20637.20) will be discussed in detail. A series of detailed maps was prepared, as described in (9), from which relative age units were determined using cross-cutting relations of grooves and superposition relations of light material. The six relative age units are: (*A*) patchily resurfaced reticulate to hummocky terrain, outlined by throughgoing grooves; (*B*) completely but shallowly resurfaced reticulate terrain having highly degraded troughs; (*C*) grooved polygons superposed on *B*; and (*D*, *E*, and *F*) groove lanes and a few grooved/resurfaced polygons. Repeatedly reactivated zones of weakness were identified, that confined both fracturing and light material emplacement within deformed polygons, and also were preferred sites of groove lane formation. In all three terrain types represented in Uruk Sulcus, dominant groove orientations are parallel to older arcuate or radial furrows. Both the groove lanes and the throughgoing zones of weakness have restricted orientations (*a*) nearly parallel to arcuate furrows and (*b*) parallel to inferred relict tidal despinning fractures (7). Smaller groove spacing in the grooved polygons than in groove lanes suggests that the grooved polygons formed when the lithosphere was relatively thinner, as is suggested in the model.

The validity of the sequence of events derived through geologic mapping was tested by measurement of the densities of craters superposed on the six relative age units and on adjacent, older dark furrowed terrain (Table 1). Densities of craters >2 km and >5 km in diameter show that the six relative age units form three larger relative age groupings: *A*, oldest; *B-C*, intermediate age; and *D-F*, youngest. In addition, *E* probably is younger than *D*. Therefore, crater-density measurements corroborate the relative age units derived through geologic mapping. Calibration of the densities using the crater-production curve of (11) shows that the duration of grooved terrain emplacement in Uruk Sulcus was $\geq 10^8$ yrs.

Each of the three major relative age groups (*A*, *B-C*, *D-F*) is dominated by a different terrain type, and the sequence of terrain types is consistent with the generalized 3-stage sequence in the model. *Stage 1* is characterized by formation of throughgoing grooves following preexisting zones of weakness, and by development of reticulate to hummocky terrain in the intervening polygons. *Stage 2* is characterized by resurfacing of the intervening polygons and formation of grooved polygons. During *stage 3*, deformation is concentrated at the sites of initial throughgoing grooves, in the form of repeated groove lane formation.

In summary, we propose that grooved terrain formation at a local scale occurs in $\geq 10^8$ yrs, as a general 3-stage process shown in Figure 1. Preexisting structures exert strong control on orientation and lateral extent of groove sets. A sequence of thinning and later thickening of the lithosphere during grooved terrain emplacement may occur.

REFERENCES: (1) Smith, B., and the Voyager Imaging Team, *Science, 204*, 951-972, 1979*a*. 599-600, 1985. (2) Smith, B., and the Voyager Imaging Team, *Science, 206*, 927-950, 1979*b*. (3) Murchie, S., and J. Head, *Lunar Planet. Sci. XVI*, (4) Lucchitta, B., *Icarus, 44*, 481-501, 1980. (5) Casacchia, R., and R. Strom, *J. Geophys. Res., 89*, B419-B428, 1984. (6) Golombek, M., and M. Allison, *Geophys. Res. Lett., 8*, 1139-1142, 1981. (7) Murchie, S., and J. Head, *Geophys. Res. Lett, 13*, 345-348, 1986. (8) Schenk, P., and W. McKinnon, *J. Geophys. Res., 90*, C775-C783, 1985. (9) Murchie, S., J. Head, P. Helfenstein, and J. Plescia, *J. Geophys. Res.*, in press, 1986. (10) Girdler, R., *Tectonophysics, 94*, 241-252, 1983. (11) Grimm, R., and S. Squyres, *J. Geophys. Res., 90*, 2013-2021, 1985. (12) Shoemaker, E., and R. Wolfe, in *The Satellites of Jupiter*, edited by D. Morrison, pp. 277-239, Univ. of Arizona, Tucson, 1982.

TABLE 1. Cumulative Crater Densities in Uruk Sulcus, $\times 10^{-6}$ km^{-2}

Unit	Area, km^2	>2 km	>5 km	>10 km	>20 km
Furrowed	193,072	–	539 ± 53	238 ± 35	41 ± 15
A	111,689	–	458 ± 64	233 ± 46	47 ± 20
B-C	151,149	992 ± 81	205 ± 37	98 ± 25	37 ± 15
D	87,821	797 ± 95	190 ± 46	98 ± 33	47 ± 23
E	48,435	681 ± 119	123 ± 40	75 ± 40	38 ± 27
F	20,750	723 ± 187	271 ± 112	133 ± 80	–

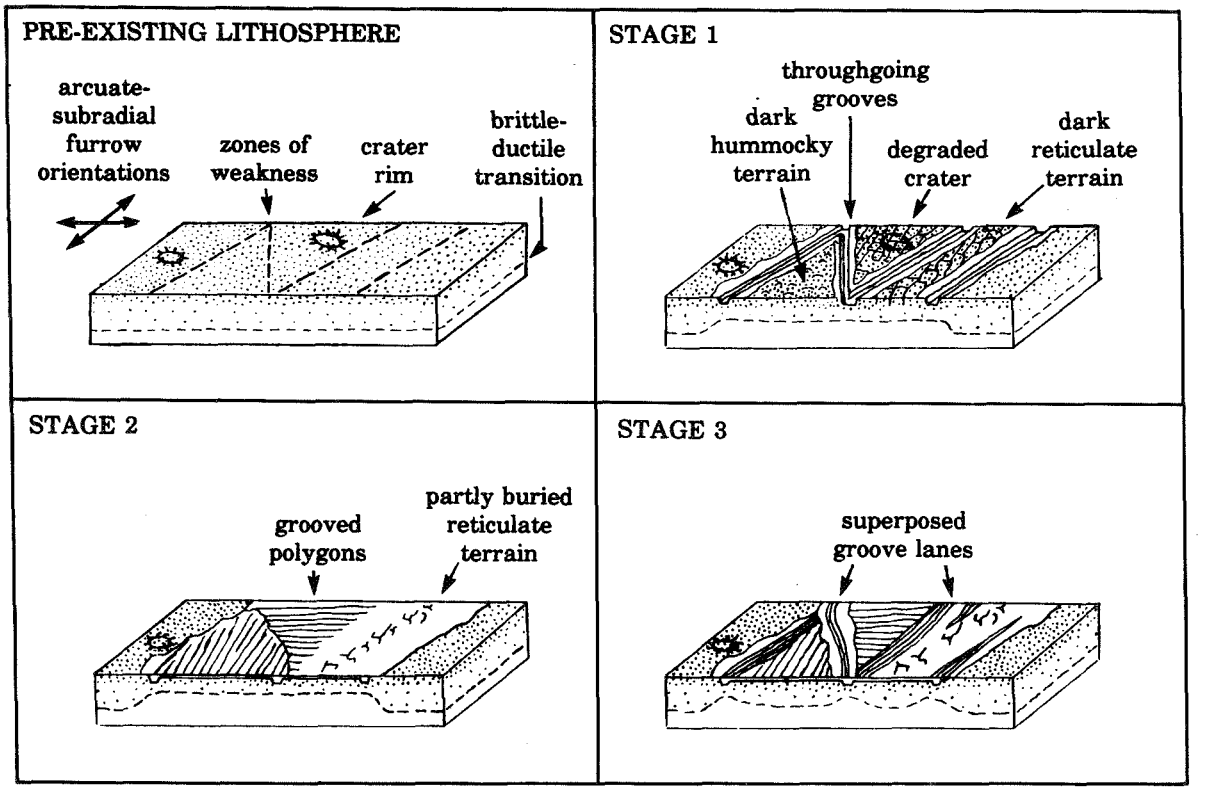

Figure 1. Schematic illustration of the generalized 3-stage sequence of events during grooved terrain formation.

STRATIGRAPHY OF THE SOUTH POLAR REGION OF GANYMEDE

R. A. De Hon, Department of Geosciences, Northeast Louisiana University, Monroe LA 71209.

This paper reports a preliminary assessment of the stratigraphy and geology in the south polar region of Ganymede. Geologic mapping is based on inspection of Voyager images and compilation on an airbrush base map at a scale of 1:5M. Illumination and resolution vary greatly in the region. Approximately half of the quadrangle is beyond the terminator. Low angle illumination over a large part of the area precludes distinction of some units by albedo characteristics.

Several types of grooved terrain (2,3) and groove related terrain occur in the southern polar region (Fig. 1). Grooves typically occur in straight to curvilinear sets or lanes. Bright lanes and grooved lanes intersect at high angles outlining polygons of dark cratered terrain. Groove sets exhibit a range of ages as shown by superposition or truncation (4) and by crater superposition ages.

The region of grooved lanes and cratered polygons passes into a region of complex grooved terrain (5; furrowed terrain of Ref. 1) characterized by subparallel sets of closely spaced groove sets lanes. Transection and truncation of groove sets in the complex grooved terrain indicate a prolonged period of complex crustal fracturing. The complex grooved terrain spans a wide range of time in its formation, but it is generally older than the smooth bright lanes and older than most bright grooved lanes. The grooves may be grouped into subparallel groove sets which in turn may be grouped into super sets made up of progressively younger sets. Most of the complex grooved terrain is older than the Gilgamesh basin and apparently older than the palimpsest associated with Hathor, but some of the grooved sets in the complex cratered terrain cut, hence are younger than, the twin palimpsests. The youngest groove sets in the complex grooved terrain transect all other sets and contain fewer grooves.

The largest basin in the polar region is Gilgamesh which consists of a 150-175 km diameter central plain surrounded by hummocky and radial basin ejecta. A clearly defined basin rim is not present. Hence, Gilgamesh has some characteristics in common with palimpsests. Ejecta and well defined secondaries from Gilgamesh are superposed on complex grooved terrain. A well defined double ringed basin

at -83°; 140° is superposed on complex grooved terrain and in turn overlain by Gilgamesh secondaries. Two palimpsests near -70°; 270° partially overlie complex cratered terrain, yet are cut by younger groove sets of the complex crater terrain.

Craters range from subdued, incomplete rings to sharp, well defined craters with bright haloes that overlie all other materials. Remnants of old, large craters are scarce. In fact, dark crated terrain, the oldest in the quadrangle does not exhibit large crater remnants. Apparently small craters are retained while larger craters are lost, perhaps by topographic relaxation.

Acknowledgements. This study represents one phase of research conducted under NASA Planetology Programs Grant NSG 7628 at Northeast Louisiana University. Geologic mapping of the south polar region of Ganymede (Jg-15, 1:5M) by Hal Masursky, William McKinnon and Rene De Hon is part of the Jovian Satellite Mapping Program.

TABLE I. RELATIVE AGES OF GEOLOGIC UNITS: Jg-15

(c3) Craters w/ bright rays
(ps) Smooth plains material
(sb) Smooth bright lane material
(gb) Bright grooved lane material
(c2) Craters without rays
(g) Gilgamesh basin material
(p) Palimpsests material (tf) Complex grooved terrain
(gd) Dark grooved terrain material
(c1) Crater remnants
(pc) Cratered plains material
(gg) Groove and groove material
(gc) Cratered and grooved material
(tc) Dark cratered terrain materials

REFERENCES

(1) De Hon, R. A. (1982) NASA Tech Mem. 85127, 349-351.
(2) Smith B. A. et al. (1979) Sci. 204, 13-32.
(3) Smith B. A. et al. (1979) Sci. 206, 9225-950.
(4) Luchitta B. K. (1980) Icarus 44, 481-501.
(5) Squyres S. W. (1981) Icarus 52, 545-559.

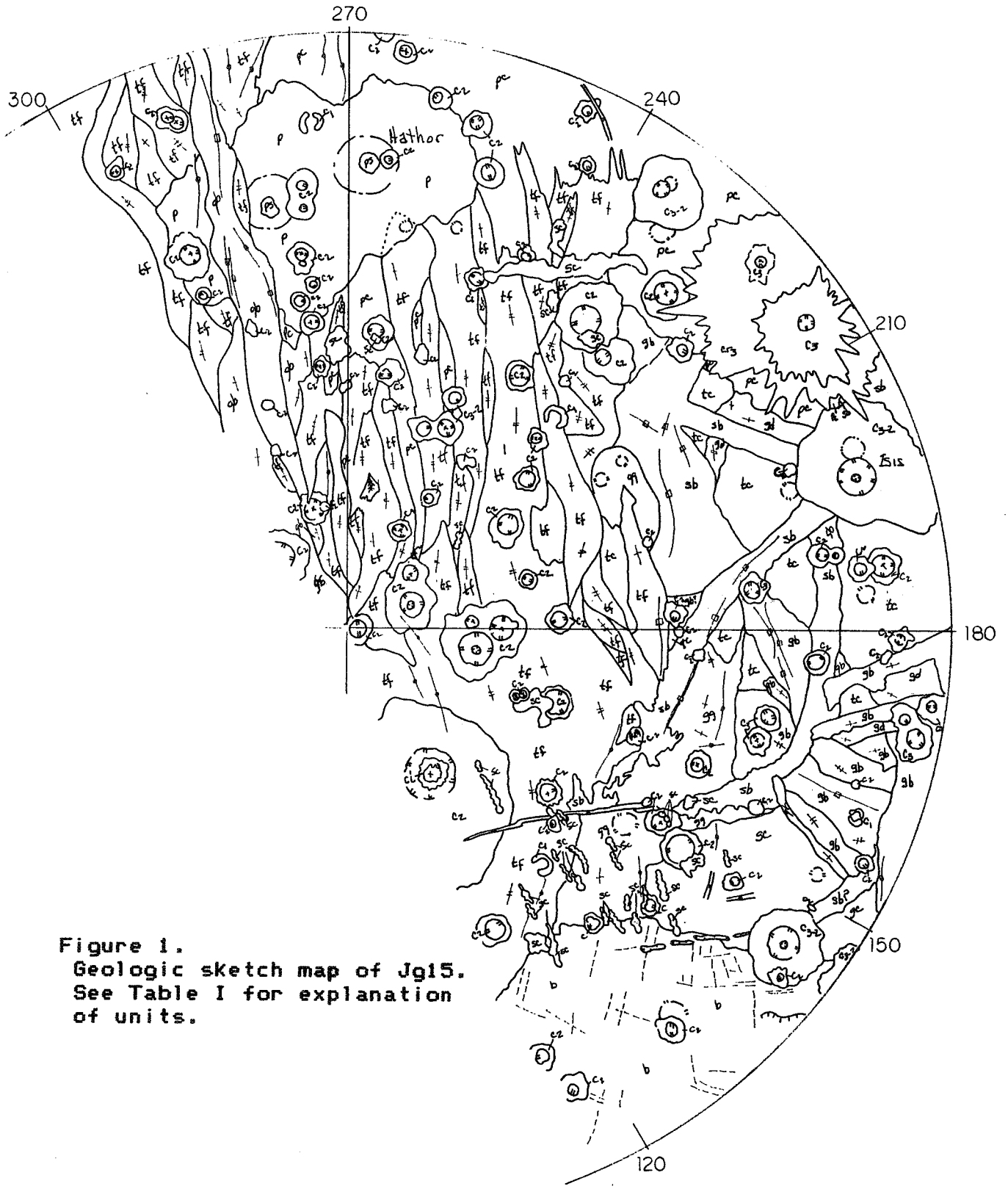

Figure 1.
Geologic sketch map of Jg15.
See Table I for explanation
of units.

CREEP OF ICE: FURTHER STUDIES

H.C. Heard[1], W.B. Durham[1], and S.H. Kirby[2]
[1]UCLLNL, Livermore, CA 94550; [2]USGS, Menlo Park, CA 94025

In the past year we have completed detailed studies of (1) the flow of high-pressure water ices II, III, and V, and (2) frictional sliding of ice I_h. Preprints describing both studies are now being circulated among interested colleagues before submittal for publication. In addition, we began work on the second phase of the current proposal--the study of the effect of impurities on the flow of ice. We summarize the results of these three projects below.

Flow of high pressure ice. Over the past two and one-half years we have tested 36 different samples of high pressure ice to pressures as high as 550 MPa and temperatures as low as 158 K. The appropriate portion of the H_2O phase diagram is shown in Figure 1. From our tests we have derived 77 independent measurements of strength (flow stress as a function of temperature, confining pressure, and strain rate) and a host of other data related to phase transformation kinetics and phase metastability in ice. The flow results for ices II, III, and V are summarized in Figure 2. Ice II is the strongest of the phases, having a strength slightly higher than that of ice I_h, and ice III is the weakest. The low strength of ice III is striking: under a fixed set of conditions ice III will flow approximately 100-1000 times faster than ice II or ice V. This is important to the evolution of a large icy moon such as Ganymede or Callisto. An ice III layer, situated between a layer of ice V and a layer of ice I_h or II, will behave over long periods essentially as a liquid, unable to transmit meaningful levels of shear stress between the layers bounding it.

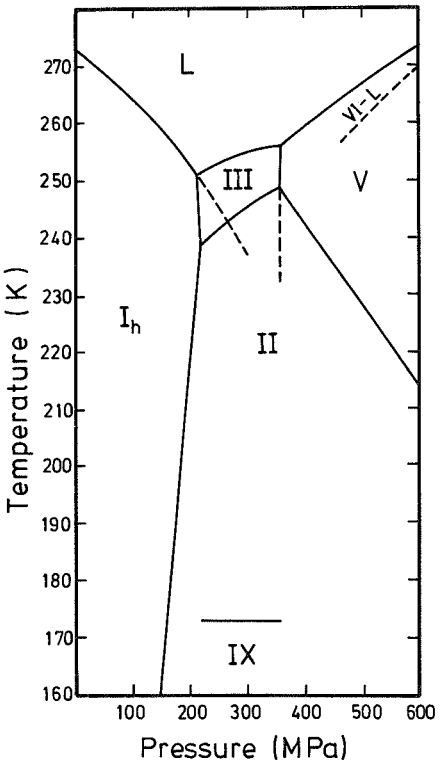

Fig. 1. H_2O phase diagram.

We have found that on the laboratory time scale of a few days, important metastable relationships exist between the phases of ice. The strongest of

these is the metastable existence of ice III in the warmer portion of the ice II stability field, a phenomenon known for many decades. What we have found is that these metastabilities endure even under large amounts of deformation, where local structural rearrangements might be expected to seed the transformation from ice III to ice II. Ice III deformed at temperatures as low as 210 K does not revert to II during deformation. The transformation from ice III to V and back (dashed line in Figure 1 at P=350 MPa) can also occur within the ice II field without producing any sign of ice II, even when the transformation is accompanied by deformation of the sample. Although it seems unlikely that such metastabilities endure over geologic time scales, the point is interesting because of the low strength of ice III and the probability that present and past temperature profiles within the icy moons are very close to the ice II-III phase boundary.

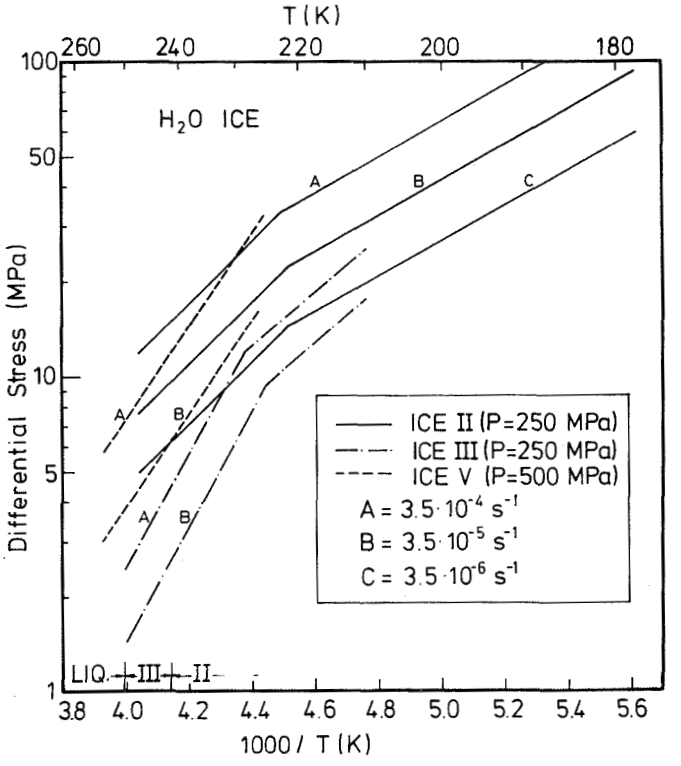

Fig. 2. Flow of ices II, III, and V

Frictional sliding in ice I_h. We can simulate sliding along existing large-scale faults in the crust of an icy moon by means of triaxial mechanical testing of cylinders of ice composed of two pieces that slide with respect to one another. The Voyager photos suggest such faults exist on the moons' surfaces, so our laboratory data should further constrain evolutionary models of the moons. We performed tests at temperatures from 77 to 115 K, near the expected surface temperatures of the moons, and at confining pressures from 0.3 to 250 MPa. The results from tests at 77 K are shown in Figure 3. Temperature turns out to play no noticeable role in the frictional characteristics of ice, nor does rate of sliding, which varied from 10^{-2} to 10^{-4} mm/s. The variable of overriding importance is the normal

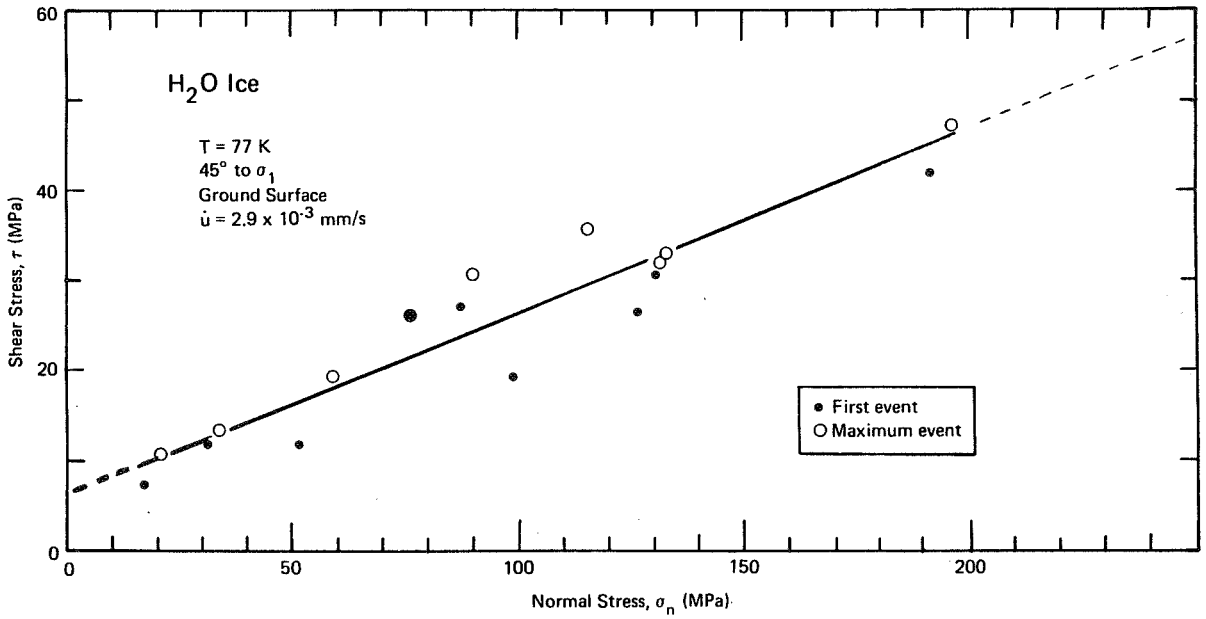

Fig. 3. Frictional strength of ice.

stress across the fault: the frictional strength rises 2 MPa for every 10 MPa increase in the normal stress (Figure 3). This strength is considerably less than that for most rocks. Applying these results to icy moons, weaker fault strength means increased tendency for deeper faults, that is, the depth at which plastic flow becomes favored over frictional sliding becomes deeper. Under extensional stresses of the order of 10 MPa, sliding on existing faults would be expected to extend to a depth of approximately 10 km in ice.

Effect of impurities on the flow of ice. This phase of the project began very recently. The first series of tests on samples of ice I_h from the important "intermediate" temperature regime (243 K to 195 K) has shown unambiguously that small amounts (less than 1%) of particulate impurities have no effect on the plastic flow properties of ice. The work will be extended to different temperature regimes, different amounts of particulate impurities, and perhaps different phases of ice. The study of dissolved impurities in water ice, especially methane and ammonia, is the subject of a current proposal to NASA.

OBSERVATIONS OF INDUSTRIAL SULFUR FLOWS AND IMPLICATIONS FOR IO

S.W. Lee, D.A. Crown, N. Lancaster, and R. Greeley, Department of Geology, Arizona State University, Tempe, Arizona 85287

The possibility of sulfur flows on the Jovian satellite Io has been discussed by several investigators [1-3]. Although the primary problem is lack of sufficient information to resolve the issue, interpretations of existing data are hampered by poor knowledge of the thermal properties and rheologic behavior of sulfur flows, especially under conditions present on Io. Relatively few natural sulfur flows occur on Earth [4-8] and only one has been seen in active flow [4]. However, recent observations of industrial sulfur flows, which are much larger than are possible to produce experimentally, may provide important information concerning natural sulfur flows on both Earth and Io.

Sulfur is mined by the Frasch process which involves drilling wells into sulfur-rich limestone or salt domes and melting the sulfur with water heated to ~ 165° C. Liquid sulfur is then pumped from the well and transported in molten form to processing plants where it is either stored as a liquid or cooled and solidified in ~ 100 m by 100 m vats with walls composed of solidified sulfur about 5 m thick and 15 m high. Liquid sulfur (99.6 % pure) at ~ 130° C is poured onto the vats at a rate of ~15 metric tons/minute (~ 7.5 m^3/min), with each "pour" totalling about 500 metric tons (~ 250 m^3 of liquid sulfur). Although this results in a total flow thickness of only 6-9 cm upon cooling, the flow is emplaced as extremely complex, thin (~ 1 cm) multiple flow units.

The flows advance in unconfined lobes and channels. Unconfined flow lobes spread rapidly, and as the flow cools and/or the local flow rate decreases, a crust forms simultaneously over the entire flow surface. Crustal flow lobes are very plastic and deform easily as flow continues beneath the crust. Breakouts along flow margins are common. Flow margins can be identified in the solidified sulfur, the surface of which is smooth and relatively featureless. Channelized flows exhibit marginal levees composed of cooling sulfur (Figure 1). Small aggregates of crystals, froth due to turbulence, and crustal plates are commonly observed on the surfaces of both channelized and unchannelized flows. Crystals and small plates collect and aggregate in slow-moving and quiescent areas of channels and along their margins and can be incorporated into fast-moving regions of flows. Crustal plates can be rafted together to form continuous and discontinuous ("sulfur lava tubes") crusts overlying the channels. Breakouts occur at channel margins and flow over levees to form additional channelized flows and lobes. Channels with crustal plates can be identified in the solidified deposits by their surface morphology (Figure 2).

Samples of overturned crust (1-2 cm thick) exhibit growth of acicular crystals 1-3 cm long into the molten sulfur; crystal growth is apparently enhanced in areas of ponded flow. Cross-sections through numerous flow units viewed in the excavated vat walls indicate that crystal growth occurs both downward from the crust and upward from the base of the flow. Crystal size apparently increases toward flow interiors. Similar features, including surface morphologies and interior structure, were noted on the natural Mauna Loa sulfur flow [9].

In one instance a "pour" was observed after a heavy rainfall which left puddles of standing water ~ 5 cm deep on the vat surface. When molten sulfur entered a puddle, the mode of flow emplacement was drastically altered; the flow advanced by thin overlapping "fingers" of sulfur (< 1 cm in diameter and commonly ~ 15 cm long). When the local flow rate decreased, molten sulfur cascaded from the top of the flow vertically into the water

forming beads and "sulfur stalactites." However, while these morphologies were observed in cross-section, the flow surfaces of the solidified deposits were smooth and relatively featureless. Nevertheless, the interaction of molten sulfur and volatiles and the resultant change in flow emplacement should be considered in the analysis of both terrestrial and Ionian sulfur volcanism.

For several "pours" a thermocouple array was used to monitor the cooling of flows. Temperatures up to ~ 109° C were recorded for dark reddish-brown molten sulfur. Previous correlations [10,11] of color with temperature indicate that below ~ 160° C liquid sulfur should be yellow to orange in color whereas dark reddish-brown sulfur is representative of much higher temperatures (> ~180° C). This apparent temperature inconsistency requires further attention and could be quite important for consideration of sulfur flows on Io because color transitions along flows have been used as evidence for the existence of sulfur flows on Io [11].

The rapid formation of a plastic crust, plus the apparently durable nature of the observed crusts, may also have important implications for the behavior of potential sulfur flows on Io. As solid sulfur is denser than liquid [10], it has been suggested that a solid crust may tend to break up and sink into the melt [12]. Such ephemeral crusts would allow relatively rapid cooling of the underlying liquid, effectively limiting flow dimensions. However, observations of extensive crusts (both "fixed" and free-floating) on flows in the vats suggest that similar crusts could occur on Io. Solid sulfur has excellent insulating properties [10] and the formation of durable crusts could significantly reduce heat loss from a flow, hence increasing the length achievable by a crusted sulfur flow. Some flow units on Io extend several hundred km [1,3]; if these are composed of sulfur, such crustal insulation would be essential.

Observations of industrial sulfur flows have provided important insights into the flow properties of molten sulfur. Continued studies and further analysis of existing data including the development of a thermal model for sulfur flows will allow a more complete understanding of terrestrial sulfur flows so that the possibility of sulfur flows on Io can be examined from a more informed perspective.

References

[1] Sagan, C., 1979, *Nature 280*, 750-753.
[2] Schaber, G., 1981, *Icarus 43*, 302-333.
[3] Pieri, D., et al., 1981, *NASA TM-84211*, 41-43.
[4] Watanabe, T., 1940, *Japanese J. Geol. Geogr. 17*, 289-310.
[5] Banfield, A., 1954, *Canadian Mining and Metallurgical Bull. 47*, 769-775.
[6] Colony, W., and Nordlie, B., 1973, *Econ. Geol. 68*, 371-380.
[7] Skinner, B., 1970, *Pacific Sci. 24*, 144-145.
[8] Naranjo, J., 1985, *Nature 313*, 778-780.
[9] Greeley, R., et al., 1984, *Icarus 60*, 189-190.
[10] Theilig, E., 1982, *NASA CR-3594*, 34 pp.
[11] Pieri, D., et al., 1984, *Icarus 60*, 685-700.
[12] Fink, J., et al., 1983, *Icarus 56*, 38-50.

Acknowledgements. This work was performed under NASA grant NAGW-132. We acknowledge with gratitude the assistance of Eilene Theilig.

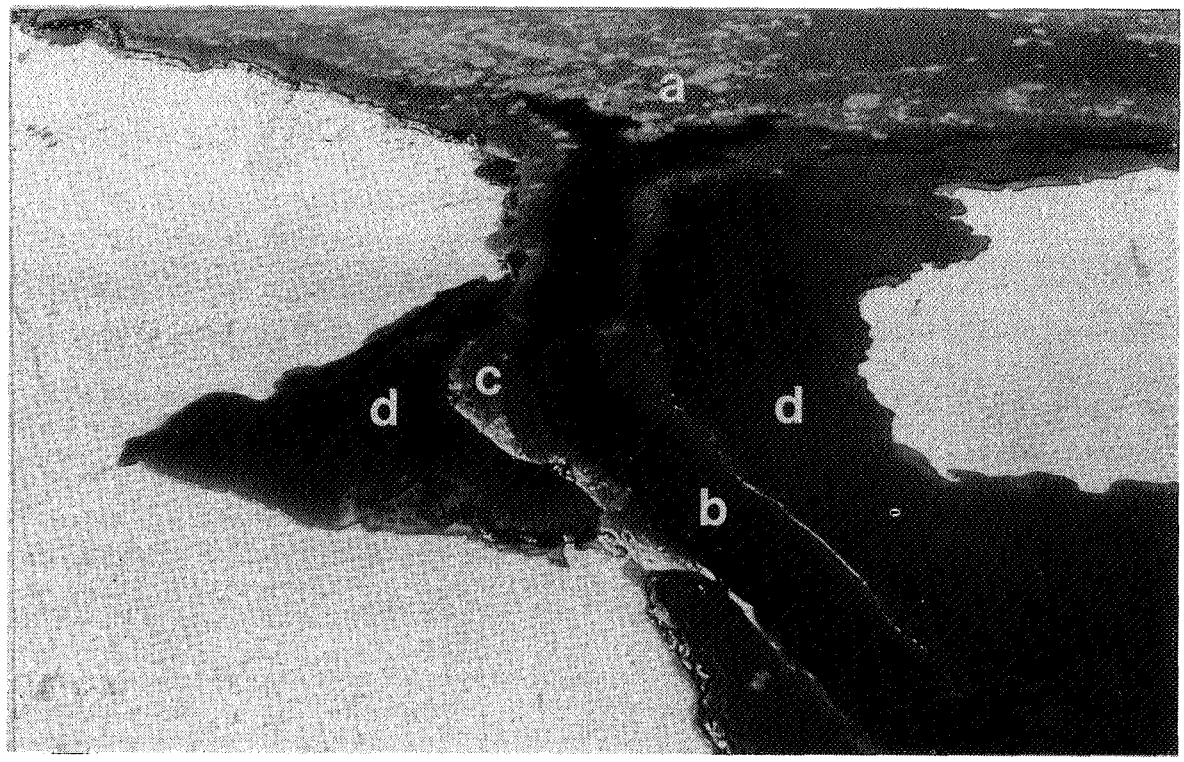

Figure 1. Molten, channelized sulfur flow over solidified sulfur vat surface. Shown are (a) crusted over, unconfined flow lobe from which channel originates, (b) uncrusted channelized flow, (c) partially solidified marginal levees, and (d) breakout flows from the channel margin. Field of view is approximately the same size as in Figure 2.

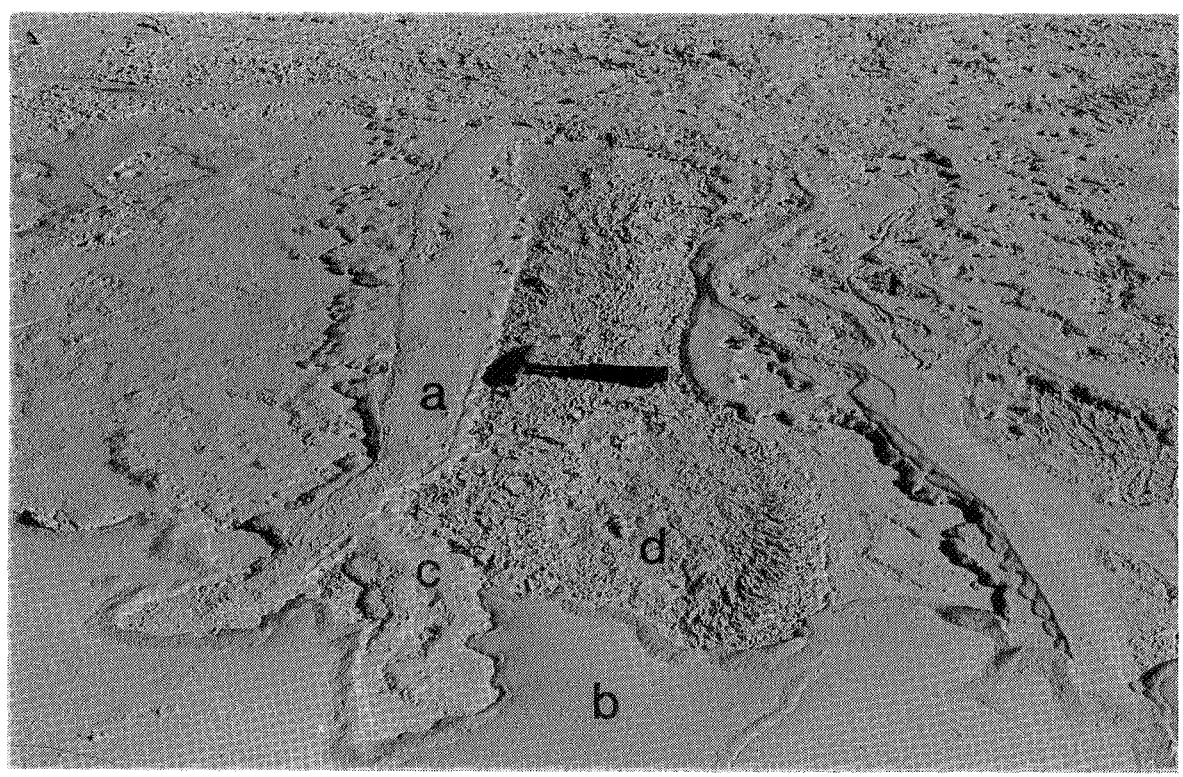

Figure 2. Portion of surface of solidified sulfur vat showing (a) a channelized flow with crustal plates, (b) an unconfined flow, (c) a breakout flow over a channel levee, and (d) rough surface texture with plates and flow lineaments.

CHAPTER 13

GEOLOGIC MAPPING, CARTOGRAPHY, AND GEODESY

GEOLOGY OF IO

R. Greeley[1], R.A. Craddock[1], D.A. Crown[1], L.A. Leshin[1], and G.G. Schaber[2], (1) Department of Geology, Arizona State University, Tempe, Arizona 85287 (2) U.S. Geological Survey, Flagstaff, Arizona 86001

Geologic mapping of Io has been completed at 1:15,000,000 scale for an area lying between +40° and -90° latitude and 230° and 45° longitude, which includes portions of the Ruwa Patera quadrangle (Ji2) and the Lerna Region (Ji4) and the westernmost section of the Colchis Region (Ji3) (see Figure 1). Image resolution in the mapped area is commonly 0.5 - 2 km/pxl. High resolution areas (< .5 km/pxl) are located near the south pole (Lerna Region) and in eastern Ruwa Patera quadrangle. Geologic maps for the Ruwa Patera quadrangle (Ji2) [1] and the Lerna Region (Ji4) [2] have been produced at 1:5,000,000 scale. The present effort reexamines the previously mapped areas and synthesizes the geology of Io on a global scale.

Complications to mapping the surface of Io include: a lack of topographic information; the presence of SO_2 frost [3], dark mantling deposits [4], near surface gases [5], and eruption plumes [6] all of which obscure underlying materials; the coalescence of flows from adjacent vents; and the anastomosing of flows from single vents. In the present refinement of Io's geology an attempt has been made to associate volcanic flows with their source vent(s) and to provide a classification of volcanoes from which to analyze the roles of various styles of volcanism in the formation of Io's surface. Future work will extend the mapping and volcano classification into the less well imaged regions where possible to create the most complete representation of Io's surface.

The following materials were used to facilitate the production of the map: 1:15,000,000 shaded airbrush relief base maps of Io, 1:5,000,000 shaded airbrush relief maps of the Ruwa Patera, Lerna, and Colchis Regions, 1:5,000,000 geologic maps of the Ruwa Patera quadrangle [1] and the Lerna Region [2], Voyager photomosaics, Voyager images, and color photomosaics prepared by A.S. McEwen (Arizona State University and U.S. Geological Survey).

The surface of Io consists of volcanic vents and their associated deposits, plains, and mountains [7]. Fifteen geologic units have been defined to describe the types of materials composing these major physiographic terranes. Examination of the flow deposits associated with volcanic vents with regard to albedo, texture, surface morphology, and apparent relief suggests the following categories of flow materials: patera flows, plains-forming flows, lobate flows, breakout flows, tholi, shield materials [8], vent cone materials, and fissure flows. The plains are divided into interpatera plains and layered plains units, and the mountain materials include smooth and grooved units.

Although local stratigraphic relations are observed in many areas, development of global stratigraphy is extremely difficult due to the lack of topographic information and the absence of impact craters. Generally, the mountain and plains units appear to be older than vent and flow materials. In addition to the plume materials and frost present, low albedo vent and flow materials are apparently the youngest deposits on Io's surface. As is the case in terrestrial volcanology, the various types of volcanoes are observed in different stages of evolution and contrasting styles of volcanism can be associated with the same vent (e.g. -19°, 325°).

References

[1] Schaber, G., et al., 1985, in review. [2] Whitford-Stark, J., et al., 1985, manuscript. [3] McCauley, J.F., et al., 1979, *Nature, 280*, 736-738, [4] Carr, M.H., et al., 1979, *Nature, 280*, 729-733. [5] Lee, S.W., and Thomas, P.C., 1980, *Icarus, 44*, 280-290. [6] Strom, R.G., et al., 1979, *Nature, 280*, 733-736. [7] Schaber, G.G., 1982, *Satellites of Jupiter*, 556-597. [8] Moore, J., et al., 1986, *Icarus, 67*, 181-183.

Acknowledgements. This work was performed under NASA grant NAGW-132. We acknowledge with gratitude photographic work by Dan Ball and drafting by Sue Selkirk.

Fig. 1a

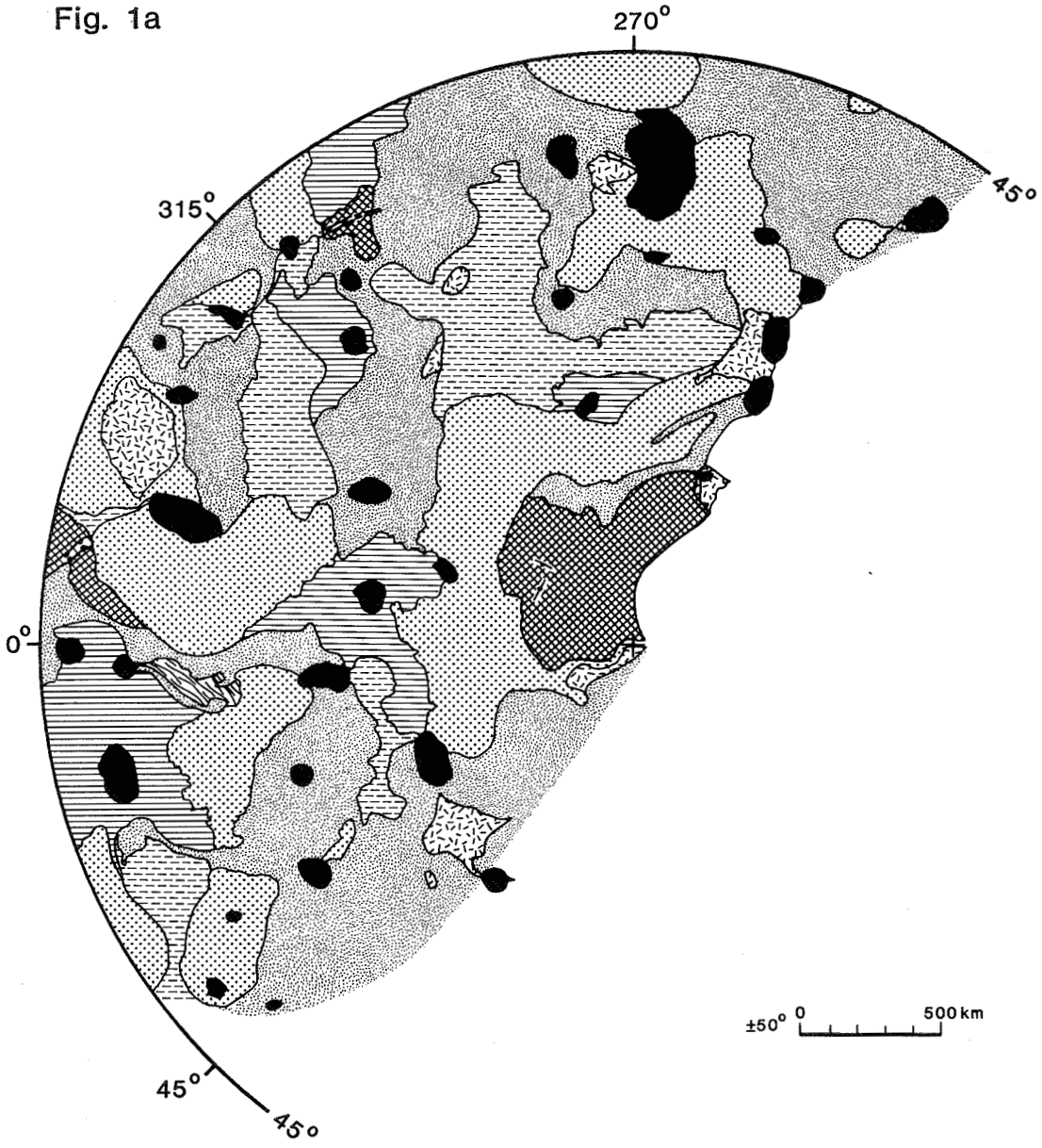

LEGEND

contact

volcanic fissure

PLAINS MATERIALS

plains materials, intervent

plains materials, layered

MOUNTAIN MATERIALS

mountain materials

VENT FLOOR MATERIALS

vent floor materials

FLOW MATERIALS

flow materials, patera

flow materials, plains-forming

flow materials, lobate

flow materials, breakout

flow materials, tholus

flow materials, shield

flow materials, vent cone

flow materials, fissure

flow materials, undifferentiated

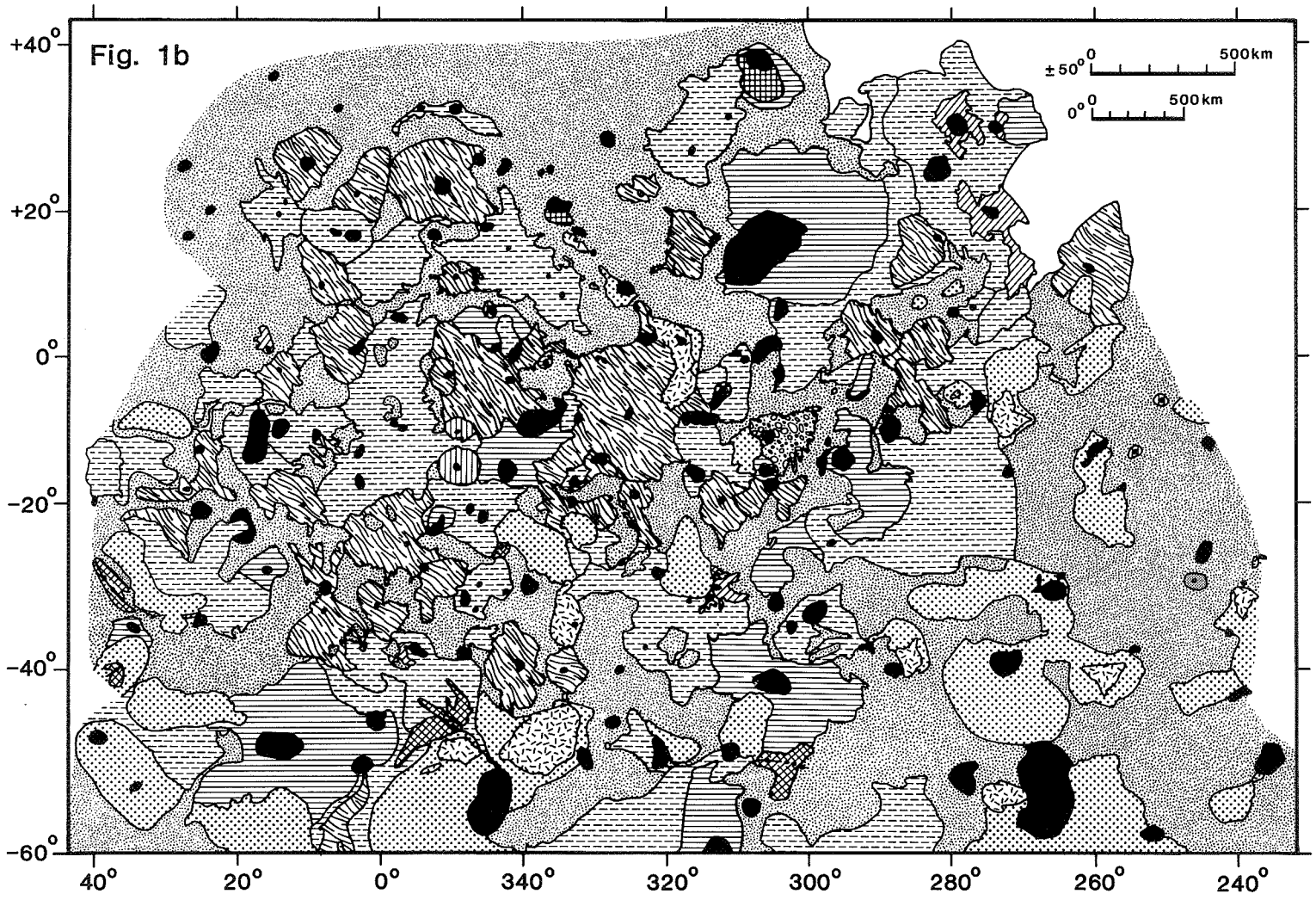

Figure 1. Preliminary geologic sketch maps of the polar (a) and equatorial (b) regions of Io as mapped on a 1:15,000,000 base. Major units are shown; however, structural features are not included.

Large Scale Topography of Io

R.W. Gaskell and S.P. Synnott (JPL/Caltech)

In order to investigate the large scale topography of Io we are using both limb observations and stereographic techniques applied to landmarks. The raw data for this study consists of Voyager 1 images of Io, 800 x 800 arrays of picture elements each of which can take on 256 possible brightness values. In analyzing this data we have had to identify and locate landmarks and limb points on the raw images, remove the image distortions caused by the camera electronics and translate the corrected locations into positions relative to a reference geoid. Minimizing the uncertainty in the corrected locations is crucial to the success of this project. In our highest resolution frames, an error of a tenth of a pixel in image space location can lead to a 300 meter error in true location. In our lowest resolution frames, the same error can lead to an uncertainty of several kilometers.

We have developed techniques to determine pixel-line positions of landmarks in Voyager images to sub-pixel accuracy. Instead of using the outline of a feature to define the landmark, we use the brightness data on the interior as well. Thus, for our purposes, a landmark is a circular patch of the surface whose variations in albedo or topography are sufficiently distinct to make identification possible in a variety of viewing situations. At the same time, the variations should be simple enough to allow for modeling with a relatively small number of parameters. This enables us to fit both the parameters in a brightness model and the offsets of the landmark positions from their nominal values simultaneously over a number of pictures.

For albedo variations, we model the brightness data as the sum of a few terms of the form

$$\Gamma^2 S/[(x-X)^2+(y-Y)^2+\Gamma^2].$$

Such a term produces a "bump" in the albedo of strength S at the point X,Y. Its half width at half maximum is Γ. Note that if S is negative,the "bump" becomes a "dip". For variations in topography, we use a few terms of the form

$$\Gamma^2 H[s_x(x-X)+s_y(y-Y)]/[(x-X)^2+(y-Y)^2+\Gamma^2]^2.$$

This form results from illumination of a topographic "bump" of the form $\Gamma^2 H/[(x-X)^2+(y-Y)^2+\Gamma^2]$ when the local sun vector has components s_x, s_y, s_z.

These parameterizations are useful for several reasons. First, in many cases they mimic the actual structure of the surface. This allows us to use a minimum number of terms. Second, if the "bumps" are sufficiently far apart, their parameters may be treated as if they were uncorrelated. Finally, this form of the model allows us to simplify the estimation process by doing some of the work analytically.

Image space locations of points lying on the limb are found by comparing the observed brightness dropoff in the neighborhood of the limb with that from an ideal surface having a possible (solved for) slow spatial variation in albedo. Before the comparison is made, the ideal brightness is convolved with a camera point spreading model.

The distortions of the image can be estimated from the distortion of the pattern of reseaus. It is difficult to locate reseaus precisely if the brightness is changing rapidly in their neighborhood.

But it is just such regions, limbs or areas of distinctive albedo fluctuations for example, which are of interest to us. We have developed a model for this distortion which can determine reseau locations to better than 0.1 pixels. It involves not only the effect of the brightness distribution within the picture but also the nonlinearity of the transfer function and the existence of charge outside of the region read by the vidicon scanning beam. In effect, it allows us to interpolate more reliably between reseaus.

The determination of the location of landmarks relative to the reference geoid has been speeded up considerably since our earlier studies. The key to this improvement is that the landmark locations relative to the body fixed frame are not directly correlated. They affect each other only through their mutual relationship to the camera pointing. Once the landmarks have been located in a reference frame which is rotating with Io, the center of that frame is determined relative to the geoid center by requiring that the mean square height of landmarks and limb points be a minimum.

Our latest results for landmark heights on Io show some softening from those of a year ago. This is primarily due to the elimination of errors which were not recognized then. The geoid, obtained from limb fitting and consistent with the landmark findings, has semi axes of 1832.6, 1821.9 and 1819.3 km with uncertainties of a few kilometers. The area of Pele is higher than the adjacent regions by about 4 km. Loki, Amaterasu, Manua and Fuchi Pateras are depressed as is Marduk. For the 120 landmarks which appear in three or more frames, the average height, relative to the geoid, is -1.4 km while the dispersion in heights is 2.8 km.

These results are preliminary. We have applied our landmark techniques to only twelve images and about one half of Io's surface. Since there are at least 50 more pictures available, we should be able to greatly improve both the extent and density of our coverage. By using pictures taken with different colors than the violet ones currently being used, we can check the consistency of our solutions and locate landmarks whose contrast is better at those frequencies. We are also studying the effect of satellite ephemeris and spacecraft trajectory errors on these results. Such errors will generally cause a bias in the height results which varies slowly with latitude and longitude. We suspect that the relative heights of neighboring landmarks will remain approximately the same. There is some evidence that such errors do exist and should therefore be solved out. For example, an apparent depression of the region near 180° (Colchis Regio) may be a symptom of this problem. However, most of the landmarks in this region are dark spots and these have been found to be low in other regions too.

THE GALILEAN SATELLITE GEOLOGICAL MAPPING PROGRAM, 1986

B.K. Lucchitta, U.S. Geological Survey, Flagstaff, AZ 86001

The Galilean Satellite Geological Mapping Program was established to illuminate detailed geologic relations on the four large satellites of Jupiter. The program involves about 40 investigators from various universities, research institutes, and government offices in the United States, England, Germany, and Italy. A total of 24 researchers were assigned to map 15 quadrangles on Ganymede, 15 to map 6 quadrangles on Io, and 3 to map 2 quadrangles on Europa. Maps for these three bodies are at a scale of 1:5 million except for three on Io that cover selected areas where high-resolution pictures permit compilation at 1:2 and 1:1 million scales. A 1:15,000,000-scale map of Callisto has been assigned; from it, quadrangles containing useful geologic information will be extracted later for mapping at a scale of 1:5,000,000.

During 1986 all remaining preliminary base materials were sent to the mappers. Final airbrush base materials for Jg3, 4, 6, 7, 8, 9 and 10 are now completed, and those for Jg1 and 12 are being reproduced photographically. Airbrush revisions are not yet completed on the major maps Jg5, 13, and 15 nor on the peripheral maps Jg2, 11, and 14.

One geologic map (Ji2c) has USGS Director's approval and is being drafted for publication. Two maps (Ji2a and Jg8) are undergoing USGS editorial review, one (Ji4) is being revised by the author after technical reviews, and three (Ji2, Jg3, and Jg4) are in technical review. Geological results and changes in previously established guidelines were discussed at a meeting in March 1986 in Houston, and a report detailing the changes was sent to the mappers in May. In addition, copies of all preliminary geologic maps and explanations were sent to members of the Galileo imaging team to aid in advance planning of the mission.

CARTOGRAPHY OF IRREGULARLY SHAPED SATELLITES

R.M. Batson and Kathleen Edwards, U.S. Geological Survey, Flagstaff, AZ 86001

Irregularly shaped satellites, such as Phobos and Amalthea, do not lend themselves to mapping by conventional methods because mathematical projections of their surfaces fail to convey an accurate visual impression of landforms and because large and irregular scale changes make their features difficult to measure on maps. A digital mapping technique has therefore been developed by which maps are compiled from digital topographic and spacecraft image files. The digital file is geometrically transformed as desired for human viewing, either on video screens or on hard copy. Digital files of this kind consist of digital images superimposed on another digital file representing the three-dimensional form of a body.

The three-dimensional digital topographic files can be compiled by two methods: stereoscopic photogrammetry and control-point triangulation in conjunction with sculptured models. Stereoscopic photogrammetry provides the strongest analytical tool for deriving the three-dimensional form. We have compiled a digital image/topography mosaic of Miranda, based on topographic compilations [1] and on Voyager 2 images [2]. This file has been used to make 180 topographically corrected global views that have been incorporated into a movie. Selected members of this set will be produced as slides for general distribution, and several others will be used in a published image map of Miranda.

Existing stereoscopic-image coverage is inadequate for most of the irregular bodies because illumination variations make stereoscopic viewing difficult or impossible. There is sufficient stereoscopic convergence, however, to triangulate latitudes, longitudes, and radii for a collection of control points. Measurements can also be made indirectly, from a sculptured model. The sculpturing is performed through successive comparisons of illuminated models and similarly illuminated spacecraft images. A plaster model has been made with Mariner 9 images [3], but techniques are now available for doing the work digitally.

We have compiled a contour map of radii of Phobos on a spherical (simple cylindrical) array of latitudes and longitudes, based on the data of [3,4,5]. A "digital radius model" was then made by interpolation from the contour map. This model was converted from the spherical system (latitude, longitude, and radius) to the perspective view of a spacecraft image (X, Y, and Z), and the model was digitally shaded to simulate the spacecraft image [6]. Comparison of the resulting synthetic spacecraft image with the actual spacecraft image provides a basis for further sculpturing of the digital radius model.

We expect to produce an accurate geometric model of Phobos by iteration of this process, and we will then compile a three-dimensional mosaic of spacecraft images by the technique used for Miranda mapping. Similar mosaics are planned for Deimos, Amalthea, Hyperion, Epimetheus, and Janus.

References

[1] Wu, S.S.C., Schafer, F.J., Jordan, Raymond, and Howington, Annie-Elpis (1987), Voyager Photogrammetry: Reports of the Planetary Geology and Geophysics Program-1986, NASA TM (this volume).

[2] Batson, R.M., Edwards, Kathleen, and Skiff, B.A., 1981, Orthophoto mosaics and three dimensional transformations of Viking Orbiter pictures: Reports of the Planetary Geology Program-1981, NASA TM 84211, p. 493-495.

[3] Turner, R.J., 1978, A model of Phobos: Icarus, v. 33, p. 116-140.

[4] Duxbury, T.C., 1974, Phobos: control network analysis: Icarus, v. 23, p. 290-299.

[5] Duxbury, Thomas C., Callahan, J.D., and Ocampo, A., 1984, Phobos: close encounter imaging from the Viking Orbiters: NASA Reference Publication 1109, 51 p.

[6] Batson, R.M., Edwards, Kathleen, and Eliason, E.M., 1975, Computer-generated shaded-relief images: Jour. Research, U.S. Geol. Survey, vol. 3, no. 4, p. 401-408.

VOYAGER CARTOGRAPHY

R.M. Batson, E.M. Lee, and K.F. Mullins, U.S.Geological Survey, Flagstaff, AZ 86001

The Jovian and Saturnian satellites are being mapped at several scales from Voyager 1 and 2 data [1,2,3]. The maps are specially formatted color mosaics [4], controlled photomosaics, and airbrush maps.

At 1:5,000,000 scale, mapping of Io, Europa, and Ganymede is complete and mapping of Callisto is approximately 30% complete. At 1:15,000,000 scale, mapping of Io and Europa mapping is complete, and mapping of Ganymede is approximately 40% complete.

A controlled mosaic of Rhea has been compiled as a Digital Image Model (DIM) in the same format as is being used for Mars [5]. The mosaic is being formatted for publication as a two-sheet set (Lambert Azimuthal Equal Area, Mercator, and Polar Stereographic projections). Magnetic tape copies of the DIM have been distributed to Regional Planetary Image Facilities and other interested users. The DIM has a scale of 1/16 degree/pixel, corresponding to approximately 833 m/pixel on Rhea.

Details of the status of the various map series are reported quarterly to Planetary Geology Principal Investigators.

References

[1] Batson, R.M., Bridges, P.M., Inge, J.L., Isbell, C.E., Masursky, Harold, Strobell, M.E., and Tyner, R.L., 1980, Mapping the Galilean satellites of Jupiter with Voyager data: Photogrammetric Engineering and Remote Sensing, 46, 10, p. 1303-1312.

[2] Batson, R.M., Bridges, P.M., and Mullins, K.F., 1981, Voyager cartography: Reports of the Planetary Geology Program-1981, NASA TM 84211, p. 484-485.

[3] Batson, R.M., Bridges, P.M., Inge, J.L., Lee, E.M., Masursky, Harold, Mullins, K.F., Skiff, B.A., and Strobell, M.E., 1984, Voyager 1 and 2 atlas of six Saturnian satellites: NASA Spec. Pub. SP 474, 175 p.

[4] McEwen, A.F., and Soderblom, L.A., 1984, High-resolution color images of Io: Reports of the Planetary Geology Program-1983, NASA TM 86246, p. 38.

[5] Batson, R.M., 1986, Digital cartography of Mars: Reports of the Planetary Geology and Geophysics Program-1986, NASA TM (this volume).

ASPECTS OF VOYAGER PHOTOGRAMMETRY

Sherman S. C. Wu, Francis J. Schafer, Raymond Jordan and Annie-Elpis Howington, U.S. Geological Survey, Flagstaff, Arizona 86001

In January 1986, Voyager 2 took a series of pictures of Uranus and its satellites with the Imaging Science System (ISS) on board the spacecraft (Smith et al., 1986). Based on six stereo-images from the ISS narrow-angle camera, a topographic map was compiled of the southern hemisphere of Miranda, one of Uranus' moons (Fig. 1). Assuming a spherical figure, a 20-km surface relief is shown on the map. The images used were FSC268-4611, -4614, -1617, -4626, and -4629. With three additional images (FSC268-4409, -4413, and -4630) from the ISS wide-angle camera, a control network of Miranda's southern hemisphere was established by analytical photogrammetry, producing 88 ground points for the control of multiple-model compilation on the AS-11AM analytical stereoplotter.

The calibrated focal lengths of the wide-angle and narrow-angle cameras on board the spacecraft are, respectively, 200.77 mm and 1,503.49 mm (Davies et al., 1979). Each frame of the two cameras consists of 800 x 800 image elements with a pixel size of 14)m. Both cameras have a grid of 202 reseau marks. Calibration of reseau coordinates has an accuracy of better than 2)m (Benesh and Jepsen, 1978). Residuals of images produced from the Optronics Photowrite range from 8 to 17)m. Decalibration was made by the U.S. Geological Survey image-processing facility in Flagstaff, using reseau calibration data. For the control network, coordinate measurements were further corrected by a second-degree polynomial. Residuals of measurements were then reduced to 6 to 8)m, about half an image element. Images used for map compilation were obtained at altitudes ranging from 30,000 to 42,000 km. Control-network adjustment has a precision of about 375 m.

Digital terrain data from the topographic map of Miranda have also been produced. By combining these data and the image data from the Voyager 2 mission, perspective views or even a movie of the mapped area can be made.

The application of these newly developed techniques to Voyager 1 imagery, which includes a few overlapping pictures of Io and Ganymede, enables the compilation of contour maps or topographic profiles of these bodies on the analytical stereoplotters.

References

Benesh, M., and Jepsen, P., 1978, Voyager Imaging Science System calibration report: Jet Propulsion Laboratory 618-802, 287 p.

Davies, M. E., Hange, T. A., Katayama, F. Y., and Roth, J. A., 1979, Control network for the Galilean satellites, November 1979: R-2532 - JPL/NASA, The Rand Corporation.

Smith, B. A., Soderblom, L. A., Beebe, R., Bliss, D., Boyce, J. M., Brahic, A., Briggs, G. A., Brown, R. H., Collins, S. A., Cook, A. F., II, Croft, S. K., Cuzzi, J. N., Danielson, G. E., Davies, M. E., Dowling, T. E., Godfrey, D., Hansen, C. J., Harris, C., Hunt, G. E., Ingersoll, A. P., Johnson, T. V., Krauss, R. J., Masursky, H., Morrison, D., Owen, T., Plescia, J. B., Pollack, J. B., Porco, C. C., Rages, K., Sagan, C., Shoemaker, E. M., Sromovsky, L. A., Stoker, C., Strom, R. G., Suomi, V. E., Synnott, S. P., Terrile, R. J., Thomas, P., Thompson, W. R., and Veverka, J., 1986, Voyager 2 in the Uranian System: Imaging Science Results: Science, 233, 43-64.

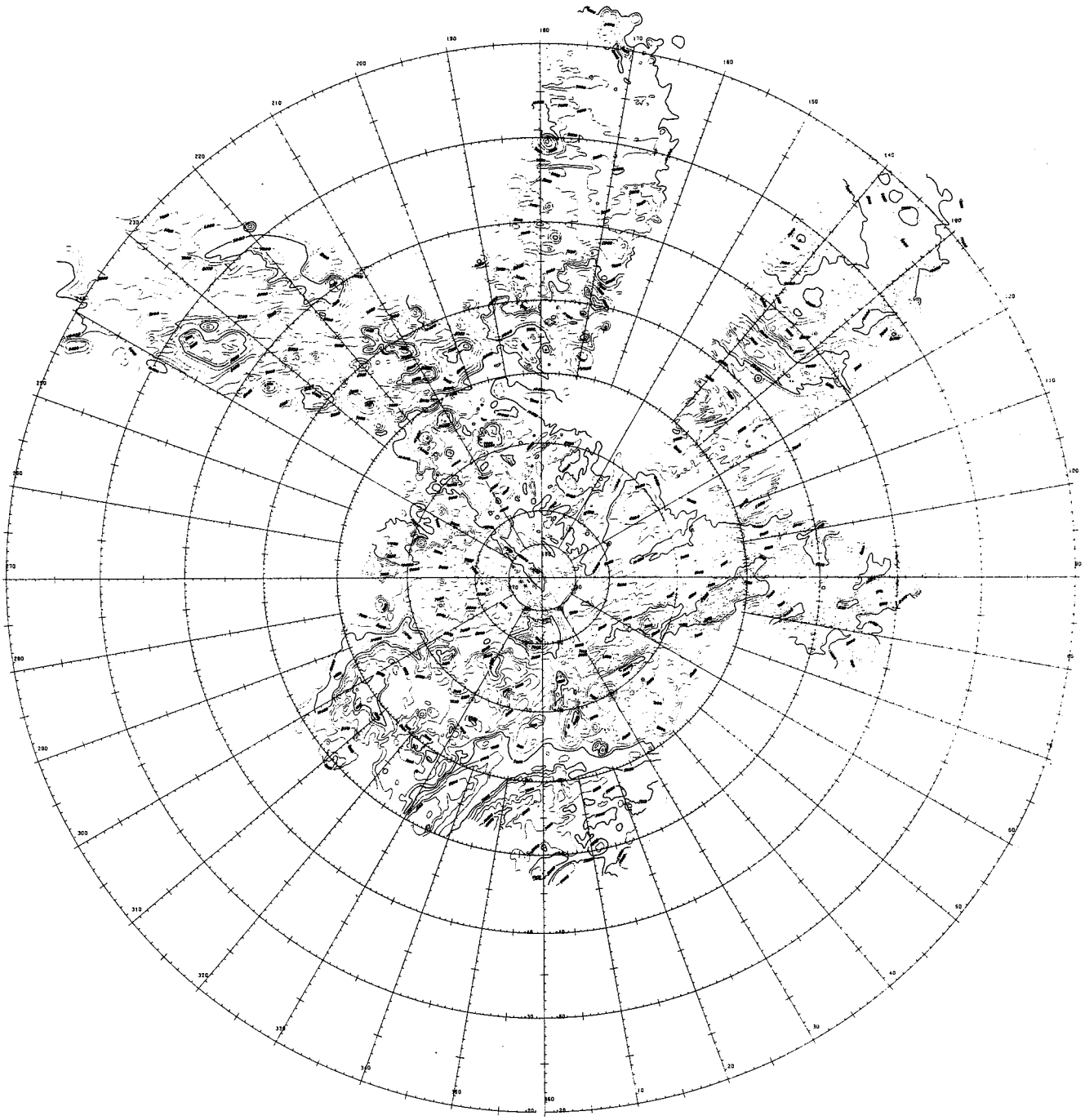

Figure 1. Topographic map of the southern hemisphere of Miranda, one of Uranus' satellites. Compilation scale is 1:1 million and contour interval is 1,000 m. The projection is Polar Stereographic.

PROGRESS IN COMPILATION OF THE 1:2,000,000-SCALE TOPOGRAPHIC MAP SERIES OF MARS

Sherman S. C. Wu, Raymond Jordan, and Francis J. Schafer, U.S. Geological Survey, Flagstaff, Arizona 86001

The application of special photogrammetric techniques (Wu et al., 1982) has enabled the systematic mapping of Mars' topography at a scale of 1:2,000,000, using high-altitude Viking Orbiter pictures. In fiscal year 1986, compilation was completed of the 24 subquadrangles that make up the quadrangles MC-12, MC-13, MC-14, MC-15, MC-20, and MC-21. This work completes compilation of the 60 topographic maps covering the equatorial belt (lat ±30°). The remaining 80 subquadrangles of Mars are planned to be completed within 3 years (27, 27, and 26 subquadrangles, in fiscal years 1987, 1988, and 1989, respectively).

Elevations on all topographic maps are relative to the Mars topographic datum (Wu, 1981). The maps have a contour interval of 1 km and a precision of ±1 km. The equatorial-belt maps are Mercator projections having true scale at lat ±27.476°. These maps provide more precise information than do those previously available and they will help in understanding the geologic processes that have shaped the Martian surface.

References

Wu, S. S. C., 1981, A method of defining topographic datums of planetary bodies: Annales de Géophysique, AGEPA 7, Tome 37, fasc. 1, p. 147-160.

Wu, S. S. C., Elassal, A. A., Jordan, Raymond, and Schafer, F. J., 1982, Photogrammetric application of Viking orbital photography: Planetary and Space Science, vol. 30, no. 1, p. 45-55.

MARS DIGITAL TERRAIN MODEL

Sherman S. C. Wu and Annie-Elpis Howington, U.S. Geological Survey, Flagstaff, Arizona 86001

The Mars Digital Terrain Model (DTM) is the result of a new project to (1) digitize the series of 1:2,000,000-scale topographic maps of Mars, which are being derived photogrammetrically under a different project (Wu et al., 1985), and (2) reformat the digital contour information into rasters of elevation that can be readily registered with the Digital Image Model (DIM) of Mars (Batson, 1986). Derivation of DTM's involves interpolation of elevation values into 1/64-degree resolution and transformation of them to a sinusoidal equal-area projection. Digital data are produced in blocks corresponding with the coordinates of the original 1:2,000,000-scale maps, e.g., the dimensions of each block in the equatorial belt are 22.5° of longitude and 15° of latitude. This DTM is not only compatible with the DIM, but it can also be registered with other data such as geologic units or gravity. It will be the most comprehensive record of topographic information yet compiled for the Martian surface. Once the Mars DTM's are established, any enhancement of Mars topographic information made with updated data, such as data from the planned Mars Observer Mission, will be by mathematical transformation of the DTM's, eliminating the need for recompilation.

Experimental work has begun on the subquadrangles MC-8NW and MC-9NW, following two different procedures. In the first procedure, for MC-8NW, the digital contour data in the Mercator projection (Fig. 1a) were interpolated to produce a digital terrain model (Fig. 1b), and then the resulting rasters were transformed into the sinusoidal projection (Fig. 1c). Following the second procedure, for MC-9NW, digital contour data were directly transformed into sinusoidal projection (Fig. 2a), and then the transformed contour data were interpolated (Fig. 2a) into rasters with the same projection (Fig. 2b). This second procedure eliminates one step, and thus saves computer time and preserves resolution, particularly for those maps having dense contour lines. Its only disadvantage is that no file can be established for digital contour data in the Mercator projection. Either procedure can be employed for the DTM's, although, as noted, the second one is more practical where the density of contour lines is high.

In fiscal year 1987, completion of DIM's for 50 Mars subquadrangles is planned. Fifty more DTM's are scheduled for completion in FY-88 and an addition 40 in FY-89.

References

Batson, R. M., 1986, A digital image model of Mars, in Reports of Planetary Geology and Geophysics Program-1985, National Aeronautics and Space Administration Technical Memorandum 88383, p. 577-579.

Wu, S. S. C., Jordan, Raymond, and Schafer, F. J., 1985, Compilation of the Mars 1:2,000,000-scale topographic map series, in Reports of Planetary Geology and Geophysics Program-1984, National Aeronautics and Space Administration Technical Memorandum 87563, p. 612-613.

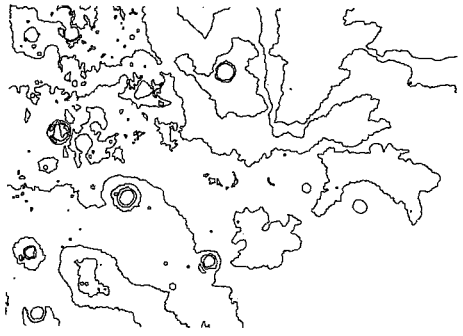

(a)

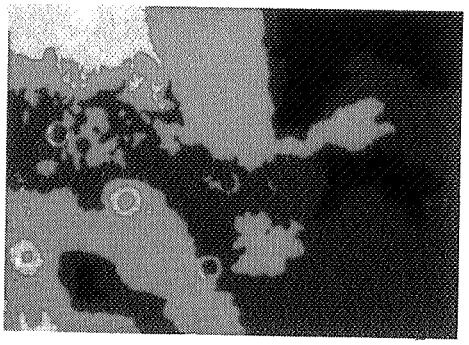

(b)

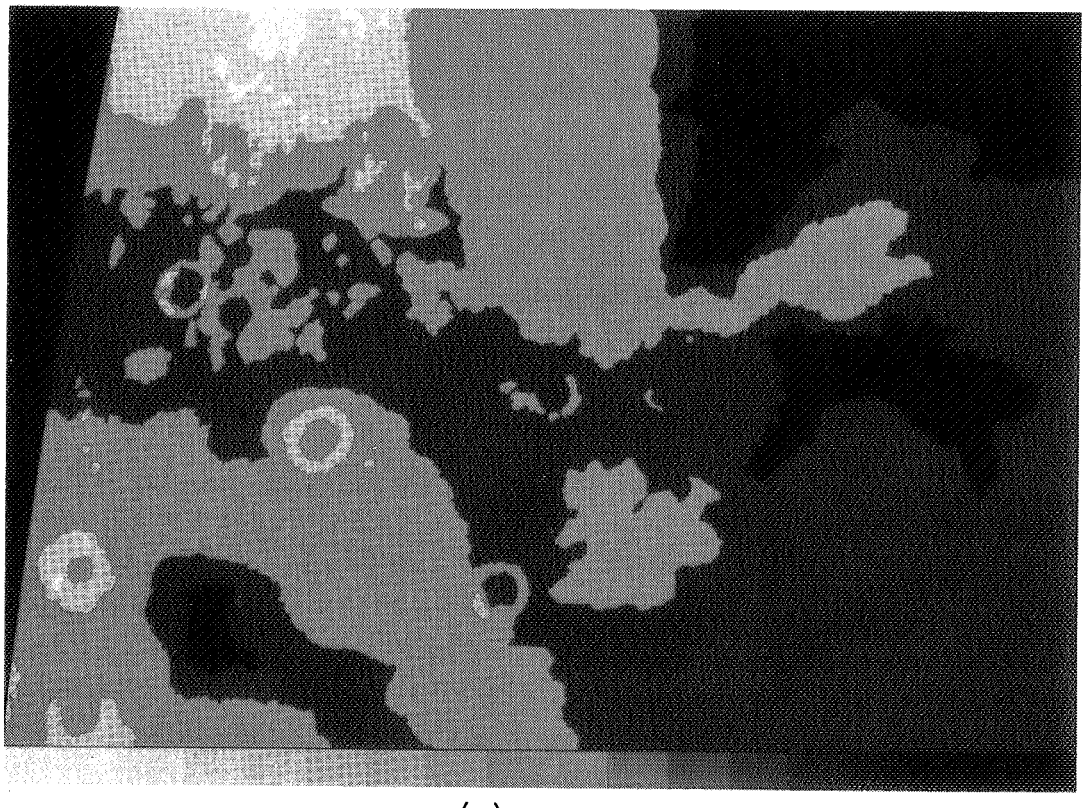

(c)

Figure 1. Digital terrain model of the northwest part of the Coprates quadrangle (MC-18NW) of Mars. (a) Digital contour data in Mercator projection, (b) digital terrain model in Mercator projection, (c) digital terrain model in sinusoidal equal-area projection.

(a)

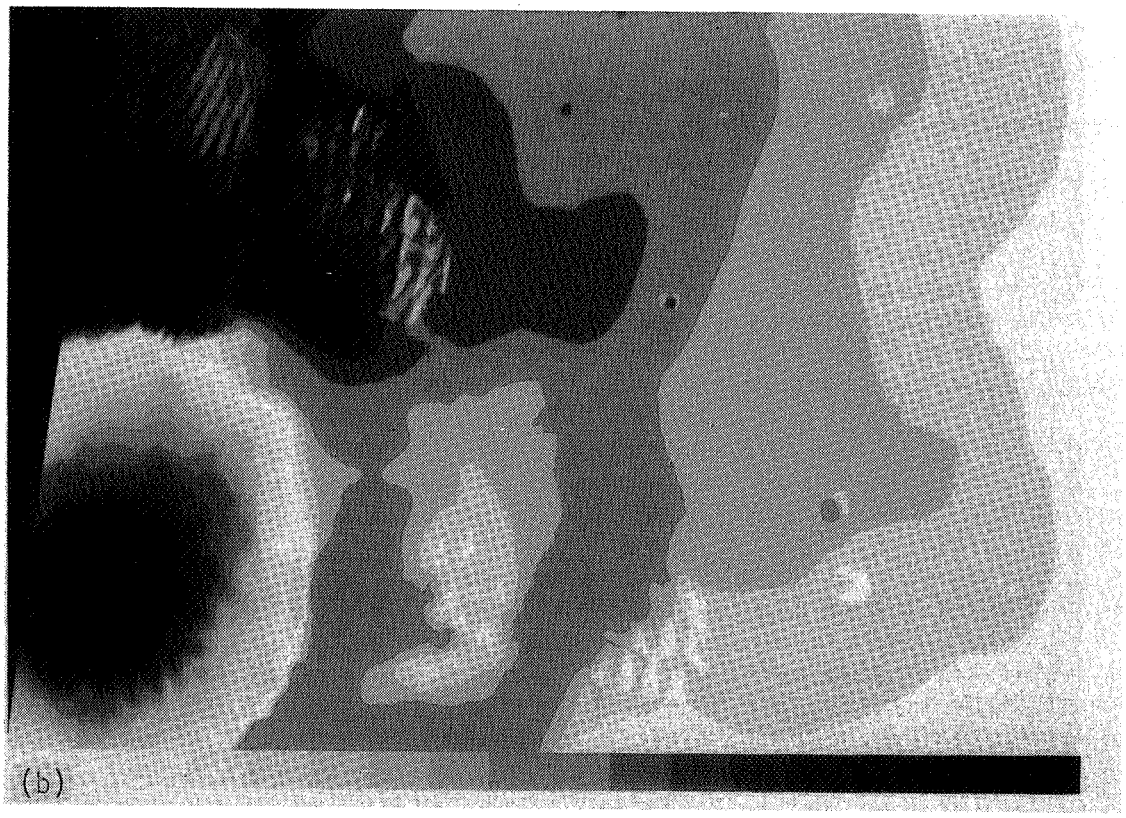

Figure 2. Digital terrain model of the northwest part of the Margaritifer Sinus quadrangle (MC-19NW) of Mars. (a) Digital contour data in sinusoidal equal-area projection, (b) digital terrain model in sinusoidal projection.

DIGITAL CARTOGRAPHY OF MARS

R.M. Batson, U.S.Geological Survey, Flagstaff, AZ 86001

Mars Medium-Resolution Digital Image Model:

A medium-resolution Digital Image Model (DIM) of Mars is being compiled [1]. A DIM is a mosaic of radiometrically corrected, photometrically modelled spacecraft images displaying accurate reflectance properties at uniform resolution, and geometrically tied to the best available control. The Mars medium-resolution DIM contains approximately 4700 Viking Orbiter image frames that were used to compile the recently completed 1:2,000,000-scale controlled photomosaic series of Mars. This DIM provides a planimetric control base to which all other Mars maps will be registered. A similar control base of topographic elevations (Digital Terrain Model, or DTM) is also being compiled [2]. These poducts are scheduled for completion in 1989.

The DIM and DTM databases are, in effect, sets of bins whose locations are defined by latitude and longitude coordinates. Each bin contains a coded value for the reflectance (in the case of DIM's) or the elevation (in DTM's) of the Martian surface at that point. Map products are made from the models by moving the values in the bins to rectangular coordinates specified by whatever map projection has been selected and by writing the array as a digital image.

The reflectance at each bin (i.e., the pixel location in the DIM) is derived as a function of radiometric camera sensitivity, surface properties, and illumination geometry. The presence of some visible seams between image frames in the mosaics is a result of the fact that each of these parameters is imperfectly known.

Geometric positions of images are controlled by the Rand control net [3], by the topographic control net [4], and by adjustment of each frame for optimum fit to surrounding images. Once the position of each frame is adopted, a revised camera orientation matrix is computed and stored so that future geometric projections will be repeatable. Any image in the resulting digital mosaic becomes a valid control point for mosaics at both higher and lower resolutions. Points defined in the original control nets will not be used to control future mosaics, because their spacing is inadequate for high-resolution mosaics and because the images by which they are defined are shifted slightly in the final compilation.

Mars High-Resolution Digital Image Models:

High-resolution DIM's of Mars are being compiled with Viking Orbiter images to support the recently announced 1:500,000-scale Mars geologic mapping program. A total of 110 controlled photomosaics was previously prepared in the Mars Transverse Mercator (MTM) format at 1:500,000 scale by manual methods; similar controlled mosaicking will now be done digitally. Images in these mosaics commonly have resolutions of 10 to 50 m/pixel, whereas the medium-resolution DIM described above is being compiled at a uniform resolution of approximately 230 m/pixel. The high-resolution DIM's will cover areas

of scientific interest where existing data support the mapping; there is no intention to map the entire planet at these resolutions.

High-resolution DIM's have high relative planimetric accuracies because individual frame positions are adjusted by image-matching. Absolute positional accuracy, however, is not commensurate with the resolution of the mosaics for two primary reasons: (1) the medium-resolution DIM used as a control base is itself tied to a control net that has standard errors of approximately 5 km, and (2) images in the mosaic have much higher resolution (commonly 20 times higher) than the base mosaic, resulting in large image-placement ambiguities. An unfortunate result of this condition is that high-resolution mosaics compiled during one time period may not join adjacent mosaics compiled during another time period. There are neither data nor resources to remedy this condition by compiling a high-resolution control net of Mars.

High-resolution DIM's can be compiled only after the medium-resolution segments in which they lie are complete, because of the requirement for control. Compilation priorities are defined by scientific interest in particular areas and by operational efficiency. Priority compilation of specific areas may be requested through the Planetary Cartography Working Group (PCWG).

Digital files containing the high-resolution image mosaics will be distributed to the Regional Planetary Image Facilities. Hard-copy mosaics will be made on the MTM format and published at 1:500,000 scale.

References

[1] Batson, R.M., 1986, Digital image models of planetary surfaces: Lunar and Planetary Science Conference, Seventeenth, Abstracts, Part 1, March 17-21, Houston, p. 34-35.

[2] Wu, S.S.C., and Howington, Annie-Elpis, 1986, A Mars digital terrain model and sample correlation with a Mars digital image model: Reports of the Planetary Geology and Geophysics Program-1985, National Aeronautics and Space Administration Technical Memorandum 88383, p. 608-611.

[3] Davies, M.E., 1986, The control network of Mars: October, 1985: Reports of the Planetary Geology and Geophysics Program-1985, National Aeronautics and Space Administration Technical Memorandum 88383, p. 591.

[4] Wu, S.S.C., Jordan, Raymond, and Schafer, F.J., 1986, Status of compilation of the Mars 1:2,000,000-scale topographic map series: Reports of the Planetary Geology and Geophysics Program-1985, National Aeronautics and Space Administration Technical Memorandum 88383, p. 618-619.

THE CONTROL NETWORK OF MARS: OCTOBER 1986

Merton E. Davies, The RAND Corporation, Santa Monica, CA 90406

The control network of Mars is composed of Mariner 9 frames which essentially give full coverage of the planet at low resolution. Superimposed and tied to this network are strips of Viking mapping frames (resolution 100-250 m per pixel) which encircle the equator and 60° north latitude and multiple longitude ties between these latitude strips. There are multiple ties between these strips and the Viking 1 lander site. In the future another strip will be established at 60° south latitude.

Because the Viking 1 lander site has been accurately located, the coordinates of points in its vicinity can be determined with an error of less than 100 m relative to an inertial coordinate system. The 0° meridian on Mars is defined by the small crater Airy-0 and the error in longitude of points near Airy-0 is less than 40 m. Within the Viking mapping strips, the standard error of the coordinates of the control points is estimated to be less than 3 km and in the Mariner 9 region, the errors might be as large as 10 km.

The horizontal coordinates of the control points on Mars have been updated with a single-block planetwide analytical triangulation computed in September 1982 (Davies and Katayama, 1983). The computation contained 47,524 measurements of 6,853 points on 1811 pictures. These comprised 1054 Mariner 9 and 757 Viking frames. The overdetermination factor was 2.48 and 19,139 normal equations were solved. The standard error of measurement was 18.06 μm. Since that time additional Viking pictures and points have been added to the data set; included were some high resolution frames near Airy-0.

Recently the effort has been to convert the entire data set to J2000; this has gone slower than expected. The J2000 network now contains 28,004 measurements of 4,591 points on 1213 pictures. These comprised 1052 Mariner 9 and 161 Viking frames. The overdetermination factor was 2.18 and 12,821 normal equations were solved. The standard error of measurement was 12.96 μm. The longitude of the Viking 1 lander site was 48°.045 and the latitude 22°.480.

References

Davies, M. E., and F. Y. Katayama, "The 1982 Control Network of Mars," J. Geophys. Res., Vol. 88, No. 89, September 10, 1983, pp. 7503-7504.

A UNIFIED LUNAR CONTROL NETWORK

Merton E. Davies and Tim R. Colvin, The RAND Corporation, Santa Monica, CA 90406
Donald L. Meyer, Defense Mapping Agency, Aerospace Center, St. Louis AFS, MO 63118

At this time, control on the Moon is composed of a number of independent regional networks. These networks frequently have different origins but never have common ties, even in overlapping areas. The objective of the unified network program is to tie the regional networks into a single consistent planetwide control network. The plan is to start with the best defined regions, create common ties with neighboring data sets, and then expand into poorly defined regions.

The most accurately defined points on the Moon are locations of the laser ranging retroreflectors (Ferrari et al., 1980) and the VLBI measurements of the locations of the Apollo 15, 16, and 17 ALSEP stations (King et al., 1976). Recent values for the coordinates of the retroreflectors have been received from Williams and Dickey, 1986. The accuracy of these locations is about 30 m and their locations are used to define the center-of-mass and, hence, the origin of the unified lunar coordinate system. The coordinates of the retroreflectors are given in both principal axis and mean Earth/Polar axis systems. Mean Earth/Polar axis coordinates have been recommended by the IAU (Davies et al., 1980) for the moon. The difference in the coordinates is important, more than 600 m in latitude and longitude.

The Apollo 15, 16 and 17 ALSEP stations have been identified on Apollo panoramic photography and their locations transferred to Apollo mapping frames. Thus, their coordinates are available in the control network computations.

Three control networks have been computed based on the Apollo mapping pictures. They are the DMA/A15 system (Schimerman, 1976), the NOS/USGS system (Doyle et al., 1977), and the DMA/603 system (DMAC Contract Report, 1981). The DMA/A15 system contained 1284 pictures and 9940 points, the NOS/USGS system contained 1244 pictures and 5324 points, and the DMA/603 system contained 603 pictures and 5346 points. The coordinates of points in one system can be transferred to another system by interpolation between nearby common points. Thus the coordinates of the three ALSEP stations which are available in DMA/A15 coordinates, are transferred to NOS/USGS and DMA/603 coordinates. The coordinates are based on picture measurements and the photogrammetic solutions and can then be compared to the coordinates derived by King et al., 1976 and Ferrari et al., 1980.

In order for the control network to have the same origin and mean Earth/Polar axis coordinate system defined by Ferrari et al., 1980, the coordinates of the ALSEP stations should be identical. The RMS of the true distance between corresponding ALSEP points is 333 m for the DMA/A15, 2110 m for NOS/USGS, and 308 m for DMA/603. Transformations permitting translation, rotation, and scale (7 parameters) have been computed for each control system to minimize the distances between these corresponding points. The RMS of the residuals after the transformations is 73 m for DMA/A15, 76 m for NOS/USGS, and 58 m for DMA/603. After the transformation, the coordinates of points in all three systems are quite similar. The DMA/603 transformed system was selected as the preferred system and called DMA/603 MOD.

Many control networks have been computed based on pictures of the Moon taken through telescopes; these cover the Earth-facing region. Probably the most carefully prepared network is that published by Meyer, 1980. This is the one incorporated into the present program. 130 points common to Meyer's and the Apollo networks were selected and transformation parameters computed to shift Meyer's coordinates to the DMA/603 MOD network. The RMS of the residuals of this transformation is 808 m. The mean shift of the coordinates was 1352 m, with a maximum of 2336 m and a minimum of 803 m. All 1088 points from Meyer's network were transformed to the DMA/603 MOD system. The mean shift of the coordinates of all of the points was 1390 m with a maximum of 2603 m and a minimum of 493 m.

References

Davies, M. E. et al., "Report of the IAU Working Group on Cartographic Coordinates and Rotational Elements of the Planets and Satellites," Celestial Mechanics, Vol. 22, January 1980, pp. 205-230.

Doyle, Frederick J., Atef A. Elassal, and James R. Lucas, "Selenocentric Geodetic Reference System," National Oceanic and Atmospheric Administration, Technical Report NOS70NGS5, February 1977.

Ferrari, A. J., W. S. Sinclair, W. L. Sjogren, J. G. Williams, and C. F. Yoder, "Geophysical Parameters of the Earth-Moon System," J. Geophys. Res., Vol. 85, No. B7, July 10, 1980, pp. 3939-3951.

King, R. W., C. C. Counselman III, I. I. Shapiro, "Lunar Dynamics and Selenodesy: Results from Analysis of VLBI and Laser Data," J. Geophys. Res., Vol. 81, No. 35, December 10, 1976, pp. 6251-6256.

Meyer, Donald L., Selenocentric Control System (1979), Defense Mapping Agency, DMA TR 80-001, April 1980.

Report on Lunar Control under Contract No. W-14, 453, Defense Mapping Agency Aerospace Center, St. Louis AFS, MO 63118, October 1981.

Schimerman, Lawrence A., The Expanding Apollo Control System, Defense Mapping Agency Aerospace Center, August 1976.

Williams, J. G. and J. O. Dickey, Coordinates of the Lunar Laser Retroreflectors, Letter to M. E. Davies, June 18, 1986.

THE CONTROL NETWORKS OF THE SATELLITES OF JUPITER

Merton E. Davies, The RAND Corporation, Santa Monica, CA 90406

Geodetic control networks are being computed photogrammetrically for the large satellites of Jupiter, using pictures from the Voyager 1 and 2 encounters. Control points have been identified on the satellites and their coordinates computed by single-block analytical triangulation. The data sets have been converted from the B1950 to the J2000 inertial coordinate system to be compatible with future flight missions.

STATUS OF THE CONTROL NETWORKS

	Io	Europa	Ganymede	Callisto
Points	640	179	1884	818
Pictures, V1	209	53	152	159
V2	43	67	150	96
Measurements	11,164	3,847	25,780	14,628
Normal Equations	2,036	718	4,674	2,401
Overdetermination	5.48	5.36	5.52	6.09
Standard Error, μm	10.31	10.50	9.31	11.57

CHAPTER 14

SPECIAL PROGRAMS

MICROVAX-BASED DATA MANAGEMENT AND REDUCTION SYSTEM FOR THE REGIONAL PLANETARY IMAGE FACILITIES

R. Arvidson, E. Guinness, S. Slavney, B. Weiss, McDonnell Center for the Space Sciences, Department of Earth and Planetary Sciences, Washington University, Saint Louis, Missouri 63130

This abstract is a progress report for the RPIF prototype image data management and reduction system being jointly implemented by Washington University and the USGS, Flagstaff. The system will consist of a MicroVAX with a high capacity (~300 megabyte) disk drive, a compact disk player, an image display buffer, a videodisk player, USGS image processing software, and SYSTEM 1032 - a commercial relational database management package. The USGS, Flagstaff, will transfer their image processing software, including radiometric and geometric calibration routines, to the MicroVAX environment. Washington University will have primary responsibility for developing the database management aspects of the system and for integrating the various aspects into a working system. This abstract stresses Washington University's role in the development of the prototype system.

The MicroVAX system will replace the current BIRP search, retrieval, and videodisk display system for planetary image data. The new system will have more capability than BIRP in that it will allow one to: 1) search a high level catalog for standard RPIF holdings, such as Viking Lander Team Data Record prints; 2) get background information on planetary missions, spacecraft and imaging instruments; 3) search selected SEDR data sets; and 4) perform image processing procedures on digital image data, including radiometric and geometric calibration. In addition, the database management portion of the system will provide capabilities to easily update the database and to sort the data by user-chosen parameters.

Initial prototype systems are in place at Washington University and the USGS, Flagstaff. The prototype effort is concentrating on Viking and Voyager digital data products, since digital image data and documentation from those missions are currently most accessible. These data should also be in demand over the next several years in order to support the upcoming Galileo and Mars Observer missions. In addition, an initial high level catalog of standard RPIF holdings will be included.

The RPIF database will contain a variety of information on the datasets housed in the RPIFs. Examples of datasets are: strip contact prints of Voyager images, Viking Orbiter image mosaics, 1:5 million scale geologic maps, and digital tapes of Viking Orbiter images. The database can be thought of as being divided into a descriptive level (high level) and a detailed level. The high level catalog information for a dataset will include such things as a description of the dataset, the data format and location of the product within an RPIF, where and by whom the data were produced, and a brief list of references where further documentation can be found. The database will also include frequently requested information on planets, planetary missions, and spacecraft instruments (particularly calibration information), and general information on the RPIFs, such as where they are located and who the directors and data managers are. The database will not include a large number of documents and references. Instead, it will catalog a few key references to provide users with a starting point for finding additional reference material. The detailed level catalog will

contain selected SEDR data similar to that found in BIRP files. Additional detailed data will be added to the database in the future.

It is expected that users of the RPIF database will have a wide range of expertise in computers as well as planetary science, although the system will be primarily used by planetary scientists and graduate students. In addition, RPIF visitors from the general public, such as science teachers, may occasionally access the database. Thus, the design of the RPIF database system will have to account for the varying capabilities and needs of this diverse set of users. TAE (Transportable Applications Executive) is being used to provide a friendly, menu-driven user interface to the system. Interaction with the database will be through the use of TAE, augmented with SYSTEM 1032 forms. The interface will support menus and on-line help, which will allow novice users to access the data with a minimum of assistance. The interface will also have the capability of allowing more advanced users to quickly access data by directly entering commands and executing command procedures. The same user interface will be used for both the database and image processing functions, so that users can access the database and process data within a single environment.

A major part of the information stored in the high level and detailed catalogs will also be integrated into the central Planetary Data System (PDS) catalog and database being developed on the Britton-Lee database machine at JPL. The MicroVAX database design is compatible with the PDS catalog. We have taken advantage of the relevant database design work already done by PDS and have also made the needs of the RPIFs known to PDS in order to influence their further design work. A certain level of compatibility between the RPIFs and PDS will be important for users who need to access both database systems.

The MicroVAX prototype project will be completed by March 1987 and will then be available for testing and evaluation by the RPIF Directory and Data Managers. It is important to note that during 1986 the RPIF Data Managers have assumed an active role in helping compile information for the high level catalog. At their meeting in March 1986 they each agreed to take responsibility for at least one planetary mission, submitting catalog information to Washington University for all data sets produced by that mission. We hereby acknowledge those contributions and thank the RPIF Data Managers for their help.

MARTIAN TERRAINS

Harold Masursky, M.G. Chapman, P.A. Davis, A.L. Dial, Jr., and M.E. Strobell, U.S. Geological Survey, Flagstaff, AZ 86001

Terrain studies of candidate landing sites for a future rover/sample-return mission to Mars are being conducted to evaluate the geologic and trafficability aspects of each site. An optimum site should have geologic units of widely diverse ages and chemical compositions occurring in close enough proximity and in smooth enough terrain so that a roving vehicle of limited traverse ability (±100 km) could collect representative samples.

In FY 1986, geologic maps were compiled at 1:500,000 and 1:2 million scales of the Mangala Valles, Kasei Valles, Chasma Boreale (north polar) and Planum Australe (south polar) areas, and a study was begun of the topography and surface-roughness characteristics of the Mangala Valles site. Geologic mapping has been greatly facilitated by specially enhanced, high-resolution Viking photographs, such as that shown in Fig. 1, which clarify stratigraphic relations of units that were unrecognized earlier. Photoclinometric profiles of topographic features (Davis and Soderblom, 1984), provide width and depth measurements of four classes of channels, the thickness of some volcanic units, and the throw on some faults. Estimates of the surface roughness of units are being calculated using a newly developed USGS computer program and using measurements derived from Earth-based radar by Tommy Thompson of JPL and Richard Simpson of Stanford.

Studies of the Mangala Valles site are virtually complete. A long, complex geologic history is indicated by stratigraphic relations (Fig. 2) shown on the maps; crater counts of geologic units (Table 1) confirm these relations. Crater-density numbers, when compared with the second model of Neukum and Hiller's (1981) calibration curve, indicate that map units range in age from 4.0 to 0.6 Ga. (The number of craters retained on the youngest unit, Amazonian textured plains material (Table 1), is not sufficient to determine a valid age.) In this area, the ancient cratered terrain of Mars is partly covered by a thick sequence of lobate volcanic units, probably basaltic lava flows, and younger, possibly felsic, volcaniclastic rocks. At least three episodes of small-channel formation have been identified and dated (Table 1). Although many investigators have theorized that most, if not all, Martian channels are ancient (Sharp and Malin, 1975; Carr and Clow, 1981; Pieri, 1980; Baker and Partridge, 1986), our studies show that the small channels appear to range in age as widely as do the large outwash channels (Masursky et al., 1977). However, it is hard to determine whether very narrow channels are volcanic or fluvial in origin. Channels that emerge from the distal end of a lava flow and have leveed banks are probably volcanic in origin; those with tributaries or with alluvial deposits at their mouths are probably fluvial.

Enhanced images, such as that of Fig. 1, show some lava flows pouring over a fault scarp, other flows that stop at the scarp, and one flow that appears to be cut by the scarp. Wide, theater-headed channels dissect some of these flows. Fault movement, lava flows, and channel formation can be dated precisely from these geologic relations.

On photoclinometric profiles of a fault scarp that marks the boundary between the southern highlands and the northern low plains east of Mangala Valles, we measured slopes that range from 8° to 25° and

throw that ranges from 70 m to 2 km.

Ancient degraded channels range in width from 0.7 to 4 km and in depth from 33 to 112 m; the longest channel is 80 km long. Two branches of the main Mangala Valles system are, where measured, 5 and 4.5 km wide and 200 and 300 m deep, respectively; their lengths are 80 and 60 km. North-trending, theater-headed channels are 1 to 3 km wide, 100 to 1500 m deep, and 6 to 60 km long. Young, narrow channels that lie inside and extend beyond the mouths of theater-headed channels are 300 to 800 m wide, 20 to 60 m deep, and 20 to 70 km long.

Profiles of the putative volcaniclastic unit show it to be about 1 km thick where it embays one crater and spills into another.

At the Kasei Valles site, one geologic map at 1:2 million scale and 2 geologic maps at 1:500,000 scale have been completed. The site appears smooth on available low-resolution images and is thus attractive to engineers. However, geologic units are more dispersed than at other sites and long traverses would be needed to collect varied samples.

Geologic maps at 1:2 million and 1:500,000 scales of the Chasma Boreale (north polar) and Planum Australe (south polar) areas show deposits of layered ice overlying deposits of mixed ice and detritus; young dune deposits are also present at the north polar site. A drill mounted on a rover could obtain meter-thick cores of these deposits. Ice phases of the deposits would have to be analyzed in situ; rock inclusions could be analyzed in terrestrial laboratories. These sites also appear to be topographically bland, but they are attractive because layered terrains are easily accessible to direct sampling or drilling.

Geologic maps of the Memnonia and Olympus Rupes sites were prepared earlier and the sites are still being considered. The Memnonia area (mapped by D. Scott in Masursky et al., 1984) displays a wide variety of rock types and compositions, but it lacks channel deposits found at the nearby Mangala site. At the Olympus Rupes site (Morris, 1982), at least three basaltic units were mapped that represent stages in the development of Olympus Mons. When 1:500,000-scale bases for these sites are produced, mapping will be transferred to them.

Studies of the Elysium Mons, Candor Chasma, and Nilosyrtis Mensae sites will be completed in FY 1987. Additional sites that contain channels with stratigraphically dateable ages will be sought and mapped.

We thank our USGS colleagues who have contributed greatly to this study. Image enhancements are being obtained by Bonnie Duck and Jo Ann Bowell, using a program modified by Eric Eliason. Photoclinometric profiles are being generated by P.L. Davis and M. G. Chapman, using a technique developed by Davis and Soderblom (1984). Measurements of terrain roughness are being obtained by combining a formula that obtains surface roughness indicator values with photometric scans (A. Acosta, R. Gurule, personal commun.).

References

Baker, V.R., and Partridge, J.B., 1986, JGR, 91, 3561-3572. Carr, M.H. and Clow, G.D., 1981, Icarus, 48, 91-117. Davis, P.A. and Soderblom, L.A., 1984, JGR, 89, 9449-9457. Masursky, H., Boyce, J.M., Dial, A.L. Jr., Schaber, G.G., and Strobell, M.E., 1977, JGR, 82, 4016-4038. Masursky, H., Scott, D.H., Morris, E.C., Strobell, M.E., and Dial, A.L, Jr., 1984, NASA TM 36246, 324-326. Morris, E.C., 1982, NASA TM 85127, 134-135. Neukum, G. and Hiller, K., 1981, JGR, 86, 3097-3121. Pieri, D., 1980, NASA TM 81979, 1-160. Sharp, R.P., and Malin, M.C., 1975, GSA Bull., 86, 593-609. Tanaka, LPI 17th Proc., in press.

Ga *	System **	Geologic Unit	Cumulative Number of Craters Per 10^6 km^2 500 m	1 km	2km	Age Range of Channels
<0.6	Amazonian	Apt		130±90		
0.6		Aps	3400±1800	340±90	7±4	
1.0		Apl	4200±1000	440±160	70±50	
1.5		Grooved Mangala Floor		700±500		
2.5						ch_4 (narrow)
2.6		AHpi	4000±600	1,200±400 1,230±370	80±35	
3.2	Hesperian	Hpl	16,000±2,000	1,600±400	160±100	ch_2 (theater headed) (Labou Ascopus, Padus)
3.3		Hpr	17,000±2,000	1,900±300	260±100	ch_3
3.4		Hpi	17,000±2,500	2,400±300	360±140	
3.7	Noachian	NHpi	19,000±2,500	3,000±800	460±300	ch_1 (Degraded)
4.0		Nc	40±40 km diam./10^6 km^2			

* 1 Ga Wl B. y., ages derived from model II curve, Neukum and Hiller, 1981

**Divisions taken from Tanaka, in press

Table I. Ages of geologic units and channels, Mangala Valles region, Mars

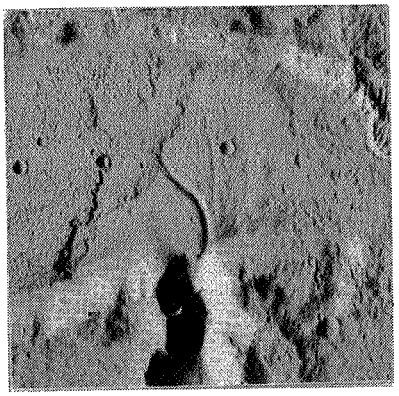

Fig. 1 Abus Valles; part of VO 455 S 11; East Mangala area, Mars

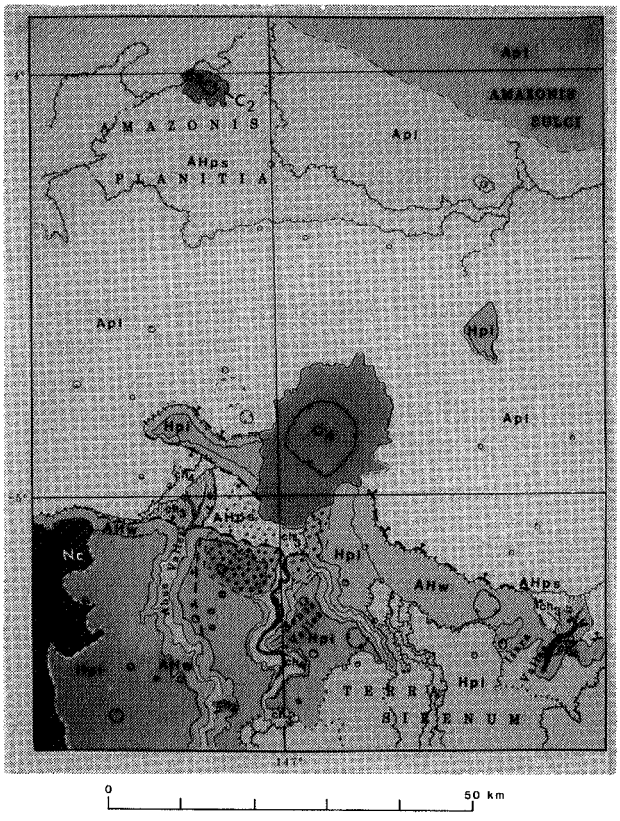

Fig. 2 Geologic map of the East Mangala landing site on Mars

MANGALA EAST

UNITS

- Apt — Amazonian textured plains material
- Apl — Amazonian lobate plains material
- AHps — Amazonian-Hesperian smooth plains material
- AHw — Amazonian-Hesperian wall unit
- Hpl — Hesperian lobate plains material
- Hpi — Hesperian intercrater plains material
- Nc — Noachian heavily cratered plains material

CHANNEL MATERIAL

- ch_4 — Youngest channel floor material
- ch_3 — Young channel floor material and alluvium

CRATER MATERIAL

- C_4 — Young sharp-rimmed crater material with discontinuous secondary crater ejecta
- C_2 — Subdued crater material
- Thin eolian deposits

MAP SYMBOLS

- Contact--Long dashed where approximately located; short dashed where inferred; dotted where buried
- Fault--Approximately located, dotted where concealed. Bar and ball on downthrown side
- Crater rim; dashed where buried
- 13 14 Proposed rover traverse
- Flow front

The Mars Observer Camera

M. C. Malin[1], G. E. Danielson[2], A. P. Ingersoll[2], H. Masursky[3], J. Veverka[4], T. Soulanille[5], and M. Ravine[5]

[1] Department of Geology, Arizona State University, Tempe, AZ 85287

[2] Division of Geological and Planetary Sciences, California Institute of Technology, Pasadena, CA 91125

[3] U. S. Geological Survey, Branch of Astrogeology, Flagstaff, AZ 86001

[4] Center for Radiophysics and Space Research, Cornell University, Ithaca, NY 14853

[5] Mars Observer Camera Western Project Office, 55 N. St. Johns Ave., Pasadena, CA 91103

A camera designed to operate under the extreme constraints of the Mars Observer mission was selected by NASA in April, 1986. Contingent upon final confirmation in mid-November, the Mars Observer Camera (MOC) will begin acquiring images of the surface and atmosphere of Mars in September-October, 1991. The MOC incorporates both a wide angle system for low resolution global monitoring and intermediate resolution regional targeting, and a narrow angle system for high resolution selective surveys. Camera electronics provide control of image clocking and on-board, internal editing and buffering to match whatever spacecraft data system capabilities are allocated to the experiment.

The objectives of the MOC experiment are to:

1) obtain global, synoptic views of the martian surface and atmosphere in order to study meteorological, climatological, and related surface changes during the course of the mission. Global monitoring observations can yield complete coverage of the planet at approximately 7.5 km/pixel in a single 24-hour period.

2) examine and monitor surface and atmospheric features at moderate resolution for changes on timescales of hours, days, weeks, months, and years. The regional targeting mode (used to monitor such time-variable features as lee clouds, the polar cap edge, and wind streaks) will have a resolution of better than 300 m/pixel at the nadir, diminishing to better than 2 km at the limb

3) systematically examine local areas at extremely high resolution in order to quantify surface/atmosphere interactions and geological processes that operate on short timescales and at extremely small spatial scales. Candidate areas for intensive study include layered slopes within the polar layered terrain and the migrating edge of the seasonal polar cap. In the high resolution sampling mode, each image covers more than 2.5 km X 2.5 km at approximately 1.4 m/pixel. Additional capability within the high resolution system allows longer areas to be imaged at reduced resolution (at 11.2 m/pixel, roughly 2.7 km X 180 km).

The MOC has two sets of optics: a very short focal length (9.7 mm) "fish-eye" lens and a very long focal length (3.5 m) Ritchey-Chretién telescope, each with its own detector assembly of CCD line arrays, and a shared electronics assembly (Figure 1). The optics are nadir pointing. In operation, the motion of the spacecraft generates the image by "pushing" the line arrays, oriented perpendicular to the velocity and nadir vectors, along the ground track. The cross-track dimension of the image is defined by the length of each CCD detector while the along-track dimension is defined by the length of time the detectors are active. The actual ground track velocity will determine the line exposure time. The cameras are electronically shuttered (i.e., the accumulated charges are shifted from the CCD in a fraction of the time required to advance one resolution element). Fixed spectral filters over each CCD array optimize system optical performance. The wide angle system has two detectors with different color filters, allowing two-color observations to distinguish between dust and condensate clouds, and to distinguish atmospheric from surface phenomena.

The MOC electronics will be among the most advanced to be flown in space. A 32-bit processor, three high speed gate arrays, and 12 megabytes of random access memory (RAM) provide considerable flexibility in instrument operation, even within the limited resources available to the experiment. The electronics will have processing capabilities approximately equal to a VAX-11 computer, within a package 23 X 23 X 10 cm, about 3 kg in mass, and using about 7 watts of power.

Under present data rate plans, the MOC will acquire several thousand images during the nominal mission (one Mars year), including low resolution global images, and several high resolution images, every day. Although the camera cannot be pointed at specific targets, representative areas of Mars should be accessible to imaging several times during the mission. As mission planning becomes more settled, the MOC Investigation Team will solicit community input for targeting observations.

MARS OBSERVER CAMERA

3.5 m f/10 Telescope and 9.7 mm f/6 Fish-Eye Lens

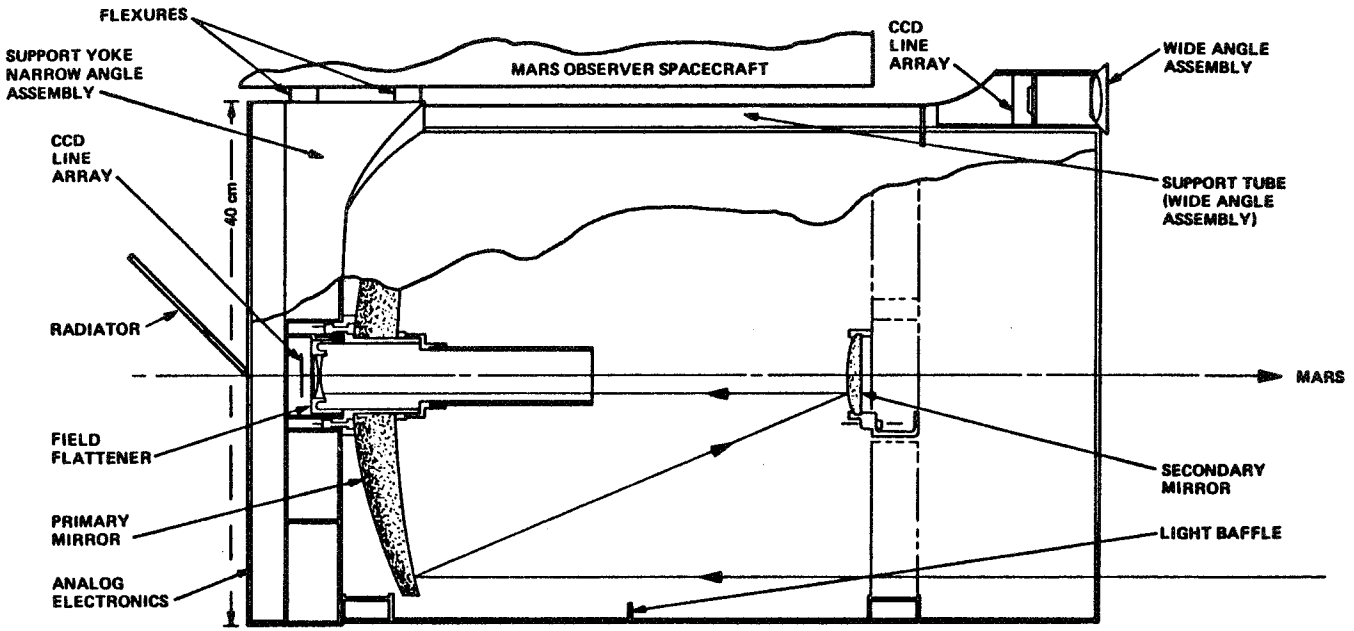

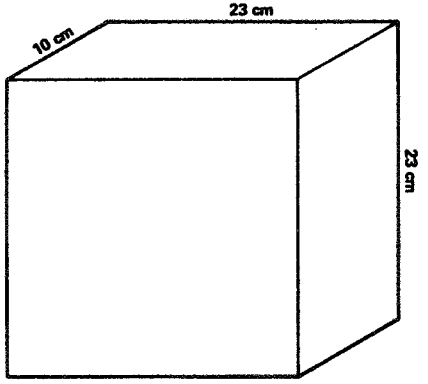

ELECTRONICS ENCLOSURE (LOCATED INSIDE SPACECRAFT)

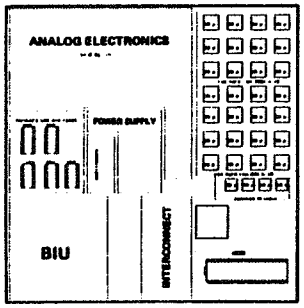

PROCESSOR BOARD
- MICROPROCESSOR
- ANALOG ELECTRONICS
- POWER SUPPLY
- BIU

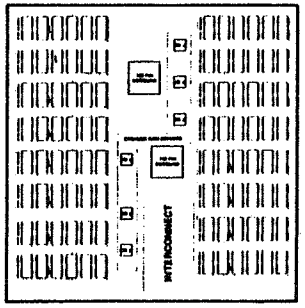

BUFFER MEMORY BOARD(S) (ONE OR FOUR)

PLANETARY NOMENCLATURE

M.E. Strobell and Harold Masursky, U.S. Geological Survey, Flagstaff, AZ

In fiscal year 1986, names were chosen for prominent features on the 5 previously known Uranian satellites and for features on the largest of the 10 satellites discovered by Voyager 2 (Table 1). The names of the five large satellites are taken mostly from Shakespeare, and most are spirits; therefore Shakespearean and spirit themes were used to choose names for topographic features on the satellites. Crater names and most other feature names on Miranda, Oberon, and Titania are from Shakespeare; features on Ariel are named for bright spirits and those on Umbriel are named for dark spirits, all taken from worldwide mythologies. Preliminary coordinates for these features, listed in Table 1, are derived from shaded relief maps of the satellites that will be published in 1987. Orbital elements have been established for the 10 new satellites by S.P. Synott, and a paper describing this work is in progress; satellite positions are being reviewed by Commission 16 of the IAU. The moon 1985 U1 is informally designated "Puck". The nine small satellites discovered in 1986 are being named for Shakespearean heroines; these names will be listed in the 1987 version of the Annual Gazetteer of Planetary Nomenclature.

Although almost 8000 requests to name the newly discovered Uranian satellites for the seven members of the Challenger crew were received (and answered), the Outer Planets Task Group could not reach a consensus on such a proposal. As an alternative suggestion, the Lunar Task Group has proposed that seven craters on the far side of the Moon, within crater Apollo and near craters honoring other American astronauts, be named for the Challenger crew members. This proposal has been favorably received and will be provisionally accepted soon.

Nearly 300 copies of the 1986 edition of the Gazetteer of Planetary Nomenclature were distributed to data facility centers and to interested scientists who requested a copy.

Names adopted by the IAU General Assembly at its triennial meeting in November 1985 at New Delhi, India, have been published (IAU, 1986). Since the New Delhi meeting, additional names have been proposed and provisionally approved for the Uranian satellite features and for 11 features on Mars, 5 on Ganymede, and 5 on Callisto. Nomenclature is now complete on the 1:5 million-scale series of Ganymede maps, and maps of Callisto at the same scale are being generated. The five proposed names on Callisto will become the names of quadrangles as well as features.

A chapter describing the history, methodology, and importance of planetary nomenclature has been completed and will be published in 1987 as part of a book on Planetary Cartography.

Anticipated nomenclature tasks for fiscal year 1987 include the following: (1) correcting and updating the Gazetteer of Planetary Nomenclature; (2) reviewing and naming features on new maps of Mars and Callisto; (3) updating nomenclature chapters for revised atlases of Mars and Jupiter; (4) and writing three chapters and editing all chapters for an illustrated NASA publication on Planetary Nomenclature.

Reference

International Astronomical Union, 1986, Working Group for Planetary System Nomenclature, in 19th General Assembly, New Delhi, 1985, Proceedings: International Astronomical Union Transactions, v. 19B, p. 340-353.

TABLE 1
URANIAN SATELLITE NOMENCLATURE

MIRANDA: (Human characters from The Tempest)

Crater: (Human from Tempest)		
Alonso	45°S	350°E
Ferdinand	35°S	205°E
Francisco	75°S	240°E
Gonzalo	30°S	90°E
Prospero	35°S	330°E
Stephano	40°S	235°E
Trinculo	75°S	165°E

Chasma: (Place from Shakespeare)		
Arden	10-60°S	30-120°E
Elsinore	15-45°S	210-300°E
Inverness	40-90°S	0-360°E

Regio: (Place from Shakespeare)		
Dunsinane	10-70°S	350-75°E
Mantua	10-90°S	750-300°E
Silicia	10-50°S	295-340°E

Rupes: (Place from Shakespeare)		
Argier Rupēs	40-50°S	310-340°E
Verona Rupēs	10-40°S	340-350°E

ARIEL: (Light spirits)

Crater: (Light spirit, indiv.)		
Abans	15°S	251°E
Agape	47°S	337°E
Ataksak	54°S	223°E
Befana	18°S	27°E
Berylune	23°S	328°E
Deive	24°S	23°E
Djadek	19°S	248°E
Domovoy	72°S	342°E
Finvara	18°S	20°E
Gwyn 77°S	20°E	
Huon 32°S	65°E	
Laica	22°S	43°E
Mab	39°S	351°E
Melusina	54°S	10°E
Onagh	23°S	243°E
Rima 19°S	260°E	
Yangoor	69°S	276°E

Chasma: (Light spirit, class)		
Brownie	15-20°S	335-355°E
Kachina	24-40°S	210-280°E
Kewpie	15-40°S	315-340°E
Korrigan	13-37°S	329-2°E
Kra	30-35°S	345-5°E
Pixie	20-25°S	350-15°E
Sylph	43-52°S	329-18°E

Vallis: (Light spirit, class)		
Leprechaun	10°S	355-25°E
Sprite	9-17°S	325-358°E

UMBRIEL: (Dark spirits)

Crater: (Dark spirit, indiv.)		
Alberich	35°S	45°E
Fin	38°S	29°E
Gob	18°S	28°E
Kanaloa	10°S	345°E
Malingee	22°S	15°E
Minepa	44°S	12°E
Setibos	30°S	346°E
Skynd	3°S	333°E
Vuver	5°S	312°E
Wokolo	30°S	0°
Wunda	8°S	275°E
Zlyden	24°S	328°E

TITANIA: (Shakespeare)

Crater: (Shakes. minor females)		
Adriana	20°S	5°E
Bona	56°S	350°E
Calphurnia	43°S	290°E
Elinor	45°S	335°E
Gertrude	10°S	288°E
Imogen	24°S	322°E
Iras	20°S	340°E
Jessica	55°S	285°E
Katherine	51°S	332°E
Lucetta	15°S	278°E
Marina	15°S	317°E
Mopsa	11°S	305°E
Phrynia	25°S	310°E
Ursula	13°S	47°E
Valeria	35°S	7°E

Chasma: Place from Shakespeare		
Belmont	6-11°S	25-40°E
Messina	5-35°S	331-13°E
Rousillon	7-25°S	17-38°E

OBERON: (Shakespeare)

Crater: (Shakespearean heroes)		
Antony	28°S	65°E
Caesar	28°S	65°E
Coriolanus	11°S	347°E
Falstaff	22°S	10°E
Hamlet	48°S	45°E
Lear 10°S		31°E
Macbeth	59°S	117°E
Othello	67°S	45°E
Romeo	30°S	90°E

Chasma: (spirit place)	
Mommur Chasma	10-20°S, 300-340°E

"PUCK": 1985 U1

Crater: (Mischievous spirit)
Bogle
Butz
Lob

ENHANCED LANDSAT IMAGES OF ANTARCTICA AND PLANETARY EXPLORATION*

B. K. Lucchitta, J. A. Bowell, K. Edwards, E. M. Eliason, and H. M. Ferguson, U.S. Geological Survey, 2255 N. Gemini Drive, Flagstaff, Arizona 86001

Since early in the Landsat program, black-and-white paper prints of band 7 (near infrared) of the Landsat multispectral scanner have been used extensively to prepare semicontrolled maps of Antarctica. Only recently, however, have image-processing techniques been employed to enhance fine detail and to make controlled image-mosaic maps in color. These techniques--restoration of badly saturated images, special stretches to bring out structures in snow and ice, and high-pass filters combined with ratioing to enhance detail--have led to a number of important results. The processed images show many subtle structures in the ice, such as flow lines on ice streams and ice shelves, ridges or double ridges on ice rises, peculiar splotchy surface markings on ice sheets, and the subsurface topography of ice-covered mountains where the ice cover is thin. Large transverse crevasses on the floating part of glaciers and ice streams retain their identities over many years, so that glacier velocities can be measured on repetitive pictures. Landsat multispectral images of Antarctica also help to expand our knowledge of extraterrestrial bodies by showing bare-ice areas as bright blue patches; on such patches meteorites tend to be concentrated and are collected. Many subtle flow features in Antarctic ice streams resemble features at the mouths of Martian outflow channels, which suggests that the channels also contained ice. Furthermore, flow lines in Antarctic ice sheets that merge with ice shelves resemble Martian flow features associated with dissected terrain along the Martian northern highland margin, and support the concept that ice was involved in the transport of material from the southern highlands to the northern lowland plains. In Antarctica, as on Mars, the virtual absence of fluvial activity over millions of years has permitted the growth of glacial and eolian features to unusually large sizes.

*(Published in Geological Society of America, Abstracts with Programs, 1986, v. 18, no. 6, p. 677.)

AUTHOR INDEX

NASA
National Aeronautics and Space Administration

Report Documentation Page

1. Report No.	2. Government Accession No.	3. Recipient's Catalog No.
NASA TM-89810		

4. Title and Subtitle	5. Report Date
Reports of Planetary Geology and Geophysics Program - 1986	May 1987
	6. Performing Organization Code: EL

7. Author(s)	8. Performing Organization Report No.
	10. Work Unit No.

9. Performing Organization Name and Address	11. Contract or Grant No.
Planetary Geosciences Program Solar System Exploration Division Office of Space Science and Applications	13. Type of Report and Period Covered: Technical Memorandum

12. Sponsoring Agency Name and Address	14. Sponsoring Agency Code
National Aeronautics and Space Administration Washington, DC 20546	

15. Supplementary Notes

16. Abstract

This is a compilation of abstracts of reports from Principal Investigators of NASA's Planetary Geology and Geophysics Program, Office of Space Science and Applications.

The purpose is to document in summary form research work conducted in this program during 1986. Each report reflects significant accomplishments within the area of the author's funded grant or contract.

17. Key Words (Suggested by Author(s))	18. Distribution Statement
planetary geology and geophysics solar system evolution planetary geologic processes formation and evolution of planets	Unclassified - Unlimited Subject Category 91

19. Security Classif. (of this report)	20. Security Classif. (of this page)	21. No. of pages	22. Price
Unclassified	Unclassified	580	A25

NASA-Langley, 1987